Biochemical and Biophysical Research Communications 420 (2012) 699–703

Contents lists available at SciVerse ScienceDirect

Biochemical and Biophysical Research Communications

journal homepage: www.elsevier.com/locate/ybbrc

Mini Review

How do tumor stem cells actively escape from host immunosurveillance?

Yao Qi [a,b], Run-Mei Li [b], Fan-Ming Kong [a,b], Hui Li [b], Jin-Pu Yu [b], Xiu-Bao Ren [a,b,*]

[a] Department of Biotherapy, Tianjin Medical University Cancer Institute and Hospital, Tianjin 300060, China
[b] Key Laboratory of Cancer Prevention and Therapy, Tianjin Medical University Cancer Institute and Hospital, Tianjin 300060, China

ARTICLE INFO

Article history:
Received 11 March 2012
Available online 23 March 2012

Keywords:
Tumor stem cells
Immune escape
Microenvironment
Tumorigenesis

ABSTRACT

Tumor stem cells (TSCs) are considered as the "seeds" in tumor development, metastasis and recurrence. Despite the various immunosurveillance mechanisms in the host, TSCs may possess the phenotypic and functional properties to evade host immunosurveillance and immune-mediated rejection in immunologically intact individuals. The mechanisms of TSC recognition and their consequent destruction are actively disturbed by various processes, including altered immunogenicity of TSCs, production of TSC-derived regulatory molecules, and interaction of TSCs with tumor-infiltrating immune cells. In addition to these TSC-mediated mechanisms, the diverse mesenchymal cells and cytokines in the tumor microenvironment are contribute to TSC immune escape. Recent mechanistic studies provide a more comprehensive understanding of TSCs in the biology, prevention, and therapy of solid tumors. This review will focus on the latest findings for mechanisms underlying TSCs' escape from the attack of immune system.
© 2012 Elsevier Inc. All rights reserved.

1. Introduction

In recent years, evidence has accumulated pointing to the existence of a new dimension of intratumor heterogeneity and a hitherto-unappreciated subclass of neoplastic cells within tumors, termed tumor stem cells (TSCs). TSCs were first described in acute myeloid leukemia (AML), where a small, distinct population of cells was capable of generating leukemia in mice [1]. The demonstration that a TSC population initiates leukemia has galvanized scientific research to identify stem cells in other cancers. To date, human TSCs were identified in a variety of other tissues including breast, brain, prostate, lung, colon and pancreatic tumors and their corresponding cell lines [2–6]. TSCs are a unique cell population that can rapidly proliferate and self-renew, and share transcriptional profiles with normal somatic stem cells. In the TSC model, tumors are organized as a cellular hierarchy maintained by a small fraction of TSCs that need to be eliminated in order to eradicate the tumor [7]. The hypothesis of TSCs proposes the role of TSCs as the root of tumor development and metastasis, with the capability to give rise to diverse cellular progenies found in a particular tumor sample. Factors in the tumor microenvironment appear to promote the self-renewal and proliferation of TSCs.

One prominent characteristic of TSCs is to evade host immune surveillance effectively. Critical links between TSC, tumor progression, and therapy resistance have emerged, and proof-of-principle now has been established that selective ablation of TSC can inhibit tumorigenic growth in experimental animal models [8]. Therefore, demonstration of a specific relationship of TSC to the evasion of host antitumor immunity would have important implications for cancer therapy. The mechanisms of TSC recognition and their consequent destruction are actively disturbed by a number of processes, such as altered immunogenicity of TSCs, production of TSC-derived regulatory molecules, and interaction of TSCs with tumor-infiltrating immune cells. Consequently, immune system is in a state of tolerance to TSCs. Studies of these mechanisms provide new insight into tumor prevention and treatment.

2. The mechanisms of TSC-induced immune tolerance

2.1. The phenotypic properties of TSCs

T lymphocytes play a central role in the antitumor immune response. However, the degree of natural antitumor immunity may be limited and often insufficient to destroy a rapidly growing neoplasm containing a TSC pool. It was recently reported that TSCs could predominantly lose MHC class I molecules, and selectively silence the expression of tumor-associated antigens (TAAs), whose levels were associated with differentiation, leading to resistance to immune rejection. MHC class I molecules play a key role in the immune recognition of transformed cells [9]. Selective or general downregulation of MHC class I molecules may suppress the ability of class I MHC-restricted CTLs to lyse TSCs [10]. Recent studies reveal that ABCB5+ malignant melanoma initiating cells (MMIC) might evade host immunosurveillance when MHC class I molecules is absent or downregulated [11]. Moreover, MMIC did not express

* Corresponding author. Address: Department of Biotherapy, Tianjin Medical University Cancer Institute and Hospital, Huanhuxi Road, Hexi District, Tianjin 300060, China. Fax: +86 22 23558988.
E-mail address: rwziyi@yahoo.com (X.-B. Ren).

0006-291X/$ - see front matter © 2012 Elsevier Inc. All rights reserved.
http://dx.doi.org/10.1016/j.bbrc.2012.03.086

tumor-associated antigen MART-1 (melanoma antigen recognized by T cells 1) at significant levels, and therefore preferentially evade the antitumor immune response. Wu et al. [12] investigated the immunogenicity of CD133+ cells in two human astrocytoma and two glioblastoma multiforme samples. Flow cytometry analysis revealed that the majority of CD133+ cells did not express detectable MHC class I molecules or natural killer (NK) cell activating ligands on their cell surface, which may render them resistance to adaptive and innate immune surveillance. When they incubated CD133+ cells with INF-γ, a significantly increased percentage of CD133+ cells that were positive for MHC class I molecules and NK cell activating ligands was detected, suggesting enhanced recognition and destruction of TSCs by immune cells.

In addition, Di Tomaso and colleagues [13] detected defects in antigen-processing machinery (APM) components expression in the cultured population of glioblastoma multiforme-derived tumor stem cells (GBM–TSCs). APM molecules included MHC class I molecules and their heavy chains (i.e., A-HC), β2-microglobulin, constitutive proteasome subunits (delta, MB1, and Z), immunoproteasome (LMP2, LMP7, and LMP10), transporter molecules (TAP), and chaperon molecules (tapasin, calnexin, calreticulin, and ERp57). They found negative or low level of expression of HLA-A, HLA-B, HLA-C molecules, A-HC and the β2-microglobulin by most GBM-TSC and corresponding FBS tumor cell lines, moreover, in most cases with higher levels in FBS tumor cells than in TSCs. These results are in line with the previously reported defective expression of MHC and APM molecules in a variety of human tumors [14,15], indicating that low efficiency in antigen processing and presentation occur in TSCs isolated from these tumor types. Therefore, TSCs may display unique phenotypes, such as downregulation of MHC class I molecules, TAAs associated with differentiation and APM components to effectively evade host immunosurveillance.

2.2. The functional properties of TSCs

Antitumor immune responses can be detected in tumor-bearing host and are particularly relevant to disease progression and antitumor therapeutic outcomes in highly immunogenic tumors [16]. To avoid the attack of immune system, TSCs may induce immunogenic tolerance through functional inactivation of antigen-reactive T lymphocytes or activation of Treg cells. The mechanism that has been implicated in the induction of anergy is direct T cell inhibition via secretion of immunosuppressive cytokines, including IL-4, IL-10 and TGF-β. Researchers detected high levels of IL-4 and IL-4R in CD133+ stem-like cells in colon cancer. Consistently, colon cancer stem cells promote tumor growth and prevent cell death via autocrine signaling of IL-4. IL-4 has previously been reported to suppress apoptosis by enhancing the expression of anti-apoptotic proteins cFLIP, Bcl-xL, and PED in many tumor cell lines, including chronic lymphocytic leukemia B cells [17], as well as prostate, breast, and bladder tumor cell lines [18]. Additionally, IL-4 has the capability of inhibiting the proliferation and immune responses of Th1 cells, and also exhibits immunoregulatory effect on B cells, mastocytes, and macrophages. Therefore, blockage of IL-4 in these tumor cells has a significant growth-inhibitory effect [19]. Hence, TSCs may signal through IL-4 autocrine to up-regulate the expression of anti-apoptotic proteins, inhibit the apoptosis of tumor cells and induce immune tolerance. Recent evidence shows that glioma stem cells (GSCs) can prevent CTL mediated specific immune cytotoxicity [20], and GBM–TSCs can strongly inhibit the proliferation of CD4+ T cells. In addition, PBMCs co-cultured with GBM–TSCs secrete lower levels of IFN-γ and higher levels of IL-10, and contained increased percentages of cells expressing Fox-P3 and CD25. A subpopulation of $CD14^{low}$, $CD11c^{high}$ $CD123^{high}$ HLA-DRinterm plasmacytoid DCs exhibiting the capacity to promote Treg phenotype and function are detected when PB CD14+ monocytes are co-cultured with GBM–TSCs [21]. Therefore, TSCs can induce high levels of Treg cells to suppress the antitumor responses. Treg cells capable of inhibiting autologous T cell proliferation might also be involved in suppressing the antitumor immune response in cancer patients. Specifically, Treg cells are actively recruited from the blood and selectively accumulate in the tumor microenvironment, where they may form a dense infiltrate shielding the neoplasm from immune responses [22,23]. It is notable that the TGF-β signaling pathway is specifically activated in the TSC fraction of breast cancers [24], and secreted morphogens in the TGF-β super family as well as their receptors are preferentially expressed by CD133+ brain tumor TSCs [25] and by ABCB5+ MMICs [26]. It was shown that TGF-β negatively influences antitumor capabilities of host cytotoxic $CD8^+$ lymphocytes. This activity is multi-directional and is based on the impairment of Fas-mediated apoptosis of tumor cells, downregulation of IFN-γ secretion and disturbed expression of perforin and granzymes by cytotoxic $CD8^+$ lymphocytes [27]. Indeed, T cell-specific blockade of TGF-β signaling was found to enhance the antitumor immune response in mice challenged with live tumor cells [28]. Taken together, these findings suggest that TSCs may induce anergy in antigen-reactive T lymphocytes through secretion of immunosuppressive factors such as IL-4, IL-10, or TGF-β to promote tumor immune evasion. Moreover, TSCs may induce high levels of Treg cells to simultaneously suppress the antitumor immune response and ultimately promote tumorigenic growth.

Immunogenic tolerance may also be achieved through clonal anergy of macrophages and DCs. Macrophages constitute one of the major immune cell populations responsible for both tumor rejection and promotion. The high expression of CD47 on leukemia stem cells (LSCs) of AML patients can reduce the macrophage-induced phagocytosis of LSCs and decrease the clearance of innate immune system of organism to LSCs [29]. CD47, also known as integrin-associated protein (IAP), is an immunoglobulin-like protein. It can inhibit the phagocytosis of macrophages through binding with signal regulatory protein α chain of inhibitory receptor on macrophage (SIRPα) [30]. Disruption of the CD47–SIRPα interaction with a monoclonal antibody (B6H12.2 or BRIC126) against CD47 will preferentially enable the phagocytosis of AML–LSCs by human macrophages [31]. In addition, SIRPα is also expressed on DCs, and upon interaction with CD47 on human LSCs, initiating a signal transduction cascade resulting in inhibition of DCs activation [30]. Moreover, functional inactivation of DCs, a major type of antigen-presenting cells of myeloid or plasmacytoid origin [32], can affect the activation of initial T cells and inhibit the adaptive immune response. It is noteworthy that researchers found that the CD200 expression was significantly higher in the TSC fractions originated from prostate, breast, colon and brain. Additionally, CD200 was co-expressed with markers of TSCs [33]. CD200 is a type Ia membrane protein that functions as a co-stimulatory molecules, which exerts suppressive effects through binding to the CD200R. CD200R is present on the surface of myeloid DCs, monocyte/macrophage lineage and on T lymphocytes [34]. It was shown that stimulation of CD200R on DCs triggered tumor supporting reactions mediated by Th2 cytokines and increased Treg activity, which are thought to hamper tumor-specific effector T cell immunity [35], whereas blockade of CD200/CD200R interactions with monoclonal anti-CD200 antibodies resulted in a shift towards Th1 activity and attenuated immune tolerance [36,37].

In addition to the mechanisms reviewed above, researches have found that knock-down of CD133 expression could inhibit proliferation of U251 human glioma cells and decrease the colony forming ability and alter the cell cycle distribution in Huh-7 human hepatocellular carcinoma cells [38]. Clinical studies suggest that the prevalence of CD133+ TSCs is related to poor prognosis [39]. Liu et al. [40] isolated tumor cells from human glioblastoma, and

observed that CD133+ cells expressed higher levels of markers associated with neural precursors, such as CD90, CD44, CXCR4, Nestin, Msi1 and MELK. Likewise, CD133+ cells also expressed higher mRNA levels of genes that inhibit apoptosis, including Bcl-2, Bcl-xL, FLIP, c-I AP2, XIAP and NAIP. However, expression of the pro-apoptotic gene Bax was down regulated in these cells. In summary, TSCs may possess the phenotypic and functional properties to evade host immunosurveillance, and foster tumor initiation and growth.

Taken together, immunobiological differences between TSC and autologous tumor cell lines emerge for several phenotypic and functional aspects. A general explanation for such differences may lie in the less differentiated stage of TSC compared with the more differentiated tumor cells as can be seen from differences in the expression of stemness-related markers. Such a lower differentiation stage of TSC appears to be associated with a weaker expression of molecules (MHC-I, NKG2D) that are crucial for T-cell and NK cell recognition of antigens and to a more accentuated immunosuppressive activity [13].

3. The role of TSC-associated immune microenvironment

Tumor microenvironment provides the soil for TSC self-renewal and maintenance by stimulating essential signaling pathways in TSCs and inducing the secretion of soluble cytokines that promotes angiogenesis and sustained growth of TSCs. Alterations of the local tumor microenvironment provide additional mechanisms for TSCs to escape the host immune surveillance.

Global gene expression profiling showed that GREMLIN 1 was expressed at a significantly higher level in basal cell carcinoma (BCC) stromal cells, compared to those from normal skin. GREMLIN 1 encodes a secreted antagonist of the bone morphogenetic protein (BMP) pathway. Antagonists of the BMP pathway are important in stem and progenitor cell biology as regulators of the balance between expansion and differentiation, which is consistent with the effect of BMP antagonists in cancer [41]. BMPs trigger a significant reduction in the stem-like, tumor-initiating precursors of human glioblastomas, and effectively block tumor growth and associated mortality that occur in 100% of mice after intracerebral grafting of human GBM cells [25]. As key components of tumor matrix, BMPs antagonists create a favorable microenvironment for the generation and expansion of tumor cells. Gangliosides can interact with the antigenic ganglioside-binding motif of the extracellular domain of CD133 [42]. Ganglioside is produced at high levels in some tumors, such as GM1, GM2, GM3 and GD3, and can be detected at high concentrations in the sera of tumor patients. Gangliosides can inhibit multiple steps of cell signal transduction events, including generation and presentation of antigens, proliferation of T cells, and secretion of cytokines (e.g., INF-γ). Membrane enrichment of human monocytes with purified exogenous gangliosides potently inhibited ligand-induced activation and upregulation of IL-1R-associated kinase-M (IRAK-M) [43]. Therefore, in the tumor microenvironment, gangliosides can induce tolerance to TLR signaling, leading to blunted activation of innate immune responses. In addition, integrin-mediated cell attachment to extracellular matrix plays a critical role in cell signaling and thereby regulates cellular shape, motility, and the cell cycle. Integrin mutations or upregulation in squamous-cell carcinoma can expand the TSC fraction by inhibiting differentiation or apoptosis [44]. Various integrin receptors are highly up-regulated in pancreatic cancer, which can evoke phenotypes and signaling pathways that regulate tumor cells growth and migration, and render tumor cells ability to escape apoptosis induced by chemotherapy and radiotherapy [45]. Besides, various soluble cytokines that constitute the tumor microenvironment, such as metalloproteinases (MMPs), VEGF, etc., can affect tumor cells signaling pathways and promote the growth and progression of tumor [46–48]. However, the mechanisms about how these cytokines interact with TSCs remains to be explored.

An assemblage of distinct cell types constitutes TSC-associated immune microenvironment. It is worth noting that an emerging role of mesenchymal stem cells (MSCs) in immunomodulation on TSCs has been supported by recent studies. MSCs may secrete TGF-β to mediate suppression of T cell proliferation, as antibodies against TGF-β were found to partially restore T cell activation and proliferative responses in MSC/T lymphocyte co-cultures [49,50]. It is noteworthy that MSCs can induce tolerance to alloantigens via the generation and recruitment of Treg cells as demonstrated both in vitro and in experimental animal models [51]. Moreover, in a murine melanoma model, Treg cell induction by MSCs fostered tumor growth, even in allogeneic mouse recipients [52]. So it was shown that MSCs could induce an immunosuppressive microenvironment to help TSCs escape from immunosurveillance. Other evidence [53] suggested that brain TSCs exist in vascular niches, into which endothelial cells secrete soluble cytokines that maintain these cells in a self-renewing and undifferentiated state. In orthotopic brain tumor xenografts, increasing the number of endothelial cells or blood vessels could expand the TSCs pool and accelerate the initiation and growth of tumor. Researchers further found that compared to CD133− tumor cells, vascular endothelial cells interact closely with the Nestin+/CD133+ brain tumor cells in co-cultures. In addition, other studies reported that microvascular endothelial cells could significantly increase proliferation and inhibit apoptosis of native human AML blasts via releasing IL-3, IL-6, and granulocyte colony-stimulating factors. In general, vascular endothelial cells constitute a niche of microenvironment that promotes the initiation of brain tumors by TSCs [54]. Additionally, tumor-associated fibroblasts play a critical role in promoting the proliferation of CD44+ CD24− breast cancer stem cells via their ability to secrete SDF-1, which may be mediated to SDF-1/CXCR4 signaling [55].

The irregular vasculature in solid tumors creates hypoxic regions, which provide an advantage to tumor growth and are linked to poor patient survival and therapeutic resistance [56]. Hypoxia induces the expression of hypoxia-inducible factors (HIFs) in tumor cells. The transcription factor HIFs are critical to TSCs maintenance and angiogenesis. In addition, HIFs can induce specific gene expression to promote tumor occurrence and development. Researchers found that hypoxia-inducible factor HIF2α and multiple HIF-regulated genes are preferentially expressed in GSCs compared to non-stem tumor cells and normal neural progenitors through detecting GSCs responses to hypoxia, and that HIF2α co-localizes with TSCs markers in tumor specimens. Targeting HIFs in GSCs could inhibit self-renewal, proliferation and survival in vitro, and attenuate tumor initiation potential of GSCs in vivo [57]. Furthermore, due to hypoxia-regulated angiogenesis, anti-angiogenic drugs are expected to inhibit tumor growth, at least in part, by disrupting a TSC vascular niche, which is important for the maintenance of TSCs [58].

4. Problems and future vision

TSCs can evade immunosurveillance effectively, and tumor-associated immune microenvironment assists TSCs to escape various lethal effects via providing factors that can promote TSCs proliferation and survival. However, questions need to be fully addressed include how the host immune system identifies TSCs, and what are the specific effects and mechanisms of TSC-induced tumor immune tolerance. In addition, immunotherapies targeting TSCs just start to emerge. Currently, the understanding of

TSC-associated microenvironment remains obscure, and the dynamic interplay between tumor and the microenvironment remains unclear. Areas that require urgent investigations include how TSC-derived signals interact with cells and cytokines in the microenvironment. A series of therapeutic strategies targeting TSCs have been developed, such as inhibiting proliferation, promoting differentiation, inducing apoptosis, destructing microenvironment and enhancing the sensitivity of chemoradiation [53,59,60]. Preliminary experimental results indicate that these strategies can target TSCs and inhibit their functions only with limited success. Therefore, it requires further in-depth investigation to decipher the rational basis for treatment development. Exploration of the mechanisms of TSC escape from immunosurveillance will shed light on future pre-clinical studies to establish effective therapies targeting TSCs, and may bring new hopes for improving care of cancer patients.

Acknowledgments

This work was supported partially by the National Natural Science Funds (No. 81171983), and by the Tianjin Key Natural Science Funds (No. 11JCYBJC13200).

References

[1] T. Lapidot, C. Sirard, et al., A cell initiating human acute myeloid leukaemia after transplantation into SCID mice, Nature 367 (1994) 645–648.
[2] M. Al Hajj, M.S. Wicha, et al., Prospective identification of tumorigenic breast cancer cells, Proc. Natl. Acad. Sci. USA 100 (2003) 3983–3988.
[3] A.T. Collins, P.A. Berry, et al., Prospective identification of tumorigenic prostate cancer stem cells, Cancer Res. 65 (2005) 10946–10951.
[4] C. Li, D.G. Heidt, et al., Identification of pancreatic cancer stem cells, Cancer Res. 67 (2007) 1030–1037.
[5] L. Ricci-Vitiani, D.G. Lombardi, et al., Identification and expansion of human colon-cancer-initiating cells, Nature 445 (2007) 111–115.
[6] S.K. Singh, I.D. Clarke, et al., Identification of a cancer stem cell in human brain tumors, Cancer Res. 63 (2003) 5821–5828.
[7] C.T. Jordan, M.L. Guzman, Cancer stem cells, N. Engl. J. Med. 355 (12) (2006) 1253–1261.
[8] Z.F. Yang, D.W. Ho, et al., Significance of CD90(+) cancer stem cells in human liver cancer, Cancer Cell 13 (2008) 153–166.
[9] D.T. Guerry, M.A. Alexander, et al., HLA-DR histocompatibility leukocyte antigens permit cultured human melanoma cells from early but not advanced disease to stimulate autologous lymphocytes, J. Clin. Invest. 73 (1) (1984) 267–271.
[10] N. Aptsiauri, T. Cabrera, et al., Role of altered expression of HLA class I molecules in cancer progression, Adv. Exp. Med. Biol. 601 (2007) 123–131.
[11] T. Schatton, M.H. Frank, Antitumor immunity and cancer stem cells, Ann. NY Acad. Sci. 1176 (2009) 154–169.
[12] A. Wu, S. Wiesner, et al., Expression of MHC-I and NK ligands on human CD133$^+$ glioma cells: possible targets of immunotherapy, J. Neuro Oncol. 83 (2) (2007) 121–131.
[13] T. Di Tomaso, S. Mazzoleni, et al., Immunobiological characterization of cancer stem cells isolated from glioblastoma patients, Clin. Cancer Res. 16 (2010) 800–813.
[14] A. Pandha, A. Rigg, et al., Loss of expression of antigen-presenting molecules in human pancreatic cancer and pancreatic cell lines, Clin. Exp. Immunol. 148 (2007) 127–135.
[15] A. Johnsen, J. France, et al., Down-regulation of the transporter for antigen presentation, proteasome subunits, and class I major histocompatibility complex tumor cell lines, Cancer Res. 58 (1998) 3660–3667.
[16] S.A. Rosenberg, N.P. Restifo, et al., Adoptive cell transfer: a clinical path to effective cancer immunotherapy, Nat. Rev. Cancer 8 (4) (2008) 299–308.
[17] M. Dancescu, M. Rubio-Trujillo, et al., Interleukin 4 protects chronic lymphocytic leukemic B cells from death by apoptosis and upregulates Bcl-2 expression, J. Exp. Med. 176 (1992) 1319–1326.
[18] C. Conticello, F. Pedini, et al., IL-4 protects tumor cells from anti-CD95 and chemotherapeutic agents via up-regulation of antiapoptotic proteins, J. Immunol. 172 (2004) 5467–5477.
[19] M. Todaro, P.M. Alea, et al., Colon cancer stem cells dictate tumor growth and resist cell death by production of interleukin-4, Cell Stem Cell 1 (4) (2007) 389–402.
[20] J.A. Trapani, V.R. Sutton, Granzyme B: pro-apoptotic, antiviral and antitumor functions, Curr. Opin. Immunol. 15 (2003) 533–543.
[21] M.K. Sabbagh, Igal Ifergan, et al., Human glioblastoma cancer stem cells promote intra-tumoral immune regulatory functions, Clin. Immunol. 131 (1) (2009) 38.
[22] M. Ahmadzadeh, A. Felipe-Silva, et al., FOXP3 expression accurately defines the population of intratumoral regulatory T cells that selectively accumulate in metastatic melanoma lesions, Blood 112 (13) (2008) 4953–4960.
[23] R.A. Clark, S.J. Huang, et al., Human squamous cell carcinomas evade the immune response by down-regulation of vascular E-selectin and recruitment of regulatory T cells, J. Exp. Med. 205 (10) (2008) 2221–2234.
[24] M. Shipitsin, L.L. Campbell, et al., Molecular definition of breast tumor heterogeneity, Cancer Cell 11 (3) (2007) 259–273.
[25] S.G. Piccirillo, B.A. Reynolds, et al., Bone morphogenetic proteins inhibit the tumorigenic potential of human brain tumour-initiating cells, Nature 444 (7120) (2006) 761–765.
[26] T. Schatton, G.F. Murphy, et al., Identification of cells initiating human melanomas, Nature 451 (7176) (2008) 345–349.
[27] A.G. Jarnicki, J. Lysaght, et al., Suppression of antitumor immunity by IL-10 and TGF-beta-producing T cells infiltrating the growing tumor: influence of tumor environment on the induction of CD4$^+$ and CD8$^+$ regulatory T cells, J. Immunol. 177 (2) (2006) 896–904.
[28] L. Gorelik, R.A. Flavell, Immune-mediated eradication of tumors through the blockade of transforming growth factor-beta signaling in T cells, Nat. Med. 7 (2001) 1118–1122.
[29] S. Jaiswal, C.H. Jaieson, et al., CD 47 is upregulated on circulating hematopoietic stem cells and leukemia cells to avoid phagocytosis, Cell 138 (2) (2009) 271–285.
[30] A.N. Barclay, M.H. Brown, The SIRP family of receptors and immune regulation, Nat. Rev. Immunol. 6 (6) (2006) 457–464.
[31] R. Majeti, M.P. Chao, et al., CD47 is an adverse prognostic factor and therapeutic antibody target on human acute myeloid leukemia stem cells, Cell 138 (2) (2009) 286–299.
[32] M. Colonna, G. Trinchieri, Plasmacytoid dendritic cells in immunity, Nat. Immunol. 5 (2004) 1219–1226.
[33] T.B. Kawasaki, T. Mistree, et al., Co-expression of the tolerogenic glycoprotein, CD200, with markers for cancer stem cells, Biochem. Biophys. Res. Commun. 364 (2007) 778–782.
[34] A.N. Barclay, G.J. Wright, et al., CD200 and membrane protein interactions in the control of myeloid cells, Trends Immunol. 23 (2002) 285–290.
[35] T.J. Curiel, G. Coukos, et al., Specific recruitment of regulatory T cells in ovarian carcinoma fosters immune privilege and predicts reduced survival, Nat. Med. 10 (2004) 942–949.
[36] Anke Kretz-Rommel, Fenghua Qin, et al., CD200 expression on tumor cells suppresses antitumor immunity: new approaches to cancer immunotherapy, J. Immunol. 178 (2007) 5595–5605.
[37] T.P. Rygiel, G. Karnam, et al., CD200–CD200R signaling suppresses anti-tumor responses independently of CD200 expression on the tumor, 2011, p. 10 (Epub ahead of print).
[38] J. Yao, T. Zhang, et al., Effect of CD133/prominin-1 antisense oligodeoxynucleotide on in vitro growth characteristics of Huh-7 human hepatocarcinoma cells and U251 human glioma cells, Oncol. Rep. 22 (4) (2009) 781–787.
[39] J.P. Jianfei, L.B. Keith, Glioma stem cell research for the development of immunotherapy, Neurosurg. Clin. N. Am. 21 (1) (2010) 159–166.
[40] G. Liu, X. Yuan, et al., Analysis of gene expression and chemoresistance of CD133$^+$ cancer stem cells in glioblasoma, Mol. Cancer 5 (2006) 67.
[41] J.B. Sneddon, H.H. Zhen, et al., Bone morphogenetic protein antagonist gremlin 1 is widely expressed by cancer-associated stromal cells and can promote tumor cell proliferation, Proc. Natl. Acad. Sci. USA 103 (40) (2006) 14842–14847.
[42] N. Taieb, M. Maresca, et al., The first extracellular domain of the tumour stem cell marker CD133 contains an antigenic ganglio-side-binding motif, Cancer Lett. 278 (2) (2009) 164–173.
[43] W. Shen, K. Stone, et al., Inhibition of TLR activation and up-regulation of IL-1R-associated kinase-M expression by exogenous gangliosides, J. Immunol. 180 (7) (2008) 4425–4432.
[44] S.M. Janes, F.M. Watt, New roles for integrins in squamous-cell carcinoma, Nat. Rev. Cancer 6 (3) (2006) 175–183.
[45] J.J. Grzesiak, J.C. Ho, et al., The integrin–extracellular matrix axis in pancreatic cancer, Pancreas 35 (4) (2007) 293–301.
[46] A. Orimo, R.A. Weinberg, Stromal fibroblasts in cancer: a novel tumor-promoting cell type, Cell Cycle 5 (15) (2006) 1597–1601.
[47] M. Dong, G.C. Blobe, Role of transforming growth factor-beta in hematologic malignancies, Blood 107 (12) (2006) 4589–4596.
[48] C.M. Overall, O. Kleifeld, Tumor microenvironment-opinion: validating matrix metalloproteinases as drug targets and anti-targets for cancer therapy, Nat. Rev. Cancer 6 (3) (2006) 227–239.
[49] J. Liu, X.F. Lu, et al., Suppression of human peripheral blood lymphocyte proliferation by immortalized mesenchymal stem cells derived from bone marrow of Banna Minipig inbred-line, Transplant. Proc. 36 (10) (2004) 3272–3275.
[50] A. Taylor, J. Verhagen, et al., Mechanisms of immune suppression by interleukin-10 and transforming growth factor-beta: the role of T regulatory cells, Immunology 117 (4) (2006) 433–442.
[51] Di Ianni, Del Papa, et al., Mesenchymal cells recruit and regulate T regulatory cells, Exp. Hematol. 36 (3) (2008) 309–318.
[52] F. Djouad, P. Plence, et al., Immunosuppressive effect of mesenchymal stem cells favors tumor growth in allogeneic animals, Blood 102 (10) (2003) 3837–3844.

[53] C. Calabrese, H. Poppleton, et al., A perivascular niche for brain tumor stem cells, Cancer Cell 11 (1) (2007) 69–82.
[54] K. Hatfield, A. Ryningen, Microvascular endothelial cells increase proliferation and inhibit apoptosis of native human acute myelogenous leukemia blasts, Int. J. Cancer 119 (10) (2006) 2313–2321.
[55] M.Z. Huang, Y.Q. Li, Breast cancer stromal fibroblasts promote the generation of $CD44^+$ $CD24^-$ cells through SDF-1/CXCR4 interaction, J. Exp. Clin. Cancer Res. 29 (80) (2010).
[56] L.M. Postovit, D.E. Abbott, et al., Hypoxia/reoxygenation: a dynamic regulator of lysyl oxidase-facilitated breast cancer migration, Cell Biochem. 103 (2008) 1369–1378.
[57] Z.Z. Li, S.P. Bao, et al., Hypoxia-inducible factors regulate tumorigenic capacity of glioma stem cells, Cancer Cell 15 (2009) 501–513.
[58] Y. Zhao, Q. Bao, et al., Cancer stem cells and angiogenesis, Semin. Cancer Biol. 19 (4) (2009) 279–284.
[59] L. Jin, K. Hope, et al., Targeting of CD44 eradicates human acute myeloid leukemic stem cells, Nat. Med. 12 (10) (2006) 1167–1174.
[60] R. Ohno, N. Asou, Treatment of acute promyelocytic leukemia: strategy toward further increase of cure rate, Leukemia 17 (8) (2003) 1454–1463.

Biochemical and Biophysical Research Communications 420 (2012) 704–709

Contents lists available at SciVerse ScienceDirect

Biochemical and Biophysical Research Communications

journal homepage: www.elsevier.com/locate/ybbrc

Comparative autoantibody profiling before and after appearance of malignance: Identification of anti-cathepsin D autoantibody as a promising diagnostic marker for lung cancer

Xue Luo [a,b], Feng Lu [c], Hong-Li Wang [a], Na Wang [a], Wei-Hua Li [a], Ning Guo [a], Hong-Xia Wang [a], Qing Xia [a,*]

[a] National Center of Biomedical Analysis, 27 Taiping Road, Beijing 100850, China
[b] Department of Occupational Health, Third Military Medical University, 30 Gao Tan Yan Road, Chong qing 400038, China
[c] Department of Molecular Immunology, Institute of Basic Medical Science, 27 Taiping Road, Beijing 100850, China

ARTICLE INFO

Article history:
Received 17 January 2012
Available online 28 January 2012

Keywords:
Lung cancer
Autoantibodies
Proteomics
Cathepsin D

ABSTRACT

Cancer patients frequently develop autoantibodies. To test the hypothesis that the appearance of autoantibodies precedes the clinical diagnosis of cancer, we applied an immunoproteomic approach to compare autoantibody profiles before and after appearance of malignances. Proteins from A549 cells, a lung adenocarcinoma cell line, were separated by two dimensional electrophoresis and then immunoblotted with serum samples from 8 individuals who were eventually diagnosed with lung cancer. Compared with autoantibody profiles from 3 years prior to the appearance of malignances, 21 immunoreactive spots newly appeared or presented with stronger staining intensity when clinical diagnoses were made. Among them, 10 matched spots on 2-DE gels were identified by mass spectrometry analysis as 5 proteins. With immunoprecipitation analysis, the antigenicity of protein cathepsin D was confirmed, and notably, in lung cancer sera, the occurrences of autoantibodies against the specific forms of cathepsin D differed significantly from the control groups ($p < 0.05$). Our findings suggest that harnessing immunity may have utility for early cancer marker discovery, and that comparing autoantibodies to specific forms of cathepsin D may be a promising early marker of lung cancer.

© 2012 Published by Elsevier Inc.

1. Introduction

Lung cancer remains at epidemic proportions and continues to be the leading cause of cancer death in both males and females. Early tumor markers to detect lung cancers when they are smaller and presumably at earlier and more curable stages are urgently needed to improve its survival rate. Theoretically, there is no detection instrument that rivals the sensitivity and specificity of the immune system. Hence, one promising approach to early detection is to identify and examine the immune response to cancer, as opposed to the cancer itself [1].

In the present study, we evaluated a prospectively assembled collection of frozen serum samples to test the hypothesis that the appearance of autoantibodies precedes the diagnosis of lung cancer. We analyzed the immunoreactivity of serum antibodies to proteins from A549 cells in lung cancer patients by immunoproteomic technique. Specially, we compared the autoantibody profiles of sera sample from 8 lung cancer patients, whose sera were collected at the time of diagnosis and correspondingly 3 years before the appearance of malignancy. By comparing each pair of immunoblot patterns, 21 immunoreactive spots newly appeared or presented with stronger staining intensity in sera after the diagnosis than observed in the 3 years prior to diagnosis. Among them, 10 matched spots on 2-DE gels were identified by mass spectrometry as 5 proteins. With immunoprecipitation analysis, the antigenicity of protein cathepsin D was further confirmed, and the occurrences of autoantibody to cathepsin D were also demonstrated in lung cancer patients.

2. Materials and methods

2.1. Sera and Cell line

Since 2002, the Department of Laboratory Diagnostics (General Hospital, Chinese PLA), has stored serum samples (at −70 °C) which were obtained from annual physical examinations of Chinese Armed Forces. A review of medical records identified 8 individuals who were clinically diagnosed with lung cancer and for whom stored serum samples were obtained before the discovery of a malignancy. Serum samples of these 8 patients with lung cancer at the time of diagnosis and correspondingly 3 years, 2

* Corresponding author. Address: Department of Molecular Immunology, Institute of Basic Medical Science, 27 Taiping Road, Beijing 100850, China. Fax: +86 10 68159436.
E-mail address: xiaqing@proteomics.cn (Q. Xia).

0006-291X/$ - see front matter © 2012 Published by Elsevier Inc.
doi:10.1016/j.bbrc.2012.01.107

years, and 1 year before diagnosis, were enrolled in this study. For immunoprecipitation analysis, Sera from malignant ($n = 47$) and nonmalignant ($n = 23$) lung disease patients and 20 healthy subjects were analyzed. The malignant samples were comprised of squamous cell carcinoma ($n = 14$), adenocarcinoma ($n = 15$), and small cell carcinoma ($n = 18$; Table 1). Informed consent was obtained from all study participants.

The A549 cell line used in this study was cultured in DMEM supplemented with 10% fetal bovine serum, 100 units/ml penicillin, and 100 unites/ml streptomycin.

2.2. 2-DE and Western blot

Proteins derived from the extracts of A549 cells were separated by 2-DE as described previously. The 2-DE images were captured using ImageScanner (Amersham Pharmacia Biotech). For hybridization with serum, unstained PVDF membranes were incubated with serum obtained from patients or with normal control serum at a 1:500 dilution for 1 h at room temperature.

2.3. Protein identification by MS analysis

After the Western blot and film exposure to the PVDF membrane incubated with ECL, we stained the PVDF membranes with CBB R250. The profile of the proteins on the membrane was the same as that of the map of 2-DE gels visualized by CBB R250 staining. We put the film exposed to the PVDF membrane (which was incubated with the ECL reagents) onto the stained PVDF membrane to localize the exposed spot on the PVDF membrane. We matched the spots on the PVDF membrane to the 2-DE map of the same sample. Next, we excised the identified protein spots from the 2-DE gel stained by CBB R250 and processed them for mass spectrometry analysis as described previously [5]. Protein identification was repeated at least twice using spots from different gels. Briefly,

Table 1
The pathological characteristics and the five forms of cathepsin D distribution in patients with lung cancer and controls.

Feature	No. cases examined	Cathepsin D-Abs+ (%)				
		66 kDa	52 kDa	48 kDa	42 kDa	34 kDa
Control						
Health	20	0 (0)	4 (20.0)	3 (15)	2 (10)	2 (10)
Nonmalignant lung disease	23	0 (0)	5 (21.7)	4 (17.4)	2 (8.7)	3 (13.0)
Lung cancer	47	17 (36.2)[A]	42 (89.4)[A]	29 (61.7)[A]	16 (34.0)[A]	28 (59.6)[A]
Sex						
Male	28	14 (50.0)[B]	25 (89.3)	15 (53.6)	11 (39.3)	15 (53.6)
Female	19	3 (15.8)	17 (89.5)	14 (73.7)	5 (26.3)	13 (68.4)
Age at diagnosis (yr)						
⩾60	20	12 (60.0)	18 (90.0)	15 (75.0)	9 (45.0)	16 (80.0) [C]
<60	27	15 (55.6)	24 (88.9)	14 (51.9)	7 (25.9)	12 (44.4)
Stage						
Early disease (1–2)	13	4 (30.8)	9 (69.2)[D]	7 (53.8)	2 (15.4)	8 (61.5)
Advanced disease (3–4)	34	13 (38.2)	33 (97.1)	22 (64.7)	14 (41.2)	20 (58.8)
Histologic type						
Adenocarcinoma	15	5 (33.3)	13 (86.7)	7 (46.7)	3 (20.0)[E]	5 (33.3)[F]
Squamous cell carcinoma	14	9 (64.3)[G]	13 (92.3)	9 (64.3)	9 (64.3)[G]	10 (71.4)
Small cell carcinoma	18	3 (16.7)	16 (83.3)	13 (72.2)	4 (22.2)	13 (72.2)

Note: A: lung cancer vs. healthy control and nonmalignant lung disease; B: male vs. female; C: <60 vs. >60; D: early disease vs. advanced disease; E: adenocarcinoma vs. squamous cell carcinoma; F: adenocarcinoma vs. small cell carcinoma; G: squamous cell carcinoma vs. small cell carcinoma; significantly different by χ^2-square test.

Table 2
Autoantigens Proteins identified by PMF.

Item No.	Spot No.	Acc No.	Protein name	M_{Theor}	M_{obv}	pI_{Theor}	pI_{obv}	Score	Sequence coverage (%)	Number of matched peptides	Number of non-matched peptides	RMS error (ppm)
1.	4	gi|4503571	Enolase 1	47139	47290	7.01	7.37	145	41	13	4	97
2.	5	gi|4503571	Enolase 1	47139	47290	7.01	7.09	143	38	12	2	48
3.	6	gi|4503571	Enolase 1	47139	47290	7.01	6.94	160	57	20	13	30
4.	7	gi|4503571	Enolase 1	47139	47290	7.01	7.40	118	37	13	7	121
5.	11	gi|4504447	Heterogeneous nuclear ribonucleoprotein A2/B1 isoform A2	35984	41120	8.67	7.29	153	55	16	17	62
6.	12	gi|154355000	KH-type splicing regulatory protein (FUSE binding protein 2)	68393	76330	8.52	7.51	245	44	26	9	42
7.	13	gi|154355000	KH-type splicing regulatory protein (FUSE binding protein 2)	68393	76330	8.52	7.38	232	45	24	9	81
8.	16	gi|4505753	Phosphoglycerate mutase 1	28786	27100	6.67	7.37	128	43	10	3	64
9.	17	gi|4504447	Heterogeneous nuclear ribonucleoprotein A2/B1 isoform A2	35984	22820	8.67	8.35	105	43	13	26	54

pI_{Theor} and M_{Theor}, calculated isoelectric point and molecular weight according to the protein sequence; pI_{obv} and M_{obv}, the calculation of experimental *pI* and *Mr* based on migration of the protein spot on 2-DE gels.

Peptide mass finger printings (PMF) were acquired using a MALDI-TOF REFLEX III instrument (Bruker Daltonics, Bremen, Germany). Nine spots (Table 2) and protein band (66 kDa) immunoprecipitated from cell lysates were analyzed by NanoLC–HDMS MS/MS on Acquity™ Nano UPLC system (Waters Corp., Milford, USA) and a Synapt high-definition mass spectrometry (HDMS) with nanospray ion source (Waters). Spot eight was analyzed by NanoLC–FT ICR MS/MS on 9.4T APEX Qe (Bruker Daltonics, Billerica, MA, USA) with an HApollo II nanoESI source in positive ion mode. PMF data was searched on local Mascot v2.1 against NCBInr 070815 (5371018 sequences; 1856562799 residues). The MS/MS ion database search was conducted using Mascot on the freely accessed internet website (http://www.matrixscience.com); the database is the non-redundant protein database NCBInr 20070926 (5519594 sequences; 1911975371 residues).

2.4. Immunoprecipitation

Immunoprecipitations were performed by incubating whole cell extracts from A549 cells with polyclonal anti-cathepsin D antibody (SC10725, Santa Cruz Biotechnology) and preincubated with protein A/G-Sepharose (Santa Cruz Biotechnology).

2.5. Statistical analysis

The chi-squared (χ^2) test was used to compare the association between the presence of the five forms of cathepsin-D and several clinicopathologic parameters, as well as differences between the lung cancer and normal groups. All comparisons were two-tailed, and $P < 0.05$ was considered statistically significant. All data analysis was performed with SPSS V11.5 (SPSS, Inc., Chicago, IL).

3. Results

3.1. Comparison of autoantibody profiles of serum samples

To observe the changing of humoral response during the process of tumorigenesis, we compared autoantibody profiles of 8 individuals newly diagnosed with lung cancer and correspondingly 3 years before the diagnosis. We first attempted to establish their autoantibody profiles individually. A549 cellular proteins were separated by 2-DE (Fig. 1A) and transferred onto PVDF membranes. These 8 pairs of serum samples were investigated for antibodies to A549 cell protein extracts individually. Each membrane was treated with one 1:500 diluted serum sample as the primary antibody and with 1:10000 diluted sheep antihuman IgG as secondary antibody. Western Blotting with each serum sample was repeated at least twice, and the results were highly replicable. Two of the 8 patients had the same autoantibody patterns before and after clinical diagnosis, while distinct changes of autoantibody profiles were observed in the other six pairs of serum samples. Generally, compared with that of prediagnosis, numbers of immunoreactive spots increased and the intensity was stronger in autoantibody profile at the time of the diagnosis. As representative results of WB (Fig. 1B) three years before appearance of malignancy, no obvious immunoreactive spots could be observed in serum from Patient 1, while seven (spots 1–7) immunoreactive spots appeared when clinical diagnosis was confirmed. All together, compared with 3 years before the diagnosis, 21 immunoreactive spots newly appeared or with stronger staining intensity were observed in sera after the diagnosis was confirmed. Among them, 10 matched spots on 2-DE gels were identified by MS analysis, as indicated in Fig. 1A.

3.2. Identification of immunoreactive protein spots

These 10 matched positive spots were excised from the corresponding CBB R250 stained 2-DE gels, in-gel digested by trypsin. The resulting peptides were analyzed by MALDI-TOF MS and ESI-MS/MS. Spot eight was subjected to NanoLC–FT ICR MS/MS analysis on 9.4T APEX Qe. A total of 5 proteins were identified from 10 spots, since some contiguous spots with similar molecular mass were identified to be isoforms of 1 protein. The contiguous spots 4, 5, 6, and 7 were identified as Enolase 1, spots 12, 13 as KH-type splicing regulatory protein (FUSE binding protein 1, FBP1), and spots 11, 17 as heterogeneous nuclear ribonucleoprotein A2/B1 (hnRNP-A2/B1) isoform A2 (Table 2). For spot eight, protein mixture of cathepsin D preproprotein and tyrosine was identified with low confidence by PMF; therefore, NanoLC-Q-FT ICR MS/MS was

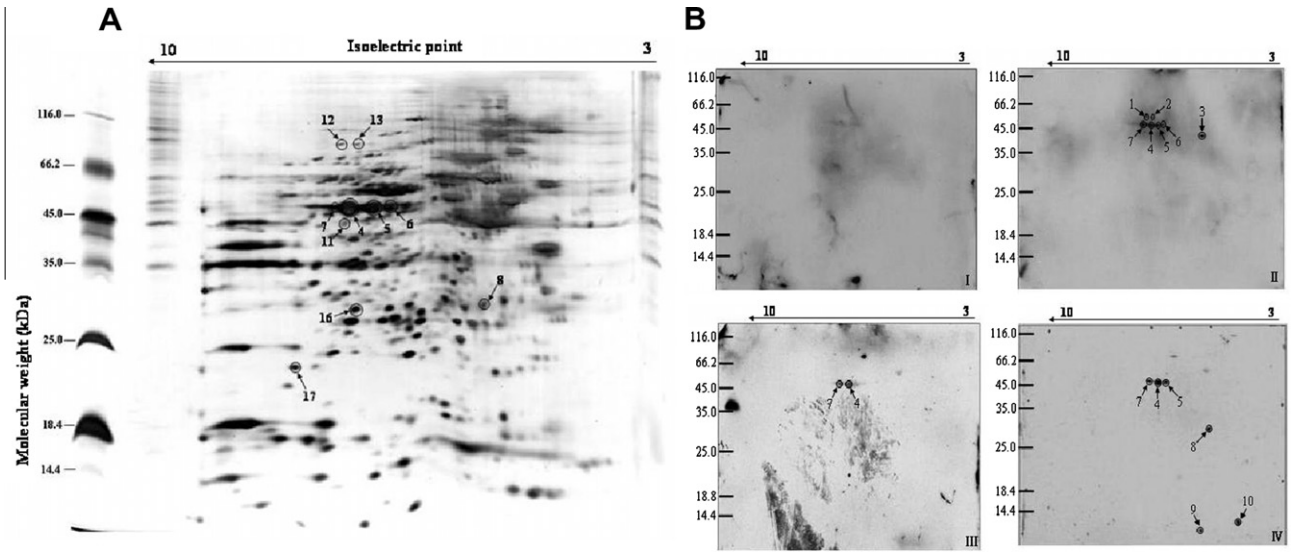


Fig. 1. Comparison of autoantibody profiles of sera from individuals before and after diagnosed with lung cancer. (A) CBB R250 staining of A549 cell-derived proteins separated by two-dimensional PAGE. Ten spots that differentially recognized by serum 3 years before and after clinical diagnosis, and got identification by MS analysis are circled and marked. The original gel size was $8 \times 7 \times 1.0$ mm^3. After transferred onto nitrocellulose membranes, proteins were reacted with serum samples diluted at 1/500 from 8 pairs of individuals who eventually developed into lung cancer. (B) Representative 2D-immunoblotting patterns of A549 cell proteins with sera sample from Patient 1 before (i) and after diagnosis (ii), and from Patient 2 before (iii) and after diagnosis (iv).

used for further confirmation (Table 3). For ESI MS/MS measurements, 4 proteins were identified from 8 spots, Enolase 1 from spot 4, 5, 6 and 7; FBP1 from spot 12, 13, and phosphoglycerate mutase 1 from spot 16. Cathepsin D preproprotein from spot 8 was identified by both nanoLC ESI–MS/MS and 9.4T Q-FT. However, spot 11, 17 did not show confident results by ESI MS/MS.

Table 3
Autoantigens proteins identified by MS/MS.

Item No.	Spot No. or band	Acc No.	Protein name	M_{Theor}	M_{obv}	pI_{Theor}	pI_{obv}	Score	Sequence Coverage (%)	Number of matched peptides	RMS error (ppm)	Instrument
1.	4	gi|4503571	Enolase 1	47139	47290	7.01	7.37	1324	50	25	14	HDMS
2.	5	gi|4503571	Enolase 1	47139	47290	7.01	7.09	903	38	18	67	HDMS
3.	6	gi|4503571	Enolase 1	47139	47290	7.01	6.94	444	23	12	103	HDMS
4.	7	gi|4503571	Enolase 1	47139	47290	7.01	7.40	147	12	4	43	HDMS
5.	8	gi|4503143	Cathepsin D preproprotein Tyrosine	44524	28820	6.10	5.76	235	37	11	3	9.4T Q-FT-MS/MS
6.	12	gi|154355000	KH-type splicing regulatory protein (FUSE binding protein 2)	68393	76330	8.52	7.51	207	6	4	21	HDMS
7.	13	gi|154355000	KH-type splicing regulatory protein (FUSE binding protein 2)	68393	76330	8.52	7.38	145	4	3	18	HDMS
8.	16	gi|4505753	Phosphoglycerate mutase 1	28786	27100	6.67	7.37	216	12	4	18	HDMS
9.	66 kDa band	gi|4503143	Cathepsin D preproprotein	44524	28820	6.10	5.76	299	14	6	42	HDMS

pI_{Theor} and M_{Theor}, calculated isoelectric point and molecular weight according to the protein sequence; pI_{obv} and M_{obv}, the calculation of experimental *pI* and *Mr* based on migration of the protein spot on 2-DE gels.

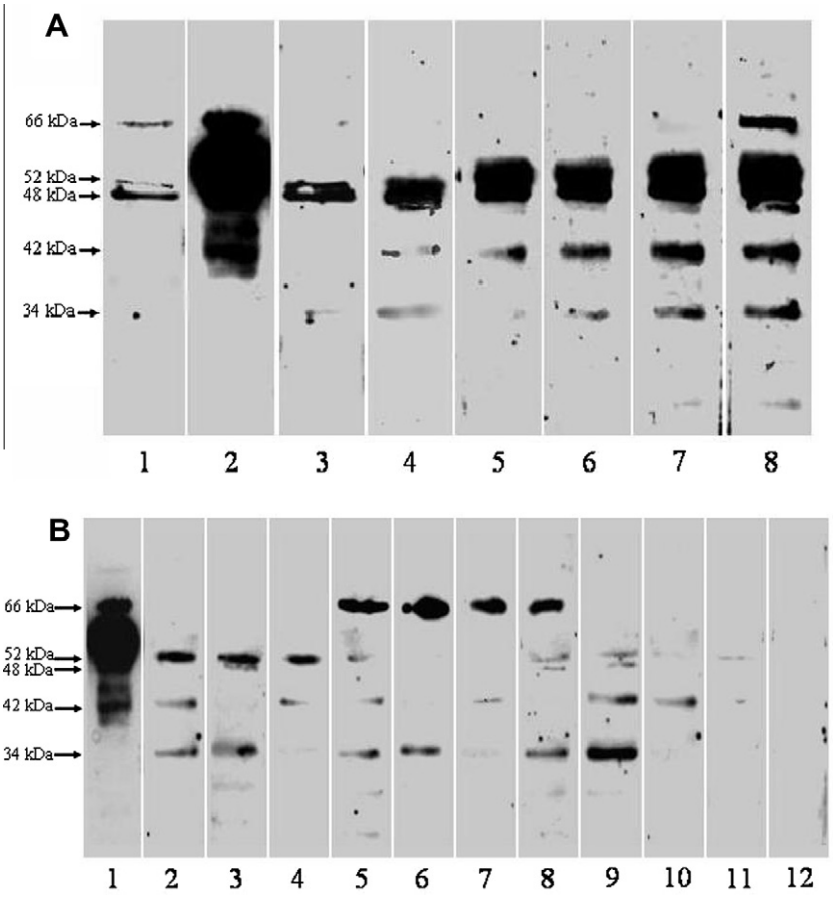


Fig. 2. Validation of the antigenicity of cathepsin D. (A) Western blot analysis of proteins, immunoprecipitated from A549 cells by anti-cathepsin D antibody and separated by 1-D PAGE, was performed with sera from Patient 2 collected when the diagnosis was made and correspondingly 1, 2, 3 years before discovery of malignancy. Whole cell extracts (WCL) were immunoprecipitated with an anti-cathepsin D antibody, and equal amounts of the immunoprecipitated protein were used for immunoblot analysis with anti- cathepsin D antibody (lane 2), sera from Patient 2 (lane 8), and his sera before discovery of malignancy [before 3 years (lane 5), 2 years (lane 6), and 1 year (lane 7)]. Lane 1, input; Lane 3, serum from healthy control; Lane 4, serum from patient with nonmalignant lung disease. (B) Occurrence of cathepsin D autoantibodies in serum from lung cancer patients. In order to find out the occurrence of cathepsin D autoantibody in cancer, Western blot analysis of proteins, immunoprecipitated from A549 cells by anti-cathepsin D antibody and separated by 1-D PAGE, was performed with 47 lung cancer patient sera, 20 normal control sera and 23 nonmalignant lung disease sera. Only typical results are shown. Lane 1, immunoblot analysis with anti-cathepsin D antibody. Lanes 2–10, sera from patients with lung cancer. Lane 11, serum from patent with nonmalignant lung disease. Lane 12, sera from healthy volunteer.

3.3. Confirmation of the antigenicity of cathepsin D in lung cancer patients

Spot 8, which was negative in sera from Patient 2 three years before the appearance of cancer and showed strong staining intensity when the diagnosis confirmed (Fig. 1B III, IV), was identified to be cathepsin D preproprotein with MS analysis. In order to confirm the antigenicity of cathepsin D, an additional type of experiment was conducted. Western blot analysis of proteins, immunoprecipitated from A549 cells by anti-cathepsin D antibody and separated by 1-D PAGE, was performed with sera from Patient 2 (Fig. 2). Whole cell lysates (WCL) were immunoprecipitated with an anti-cathepsin D antibody, and equal amounts of the immunoprecipitated protein were used for immunoblot analysis with anti-cathepsin D antibody (Fig. 2, lane 2), sera from Patient 2 the year when diagnosis confirmed (lane 8), as well as 3 years (lane 5), 2 years (lane 6), and 1 year (lane 7) before discovery of malignancy respectively. All of the four serum samples showed positive reactivity against pro-forms of cathepsin D (48, 52 kDa), while the intensity of immunoreactivity to mature molecular weight form (34 kDa) increased by degree. Interestingly enough, besides recognizing the three well-known forms (34, 48, 52 kDa), a novel form of cathepsin D (66 kDa) was recognized by sera at the year of diagnosis, while negative or weakly recognized in the three prediagnosis periods, normal control (lane 3) and nonmalignant lung disease (lane 4).

3.4. Occurrence of cathepsin D autoantibodies in sera from lung cancer patients

To examine the occurrence of cathepsin D autoantibody in lung cancer, the immunoprecipitation analysis was performed with lung cancer patient as well as control sera. Sera from 43 of 47 lung cancer, 4 of 20 healthy control, and 6 of 23 nonmalignant lung disease subjects showed positive reactivity against cathepsin D. Notably, two other forms with molecular weight as 66 and 42 kDa were observed immunoreactive in lung cancer (Fig. 2B), except for three well-known forms (52, 48, 34 kDa) of cathepsin D. Statistic analysis showed that positive reactivity against five forms of cathepsin D was significantly higher in the lung cancer group when compared to control groups (Table 1).

3.5. Identification of 66 kDa protein the band by NanoLC–HDMS MS/MS

In the present study, 66 kDa, which showed a sensitivity of 36.2% and a specificity of 100% to lung cancer patients, was an area of interest. We confirmed that it was a novel form of cathepsin D by immunoprecipitation and Synapt HDMS DDA (the latest Q-TOF premiere version) analysis. A549 cells were lysed and immunoprecipitations were performed by incubating whole cell extracts with polyclonal anti-cathepsin D antibody. Immunoprecipitates were separated by SDS-PAGE and stained with CBB R250. Interest band (66 kDa) was excised and subjected to in-gel tryptic digestion. The resulting peptides were analyzed by ESI–MS/MS (Fig. 3, Table 3) and showed that 66 kDa form cathepsin D might be another type modification isoform of cathepsin D in lung cancer patients.

4. Discussion

Since tumor-reactive antibodies are elicited and detectable prior to the development of a palpable tumor or circulating antigens, the assessment of the tumor-reactive immune response against autoantigens should represent an early diagnostic and

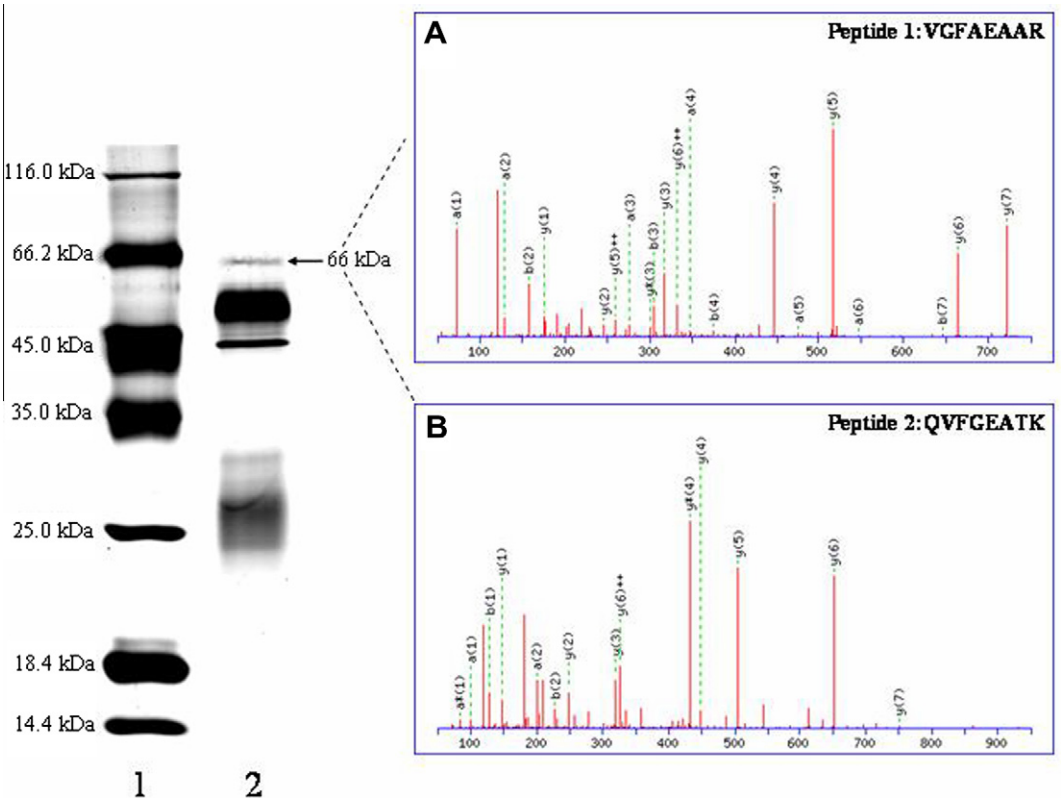


Fig. 3. Identification of protein (66 kDa band) with immunoprecipitation followed by MS/MS analysis. Proteins from cell lysates were immunoprecipitated with antibodies to cathepsin D and then processed for NanoLC–HDMS MS/MS analysis on 9.4T APEX Qe. Lane 1, standard protein molecular marker; Lane 2, proteins immunoprecipitated from A549 cells by anti-cathepsin D antibody and then separated by 1-D SDS–PAGE. (A) MS/MS spectra for inferred peptide1 VGFAFAAR and (B) inferred peptide 2 QVFGEATK.

prognostic marker [2]. Although there are many reports of autoantibodies in patients with malignancies, including lung cancer [3], to our knowledge, this is the first report on the comparative analysis of global autoantibody profiles of sera from lung cancer patients before and after clinical diagnosis. In the present study, we found 21 immunoreactive spots newly appeared or with stronger staining intensity in sera after the diagnosis compared with that of correspondingly 3 years before the diagnosis, and with MS analysis, 10 matched spots on 2-DE gels were identified as 5 proteins. Lung cancer was preceded by or coincided with seroconversion from antibody negative to positive status, suggesting that the novel immune responses are driven by proteins involved in the transformation process, and the five identified autoantigens might be candidates for such tumor markers in lung cancer.

Enolase 1 autoantibody has been detected in the sera from lung cancer patients [4] and also in more than 50% of healthy individuals with low titers [5]. In the present study, we found changes of titer and/or pattern of anti-enolase 1 autoantibody in lung cancer patients' sera. The profile of the spots of enolase 1 antibody in the sera from Patient 1 (after diagnosis) showed three continuously connected spots at the pI range from 6.94 to 7.37 in the 2D blot profile, while only weak intensity could be observed in the sera from the same individual 3 years before appearance of malignancy (Fig. 1BI–II). FBP1 is one of the three far-upstream element binding protein (FBP) family members. Recent findings have shown that FBP is essential for c-myc expression, and reductions in FBP levels reduce c-myc expression and correlate with slower cell growth [6]. To our knowledge this is the first report on FBP1 recognized as an autoantigen by sera from patients with lung cancer, and it will require more data from a larger group of patients to determine whether autoantibodies to FBP1 are a chance observation or occur more frequently in patients with lung cancer.

Cathepsin D is a lysosomal acid proteinase, which is translated as preprocathepsin D in rough endoplasmic reticulum. In normal cells, the mature cathepsin D (34 kDa) participates in intracellular protein catabolism, hormone and antigen processing, as well as in the apoptotic pathway, and its preform, procathepsin D (pCD52, 48 kDa) is believed to cause enhanced proliferation and neoplastic transformation [7,8]. Bosschers et al. [2] demonstrated that circulating pro-forms of cathepsin D (52, 48 kDa) were detected in 31 of 40 endometrial cancer patients and none of the control volunteers. Circulating IgG reactive with cathepsin D could be demonstrated in 29/31 patients with circulating procathepsin D, while none of the normal controls. In this study, anti-cathepsin D was identified as a newly appeared autoantibody in a patient who was diagnosed with lung cancer, whereas the corresponding specific signal was undetectable in serum correspondingly 3 years before the appearance of malignancy (spot eight in Fig. 1B IV). In the following immunoprecipitation analysis, anti-cathepsin D autoantibodies were observed in 91.5% lung cancer patients, while only 20% of normal controls and 26.1% patients with nonmalignant lung disease did. In contrast to current assays for circulating cathepsin D, the presence of antibodies reactive with specific epitopes of cathepsin D is associated with not only the over expression of cathepsin D, but also the presence of the aberrant processing and modification of the pro-enzyme. Since immune responses generally precede detectable circulating antigen, the assessment of antibodies against these specific epitopes may be a more useful diagnostic or prognostic marker than current assays measuring circulating antigen. In this sense, these results strongly suggest that serum anti-cathepsin D autoantibodies would become a possible novel early tumor marker in lung cancer.

Notably, besides the occurrence, the pattern of anti-cathepsin D autoantibodies was different between lung cancer patients and control groups. Specifically, the patterns of anti-cathepsin D autoantibodies were more diverse in that each patient had one main intense reaction. Of the 43 patients producing antibodies reactive with cathepsin D, 7 (16%) had most intense reaction against 66 kDa band, 17 (39.5%) against 52 kDa, 5 (11.6%) against 48 kDa, and 14 (32.6%) against the 34 kDa band. While in the four normal controls and six patients with nonmalignant lung disease-producing antibodies, the most intense reaction appeared to be directed at the procathepsin D bands (52 kDa). Sreenavasa et al. [9] isolated cathepsin D from human ovarian tumor cell line UL-1 and was further analyzed by immunoblotting with three sera samples from ovarian cancer patients. They found that the patient-derived antibodies reacted with three forms (52, 48, 32 kDa) and the most intense reaction was directed at the procathepsin D bands (48, 52 kDa), while only weak reactivity with mature 34 kDa cathepsin D. Whether the immune response to the novel forms of cathepsin D (66 kDa) arise from altered glycosylation or other mechanisms still needs further studies. However, these results suggest that novel immune responses to cathepsin D are driven by the process of malignant transformation, and the detection of autoantibodies against specific forms of cathepsin D might have utility for the diagnosis of lung cancer. It still requires more data from a larger group of patients to determine whether the diverse pattern of autoantibodies to cathepsin D is associated with the histology, progression and response to therapy in lung cancer.

Although the data gathered in this paper are somewhat preliminary, it is of interest to perform further studies on the antigens detected in this study, which might be candidates of diagnostic marker and therapy targets in lung cancer. It is necessary to analyze a larger number of samples to identify the relative specific lung cancer-associated autoantibodies and the specific antigens recognized by these autoantibodies.

Acknowledgments

This work was supported by grants from the National Natural Science foundation of China (No. 81171919) and the National Basic Research Program of China (973 Program; 2011CB910602).

References

[1] O.J. Finn, Immune response as a biomarker for cancer detection and a lot more, N. Engl. J. Med. 353 (2005) 1288–1290.
[2] J.R. Bosscher, C. Gercel-Taylor, C.S. Watkins, D.D. Taylor, Epitope recognition by anti-cathepsin D autoantibodies in endometrial cancer patients, Gynecol. Oncol. 81 (2001) 138–143.
[3] F. Fernandez-Madrid, P.J. VandeVord, X. Yang, R.L. Karvonen, P.M. Simpson, M.J. Kraut, J.L. Granda, J.E. Tomkiel, Antinuclear antibodies as potential markers of lung cancer, Clin. Cancer Res. 5 (1999) 1393–1400.
[4] A. Fujii, M. Yoneda, T. Ito, O. Yamamura, S. Satomi, H. Higa, A. Kimura, M. Suzuki, M. Yamashita, T. Yuasa, H. Suzuki, M. Kuriyama, Autoantibodies against the amino terminal of alpha-enolase are a useful diagnostic marker of Hashimoto's encephalopathy, J. Neuroimmunol. 162 (2005) 130–136.
[5] W.H. Li, J. Zhao, H.Y. Li, H. Liu, A.L. Li, H.X. Wang, J. Wang, K. He, B. Liang, M. Yu, B.F. Shen, X.M. Zhang, Proteomics-based identification of autoantibodies in the sera of healthy Chinese individuals from Beijing, Proteomics 6 (2006) 4781–4789.
[6] K. Matsushita, T. Tomonaga, H. Shimada, A. Shioya, M. Higashi, H. Matsubara, K. Harigaya, F. Nomura, D. Libutti, D. Levens, T. Ochiai, An essential role of alternative splicing of c-myc suppressor FUSE-binding protein-interacting repressor in carcinogenesis, Cancer Res. 66 (2006) 1409–1417.
[7] J.P. Brouillet, F. Dufour, G. Lemamy, M. Garcia, N. Schlup, J. Grenier, J.C. Mani, H. Rochefort, Increased cathepsin D level in the serum of patients with metastatic breast carcinoma detected with a specific pro-cathepsin D immunoassay, Cancer 79 (1997) 2132–2136.
[8] A. Vashishta, S.S. Ohri, M. Proctor, M. Fusek, V. Vetvicka, Role of activation peptide of procathepsin D in proliferation and invasion of lung cancer cells, Anticancer Res. 26 (2006) 4163–4170.
[9] S.R. Chinni, C. Gercel-Taylor, G.E. Conner, D.D. Taylor, Cathepsin D antigenic epitopes identified by the humoral responses of ovarian cancer patients, Cancer Immunol. Immunother. 46 (1998) 48–54.

Biochemical and Biophysical Research Communications 420 (2012) 710–713

Contents lists available at SciVerse ScienceDirect

Biochemical and Biophysical Research Communications

journal homepage: www.elsevier.com/locate/ybbrc

Quantitative analysis of extension–torsion coupling of actin filaments

Shinji Matsushita [a,b,*], Yasuhiro Inoue [a,b], Taiji Adachi [a,b]

[a] Department Microengineering, Graduate School of Engineering, Kyoto University, Sakyo, Kyoto 606-8501, Japan
[b] Department of Biomechanics, Research Center for Nano Medical Engineering, Institute for Frontier Medical Sciences, Kyoto University, Sakyo, Kyoto 606-8507, Japan

ARTICLE INFO

Article history:
Received 3 February 2012
Available online 15 February 2012

Keywords:
Actin filament
Extension–torsion coupling stiffness
Thermal fluctuation
Molecular dynamics simulation
Cell mechanics
Molecular biomechanics

ABSTRACT

Actin filaments have a double-helix structure consisting of globular actin molecules. In many mechanical cellular activities, such as cell movement, division, and shape control, modulation of the extensional and torsional dynamics of the filament has been linked to regulatory actin-binding protein functions. Therefore, it is important to quantitatively evaluate extension–torsion coupling of filament to better understand the actin filament dynamics. In the present study, the extension–torsion coupling was investigated using molecular dynamics simulations. We constructed a model for the actin filament consisting of 14 actin subunits in an ionic solvent as a minimal functional unit, and analyzed longitudinal and twisting Brownian motions of the filament. We then derived the expected value of energy associated with extension and torsion at equilibrium, and evaluated the extension–torsion stiffness of the filament from the thermal fluctuations obtained from the MD simulations. The results demonstrated that as the analyzed sampling-window duration was increased, the extension–torsion coupling stiffness evaluated on a nanosecond scale tended to converge to a value of 7.6×10^{-11} N. The results obtained from this study will contribute to the understanding of biomechanical events, under mechanical tension and torque, involving extension–torsion coupling of filaments.

© 2012 Elsevier Inc. All rights reserved.

1. Introduction

Actin filaments, the major components of the actin cytoskeleton, display filament-scale extensional, torsional and bending motions. Because of their double-helix structure consisting of globular actin molecules, torsional motions of the filaments couple with bending and extensional ones. In order to clarify these unique mechanically coupled motions, various studies have measured mechanical properties of actin filaments such as their extensional stiffness [1,2], torsional stiffness [2–4], bending stiffness [5], and torsion-bending coupling stiffness [6]. However, extension–torsion coupling, which is fundamental in a variety of functional processes when the filaments are under mechanical forces such as tensions and torques, has not been evaluated.

Extension–torsion coupling in actin filaments is important for actomyosin interaction processes. Actin filaments serve as tracks for contractile myosin molecular motors, which produce tensile forces on the filaments when sliding along them. In addition, it has been reported that torque was also generated around the filament axis as a result of extension–torsion coupling [7], and this may play a biological role in muscle contraction [8]. Furthermore, experiments using gliding assays [9,10], in which actin filaments were stretched and moved by nonprocessive myosin motors, demonstrated that the gliding actin filaments twisted and rotated around their axes while moving over a surface decorated with myosins, indicating that this twisting motion is crucial for efficient gliding. Thus, tensions and torques modulate the gliding behavior of filaments via extension–torsion coupling during actomyosin interaction processes.

In addition, extension–torsion coupling is critical for actin dynamics involving mechanosensitive actin-binding proteins. For example, tension acting on the filaments modulates their twisting dynamics and thus the affinity of the actin depolymerizing proteins, cofilins, for the actin filaments [11]. Therefore, to understand biomechanical events involving mechanical tension and torque, it is essential to carry out a quantitative evaluation of the extensional and torsional behavior of the filaments, and in particular their extension–torsion coupling stiffness.

Our previous study [2] successfully evaluated the extensional and torsional stiffness of a single actin filament based on an analysis of thermal fluctuations in the molecular structure using a molecular dynamics (MD) method, and demonstrated that this was a valid method for evaluating the stiffness. Furthermore, for the actin monomers [12] and filaments [13–15], MD simulations have successfully analyzed their structural and dynamic properties. The present study quantitatively evaluates the extension–torsion

* Corresponding author. Address: Department of Biomechanics, Research Center for Nano Medical Engineering, Institute for Frontier Medical Sciences, Kyoto University, 53 Kawahara-cho, Shogoin, Sakyo, Kyoto 606-8507, Japan. Fax: +81 75751 4854.
E-mail address: matsushita@frontier.kyoto-u.ac.jp (S. Matsushita).

0006-291X/$ - see front matter © 2012 Elsevier Inc. All rights reserved.
doi:10.1016/j.bbrc.2012.02.048

coupling stiffness of a filament through a statistical-mechanics approach. We construct a model of a half-turn structure of an actin filament in an ionic solvent and analyze its longitudinal and twisting Brownian motions in thermal equilibrium using MD simulations. We then derive the expected value of energy associated with extension and torsion at equilibrium, including an extension–torsion coupling term, and evaluate the extension–torsion stiffness of the actin filament from the thermal fluctuations obtained from the MD simulations. Based on these results, we discuss the extension–torsion coupling of actin filament under uniaxial tension.

2. Materials and methods

The 2.0 Å resolution X-ray crystallographic structure of an actin filament, obtained from the protein data bank (PDB code: 1MVW) [16,17], is shown in Fig. 1. From an original structure derived from rabbit skeletal muscle with six myosins, an actin filament consisting of 14 actin subunits was extracted. ADP was then placed into the individual actin subunits in the filament, with the ADP coordinates being obtained from the ADP-bound monomer structure (PDB code: 1J6Z) [18]. The actin filament was placed in a water box, with the water molecules being simulated using the TIP3P model [19]. Counter ions, Na^+ and Cl^-, counter ions were added to the water to a total concentration of 30 mM.

MD simulation was performed using NAMD 2.6 [20] with the CHARMM27 force field for proteins [21]. We applied periodic boundary conditions for the simulations, in which van der Waals interactions were calculated with a cutoff of 13 Å and electrostatic interactions were calculated using the particle mesh Ewald method [22]. A multiple time-stepping algorithm was used with a two-fs step. The MD simulations were performed in an NPT ensemble (pressure = 1 atm, temperature = 310 K), in which the pressure was controlled by the hybrid Nosé-Hoover Langevin piston method and the temperature was controlled using Langevin dynamics. After relaxing the water molecules for 200 ps with all the protein atoms fixed, a free dynamics simulation for the entire system was performed for 12 ns to obtain the equilibrium structure.

To analyze the longitudinal and twisting behavior of the filament, the length of the filament, $L(t)$, is defined [2] as

$$L(t) = z_{\mathrm{plus}}(t) - z_{\mathrm{minus}}(t), \tag{1}$$

where $z_{\mathrm{plus}}(t)$ and $z_{\mathrm{minus}}(t)$ are the positions along the z-axis of the centers of mass of two actin subunits at the plus and minus ends, respectively, as shown in Fig. 1. In addition, the twist angle $\Theta(t)$ of the actin filament helix structure is defined [2] as

$$\Theta(t) = cos^{-1}\left(\frac{\boldsymbol{n}_{plus}(\boldsymbol{t})}{|\boldsymbol{n}_{plus}(\boldsymbol{t})|}\cdot\frac{\boldsymbol{n}_{minus}(\boldsymbol{t})}{|\boldsymbol{n}_{minus}(\boldsymbol{t})|}\right), \tag{2}$$

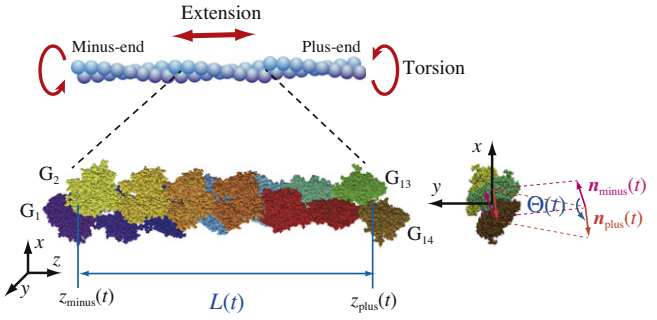


Fig. 1. Actin filament structural model used in the MD simulations. Filament length $L(t)$ is defined in Eq. (1) as the distance between the plus and minus ends of the filament. Twist angle $\Theta(t)$ is defined by Eq. (2) as the angle between the directional vectors of the plus and minus ends, projected onto the xy plane.

where $\boldsymbol{n}_{\mathrm{plus}}(t)$ and $\boldsymbol{n}_{\mathrm{minus}}(t)$ are the directional vectors between the centers of mass of two actin subunits at the plus and minus ends, respectively, projected onto the xy plane, as shown in Fig. 1.

3. Results and discussion

3.1. Theoretical evaluation for mean energy of thermally fluctuating filament with extension–torsion coupling

The extensional and torsional dynamics of the filament can be described using elastic properties that assume an isotropic and homogeneous material. The quadratic form of the total elastic free energy stored in the actin filament under deformation, that includes contributions from extension and torsion, as well as coupling that may exist between these motions, is defined by

$$U = \frac{1}{2}k_{\mathrm{ext}}\Delta L^2 + \frac{1}{2}k_{\mathrm{tor}}\Delta\Theta^2 + k_{\mathrm{ext-tor}}\Delta L\Delta\Theta, \tag{3}$$

where the first term corresponds to extension, the second to torsion, and the third to extension–torsion coupling; the constants k_{ext} and k_{tor} are the extensional and torsional stiffnesses of the half-turn filament structure, respectively, $k_{\mathrm{ext\text{-}tor}}$ is the extension–torsion coupling stiffness, and $\Delta\alpha$ ($\alpha = L, \Theta$) indicates the elongation and angle of twist from the mean value $<\alpha>$, i.e., $\Delta\alpha = \alpha - <\alpha>$. To conserve convexity of the quadratic energy form,

$$k_{\mathrm{ext}}k_{\mathrm{tor}} - k_{\mathrm{ext-tor}}^2 > 0 \tag{4}$$

is required.

Here, we derive the mean value of the extensional and torsional energies of the thermally fluctuating filament in a canonical ensemble, $\frac{1}{2}k_{\mathrm{ext}} < \Delta L^2 >$ and $\frac{1}{2}k_{\mathrm{tor}} < \Delta\Theta^2 >$, respectively, in terms of the extensional and torsional stiffness k_{ext} and k_{tor} and the extension–torsion coupling stiffness $k_{\mathrm{ext\text{-}tor}}$, as

$$\frac{1}{2}k_{\mathrm{ext}} < \Delta L^2 >= -k_{\mathrm{B}}Tk_{\mathrm{ext}}\frac{\partial}{\partial k_{\mathrm{ext}}}\log Z \qquad = \frac{1}{2}k_{\mathrm{B}}T\frac{1}{1-\frac{k_{\mathrm{ext-tor}}^2}{k_{\mathrm{ext}}k_{\mathrm{tor}}}}, \tag{5}$$

$$\frac{1}{2}k_{\mathrm{tor}} < \Delta\Theta^2 >= -k_{\mathrm{B}}Tk_{\mathrm{tor}}\frac{\partial}{\partial k_{\mathrm{tor}}}\log Z \qquad = \frac{1}{2}k_{\mathrm{B}}T\frac{1}{1-\frac{k_{\mathrm{ext-tor}}^2}{k_{\mathrm{ext}}k_{\mathrm{tor}}}}. \tag{6}$$

The extension–torsion coupling energy is similarly derived as

$$k_{\mathrm{ext-tor}} < \Delta L\Delta\Theta >= -k_{\mathrm{B}}Tk_{\mathrm{ext-tor}}\frac{\partial}{\partial k_{\mathrm{ext-tor}}}\log Z = k_{\mathrm{B}}T\frac{1}{1-\frac{k_{\mathrm{ext}}k_{\mathrm{tor}}}{k_{\mathrm{ext-tor}}^2}}, \tag{7}$$

where Z is the partition function

$$Z = \iint \exp(-\frac{U}{k_{\mathrm{B}}T})d(\Delta L)d(\Delta\Theta) = 2\pi k_{\mathrm{B}}T(k_{\mathrm{ext}}k_{\mathrm{tor}} - k_{\mathrm{ext-tor}}^2)^{-\frac{1}{2}}, \tag{8}$$

k_{B} is the Boltzmann constant, and T is the absolute temperature.

As indicated by Eqs. (5) and (6), the mean value of the extension and torsion energies, taking into account the effect of extension–torsion coupling, are larger than $\frac{1}{2}k_{\mathrm{B}}T$ by a coupling correction factor γ, defined as

$$\gamma = \left(1 - \frac{k_{\mathrm{ext-tor}}^2}{k_{\mathrm{ext}}k_{\mathrm{tor}}}\right)^{-1}. \tag{9}$$

Based on $k_{\mathrm{ext}} > 0$, $k_{\mathrm{ext}} > 0$ and Eq. (4), the coupling correction factor satisfies $\gamma \geqslant 1$. When the coupling correction factor $\gamma = 1$, that is $k_{\mathrm{ext\text{-}tor}} = 0$, Eqs. (5) and (6) correspond to the law of equipartition of energy in the absence of extension–torsion coupling.

In this way, the three stiffnesses in Eq. (3) can be associated with terms of extensional, torsional and extension–torsion coupling mo-

tions. We can evaluate the extension–torsion coupling stiffness $k_{\text{ext-tor}}$ by analyzing the thermal fluctuations of the filament.

3.2. Evaluation of the extension–torsion coupling stiffness using MD simulation

By analyzing $<\Delta L^2(t)>_{\Delta t}$, $<\Delta\Theta^2(t)>_{\Delta t}$ and $<\Delta L(t)\Delta\Theta(t)>_{\Delta t}$, where $<>_{\Delta t}$ indicates an average over the sampling-window duration Δt $\left(t-\frac{\Delta t}{2}\le t<t+\frac{\Delta t}{2}\right)$, based on the thermal fluctuations of the filament obtained from the MD simulations, we evaluate k_{ext}, k_{tor} and $k_{\text{ext-tor}}$ from Eqs. (5)–(7) as

$$k_{\text{ext}}=\frac{k_{\text{B}}T}{<\Delta L^2>_{\Delta t}\left(1-\frac{<\Delta L\Delta\Theta>^2_{\Delta t}}{<\Delta L^2>_{\Delta t}<\Delta\Theta^2>_{\Delta t}}\right)}, \tag{10}$$

$$k_{\text{tor}}=\frac{k_{\text{B}}T}{<\Delta\Theta^2>_{\Delta t}\left(1-\frac{<\Delta L\Delta\Theta>^2_{\Delta t}}{<\Delta L^2>_{\Delta t}<\Delta\Theta^2>_{\Delta t}}\right)}, \tag{11}$$

$$k_{\text{ext-tor}}=\frac{k_{\text{B}}T}{\frac{<\Delta L^2>_{\Delta t}<\Delta\Theta^2>_{\Delta t}}{<\Delta L\Delta\Theta>_{\Delta t}}-<\Delta L\Delta\Theta>_{\Delta t}}. \tag{12}$$

For the 25 ns equilibrium MD simulation, we monitored the filament length and angle of twist, and calculated the variance and the covariance in the elongation and angle of twist, $<\Delta L^2(t)>_{\Delta t}$, $<\Delta\Theta^2(t)>_{\Delta t}$ and $<\Delta L(t)\Delta\Theta(t)>_{\Delta t}$, for different sampling-window durations Δt = 0.5, 1.0, 2.0, 4.0, 8.0 and 16.0 ns. Fig. 2A shows the dependence of the covariance $<\Delta L(t)\ \Delta\Theta\ (t)>_{\Delta t}$ on Δt. From the figure, we found that the mean value of the covariance exhibits no significant dependence on Δt, and has an almost constant value of $\sim -5\times10^{-3}$ Å rad, whereas the standard deviation decreases with Δt increasing. For the longest sampling-window duration Δt = 16.0 ns, the mean value of covariance, $\overline{<\Delta L(t)\Delta\Theta(t)>_{16\text{ ns}}}$, was $\sim -5.4\times10^{-3}$ Å rad, the variance in the elongation, $\overline{<\Delta L^2(t)>_{16\text{ ns}}}$, was ~0.036 Å^2, and the variance in the angle of twist, $\overline{<\Delta\Theta^2(t)>_{16\text{ ns}}}$, was ~0.013 rad^2.

We then estimated the extension–torsion stiffness $k_{\text{ext-tor}}$ of the actin filament based on Eq. (12). Fig. 2B shows the mean value and standard deviation of $k_{\text{ext-tor}}$ plotted against Δt. As can be seen, $k_{\text{ext-tor}}$ tends to converge to a certain value as Δt increases. As a result, for the longest sampling-window duration Δt = 16.0 ns, the value of $k_{\text{ext-tor}}$ was estimated to be 7.6×10^{-11} N.

The convergence of the extension–torsion coupling stiffness may be related to the results of a previous study [2], where it was found that the variances in the elongation and angle of twist $<\Delta L^2(t)>_{\Delta t}$ < $\Delta\Theta$ 2$(t)>_{\Delta t}$ evaluated on a nanosecond scale gradually increased and began to converge to certain values with increasing Δt. Furthermore, because in the present study the covariance $<\Delta L(t)\ \Delta\Theta\ (t)>_{\Delta t}$ was almost independent of Δt, the convergence of the extension–torsion coupling stiffness to a certain value can be understood from Eq. (12). Therefore, to more quantitatively evaluate the extension–torsion coupling stiffness, more accurate information on the variance in the elongation and angle of twist might be required.

3.3. Theoretical prediction of deformation of actin filament under tension

Because we have obtained the extension–torsion coupling stiffness $k_{\text{ext-tor}}$ in the previous section, we substitute the value into the rod model for which the total elastic free energy can be described by Eq. (1), and predict the deformation of actin filament under tension. Under uniaxial tension without torques, the elongation and angle of twist of the filaments can be expressed as

$$\Delta L=\frac{F}{k_{\text{ext}}\left(1-\frac{k^2_{\text{ext-tor}}}{k_{\text{ext}}k_{\text{tor}}}\right)}=\frac{F}{k_{\text{ext}}}\gamma, \tag{13}$$

$$\Delta\Theta=\frac{F}{k_{\text{ext-tor}}\left(1-\frac{k_{\text{ext}}k_{\text{tor}}}{k^2_{\text{ext-tor}}}\right)}=\frac{F}{k_{\text{ext-tor}}}(1-\gamma), \tag{14}$$

where F is the axial tensile force acting on the filament and γ is the coupling correction factor. Substituting the values of stiffness obtained in the previous section into Eqs. (13) and (14), we obtain $\Delta L = 0.94F$ m and $\Delta\Theta = -2.1\times10^{8}F$ rad for a tensile force F N.

Because many actin-binding proteins interact with amino-acid residues in the vicinity of surface of the actin filament, the deformations at the surface of the rod are significant. On the surface of the rod with radius R = 40 Å, which almost equals to that of the actin filament, the torsional deformation is calculated as $R\Delta\Theta = -0.84F$ m. The absolute value of torsional deformation $|R\Delta\Theta|$ and the elongation ΔL against the tension F are shown in Fig. 3. As can be seen, the order of torsional deformation at the surface is comparable with that of the elongation, indicating that the extension–torsion coupling induces the significant torsional deformation when the tension acts on the actin filament.

For example, in cytoskeletal stress fibers, which are actin bundles containing ~10–30 actin filaments [23], the actin filaments are under tension due to actomyosin interactions. Previous studies reported that tensions generated in the stress fibers were several

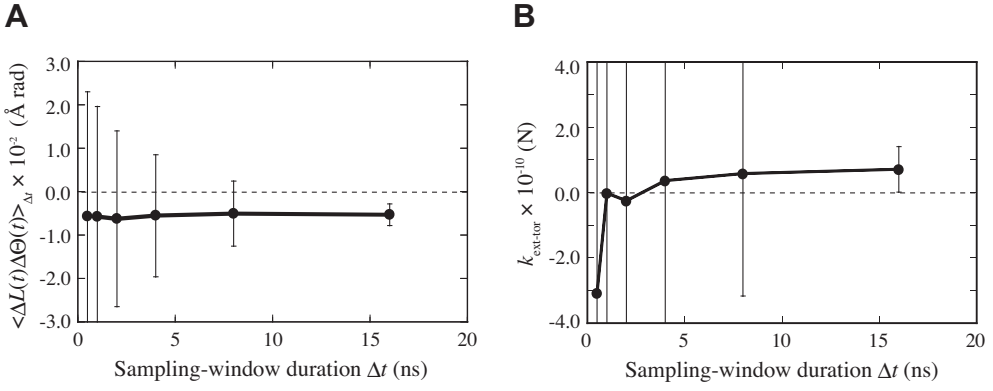


Fig. 2. Evaluation of extension–torsion coupling stiffness $k_{\text{ext-tor}}$. (A) shows the covariance in elongation and angle of twist at equilibrium $<\Delta L(t)\Delta\Theta(t)>_{\Delta t}$ for different sampling-window durations Δt. (B) shows extension–torsion coupling stiffness $k_{\text{ext-tor}}$. The black solid shows the mean value and the error bars represent the standard deviation, respectively.

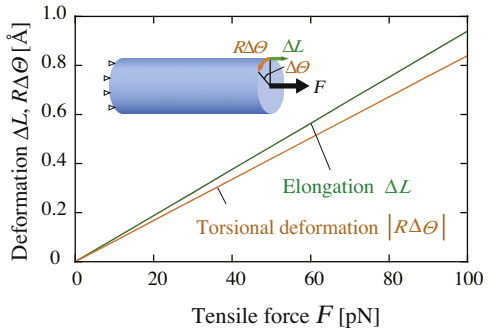


Fig. 3. Deformation of the half-turn filament under uniaxial tensile force. The elongation and torsional deformation at the surface of the rod ΔL, $R\Delta\Theta$ are plotted. The torsional deformation is comparable with the elongation due to the extension–torsion coupling.

nN [24,25], indicating that single actin filaments in stress fiber were under tensions of up to ~100 pN. As shown in Fig. 3, tension of 100 pN induces the elongation of ~0.9 Å and the torsional deformation of ~0.8 Å. These structural changes may be critical for biochemical events, such as binding of actin regulatory proteins to the filament.

3.4. Future perspectives

To clarify the mechanical behavior of actin filaments, various coarse-grained (CG) and continuum models have been developed, such as the Brownian dynamics model [13,14,26,27] and the continuum model [28,29]. By carrying out simulations using these models, the behavior of actin filaments can be analyzed on larger spatiotemporal scales than is possible in MD simulations. In particular, helical filament models have been proposed based on the wormlike chain model [30] and the Cosserat rod model [29]. The Cosserat rod model, which has the advantage of describing the geometrical microstructure of the filament, allows the relationship between the loading force and the twisting deformation to be considered. In CG and continuum simulations, the extension–torsion coupling stiffness is a fundamental parameter characterizing the filament dynamics, because the mechanical behavior of actin filaments and their interactions with actin regulatory proteins strongly depend on the nanomechanical properties of the filament. Therefore, by embedding the extension–torsion coupling stiffness obtained from our MD analysis into CG and continuum simulations, it is possible to carry out multiscale quantitative analyses of actin filaments.

4. Conflict of interest

None.

Acknowledgments

This work was supported in part by the Funding Program for the Next Generation World-Leading Researchers (LR017) from the Ministry of Education, Culture, Sports, Science and Technology in Japan. The computing system was provided by Research and Development of the Next-Generation Integrated Simulation of Living Matter, a part of the Development and Use of the Next-Generation Supercomputer Project. Shinji Matsushita was supported by the Japan Society for the Promotion of Science (JSPS) as a JSPS Fellow.

References

[1] H. Kojima, A. Ishijima, T. Yanagida, Direct measurement of stiffness of single actin-filaments with and without tropomyosin by in-vitro nanomanipulation, Proceedings of the National Academy of Sciences of the United States of America 91 (1994) 12962–12966.
[2] S. Matsushita, T. Adachi, Y. Inoue, M. Hojo, M. Sokabe, Evaluation of extensional and torsional stiffness of single actin filaments by molecular dynamics analysis, Journal of Biomechanics 43 (2010) 3162–3167.
[3] Y. Tsuda, H. Yasutake, A. Ishijima, T. Yanagida, Torsional rigidity of single actin filaments and actin-actin bond breaking force under torsion measured directly by in vitro micromanipulation, Proceedings of the National Academy of Sciences of the United States of America 93 (1996) 12937–12942.
[4] E. Prochniewicz, N. Janson, D.D. Thomas, E.M. De La Cruz, Cofilin increases the torsional flexibility and dynamics of actin filaments, Journal of Molecular Biology 353 (2005) 990–1000.
[5] B.R. McCullough, L. Blanchoin, J.L. Martiel, E.M. De La Cruz, Cofilin increases the bending flexibility of actin filaments: implications for severing and cell mechanics, Journal of Molecular Biology 381 (2008) 550–558.
[6] E.M. De La Cruz, J. Roland, B.R. McCullough, L. Blanchoin, J.L. Martiel, Origin of twist-bend coupling in actin filaments, Biophysical Journal 99 (2010) 1852–1860.
[7] J.M. Gillis, E.J. Obrien, Effect of calcium-ions on structure of reconstituted muscle thin-filaments, Journal of Molecular Biology 99 (1975) 445–451.
[8] Y. Maeda, I. Matsubara, N. Yagi, Structural-changes in thin-filaments of crab striated-muscle, Journal of Molecular Biology 127 (1979) 191–201.
[9] A. Vilfan, Twirling motion of actin filaments in gliding assays with nonprocessive myosin motors, Biophysical Journal 97 (2009) 1130–1137.
[10] T. Nishizaka, T. Yagi, Y. Tanaka, S. Ishiwata, Right-handed rotation of an actin filament in an invitro motile system, Nature 361 (1993) 269–271.
[11] K. Hayakawa, H. Tatsumi, M. Sokabe, Actin stress fibers transmit and focus force to activate mechanosensitive channels, Journal of Cell Science 121 (2008) 496–503.
[12] P. Dalhaimer, T.D. Pollard, B.J. Nolen, Nucleotide-mediated conformational changes of monomeric actin and Arp3 studied by molecular dynamics simulations, Journal of Molecular Biology 376 (2008) 166–183.
[13] J.W. Chu, G.A. Voth, Allostery of actin filaments: molecular dynamics simulations and coarse-grained analysis, Proceedings of the National Academy of Sciences of the United States of America 102 (2005) 13111–13116.
[14] J.W. Chu, G.A. Voth, Coarse-grained modeling of the actin filament derived from atomistic-scale simulations, Biophysical Journal 90 (2006) 1572–1582.
[15] J. Pfaendtner, E. Lyman, T.D. Pollard, G.A. Voth, Structure and dynamics of the actin filament, Journal of Molecular Biology 396 (2010) 252–263.
[16] L.F. Chen, H. Winkler, M.K. Reedy, M.C. Reedy, K.A. Taylor, Molecular modeling of averaged rigor crossbridges from tomograms of insect flight muscle, Journal of Structural Biology 138 (2002) 92–104.
[17] K.C. Holmes, D. Popp, W. Gebhard, W. Kabsch, Atomic model of the actin filament, Nature 347 (1990) 44–49.
[18] L.R. Otterbein, P. Graceffa, R. Dominguez, The crystal structure of uncomplexed actin in the ADP state, Science 293 (2001) 708–711.
[19] W.L. Jorgensen, J. Chandrasekhar, J.D. Madura, R.W. Impey, M.L. Klein, Comparison of simple potemtial functions for simulating liquid water, Journal of Chemical Physics 79 (1983) 926–935.
[20] L. Kale, R. Skeel, M. Bhandarkar, R. Brunner, A. Gursoy, N. Krawetz, J. Phillips, A. Shinozaki, K. Varadarajan, K. Schulten, NAMD2: greater scalability for parallel molecular dynamics, Journal of Computational Physics 151 (1999) 283–312.
[21] A.D. MacKerell, D. Bashford, M. Bellott, R.L. Dunbrack, J.D. Evanseck, M.J. Field, S. Fischer, J. Gao, H. Guo, S. Ha, D. Joseph-McCarthy, L. Kuchnir, K. Kuczera, F.T.K. Lau, C. Mattos, S. Michnick, T. Ngo, D.T. Nguyen, B. Prodhom, W.E. Reiher, B. Roux, M. Schlenkrich, J.C. Smith, R. Stote, J. Straub, M. Watanabe, J. Wiorkiewicz-Kuczera, D. Yin, M. Karplus, All-atom empirical potential for molecular modeling and dynamics studies of proteins, Journal of Physical Chemistry B 102 (1998) 3586–3616.
[22] T. Darden, D. York, L. Pedersen, Paticle mesh Ewald - an N.log(N) method for Ewald sums in large systems, Journal of Chemical Physics 98 (1993) 10089–10092.
[23] L.P. Cramer, M. Siebert, T.J. Mitchison, Identification of novel graded polarity actin filament bundles in locomoting heart fibroblasts: implications for the generation of motile force, Journal of Cell Biology 136 (1997) 1287–1305.
[24] S. Sugita, T. Adachi, Y. Ueki, M. Sato, A novel method for measuring tension generated in stress fibers by applying external forces, Biophysical Journal 101 (2011) 53–60.
[25] J.L. Tan, J. Tien, D.M. Pirone, D.S. Gray, K. Bhadriraju, C.S. Chen, Cells lying on a bed of microneedles: an approach to isolate mechanical force, Proceedings of the National Academy of Sciences of the United States of America 100 (2003) 1484–1489.
[26] Y. Shimada, T. Adachi, Y. Inoue, M. Hojo, Coarse-grained modeling and simulation of actin filament behaviour based on Brownian dynamics method, Molecular and Cellular Biomechanics 6 (2009) 161–173.
[27] D. Sept, A.H. Elcock, J.A. McCammon, Computer simulations of actin polymerization can explain the barbed-pointed end asymmetry, Journal of Molecular Biology 294 (1999) 1181–1189.
[28] D.M. Ming, Y.F. Kong, Y.H. Wu, J.P. Ma, Simulation of F-actin filaments of several microns, Biophysical Journal 85 (2003) 27–35.
[29] H. Yamaoka, T. Adachi, Coupling between axial stretch and bending/twisting deformation of actin filaments caused by a mismatched centroid from the center axis, International Journal of Mechanical Sciences 52 (2010) 329–333.
[30] C. Bouchiat, M.D. Wang, J.F. Allemand, T. Strick, S.M. Block, V. Croquette, Estimating the persistence length of a worm-like chain molecule from force-extension measurements, Biophysical Journal 76 (1999) 409–413.

Biochemical and Biophysical Research Communications 420 (2012) 714–720

Contents lists available at SciVerse ScienceDirect

Biochemical and Biophysical Research Communications

journal homepage: www.elsevier.com/locate/ybbrc

NAMPT pathway is involved in the FOXO3a-mediated regulation of *GADD45A* expression

Basant Kumar Thakur [a,b,*,1], Yannick Lippka [b,1], Tino Dittrich [a,b], Prakash Chandra [c], Julia Skokowa [b], Karl Welte [b,*]

[a] Department of Pediatric Hematology and Oncology, Hannover Medical School, Carl Neuberg Str-1, 30625 Hannover, Germany
[b] Department of Molecular Hematopoiesis, Hannover Medical School, Carl Neuberg Str-1, 30625 Hannover, Germany
[c] Frankfurt University Medical School, Building 57, Theodor-Stern-Kai-7, 60590 Frankfurt, Germany

ARTICLE INFO

Article history:
Received 1 March 2012
Available online 10 March 2012

Keywords:
FOXO3a
Acetylation
NAMPT
Sirtuins (SIRTs)
FK866

ABSTRACT

Nicotinamide-phosphoribosyltransferase (NAMPT), induced under stress, converts nicotinamide (NA) to nicotinamide mononucleotide (NMN), which then reacts with ATP to regenerate NAD^+. Despite the pivotal role of NAD^+ in metabolic reactions, the molecular pathways triggered by the intracellular changes in NAD^+ level in cancer cells are largely unknown. Growth Arrest and DNA Damage-inducible Gene (*GADD45A*) is regulated by multiple cellular factors which play an important role in the control of cell-cycle checkpoint, DNA repair process and signal transduction. The present study was designed to assess the significance of intracellular NAD^+ levels on the regulation of *GADD45A* expression. The results of this study demonstrate an inverse relationship between NAMPT expression and the regulation of *GADD45A* gene. Thus, an overexpression of NAMPT led to a decreased expression of *GADD45A*, whereas, the inhibition of NAMPT by the known chemical inhibitor FK866 increased the expression of *GADD45A* in cells. Inhibition of SIRT1, an NAD^+-dependent deacetylase, using shRNA also led to an increased expression of *GADD45A* gene. In further experiments we could show that the increased expression of *GADD45A* under the above experimental conditions, NAMPT inhibition by FK866, involves acetylation of FOXO3a, a member of the important family of forkhead (FOXO) proteins. This knowledge should contribute to our understanding of the role played by NAMPT and SIRT1 in the regulation of *GADD45A* expression by FOXO3a.
© 2012 Elsevier Inc. All rights reserved.

1. Introduction

GADD45 belongs to the family of stress-response genes, and its protein products regulate several cellular processes that are important to maintain the homeostasis of the cell [1,2]. These are highly inducible genes, and their expression is altered by genotoxic stress and metabolic status of the cell. GADD45A, an important member of this family, is a 18 kDa acidic protein, which is predominantly localized in the nucleus [3]. *GADD45A* was first found to be a direct target of p53 but since then several other factors have been shown to regulate its function in p53-independent manner [1]. Recently, it has been reported that *GADD45A* is a direct target gene of the tumor suppressor FOXO3a [4]. FOXO3a is a member of the important family of forkhead (FOXO) proteins which modulates the expression of several genes involved in many cell type-specific functions critical in aging, cancer and differentiation [5,6]. The functions of FOXO3a are regulated by several posttranslational modifications such as phosphorylation, ubiquitination and acetylation [6–11]. In the nucleus, FOXO3a is under tight regulation of acetylation and deacetylation. In the presence of stress factors such as H_2O_2, the acetylation of FOXO3a by histone acetylase, CREB binding protein (CREBBP) and P300 [12,13] is important for its transcriptional function. This pre-acetylated nuclear FOXO protein is subject to deacetylation by mammalian Sirtuins (SIRTs) which are NAD^+ dependent deacetylases [14]. The flux of FOXO acetylation and deacetylation regulates differentially the genes critical in fine tuning the cellular response to extracellular stress.

SIRT1, the founding member of the Sirtuin (SIRT) family has been shown to exert both, positive as well as negative impact on FOXO dependent gene expression [12,14–16]. More in-depth studies are required to understand how SIRT1 regulates FOXO3a targets. SIRT1 mediated deacetylation of FOXO3a switches its tumor suppressor function away from cell death towards stress resistance [17]. Since SIRTs depend on NAD^+ to execute deacetylation reactions, changes in NAD^+ levels, under stress and disease conditions, might alter the expression of genes regulated by FOXO3a.

Although it is known that *GADD45A* is regulated under different types of stresses or changes in extracellular conditions, its regulation under changes in intracellular NAD^+ levels is largely unknown.

* Corresponding authors. Fax: +49 511 532 9200.
E-mail addresses: thakur.basant@mh-hannover.de (B.K. Thakur), Welte.Karl.H@mh-hannover.de (K. Welte).
[1] These authors contributed equally to the work.

0006-291X/$ - see front matter © 2012 Elsevier Inc. All rights reserved.
http://dx.doi.org/10.1016/j.bbrc.2012.03.017

In this study, we demonstrate the role of NAMPT/NAD^+/SIRT1 pathway in the regulation of *GADD45A* expression by controlling the acetylation levels of FOXO3a.

2. Materials and methods

2.1. Cell lines

HEK 293T cells obtained from DSMZ (Cat No# ACC 635) were cultured in Dulbecco's modified Eagle's medium, high glucose 4.5 g/l, without L-Glu (PAA) supplemented with 10% fetal calf serum; 1% L-glutamine, 1% penicillin and 1% streptomycin at 37 °C in a humidified atmosphere of 5% CO_2. Cells were split every 2 or 3 d 1:4 or 1:5 depending on the density.

2.2. Transient transfection

Cells (0.4×10^6) were seeded in a 6 well plate (0.2×10^6/ml) and later transfected with Lipofectamin 2000 (Invitrogen) according to manufacturer's protocol. Cells were harvested after 24 h.

2.3. Virus transduction

Production of viral particles was performed by transfection of 293T cells with target vector, pGagpol vector, pEnv-VSVG vector and REV vector. Supernatant with viral particles containing shRNA sequence or overexpression construct were harvested after 36 h of transfection. For transduction cells (0.1×10^6 in 1 ml) were seeded in a 24 well plate and 24 h later 50 μl of the harvested virus supernatant and 5 μl of polybrene (2 μg/ml) was added on the cells. Cells were incubated for 1 h in incubator and afterwards centrifuged for 2 h at 37 °C and 700×*g*. After 16 h in the incubator the medium was replaced. Transduced cells positive for fluorescence were selected using FACS based method and were further cultured for the experiments.

2.4. Plasmids

For silencing of FOXO3a oligonucleotide:
Sense: GAT CCC CGG CAC AGA GTT GGA TGA AGT TTC AAG AGA ACT TCA TCC AAC TCT GTG CTT TTT GG AAA and Antisense: AGC TTT TCC AAA AAG CAC AGA GTT GGA TGA AGT TCT CTT GAA ACT TCATCC AAC TCT GTG CCG GG against FOXO3a was purchased from Qiagen and cloned into pSUPER and further sub-cloned into pRRL.SF.DsRedEx.pre. For overexpression of NAMPT we used pcDNA3.1 construct containing cDNA of NAMPT. The plasmids pcDNA3-HA-FOXO3a, FG12-shSIRT1-Scramble and FG-shSIRT1 were kindly provided by Dr. Qiang Tong. The FHRE-Luc (#1789) construct was purchased from Addgene.

2.5. Reporter gene assay

Reporter gene assay was performed using Dual-Luciferase Reporter Assay System (Promega). HEK293T cells were grown in 96 well plate with the density of 1.5×10^4 cells per 100 μl each well and transfected ($n = 6$) with 1 μg/well of target plasmids and 0.2 μg/well of reporter constructs. After 24 h cells were lysed in passive lysis buffer and the firefly luciferase and renilla luciferase activity was quantified according to manufacturer's protocol. Results are given as mean ± standard error.

2.6. Measurement of intracellular NAD^+ and ATP

Cells (0.1×10^6) were seeded in a 12 well plate (0.1×10^6/ml) and treated for the indicated time points with FK866. From that suspension 100 μl were transferred into an opaque plate for measurement of ATP with CellTiter Glo Luminescent Cell Viability Assay (Promega) according to manufacturer's instructions. The remaining cells were washed once in ice cold PBS and pelleted. The pellet was then homogenized in NAD^+ extraction buffer from the EnzyChrom NAD^+/NADH Assay Kit (Biotrend). Measurements were performed according to manufacturer's instructions.

2.7. Western blotting

Equal number of pelleted cells were washed with ice-cold phosphate-buffered saline (PBS), again pelleted and resuspended in 1.5× lämmli buffer (15% glycerol, 3% SDS, 4.5% β-mercaptoethanol, 0.2% bromophenol blue in 100 mM Tris/HCl [pH 6.8]), subsequently boiled at 95 °C for 5 min and spun in a microcentrifuge for 5 min. Samples were separated in 10% sodium dodecyl sulfate–polyacrylamide gels and transferred onto nitrocellulose membrane (Amersham Bioscience). The membranes were blocked with 5% non-fat dry milk-TBS-T (10 mM Tris/HCl [pH 8.0], 150 mM NaCl, 0.1% Tween 20) for 1 h at room temperature and incubated with primary antibody in TBS-T for 1 h at room temperature or overnight at 4 °C. After washing four times each for 5 min in TBS-T membranes were incubated with horseradish peroxidase-conjugated secondary antibody (Santa Cruz Biotechnology) for 1 h at room temperature. After washing four times each for 5 min protein bands were visualized by enhanced chemiluminescence reagent (Pierce) and by exposure to X-ray film (Agfa).

2.8. Antibodies

Antibodies to rabbit polyclonal FOXO3a (cat.-no: #9467), acetylated Lysine (cat.-no: #9441) and SIRT1 (cat.-no: #2310) were obtained from Cell Signaling. Mouse monoclonal antibody to β-actin (sc-130300) was obtained from Santa Cruz Biotechnology and rabbit polyclonal antibody to NAMPT (cat.-no: H-003-84) was obtained from Phoenix Pharmaceuticals.

2.9. Quantitative real-time PCR

RNA of cells was isolated using RNeasy Micro Kit (Qiagen). Reverse transcription was performed with 500 ng of RNA and reagents of Omniscript Reverse Transcription Kit, both according to the manufacturer's protocol. The relative mRNA levels of target genes were measured as triplicates using SYBR Green Master Mix (Applied Biosystems) and the following oligonucleotide primers (Qiagen) were used: β-actin-sense, 5′-TTC CTG GGC ATG GAG TC-3′ and β-actin-antisense, 5′-AGG TCT TTG CGG ATG TC-3′; GADD45A-sense, GTG GTG TTG TGC CTG CTG and antisense, AGG ATG TTG ATG TCG TTC TCG; FOXO3a-sense, CCC AGC CTA ACC AGG GAA GT and antisense, AGC GCC CTG GGT TTG G; NAMPT-sense, AGG GCT TTG TCA TTC CCA GA and antisense, GCC AGC AGT CTC TTG GGA AG; and SIRT1-sense CAA CTT GTA CGA CGA AGA C and SIRT1-antisense, TCA TCA CCG AAC AGA AGG. The mRNA levels were determined using the ΔΔ Ct method and results are shown as mean ± standard error.

2.10. Apoptosis assay

Apoptosis analysis was performed using the Annexin V Apoptosis Detection Kit (BD Pharmingen) according to manufacturer's instructions. Flow cytometry measurements were performed on a Navios (Beckman Coulter).

3. Results

3.1. Overexpression of NAMPT decreases the levels of GADD45A mRNA

GADD45A is an inducible gene and its protein product is important in maintaining the integrity of a cell. NAMPT is involved in the biosynthesis of NAD^+, and our group and others have shown that overexpression of NAMPT in diseased conditions is associated with high levels of intracellular NAD^+ [18]. In order to examine whether the modulation of intracellular NAD^+ levels influences the expression of *GADD45A*, we transduced 293T cells using lentiviral vector expressing cDNA of NAMPT and measured the GADD45A mRNA expression. Overexpression of NAMPT was confirmed both, at mRNA (Fig. 1A) and protein levels (Fig. 1B), using real time PCR (RT-PCR) and Western blot respectively. Strong inhibition of GADD45A mRNA expression was observed in the cells overexpressing NAMPT when was compared against mock-transduced control cells (Fig. 1C).

3.2. The expression of GADD45A mRNA is regulated by SIRT1

SIRTs belong to the family of class III HDAC and they strictly depend on NAD^+ for mediating deacetylation of target proteins [19]. SIRT1, the founding member of this family, regulates diverse cellular processes, like metabolism, aging and cancer. Therefore, we asked whether SIRT1 is involved in NAMPT mediated down regulation of GADD45A. To check the effect of SIRT1 on *GADD45A* expression, we performed shRNA mediated knock down of SIRT1. Knock down of SIRT1 was confirmed at mRNA levels using RT-PCR (Fig. 2A) and at protein levels using Western blotting (Fig. 2B). Expression of GADD45A mRNA was modestly, but significantly increased in SIRT1 knock down cells when compared against sh Scramble transduced control cells (Fig. 2C).

3.3. Inhibition of NAMPT by FK866 induced apoptosis in 293T cells and increased acetylation of FOXO3a

The tumor suppressor proteins p53 and FOXO3a are among the major targets of SIRT1. FOXO3a is subject to various posttranscriptional modifications, and these modifications determine its specificity towards the target genes. To address the mechanism behind the FK866 mediated cell death we performed Annexin V based apoptosis assay after challenging 293T cells with two different concentrations of FK866 (10 nM and 100 nM). We observed a dose dependent increase in apoptosis in 293T cells after treatment with FK866 (Fig. 3A).

The FK866 mediated killing of cancer cells involves reduction in intracellular levels of NAD^+, followed by ATP depletion. In analogy to this, we have measured the NAD^+ and ATP levels in the 293T cells after treatment with 10 and 100 nM FK866 for the indicated incubation periods. Indeed, we observed the initial decrease in

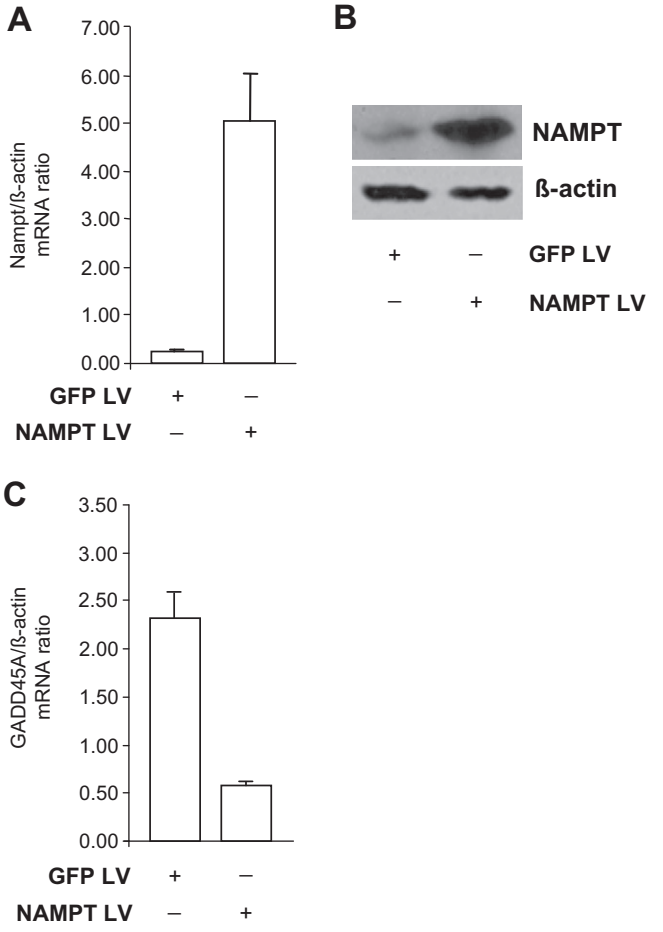


Fig. 1. Overexpression of NAMPT decreases the levels of GADD45A mRNA. 293T cells were transduced with mock GFP lentiviral (GFP LV) particles or LV particles containing NAMPT cDNA (NAMPT LV). (A) The endogenous mRNA levels of NAMPT were measured by real time PCR and (B) Western blot using NAMPT antibody was performed to check the efficiency of the transduction. (C) Endogenous GADD45A mRNA levels were detected by Real Time PCR in NAMPT overexpressed cells.

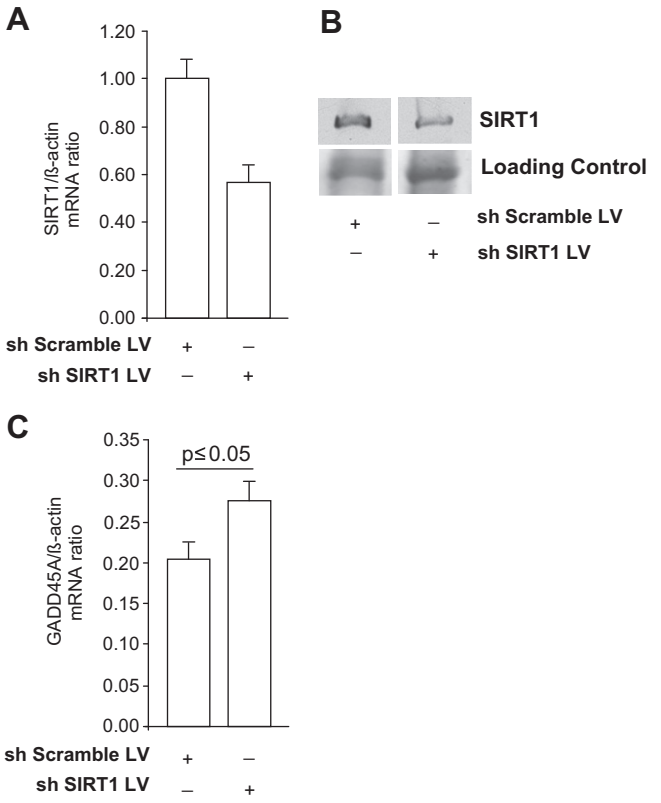


Fig. 2. The expression of GADD45A mRNA is regulated by SIRT1. Cells were transduced with control sh Scramble lentiviral (sh Scramble LV) particles or LV particles containing shRNA against SIRT1 (sh SIRT1 LV), and (A) endogenous SIRT1 mRNA levels were measured by real time PCR. (B) Western blot was performed using antibody against SIRT1 to check the efficiency of SIRT1 knockdown at protein levels. (C) Endogenous GADD45A mRNA levels were detected by Real Time PCR in SIRT1 knockdown cells. Results are shown as mean ± standard error. For calculation of the *p*-value we used an unpaired, two-tailed student's *t* test. The results were considered significant when $p \leqslant 0.05$.

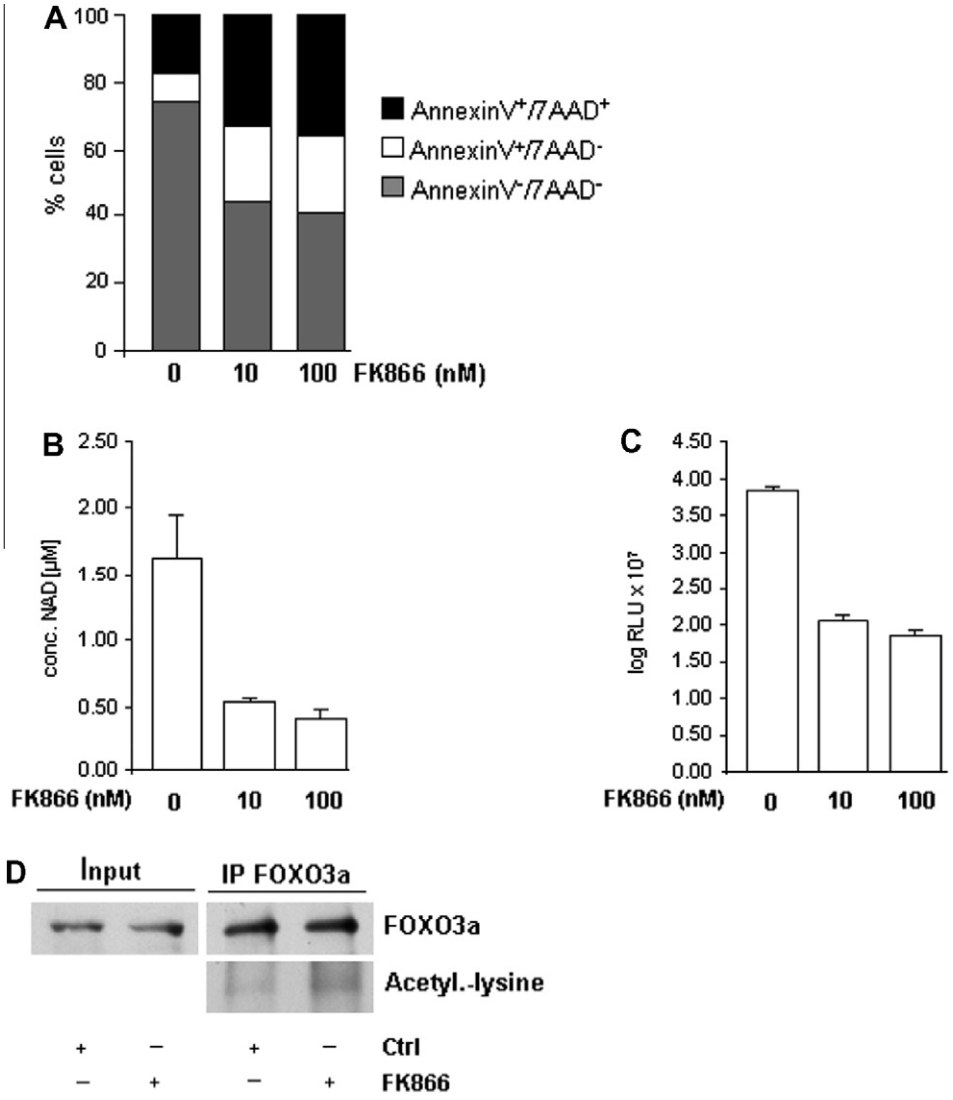


Fig. 3. Inhibition of NAMPT by FK866 induced apoptosis in 293T cells and increased acetylation of FOXO3a. (A) Percentage of Annexin V positive cells indicating apoptosis compared to viable cells was measured 48 h after treatment of 293T cells with indicated concentrations of FK866. (B) Intracellular NAD^+ concentrations were measured after treating 293T cells with 10 and 100 nM of FK866 for 24 h. (C) Intracellular levels of ATP were measured after treating 293T cells with 10 and 100 nM of FK866 for 24 h. (D) Immunoprecipitates of endogenous FOXO3a IP from 293T cell lysate were subjected to immunoblot analysis using acetylated lysine antibody. For loading control total FOXO3a was detected using FOXO3a antibody.

NAD^+ (Fig. 3B) levels followed by depletion of cellular ATP (Fig. 3C). Next, we addressed the cross talk between FOXO3a and SIRT1 in context to *GADD45A* regulation. To study this, we performed immunoprecipitation (IP) experiments with FOXO3a antibody in 293T cells treated or untreated with FK866. The IP fractions were subjected to immunoblotting using antibody against acetylated lysine. We observed a significant increase in FOXO3a acetylation in samples treated with FK866 when compared against untreated control (Fig. 3D).

3.4. Acetylation of FOXO3a is involved in regulation of GADD45A expression via NAMPT/NAD^+/SIRT1 pathway

We next explored whether decrease in FOXO3a acetylation by SIRT1 negatively regulates the transcriptional activity of FOXO3a. Since FOXO3a positively regulates the activity of FOXO response element (FHBE) [20], we monitored the transactivating potential of FOXO3a by transiently transfecting a luciferase reporter under the control of FHBE in the absence or presence of SIRT1. The ability of FOXO3a to transactivate FHBE was strongly reduced in presence of SIRT1 (Fig. 4A).

To address that FOXO3a directly regulates the expression of endogenous GADD45A mRNA, we performed shRNA based knock down of FOXO3a in 293T cells. The knock down of FOXO3a was confirmed at both, mRNA and protein levels using real time PCR (Fig. 4B) and Western blot (Fig. 4C) respectively. Strong reduction of GADD45A mRNA expression was observed in FOXO3a knock down cells (Fig. 4D), suggesting that FOXO3a positively regulates expression of *GADD45A*. To investigate the role of acetylation of FOXO3a in the regulation of *GADD45A* expression, we measured GADD45A mRNA levels in control and FOXO3a knockdown cells, in the presence or absence of FK866. In mock transduced, control cells, treatment with FK866 increased mRNA levels of GADD45A, and knock down of FOXO3a attenuated the FK866 mediated elevation of GADD45A mRNA (Fig. 4E).

4. Discussion

The interplay between FOXO3a, SIRT1 and GADD45A is the key for the modulation of several cellular processes, including response to extracellular stress, longevity, and tumor suppression. In this

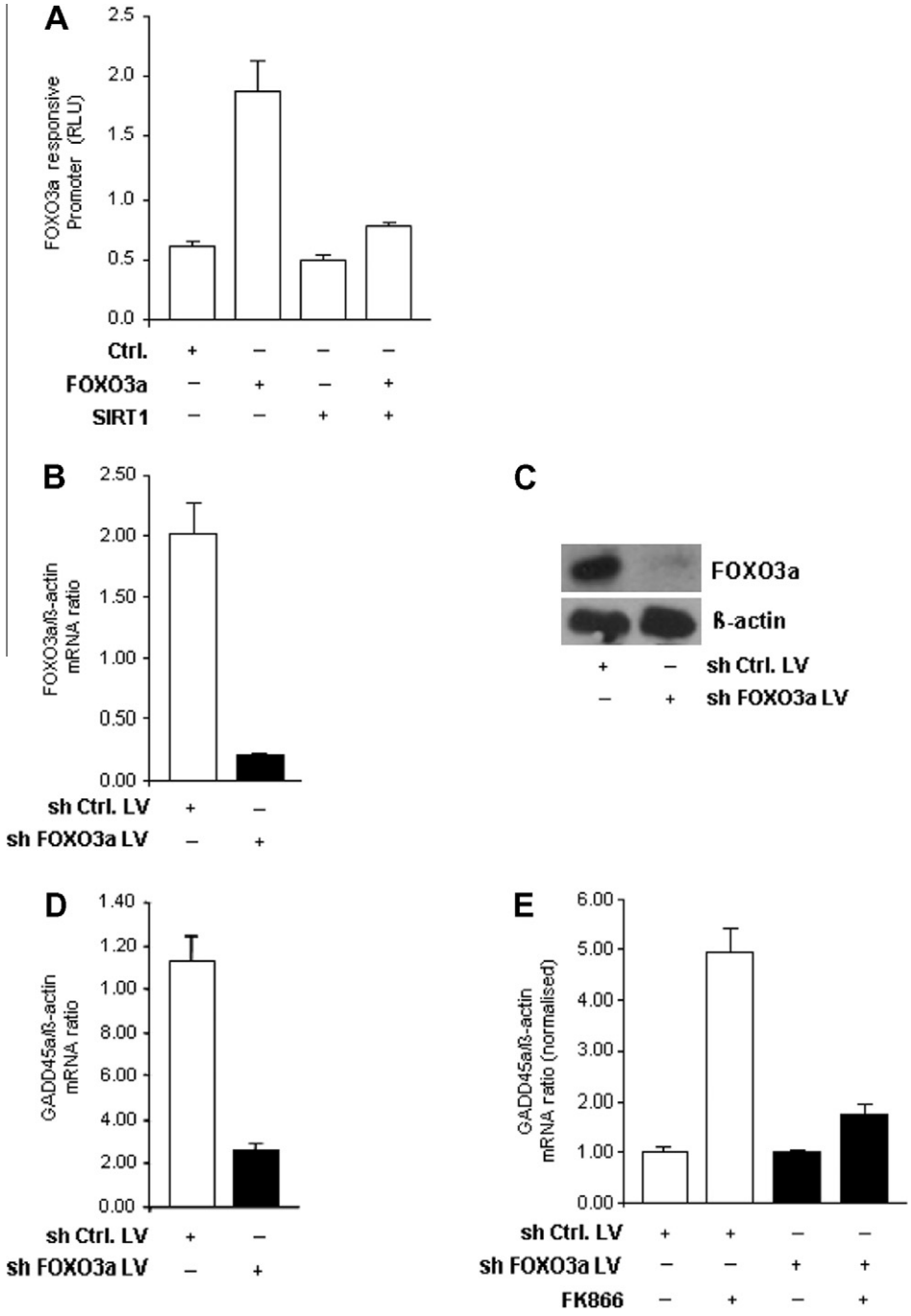


Fig. 4. Acetylation of FOXO3a is involved in regulation of GADD45A mRNA expression via NAMPT/NAD$^+$/SIRT1 pathway. (A) Reporter gene assay was performed by transiently transfecting a luciferase reporter under the control of FHBE in the absence or presence of FOXO3a and SIRT1. Cells were transduced with lentiviral vector either containing control shRNA lentiviral (sh Ctrl.) particles or FOXO3a shRNA lentiviral (sh FOXO3aLV) particles and endogenous expression of FOXO3a mRNA (B) and protein (C) was measured by real time PCR and Western blot respectively. (D) Endogenous GADD45A mRNA levels were detected by Real Time PCR in control and sh FOXO3a cells. (E) 293T cells transduced with control shRNA lentiviral or FOXO3a shRNA lentiviral, treated without or with 10 nM of FK866 and real time PCR was performed to measure the endogenous levels of GADD45A mRNA.

interplay, FOXO3a mainly responds to the extracellular signalling, SIRT1 tunes the activity of FOXO3a and GADD45A executes the signal downstream. SIRT1, the founding member of class III HDACs is a critical regulator of FOXO3a function. In context to aging, SIRT1 mediated deacetylation of FOXO3a retards the process of aging and therefore promotes longevity. On the contrary, SIRT1 mediated deacetylation of FOXO3a abrogates its tumor suppressor functions. How the function of SIRT1 is modulated under different cellular context is largely unknown, and is currently an interesting area of investigation.

Recently, we have shown that NAMPT/NAD$^+$ mediated activation of SIRT1 promotes myeloid differentiation in patients with severe congenital neutropenia [18]. On the other hand, hyperactivation of SIRT1 by overexpression of NAMPT may lead to leukemogenic transformation. FK866, a specific inhibitor of NAMPT, exerts cytotoxic activity on wide range of cancer cells via depletion of intracellular NAD$^+$ content. Although, it is quite clear that FK866 possesses anti-cancer activity, the mechanism underlying its action is largely unknown. Here we identified *GADD45A* as one of the downstream targets whose expression is regu-

lated by NAMPT/NAD$^+$/SIRT1 pathway. This is based on three lines of evidence: (1) overexpression of NAMPT, which increases NAD$^+$ levels, decreases the *GADD45A* expression (2) inhibition of SIRT1 by shRNA knock down of SIRT1 increases the *GADD45A* expression and (3) inhibition of NAMPT by FK866, which decreases NAD$^+$, increases the *GADD45A* expression.

GADD45A protein connects several signaling pathways induced by varieties of extracellular or intracellular stresses. Understanding the mechanism by which the upstream factors regulate the expression of *GADD45A* upon depletion of intracellular NAD$^+$ will lead to better approaches to target malignant cells. Our recently published data suggest that FK866 mediated killing of AML cells involves acetylation dependent dephosphorylation of AKT [21]. Decrease in NAD$^+$ levels in cancer cells can have global influence on wide range of SIRT1 dependent downstream targets. To identify the upstream regulator of *GADD45A* expression upon decrease in NAD$^+$ levels, we performed immunoblot analysis of the protein lysate prepared from FK866 treated 293T cells (data not shown). Using this approach, we identified FOXO3a to be among the targets that were significantly acetylated upon inhibition of NAMPT by FK866. Previously, it has been reported that acetylation of FOXO3a is triggered by oxidative stress, and SIRT1 mediated deacetylation of FOXO3a positively regulates the expression of *GADD45A* [20]. Intriguingly, our data suggest that acetylation of FOXO3a, as a result of NAMPT inhibition by FK866, is required to activate *GADD45A* expression. In presence of oxidative stress the induced acetylation of FOXO3A depends on the increase in FOXO3A interaction with SIRT1, and it is suggested that during stress multiple factors are recruited to promote the interaction between FOXO3a and SIRT1 [20]. Therefore, we addressed how depletion of intracellular NAD$^+$ influences the interaction between FOXO3A and SIRT1 in HEK293T cells. We observed that the interaction between these proteins decreases in the presence of FK866 (data not shown). Further, this indicates that in context of NAD$^+$ depletion, the SIRT1 protein may recruit factors which reduce SIRT1 binding to FOXO3a, thereby promoting its acetylation. To balance the process of aging and cancer, the expression and activity of SIRT1 protein is required to be strictly regulated in a cell-specific and context-dependent manner. In case of extended longevity, the cellular resistance to stress has to be increased, and the way SIRT1 mediates this, is by tipping the balance of FOXO3a to increase the expression of DNA repair genes and decrease the expression of apoptotic genes [20]. In context of cancer, FOXO3a mediated expression of target gene relevant in tumor suppression has to be increased [4], and one possible way to achieve this in malignant cells is by inhibiting the deacetylase activity of SIRT1. FOXO3a has been clearly shown to be involved in the transactivation of *GADD45A* [4]. Our observations that activation of *GADD45A* upon inhibition of NAMPT pathway by FK866 requires the presence of FOXO3a, adds further to our knowledge on *GADD45A* regulation by changes in cellular levels of NAD$^+$. Our findings are supported by Revollo et al. [22], showing that *GADD45A* expression is significantly downregulated in NIH3T3 cells either in presence of NAMPT or SIRT1 [22]. In addition, Wang et al. [23], have suggested that SIRT1 mediated deacetylation of FOXO3a promotes SKP2 mediated degradation of FOXO3a.

Due to their ability to reactivate aberrantly silenced tumor suppressor proteins, the inhibitors of histone deacetylases (iHDAC) are potential anti-cancer agents. Several class I and II iHDACs are currently evaluated in cancer model and in clinical trial. Due to the emerging link between metabolism and cancer, the inhibitors, like FK866 that can target class III HDACs have recently gained attention. Since cancer is considered as a heterogeneous disorder in that they differ by individual, sex, age and even the kinds of cells within the cancer themselves. Understanding the detailed molecular mechanism of the action of potential iHDACs will lead to better therapeutic application of these inhibitors. The results presented in this report contribute to our understanding of the mechanism by which FK866 exerts its anti-cancer effects. Based on our results we propose that inhibition NAMPT/NAD$^+$/SIRT1 pathway might restore the function of FOXO3a, partly by increasing the expression of *GADD45A*.

The data presented here highlights the role of NAMPT/NAD$^+$/SIRT1 pathway on the regulation of *GADD45A* expression which is mediated by FOXO3a protein. The modification of FOXO3a under the above experimental conditions is the decisive factor for the functional role of FOXO3a in the regulation of *GADD45A* expression.

Acknowledgment

We thank Dr. Michael E. Greenberg for the FHRE-Luc (#1789) plasmid which was purchased from Addgene. We thank Dr. Qiang Tong and Dr. Fei Wang (USDA/ARS Children's Nutrition Research Center, Department of Pediatrics, Baylor College of Medicine, Houston, TX 77030, USA) for providing us with the plasmids pcDNA3-HA-FOXO3a, FG12-shSIRT1-Scramble and FG-shSIRT1. We thank Dr. Axel Schambach for providing us with the lentiviral vector pRRL.SF.DsRedEx.pre. We thank the Jose Carreras Leukaemia Foundation for financing this project.

References

[1] A.J. Fornace Jr., D.W. Nebert, M.C. Hollander, J.D. Luethy, M. Papathanasiou, J. Fargnoli, N.J. Holbrook, Mammalian genes coordinately regulated by growth arrest signals and DNA-damaging agents, Mol. Cell Biol. 9 (1989) 4196–4203.
[2] M.C. Hollander, Q. Zhan, I. Bae, A.J. Fornace Jr., Mammalian GADD34, an apoptosis- and DNA damage-inducible gene, J. Biol. Chem. 272 (1997) 13731–13737.
[3] O. Kovalsky, F.D. Lung, P.P. Roller, A.J. Fornace Jr., Oligomerization of human Gadd45a protein, J. Biol. Chem. 276 (2001) 39330–39339.
[4] H. Tran, A. Brunet, J.M. Grenier, S.R. Datta, A.J. Fornace Jr., P.S. DiStefano, L.W. Chiang, M.E. Greenberg, DNA repair pathway stimulated by the forkhead transcription factor FOXO3a through the Gadd45 protein, Science 296 (2002) 530–534.
[5] K.C. Arden, Multiple roles of FOXO transcription factors in mammalian cells point to multiple roles in cancer, Exp. Gerontol. 41 (2006) 709–717.
[6] A. van der Horst, B.M. Burgering, Stressing the role of FoxO proteins in lifespan and disease, Nat. Rev. Mol. Cell Biol. 8 (2007) 440–450.
[7] T. Obsil, V. Obsilova, Structure/function relationships underlying regulation of FOXO transcription factors, Oncogene 27 (2008) 2263–2275.
[8] L.P. Van Der Heide, M.F. Hoekman, M.P. Smidt, The ins and outs of FoxO shuttling: mechanisms of FoxO translocation and transcriptional regulation, Biochem. J. 380 (2004) 297–309.
[9] P.K. Vogt, H. Jiang, M. Aoki, Triple layer control: phosphorylation, acetylation and ubiquitination of FOXO proteins, Cell Cycle 4 (2005) 908–913.
[10] H. Huang, D.J. Tindall, Dynamic FoxO transcription factors, J. Cell Sci. 120 (2007) 2479–2487.
[11] S. Reagan-Shaw, N. Ahmad, The role of forkhead-box Class O (FoxO) transcription factors in cancer: a target for the management of cancer, Toxicol. Appl. Pharmacol. 224 (2007) 360–368.
[12] H. Daitoku, M. Hatta, H. Matsuzaki, S. Aratani, T. Ohshima, M. Miyagishi, T. Nakajima, A. Fukamizu, Silent information regulator 2 potentiates Foxo1-mediated transcription through its deacetylase activity, Proc. Natl. Acad. Sci. USA 101 (2004) 10042–10047.
[13] V. Perrot, M.M. Rechler, The coactivator p300 directly acetylates the forkhead transcription factor Foxo1 and stimulates Foxo1-induced transcription, Mol. Endocrinol. 19 (2005) 2283–2298.
[14] M.C. Motta, N. Divecha, M. Lemieux, C. Kamel, D. Chen, W. Gu, Y. Bultsma, M. McBurney, L. Guarente, Mammalian SIRT1 represses forkhead transcription factors, Cell 116 (2004) 551–563.
[15] A. van der Horst, L.G. Tertoolen, L.M. de Vries-Smits, R.A. Frye, R.H. Medema, B.M. Burgering, FOXO4 is acetylated upon peroxide stress and deacetylated by the longevity protein hSir2(SIRT1), J. Biol. Chem. 279 (2004) 28873–28879.
[16] Y. Yang, H. Hou, E.M. Haller, S.V. Nicosia, W. Bai, Suppression of FOXO1 activity by FHL2 through SIRT1-mediated deacetylation, EMBO J. 24 (2005) 1021–1032.
[17] M.E. Giannakou, L. Partridge, The interaction between FOXO and SIRT1: tipping the balance towards survival, Trends Cell Biol. 14 (2004) 408–412.
[18] J. Skokowa, D. Lan, B.K. Thakur, F. Wang, K. Gupta, G. Cario, A.M. Brechlin, A. Schambach, L. Hinrichsen, G. Meyer, M. Gaestel, M. Stanulla, Q. Tong, K. Welte, NAMPT is essential for the G-CSF-induced myeloid differentiation via a NAD(+)-sirtuin-1-dependent pathway, Nat. Med. 15 (2009) 151–158.

[19] S. Imai, C.M. Armstrong, M. Kaeberlein, L. Guarente, Transcriptional silencing and longevity protein Sir2 is an NAD-dependent histone deacetylase, Nature 403 (2000) 795–800.
[20] A. Brunet, L.B. Sweeney, J.F. Sturgill, K.F. Chua, P.L. Greer, Y. Lin, H. Tran, S.E. Ross, R. Mostoslavsky, H.Y. Cohen, L.S. Hu, H.L. Cheng, M.P. Jedrychowski, S.P. Gygi, D.A. Sinclair, F.W. Alt, M.E. Greenberg, Stress-dependent regulation of FOXO transcription factors by the SIRT1 deacetylase, Science 303 (2004) 2011–2015.
[21] L. Dan, O. Klimenkova, M. Klimiankou, J.H. Klusmann, M.M. van den Heuvel-Eibrink, D. Reinhardt, K. Welte, J. Skokowa, The role of Sirtuin 2 activation by nicotinamide phosphoribosyltransferase in the aberrant proliferation and survival of myeloid leukemia cells. Haematologica (Epub ahead of print 2011 Dec 29).
[22] J.R. Revollo, A.A. Grimm, S. Imai, The NAD biosynthesis pathway mediated by nicotinamide phosphoribosyltransferase regulates Sir2 activity in mammalian cells, J. Biol. Chem. 279 (2004) 50754–50763.
[23] F. Wang, C.H. Chan, K. Chen, X. Guan, H.K. Lin, Q. Tong, Deacetylation of FOXO3 by SIRT1 or SIRT2 leads to Skp2-mediated FOXO3 ubiquitination and degradation, Oncogene 31 (2012) 1546–1557. http://dx.doi.org/10.1038/onc.2011.347.

Biochemical and Biophysical Research Communications 420 (2012) 721–726

Contents lists available at SciVerse ScienceDirect

Biochemical and Biophysical Research Communications

journal homepage: www.elsevier.com/locate/ybbrc

Nuclear envelope-localized EGF family protein amphiregulin activates breast cancer cell migration in an EGF-like domain independent manner

Hisae Tanaka [a], Yu Nishioka [a], Yuhki Yokoyama [a], Shigeki Higashiyama [b], Nariaki Matsuura [a], Shuji Matsuura [a], Miki Hieda [a,*]

[a] Osaka University Graduate School of Medicine and Health Science, 1-7 Yamadaoka, Suita, Osaka 565-0871, Japan
[b] Proteo Medicine Research Center, Ehime University, Shitsukawa, Toon, Ehime 791-0295, Japan

ARTICLE INFO

Article history:
Received 8 March 2012
Available online 16 March 2012

Keywords:
Amphiregulin
Cell migration
EGF family
Breast cancer cells

ABSTRACT

Amphiregulin (AREG), an EGF family protein, is synthesized as a type I transmembrane precursor (proAREG) and expressed on the cell surface with an extracellular EGF-like domain and an intracellular short cytoplasmic tail. The ectodomain shedding yields a soluble EGF receptor ligand (soluble AREG) which binds to EGF receptor (EGFR) and concomitantly induces migration of unshed proAREG from the plasma membrane to the nuclear envelope (NE).

AREG is known to play a potential role in breast cancer and has been intensively investigated as an EGF receptor ligand, while the function of the NE-localized proAREG remains unknown. In this study we used a truncated mutant that mimics NE-localized proAREG without shedding stimuli to discriminate between the functions of NE-localized and plasma membrane-localized proAREG and demonstrate that NE-localized proAREG activates breast cancer cell migration, but suppresses cell growth. Moreover, the present study shows that induction of cell migration by NE-localized proAREG does not require the extracellular growth factor domain or EGF receptor function. Collectively these data demonstrate a novel function mediated by the intracellular domain of proAREG and suggest a significant role for NE-localized proAREG in driving human breast cancer progression.

© 2012 Elsevier Inc. All rights reserved.

1. Introduction

Amphiregulin (AREG), an EGF family protein, is synthesized as a type I transmembrane protein (proAREG) with an extracellular EGF-like domain that binds to EGF receptor (EGFR) and regulates downstream pathways involved in cell growth, proliferation, differentiation, and migration. Ectodomain shedding at the juxtamembrane domain yields a soluble EGFR ligand (soluble AREG) and carboxyl-terminal fragments (AREG-CTF) that contain transmembrane and cytoplasmic segments (Fig. 1A). The EGF-like growth factor domain is sufficient to elicit EGFR phosphorylation; the conserved cytoplasmic tail among EGF family proteins may also have biological activities (reviewed in [1,2]). For example, membrane-anchored heparin-binding EGF like growth factor (HB-EGF) cytoplasmic tails migrate from the plasma membrane to the inner nuclear membrane (INM) [3], where they regulate gene expression [4,5]. In the case of AREG, in response to shedding stimuli, interaction between the cytoplasmic tail of proAREG and A-type lamin results in targeting of unshed proAREG from the plasma membrane to the ER and nuclear envelope (NE) including INM, and causes transient genome-wide transcriptional repression [6]. However, the physiological and pathological functions of AREG at the INM remain unknown.

AREG was originally identified as an EGFR ligand in the human breast carcinoma cell line MCF7. It is synthesized as a 252-amino acid transmembrane precursor [7,8] and is expressed in various tissues including ovary, heart, kidney, spleen and breast [9]. AREG plays roles in a wide range of biological processes, such as nerve regeneration, blastocyst implantation, and bone formation. Moreover, AREG is the most abundant EGF-like growth factor in the pubertal mammary gland and has critical functions in ductal morphogenesis in pubertal mammary gland development ([10], reviewed in [11]). In addition to these physiological roles, AREG may play role(s) in breast cancer, as suggested by research results showing that the frequency and levels of AREG protein expression are generally higher in invasive breast carcinomas than in ductal carcinomas *in situ* or in normal mammary epithelium, and its expression is more common in lymph node positive cases (reviewed in [11,12]). Furthermore, suppression of AREG expression in breast cancer cells reduces tumor formation *in vivo* [13,14]. However, previous investigations of AREG function have focused on the extracellular growth factor domain; the functions of the cytoplasmic domain, however, remain mostly unknown.

Abbreviations: AREG, amphiregulin; AREG-CTF, carboxyl terminal fragment; EGFR, EGF receptor; NE, nuclear envelope; INM, inner nuclear membrane; Br-U, bromo-uridine; H3K9me3, histone H3 lysine 9 tri-methylation.

* Corresponding author. Fax: +81 66878 8162.
E-mail address: mhieda@sahs.med.osaka-u.ac.jp (M. Hieda).

0006-291X/$ - see front matter © 2012 Elsevier Inc. All rights reserved.
http://dx.doi.org/10.1016/j.bbrc.2012.03.045

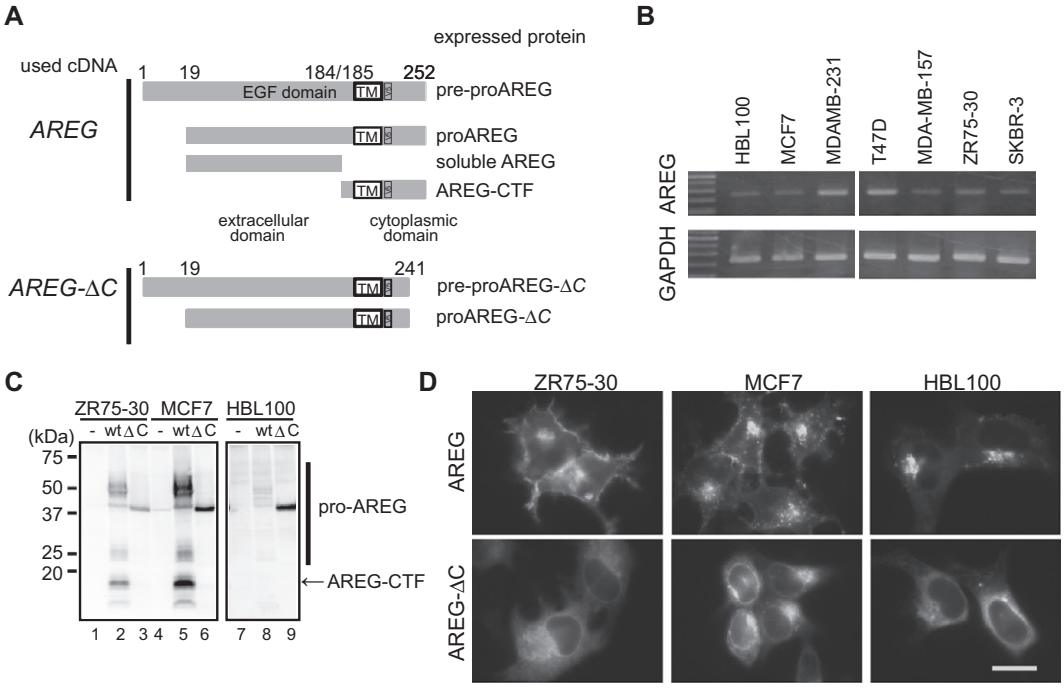


Fig. 1. NE-localized proAREG upregulates cell migration. **A.** Schematic presentation of wild type (*AREG*) and its deletion mutant (*AREG-ΔC*). AREG expressed at the plasma membrane as type I transmembrane proteins with an extracellular EGF-like domain. Ectodomain shedding at the juxtamembrane domain yields soluble AREG and carboxyl-terminal fragments (AREG-CTF) that contain transmembrane and cytoplasmic segments. A V5-epitope tag was inserted just downstream from the transmembrane domains, because the carboxyl-terminus is cleaved in response to shedding stimuli [6]. **B.** RT-PCR using cDNA derived from various breast cancer cells. **C.** ZR75-30, HBL100, and MCF7 cells were transiently transfected with empty vector (−), *AREG* (wt), or *AREG-ΔC* (ΔC) and analyzed by Western blotting using anti-AREG-C mAb#9. Multiple bands are the consequence of the multiple glycosylation sites on AREG [26]. **D.** *AREG*– or *AREG-ΔC*–transfected cells were immunostained with anti-AREG-N pAbs. Bar, 10 μm.

In the present study, we investigated the role of NE-localized proAREG in breast cancer cells using a truncated mutant that lacks the final 11 C-terminal amino acids (*AREG-ΔC*). AREG-ΔC mimics NE-localized proAREG; both proteins are localized at the NE and ER, interact with A-type lamin, and induce histone H3 lysine 9 (H3K9) tri-methylation [6]. Our results reveal a function of the AREG cytoplasmic tail in breast cancer cell migration.

2. Materials and methods

2.1. Cell culture and transfection

HBL100 and ZR75-30 were grown in RPMI. MCF7 and MDA-MB231 cells were grown in DMEM. Both media were supplemented with 10% FBS. Transfections were performed using Lipofectamine 2000 (Invitrogen). Unless otherwise stated, cells were used for each experiment 17 h after transfection.

2.2. Antibodies and reagents

Goat pAbs against the extracellular region of proAREG (anti-AREG-N pAbs) were from R&D systems. Rat mAb against the cytoplasmic domain of proAREG, clone No.9 (anti-AREG-C mAb#9) was described previously [6]. Anti-V5 epitope tag mAb was purchased from Invitrogen. A mouse anti-trimethylated histone H3K9 (anti-H3K9me3), a gift from H. Kimura (Osaka University), was described previously [15]. Mouse anti-β-tubulin mAb were from Sigma–Aldrich. Soluble AREG growth factor was purchased from R&D systems.

2.3. Immunofluorescence and TPA treatment

Cells were fixed with 4% paraformaldehyde and permeabilized with Triton X-100. Cells were then immunostained with appropriate primary and secondary antibodies (Jackson ImmunoResearch Laboratories), and viewed with an epifluorescence microscope Olympus IX81 (Olympus). For TPA treatment, 100 nM TPA (Sigma) was added to the culture medium and incubated for 30 min before fixation.

2.4. Plasmids construction

AREG with a V5 tag and lacking the carboxy-terminal 11 amino acids (*AREG-ΔC*) was previously described [6]. For the construction of the extracellular EGF-like domain (142–184 aa) deleted *AREG-ΔC* (*AREG-ΔED-ΔC*), fragments of *AREG* (1–141 aa and 185–241 aa) were amplified; *AREG-ΔED-ΔC* was amplified using overlapping PCR and followed by insertion into pME18S (neo) vector. All of the cDNA constructs were verified by DNA sequencing.

2.5. Western blotting

Cell lysate were separated and transferred to nitrocellulose. The membrane was blocked with 3% skim milk, and then incubated with the first antibody followed by HRP-conjugated second antibodies.

2.6. Matrigel invasion assay

Chemotaxicell (8 μm pore size, Kurabo, Japan) were inserted into a 24-well chamber and coated with Matrigel (BD Bioscience). Then, 1×10^5 cells were seeded into the upper chamber with medium containing 0.1% BSA without FBS. The lower chamber was filled with medium with FBS as a chemoattractant. Cells were permitted to migrate for 48 h, and then were fixed and stained with hematoxylin. The number of cells that invaded to the lower surface was counted. The experiments were repeated a minimum of 4 times.

2.7. Cell motility assay using a Boyden chamber

Polycarbonate membrane inserts (8 μm pore size, Neuro Probe Inc.) were coated with collagen-type IC (Nitta Gelatin). Then, 2.5×10^4 cells were seeded into the upper chamber with medium containing 0.1% BSA without FBS. The lower chamber was filled with medium using FBS as a chemoattractant. Cells were permitted to migrate for 3 h, and were then fixed and stained with hematoxylin. The number of cells migrating to the lower surface was counted. The experiments were repeated a minimum of 4 times.

2.8. Real-time cell motility assay

Real-time cell motility was monitored using a real-time cell analyzer, xCELLigence (Roche), according to the standard protocol. Briefly, the CIM plate was coated with collagen-type IC. Then, 5×10^4 cells (17 h after transfection) were seeded into the upper chamber with the medium containing 0.1% BSA without FBS. The lower chamber was filled with medium using FBS as a chemoattractant. The top chamber was sealed at the bottom with a microporous membrane containing gold microelectrodes. Cells were permitted to migrate and the impedance (indicated as the "cell index") was measured. The impedance value (cell index) was derived from the electrode/solution interface. When cells migrated and adhered on the electrode, the local ionic environment as well as the electrode/solution interface was affected leading to an increase in electrode impedance. As a result, the cell index was increased due to cell migration through membrane pores and adhesion on the sensor side of the membrane. The results were recorded as the value of the cell index after 8 h.

2.9. Cell growth measurement

Cell growth was measured using WST-1 reagent according to the manufacturers' protocol (Dojindo). In brief, cells were plated into 96-well plates and then transfected (time = 0). After incubation for the indicated time, WST reagent was added into the wells, and 2 h after incubation, OD_{415} was measured.

2.10. RT-PCR

Total RNA isolated using Trizol (Invitrogen) was reverse-transcribed using AMV reverse transcriptase (Sigma). PCR amplification was performed using the following primers: for AREG 5′-TCG CTCTTGATACTCGGCTCA-3′ and 5′-AGCCAGGTATTTGTGGTTCG-3′; for EGFR 3′-TGTGAGGTGGTCCTTGGGAATTTGG-5′ and 3′-TGCTGA CTATGTCCCGCCACTGGA-5′; and, for GAPDH 5′-GAAGGTGAAGGT CGGAGTC-3′ and 5′-GAAGATGGTGATGGGATTAC-3′.

2.11. Br-U incorporation

Cells were grown in 5 mM bromo-uridine (Br-U) for 30 min and fixed. This analogue does not affect the activity of the major polymerizing enzyme, RNA polymerase II. Newly synthesized Br-U-labeled RNA (Br-RNA), with the exception of nucleolar RNA, can be detected with rat anti-BrdU mAb (Abcam).

3. Results

3.1. A carboxyl terminus-deleted AREG was localized at the ER and NE without shedding stimuli in breast cancer cells

AREG supposedly contributes to breast cancer (reviewed in [11,12]). Many studies have demonstrated the functions of the extracellular domain of AREG, but the physiological role of the NE-localized pro-form (proAREG) remains unknown. To address this issue, and to discriminate between the functions of plasma membrane-localized, NE-localized, and secreted AREG, we attempted to use a truncated mutant that lacks the final 11 C-terminal amino acids (*AREG-ΔC*, Fig. 1A).

ProAREG targets the NE and ER, interacts with A-type lamin, and transiently suppresses genome-wide transcription in response to shedding stimuli, whereas AREG-ΔC is localized at the NE and ER and interacts with A-type lamin in the absence of shedding stimuli in HeLa cells [6]. To examine the effects of the cytoplasmic tail of AREG in breast cancer cells, AREG low-expressing cells were first explored. Similar to published results [16,17], most malignant breast cancer cell lines express a high level of AREG; inversely, less invasive and non-metastatic MCF7, HBL100, and ZR75-30 cells express relatively lower levels of AREG in RT-PCR (Fig. 1B). These cell lines express proAREG protein below detection levels in Western blotting (Fig. 1C, lanes 1, 4, and 7). Then, wild type *AREG* or *AREG-ΔC* were transfected into these breast cancer cells, and the expressed protein size and location was verified (Fig. 1C, D). The wild type *AREG* transfection produced 2 major forms of AREG (proAREG and AREG-CTF in Fig. 1C), whereas only the pro-form was detected in *AREG-ΔC*-transfected cells (Fig. 1C, lanes 3, 6, and 9) suggesting that AREG-ΔC would not be localized at the plasma membrane where it would be accessible to shedding proteases. Immunofluorescence microscopy showed that transfected wild-type AREG was largely localized in the plasma membrane and Golgi apparatus (Fig. 1D, upper); by contrast, AREG-ΔC protein was confined to the NE and ER in these cell lines at the steady state (Fig. 1D, lower), as with wild-type AREG following shedding stimuli. Moreover, the expression of AREG-ΔC in these breast cancer cells relatively induced H3K9me3, as with NE-localized proAREG in HeLa cells ([6], Fig. S1). These results demonstrated that AREG-ΔC is localized at the ER and NE and mimics NE-localized proAREG without shedding stimuli in breast cancer cells. We thus decided to use AREG-ΔC as a tool to examine the function(s) of NE-localized proAREG.

3.2. NE-localized proAREG activates cell motility

Since AREG reportedly associates with invasion activity in cancer cells (reviewed in [18]), we performed Matrigel invasion assay using AREG-ΔC-expressing breast cancer cells. However, there were no significant differences in invasion activity between AREG-ΔC-transfected and non-transfected cells (Fig. 2A). We next examined whether NE-localized proAREG plays a functional role in cell migration using a Boyden chamber because cell migration activity is a critical requirement for tumor cell metastasis and AREG is also known to be involved in cell migration. Interestingly, AREG-ΔC expression significantly activated cell motility in all 3 of the cell lines we examined (Fig. 2B). Expression of wild-type AREG also activated cell migration in ZR75-30 and MCF7 cells in the absence of shedding stimuli, possibly via EGFR activation or via NE-localized proAREG due to the basal level of shedding activity; the serum in the culture medium contained growth factors that induced ectodomain shedding [19]. In fact, the amount of AREG-CTF in the ZR75-30 and MCF7 cells was higher than it was in the HBL100 cells (Fig. 1C). Next, AREG-ΔC was transfected into these cell lines and cell growth was measured for 48 h. The expression of AREG-ΔC did not activate the cell growth of MCF7 cells, and, moreover, the growth of ZR75-30 and HBL100 cells was obviously suppressed (Fig. 2C).

3.3. The extracellular domain is not required for the induction of cell migration

For further investigation into the function of NE-localized proAREG, we focused on ZR75-30 cells, because they exhibited the most

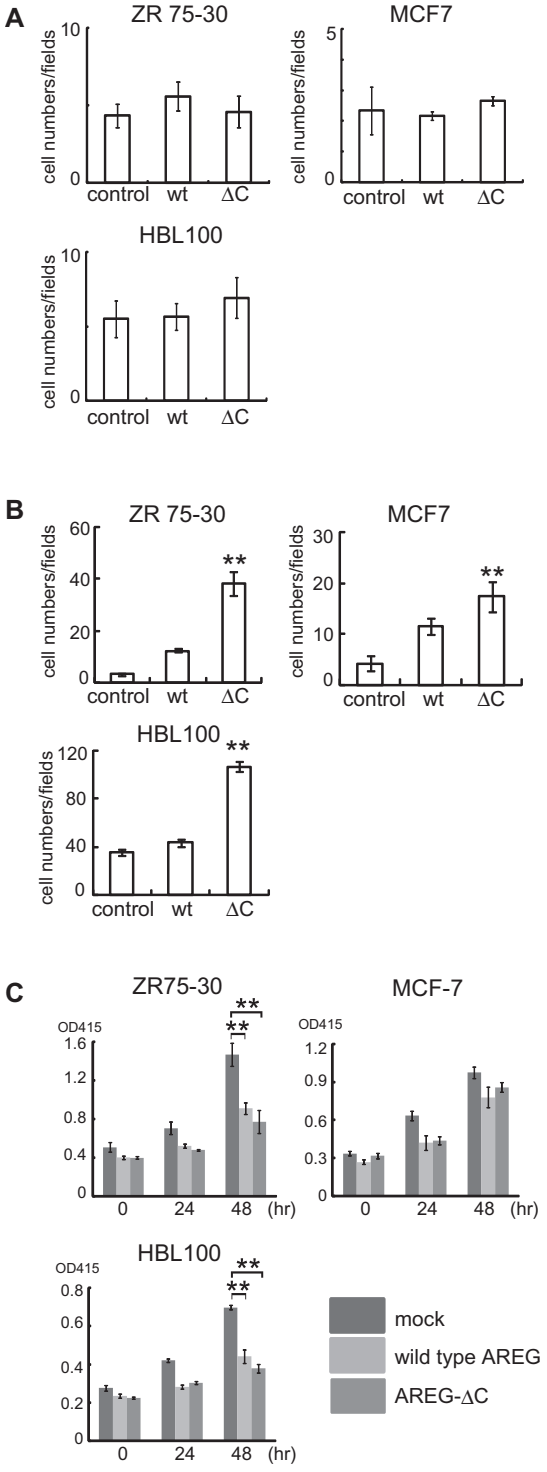


Fig. 2. NE-localized proAREG activates cell motility. A. Matrigel invasion assay was performed using *AREG*-, *AREG-ΔC*-, and empty vector-transfected cells. Results are expressed as the mean number of invaded cells/field ± SD. The transfectant with empty vector (pME18S) was used as the control for all experiments. B. Cell migration was analyzed using *AREG*-, *AREG-ΔC*-, and empty vector-transfected cells in a Boyden chamber assay. Results are expressed as the mean number of migrated cells/field ± SD. There was significant differences between the control and the AREG-ΔC expressing cells, (**$p < 0.01$). C. Transfected cells were seeded to 96-well plates (time = 0) and cell proliferation was monitored at the indicated time points. (**$p < 0.01$).

evident activated cell motility (Fig. 2B), and the expression of EGFR mRNA in ZR75-30 cells was negligible ([20]; also see below). In ZR75-30 cells, AREG-ΔC mainly localized at the ER and NE

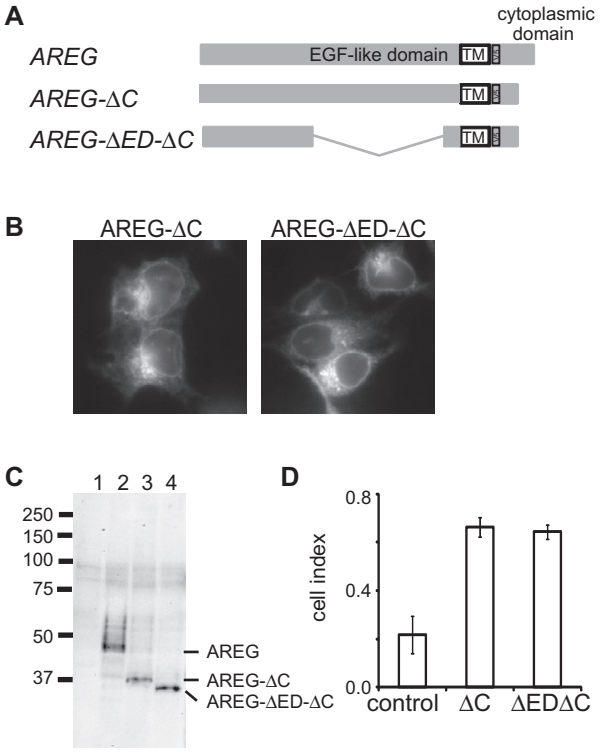


Fig. 3. The cytoplasmic domain of AREG is responsible for the upregulation of cell migration. A. Schematic representation of *AREG-ΔC* lacking the EGF-like domain (termed *AREG-ΔED-ΔC*). B. Indicated plasmids were transfected into ZR75-30 cells and immunostained with anti-AREG-C mAb#9. C. An empty vector (lane 1), wild type *AREG* (lane 2), *AREG-ΔC* (lane 3), or *AREG-ΔED-ΔC* (lane 4) were transfected into ZR75-30 cells and cell lysate were subjected to Western blotting using anti-V5mAb. D. Cell migration of *AREG-ΔC*- or AREG-ΔED-ΔC-transfected ZR75-30 cells was monitored using an xCELLigence instrument (Roche). The cell index refers to the cell migration activity (see Section 2).

(Fig. 1C) with the cytoplasmic domain of AREG-ΔC facing the nucleoplasm, whereas the extracellular domain was restricted to the lumen of the inner and outer nuclear membranes (see Fig. 4D, iv). To reveal the functional domain within NE-localized proAREG for the induction of cell migration, we deleted the extracellular EGF-like domain from AREG-ΔC (termed *AREG-ΔED-ΔC*, Fig. 3A). As with AREG-ΔC, this mutant AREG localized to the NE and ER (Fig. 3B). The expressed protein size was confirmed by Western blotting (Fig. 3C). To analyze the cell migration, a real-time cell analyzer, xCELLigence (Roche) was used because cell migration activity can be continuously monitored up to 12 h. xCELLigence showed that the expression of AREG-ΔC activated cell migration (Fig. 3D), which was consistent with the results of the Boyden chamber assay. More importantly, the AREG-ΔED-ΔC expression also induced cell motility to the same extent as AREG-ΔC (Fig. 3D). This result suggested that the extracellular EGF-like domain is not required for the induction of cell migration by NE-localized proAREG.

3.4. EGFR activation may not be required for the NE-localized proAREG induced cell migration

The fact that AREG-ΔED-ΔC could induce cell migration (Fig. 3) suggests that the NE-localized proAREG-induced cell migration is not dependent on EGFR activation. To examine this possibility, the expression level of EGFR was analyzed. In agreement with the published data [20], EGFR mRNA expression was negligible in PCR analysis (~35 cycles) using cDNA from ZR75-30 cells, while we did observe an amplicon corresponding to EGFR using the same

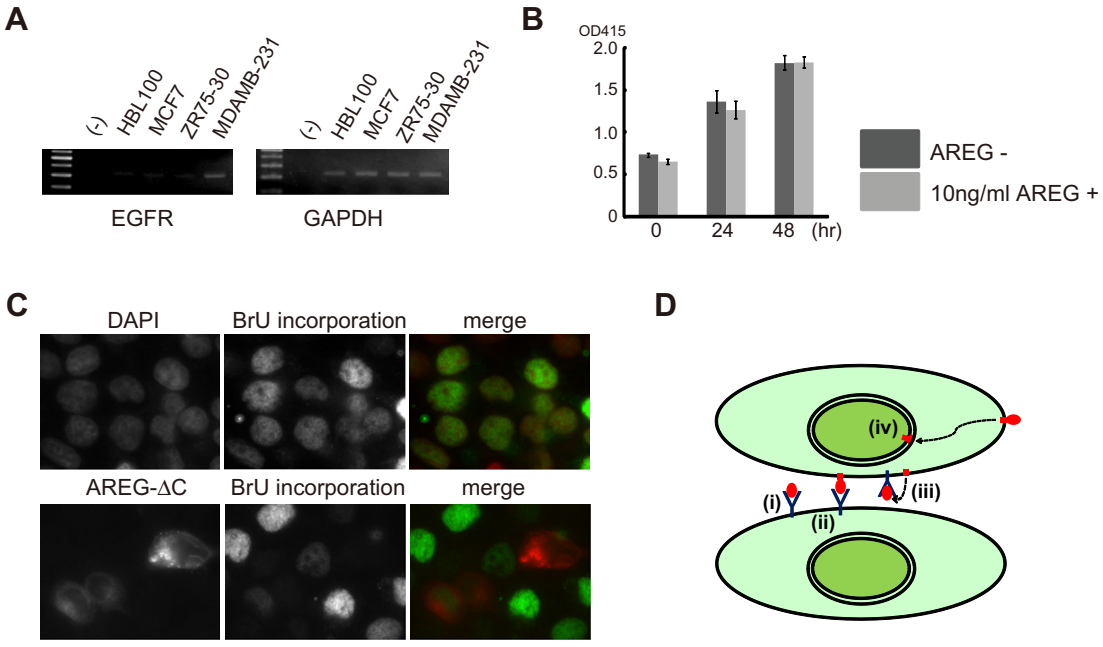


Fig. 4. (A) RT-PCR analysis using cDNA derived from indicated breast cancer cells. (B) Soluble AREG corresponding to growth factor domain (R&D systems), which is known to activate the EGFR was added to the culture medium, and the cell growth was measured. (C) Synthesis of RNA transcripts was monitored using incorporation of Br-U [27]. *AREGΔC* or empty vector was transfected into ZR75-30 cells. 5 mM Br-U was added to the culture medium 30 min prior to fixation. After fixation, Br-U incorporated mRNA was stained with anti-Br-U mAb. (D) A schematic presentation of the signaling pathway induced by AREG; paracrine (i), juxtacrine (ii), autocrine (iii), and NE-localized proAREG (iv). ProAREG targets from the plasma membrane to the NE, and NE-localized proAREG activates the signaling pathway via an intracellular domain.

amount of cDNA from MDA-MB231 cells (Fig. 4A). Western blots using ZR75-30 cell lysate also did not detect EGFR (data not shown). However, no detection of EGFR mRNA and protein is not conclusive proof of a lack of protein expression, so we added soluble AREG to the culture medium to activate the EGFR, and measured the cell growth. As a result, exogenously added soluble AREG (10 ng/ml or 100 ng/ml) did not effect on cell growth (Fig. 4B and data not shown). These results suggested that NE-localized proAREG contributes to the activation of cell motility possibly via an intracellular domain.

To examine the molecular mechanism of the induction of cell migration, transcriptional activity was measured because the expression of AREG-ΔC induced H3K9me3 ([6] and Fig. S1), which is a repressive marker for transcription, and NE-localization of proAREG repressed genome-wide transcriptional activity [6]. As a result, BrU incorporation intensity decreased by ~60% in AREG-ΔC positive cells (Fig. 4C) suggesting a transcriptional-regulation independent mechanism (as discussed below).

4. Discussion

4.1. Activation of cell migration by NE-localized proAREG

AREG is known to function in cell migration through the activation of EGFR. In addition to this function, our data reveals that NE-localized proAREG activates cell migration. Several lines of evidence have suggested that NE-localized proAREG-induced cell motility is independent of EGFR. First, cell migration is activated by the expression of AREG-ΔC (Fig. 2), in which the extracellular growth factor domain is restricted in the lumen of ER/NE (please see Fig. 4D). Second, the extracellular growth factor domain is not required for the activation of cell migration (Fig. 3). And third, AREG-ΔC induces the cell migration of ZR75-30 cells in which EGFR expression is negligible (Fig. 4). Therefore, we concluded that NE-localized proAREG contributes to the activation of cell motility via the intracellular domain.

4.2. How does NE-localized proAREG promote cell migration?

We found that NE-localization of proAREG causes the activation of cell migration, and that it is dependent on its cytoplasmic tail. Moreover, the activation of cell migration does not require EGFR function, but does occur concomitantly with a slight increase in a specific histone modification, H3K9me3 ([6], Fig. S1A). Cell migration cues reportedly induce global changes in chromatin organization, particularly in elevated H3K9me3 [21]. Efficient cell migration requires chromatin condensation [22] and genome-wide chromatin structure is suggested to play a function(s) in cell migration [23,24]. Based on this, we proposed a model for the molecular mechanism of cell migration promoted by NE-targeted proAREG (Fig. 4D, iv): first, proAREG is translocated to the INM via interaction with A-type lamin; subsequently, H3K9 methylation is elevated (but the molecular mechanism remains unknown); finally, chromatin structure via regulation of histone methylation may control cell migration. It is possible to propose several explanations for the role of chromatin organization in the regulation of cell migration. One viable possibility is that the NE-localized proAREG/lamin complex may work as a platform for the LINC complex [25], in which SUN-domain-containing proteins interact with chromatin in the nucleoplasm and with KASH-containing proteins in the NE lumen that, in turn, interact with the cytoskeleton.

4.3. Role of proAREG in breast cancer cells

The expression of AREG and its cell surface receptor EGFR are known to be involved in cancer cell progression and migration. Autocrine, paracrine and juxtacrine signaling pathways (extracellular signaling pathways, Fig. 4D i, ii, and iii) have been used to explain the effects of AREG on cancer cells via EGFR activation. In addition to these effects, we demonstrated that proAREG can activate cell migration through a novel signaling pathway by the carboxyl terminus of NE-localized proAREG (intracellular signaling pathway, Fig. 4D iv). Moreover, our results also showed that

NE-localized proAREG suppresses the cell growth of breast cancer cells (Fig. 2C), while the expression of EGFR in the same cells (ZR75-30) is not high enough to respond to the addition of soluble AREG (Fig. 4A, B). The shedding stimuli yields EGFR ligand and simultaneously triggers the NE targeting of AREG [6]. Thus, in most cases these signaling pathways are well coordinated, and collapsed coordination between extracellular and intracellular signaling pathways might activate cancer cell progression. Enhanced cell motility is one of the hallmarks of cancer cells, whereas altered histone modifications correlate with prognostic factors in a wide range of cancers, including breast cancer. Thus, our proposed model, in which NE-targeted proAREG plays a functional role in cell migration (in this paper) and simultaneous upregulated H3K9 methylation ([6], Fig. S1), can explain the association of aggressive breast cancer with AREG expression. In summary, it is evident that the EGF family protein AREG has two functional domains, extracellular and intracellular/cytoplasmic; the AREG cytoplasmic domain activates a novel signaling pathway that regulates cell migration.

Acknowledgments

We thank Dr. T. Kurokawa and Dr. T. Honda (Wako Pure Chemical) for valuable discussions, Dr. H. Kimura (Osaka University) for anti-H3K9me3mAb and Ms. H. Sasaki for technical assistance. This study was performed as part of a joint research program with Wako Pure Chemical Industries Ltd., and was supported by Grants from the Ministry of Education, Culture, Sports, Science and Technology of Japan; by a Grant-in-Aid for Scientific Research on Innovative Areas to MH; and, by a Grant-in-Aid for Scientific Research (C) to MH.

Appendix A. Supplementary data

Supplementary data associated with this article can be found, in the online version, at http://dx.doi.org/10.1016/j.bbrc.2012.03.045.

References

[1] S. Higashiyama, H. Iwabuki, C. Morimoto, M. Hieda, M, H. Inoue, N. Matsushita, Membrane-anchored growth factors, the epidermal growth factor family: beyond receptor ligands, Cancer Sci. 99 (2008) 214–220.
[2] S.R. Schneider, E. Wolf, The epidermal growth factor receptor ligands at a glance, J. Cell Physiol. 218 (2009) 460–466.
[3] M. Hieda, M. Isokane, M. Koizumi, C. Higashi, T. Tachibana, M. Shudou, T. Taguchi, Y. Hieda, S. Higashiyama, Membrane-anchored growth factor, HB-EGF, on the cell surface targeted to the inner nuclear membrane, J. Cell Biol. 180 (2008) 763–769.
[4] D. Nanba, A. Mammoto, K. Hashimoto, S. Higashiyama, Proteolytic release of the carboxy-terminal fragment of proHB-EGF causes nuclear export of PLZF, J. Cell Biol. 163 (2003) 489–502.
[5] Y. Kinugasa, M. Hieda, M. Hori, S. Higashiyama, The carboxyl-terminal fragment of pro-HB-EGF reverses Bcl6-mediated gene repression, J. Biol. Chem. 282 (2007) 14797–14806.
[6] M. Isokane, M. Hieda, S. Hirakawa, M. Shudou, K. Nakashiro, K. Hashimoto, H. Hamakawa, S. Higashiyama, The PM-anchored growth factor, pro-amphiregulin, binds A-type lamin and regulates global transcription, J. Cell Sci. 121 (2008) 3608–3618.
[7] M. Shoyab, V.L. McDonald, J.G. Bradley, G.J. Todaro, Amphiregulin: a bifunctional growth-modulating glycoprotein produced by the phorbol 12-myristate 13-acetate-treated human breast adenocarcinoma cell line MCF7, Proc. Natl. Acad. Sci. USA 85 (1988) 6528–6532.
[8] M. Shoyab, G.D. Plowman, V.L. McDonald, J.G. Bradley, G.J. Todaro, Structure and function of human amphiregulin: a member of the epidermal growth factor family, Science 243 (1989) 1074–1076.
[9] G.D. Plowman, J.M. Green, V.L. McDonald, M.G. Neubauer, C.M. Disteche, G.J. Todaro, M. Shoyab, The amphiregulin gene encodes a novel epidermal growth factor-related protein with tumor-inhibitory activity, Mol. Cell Biol. 10 (1990) 1969–1981.
[10] L. Ciarloni, S. Mallepell, C. Brisken, AR is an essential mediator of estrogen receptor alpha function in mammary gland development, Proc. Natl. Acad. Sci. USA 104 (2007) 5455–5460.
[11] J. McBryan, J. Howlin, S. Napoletano, F. Martin, Amphiregulin: role in mammary gland development and breast cancer, J. Mammary Gland Biol. Neoplasia 13 (2008) 159–169.
[12] N.E. Willmarth, S.P. Ethier, Amphiregulin as a novel target for breast cancer therapy, J. Mammary Gland Biol. Neoplasia 13 (2008) 171–179.
[13] L. Ma, C. Gauville, Y. Berthois, A. Degeorges, G. Millot, P.M. Martin, F. Calvo, Role of epidermal-growth-factor receptor in tumor progression in transformed human mammary epithelial cells, Int. J. Cancer 78 (1998) 112–119.
[14] L. Ma, C. Gauville, Y. Berthois, G. Millot, G.R. Johnson, F. Calvo, Antisense expression for amphiregulin suppresses tumorigenicity of a transformed human breast epithelial cell line, Oncogene 18 (1999) 6513–6520.
[15] H. Kimura, Y. Hayashi-Takanaka, Y. Goto, N. Takizawa, N. Nozaki, The organization of histone H3 modifications as revealed by a panel of specific monoclonal antibodies, Cell Struct. Funct. 33 (2008) 61–73.
[16] S. LeJeune, R. Leek, E. Horak, G. Plowman, M. Greenall, A.L. Harris, Amphiregulin, epidermal growth factor receptor, and estrogen receptor expression in human primary breast cancer, Cancer Res. 53 (1993) 3597–3602.
[17] S. Li, G.D. Plowman, S.D. Buckley, G.D. Shipley, Heparin inhibition of autonomous growth implicates amphiregulin as an autocrine growth factor for normal human mammary epithelial cells, J. Cell Physiol. 153 (1992) 103–111.
[18] B. Busser, L. Sancey, E. Brambilla, J. Coll, A. Hurbin, The multiple roles of amphiregulin in human cancer, Biochim. Biophys. Acta 1816 (2011) 119–131.
[19] M. Hirata, T. Umata, T. Takahashi, M. Ohnuma, Y. Miura, R. Iwamoto, E. Mekada, Identification of serum factor inducing ectodomain shedding of proHB-EGF and studies of noncleavable mutants of proHB-EGF, Biochem. Biophys. Res. Commun. 283 (2001) 915–922.
[20] J.M. Rae, J.O. Scheys, K.M. Clark, R.B. Chadwick, M.C. Kiefer, M.E. Lippman, EGFR and EGFRvIII expression in primary breast cancer and cell lines, Breast Cancer Res. Treat. 87 (2004) 87–95.
[21] G. Gerlitz, I. Livnat, C. Ziv, O. Yarden, M. Bustin, O. Reiner, Migration cues induce chromatin alterations, Traffic 8 (2007) 1521–1529.
[22] G. Gerlitz, M. Bustin, Efficient cell migration requires global chromatin condensation, J. Cell Sci. 123 (2010) 2207–2217.
[23] Y. Seki, M. Yamaji, Y. Yabuta, M. Sano, M. Shigeta, Y. Matsui, Y. Saga, M. Tachibana, Y. Shinkai, M. Saitou, Cellular dynamics associated with the genome-wide epigenetic reprogramming in migrating primordial germ cells in mice, Development 134 (2007) 2627–2638.
[24] G. Gerlitz, M. Bustin, The role of chromatin structure in cell migration, Trends Cell Biol. 21 (2011) 6–11.
[25] M. Crisp, Q. Liu, K. Roux, J.B. Rattner, C. Shanahan, B. Burke, P.D. Stahl, D. Hodzic, Coupling of the nucleus and cytoplasm: role of the LINC complex, J. Cell Biol. 172 (2005) 41–53.
[26] C.L. Brown, K.S. Meise, G.D. Plowman, R.J. Coffey, P.J. Dempsey, Cell surface ectodomain cleavage of human AR precursor is sensitive to a metalloprotease inhibitor. Release of a predominant N-glycosylated 43-kDa soluble form, J. Biol. Chem. 273 (1998) 17258–17268.
[27] F.J. Iborra, D.A. Jackson, P.R. Cook, The path of transcripts from extranucleolar synthetic sites to nuclear pores: transcripts in transit are concentrated in discrete structures containing SR proteins, J. Cell Sci. 111 (1998) 2269–2282.

Biochemical and Biophysical Research Communications 420 (2012) 727–732

Contents lists available at SciVerse ScienceDirect

Biochemical and Biophysical Research Communications

journal homepage: www.elsevier.com/locate/ybbrc

Nitric oxide produced by cytochrome c oxidase helps stabilize HIF-1α in hypoxic mammalian cells

Kerri A. Ball, Andrew W. Nelson, Daniel G. Foster, Robert O. Poyton *

Department of Molecular, Cellular, and Developmental Biology, University of Colorado, Boulder, CO 80309-0347, USA

ARTICLE INFO

Article history:
Received 9 March 2012
Available online 17 March 2012

Keywords:
Cytochrome c oxidase
Mitochondria
Hypoxia
Hypoxic inducible factor
Superoxide
Nitric oxide

ABSTRACT

The mitochondrial respiratory chain has been reported to play a role in the stabilization of HIF-1α when mammalian cells experience hypoxia, most likely through the generation of free radicals. Although previous studies have suggested the involvement of superoxide catalyzed by complex III more recent studies raise the possibility that nitric oxide (NO) catalyzed by cytochrome c oxidase (Cco/NO), which functions in hypoxic signaling in yeast, may also be involved. Herein, we have found that HEK293 cells, which do not express a NOS isoform, possess Cco/NO activity and that this activity is responsible for an increase in intracellular NO levels when these cells are exposed to hypoxia. By using PTIO, a NO scavenger, we have also found that the increased NO levels in hypoxic HEK293 cells help stabilize HIF-1α. These findings suggest a new mechanism for mitochondrial involvement in hypoxic signaling in mammalian cells.

© 2012 Elsevier Inc. All rights reserved.

1. Introduction

Several studies have implicated the mitochondrial respiratory chain in the induction of hypoxic genes (hypoxic signaling) when eucaryotic cells experience hypoxia and have proposed that increased mitochondrial free radicals produced by hypoxic mitochondria are involved [5,9,20]. As yet, the mitochondrial free radical(s) involved in hypoxic signaling has (have) not been conclusively identified. Early evidence suggested the involvement of superoxide produced by complex III [8,11]. However, it has been demonstrated more recently that hypoxic mitochondria also produce nitric oxide (NO), catalyzed by cytochrome c oxidase (Cco/NO) [6,7], and there is growing evidence that cell and tissue NO levels increase under hypoxic conditions [34]. Moreover, several lines of evidence indicate a role for Cco and NO in hypoxic signaling in yeast cells [6,7,32].

Hypoxic signaling in mammalian cells has been addressed largely by examining HIF-1, a dimeric hypoxic transcription factor, whose alpha subunit, HIF-1α, is susceptible to degradation after prolyl hydroxylation in normoxic cells and which becomes stabilized under hypoxia [14]. It is now well established that mitochondria play a role in the hypoxic stabilization of HIF-1α and it has been demonstrated that cytochrome c, which is required for Cco/NO activity, helps stabilize HIF-1α in murine cell lines exposed to hypoxia [26]. Current understanding of the role of NO in HIF-1α stability is still evolving. While several early studies reported that NO destabilizes HIF-1α in hypoxic cells [15,25,33] recent studies have revealed a more complex picture in which NO levels are important. Indeed, it now appears that short term exposure to NO leads to the stabilization of HIF-1α either in normoxic or hypoxic cells while longer term exposure destabilizes HIF-1α [3,4]. Similarly, high doses of NO have been reported to stabilize HIF-1α independently of O_2 concentration whereas low levels of NO destabilize HIF-1α under hypoxic conditions [27]. These latter studies have used human osteocarcinoma cells treated with exogenous NO donors (e.g., GSNO) [4] or HEK293 cells with an overexpressed transfected exogenous iNOS isoform or in the presence of exogenous NO donors [27]. Consequently, it is not clear if the intracellular NO levels produced in these studies were in the physiological range or if either cell type experienced an increase in NO from endogenous sources when exposed to hypoxia. Also unclear is whether NO produced from Cco/NO plays a role in the stabilization of HIF-1α in hypoxic cells. These questions are addressed in this study with untransfected HEK293 cells.

2. Materials and methods

2.1. Cell culture

Human embryonic kidney cells, HEK293 (Invitrogen 11625-019: 293F), were grown to >80% confluence in Dulbecco's modified eagle medium (DMEM; Gibco 10569) supplemented with 10% FBS and 1% Penicillin–Streptomycin at 37 °C in a humidified atmosphere of air supplemented with 5% CO_2. To harvest, confluent HEK293 adherent cells were washed once with PBS pH 7.4 and

* Corresponding author. Address: 347 UCB Boulder, CO 80309-0347, USA. Fax: +1 303 492 8783.
E-mail address: Robert.Poyton@colorado.edu (R.O. Poyton).

0006-291X/$ - see front matter © 2012 Elsevier Inc. All rights reserved.
http://dx.doi.org/10.1016/j.bbrc.2012.03.050

removed from the culture plate using 0.05% trypsin–EDTA solution. A 10% FBS solution was added and the harvested cells were washed twice with PBS and then suspended in the appropriate buffer.

2.2. Hypoxic shifts

Confluent HEK293 cells were placed in a Biospherix Pro-ox C-Chamber inside a 37 °C incubator with fresh media without FBS supplement. O_2 concentration in the Biospherix C-Chamber was controlled using the Pro-ox Model C21 Biospherix regulator that balances air and N_2 to achieve the desired O_2 concentration while CO_2 is regulated independently and held constant at 5% for all experiments. Cells were shifted from atmospheric O_2 concentrations to 2%, 1%, or 0% O_2 and maintained at the desired O_2 concentration for varying lengths of time (typically 3 h). The media used during the hypoxic shifts were DMEM or Phenol-free DMEM (Gibco 31053) with 100 mg/L Sodium Pyruvate added to match Gibco 10569 DMEM composition.

2.3. Measurement of NO production

2.3.1. NO electrode assay

HEK293 adherent cells were harvested and then suspended in Electrode Assay Buffer (75 mM mannitol, 25 mM sucrose, 100 mM KCl, 10 mM KH_2PO_4, 10 mM Tris, 50 μM EDTA, adjusted to a final pH of 7.0) with 2% n-dodecyl-R-D maltoside to solubilize the cells. The cell lysate was clarified by centrifuged at 3000×*g*, treated with 1X phosphatase inhibitor cocktail (Sigma P5726) to stabilize activity [13], aliquoted for single use, and stored in liquid nitrogen. Samples were assayed immediately after thawing. Cell lysate NO production was measured simultaneously with O_2 consumption, with the Innovative Instruments in NOII system using the TMPD/ascorbate method as previously described [2]. Briefly, measurements were performed at 30 °C in a closed WPI NOCHM-4 multi-port thermostatic measurement chamber using amiNO-700 and OXY-2 Clark-type electrodes. Cell lysate (3 mg/mL), superoxide dismutase (5000 units), 10 mM ADP, 10 μM mammalian cytochrome c, 0.5 mM ascorbate, and 0.5 mM TMPD were added to the assay chamber; the O_2 concentration was drawn down to 0% by the respiring lysate, and then sodium nitrite ($NaNO_2$) (1 mM) was added to the assay chamber to initiate NO production. The NO scavenger, PTIO (2-Phenyl-4,4,5-tetramethylimidazoline-3-oxide-1-oxyl) was used to validate the NO specificity of the electrode signal. The NO electrode was calibrated with a series of known concentrations of NO (10, 20, 40, 80, 100 nM) generated by mixing 1 μM $NaNO_2$ with 0.1 M KI_2 and 0.1 M H_2SO_4.

2.3.2. Measurement of NO Levels using DAF-2DA fluorescent dye

Confluent HEK293 cells were harvested and resuspended in Reaction Buffer (PBS pH 7.4, 110 mg/L Sodium Pyruvate, 4.5 g/L glucose). The fluorescent probe, DAF-2DA (4,5-Diaminofluorescein diacetate; Cayman Chemical 85165), was added to a concentration of 11 μM [18] and 150 μL (~20×10^4 cells per well) of each fraction was added in replicate to a black 96-well plate. NO related fluorescence signals (Ex/Em 485/538) were measured following 1 h of normoxia (atmospheric O_2, 5% CO_2, 37 °C) [30] and following up to 3 h of hypoxia (1% O_2, 5% CO_2, balanced N_2, 37 °C). Changes in NO levels were determined by calculating the difference in fluorescence in cells prior to entering the hypoxic chamber and immediately after removal.

2.4. Measurement of HIF

2.4.1. Nuclear protein isolation

Nuclear and cytoplasmic extracts were obtained using a Nuclear Extract Kit (Active Motif 40010) per kit instructions. Briefly, media was aspirated from adherent HEK293 cells and the cells were washed and scraped with ice-cold PBS containing Phosphatase Inhibitor (Active Motif 102146). They were then pelleted, resuspended, and incubated in Hypotonic Buffer (Active Motif 100505). Next, detergent (Active Motif 100512) was added, the sample was vortexed 10 s at the highest setting, and the sample was centrifuged for 30 s at 14,000×*g*. The supernatant (cytoplasmic fraction) was removed and saved. The nuclear pellet was lysed (Lysis Buffer, Active Motif 100534) and the nuclear protein fraction was collected. All protein fractions were stored at −80 °C and used within 1 week of collection.

2.4.2. Active HIF-1 analysis

Active HIF results were obtained using a HIF-1 Activation Assay Kit (Active Motif 47096) per kit instructions. Briefly, the kit contains a 96-well plate with immobilized HRE oligonucleotide (5′-TACGTGCT-3′) from the EPO gene. Nuclear extract (20 μg/well) was incubated with Binding Buffer and bound HIF was detected by absorbance at 450 nm with HIF-1α antibody followed by an HRP conjugate antibody.

2.4.3. Total HIF-1α analysis

Nuclear and/or cytoplasmic protein fractions were run on a 4–20% polyacrylamide gel and transferred to a PVDF membrane. The membrane was blocked with 5% Blotto-PBS Solution and washed in PBS with 0.1% Tween-20. The following antibodies were used: anti-HIF-1α (BD-Bioscience 610958 at 1:1000); anti-tubulin (Santa Cruz sc-58666 at 1:2000 or NeoMarkers at 1:8000); anti-Histone H2B (Cell Signaling 2934S at 1:30,000); and anti-mouse HRP (ThermoFisher PI31430 at 1:20,000). Western Lightning (PerkinElmer NEL105001) was used to visualize bands on Kodak X-OMAT Blue XB Imaging Film. Bands were quantified using a previously described Photoshop Method [29].

3. Results and discussion

3.1. HEK293 cells possess Cco/NO activity

Although Cco/NO activity is enhanced under hypoxic conditions it is operable over a wide range of O_2 levels [2,7] and functions at physiological NO_2^- concentrations (~10 μM) [2]. The NO_2^--reductase activity of Cco and other proteins (e.g., xanthine oxidase, and hemoglobin) [6,16,23] are generally assayed at NO_2^- concentrations that exceed 1 mM in order to achieve high signal to noise ratios. So far, Cco/NO activity has been demonstrated in yeast, rat, mouse brain, plant, and human endothelial cell mitochondria as well as with purified Cco [2,6,17,21,32]. In order to determine if HEK293 cells also possess Cco/NO activity we used the previously described TMPD/ascorbate assay [2]. To improve signal level assays are generally done at O_2 concentrations below 15 μM O_2. As shown in Fig. 1A, solubilized HEK293 cell lysates begin producing NO in this assay immediately upon the addition of NO_2^-. This signal returns to baseline with the addition of the NO scavenger, PTIO. It is notable that no activity is observed when the phosphatase inhibitor cocktail is omitted from the lysate during cell lysate preparation. As expected, NO synthesis is inhibited by azide but not L-NAME (Fig. 1B).

To our knowledge this is the first report which demonstrates that HEK293 cells possess Cco/NO activity. It is likely that the failure of an earlier study to find this activity in HEK293 cells transfected with iNOS [31] was the result the dephosphorylation of Cco during detergent lysis of the cells. Indeed, as shown in Fig. 1B, no Cco/NO activity could be measured in the absence of a phosphatase inhibitor. This finding suggests that Cco/NO activity, like Cco/H_2O activity, is regulated by phosphorylation [1,13].

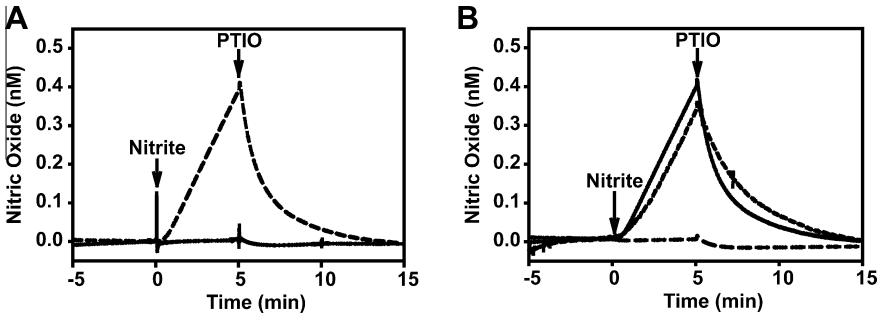


Fig. 1. HEK293 cells have Cco/NO activity. (A) HEK293 cell lysates were prepared either with (dashed line) or without (solid line) phosphatase inhibitor. NO production was measured under anoxic conditions with the Innovative Instruments in NOII system as described in Section 2 using 3 mg/mL cell lysate. 1 mM $NaNO_2$ was added as indicated. The NO scavenger, PTIO, was added at the time indicated to confirm the specificity of the observed signal. (B) The effects of sodium azide (5 mM; long dashed line) or L-NAME (1 mM; short dashed line) on Cco/NO activity in phosphatase inhibitor-treated HEK293 cell lysates were measured as described in Panel (A).

3.2. Endogenous NO levels increase in hypoxic HEK293 cells

HEK293 cells have been used extensively to examine mitochondrial involvement in hypoxic signaling and mammalian gene induction and it has been reported that HEK293 cells transfected with i-NOS release NO into the surrounding medium when exposed to hypoxia [31]. While interesting, it is unlikely that these findings with HEK293 cells transfected with an exogenousi-NOS are relevant to normal HEK293 cells because these cells by themselves do not express any NOS isoforms [10]. Similarly, these previous findings do not address whether intracellular NO levels change in hypoxic untransformed HEK293 cells or whether NO generated from an endogenous source affects HIF-1 stability in these cells when they are exposed to hypoxia. To examine these questions we first determined whether exposure to hypoxia increases intracellular NO levels in HEK293 cells by using an NO sensitive dye, DAF-2DA. Previously, we and others have reported that DAF-2DA is specific for NO and NO oxidation products and does not react to any measureable extent with other reactive oxygen species (e.g., superoxide and hydrogen peroxide) *in vivo* under our assay conditions [22,35]. As shown in Fig. 2A, HEK293 cells experience an increase in NO-related signals upon exposure to hypoxia. This increase begins after about 30 min of exposure to hypoxia, plateaus after about 2 h, and is unaffected by added L-NAME, a general NOS inhibitor. Moreover, the level of NO produced is elevated in a dose-dependent manner by added exogenous NO_2^- (Fig. 2B) and is reduced by cyanide (Fig. 2C), which inhibits Cco/NO activity [2]. Oxypurinol, a xanthine oxidase inhibitor, has no effect on the increase in hypoxic NO production (Fig. 2D). Together, these findings indicate that hypoxia increases endogenous NO levels in HEK293 cells, which do not express a NOS isoform, and suggest that new NO synthesis, catalyzed by Cco/NO, is responsible for the increase. These results also do not support the view that the increase in intracellular NO observed merely reflects the release on

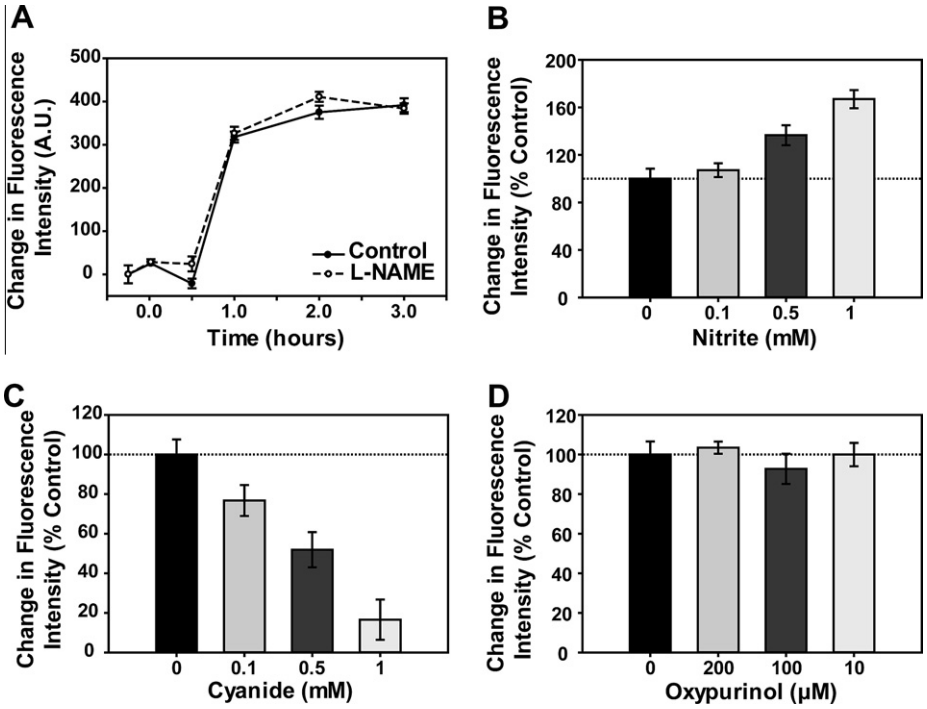


Fig. 2. Effect of hypoxia on NO levels in HEK293 cells. (A) NO levels were measured in HEK293 cells at different times after exposure to hypoxia (1% O_2) using the NO-scavenging fluorescent probe, DAF-2DA, in the presence (open circles; solid line) or absence (closed circles; dashed line) of 1 mM L-NAME. (B-D) NO levels were measured in HEK293 cells using DAF-2DA as described in above, following 3 h of hypoxic incubation (1% O_2) in the presence of the indicated concentrations of (B) $NaNO_2$, (C) potassium cyanide, or (D) oxypurinol. For all assays, the change in fluorescence intensity is represented as the percent of signal compared to the untreated hypoxic control.

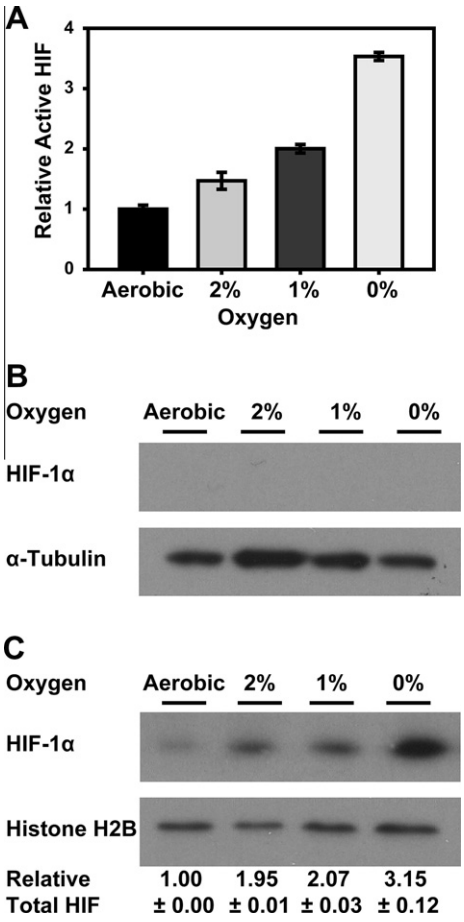


Fig. 3. HIF-1 expression levels increase as O_2 concentrations decrease. HEK293 cells were shifted to 0%, 1%, or 2% O_2 for 3 h, as described in Section 2 or were left at atmospheric O_2 levels. An Active Motif® nuclear extraction kit was used to produce cytosolic and nuclear extracts. (A) The nuclear extract was examined using an Active Motif® HIF-1 ELISA assay for active HIF-1 levels. (B) The cytosolic fraction was analyzed by immunoblotting using anti-HIF-1α and anti-α-Tubulin antibodies. (C) The nuclear fraction was analyzed by immunoblotting using anti-HIF-1α and anti-Histone H2B antibodies. Quantitation was as described in Section 2.

NO from Cco, rather than new NO synthesis by Cco/NO, because cyanide inhibits the increase in intracellular NO levels. Indeed, if Cco bound NO is merely released from Cco under hypoxia then NO levels should increase in the presence of cyanide, as the enzyme becomes reduced [31].

3.3. HIF-1 expression levels in hypoxic cells are affected by Cco/NO inhibitors and endogenously produced NO

Under hypoxia NO has been reported previously to both increase and decrease HIF-1α stability. Early studies suggested that this dual effect of NO was concentration dependent where high concentrations of NO stabilize HIF-1α irrespective of O_2 concentration and low levels destabilize HIF-1α in hypoxic cells [27]. More recent studies have reported that acute exposure to NO stabilizes HIF-1α while longer term exposure to NO destabilizes HIF-1α [3,4]. Because these latter studies made use of an exogenous NO donor it appears that the two phases are a reflection of the amount of NO released to the cells and that the latter phase is a reflection of the reduced release kinetics from the NO donor. Consequently, it is not clear how these results translate to the changes in endogenous NO synthesis during hypoxia that are reported in this study.

In order to ask if the increase in endogenously produced NO in hypoxic cells affects HIF-1 levels we first looked at the expression of HIF in the HEK293 cell line used above. Cells grown in an air-5% CO_2 mixture were exposed to reduced O_2 levels of 2% O_2, 1% O_2, or 0% O_2 with 5% CO_2 and balanced N_2 for 3 h. Then, both active HIF-1 levels and HIF-1α subunit levels were determined. From Fig. 3A it is clear that this cell line expressed HIF activity at nominal levels under aerobic conditions and that this activity increased under hypoxic (1 or 2% O_2) or anoxic conditions. As expected, immunoblot analysis of both cytosolic and nuclear fractions revealed the complete absence of HIF-1α in the cytosol at all O_2 concentrations, indicating that the increase in HIF-1 activity coincides with an increase in nuclear but not cytosolic HIF-1α levels (Fig. 3B and C).

Having demonstrated that HEK293 cells have Cco/NO activity, which is responsible for the increase in endogenous NO levels in hypoxic cells, we next asked if this Cco/NO affects HIF-1 and HIF-1α levels under hypoxia. This was done first by examining whether azide, a Cco/NO inhibitor, affects HIF-1 levels in hypoxic cells. From Fig. 4A it is clear that active HIF-1 levels do not increase in cells treated with azide, either in the presence or absence of L-NAME. The finding that azide affects the hypoxic stabilization of HIF-1

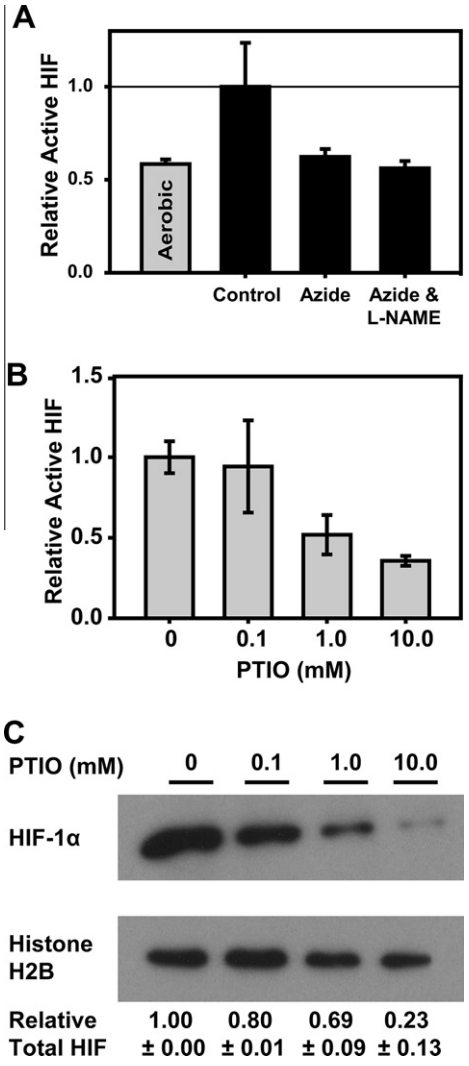


Fig. 4. Azide and PTIO prevent the accumulation of HIF-1 in hypoxic cells. HEK293 cells were shifted to 1% O_2 for 3 h as described in Section 2 or were left at atmospheric O_2 levels (A) in the presence or absence sodium azide (5 mM) and/or L-NAME (1 mM), as indicated or (B) in the presence of PTIO at the indicated concentrations. Active HIF-1 levels were measured as described in the legend to Fig. 3. (C) Nuclear HIF-1α levels in the PTIO samples were evaluated by immunoblot analysis using anti-HIF-1α and anti-Histone H2B antibodies. Quantitation was as described in Section 2.

supports and extends a previous observation that azide inhibits the accumulation of HIF-1α in hypoxic HEK293 cells [12]. We next asked if the increased NO levels generated by Cco/NO in hypoxic cells affect HIF-1 or HIF-1α levels. This was done by using the cell permeable NO scavenger, PTIO, to deplete intracellular NO levels in HEK293 cells exposed to hypoxia (1% O_2). From Fig. 4B it is clear that added PTIO diminishes active HIF levels in a concentration dependent manner. This decrease in active HIF levels parallels a decrease in HIF-1α levels in these cells (Fig. 4C).

Together, these findings support the conclusion that NO produced by Cco/NO in hypoxic HEK293 cells plays a role in the stabilization of HIF-1α. Previous efforts to understand the effects of NO on HIF-1α stability under hypoxia have focused largely on the effects of NO on the prolyl hydroxylases (PHDs) that hydroxylate HIF-1α. They have revealed that exposing cells to exogenous NO-donors reduces HIF-1α hydroxylation [28] and that NO has an inhibitory effects on PHDs 1–3 *in vitro*. It is not yet clear how NO inhibits PHDs but it has been proposed to compete with O_2 for binding to the ferrous iron at the active site on these enzymes [28]. It is not yet known if NO also functions in the nitrosylation or tyrosine nitration of HIF-1 protein side chains in hypoxic cells or if NO exerts its effect on HIF-1α indirectly by affecting proteins with which it interacts or which function in other HIF-1α post-translational modifications. In this latter regard it is interesting that the hypoxic deacetylation of HIF-1α is catalyzed by SIRT1 [24] and that NO modulates the deacetylase activity of SIRT1 [19].

3.4. Mitochondrial involvement in hypoxic signaling

It is clear that the identification of mitochondria as the intracellular source of NO generated in hypoxic cells is crucial to understanding the role of NO in HIF-1α stabilization and hypoxic signaling. Indeed, the findings reported here support a new model for mitochondrial involvement in hypoxic signaling [32]. This model takes into account the finding that hypoxic mitochondria produce both superoxide and NO and proposes that the predominant mitochondrially-generated signals in hypoxic cells are either peroxynitrite (ONOO-) or NO. Because these free radicals are highly reactive and unstable it is unlikely that they diffuse over the great distances that separate the mitochondrial reticulum and the nucleus. Indeed, it is more likely that these free radicals initiate signaling via S-nitrosylation, or tyrosine nitration and that these modifications activate the signaling pathway between the mitochondrion and HIF-1 in the nucleus. Attempts to identify these proteins are currently underway.

Acknowledgment

This work was supported by National Institutes of Health Grant GM30228 to R.O. P.

References

[1] R. Acin-Perez, D.L. Gatti, Y. Bai, G. Manfredi, Protein phosphorylation and prevention of cytochrome oxidase inhibition by ATP: coupled mechanisms of energy metabolism regulation, Cell Metab. 13 (2011) 712–719.
[2] K.A. Ball, P.R. Castello, R.O. Poyton, Low intensity light stimulates nitrite-dependent nitric oxide synthesis but not oxygen consumption by cytochrome c oxidase: implications for phototherapy, J. Photochem. Photobiol. B 102 (2011) 182–191.
[3] U. Berchner-Pfannschmidt, S. Tug, M. Kirsch, J. Fandrey, Oxygen-sensing under the influence of nitric oxide, Cell Signal 22 (2010) 349–356.
[4] U. Berchner-Pfannschmidt, H. Yamac, B. Trinidad, J. Fandrey, Nitric oxide modulates oxygen sensing by hypoxia-inducible factor 1-dependent induction of prolyl hydroxylase 2, J. Biol. Chem. 282 (2007) 1788–1796.
[5] J.K. Brunelle, E.L. Bell, N.M. Quesada, K. Vercauteren, V. Tiranti, M. Zeviani, R.C. Scarpulla, N.S. Chandel, Oxygen sensing requires mitochondrial ROS but not oxidative phosphorylation, Cell Metab. 1 (2005) 409–414.
[6] P.R. Castello, P.S. David, T. McClure, Z. Crook, R.O. Poyton, Mitochondrial cytochrome oxidase produces nitric oxide under hypoxic conditions: implications for oxygen sensing and hypoxic signaling in eukaryotes, Cell Metab. 3 (2006) 277–287.
[7] P.R. Castello, D.K. Woo, K. Ball, J. Wojcik, L. Liu, R.O. Poyton, Oxygen-regulated isoforms of cytochrome c oxidase have differential effects on its nitric oxide production and on hypoxic signaling, Proc. Natl. Acad. Sci. USA 105 (2008) 8203–8208.
[8] N.S. Chandel, D.S. McClintock, C.E. Feliciano, T.M. Wood, J.A. Melendez, A.M. Rodriguez, P.T. Schumacker, Reactive oxygen species generated at mitochondrial complex III stabilize hypoxia-inducible factor-1alpha during hypoxia: a mechanism of O_2 sensing, J. Biol. Chem. 275 (2000) 25130–25138.
[9] R. Dirmeier, K.M. O'Brien, M. Engle, A. Dodd, E. Spears, R.O. Poyton, Exposure of yeast cells to anoxia induces transient oxidative stress. Implications for the induction of hypoxic genes, J. Biol. Chem. 277 (2002) 34773–34784.
[10] N.T. Eissa, J.W. Yuan, C.M. Haggerty, E.K. Choo, C.D. Palmer, J. Moss, Cloning and characterization of human inducible nitric oxide synthase splice variants: a domain, encoded by exons 8 and 9, is critical for dimerization, Proc. Natl. Acad. Sci. USA 95 (1998) 7625–7630.
[11] R.D. Guzy, B. Hoyos, E. Robin, H. Chen, L. Liu, K.D. Mansfield, M.C. Simon, U. Hammerling, P.T. Schumacker, Mitochondrial complex III is required for hypoxia-induced ROS production and cellular oxygen sensing, Cell Metab. 1 (2005) 401–408.
[12] T. Hagen, C.T. Taylor, F. Lam, S. Moncada, Redistribution of intracellular oxygen in hypoxia by nitric oxide: effect on HIF1alpha, Science 302 (2003) 1975–1978.
[13] S. Helling, S. Vogt, A. Rhiel, R. Ramzan, L. Wen, K. Marcus, B. Kadenbach, Phosphorylation and kinetics of mammalian cytochrome c oxidase, Mol. Cell Proteomics 7 (2008) 1714–1724.
[14] L.E. Huang, Z. Arany, D.M. Livingston, H.F. Bunn, Activation of hypoxia-inducible transcription factor depends primarily upon redox-sensitive stabilization of its alpha subunit, J. Biol. Chem. 271 (1996) 32253–32259.
[15] L.E. Huang, W.G. Willmore, J. Gu, M.A. Goldberg, H.F. Bunn, Inhibition of hypoxia-inducible factor 1 activation by carbon monoxide and nitric oxide. Implications for oxygen sensing and signaling, J. Biol. Chem. 274 (1999) 9038–9044.
[16] Z. Huang, S. Shiva, D.B. Kim-Shapiro, R.P. Patel, L.A. Ringwood, C.E. Irby, K.T. Huang, C. Ho, N. Hogg, A.N. Schechter, M.T. Gladwin, Enzymatic function of hemoglobin as a nitrite reductase that produces NO under allosteric control, J. Clin. Invest. 115 (2005) 2099–2107.
[17] A.U. Igamberdiev, R.D. Hill, Plant mitochondrial function during anaerobiosis, Ann. Bot. (Lond) 103 (2008) 259–268.
[18] H. Kojima, N. Nakatsubo, K. Kikuchi, S. Kawahara, Y. Kirino, H. Nagoshi, Y. Hirata, T. Nagano, Detection and imaging of nitric oxide with novel fluorescent indicators: diaminofluoresceins, Anal. Chem. 70 (1998) 2446–2453.
[19] M.D. Kornberg, N. Sen, M.R. Hara, K.R. Juluri, J.V. Nguyen, A.M. Snowman, L. Law, L.D. Hester, S.H. Snyder, GAPDH mediates nitrosylation of nuclear proteins, Nat. Cell Biol. 12 (2010) 1094–1100.
[20] K.E. Kwast, P.V. Burke, B.T. Staahl, R.O. Poyton, Oxygen sensing in yeast: evidence for the involvement of the respiratory chain in regulating the transcription of a subset of hypoxic genes, Proc. Natl. Acad. Sci. USA 96 (1999) 5446–5451.
[21] Z. Lacza, A.V. Kozlov, E. Pankotai, A. Csordas, G. Wolf, H. Redl, M. Kollai, C. Szabo, D.W. Busija, T.F. Horn, Mitochondria produce reactive nitrogen species via an arginine-independent pathway, Free Radic. Res. 40 (2006) 369–378.
[22] B. Li, C. Skinner, P.R. Castello, M. Kato, E. Easlon, L. Xie, T. Li, S.P. Lu, C. Wang, F. Tsang, R.O. Poyton, S.J. Lin, Identification of potential calorie restriction-mimicking yeast mutants with increased mitochondrial respiratory chain and nitric oxide levels, J. Aging Res. 2011 (2011) 673185.
[23] H. Li, A. Samouilov, X. Liu, J.L. Zweier, Characterization of the effects of oxygen on xanthine oxidase-mediated nitric oxide formation, J. Biol. Chem. 279 (2004) 16939–16946.
[24] J.H. Lim, Y.M. Lee, Y.S. Chun, J. Chen, J.E. Kim, J.W. Park, Sirtuin 1 modulates cellular responses to hypoxia by deacetylating hypoxia-inducible factor 1alpha, Mol. Cell 38 (2010) 864–878.
[25] Y. Liu, H. Christou, T. Morita, E. Laughner, G.L. Semenza, S. Kourembanas, Carbon monoxide and nitric oxide suppress the hypoxic induction of vascular endothelial growth factor gene via the 5' enhancer, J. Biol. Chem. 273 (1998) 15257–15262.
[26] K.D. Mansfield, R.D. Guzy, Y. Pan, R.M. Young, T.P. Cash, P.T. Schumacker, M.C. Simon, Mitochondrial dysfunction resulting from loss of cytochrome c impairs cellular oxygen sensing and hypoxic HIF-alpha activation, Cell Metab. 1 (2005) 393–399.
[27] J. Mateo, M. Garcia-Lecea, S. Cadenas, C. Hernandez, S. Moncada, Regulation of hypoxia-inducible factor-1alpha by nitric oxide through mitochondria-dependent and -independent pathways, Biochem. J. 376 (2003) 537–544.
[28] E. Metzen, J. Zhou, W. Jelkmann, J. Fandrey, B. Brune, Nitric oxide impairs normoxic degradation of HIF-1alpha by inhibition of prolyl hydroxylases, Mol. Biol. Cell 14 (2003) 3470–3481.
[29] L.P. Miller, Quantifying western blots without expensive commercial quantification software 1–8 (2007) (Online).
[30] N. Nakatsubo, H. Kojima, K. Kikuchi, H. Nagoshi, Y. Hirata, D. Maeda, Y. Imai, T. Irimura, T. Nagano, Direct evidence of nitric oxide production from bovine aortic endothelial cells using new fluorescence indicators: diaminofluoresceins, FEBS Lett. 427 (1998) 263–266.
[31] M. Palacios-Callender, V. Hollis, M. Mitchison, N. Frakich, D. Unitt, S. Moncada, Cytochrome c oxidase regulates endogenous nitric oxide availability in respiring cells: a possible explanation for hypoxic vasodilation, Proc. Natl. Acad. Sci. USA 104 (2007) 18508–18513.

[32] R.O. Poyton, K.A. Ball, P.R. Castello, Mitochondrial generation of free radicals and hypoxic signaling, Trends Endocrinol. Metab. 20 (2009) 332–340.
[33] K. Sogawa, K. Numayama-Tsuruta, M. Ema, M. Abe, H. Abe, Y. Fujii-Kuriyama, Inhibition of hypoxia-inducible factor 1 activity by nitric oxide donors in hypoxia, Proc. Natl. Acad. Sci. USA 95 (1998) 7368–7373.
[34] E.E. van Faassen, S. Bahrami, M. Feelisch, N. Hogg, M. Kelm, D.B. Kim-Shapiro, A.V. Kozlov, H. Li, J.O. Lundberg, R. Mason, H. Nohl, T. Rassaf, A. Samouilov, A. Slama-Schwok, S. Shiva, A.F. Vanin, E. Weitzberg, J. Zweier, M.T. Gladwin, Nitrite as regulator of hypoxic signaling in mammalian physiology, Med. Res. Rev. 29 (2009) 683–741.
[35] X. Zhou, P. He, Improved measurements of intracellular nitric oxide in intact microvessels using 4,5-diaminofluorescein diacetate, Am. J. Physiol. Heart Circ. Physiol. 301 (2011) H108–H114.

Biochemical and Biophysical Research Communications 420 (2012) 733–737

Contents lists available at SciVerse ScienceDirect

Biochemical and Biophysical Research Communications

journal homepage: www.elsevier.com/locate/ybbrc

Study of the electrostatic effects of mutations on the surface of dehaloperoxidase-hemoglobin A

Junjie Zhao [a], Jennifer Rowe [a], Jocelyn Franzen [a], Chi He [b], Stefan Franzen [a,*]

[a] Department of Chemistry, North Carolina State University, Raleigh, NC 27695, United States
[b] Department of Chemistry, Zhejiang University, Hangzhou, China

ARTICLE INFO

Article history:
Received 2 March 2012
Available online 17 March 2012

Keywords:
Surface mutation
Electrostatic interaction
Isoelectric focusing
Ionic strength effect
Enzyme kinetics

ABSTRACT

Point mutations of dehaloperoxidase-hemoglobin A (DHP A) that affect the surface charge have been prepared to study the interaction between DHP A with its substrate 2,4,6-trichlorophenol (TCP). Kinetic studies of these surface mutations showed a correlation, in which the more positively charged mutants have increased catalytic efficiency compared with wild type DHP A. As a result, the hypothesis of this study is that there is a global electrostatic interaction between DHP A and TCP. The electrostatic nature of substrate binding was further confirmed by the result that kinetic assays of DHP A were affected by ionic strength. Furthermore, isoelectric focusing (IEF) gel study showed that the pI – 6.8 for DHP A, which indicates that DHP A has a slight negative charge pH 7, consistent with the kinetic observations.

© 2012 Elsevier Inc. All rights reserved.

1. Introduction

Dehaloperoxidase-hemoglobin A was first isolated from the terebellid polychaete *Amphitrite ornata* [1], and subsequently cloned and expressed into *Escherichia coli* cells. [2] DHP A is a bifunctional protein which can function as both a hemoglobin and a peroxidase [1,3]. As a hemoglobin, DHP A can cycle between oxy and deoxy states by reversibly binding diatomic oxygen, and therefore serves an essential role in oxygen storage and transport in *A. ornata* [3]. As a peroxidase, DHP A can catalyze the oxidation of 2,4,6-trihalophenol (2,4,6-TXP) to the corresponding 2,6-dihaloquinone (2,6-DXQ) (X = I, Br, Cl, F) using H_2O_2 as a co-substrate (Scheme 1) [1]. Peroxidase activity can be inhibited in the presence of 4-bromophenol (4-BP) [4]. This observation is significant because of the prevalence of 4-BP in coastal ecosystems where *A. ornata* is found [5].

DHP A is a unique heme protein because it has an internal binding site for inhibitor 4-BP [4,6,7]. Based on the available data we suggest that there is an external binding site for substrates such as 2,4,6-TXPs [4,8]. The mechanism has been characterized using a two-site competitive inhibition model [4]. The internal binding site of inhibitor 4-BP has been demonstrated by X-ray crystallography and resonance Raman spectroscopy as the distal pocket immediately above heme Fe [4]. The correlated evidence from X-ray crystallography, NMR and RR spectroscopy, strongly suggests that there is an external binding site for substrates such as 2,4,6-TXPs [4,8]. However, the exact binding site of TXP has not yet been determined.

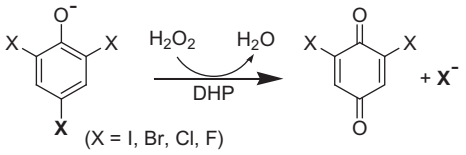
Extensive mutagenesis of DHP A has been carried out at residues around the distal pocket, which surrounds the heme iron [9–12]. The heme iron is the active site for H_2O_2 activation in the peroxidase function. The mutagenesis studies have supplied information relevant to the catalytic mechanism of DHP A and the role played by important conserved residues [9,13]. However, surface residues of DHP A have not been studied in any detail. The role of charged surface residues has been studied in some other hemeproteins such as Cytochrome c6 and Cytochrome P450scc, which show the importance of electrostatic contacts in hemeprotein–protein and hemeprotein–ferredoxin interactions, respectively, for electron transfer [14,15]. Since the substrate of DHP A is negatively charged at pH 7, as shown in Scheme 1, it is possible that there is electrostatic interaction between DHP A and substrate. In this study, we have tested the hypothesis that surface charge affects the rate of substrate binding and thereby the catalytic efficiency.

To test the hypothesis, we initiated a systematic study of the effect of mutation of charged surface amino acid residues. Our studies have mainly used TCP as a substrate, because of the higher solubility compared with 2,4,6-tribromophenol (TBP), which is the native substrate. Considering that DHP A has at the greatest activity at pH 7.4, we reasoned the Coulombic effects could be significant [16]. At pH 7.4, the substrate TCP is negatively charged,

Abbreviations: DHP A, dehalperoxidase-hemoglobin A; 2,4,6-TXP, 2,4,6-trihalophenol; 2,6-DXQ, 2,6-dihaloquinone (X = I, Br, Cl, F); TCP, 2,4,6-trichlorophenol; TBP, 2,4,6-tribromophenol; DCQ, 2,6-dichloroquinone; 4-BP, 4-bromophenol; IEF, isoelectric focusing.

* Corresponding author.
E-mail address: Stefan_Franzen@ncsu.edu (S. Franzen).

0006-291X/$ - see front matter © 2012 Elsevier Inc. All rights reserved.
http://dx.doi.org/10.1016/j.bbrc.2012.03.053



Scheme 1. Oxidative–dehalogenation of TXP to yield DXQ as catalyzed by DHP in the presence of H_2O_2.

since it is has a pK_a of 6.2. It was hypothesized that negatively charged TCP might interact with charged residues (lysine, arginine, glutamate or aspartate) on the surface of protein. The results presented herein show that this is indeed the case, but that specific locations are not important to the effect, which appears to be a global electrostatic effect of the protein surface. In present work, different residues are mutated (Table 1) on the surface of DHP A in order to test their effect on the kinetics of the turnover of TCP. Moreover, the electrostatic nature of the interaction between TCP and DHP A was also tested by a study of the ionic strength dependence of the enzymatic rate.

2. Materials and methods

2.1. Materials

Buffer salts were purchased from Fisher Scientific. All other reagents and biochemicals were purchased from Sigma–Aldrich and used without further purification. Deionized water is provided by Barnstead system. The E.Z.N.A plasmid mini kit I was purchased from Omega bio-tek, Inc. The QuikChange II site-directed mutagenesis kit was purchased from Stratagene (La Jolla, CA). The required oligo-nucleotides were synthesized by IDT DNA Technologies, Inc.

2.2. Plasmid preparation, protein purification and preparation

Mutations listed in Table 1 were generated with the QuikChange II site-directed mutagenesis kit. Mutagenesis (melt (95 °C, 30 s), anneal (55 °C, 60 s), and extension (68 °C, 6 min)) was performed for 16 cycles. The plasmid encoding DHP A was used as a template to generate the mutation using different mutagenic primers (Table S1, Supporting information). The plasmids were extracted using the E.Z.N.A plasmid mini kit I. The presence of the desired mutation was confirmed by sequencing. Protein was expressed, purified and prepared in ferric form as previously described [8,12] with only minor modification.

2.3. Enzyme kinetic assays

Experiments of surface mutants kinetic assays were conducted in 150 mM potassium phosphate (KP_i) buffer at pH 7 and kinetic assays of DHP A were conducted in 10 mM KP_i pH 7 buffer with the gradual addition of NaBr. Kinetic spectra were collected with an Agilent 8453 UV–Vis spectrometer equipped with a temperature control system and Hewlett Packard UV–Visible Chemstation software set to kinetics mode. The concentration of enzyme in each sample was about 2.4 μM. The temperature was equilibrated to 20 °C and a 500-fold excess of H_2O_2 was added to the quartz cuvette to initiate the assay. Spectra were acquired every 3 s for 2 min, monitoring the formation of DCQ at 273 nm. The initial velocity, V_0 of enzyme turnover was calculated for each concentration of TCP and V_0 versus TCP concentration data were fit independently to the Michaelis–Menten equation using non-linear fitting curve in Igor Pro5.0.

Table 1
Surface mutations of DHP A made on different heme edges.

K99Q α edge	N61D δ edge
K99A α edge	N61 K δ edge
N96D α edge	K58A δ edge
R33Q β edge	K51A γ edge
R33A β edge	K87A γ edge
K36A β edge	

2.4. Isoelectric focusing study of DHP A

IEF standards and ferric DHP A were loaded into an IEF ready gel pH 5–8 (Bio-Rad Laboratories, Inc. CA). The gels were run under 100 V for 60 min, 250 V for 60 min and 500 V for 30 min. Gels were stained by Coomassie blue for 45 min and destained in 40% methanol and 10% acetic acid for 120 min.

3. Results

3.1. Mutagenesis, expression and purification of surface mutants of DHP A

The mutants K99A and K99Q were not expressed in *Escherichia coli*. The other surface mutants given in Table 1 have an expression yield similar to wild type DHP A.

3.2. Enzyme kinetics study of the surface mutants of DHP A

The rate scheme for DHP as a peroxidase catalyst is shown in Scheme 2, in which H_2O_2 activation is the first step with rate constant k_1 and substrate bindings are the second and third steps with rate constants k_2 and k_3, respectively.

The Michaelis–Menten equation derived from Scheme 2 and the corresponding V_{max}, K_m and k_{cat}/K_m are shown as follows [17]:

$$V_0 = \frac{V_{max}[\text{substrate}]}{K_m + [\text{substrate}]} \quad V_{max} = k_1[H_2O_2][E]_T$$

$$K_m = \left(\frac{1}{k_2} + \frac{1}{k_3}\right)k_1[H_2O_2] \quad K_{cat}/K_m = \frac{k_2k_3}{k_2 + k_3}$$

Fig. 1 shows the comparison of the catalytic rates of wild-type DHP A with other surface mutations listed in Table 1. The data are presented in the form of Michaelis–Menten rate saturation plots. Table 2 summaries the kinetic parameters of the surface mutants obtained from fits to the Michaelis–Menten plots. The enzyme concentration used for each mutant is 2.4 μM. Compared with wild-type DHP A, catalytic efficiency k_{cat}/K_m of N61 K is increased by a factor of 1.21. However, the rest of mutants listed in Table 2 showed a decrease in k_{cat}/K_m relative to wild type DHP A from 11.1% (N61D) to 40.9% (R33Q).

3.3. Study of ionic strength effects of DHP A kinetics

Fig. 2 shows the catalytic efficiency k_{cat}/K_m of DHPA as a function of NaBr concentration. The k_{cat}/K_m rises with the increase of NaBr concentration from 0 to 50 mM, and then levels off, even decreases with further increase of NaBr concentration. The kinetic parameters derived from Michaelis–Menten curve fitting under different NaBr concentration are summarized in Table 3.

$$DHP + H_2O_2 \xrightarrow{k_1} Compound \quad ES + H_2O$$
$$Compound \quad ES + XAOH \xrightarrow{k_2} Compound \quad II + XAO\bullet$$
$$Compound \quad II + XAOH \xrightarrow{k_3} DHP + XAO\bullet$$

Scheme 2. Rate scheme for DHP as a peroxidase catalyst.

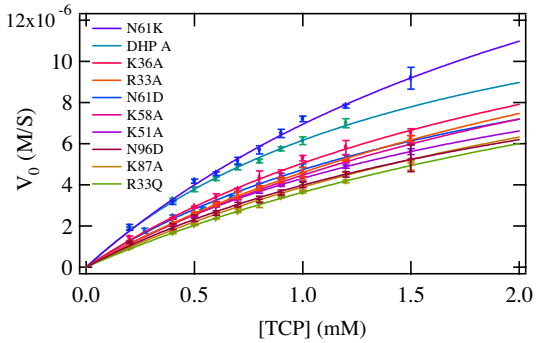


Fig. 1. Single wavelength kinetics at 273 nm (2,6-DCQ) of oxidation of 2,4,6-TCP by DHP as a function of 2,4,6-TCP concentration and enzymatic reaction initial velocities. Assay conditions were 2.4 μM DHP, 0.2 mM–1.5 mM TCP and 1.2 mM H_2O_2 in 150 mM KP buffer at pH 7 at 293 K. The Michaelis–Menten fit parameters are given in Table 2.

Table 2
Kinetic parameters of DHP A and surface mutations from the curve fitting to the Michaelis–Menten equation.

	k_{cat} (s^{-1})	K_m (mM)	k_{cat}/K_m (mM^{-1} s^{-1})
DHPA	5.62 ± 0.31	1.73 ± 0.15	3.25 ± 0.33
N61 K	11.0 ± 1.07	2.80 ± 0.37	3.92 ± 0.64
N61D	6.21 ± 0.55	2.15 ± 0.27	2.89 ± 0.44
K58A	7.70 ± 0.35	3.13 ± 0.19	2.46 ± 0.19
K51A	5.91 ± 0.14	2.29 ± 0.08	2.58 ± 0.11
K36A	7.58 ± 0.69	2.60 ± 0.32	2.92 ± 0.45
R33A	8.26 ± 0.36	3.31 ± 0.19	2.50 ± 0.18
N96D	5.81 ± 0.47	2.50 ± 0.28	2.32 ± 0.32
K87A	7.01 ± 0.59	3.32 ± 0.36	2.11 ± 0.29
R33Q	7.19 ± 0.33	3.75 ± 0.22	1.92 ± 0.14

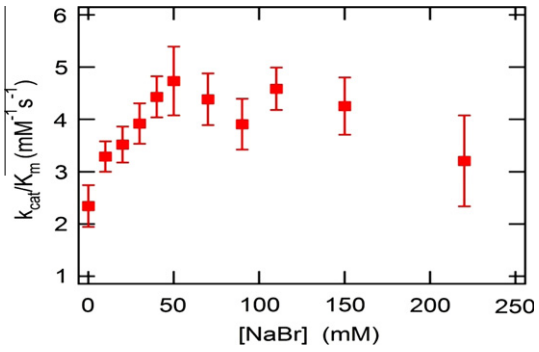


Fig. 2. Catalytic efficiency of DHP A as a function of [NaBr]. Assay conditions were 2.4 μM DHP A, 0.2 mM–1.5 mM TCP and 1.2 mM H_2O_2 in 10 mM KP_i buffer with 0–220 mM NaBr at pH 7 at 293 K. The Michaelis–Menten fit parameters are given in Table 3.

3.4. Isoelectric focusing study of DHP A

Fig. 3 shows the isoelectric focusing gel of ferric DHP A and IEF standards in different columns. IEF standards were loaded in the middle column and DHP A was loaded on the two sides. By comparing with IEF standards, DHP A has a clear single band between pH 6.5 and 7, which is estimated around 6.8. It suggests DHP A is negatively charged under pH 7.

4. Discussion

It appears that there is a correlation of increasing overall negative charge on the surface of DHP with increasing repulsion of the substrate, which can be considered as a general electrostatic effect

Table 3
Kinetic parameters of DHP A in different [NaBr] from the curve fitting to the Michaelis–Menten equation.

[NaBr] mM	k_{cat} (s^{-1})	K_m (mM)	k_{cat}/K_m (mM^{-1} s^{-1})
0	16.2 ± 1.80	6.90 ± 0.89	2.34 ± 0.40
10	10.7 ± 0.58	3.26 ± 0.23	3.29 ± 0.29
20	11.3 ± 0.67	3.22 ± 0.25	3.52 ± 0.34
30	10.2 ± 0.59	2.60 ± 0.21	3.92 ± 0.39
40	10.5 ± 0.54	2.36 ± 0.17	4.43 ± 0.39
50	11.1 ± 0.89	2.33 ± 0.27	4.74 ± 0.66
70	9.94 ± 0.65	2.27 ± 0.21	4.39 ± 0.50
90	10.5 ± 0.77	2.69 ± 0.27	3.91 ± 0.48
110	8.36 ± 0.41	1.82 ± 0.14	4.59 ± 0.41
150	10.6 ± 0.80	2.49 ± 0.26	4.25 ± 0.55
220	15.1 ± 2.59	4.70 ± 0.99	3.21 ± 0.87

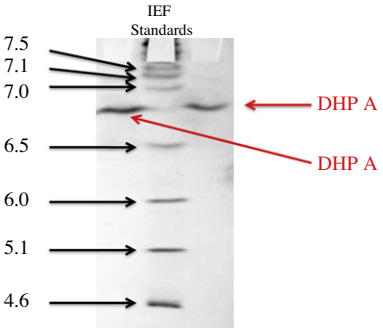


Fig. 3. Isoelectric focusing (IEF) gel of DHP A (left and right columns) with IEF standards (middle column).

on substrate binding. This correlation is based on the observation that mutants with more negative charge than wild type DHP A have lower catalytic efficiency than those with less negative charge. Based on these observations, it is hypothesized that the interaction between substrate TCP and DHP is electrostatic in nature.

The pK_a of substrate TCP is 6.2, so that substrate is mostly in the anionic conjugate base form at neutral pH. The change of charged amino acids on the surface of enzyme might affect the binding of TCP by DHP A. In the catalytic reaction cycle of DHP A (Scheme 2), steps 2 and 3 are the substrate binding steps with rate constants k_2 and k_3, respectively. Based on the expressions of V_{max} and K_m, it is K_m which is dependent of substrate binding rate constants k_2 and k_3 instead of V_{max}. However, K_m is also related to the H_2O_2 activation rate constant k_1 and [H_2O_2] concentration. Therefore, the effect of mutation on the catalytic efficiency, k_{cat}/K_m, was deemed the best independent measure of the effect on the substrate binding rate constants, k_2 and k_3.

The mutants, K36A, K51A, K58A and K87A give rise to a reduction in positive charge on the protein surface by mutating lysines at 36, 51, 58 and 87 into alanines, respectively. R33A and R33Q mutations are designed to also reduce the charge by one unit by mutating Arg33 into Ala33 and Gln33, respectively. N61D and N96D mutations are mutations of neutral charged N61, N96 into D61 and D96, respectively. Therefore, the overall charges of K36A, K51A, K58A, K87A, R33A, R33Q, N96D and N61D are more negative compared with DHP A. It is observed that all these mutations have slightly smaller k_{cat}/K_m values compared with DHP A, which suggests smaller values of k_2 and k_3 in the mutants relative to wild type DHP A. The N61 K mutation, which consists of a mutation of neutral Asn61 into positively charged Lys61 has an opposite effect. The overall charge of N61 K is less negative compared with DHP A, resulting that N61 K has higher k_{cat}/K_m value than wild type DHP A.

We used the ionic strength dependence of the catalytic efficiency as a test of the electrostatic model. In electric double layer theory, Debye length is proportional to the square root of the reciprocal of ionic strength. Therefore, the salt concentration would affect the kinetic activity of DHP. The catalytic efficiency of DHP A is tested in different [NaBr] and shown in Table 3 and Fig. 2. With the increase of [NaBr], the catalytic efficiency increases and then levels off followed by a slight decrease. We believe that the decrease is due to the binding of Br^- to the heme iron at high concentration. Obviously, this binding would tend to inhibit the enzyme. Thus the range over which ionic strength effects can be measured is from 0 to 100 mM. These results indicate that a high concentration of NaBr screens the charge of protein in solution. If DHP A is positively charged, the catalytic efficiency should decrease with increasing ionic strength. Otherwise, the catalytic efficiency should increase proportional to the ionic strength. Based on the result in Fig. 2, it is believed DHP A is mostly negatively charged at PH 7. And this is consistent with the result of IEF gel study, shown in Fig. 3, which shows that pI of wild type DHP A is around 6.8.

The activation of H_2O_2, which occurs at the heme Fe atom may also be affected by surface electrostatics. Studies of the binding and reactions at the heme active site have been conducted by resonance Raman spectroscopy [4,18], and electron paramagnetic resonance (EPR) [11,12,19–21]. These studies show that substrate and inhibitor binding are competitive. However, more important for the present result is the observation that substrate binding appears to involve an interaction with the distal histidine that strengthens its ability to hydrogen bond with water bound to Fe(III) at the active site of DHP A. One can infer that substrate binding could be a trigger for initiation of enzymatic activity. However, in the native hemoglobin function the enzyme would be found in the oxy form, Fe(II)–O_2, and therefore the question arises as to how substrate binding could trigger a change from hemoglobin to peroxidase function. Recent evidence suggests that activation requires displacement of bound O_2 [22,23]. According to kinetic Scheme 2 the effect on k_{cat}/K_m measures an effect on k_2 and k_3, there is no direct evidence that surface electrostatics affect k_1 [17]. However, paradoxically, substrate binding may be required to initiate enzyme function and thus to therefore may actually play a role in the k_1 process as well [24]. It is possible that the kinetic scheme for a dehaloperoxidase-hemoglobin is more complex than Scheme 2 would indicate.

The long-range electrostatic nature of the interaction of substrate TCP and DHP A has been confirmed by kinetic studies of surface mutations and ionic strength. The kinetic studies on DHP A with various surface mutations show that there is a correlation of increasing positive surface charge and catalytic efficiency compared with wild type DHP A. The increase in DHP A catalytic efficiency with increasing ionic strength indicates that DHP A has a negative charge at pH 7. This conclusion is confirmed by an IEF gel study of DHP A, which shows pI – 6.8 for DHP A, although this result suggests that the charge is relatively modest. Understanding electrostatic nature of the interaction between DHP A and substrate may help further in understanding the external binding site of substrate TCP. On the basis of the present work, we suggest electrostatic control of substrate binding may play a role elsewhere in biochemistry. For example, once glucose is phosphorylated by glucose-6-phosphorylase, glucose-6-phosphate and every subsequent substrate in the tricarboxylic acid cycle is negatively charged. The present study suggests the hypothesis that electrostatic control over the binding of substrates may provide an aspect of directional control over the trajectories of substrates in complex biochemical cycles.

Acknowledgments

S.F. gratefully acknowledges support through Army Research Office Grant LS-552685.

Appendix A. Supplementary data

Supplementary data associated with this article can be found, in the online version, at doi:10.1016/j.bbrc.2012.03.053.

References

[1] Y.P. Chen, S.A. Woodin, D.E. Lincoln, C.R. Lovell, An unusual dehalogenating peroxidase from the marine terebellid polychaete *Amphitrite ornata*, J. Biol. Chem. 271 (1996) 4609–4612.
[2] J. Belyea, L.B. Gilvey, M.F. Davis, M. Godek, T.L. Sit, S.A. Lommel, S. Franzen, Enzyme function of the globin dehaloperoxidase from *Amphitrite ornata* is activated by substrate binding, Biochemistry 44 (2005) 15637–15644.
[3] R.E. Weber, C. Mangum, H. Steinman, C. Bonaventura, B. Sullivan, J. Bonaventura, Hemoglobins of two terebellid polychaetes: Enoplobranchus sanguineus and *Amphitrite ornata*, Comp. Biochem. Physiol. A Comp. Physiol. 56 (1977) 179–187.
[4] M.K. Thompson, M.F. Davis, V. de Serrano, F.P. Nicoletti, B.D. Howes, G. Smulevich, S. Franzen, Internal binding of halogenated phenols in dehaloperoxidase-hemoglobin inhibits peroxidase activity, Biophys. J. 99 (2010) 1586–1599.
[5] D.E. Lincoln, K.T. Fielman, R.L. Marinelli, S.A. Woodin, Bromophenol accumulation and sediment contamination by the marine annelids Notomastus lobatus and Thelepus crispus, Biochem. Syst. Ecol. 33 (2005) 559–570.
[6] M.W. LaCount, E. Zhang, Y.P. Chen, K. Han, M.M. Whitton, D.E. Lincoln, S.A. Woodin, L. Lebioda, The crystal structure and amino acid sequence of dehaloperoxidase from *Amphitrite ornata* indicate common ancestry with globins, J. Biol. Chem. 275 (2000) 18712–18716.
[7] L. Lebioda, M.W. LaCount, E. Zhang, Y.P. Chen, K. Han, M.M. Whitton, D.E. Lincoln, S.A. Woodin, An enzymatic globin from a marine worm, Nature (London) 401 (1999) 445.
[8] M.F. Davis, H. Gracz, F.A.P. Vendeix, V. de Serrano, A. Somasundaram, S.M. Decatur, S. Franzen, Different modes of binding of mono-, Di-, and trihalogenated phenols to the hemoglobin Dehaloperoxidase from *Amphitrite ornata*, Biochemistry 48 (2009) 2164–2172.
[9] S. Franzen, J. Belyea, L.B. Gilvey, M.F. Davis, C.E. Chaudhary, T.L. Sit, S.A. Lommel, Proximal cavity, distal histidine, and substrate hydrogen-bonding mutations modulate the activity of *Amphitrite ornata* Dehaloperoxidase, Biochemistry 45 (2006) 9085–9094.
[10] E.L. D'Antonio, J. D'Antonio, V. De Serrano, H. Gracz, M.K. Thompson, R.A. Ghiladi, E.F. Bowden, S. Franzen, The functional consequences of the creation of an Asp–His–Fe triad in a 3/3 globin, Biochemistry (2011 A.S.A.P.).
[11] J. D'Antonio, E.L. D'Antonio, M.K. Thompson, E.F. Bowden, S. Franzen, T. Smirnova, R.A. Ghiladi, Spectroscopic and mechanistic investigations of Dehaloperoxidase B from *Amphitrite ornata*, Biochemistry 49 (2010) 6600–6616.
[12] J. Feducia, R. Dumarieh, L.B.G. Gilvey, T. Smirnova, S. Franzen, R.A. Ghiladi, Characterization of Dehaloperoxidase compound ES and its reactivity with trihalophenols, Biochemistry 48 (2009) 995–1005.
[13] J. Zhao, R. Dumarieh, M.K. Thompson, V. deSerrano, R. Ghiladi, S. Franzen, Role of distal histidine in the activation and protection of heme in dehaloperoxidase-hemoglobin A, Journal of Physical Chemistry B, submitted for publication.
[14] N.V. Strushkevich, T.N. Azeva, G.I. Lepesheva, S.A. Usanov, Role of positively charged residues Lys267, Lys270, and Arg411 of cytochrome P450scc (Cyp11A1) in interaction with adrenodoxin, Biochemistry-Moscow 70 (2005) 664–671.
[15] F.P. Molina-Heredia, A. Diaz-Quintana, M. Hervas, J.A. Navarro, M.A. De la Rosa, Site-directed mutagenesis of cytochrome c(6) from Anabaena species PCC 7119 – Identification of surface residues of the hemeprotein involved in photosystem I reduction, Journal of Biological Chemistry 274 (1999) 33565–33570.
[16] S. Franzen, L.B. Gilvey, J.L. Belyea, The pH dependence of the activity of dehaloperoxidase from *Amphitrite ornata*, Biochim. Biophys. Acta Proteins Proteomics 1774 (2007) 121–130.
[17] H.A. Ma, M.K. Thompson, J. Gaff, S. Franzen, Kinetic analysis of a naturally occurring bioremediation enzyme: Dehaloperoxidase-Hemoglobin from *Amphitrite ornata*, J. Phys. Chem. B 114 (2010) 13823–13829.
[18] F.P. Nicoletti, M.K. Thompson, B.D. Howes, S. Franzen, G. Smulevich, New insights into the role of distal histidine flexibility in ligand stabilization of Dehaloperoxidase-hemoglobin from *Amphitrite ornata*, Biochemistry 49 (2010) 1903–1912.

[19] T.I. Smirnova, R.T. Weber, M.F. Davis, S. Franzen, Substrate binding triggers a switch in the iron coordination in Dehaloperoxidase from *Amphitrite ornata*: HYSCORE experiments, J. Am. Chem. Soc. 130 (2008) 2128–2129.

[20] R. Davydov, R.L. Osborne, S.H. Kim, J.H. Dawson, B.M. Hoffman, EPR and ENDOR studies of cryoreduced Compounds II of peroxidases and myoglobin. Proton-coupled electron transfer and protonation status of ferryl hemes, Biochemistry 47 (2008) 5147–5155.

[21] R. Davydov, R.L. Osborne, M. Shanmugam, J. Du, J.H. Dawson, B.M. Hoffman, Probing the oxyferrous and catalytically active ferryl states of *Amphitrite ornata* Dehaloperoxidase by cryoreduction and EPR/ENDOR spectroscopy. Detection of Compound I, J. Am. Chem. Soc. 132 (2010) 14995–15004.

[22] J. Du, M. Sono, J.H. Dawson, Functional switching of *Amphitrite ornata* Dehaloperoxidase from O-2-binding globin to peroxidase enzyme facilitated by halophenol substrate and H_2O_2, Biochemistry 49 (2010) 6064–6069.

[23] J. D'Antonio, R.A. Ghiladi, Reactivity of deoxy- and oxyferrous Dehaloperoxidase B from *Amphitrite ornata*: identification of Compound II and its ferrous-hydroperoxide precursor, Biochemistry 50 (2011) 5999–6011.

[24] M.K. Thompson, R.A. Ghiladi, S. Franzen, The Dehaloperoxidase Paradox, Biochim. Biophys. Acta A.S.A.P. (2012).

Biochemical and Biophysical Research Communications 420 (2012) 738–742

Contents lists available at SciVerse ScienceDirect

Biochemical and Biophysical Research Communications

journal homepage: www.elsevier.com/locate/ybbrc

Rapid detection of microbial DNA by a novel isothermal genome exponential amplification reaction (GEAR) assay

Jothikumar Prithiviraj [a], Vincent Hill [b], Narayanan Jothikumar [b,*]

[a] Georgia Tech, Institute of Bioengineering and Biosciences, 315 Ferst Drive, Atlanta, GA 30332, USA
[b] Centers for Disease Control and Prevention, National Center for Emerging and Zoonotic Infectious Diseases, Waterborne Disease Prevention Branch, 1600 Clifton Road, Atlanta, GA 30329, USA

ARTICLE INFO

Article history:
Received 5 March 2012
Available online 17 March 2012

Keywords:
Molecular
Isothermal amplification
Nucleic acids
Diagnosis
Real-time monitoring

ABSTRACT

In this study we report the development of a simple target-specific isothermal nucleic acid amplification technique, termed genome exponential amplification reaction (GEAR). *Escherichia coli* was selected as the microbial target to demonstrate the GEAR technique as a proof of concept. The GEAR technique uses a set of four primers; in the present study these primers targeted 5 regions on the 16S rRNA gene of *E. coli*. The outer forward and reverse Tab primer sequences are complementary to each other at their 5′ end, whereas their 3′ end sequences are complementary to their respective target nucleic acid sequences. The GEAR assay was performed at a constant temperature 60 °C and monitored continuously in a real-time PCR instrument in the presence of an intercalating dye (SYTO 9). The GEAR assay enabled amplification of as few as one colony forming units of *E. coli* per reaction within 30 min. We also evaluated the GEAR assay for rapid identification of bacterial colonies cultured on agar media directly in the reaction without DNA extraction. Cells from *E. coli* colonies were picked and added directly to GEAR assay mastermix without prior DNA extraction. DNA in the cells could be amplified, yielding positive results within 15 min.

Published by Elsevier Inc.

1. Introduction

The polymerase chain reaction (PCR) is used as a standard analytical technique in molecular biology [1,2]. However, PCR requires an energy intensive thermal cycler for heating and cooling cycles during the amplification of DNA and is not field portable. Several isothermal amplification techniques have been reported for amplification of DNA or RNA in a simple heating block or water bath. Previously reported isothermal amplification techniques have some limitations, including requiring more than one enzyme, more than two primers, modification of a primer, or the requirement of RNA. A wide variety of isothermal amplification techniques have been reported, including Strand Displacement Amplification (SDA) [3], Rolling Circle Amplification (RCA) [4], Loop-Mediated Isothermal Amplification (LAMP) [5,6], Multiple Displacement Amplification (MDA) [7], Helicase-Dependent Amplification (tHDA) [8,9], Isothermal and Chimeric primer-initiated Amplification of Nucleic acids (ICAN) [10], self-sustained sequence replication reaction (3SR) [11], nucleic acid sequence-based amplification (NASBA) [12], Transcription Mediated Amplification (TMA) [13], Exponential Amplification Reaction (EXPAR) [14], Single Primer Isothermal Amplification (SPIA) [15], Smart Amplification Process (SmartAmp) [16] and cross-priming amplification (CPA) [17,18]. SDA, SPIA, NASBA, TMA, ICAN and tHDA require multiple enzymes (two or more) and require rigorous optimization. Only a few of these isothermal amplification techniques (e.g., LAMP and SmartAmp) can be efficiently performed at temperatures of $\geqslant$60 °C to increase the specificity of amplification. A new isothermal amplification technique would be useful that combines simple design (e.g., $\leqslant$4 primers), cost-efficiency (e.g., using a single enzyme), and robustness (e.g., amplication at temperatures $\geqslant$60 °C) for the development of field and point of care testing (POCT).

We describe in this report a selective real-time based isothermal amplification assay with four primers that can prime to extend on target sequences at a constant temperature, named genome exponential amplification reaction (GEAR) technique. The GEAR technique differs from the LAMP technique by three distinct features. First, GEAR assays use Tab primers (FT and BT) targeting three genomic regions, whereas LAMP assays consist of inner primers (FIP and BIP) targeting four regions on the target gene. Second, primer design for the GEAR technique differs from the LAMP technique in that the 5′ end between forward and reverse primers are complementary [LAMP inner primers (FIP and BIP) do not form a complementary structure at the 5′ end]. Third, GEAR assays do

* Corresponding author. Address: Centers for Disease Control and Prevention, National Center for Emerging and Zoonotic Infectious Diseases, Waterborne Disease Prevention Branch, 1600 Clifton Road NE, Mail Stop D-66, Atlanta, GA 30329, USA.
E-mail address: jin2@cdc.gov (N. Jothikumar).

0006-291X/$ - see front matter Published by Elsevier Inc.
http://dx.doi.org/10.1016/j.bbrc.2012.03.055

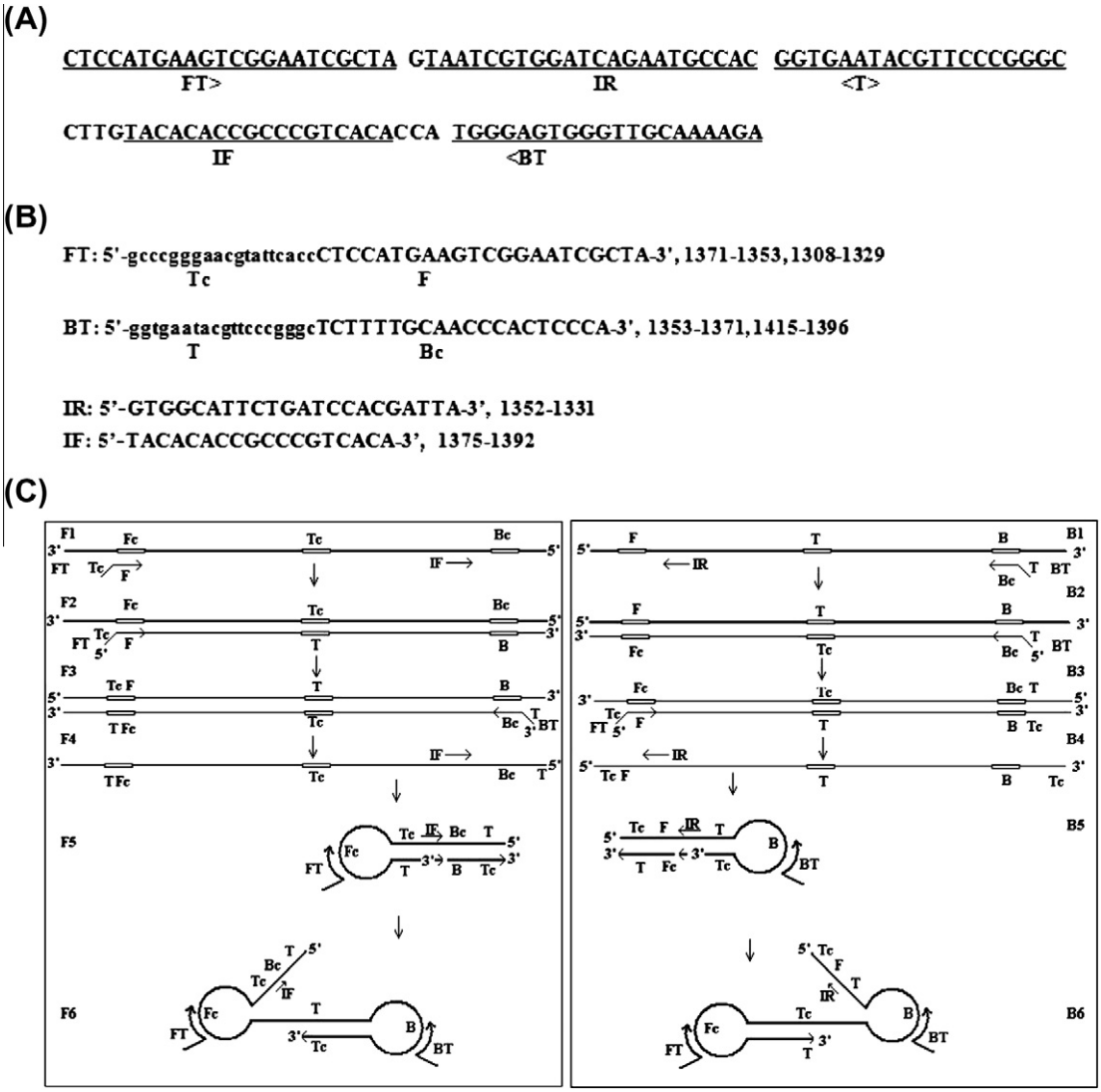


Fig. 1. (A) Nucleotide sequences of 16S rRNA and locations of primers are underlined. (B) The construction of Tab primer pairs FT/BT are shown for GEAR assay for the detection of *E. coli*. Tab sequence regions (small case letters) of the forward and reverse primers self-hybridize in the absence of amplification. Inner primers IR and IF accelerates the amplification reaction. The sequence positions are numbered based on the GenBank accession number GU594309. (C) A schematic presentation of isothermal amplification is illustrated. The primers FT (left box) anneals to the anti-sense strand DNA and the primer BT (right box) anneals to the sense strand DNA. The amplification step produces C-clamp like DNA structure in series of cycling stages of F1 through F6 and B1 through B6 respectively for primers FT and BT.

not require outer primers (F3 and B3), whereas LAMP assay requires two outer primers (F3 and B3).

The main objective of the present study was to demonstrate an application of the GEAR technique. We chose *Escherichia coli* as a model target organism for the purpose of easy quantitation in terms of culturing and targeting the 16S rRNA target gene due to the presence of high copy numbers per cell.

2. Materials and methods

2.1. Primer sequences

The primers for the GEAR assay were designed to target the 16S rRNA region of *E. coli* (Fig. 1A). The Tab primers for the GEAR assay are shown in Fig. 1B. The upper case 3′ sequence of the forward primer is complementary to the target sequence with *E. coli* (position 1308-1329; GenBank accession # GU594309). The upper case 3′ sequence of the reverse primer is complementary to the *E. coli* target sequence (position 1415-1396; GenBank accession # GU594309). The lower case residues correspond to 5′end Tab sequence. In the FT primer sequence, the lower case letter sequence forms complementary to the 5′ end of the BT primer (position 1371-1353 in FT and position 1353-1371 in BT; GenBank accession # GU594309) having a lower case letter sequence. The sequences of accelerated primers IR and IF were 5′-GTGGCATTCTGATCCACGATTA-3′ (position 1352-1331; GenBank accession # GU594309) and 5′-TACACACCGCCCGTCACA-3′ (position 1375-1392; GenBank accession # GU594309) respectively (Fig. 1B).

2.2. The sensitivity of the GEAR assay

The sensitivity of the GEAR assay was demonstrated using DNA extracted from 2×10^6 *E. coli* CFU (ATCC 11775) per ml stock cells. A 10-fold DNA dilution series (corresponding to 2×10^6–2×10^{-1} CFU) was used to evaluate the sensitivity of the GEAR assay. This 10-fold serial dilution resulted in 2000, 200, 20, 2, and 0.2 CFU per reaction. All isothermal amplification assays were performed in triplicate.

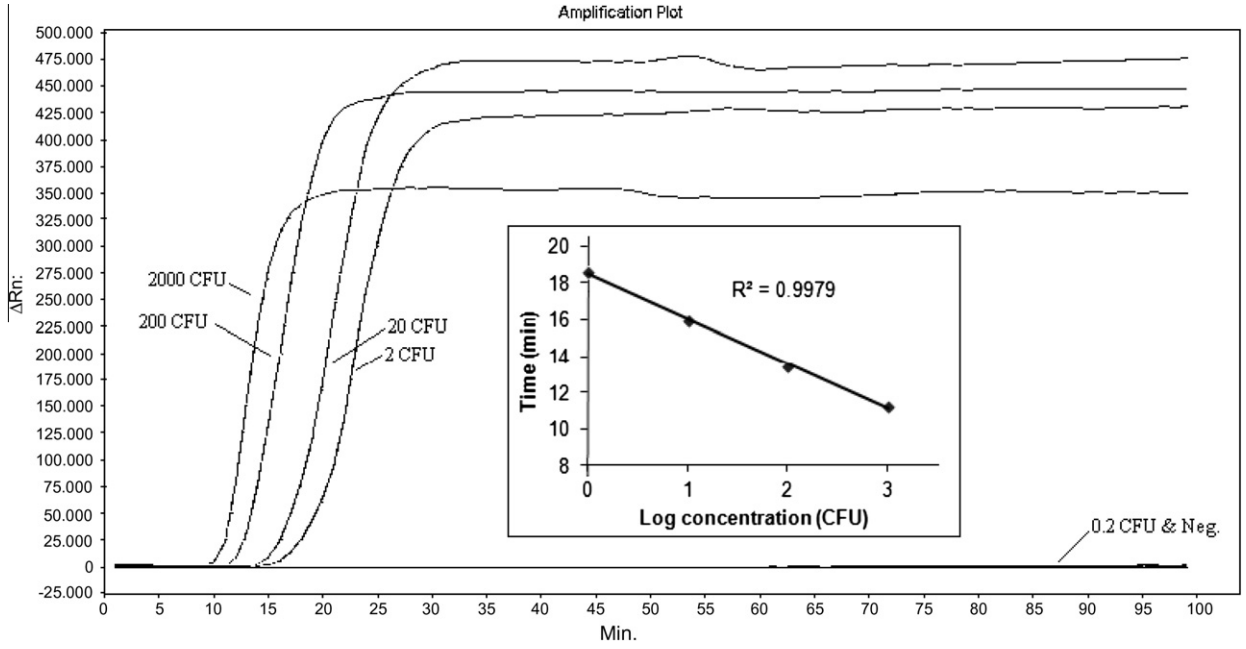


Fig. 2. Quantitation of serially diluted DNA by GEAR assay amplification. Isothermal amplification plot represents amplification products as observed through real-time fluorescence monitoring at different concentrations of DNA. DNA concentration represents CFU equivalents. Each "cycle" represents 1 min of reaction time. The insert figure presents the standard curve obtained by plotting the value of crossing threshold (Ct) versus the concentration of CFU equivalents. Data represent the mean of four replicates for each standard dilution.

2.3. Real-time isothermal amplification protocols

Standard GEAR assays were carried out by using the specific primer combination, FT/BT/IR/IF. The GEAR assay was performed with a Loopamp DNA amplification kit (Eiken Chemical, Japan). Briefly, a total reaction volume of 20 μl consisted of 2× buffer, 1.2 μM SYTO9, 0.8 μl (8 U) *Bst* DNA polymerase and 1 μM of each primer FT, BT, IF and IR. A DNA template volume of 1 μl was added to the reaction mixture. For detection limit testing, the DNA template was equivalent to a known concentration of CFU per reaction as quantified by spread plating on nutrient agar. Negative controls with no template DNA (replaced with nuclease free water) were performed for each reaction series. The reaction was carried out under isothermal condition at 60 °C for 90 min and fluorescence signal was acquired every minute using an ABI 7500 Real-time PCR System (Applied Biosystems, Foster City, CA). A total of 5 μl of the GEAR product was electrophoresed in 2% agarose gels containing Glow Red stain (Biotium, Hayward, CA) and visualized by UV transilluminator at 365 nm.

2.4. Bacterial culture

A known quantity of *E. coli* (Bio-Ball strain NCTC 9001–Equivalent ATCC Strain 11775) was obtained as "30 CFU Bio-Balls" from BTF Pty. Ltd. (Australia). One 30 CFU Bio-Ball was dissolved in 100 μl of sterile water. After 30 s, the whole volume was spread onto nutrient agar plate and plates were incubated at 37 °C overnight to obtain isolated colonies. A stab of bacterial cells was picked from an individual colony grown on a nutrient agar plate with the help of sterile aerosol barrier P-20 tip with a simple touch on the surface of the colony. Picked cells were transferred directly into the 20 μl reaction mix. Standard isothermal amplification reactions were carried out by non-accelerated GEAR assay using two primers (FT/BT) or accelerated GEAR assay using four primers (FT/BT/IR/IF) for *E. coli*. Appropriate negative controls were included for each set of run.

3. Results

3.1. Development of GEAR assay

The mechanism of isothermal DNA amplification is illustrated in Fig. 1C with four primers (FT/BT/IR/IF). The illustration of isothermal amplification in the figure is based on a pair of Tab primers (FT/BT) and accelerated primers (IR/IF). The lowercase residue of the 5′ end Tab sequence of the forward primer is complimentary to the 5′ end Tab sequence of the reverse primer. The uppercase residue of the 3′ end of the forward and revere primers hybridize to specific regions of target nucleic acid sequence that can prime and extend on the target nucleic acids (Fig. 1C). Initially, the main purpose for the use of lowercase residue 5′ end Tab sequence is to hybridize to the extension product to enable easy separation of amplified products shown in sequence F2 and B2 intermediate (Fig. 1C). As GEAR isothermal amplification progresses, the 5′ end Tab sequences are incorporated into the amplified products, leading to exponential self-amplification. The speed and sensitivity of the assay was further improved with an additional pair of primers (IR and IF).

3.2. The sensitivity of the GEAR assay

When only the two Tab primers were used (FT/BT), the sensitivity the GEAR assay was relatively low (limit of detection for the *E. coli* target was 1000 CFU/reaction) and the time-to-detection was relatively long (50 min; data not shown). When the GEAR assay was performed with outer (FT/BT) and inner (IR/IF) primers, the measured detection limit for the *E. coli* target was two cells per reaction (Fig. 2). Gel electrophoresis images showed that consistent amplification product sizes were formed by the GEAR assay (Fig. 3). The average and standard deviation of crossing threshold (Ct) values for each serial dilution were 10.2 ± 0.47, 12.4 ± 0.98, 14.9 ± 0.7 and 17.6 ± 1.8 min, respectively for the 2000, 200, 20 and 2 CFU/reaction template levels. In order to refine the limit of

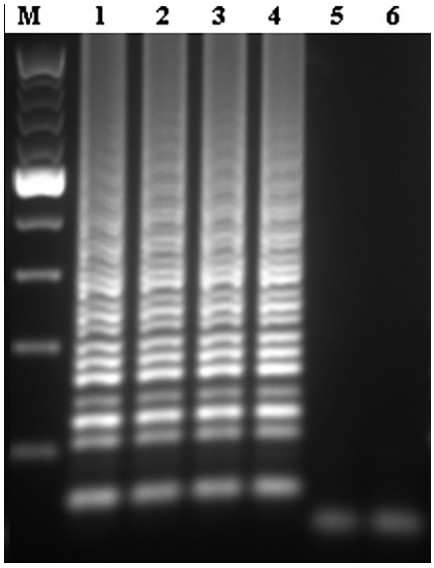


Fig. 3. Gel electrophoresis results for amplified GEAR product of *E. coli* by primers FT/BT/IR/IF from *E. coli*. Lane M; 100 bp molecular weight marker, lanes 1 through 5 are 10-fold serial dilution of the amplified product 2000, 200, 20, 2, 0.2 CFU and lane 6, negative control.

detection further, the DNA was further serially diluted by twofold serial dilution until the diluted sample represented 1, 0.5 and 0.25 cell per reaction. Using this twofold dilution series, three of three DNA samples were positive at 1 cell per reaction, whereas only two of three were positive at 0.5 cells per reaction and there was no detection for reactions performed with 0.25 cells per reaction. The detection limit of GEAR assay was determined to be 1 CFU per reaction. The high sensitivity of the *E. coli* GEAR assay is partly attributable to the high copy numbers of the 16S rRNA gene present in *E. coli* cells.

3.3. Isothermal GEAR assay for bacterial colony analysis

Isothermal amplification using the non-accelerated GEAR assay was successful with a set of primer pair (FT/BT) using direct *E. coli* cell transfer to reaction mixes. DNA was amplified from each of the 21 *E. coli* colonies tested and positive signals were obtained in 29.6 ± 1.8 min. When the GEAR assay was performed with four primers (FT/BT/IR/IF), from each of the 21 *E. coli* colonies tested and positive signals were obtained in 13.7 ± 2.8 min.

4. Discussion

LAMP-based isothermal amplification assays have been widely reported next as alternatives to PCR assays for rapid detection of nucleic acids, with the advantage of being able to be performed at constant temperature using simple equipment (e.g., water bath or heating block). In the present study, we were able to demonstrate a novel isothermal amplification assay that offers the same benefits of the LAMP technique, including the ability to enable high throughput screening of bacterial colonies. The GEAR assay requires only four primers targeting five target regions in contrast to the LAMP assay that requires six primers to target eight regions. The isothermal amplification of the reaction proceeds due to the presence of the Tab sequence in the primer and resulting conformational change during the amplification. In a previous study, the detection limit of a PCR assay targeting the 16S rRNA gene of *E. coli* was reported to be three cells [19]. The 16S rRNA-based accelerated GEAR assay was able to achieve a similar detection limit (one *E. coli* cell per reaction).

A typical positive GEAR assay produced a ladder of multiple bands on an agarose gel (Fig. 3), suggesting that DNA with repeat target sequences were produced due to different exponential amplification stages as a result of simultaneous *Bst* DNA polymerase extension at 3′ and strand displacement at 5′ end. Inclusion of the DNA intercalating dye (SYTO9) in the reaction buffer permitted real-time monitoring of fluorescence without the need for gel electrophoresis or visual inspection of the tubes DNA amplification indicators (e.g., turbidity, precipitates).

After the initial proof of concept study to evaluate the GEAR technique, we used the GEAR assay to identify *E. coli* colonies using cells picked directly from colonies on agar plates without nucleic acid extraction. This testing demonstrated that the GEAR assay can be used to identify colonies grown on agar plates within 15 min without requiring the time and expense of extracting DNA. A similar direct amplification from agar cultures was reported by Niesen and Vogel [20] for detecting fungal organisms directly using LAMP.

The present study successfully demonstrated an application of the novel GEAR assay for isothermal amplification of *E. coli* DNA with a set of four primers. Non-accelerated (two-primer) GEAR assays were also found to be effective in enabling rapid amplification of DNA from bacterial colony picks from agar plates, indicating that this technique could be useful for enabling rapid screening of bacterial isolates. The ability of new GEAR assay to detect as low as 1 cell per reaction within an hour suggests that this technique could also be effective in the development of biosensor-based analytical instruments. The GEAR technique provides a cost-effective alternative for rapid isothermal molecular analysis of clinical, environmental, or biological samples in field settings or point of care facilities.

5. Disclaimer

Use of trade names and commercial sources is for identification only and does not imply endorsement by the Centers for Disease Control and Prevention or the U.S. Department of Health and Human Services. The findings and conclusions in this presentation are those of the authors and do not necessarily represent those of the Centers for Disease Control and Prevention.

References

[1] K.B. Mullis, F.A. Faloona, Specific synthesis of DNA in vitro via a polymerase-catalyzed chain reaction, Methods Enzymol. 155 (1987) 335–350.
[2] R.K. Saiki, D.H. Gelfand, S. Stoffel, S.J. Scharf, R. Higuchi, G.T. Horn, et al., Primer-directed enzymatic amplification of DNA with a thermostable DNA polymerase, Science 239 (1988) 487–491.
[3] G.T. Walker, M.S. Fraiser, J.L. Schram, M.C. Little, J.G. Nadeau, D.P. Malinowski, Strand displacement amplification–an isothermal, in vitro DNA amplification technique, Nucleic Acids Res. 20 (1992) 1691–1696.
[4] P.M. Lizardi, X. Huang, Z. Zhu, P. Bray-Ward, D.C. Thomas, D.C. Ward, Mutation detection and single-molecule counting using isothermal rolling-circle amplification, Nat. Genet. 19 (1998) 225–232.
[5] T. Notomi, H. Okayama, H. Masubuchi, T. Yonekawa, K. Watanabe, N. Amino, et al., Loop-mediated isothermal amplification of DNA, Nucleic Acids Res. 28 (2000) E63.
[6] K. Nagamine, T. Hase, T. Notomi, Accelerated reaction by loop-mediated isothermal amplification using loop primers, Mol. Cell. Probes 16 (2002) 223–229.
[7] F.B. Dean, S. Hosono, L. Fang, X. Wu, A.F. Faruqi, P. Bray-Ward, et al., Comprehensive human genome amplification using multiple displacement amplification, Proc. Natl. Acad. Sci. U. S. A. 99 (2002) 5261–5266.
[8] M. Vincent, Y. Xu, H. Kong, Helicase-dependent isothermal DNA amplification, EMBO Rep. 5 (2004) 795–800.
[9] J. Goldmeyer, H. Kong, W. Tang, Development of a novel one-tube isothermal reverse transcription thermophilic helicase-dependent amplification platform for rapid RNA detection, J. Mol. Diagn. 9 (2007) 639–644.
[10] T. Uemori, H. Mukai, O. Takeda, M. Moriyama, Y. Sato, S. Hokazono, et al., Investigation of the molecular mechanism of ICAN, a novel gene amplification method, J. Biochem. 142 (2007) 283–292.
[11] J.C. Guatelli, K.M. Whitfield, D.Y. Kwoh, K.J. Barringer, D.D. Richman, T.R. Gingeras, Isothermal, in vitro amplification of nucleic acids by a multienzyme

reaction modeled after retroviral replication, Proc. Natl. Acad. Sci. U. S. A. 87 (1990) 1874–1878.
[12] J. Compton, Nucleic acid sequence-based amplification, Nature 350 (1991) 91–92.
[13] R. Pasternack, P. Vuorinen, A. Miettinen, Evaluation of the Gen-Probe *Chlamydia trachomatis* transcription-mediated amplification assay with urine specimens from women, J. Clin. Microbiol. 35 (1997) 676–678.
[14] J. Van Ness, L.K. Van Ness, D.J. Galas, Isothermal reactions for the amplification of oligonucleotides, Proc. Natl. Acad. Sci. U. S. A. 100 (2003) 4504–4509.
[15] N. Kurn, P. Chen, J.D. Heath, A. Kopf-Sill, K.M. Stephens, S. Wang, Novel isothermal, linear nucleic acid amplification systems for highly multiplexed applications, Clin. Chem. 51 (2005) 1973–1981.
[16] Y. Mitani, A. Lezhava, Y. Kawai, T. Kikuchi, A. Oguchi-Katayama, Y. Kogo, et al., Rapid SNP diagnostics using asymmetric isothermal amplification and a new mismatch-suppression technology, Nat. Methods 4 (2007) 257–262.
[17] R. Fang, X. Li, L. Hu, Q. You, J. Li, J. Wu, et al., Cross-priming amplification for rapid detection of *Mycobacterium tuberculosis* in sputum specimens, J. Clin. Microbiol. 47 (2009) 845–847.
[18] Z. Yulong, Z. Xia, Z. Hongwei, L. Wei, Z. Wenjie, H. Xitai, Rapid and sensitive detection of *Enterobacter sakazakii* by cross-priming amplification combined with immuno-blotting analysis, Mol. Cell. Probes 24 (2010) 396–400.
[19] Y.L. Tsai, B.H. Olson, Rapid method for separation of bacterial DNA from humic substances in sediments for polymerase chain reaction, Appl. Environ. Microbiol. 58 (1992) 2292–2295.
[20] L. Niessen, R.F. Vogel, Detection of *Fusarium graminearum* DNA using a loop-mediated isothermal amplification (LAMP) assay, Int. J. Food Microbiol. 140 (2010) 183–191.

Biochemical and Biophysical Research Communications 420 (2012) 743–749

Contents lists available at SciVerse ScienceDirect

Biochemical and Biophysical Research Communications

journal homepage: www.elsevier.com/locate/ybbrc

Role of bone marrow cells in the development of pancreatic fibrosis in a rat model of pancreatitis induced by a choline-deficient/ethionine-supplemented diet

Shingo Akita [a,1], Koji Kubota [a,1], Akira Kobayashi [a,*], Ryosuke Misawa [a], Akira Shimizu [a], Takenari Nakata [a], Takahide Yokoyama [a], Masafumi Takahashi [b], Shinichi Miyagawa [a]

[a] Department of Surgery, Shinshu University School of Medicine, 3-1-1 Asahi, Matsumoto, Nagano 390-8621, Japan
[b] Center for Molecular Medicine Division of Bioimaging Sciences, Jichi Medical University, 3311-1 Yakushiji, Shimono, Tochigi 329-0498, Japan

ARTICLE INFO

Article history:
Received 22 February 2012
Available online 23 March 2012

Keywords:
Bone marrow cell
Pancreatic stellate cell
Pancreatic fibrosis
Choline-deficient/ethionine-supplemented diet

ABSTRACT

Bone marrow cell (BMC)-derived myofibroblast-like cells have been reported in various organs, including the pancreas. However, the contribution of these cells to pancreatic fibrosis has not been fully discussed. The present study examined the possible involvement of pancreatic stellate cells (PSCs) originating from BMCs in the development of pancreatic fibrosis in a clinically relevant rat model of acute pancreatitis induced by a choline-deficient/ethionine-supplemented (CDE) diet. BMCs from female transgenic mice ubiquitously expressing green fluorescent protein (GFP) were transplanted into lethally irradiated male rats. Once chimerism was established, acute pancreatitis was induced by a CDE diet. Chronological changes in the number of PSCs originating from the donor BMCs were examined using double immunofluorescence for GFP and markers for PSCs, such as desmin and alpha smooth muscle actin (αSMA), 1, 3 and 8 weeks after the initiation of CDE feeding. We also used immunohistochemical staining to evaluate whether the PSCs from the BMCs produce growth factors, such as platelet-derived growth factor (PDGF) and transforming growth factor (TGF) β1. The percentage of BMC-derived activated PSCs increased significantly, peaking after 1 week of CDE treatment (accounting for 23.3 ± 0.9% of the total population of activated PSCs) and then decreasing. These cells produced both PDGF and TGFβ1 during the early stage of pancreatic fibrosis. Our results suggest that PSCs originating from BMCs contribute mainly to the early stage of pancreatic injury, at least in part, by producing growth factors in a rat CDE diet-induced pancreatitis model.

© 2012 Elsevier Inc. All rights reserved.

1. Introduction

Several previous studies have suggested that pancreatic stellate cells (PSCs) play a major role in the development of pancreatic fibrosis [1–7]. Under physiological conditions, PSCs are present in the periacinar and periductular spaces and characteristically exhibit long cytoplasmic processes. Quiescent PSCs contain vitamin A-containing lipid droplets in their cytoplasm and exhibit intermediate filament proteins, such as desmin and glial fibrillary acid protein (GFAP). Once pancreatic injury occurs, PSCs are activated and transform into myofibroblast-like cells, accompanied by the loss of the lipid droplets containing vitamin-A and the expression of alpha smooth muscle actin (αSMA), a cytoskeletal protein [1,2]. Activated PSCs produce not only extracellular matrix (ECM) proteins that promote fibrosis, but some cytokines and growth factors, such as platelet-derived growth factor (PDGF), transforming growth factor (TGF) β1, and activin-A [8–10], which are known to be activators of PSCs [4,8–15]. These results suggested that PSCs possess autocrine loops, leading to persistent PSC activation, and thereby promoting the development of fibrosis.

Circulating bone marrow cell (BMC)-derived myofibroblast-like cells are reportedly prominent in a number of organs, such as the liver [16–18], heart [19,20], skin [21], kidney [22], lung [23] and gut [24]. Recently, Marrache et al. reported that PSCs could also originate from BMCs [25]. However, the contribution of PSCs originating from BMCs to pancreatic fibrosis remains largely unknown.

In the present study, we examined the contribution of PSCs derived from BMCs to the development of pancreatic fibrosis in a rat model of CDE diet-induced chronic pancreatitis. We investigated the chronological changes in the number of PSCs originating from donor BMCs at 1, 3 and 8 weeks after the initiation of CDE feeding. We also used immunohistochemical staining to evaluate whether these cells can produce growth factors, such as platelet-derived growth factor (PDGF) and transforming growth factor (TGF) β1.

* Corresponding author. Fax: +81 263 35 1282.
E-mail address: kbys@shinshu-u.ac.jp (A. Kobayashi).
[1] The first two authors contributed equally to this work.

0006-291X/$ - see front matter © 2012 Elsevier Inc. All rights reserved.
http://dx.doi.org/10.1016/j.bbrc.2012.03.060

2. Materials and methods

2.1. Animals

Lewis rats were purchased from Japan SLC Inc. (Shizuoka, Japan). Lewis transgenic rats that ubiquitously express enhanced-GFP under the control of the cytomegalovirus enhancer-chicken β-actin enhancer promoter (GFP-transgenic rats [26,27]) were a gift from PhoenixBio Co. (Tochigi, Japan). Animals were housed at a constant temperature of 18–20 °C under a 12-h light/12-h dark cycle. All the procedures involving rats were approved by the Shinshu University Institutional Animal Care and Use Committee.

2.2. Bone marrow transplantation

Recipient rats (8 weeks male Lewis rats) were subjected to 10 Gy of total body irradiation using a linear accelerator (MBR-1505RS; Hitachi Medical Corporation, Tokyo, Japan). Briefly, BMCs were harvested from the thigh of a donor female GFP-transgenic rat, suspended in phosphate-buffered saline (PBS), and filtered through a 70-μm nylon mesh (Becton and Dickinson Company, Franklin Lakes, NJ). Red blood cells were eliminated by washing the BMCs in ammonium chloride-potassium (ACK) buffer (150 mM NH_4Cl, 10 mM $KHCO_3$, 0.1 mM EDTA) for 10 min on ice and then resuspended in Dulbecco's modified Eagle Medium (DMEM) at 1×10^8 cells/mL. Each recipient rat received 5×10^7 BMCs via the tail vein. To confirm the success of the bone marrow transplantation (BMT), hematological reconstitution was confirmed using a flow cytometry analysis (FACS Calibur; Becton Dickinson and Company) and fluorescence microscopy (BX60 fluorescence microscope; Olympus, Tokyo, Japan) at 6 weeks after the BMT.

2.3. Choline-deficient/ethionine-supplemented diet

Six weeks after the BMT, the rats were fed a choline-deficient diet containing 0.1% DL-ethionine (CDE diet; Oriental Yeast Co. Ltd., Tokyo, Japan) to induce pancreatic fibrosis. We studied five groups of rats: (1) CDE-fed for 1 week; (2) CDE-fed for 3 weeks; (3) CDE-fed for 8 weeks; (4) BMT only; and (5) no BMT (summarized in Fig. 1).

2.4. Histological analysis

The histological analysis was performed using hematoxylin and eosin (HE), Masson Trichrome (MT) and immunohistochemical staining. Pancreas tissues were fixed in 4% paraformaldehyde (PFA), embedded in paraffin, and cut into 3-μm-thick sections. The primary antibodies that were used anti-desmin (DAKO, Carpentaria, CA, USA), anti-alpha smooth muscle actin (αSMA; Sigma–Aldrich, St. Louis, MO, USA), anti-GFP (MEDICAL & BIOLOGICAL LABORATORIES Co. Ltd., Nagoya, Japan) and (Abcam, Cambridge, MA), anti-type I collagen (CALBIOCHEM, Darmstadt, Germany), anti-PDGF (Abcam), and anti-TGFβ1 (Santa Cruz Biotechnology, Santa Cruz, CA, USA). The primary antibodies were detected using the DAB method (DAKO) or combinations of Alexa Fluor 488-, 555- and 647-conjugated secondary antibodies (Invitrogen, Carlsbad, CA, USA). The cell nuclei were stained with DAPI (Invitrogen).

2.5. Fluorescence in situ hybridization

The paraformaldehyde-fixed sections (3 μm) were incubated with a rat Y chromosome probe labeled with fluorescein isothiocyanate (FITC) (STAR FISH, Cambio, Cambridge, UK) overnight at 37 °C. Slides were counterstained with anti-FITC (Beckman Coulter, Fullerton, CA, USA) and anti-GFP (MEDICAL & BIOLOGICAL LABORATORIES), which were detected using Alexa Fluor 488- and 555-conjugated secondary antibodies (Invitrogen).

2.6. Cell counting

The number of desmin-, αSMA-, and GFP-desmin- or GFP-αSMA-positive cells was counted in 20 randomly selected images at a magnification of ×400 in each pancreas section. Microscopic images were obtained using an Olympus BX60 fluorescence microscope (Melvile, NY) or a BZ-8000 fluorescence microscope (KEYENCE, Osaka, Japan).

2.7. Statistical analysis

Data are expressed as the mean ± SD. Statistical significance was evaluated using the Student *t*-test; the statistical analysis was performed using Microsoft Excel (Microsoft, Redmond, WA) and Excel Toukei (Social Survey Research Information Co. Ltd., Tokyo, Japan). Differences were considered significant at $P < 0.05$.

3. Results

3.1. Analysis of chimerism

We first confirmed the hematologic reconstitution, as described previously [28], after lethal irradiation and BMT by examining the peripheral blood cells at 6 weeks after BMT using flow cytometry and direct visualization with fluorescence microscopy. All myeloid and lymphocytic lineages of the BMT rats exhibited GFP labeling in 93–96% of the cells. GFP expression of BMCs was routinely

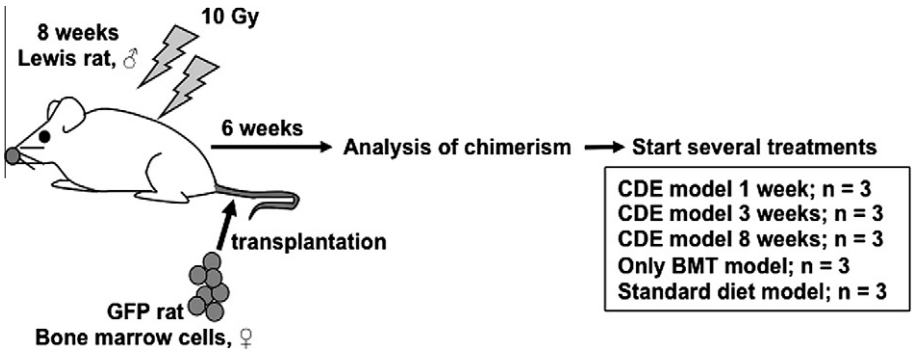


Fig. 1. Experimental design. Eight-week-old Lewis male recipient rats were irradiated and transplanted with bone marrow cells from 8 weeks old GFP transgenic female donor rats. After the stable establishment of peripheral chimerism, the BMT rats were fed a CDE diet to induce pancreatitis. Their pancreases were then analyzed at 1, 3 and 8 weeks after the start of CDE feeding.

observed by direct visualization with fluorescence microscopy at the time of expiration (Supplementary Data 1).

3.2. Progression of pancreatic fibrosis in CDE diet-fed rats

Pathological changes in the pancreas after CDE feeding were examined using HE and MT staining (Fig. 2A). While no obvious histological changes were observed in the control groups (Fig. 2Aa–d), CDE treatment resulted in early-stage pancreatitis after 1 week, characterized by the distention of the pancreatic duct, an enlarged acinus cavity between acinar cells, a reduction in the number as well as the destruction of acini, and the atrophy of acinar cells (Fig. 2Ae). MT staining confirmed fibrosis in the interstitium (Fig. 2Af). Hyperplasia of the tubular structures resembling the pancreatic duct and abnormal vacuolization in the acinar cells became marked at 3 weeks of CDE treatment. The reduction/destruction of the acini progressed, and tubular complexes were formed in some areas (Fig. 2Ag). The intercellular fibrosis developed into interlobular fibrosis (Fig. 2Ah). After 8 weeks of CDE treatment, pancreatic steatosis occurred and thin septa, extensive bridging fibrosis, and a nodular appearance were observed (Fig. 2Ai, j).

3.3. Consumption of CDE diet activates PSCs

PSCs were identified based on the expressions of desmin, a marker of quiescent and activated PSCs, and αSMA, a marker of activated PSCs. A markedly larger number of desmin-positive cells were observed after 3 weeks of the CDE diet, compared with after 1 week (Fig. 2B). Meanwhile, the number of αSMA-positive cells was significantly higher after 1 week of CDE treatment, compared with the number in control rats, and peaked after 3 weeks of CDE treatment (Fig. 2C). No further increases in the numbers of desmin- and αSMA-positive cells were observed after 8 weeks of treatment (Fig. 2B, C). Pancreatic fibrosis is also characterized by the extensive deposition of ECM (mainly type I collagen), and activated PSCs with a myofibroblastic phenotype express a high amount of type I collagen [29,30]. Immunostaining for type I collagen showed similar results to those for MT staining, and αSMA was co-expressed with collagen type I (Supplementary Data 2). No significant

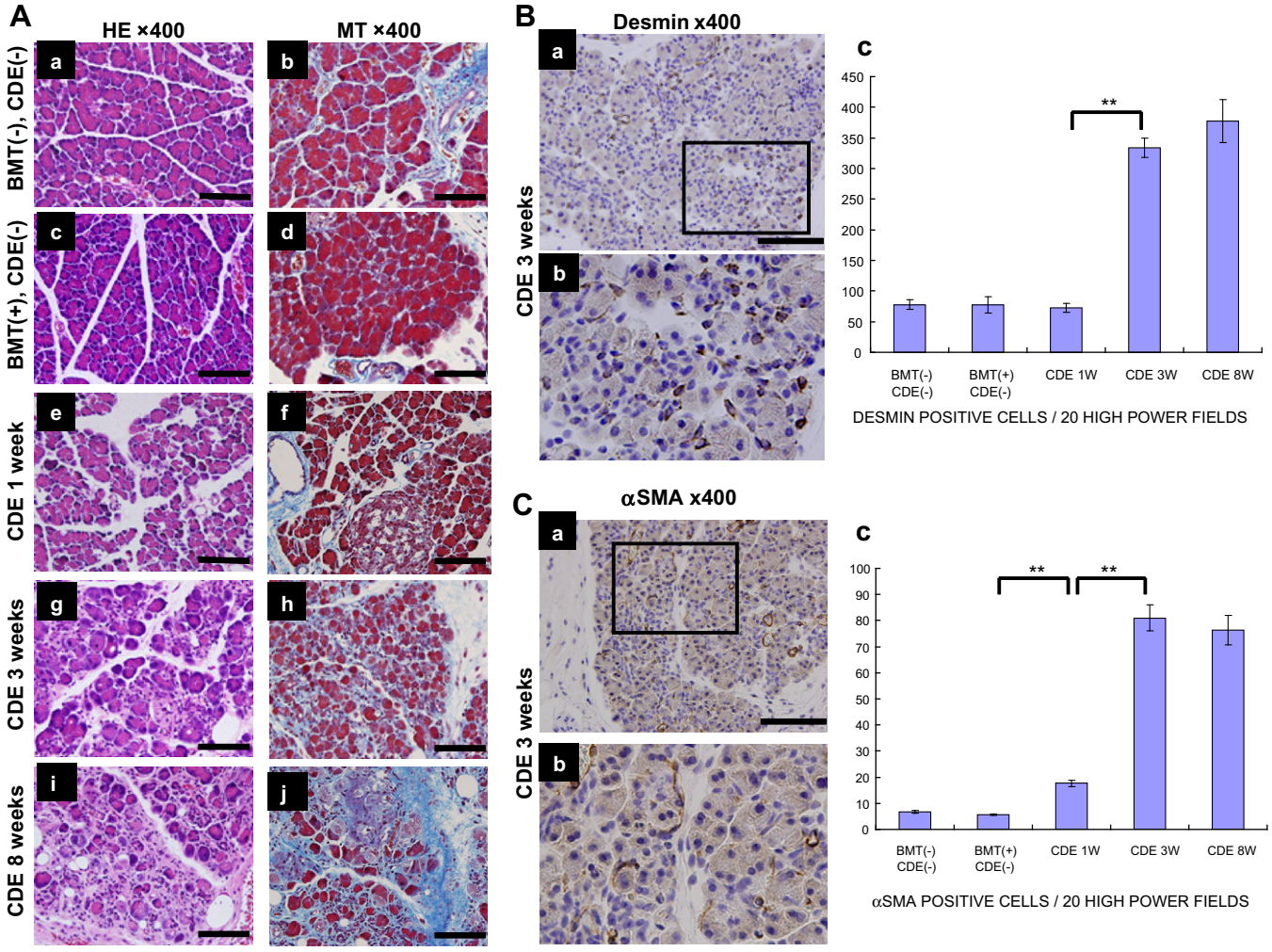


Fig. 2. Histology of pancreases from rats fed a CDE diet and examination of desmin- and αSMA-positive cells in pancreases from rats fed a CDE diet. (A) Right panels; HE staining. Left panels; MT staining. (a, b) Non-BMT and non-CDE treatment. (c, d) 14 weeks after BMT without CDE treatment. (e, f) 1 week after CDE treatment. (g, h) 3 weeks after CDE treatment. (i, j) 8 weeks after CDE treatment. (×400) Bar = 5 μm. (B) (a) Immunohistochemical analysis of desmin after 3 weeks of CDE treatment. (b) Enlargement of the framed area in panel a. (c) Number of desmin-positive cells counted in 20 randomly selected high-power fields. The columns and bars represent the mean ± SDs. (C) (a) Immunohistochemical analysis of αSMA after 3 weeks of CDE treatment. (b) Enlargement of the framed area in panel a. (c) Number of αSMA-positive cells counted in 20 randomly selected high-power fields. Columns and bars represent means ± SDs. (B, C) Bar = 5 μm. $^{**}P < 0.01$.

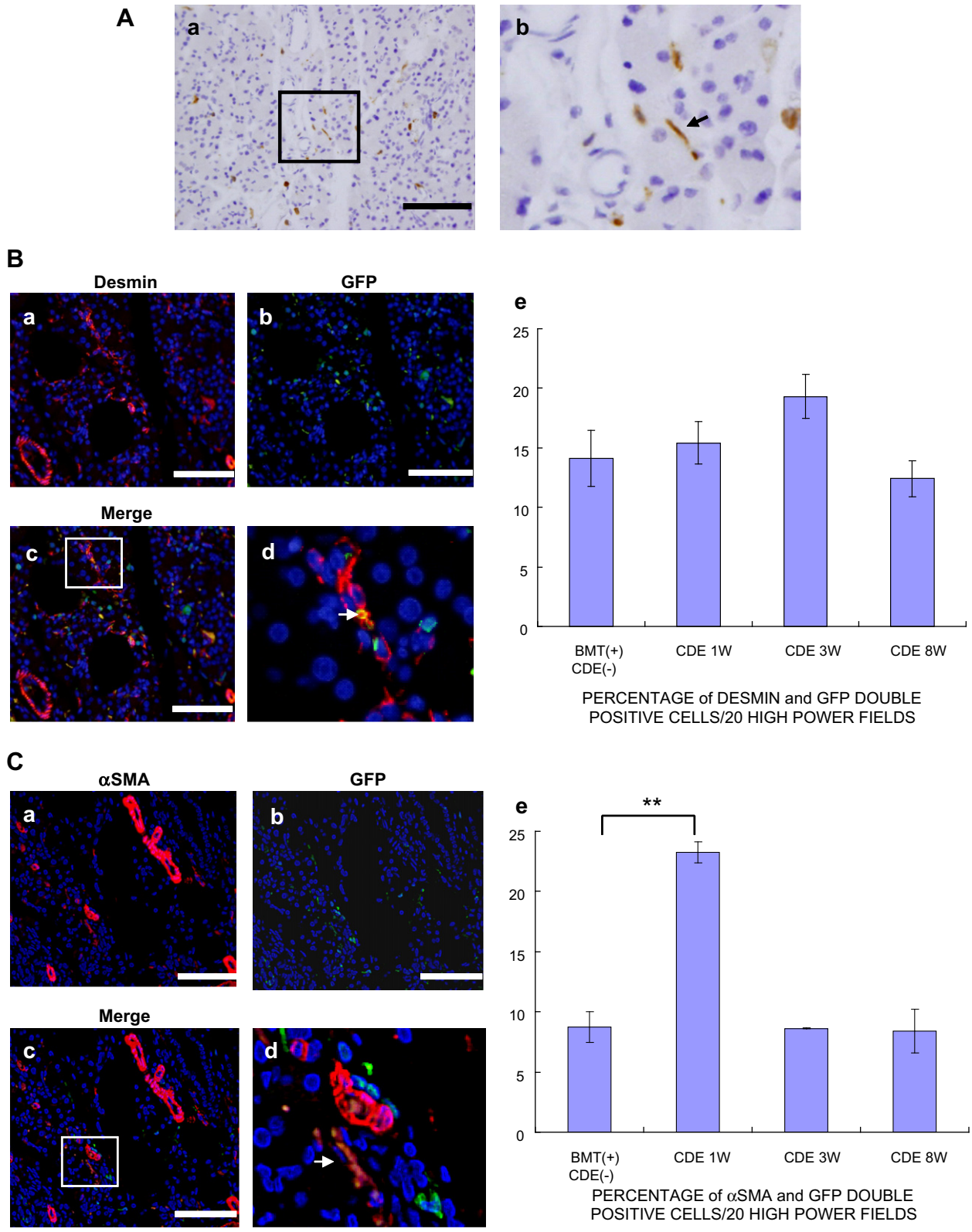


Fig. 3. Immunohistochemical analysis of GFP-positive cells in the pancreas and co-expression of GFP with PSC markers. (A) Immunohistochemical analysis of GFP after 1 week of CDE treatment. (b) Enlargement of the framed area in panel a. Spindle-shaped GFP-positive cells were observed in the periacinar region (black arrow). (B) Immunofluorescent staining for (a) desmin (shown in red) and (b) GFP (shown in green). (c) Merged photograph. (d) Enlargement of the framed area in panel c. The white arrows indicate GFP and desmin double-positive cells. The nuclei were counterstained with DAPI (blue). (e) Percentage of desmin and GFP double-positive cells among all desmin-positive cells in 20 randomly selected high-power fields. The columns and bars represent the means ± SDs. (C) Immunofluorescent staining for (a) αSMA (shown in red) and (b) GFP (shown in green). (c) Merged photograph. (d) Enlargement of the framed area in panel c. The white arrows indicate GFP and αSMA double-positive cells. The nuclei were counterstained with DAPI (blue). (e) Percentage of αSMA and GFP double-positive cells among all αSMA-positive cells in 20 randomly selected high-power fields. The columns and bars represent the means ± SDs. (A) Bar = 5 μm. (B, C) Bar = 10 μm.

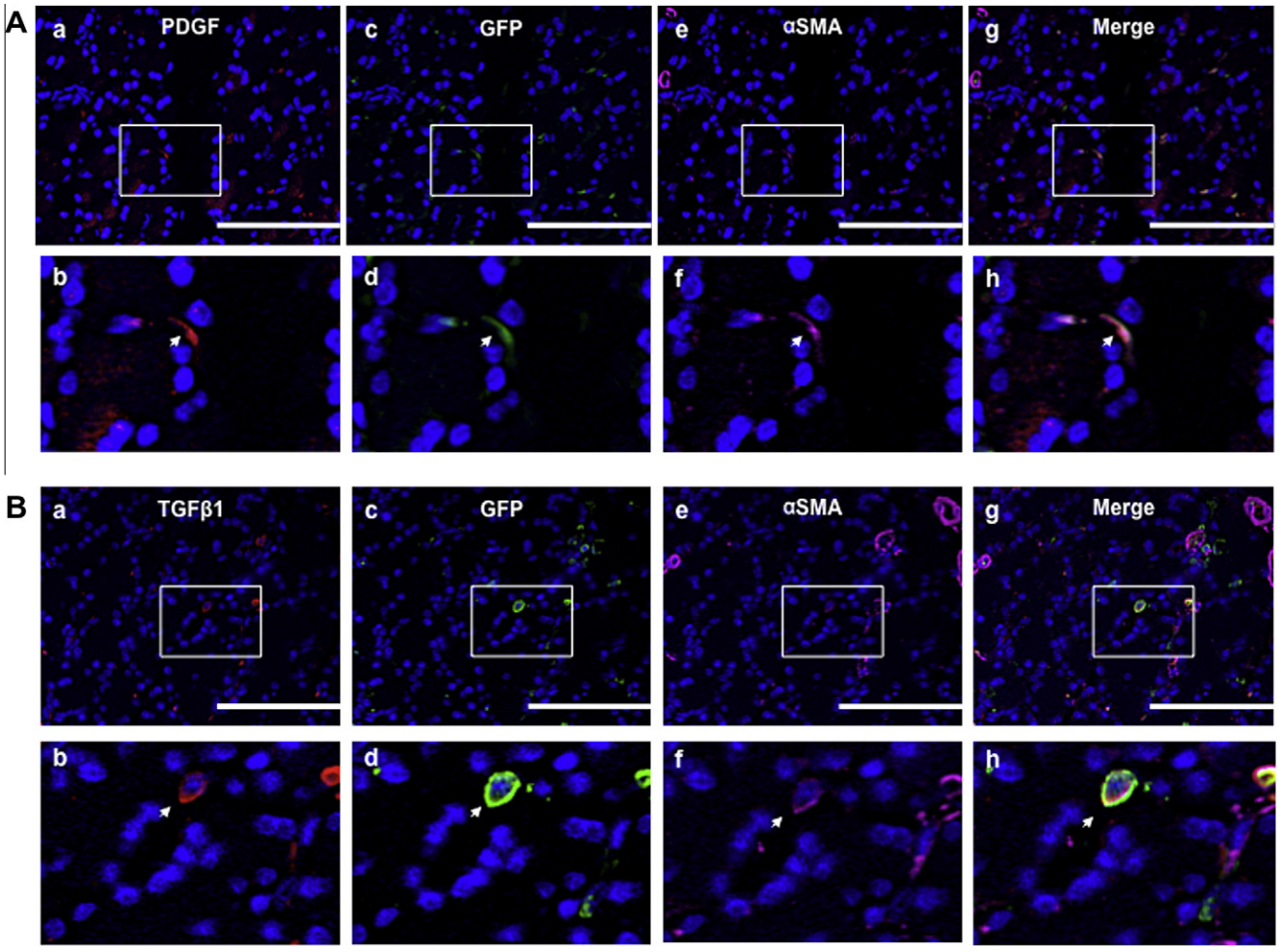


Fig. 4. Co-expression of GFP-αSMA with growth factors. (A) Immunofluorescent staining for (a, b) PDGF (shown in red), (c, d) GFP (shown in green), and (e, f) αSMA (shown in reddish purple); (g, h) merged image. The nuclei were counterstained with DAPI (blue). (b, d, f, h) Enlargement of the framed area in panels a, c, e, and g. The white arrows indicate GFP-αSMA-PDGF-positive cells. (B) Immunofluorescent staining for (a, b) TGFβ1 (shown in red), (c, d) GFP (shown in green), and (e, f) αSMA (shown in reddish purple); (g, h) merged image. The nuclei were counterstained with DAPI (blue). (b, d, f, h) Enlargement of the framed area in panels a, c, e, and g. The white arrows indicate GFP-αSMA-TGFβ1-positive cells. Bar = 10 μm.

changes in the number of desmin- and αSMA-positive cells were defected in BMT rats without CDE treatment (Fig. 2B, C).

3.4. Bone marrow-derived PSCs

The pancreas of each GFP transgenic rat was extensively stained with anti-GFP antibody (Supplementary Data 3A). In the pancreases of rats treated without BMT or CDE treatment (negative control group), no GFP-positive cells were observed (Supplementary Data 3B). Only a few GFP-positive cells were visible in the BMT alone group (Supplementary Data 3C); these cells were first detected after 1 week of CDE treatment (Fig. 3A), increased markedly after 3 weeks of treatment, and did not increase any further after 8 weeks of treatment (Supplementary Data 3D, E). From a morphological point of view, spindle-shaped cells in the periacinar and periductular spaces were observed after 1 week of CDE treatment; these cells were similar to the shape and location of the PSCs (Fig. 3A). No GFP-expressing islet cells, acinar cells, or duct cells were identified in any of the treatment groups at any of the time points (Fig. 3A, Supplementary Data 3).

Next, we examined whether the PSCs had differentiated from the donor BMCs or arose from local cell fusion events using fluorescent in situ hybridization with a rat Y chromosome probe that fluoresced negatively in the cells from donor female GFP transgenic rats. The results showed that the GFP-positive cells were all Y chromosome negative, suggesting that the donor BMCs had differentiated directly from the PSCs (data not shown).

To examine the contribution of BMCs to PSCs, we performed double immunofluorescence staining for GFP (green) and desmin (red) or αSMA (red). BMC-derived PSCs were observed in the BMT alone group (without pancreas injury), accounting for 13.7 ± 3.3% of all the desmin-positive cells. After the initiation of the CDE diet, this figure did not change significantly throughout the observation period, although it appeared to reach a small peak at 3 weeks (Fig. 3B). On the other hand, the percentage of activated PSCs of BMC origin out of all the αSMA-positive cells increased significantly and peaked after 1 week of CDE treatment, accounting for 23.3 ± 0.9% of the total population of activated PSCs. The ratio decreased thereafter to the same degree as that seen in the BMT alone group (Fig. 3C).

3.5. Activated PSCs derived from BMC produce growth factors such as PDGF and TGFβ1

To further examine the characteristics of the BMC-derived PSCs, we performed a triple-immunohistochemical analysis for PDGF or TGFβ1 in addition to GFP and αSMA, and confirmed that the αSMA-GFP double-positive cells coexpressed PDGF (Fig. 4A) and TGFβ1

(Fig. 4B) already after 1 week of CDE treatment before starting of pancreatic fibrosis. However, not only the PSCs, but also other cells, such as acinar cells, inflammatory cells, ductal cells, and endothelial cells, produced PDGF and TGF (Supplementary Data 4).

4. Discussion

In the present study, we showed that BMC-derived PSCs contributed mainly to the early stage of pancreatic fibrosis and that these cells produced growth factors such as PDGF and TGFβ1 in a rat model of CDE diet-induced pancreatitis.

We used a CDE diet to induce pancreatitis in the present study because CDE diet-induced pancreatitis is similar to the human disease in terms of its natural history, histological findings, and biochemical changes. Indeed, CDE diet-induced pancreatitis shares the same histological parenchymal alterations as those occurring in humans, including inflammation, fibrosis, and the loss of exocrine and endocrine tissue [31–34].

In the present study, we examined the time course of developing pancreatitis in a rat CDE diet model at 1, 3 and 8 weeks after its initiation. Our results showed that acute pancreatitis developed after 1 week of CDE feeding and progressed to pancreatic fibrosis after 3 weeks, persisting until 8 weeks.

The BMC origin of PSCs has been observed in two animal models of chemically induced pancreatitis [25,35–37] in which dibutyltin dichloride or cerulean was used. Hence, this is the first study to confirm the contribution of BMCs to the population of activated PSCs in a rat CDE diet-induced pancreatitis model. Our study revealed that approximately one-fourth of the activated PSCs were derived from BMCs at 1 week after the initiation of the CDE diet, namely during the acute pancreatitis phase. After 3 weeks of the CDE diet and the progression of pancreas injury and fibrosis, the percentage of BMC-derived activated PSCs out of the total population of activated PSCs returned to the control level. These results suggested that BMC-derived activated PSCs might play an important role during the early stage of pancreatic injury in the rat CDE diet-induced pancreatitis model.

Proinflammatory cytokines mediate pancreatic inflammation and fibrosis. Several studies have suggested that activated PSCs have an autocrine effect through the production of cytokines and growth factors, such as PDGF, TGFβ1 and activin-A [8–10]. PDGF acts as a profibrogenic cytokine though the activation and proliferation of PSCs and contributes to the migration potential of PSCs [12], and TGFβ1 activates PSCs to promote ECM secretion [13]. However, previous studies [25,35–37] have not examined whether BMC-derived activated PSCs produce growth factors such as PDGF and TGFβ1. This study revealed that these cells do produce PDGF and TGFβ1, suggesting their involvement in the development of fibrosis during the early stage of pancreatitis.

In conclusion, our results suggested that BMC-derived activated PSCs may contribute to the early stage of pancreatic injury, at least in part, by producing growth factors such as PDGF and TGFβ1 in the rat CDE diet-induced pancreatitis model.

Acknowledgments

The authors thank Phoenix Bio Co. (Tochigi, Japan) for providing the GFP-transgenic rats.

Appendix A. Supplementary data

Supplementary data associated with this article can be found, in the online version, at http://dx.doi.org/10.1016/j.bbrc.2012.03.060.

References

[1] M.V. Apte, P.S. Haber, T.L. Applegate, I.D. Norton, G.W. McCaughan, M.A. Korsten, R.C. Pirola, J.S. Wilson, Periacinar stellate shaped cells in rat pancreas: identification, isolation, and culture, Gut 43 (1998) 128–133.
[2] M.G. Bachem, E. Schneider, H. Gross, H. Weidenbach, R.M. Schmid, A. Menke, M. Siech, H. Beger, A. Grunert, G. Adler, Identification, culture, and characterization of pancreatic stellate cells in rats and humans, Gastroenterology 115 (1998) 421–432.
[3] A. Masamune, T. Shimosegawa, Signal transduction in pancreatic stellate cells, J. Gastroenterol. 44 (2009) 249–260.
[4] M.B. Omary, A. Lugea, A.W. Lowe, S.J. Pandol, The pancreatic stellate cell: a star on the rise in pancreatic diseases, J. Clin. Invest. 117 (2007) 50–59.
[5] M.G. Bachem, M. Schunemann, M. Ramadani, M. Siech, H. Beger, A. Buck, S. Zhou, A. Schmid-Kotsas, G. Adler, Pancreatic carcinoma cells induce fibrosis by stimulating proliferation and matrix synthesis of stellate cells, Gastroenterology 128 (2005) 907–921.
[6] R.F. Hwang, T. Moore, T. Arumugam, V. Ramachandran, K.D. Amos, A. Rivera, B. Ji, D.B. Evans, C.D. Logsdon, Cancer-associated stromal fibroblasts promote pancreatic tumor progression, Cancer Res. 68 (2008) 918–926.
[7] A. Vonlaufen, S. Joshi, C. Qu, P.A. Phillips, Z. Xu, N.R. Parker, C.S. Toi, R.C. Pirola, J.S. Wilson, D. Goldstein, M.V. Apte, Pancreatic stellate cells: partners in crime with pancreatic cancer cells, Cancer Res. 68 (2008) 2085–2093.
[8] F.W. Shek, R.C. Benyon, F.M. Walker, P.R. McCrudden, S.L. Pender, E.J. Williams, P.A. Johnson, C.D. Johnson, A.C. Bateman, D.R. Fine, J.P. Iredale, Expression of transforming growth factor-beta 1 by pancreatic stellate cells and its implications for matrix secretion and turnover in chronic pancreatitis, Am. J. Pathol. 160 (2002) 1787–1798.
[9] P.A. Phillips, M.J. Wu, R.K. Kumar, E. Doherty, J.A. McCarroll, S. Park, R.C. Pirola, J.S. Wilson, M.V. Apte, Cell migration: a novel aspect of pancreatic stellate cell biology, Gut 52 (2003) 677–682.
[10] N. Ohnishi, T. Miyata, H. Ohnishi, H. Yasuda, K. Tamada, N. Ueda, H. Mashima, K. Sugano, Activin A is an autocrine activator of rat pancreatic stellate cells: potential therapeutic role of follistatin for pancreatic fibrosis, Gut 52 (2003) 1487–1493.
[11] P.A. Phillips, J.A. McCarroll, S. Park, M.J. Wu, R. Pirola, M. Korsten, J.S. Wilson, M.V. Apte, Rat pancreatic stellate cells secrete matrix metalloproteinases: implications for extracellular matrix turnover, Gut 52 (2003) 275–282.
[12] T. Luttenberger, A. Schmid-Kotsas, A. Menke, M. Siech, H. Beger, G. Adler, A. Grunert, M.G. Bachem, Platelet-derived growth factors stimulate proliferation and extracellular matrix synthesis of pancreatic stellate cells: implications in pathogenesis of pancreas fibrosis, Lab. Invest. 80 (2000) 47–55.
[13] E. Schneider, A. Schmid-Kotsas, J. Zhao, H. Weidenbach, R.M. Schmid, A. Menke, G. Adler, J. Waltenberger, A. Grunert, M.G. Bachem, Identification of mediators stimulating proliferation and matrix synthesis of rat pancreatic stellate cells, Am. J. Physiol. Cell. Physiol. 281 (2001) C532–C543.
[14] P. Mews, P. Phillips, R. Fahmy, M. Korsten, R. Pirola, J. Wilson, M. Apte, Pancreatic stellate cells respond to inflammatory cytokines: potential role in chronic pancreatitis, Gut 50 (2002) 535–541.
[15] K. Hama, H. Ohnishi, H. Aoki, H. Kita, H. Yamamoto, H. Osawa, K. Sato, K. Tamada, H. Mashima, H. Yasuda, K. Sugano, Angiotensin II promotes the proliferation of activated pancreatic stellate cells by Smad7 induction through a protein kinase C pathway, Biochem. Biophys. Res. Commun. 340 (2006) 742–750.
[16] S. Baba, H. Fujii, T. Hirose, K. Yasuchika, H. Azuma, T. Hoppo, M. Naito, T. Machimoto, I. Ikai, Commitment of bone marrow cells to hepatic stellate cells in mouse, J. Hepatol. 40 (2004) 255–260.
[17] T. Kisseleva, H. Uchinami, N. Feirt, O. Quintana-Bustamante, J.C. Segovia, R.F. Schwabe, D.A. Brenner, Bone marrow-derived fibrocytes participate in pathogenesis of liver fibrosis, J. Hepatol. 45 (2006) 429–438.
[18] F.P. Russo, M.R. Alison, B.W. Bigger, E. Amofah, A. Florou, F. Amin, G. Bou-Gharios, R. Jeffery, J.P. Iredale, S.J. Forbes, The bone marrow functionally contributes to liver fibrosis, Gastroenterology 130 (2006) 1807–1821.
[19] P.Y. Chu, J. Mariani, S. Finch, J.R. McMullen, J. Sadoshima, T. Marshall, D.M. Kaye, Bone marrow-derived cells contribute to fibrosis in the chronically failing heart, Am. J. Pathol. 176 (2010) 1735–1742.
[20] S.B. Haudek, Y. Xia, P. Huebener, J.M. Lee, S. Carlson, J.R. Crawford, D. Pilling, R.H. Gomer, J. Trial, N.G. Frangogiannis, M.L. Entman, Bone marrow-derived fibroblast precursors mediate ischemic cardiomyopathy in mice, Proc. Natl. Acad. Sci. USA 103 (2006) 18284–18289.
[21] Y. Yamaguchi, T. Kubo, T. Murakami, M. Takahashi, Y. Hakamata, E. Kobayashi, S. Yoshida, K. Hosokawa, K. Yoshikawa, S. Itami, Bone marrow cells differentiate into wound myofibroblasts and accelerate the healing of wounds with exposed bones when combined with an occlusive dressing, Br. J. Dermatol. 152 (2005) 616–622.
[22] J. Li, J.A. Deane, N.V. Campanale, J.F. Bertram, S.D. Ricardo, The contribution of bone marrow-derived cells to the development of renal interstitial fibrosis, Stem Cells 25 (2007) 697–706.
[23] N. Hashimoto, H. Jin, T. Liu, S.W. Chensue, S.H. Phan, Bone marrow-derived progenitor cells in pulmonary fibrosis, J. Clin. Invest. 113 (2004) 243–252.
[24] G. Ishii, T. Sangai, K. Sugiyama, T. Ito, T. Hasebe, Y. Endoh, J. Magae, A. Ochiai, In vivo characterization of bone marrow-derived fibroblasts recruited into fibrotic lesions, Stem Cells 23 (2005) 699–706.

[25] F. Marrache, S. Pendyala, G. Bhagat, K.S. Betz, Z. Song, T.C. Wang, Role of bone marrow-derived cells in experimental chronic pancreatitis, Gut 57 (2008) 1113–1120.
[26] Y. Hakamata, K. Tahara, H. Uchida, Y. Sakuma, M. Nakamura, A. Kume, T. Murakami, M. Takahashi, R. Takahashi, M. Hirabayashi, M. Ueda, I. Miyoshi, N. Kasai, E. Kobayashi, Green fluorescent protein-transgenic rat: a tool for organ transplantation research, Biochem. Biophys. Res. Commun. 286 (2001) 779–785.
[27] H. Inoue, I. Ohsawa, T. Murakami, A. Kimura, Y. Hakamata, Y. Sato, T. Kaneko, M. Takahashi, T. Okada, K. Ozawa, J. Francis, P. Leone, E. Kobayashi, Development of new inbred transgenic strains of rats with LacZ or GFP, Biochem. Biophys. Res. Commun. 329 (2005) 288–295.
[28] K. Kubota, J. Soeda, R. Misawa, M. Mihara, S. Miwa, H. Ise, M. Takahashi, S. Miyagawa, Bone marrow-derived cells fuse with hepatic oval cells but are not involved in hepatic tumorigenesis in the choline-deficient ethionine-supplemented diet rat model, Carcinogenesis 29 (2008) 448–454.
[29] P.S. Haber, G.W. Keogh, M.V. Apte, C.S. Moran, N.L. Stewart, D.H. Crawford, R.C. Pirola, G.W. McCaughan, G.A. Ramm, J.S. Wilson, Activation of pancreatic stellate cells in human and experimental pancreatic fibrosis, Am. J. Pathol. 155 (1999) 1087–1095.
[30] A. Casini, A. Galli, P. Pignalosa, L. Frulloni, C. Grappone, S. Milani, P. Pederzoli, G. Cavallini, C. Surrenti, Collagen type I synthesized by pancreatic periacinar stellate cells (PSC) co-localizes with lipid peroxidation-derived aldehydes in chronic alcoholic pancreatitis, J. Pathol. 192 (2000) 81–89.
[31] A.K. Banerjee, S.W. Galloway, A.N. Kingsnorth, Experimental models of acute pancreatitis, Br. J. Surg. 81 (1994) 1096–1103.
[32] P.G. Lankisch, U. Pohl, B. Goke, J. Otto, U. Wereszczynska-Siemiatkowska, H.J. Grone, G. Rahlf, Effect of FOY-305 (camostate) on severe acute pancreatitis in two experimental animal models, Gastroenterology 96 (1989) 193–199.
[33] M.A. Manso, A. Rebollo, R. Pescador, I. de Dios, Action of CCK on CDE diet-induced acute pancreatitis in rats treated with hydrocortisone, Comp. Biochem. Physiol. C Pharmacol. Toxicol. Endocrinol. 111 (1995) 257–263.
[34] S. Ida, M. Ohmuraya, M. Hirota, N. Ozaki, S. Hiramatsu, H. Uehara, H. Takamori, K. Araki, H. Baba, K. Yamamura, Chronic pancreatitis in mice by treatment with choline-deficient ethionine-supplemented diet, Exp. Anim. 59 (2010) 421–429.
[35] T. Watanabe, A. Masamune, K. Kikuta, M. Hirota, K. Kume, K. Satoh, T. Shimosegawa, Bone marrow contributes to the population of pancreatic stellate cells in mice, Am. J. Physiol. Gastrointest. Liver. Physiol. 297 (2009) G1138–G1146.
[36] G. Sparmann, M.L. Kruse, N. Hofmeister-Mielke, D. Koczan, R. Jaster, S. Liebe, D. Wolff, J. Emmrich, Bone marrow-derived pancreatic stellate cells in rats, Cell Res. 20 (2010) 288–298.
[37] C.J. Scarlett, E.K. Colvin, M. Pinese, D.K. Chang, A.L. Morey, E.A. Musgrove, M. Pajic, M. Apte, S.M. Henshall, R.L. Sutherland, J.G. Kench, A.V. Biankin, Recruitment and activation of pancreatic stellate cells from the bone marrow in pancreatic cancer: a model of tumor-host interaction, PLoS One 6 (2011) e26088.

Biochemical and Biophysical Research Communications 420 (2012) 750–754

Contents lists available at SciVerse ScienceDirect

Biochemical and Biophysical Research Communications

journal homepage: www.elsevier.com/locate/ybbrc

Specific phase arrest of cell cycle restores cell viability against tRNA cleavage by killer toxin

Megumi Shigematsu [a], Tetsuhiro Ogawa [a,*], Hiroko K. Kitamoto [b], Makoto Hidaka [a], Haruhiko Masaki [a,*]

[a] Department of Biotechnology, The University of Tokyo, Yayoi, Bunkyo-ku, Tokyo 113-8657, Japan
[b] National Institute for Agro-environmental Sciences, Kannondai, Tsukuba, Ibaraki 305-8604, Japan

ARTICLE INFO

Article history:
Received 23 February 2012
Available online 17 March 2012

Keywords:
tRNA
Killer toxin
Cell cycle

ABSTRACT

Zymocin and PaT are killer toxins that induce cell cycle arrest of sensitive yeast cells in G1 and S phase, respectively. Recent studies have revealed that these two toxins cleave specific tRNAs, indicating that the cell growth impairment is due to the tRNA cleavage. Additionally, we have previously shown that the active domain of colicin D (D-CRD), which also cleaves specific *Escherichia coli* tRNAs, statically impairs growth when expressed in yeast cells. To verify that phase-specific cell cycle arrest is also induced by the expression of D-CRD, D-CRD and the subunits of zymocin and PaT that have tRNA cleaving activity were expressed in yeast cells and cell cycle status was analyzed. Our results indicate that phase-specific arrest does not commonly occur by tRNA cleavage, and it saves the cell viability. Furthermore, the extent of protein synthesis impairment may determine the phase specificity of cell cycle arrest.

© 2012 Elsevier Inc. All rights reserved.

1. Introduction

Many bacteria produce toxins to gain an advantage over other organisms living in the same niche. To date, diverse modes of action have been reported for toxins, including cleavage of the anticodon loop of specific tRNAs. For instance, colicin E5, which is encoded by Col plasmid, was the first toxin reported to cleave $tRNA^{Tyr}$, $tRNA^{His}$, $tRNA^{Asn}$ and $tRNA^{Asp}$ of *Escherichia coli* [1]. Similarly, colicin D cleaves four isoaccepting $tRNA^{Arg}$s of *E. coli* [2]. Following these reports, two yeast killer toxins have been shown to cleave specific yeast tRNAs. Zymocin, which is produced by *Kluyveromyces lactis*, arrests the cell cycle of sensitive *Saccharomyces cerevisiae* in G1 phase [3]. Although zymocin is one of the most studied yeast killer toxins, the mechanism of cell cycle arrest had been unknown [4,5]. A few years ago, Lu et al. reported that zymocin cleaves the anticodon-loop of $tRNA^{Glu}_{mcm5s2UUC}$, $tRNA^{Lys}_{mcm5s2UUU}$, and $tRNA^{Gln}_{mcm5s2UUG}$ in sensitive yeast cells [6]. Zymocin is a heterotrimeric protein that consists of α, β and γ subunits, and the γ-subunit is responsible for tRNA cleavage activity [4,6,7]. Since the intracellular expression of the γ-subunit causes G1 arrest [8], it is conceivable that G1 arrest is due to tRNA cleavage. PaT, which is produced by *Pichia acaciae*, is another tRNA-targeting killer toxin. The gene organization on the PaT-encoding plasmid is similar to that on the zymocin-encoding plasmid, and PaT is believed to form a heterotrimeric complex similar to zymocin [9]. PaT has long been known to induce DNA damage, which was believed to induce the cell cycle arrest of sensitive cells in S phase [10,11]. However, the mechanism of DNA damage induction by PaT had remained elusive. Then Klassen et al. reported a surprising result that PaT specifically cleaves the $tRNA^{Gln}_{mcm5s2UUG}$ of sensitive yeast cells [12]. This indicates that the tRNA cleavage by PaT results in S phase arrest via DNA damage induction. Alternatively, tRNA cleavage and DNA damage induction additively contribute to S phase arrest. Similar to zymocin, intracellular expression of the active subunit of PaT (Orf2p) also causes S phase arrest [11].

We previously reported on the cellular response to tRNA cleavage by expressing the ribonuclease domains of colicin E5 and colicin D, E5-CRD and D-CRD, respectively, in yeast cells [13,14]. Intracellular expression of E5-CRD or D-CRD in yeast cells statically impairs cell growth concomitant with tRNA cleavage. Additionally, transcriptional profile of cells exposed to the tRNA cleavage was comprehensively analyzed with DNA microarray. If tRNA cleavage always leads to phase-specific cell cycle arrest, D-CRD is also expected to exhibit the same effect on sensitive cells. To explore this, the zymocin γ-subunit, PaT Orf2p and D-CRD were individually expressed in *S. cerevisiae*, and the cell cycle status and transcriptional responses to tRNA cleavage were compared. Our data indicates that specific cell cycle arrest positively effects on the viability of cells against tRNA cleavage.

Abbreviations: mcm^5s^2U, 5-methoxycarbonylmethyl-2-thiouridine; mcm^5U, 5-methoxycarbonylmethyluridine; qPCR, quantitative PCR; FACS, fluorescence-activated cell sorting.

* Corresponding authors. Fax: +81 3 5841 8016.
E-mail addresses: atetsu@mail.ecc.u-tokyo.ac.jp (T. Ogawa), amasaki@mail.ecc.u-tokyo.ac.jp (H. Masaki).

0006-291X/$ - see front matter © 2012 Elsevier Inc. All rights reserved.
http://dx.doi.org/10.1016/j.bbrc.2012.03.061

2. Materials and methods

2.1. Yeast strains, media and culture conditions

S. cerevisiae strain TM142 (*MATα ura3 leu2 trp1 his3*) was used for the killer toxin challenge assay. Strain CG379 (*MATα ade5 can1 leu2 trp1 ura3 his7* GAL+) was used for the expression of tRNA targeting toxins. The strains were cultured in YPD medium (2% glucose, 2% bacto-peptone and 1% bacto-yeast extract) at 30 °C. For the expression of toxins, CG379 was grown in YPRaff medium (2% raffinose, 2% bacto-peptone and 1% bacto-yeast extract) to an optical density at 660 nm of 0.2, and then 2% galactose was added. YPGal contains 2% galactose instead of glucose of YPD. SD and SG were used as synthetic minimum media containing glucose and galactose, respectively. A diploid strain was obtained by mating strain TM142 and TM141 (*MAT*a *ura3 leu2 trp1 his3*), and was used for cycloheximide treatment in YPD medium.

2.2. Preparation of crude killer toxins

Crude toxins were prepared from the supernatant of *K. lactis* IFO1267 and *P. acaciae* NRRL Y-18665 cultures grown in YPD medium. Each supernatant was filtered using a Vivaspin (3000 MWCO, Viva science), and then toxin activity was calculated using a multi-well plate assay, as described previously [11].

2.3. Construction of toxin-expressing strains

Plasmids for the expression of D-CRD and D-CRD (H611Y) which has less than 0.1% of the tRNA cleaving activity of wild-type have been described previously [14]. Genes encoding N-terminal FLAG-tagged D-CRD and zymocin γ-subunit, and C-terminal FLAG-tagged PaT ORF2 were polymerase chain reaction (PCR)-amplified, and cloned into *Xba*I and *Sac*I sites of pGML20, which contains a *GAL1* promoter and *ADH1* terminator. The resultant plasmids were digested with *Sph*I and *Eco*RV, and the excised toxin-coding genes were cloned into the *Sph*I–*Sma*I site of pAUR101 (TaKaRa). Homologous gene recombination in strain CG379 by pAUR101 was performed according to the manufacturer's instructions.

2.4. FACS analysis

Cells were harvested, washed with PBS and then fixed with 70% EtOH overnight. Aggregated cells were re-suspended in PBS and separated by sonication. Cells were treated with 0.5 mg/mL RNase A at 30 °C overnight, then PI was added at a final concentration of 0.025 mg/mL and incubated at 4 °C for 10 min. Cells that were re-suspended in PBS were used for FACS analysis.

2.5. Northern hybridization

RNA isolation was performed using the hot phenol method. Northern hybridization was performed as described previously [2]. The probes, which corresponded to the 3′ half of the respective tRNAs, were as follows: $tRNA^{Arg}_{ICG}$ 5′-GGACTTGAACCTGGAATCTTCTG-3′; $tRNA^{Gln}_{mcm5s2UUG}$ 5′-ATTCGAACCGGGGTTGTCCG-3′; and $tRNA^{Glu}_{mcm5s2UUC}$ 5′-TCGAACCCCGGTCTCCACG-3′.

2.6. Quantification of expression level of mRNA using quantitative RT–PCR

To quantify mRNA levels of *STE2* and *STE3*, quantitative PCR (qPCR) was performed according to the method described previously [14]. The primers were as follows: STE2-upsream 5′-GCTGTCTAGCTTTCAAACTGAT-3′; STE2-downstream 5′-AACTTTCTGGCTTCCTCATC-3′; STE3-upstream 5′-TGTCGACTATAGGATTCCAGATG-3′; and STE3-downstream 5′-TGAGCTTGAATTCTCTTCTTTTG-3′.

3. Results

3.1. Cell cycle arrest at a specific phase is not a common response to tRNA-targeting toxins

Since the toxicity of a killer toxin often varies according to the strain, the sensitivity of several experimental *S. cerevisiae* strains to killer toxins was tested first. The toxin eclipse assay showed that all *S. cerevisiae* strains tested formed a halo around zymocin-producing *K. lactis*. In contrast, some strains did not exhibit a clear sensitivity to PaT (Supplementary Fig. 1). However, a concentrated solution of crude PaT decreased the viability, indicating that TM142, which was judged tolerant of PaT by the eclipse assay, was intrinsically sensitive (Fig. 1A). Then after challenge with these toxins, cell cycle analysis was performed by Fluorescence-activated cell sorting (FACS) analysis. *S. cerevisiae* cells exposed to zymocin and PaT were arrested at G1 phase and S phase, respectively, which is consistent with previous reports (Fig. 1B) [3,11].

We previously showed that D-CRD cleaves $tRNA^{Arg}_{ICG}$, $tRNA^{Arg}_{mcm5UCU}$, and $tRNA^{Arg}_{CCU}$ of yeast cells both *in vitro* and *in vivo* [14]. The impairment of cell growth by D-CRD was static, however, the cell cycle analysis was not performed at that time. Then, genes encoding the zymocin γ-subunit, PaT Orf2p and D-CRD were chromosomally integrated, and these toxins were expressed to compare the effect of tRNA cleavage on cell cycle progression. The colony forming ability was severely impaired when D-CRD and Orf2p were expressed (Fig. 2A). In contrast, the expression of γ-subunit had a lesser effect on cell growth. When a FLAG-tag was fused to the C-terminus of γ-subunit, colony-forming activity was greatly decreased, which was comparable to that of D-CRD. However, tRNA cleavage by γ-subunit was not observed in these cells (data not shown). Therefore, we used an N-terminal FLAG-tagged γ-subunit for subsequent experiments.

Then, time dependence of tRNA cleavage of each toxin-expressing strain was analyzed. $tRNA^{Arg}_{ICG}$, $tRNA^{Glu}_{mcm5s2UUC}$ and $tRNA^{Gln}_{mcm5s2UUG}$, which were the primary targets of D-CRD, zymocin and PaT, respectively, were constantly cleaved during the experimental period (Fig. 2B). It is noteworthy that colony formation of the γ-subunit-expressing strain did not decrease appreciably despite the prolonged tRNA cleavage (Fig. 2A and B). Next, the cell cycle status of cells expressing these toxins was determined by FACS. D-CRD expression did not cause cell cycle arrest at any specific phase (Fig. 2C). The DNA histogram of the CG379 cells that expressed γ-subunit for twelve hours showed a single peak of increased DNA content, which seems to be inconsistent with the previous result that γ-subunit-expressing cells were arrested at G1 phase [8]. However, microscopic analysis showed that most of these cells were unbudded, indicating that they were arrested at G1 phase (Supplementary Fig. 2). G1 arrest was also confirmed in TM142 cells expressing γ-subunit from the chromosome (Fig. 2C). Unexpectedly, obvious phase specificity of cell cycle arrest, namely in S phase, was not observed in the Orf2p-expressing cells in this study (Fig. 2C). These findings indicate that PaT does not always induce complete S phase arrest of sensitive cells. These three toxins were then expressed from high-copy plasmids, and the ability of colony formation was tested. Colony formation of these strains was considerably lower than that of strains expressing toxin from the chromosome (Fig. 2D). Furthermore, the G1 arrest induced by γ-subunit, as shown in Fig. 2C, disappeared (Fig. 2E).

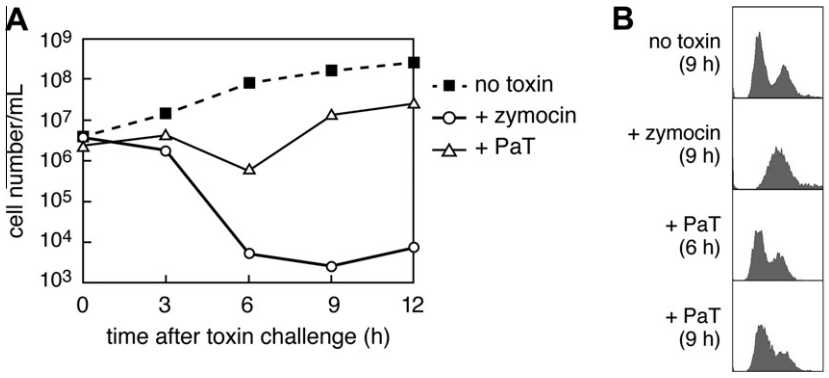


Fig. 1. Phase-specific cell cycle arrest induced by zymocin and PaT. (A) The viability of *S. cerevisiae* TM142 cells after challenge with zymocin or PaT was measured. Cells were washed to remove the toxins, spread onto YPD plates and then the CFUs were counted. (B) Cell cycle status of TM142 cells in response to the tRNA-targeting toxins was analyzed by FACS. Cells were sampled at the indicated time points in A.

3.2. G1 arrested cells expressing γ-subunit do not activate the transcription of a-cell specific gene in MATα cells

In our previous report, the transcriptional profile of D-CRD-expressing cells was analyzed by DNA microarray, and the yeast mating MAPK cascade was shown to be activated by tRNA cleavage only in *MATα* cells [14]. This conclusion depends on the fact that the transcriptional activation of a-cell specific genes such as *STE2*, *ASG7*, *BAR1* and *MFa2* occurred in D-CRD-expressing *MATα* cells. In contrast, α-cell specific genes, such as *STE3* and *MFα1*, were not transcribed in *MAT*a cells expressing D-CRD. The G1 arrest caused by the γ-subunit was reminiscent of the mating response, because activation of the mating MAPK cascade causes G1 arrest when cells receive a corresponding pheromone [15]. It was then assumed that γ-subunit activates a-cell specific genes in *MATα* cells to a much higher level than D-CRD. To verify this, the level of *STE2* transcript after the expression of γ-subunit and Orf2p in CG379 (*MATα*) cells was determined by quantitative PCR (qPCR). However, contrary to our expectations, γ-subunit did not induce *STE2* transcription (Table 1). Conversely, Orf2p expression induced the activation of *STE2* transcription, although to a lesser extent than D-CRD. Microscopic analysis showed aggregation of cells expressing D-CRD and Orf2p, but not γ-subunit (Supplementary Fig. 2), showing that the mating response was initiated in these cells.

3.3. Transcription of a-cell specific gene in MATα cells is due to translation impairment

How do Orf2p and D-CRD induce the expression of a-cell specific gene in *MATα* cells? The results suggest that inhibition of translation causes activation, since tRNA cleavage should down-regulate translation in sensitive cells [1]. Therefore, cells were treated with cycloheximide, which reversibly inhibits protein synthesis by binding to the 80S ribosome [16], and then the transcription levels of an a-cell specific gene (*STE2*) and an α-cell specific gene (*STE3*) were determined. Transcription of *STE2* dramatically increased in *MATα* cells treated with cycloheximide (Table 2). Similarly, *STE3* was activated in *MAT*a cells, however, the level of *STE3* activation was about one twenty-third compared to that of *STE2* activation in *MATα* cells. In diploid cells, both *STE2* and *STE3* were equally activated. Therefore, we concluded that the activation of a-cell specific genes in *MATα* cells is caused by impairment of protein synthesis.

4. Discussion

In this study, D-CRD, γ-subunit and Orf2p, which contain tRNA cleaving activity, were expressed in yeast cells, and the correlation between growth impairment and cell cycle status was examined. Colony formation was severely decreased by Orf2p and D-CRD. In contrast, viability was hardly affected by the γ-subunit when expressed from the chromosome, and cell cycle was arrested in G1 phase. However, cell growth was almost completely abolished when the γ-subunit was expressed from a high-copy plasmid, and the phase specificity of cell cycle arrest vanished. This result is very similar to the cellular response of strains with defects in the DNA damage checkpoint. For instance, cells lacking *RAD9* and *MEC1*, which encode DNA damage-dependent checkpoint proteins responsible for the activation of Rad53p [17], exhibit decreased colony forming ability after treatment with DNA damage agents, such as MMS and hydroxyurea [18,19]. Therefore, our results indicate that phase-specific cell cycle arrest contributes to the viability of host cells in response to tRNA cleavage by γ-subunit.

Cycloheximide treatment induced the expression of a-cell specific gene, such as *STE2*, in *MATα* cells, indicating that the activation is due to translation impairment. Then, it is acceptable to deduce the extent of protein synthesis impairment according to the activation of a-cell specific gene in *MATα* cells. Since the activation of a-cell specific gene is not induced in cells expressing γ-subunit despite of prolonged tRNA cleavage, it is assumed that the impairment of protein synthesis by γ-subunit was not sufficient for *STE2* de-repression. It has been reported that cell size increases when cells are challenged with zymocin [3], which is consistent with our result. On the contrary, protein synthesis is severely impaired by D-CRD as the transcriptional level of a-cell specific gene was the most elevated. Interestingly, in Orfp2-expressing cells, the transcription of a-cell specific gene is less activated and cell cycle arrest in S phase is incomplete. Taken together, our results suggest that the extent of protein synthesis impairment determines the phase specificity of cell cycle arrest after tRNA cleavage. Cell cycle arrest, such as G1 or S arrest, may be induced only if cells have enough energy left to activate cell cycle checkpoint.

In *S. cerevisiae*, codons for Glu and Gln are frequently used, and their cognate tRNAs, $tRNA^{Glu}_{mcm5s2UUC}$ and $tRNA^{Gln}_{mcm5s2UUG}$, which are the primary targets of zymocin and PaT, respectively, are abundantly expressed. On the other hand, the target of colicin D, $tRNA^{Arg}_{ICG}$, is abundant in *E. coli* cells, but is a minor tRNA in *S. cerevisiae*. These facts might influence the difference in cellular effects among γ-subunit, Orf2p and D-CRD. Additionally, the induction of DNA damage by PaT seems to synergistically contribute to growth impairment with tRNA cleavage, which may discriminate the effect of PaT on sensitive cells from that of zymocin. As noted above, the activity of Orf2p might be dependent on the balance between tRNA cleavage and DNA damage induction. Therefore, this suggests that the effect of Orf2p on cells varies according to the

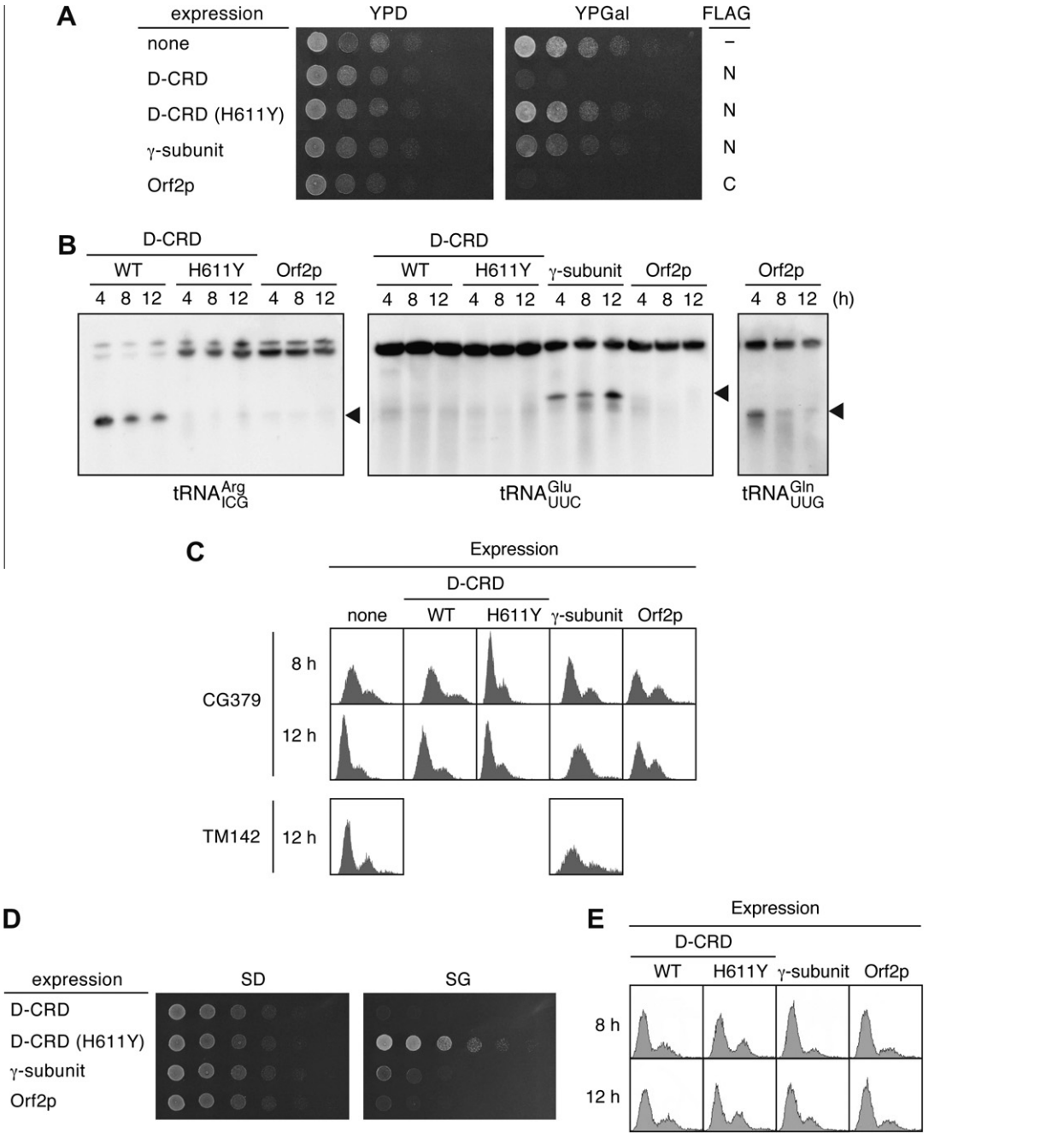


Fig. 2. Phase-specific cell cycle arrest contributes to the colony formation of sensitive cells in response to γ-subunit. (A) The colony forming ability of the CG379 cells chromosomally expressing tRNA-targeting toxins was examined. The location of the FLAG-tag on these toxins is indicated. Cultures of each strain were serially diluted five times, and then spotted onto solid medium as indicated. (B) tRNA cleavage was observed in the same toxin-expressing cells as shown in Fig. 2A. Cells were collected at the indicated times, then total RNA was prepared and northern hybridization was performed. Cleaved tRNA fragments are indicated by the arrowhead. (C) D-CRD, γ-subunit and Orf2p were expressed as seen in Fig. 2A, and these cells were harvested after 8 and 12 h of expression. The status of cell cycle progression was then analyzed by FACS. The same experiment was performed with TM142 cells expressing γ-subunit from the chromosome. (D) The colony forming ability of TM142 cells expressing the tRNA-targeting toxins from high-copy plasmid was examined as shown in Fig. 2A. (E) Cell cycle progression of toxin-expressing cells from high-copy plasmid was analyzed by FACS.

Table 1
Transcription of *STE2* mRNA after inducing the expression of tRNA targeting toxins for 4 h. Transcriptional levels were quantified by qPCR. *STE2* mRNA levels were normalized to *ACT1* mRNA, and those were shown as a ratio to wild-type value.

Expression	*STE2/ACT1*	Ratio to WT (%)
None	0.018	100
D-CRD	6.201	33565
D-CRD (H611Y)	0.020	111
γ-Subunit	0.029	155
Orf2p	1.519	8221

intracellular expression level. This could be the reason that Orf2p failed to arrest the cell cycle in S phase in this study.

Transcriptional de-repression by protein synthesis impairment was observed in both of haploid cells and diploid cells, and the a-cell specific gene in *MAT*α cells exhibited the highest activation. Cell type information is established by mating type-specific gene silencing [20]. The Tup1p-Cyc8p co-repressor is involved in the repression of a-cell specific gene transcription in both *MAT*α cells and diploid cells [21,22]. In contrast, this co-repressor is not necessary for the repression of α-cell specific genes in *MAT*a cells or dip-

Table 2
Transcription of mating-type specific genes after cycloheximide treatment. Transcriptional levels were quantified by qPCR after treatment with 50 ng/mL cycloheximide. The a-cell specific gene and α-cell specific gene are *STE2* and *STE3*, respectively. Each value was calculated as a proportion of *ACT1* mRNA, and then normalized to a mock treated sample from the same time point.

Cell type	a-cell specific gene			α-cell specific gene		
	0	1	3	0	1	3 (h)
*MAT*α	1.7	410	360	1.3	1.2	1.0
*MAT*a	1.2	3.8	3.2	1.3	27	16
*MAT*a/α	1.9	9.5	12	1.2	6.3	11

loid cells. Therefore, we assumed that transcriptional activation of a-cell specific genes in *MAT*α cells is due to decrease of Tup1p-Cyc8p co-repressor, and the expression of D-CRD actually decreased Tup1p expression (Supplementary Fig. 3).

The physiological significance of the phase-specific cell cycle arrest has yet been unknown. This may be a resistance of cells against tRNA cleavage, and yeast cells do not provide it against the ectopic expression of D-CRD, which results in the non-specific cell cycle arrest. To elucidate the mechanism of cell cycle arrest would help to know veritable cellular response to tRNA cleavage as well as the importance of cell cycle arrest itself.

Acknowledgments

We are grateful to Dr. Yoshinori Watanabe for providing FACS (Becton, Dickinson, and Company). Yeast strains *S. cerevisiae* CG379, *K. lactis* IFO1267 and *Pichia acaciae* NRRL Y-18665 were provided by the National BioResource Project (NBRP) of the Ministry of Education, Culture, Sports, Science and Technology, Japan; Japan Collection of Microorganisms; and the ARS Culture Collection, respectively. This work was supported by a Grant-in-Aid for Young Scientists (B) to T.O. from the Ministry of Education, Culture, Sports, Science and Technology of Japan.

Appendix A. Supplementary data

Supplementary data associated with this article can be found, in the online version, at doi:10.1016/j.bbrc.2012.03.061.

References

[1] T. Ogawa, K. Tomita, T. Ueda, K. Watanabe, T. Uozumi, H. Masaki, A cytotoxic ribonuclease targeting specific transfer RNA anticodons, Science 283 (1999) 2097–2100.
[2] K. Tomita, T. Ogawa, T. Uozumi, K. Watanabe, H. Masaki, A cytotoxic ribonuclease which specifically cleaves four isoaccepting arginine tRNAs at their anticodon loops, Proc. Natl. Acad. Sci. USA 97 (2000) 8278–8283.
[3] A.R. Butler, J.H. White, M.J. Stark, Analysis of the response of *Saccharomyces cerevisiae* cells to *Kluyveromyces lactis* toxin, J. Gen. Microbiol. 137 (1991) 1749–1757.
[4] M.J. Stark, A. Boyd, A.J. Mileham, M.A. Romanos, The plasmid-encoded killer system of *Kluyveromyces lactis*: a review, Yeast 6 (1990) 1–29.
[5] R. Schaffrath, K.D. Breunig, Genetics and molecular physiology of the yeast *Kluyveromyces lactis*, Fungal Genet. Biol. 30 (2000) 173–190.
[6] J. Lu, B. Huang, A. Esberg, M.J. Johansson, A.S. Byström, The *Kluyveromyces lactis* gamma-toxin targets tRNA anticodons, RNA 11 (2005) 1648–1654.
[7] D. Jablonowski, R. Schaffrath, Zymocin, a composite chitinase and tRNase killer toxin from yeast, Biochem. Soc. Trans. 35 (2007) 1533–1537.
[8] A.R. Butler, M. Porter, M.J. Stark, Intracellular expression of *Kluyveromyces lactis* toxin gamma subunit mimics treatment with exogenous toxin and distinguishes two classes of toxin-resistant mutant, Yeast 7 (1991) 617–625.
[9] D.A. McCracken, V.J. Martin, M.J. Stark, P.L. Bolen, The linear-plasmid-encoded toxin produced by the yeast *Pichia acaciae*: characterization and comparison with the toxin of *Kluyveromyces lactis*, Microbiology 140 (Pt 2) (1994) 425–431.
[10] R. Klassen, F. Meinhardt, Induction of DNA damage and apoptosis in *Saccharomyces cerevisiae* by a yeast killer toxin, Cell Microbiol. 7 (2005) 393–401.
[11] R. Klassen, S. Teichert, F. Meinhardt, Novel yeast killer toxins provoke S-phase arrest and DNA damage checkpoint activation, Mol. Microbiol. 53 (2004) 263–273.
[12] R. Klassen, J.P. Paluszynski, S. Wemhoff, A. Pfeiffer, J. Fricke, F. Meinhardt, The primary target of the killer toxin from *Pichia acaciae* is tRNA(Gln), Mol. Microbiol. 69 (2008) 681–697.
[13] T. Ogawa, M. Hidaka, K. Kohno, H. Masaki, Colicin E5 ribonuclease domain cleaves *Saccharomyces cerevisiae* tRNAs leading to impairment of the cell growth, J. Biochem. 145 (2009) 461–466.
[14] M. Shigematsu, T. Ogawa, A. Kido, H.K. Kitamoto, M. Hidaka, H. Masaki, Cellular and transcriptional responses of yeast to the cleavage of cytosolic tRNAs induced by colicin D, Yeast 26 (2009) 663–673.
[15] J. Kurjan, Pheromone response in yeast, Annu. Rev. Biochem. 61 (1992) 1097–1129.
[16] W. Stöcklein, W. Piepersberg, Binding of cycloheximide to ribosomes from wild-type and mutant strains of *Saccharomyces cerevisiae*, Antimicrob. Agents Chemother. 18 (1980) 863–867.
[17] C. Clémenson, M.C. Marsolier-Kergoat, DNA damage checkpoint inactivation: adaptation and recovery, DNA Repair (Amst) 8 (2009) 1101–1109.
[18] T.A. Weinert, G.L. Kiser, L.H. Hartwell, Mitotic checkpoint genes in budding yeast and the dependence of mitosis on DNA replication and repair, Genes Dev. 8 (1994) 652–665.
[19] A.G. Paulovich, R.U. Margulies, B.M. Garvik, L.H. Hartwell, RAD9, RAD17, and RAD24 are required for S phase regulation in *Saccharomyces cerevisiae* in response to DNA damage, Genetics 145 (1997) 45–62.
[20] J.E. Haber, Mating-type gene switching in *Saccharomyces cerevisiae*, Annu. Rev. Genet. 32 (1998) 561–599.
[21] A.D. Johnson, Molecular mechanisms of cell-type determination in budding yeast, Curr. Opin. Genet. Dev. 5 (1995) 552–558.
[22] C.A. Keleher, M.J. Redd, J. Schultz, M. Carlson, A.D. Johnson, Ssn6-Tup1 is a general repressor of transcription in yeast, Cell 68 (1992) 709–719.

Biochemical and Biophysical Research Communications 420 (2012) 755–761

Contents lists available at SciVerse ScienceDirect

Biochemical and Biophysical Research Communications

journal homepage: www.elsevier.com/locate/ybbrc

Expression and immunogenicity of novel subunit enterovirus 71 VP1 antigens

Juan Xu [b,c], Shixia Wang [b,g], Weihua Gan [d], Wenhong Zhang [e], Liwen Ju [f], Zuhu Huang [a,b], Shan Lu [a,b,g,*]

[a] Department of Infectious Diseases, The First Affiliated Hospital, Nanjing Medical University, China
[b] China–US Vaccine Research Center, The First Affiliated Hospital, Nanjing Medical University, China
[c] Department of Microbiology and Immunology, Nanjing Medical University, China
[d] Department of Pediatrics, The Second Affiliated Hospital, Nanjing Medical University, China
[e] Department of Infectious Diseases, Huashan Hospital, Fudan University, China
[f] School of Public Health, Fudan University, China
[g] Department of Medicine, University of Massachusetts Medical School, USA

ARTICLE INFO

Article history:
Received 1 March 2012
Available online 17 March 2012

Keywords:
Enterovirus 71 (EV71)
VP1 protein
DNA vaccine
Antibody responses

ABSTRACT

Hand, foot, and mouth disease (HFMD) is a common viral illness in young children. HFMD is caused by viruses belonging to the enterovirus genus of the picornavirus family. Recently, enterovirus 71 (EV71) has emerged as a virulent agent for HFMD with severe clinical outcomes. In the current report, we conducted a pilot antigen engineering study to optimize the expression and immunogenicity of subunit VP1 antigen for the design of EV71 vaccines. DNA immunization was adopted as a simple technical approach to test different designs of VP1 antigens without the need to express VP1 protein *in vitro* first. Our studies indicated that the expression and immunogenicity of VP1 protein can be improved with alternated VP1 antigen designs. Data presented in the current report revealed novel pathways to optimize the design of VP1 antigen-based EV71 vaccines.

© 2012 Elsevier Inc. All rights reserved.

1. Introduction

HFMD is a common viral illness in young children, causing fever, skin rash, and blister-like eruptions. HFMD is caused by enterovirus genus of the picornavirus family [1]. Coxsackieviruses, such as coxsackievirus A16 (CA16), are the most common cause of HFMD. Other enteroviruses, especially enterovirus 71 (EV71), have also been associated with HFMD.

Most HFMD infections do not result in serious complications; however, when the pathogen of HFMD is EV71, the disease can present with a high rate of neurological complications, including meningoencephalitis and pulmonary edema, which can occur within a few days and may lead to death. Other more serious complications, such as encephalitis, can be fatal [2,3].

EV71 is a small, non-enveloped virus with a positive-stranded RNA genome size of about 7.4 kb. While there is no structure report on EV71, the structure of viruses in this group is typified by a pentameric icosahedral outer capsid consisting of 60 copies each of four viral coat proteins VP1–VP4 [4]. VP1, VP2, and VP3 each contain in the order of 270 amino acid residues, folded into eight-stranded antiparallel sheet structures, and form the outer surface of the virus, such as in the case of coxsackievirus A9 [5]. VP4 contains only about 70 amino acids and lies on the inside of the capsid [6]. The open reading frame encoding the capsid protein VP1 is more variable and confers distinct antigenic properties to the virus [7]. Thus, the VP1 region is considered to be the most suitable region for sequence analysis to determine genetic diversity as the VP1 sequence appears to correlate with the serotype [8–10]. VP1 plays critical roles in adsorption and the uncoating process of the virus [11]. Any minor mutations in the VP1 gene have reported to lead to resistance to candidate antiviral compounds or produce a change in virulence [12–14].

The VP1 protein is the key target for vaccine development as it contains a number of important neutralization sites [15–17]. Key neutralizing antibody determinants have been found in the N-terminal half of VP1 when tested with high titer human neutralizing antibodies [18,19].

With repeated EV71 outbreaks in recent years, especially in Asian countries, a wide range of experimental EV71 vaccines have been studied, including heat-inactivated or formaldehyde-inactivated virions [20,21], EV71 virus-like particles (VLP) [22], VP1 recombinant protein [15], VP1 DNA vaccine [15,23], bacterial or viral vector expressing VP1 [19,24], and a Vero cell-adapted live attenuated virus [25]. Inactivated EV71 vaccines manufactured by several companies have started testing in clinical trials. It was shown that a recombinant *Escherichia coli*-expressed VP1 protein

* Corresponding author at: The First Affiliated Hospital of Nanjing Medical University, 300 Guangzhou Road, Nanjing 210029, China
E-mail address: shan.lu@umassmed.edu (S. Lu).

0006-291X/$ - see front matter © 2012 Elsevier Inc. All rights reserved.
http://dx.doi.org/10.1016/j.bbrc.2012.03.067

vaccine induced VP1-specific IgG and neutralizing antibody responses [15]. However, there has been limited work in expressing VP1 in mammalian cell systems.

In the current report, we conducted a pilot antigen engineering study to explore novel VP1 designs to improve the expression and immunogenicity of VP1 antigen. A DNA immunization approach was adopted to test different designs of VP1 antigens without the need to express VP1 protein *in vitro* first. Data presented in the current report provided a foundation for more work in optimizing the design of VP1-based subunit EV71 vaccines.

2. Materials and methods

2.1. Immunogen design

The natural codon usage by the *VP1* gene (Genbank Accession No. EU024958.1) from EV71 BJ4211 strain was modified with the MacVector software 7.2 against codon preference of *Homo sapiens*. A new *VP1* gene was created with codon optimized sequences. This change does not affect the amino acid sequence of the VP1 protein but may allow a higher expression in mammalian cells. The codon optimized *VP1* gene was chemically synthesized at Geneart Invitrogen (Germany).

2.2. Cloning of VP1 inserts into DNA vaccine vector

The codon optimized *VP1* genes contain two enzyme sites, Pst-I and BamH-I at the 5′ and 3′ ends, respectively. The *VP1* gene insert was removed from Geneart plasmid pGA4/VP1 and directly subcloned into DNA vaccine vector pJW4303 to generate pJW4303/VP1 (wt-VP1) DNA vaccine.

To promote secretion of the VP1 protein in a eukaryotic cell, a modified *VP1* gene insert linked to a tPA leader was created. This was produced by PCR with the template pGA4/VP1 using forward primer P1 and the reverse primer P2 (Table 1). The PCR products were then ligated into pJW4303 at the downstream of tPA leader. The resulting DNA vaccine was named pJW4303/tPA-VP1 (tPA-VP1).

The dimer form of the VP1 DNA vaccine was created by linking two copies of VP1 genes together. Insert 1 was produced by PCR using pGA4/VP1 as the template with the forward primer P1 and the reverse primer P3 (Table 1). The insert2 gene, was amplified with the forward primer P4 and the reverse primer P2 (Table 1). The two inserts were cloned into the downstream of tPA leader sequence of pJW4303 at the same time by a three-way ligation, leading to pJW4303/tPA-VP1-dimer (VP1-d).

The fusion VP1 antigen containing Fc of human IgG (VP1-Fcγ) was produced by PCR from a human Fcγ (hFc) segment from template plasmid pJW4303/gp120-hFc using forward primer P5 and backward primer P6. Similarly, mouse Fcγ (mFc) was amplified from a plasmid containing mouse IL-2-Fc with forward primer P7 and backward primer P8 (Table 1). At the same time, the plasmid pJW4303/tPA-VP1-dimer (VP1-d) was digested with Kpn-I and BamH-I to serve as the "vector" without insert2 gene. The two Fcγ genes were then fused with insert1 in the "vector" plasmid separately to produce either pJW4303/tPA-VP1-hFc (VP1-hFc) or pJW4303/tPA-VP1-mFc (VP1-mFc).

Table 1
Sequences of primers for PCR.

Name	Sequence
P1	5′-GTCACTTCGCTAGCGTGGCCGACGTGATCGAGAG-3′
P2	5′-GAGCTCGGATCCTCATCACAGGGTGG-3′
P3	5′-ATAACTGGTACCGGCTCCCAGGGTGGTGATGGCGGTCCG-3′
P4	5′-ATAGCAGGTACCGCCGGAGTGGCCGACGTGATCGAGAG-3′
P5	5′-ATAACTGGTACCGATCGCAAATGTTGTGTCGAG-3′
P6	5′-GAGCTCGGATCCTCATTTACCCGGAGACAGGGAG-3′
P7	5′-ATAACTGGTACCCATCCCAGAGGGCCCACAATC-3′
P8	5′-GAGCTCGGATCCTCATTTACCCGGAGTCCGGGAG-3′

Underlined letters were restriction sites.

2.3. In vitro expression of VP1 antigens in 293T cells

The expression of VP1 DNA vaccines was verified by transient transfection in 293T cells. Cells were seeded and grown to 50–70% confluence on 100 mm dishes, and plasmids (20 μg per dish) were mixed with 100 μl Polyethylenimine (PEI) for 15 min before being added into 293T cells. The supernatants and cell lysates were harvested at 72 h after transfection. VP1 protein expression was examined by Western blot.

2.4. DNA immunizations

NZW rabbits (~2 kg weight) were purchased from Shanghai Animal Center, Chinese Academy of Science. The rabbits were housed in the Animal Facility at the Nanjing Medical University in accordance with approved protocol.

Electroporation was used for inoculation of DNA vaccines by using electroporator SCIENTZ-2C from Scientz Co., Ltd. VP1 DNA vaccines or vector control were diluted to 1 μg/μl with normal saline and injected at four different sites in the quadriceps muscle with the dose of 200 μg per rabbit, then the injection sites were electroporated under the following parameters: 100 V, 60 ms and 60 Hz. The immunizations were given at weeks 0, 2, 4, and 8. Serum samples were taken prior to the first immunization and 2 weeks after each immunization VP1-specific antibody analysis.

2.5. Enzyme-linked immunosorbent assay (ELISA)

To measure VP1-specific antibody responses in immunized animals, 96-well plates were coated with 100 μl supernatant of VP1-d transfected cells (1:5 diluted with PBS) overnight, and washed five times with PBS containing 0.05% Tween-20 (PBST). After blocking, 100 μl of diluted rabbit serum were added in duplicate wells. After another set of washes, the plates were incubated with 100 μl of biotinylated anti-rabbit IgG (MultiSciences Biotech Co., Ltd. China) diluted at 1:2000 of Whey buffer (4% Whey, 0.5% Tween-20 in PBS). Then, 100 μl of horseradish peroxidase-conjugated streptavidin (SouthernBiotech) diluted at 1:2000 in whey buffer was added to each well. After the final wash, the plates were developed with 3,3′,5,5′-tetramethylbenzidine (TMB, Sigma) solution. The reactions were stopped by adding 50 μl of 1 M H_2SO_4, and the plates were read at an OD of 450 nm. The wells were scored positive with an OD above twice of that from the negative control serum.

2.6. Western blot

The VP1 proteins from transiently expressed 293T cell lysate (L) and supernatant (S) was subjected to denaturing SDS–PAGE and transferred onto PVDF membrane (Millipore). VP1 DNA vaccine or vector-immunized rabbit sera and EV71-infected human serum were diluted and used as the detecting antibody. Subsequently, the membranes were washed with PBST for 1 h and then reacted with HRP-conjugated goat anti-rabbit IgG at 1:10,000 dilution or HRP-conjugated rabbit anti-human IgG at 1:5000 dilution. After final wash, Western-light substrate was applied to the membranes and Kodak films were exposed to the membrane before being developed.

2.7. Indirect immunofluorescence analysis (IFA)

VP1 DNA vaccines or vector transfected 293T cells were fixed directly on the culture plates or harvested for cell smear with cooled methanol. RD cells infected with EV71 were also fixed to detect the ability of rabbit immune sera to recognize the virus. After three washes with PBS, the cells were penetrated with 0.1% Triton X-100 for 10 min at room temperature. Then blocking buffer (1% BSA, 0.1% Tween-20 in PBS) was added to cover whole cells for 1 h at room temperature. Detecting sera diluted with the same blocking buffer were put into and incubated at 4 °C overnight. Cells were washed 3 × 10 min with PBS. DyLight™488-conjugated goat anti-rabbit IgG at 1:400 dilution or DyLight™549-conjugated donkey anti-human IgG at 1:500 dilution were added and incubated in a moist cassette for 40 min at 37 °C. After another 3 × 10 min washes, the slides were examined using an inverted fluorescence microscope.

2.8. In vitro protective antibody analysis

An *in vitro* virus neutralization study was performed by a TCID50-reduction assay in Vero cells to assess the ability of the immunized sera to neutralize the EV71 virus. Serum samples were inactivated at 56 °C for 30 min before use. All serum samples were tested in triplicate and with a twofold serial dilution before mixing with equal volumes of EV71 viral isolate 10JA8-F5 containing 10^2 TCID50 and then plated onto monolayers of Vero cells growth to 85% confluence. After 48 h, the titer was read as the highest dilution that resulted in more than 50% reduction of CPE. The neutralization titer was taken as the average of the triplicates.

3. Results

In the current study, a codon optimized VP1 gene was used. The level of codon changes is shown in Supplement Fig. 1. This synthetic VP1 gene was used as the template to produce five different VP1 gene inserts (Fig. 1A). The amino acid sequence of wt-VP1 is same as the original wild type VP1 protein in the EV71 virus. The second VP1 insert (tPA-VP1) has an additional leader sequence from the human tissue plasminogen (tPA) with the objective to study if the addition of a tPA leader may increase the secretion of VP1 protein. The third VP1 insert (VP1-d) is a dimer form of VP1, which was produced by adding another copy of VP1 insert downstream of the tPA-VP1 insert – a combination of tPA-VP1 + wt-VP1 separated by a six amino acid linker (Gly-Ala-Gly-Thr-Ala-Gly). It was designed to force the VP1 molecule to form an artificial dimer. The last two VP1 inserts were built by adding the constant region (Fc) of either human or mouse immunoglobulin G (IgG) to the C-terminus of the tPA-VP1 insert. They were tested for whether the Fc domain can further facilitate the folding and secretion of VP1 protein.

The expression of VP1 DNA vaccines in 293T cells was confirmed by Western blot using an EV71 positive patient serum (Fig 1B). VP1 proteins expressed from wt-VP1 and tPA-VP1 were found mainly in 293T cell lysate, suggesting limited secretion of VP1 protein with these two VP1 insert designs. Adding an extra tPA leader did not increase the secretion of VP1. The dimer form of the VP1 design (VP1-d) was expressed as a higher molecular weight product which was expected since two copies of the VP1 sequence were included in the DNA vaccine insert. For the two VP1 insert designs with an additional C-terminal Fc component, both were expressed similarly as higher molecular weight products. However, VP1-hFc had detectable expression in supernatant while the other design with mouse Fc (VP1-mFc) did not have detectable extracellular expression.

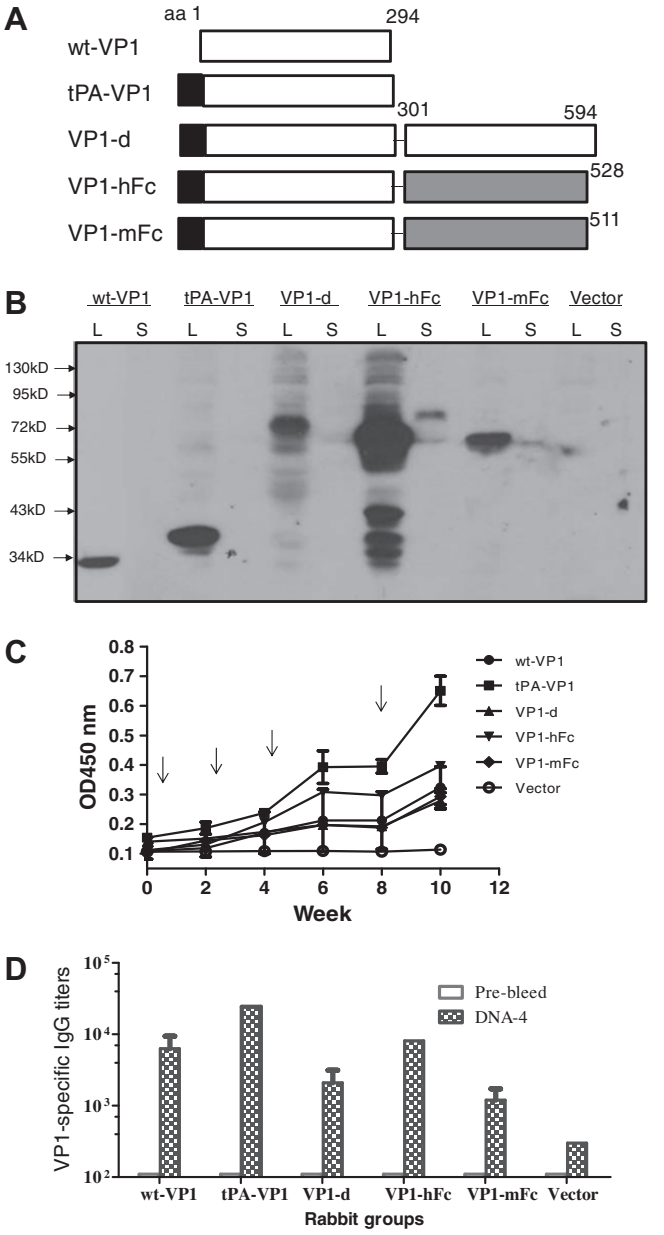


Fig. 1. (A) Schematic designs of VP1 DNA vaccines. The amino acid positions for each VP1 are indicated. (B) The Western blot of antigen expression by various VP1 DNA vaccines and the empty vector. "S" and "L" represent the supernatant and lysate of transiently transfected 293T cells, respectively. EV71 patient convalescent serum at 1:200 dilution was used as the detection antibody. (C) Temporal VP1-specific antibody responses in rabbit immune sera (1:500 dilution). Each curve represents the antibody response of five rabbits in the same group (average OD values with standard deviations). The arrows indicate the time points of DNA immunizations. (D) Peak level antibody titer in rabbit sera shown in panel C.

The immunogenicity of VP1-expressing DNA vaccines was evaluated in NZW rabbits (Fig. 1C). After three bi-weekly immunizations, positive antibody responses against VP1 antigen were detected. Animal groups receiving tPA-VP1 or VP1-hFc DNA vaccines had higher antibody responses than other groups. With another boost immunization in week 8, antibody titers in all groups were increased further (Fig. 1C). Peak level antibody titers showed that tPA-VP1 is the most immunogenic with a titer of ~1:2500. VP1-hFc and wt-VP1 groups had the next best antibody responses with titers just below 1:1000 (Fig. 1D).

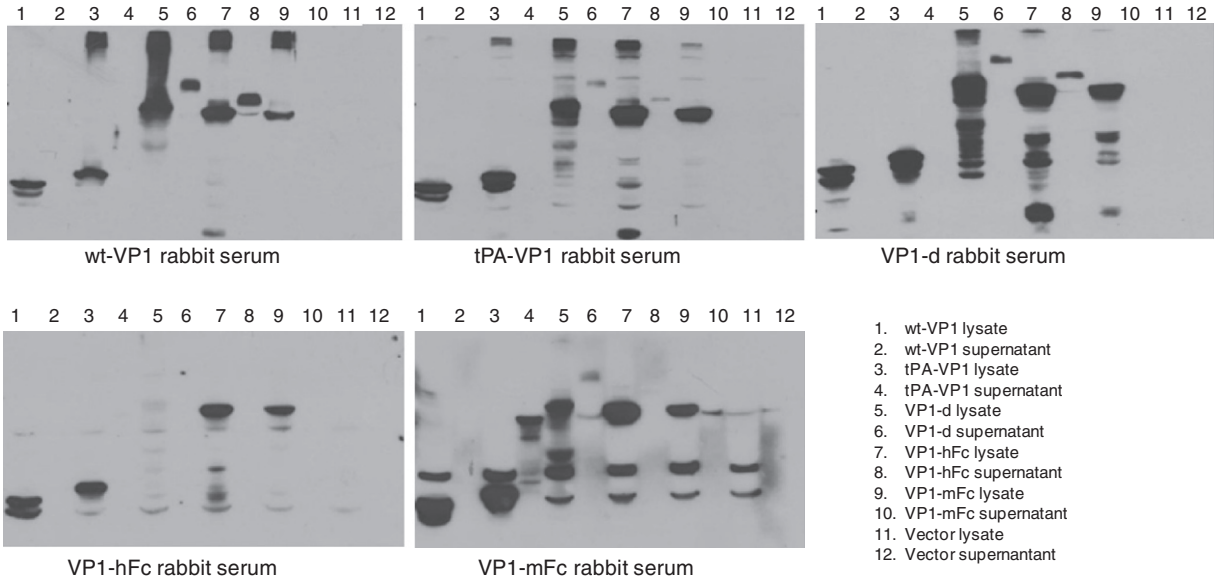


Fig. 2. Western blot analysis on the recognitions of VP1 proteins using rabbit sera (1:200 dilution) immunized with different VP1 DNA vaccines as indicated.

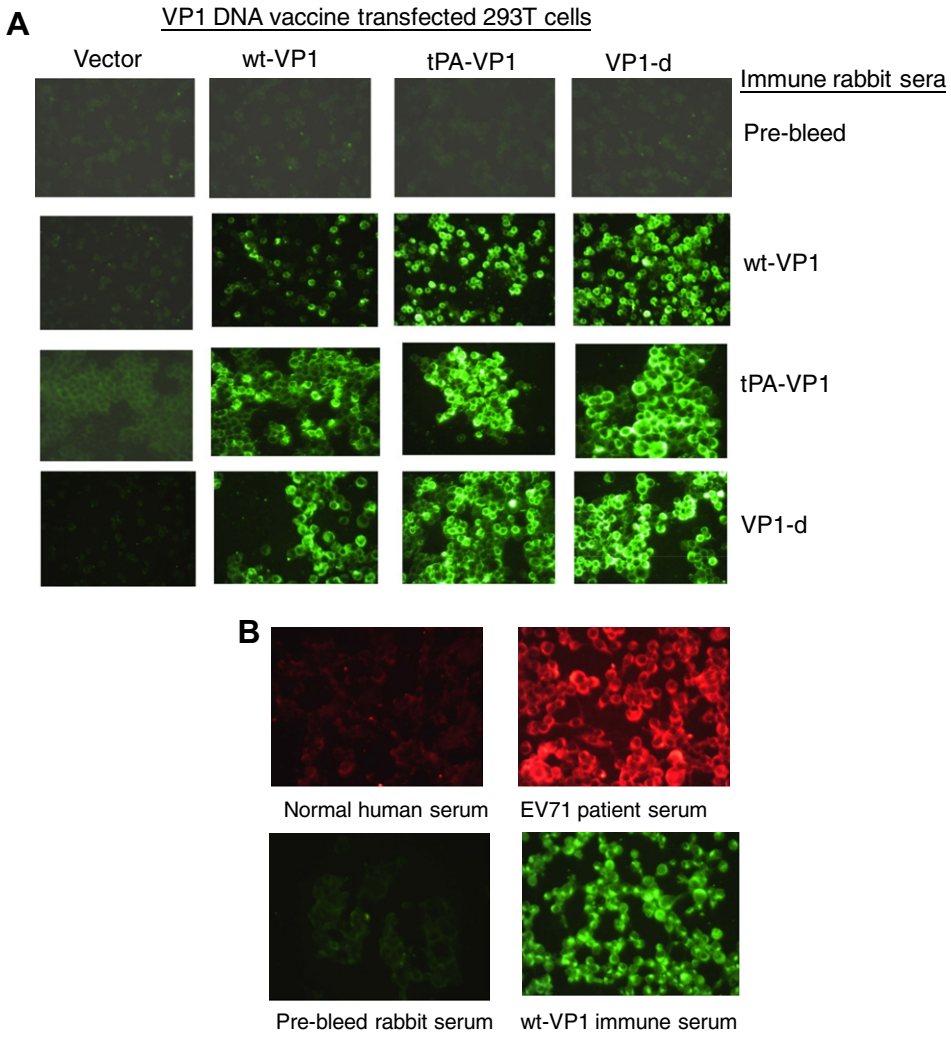


Fig. 3. (A) Detection by Immune-fluorescence assay (IFA) on the expression of VP1 proteins in 293T cells. The immune rabbit sera used in the detection (1:200 dilution) were collected at 2 weeks after the 4th DNA immunization. (B) IFA detection of EV71 viral infection of RD cells using normal human serum, EV71 patient convalescent serum, rabbit pre-bleed and wt-VP1 DNA vaccinated rabbit sera. The serum samples were at 1:200 dilution.

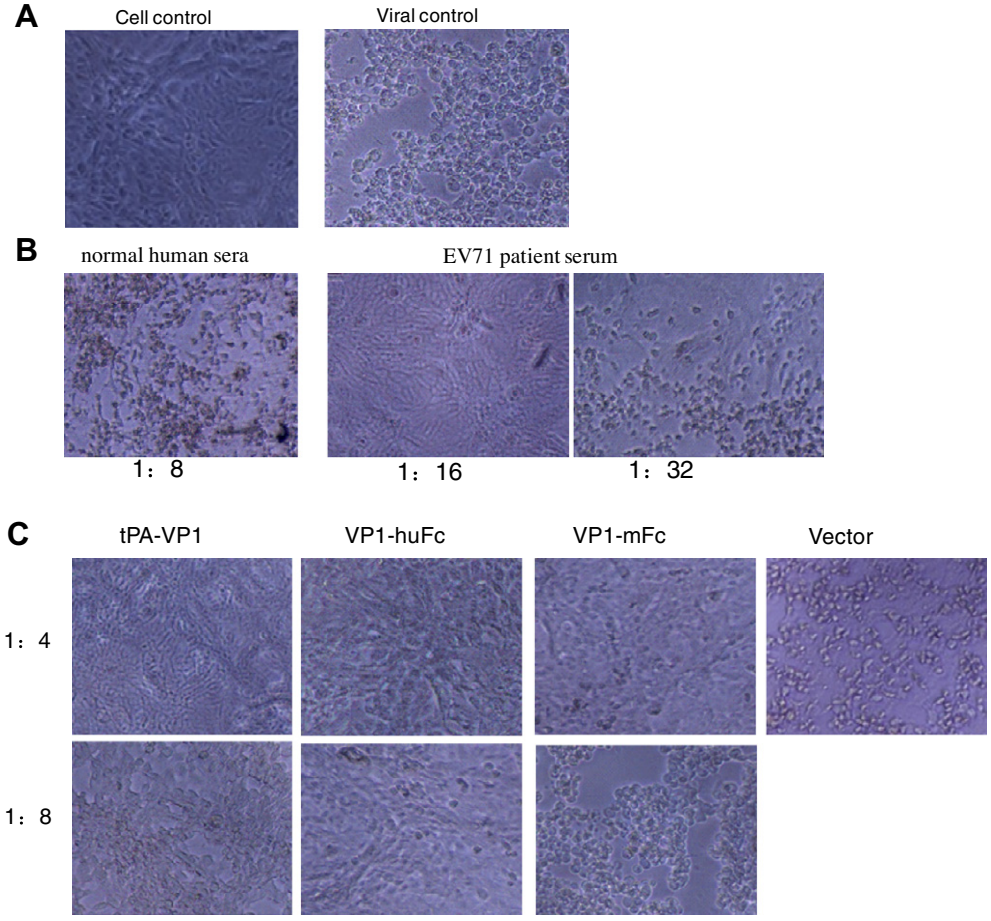


Fig. 4. Neutralizing antibody analysis against EV71 infection of RD cells. (A) RD cells with (viral control) or without (cell control) EV71 infection. (B) The EV71 viruses were pre-incubated for 1 h with either normal human serum at 1:8 dilution, or EV71 patient convalescent serum at 1:16 or 1:32 dilution before being added to RD cells. (C) The EV71 viruses were pre-incubated for 1 h anti-VP1 rabbit sera immunized at 1:4 or 1:8 dilutions before being added to RD cells. Rabbit sera were collected at 2 weeks after the 4th DNA immunization.

Western analysis was conducted to examine the antigen profile of rabbit sera (Fig. 2). First, the overall rabbit immune sera elicited by one VP1 DNA vaccine were able to recognize both the autologous and heterologous VP1 antigens. This data is consistent with results in Fig. 1B showing broad recognition by an EV71 patient serum.

Second, there is an extra high molecular weight band in the 293T cell lysate transfected with the tPA-VP1 DNA vaccine that can be recognized by rabbit sera immunized by either wt-VP1 or tPA-VP1 DNA vaccines but not by sera immunized with the other three VP1 DNA vaccines. This finding provided two pieces of useful information: (a) with the addition of tPA, small amounts of VP1 are secreted; and (b) tPA-VP1 protein can form a higher molecular weight complex that can be recognized by two rabbit sera that were elicited by the single copy VP1 antigen design (either wt-VP1 or tPA-VP1) but not by the double copy VP1 design (VP1-d) or VP1-Fc fusion designs (VP1-hFc or VP1-mFc). Together, our findings indicated that the conformation of oligomeric VP1 produced by tPA-VP1 is different from other high molecular weight VP1 complexes produced by other larger size VP1 antigens.

Third, there is an extra band (~95 kDa) in the culture supernatant of 293T cells transfected with VP1-d DNA vaccine plasmid that can be recognized by rabbit sera immunized with either wt-VP1, tPA-VP1, VP1-d or VP1-hFc, but not by that immunized with VP1-mFc. This would support the identity of this molecule as a VP1 dimer, as expected. Because a similarly secreted VP1 protein was identified with the VP1-hFc DNA vaccine and it is expected that two copies of Fc molecules will form a dimer, as in the immunoglobulin conformation, our results indicate that dimerization may be involved for VP1 protein secretion out of cells.

Finally, rabbit sera elicited by VP1-mFc recognized multiple bands with molecular weight ranging from 40 to 60 kDa in the supernatant of tPA-VP1 transfected 293T cells. However, the nature of such reactivity is not clear as there is high background of non-specific recognition at the 43 kDa level across different cell lysates from all five DNA vaccine inserts.

Indirect immunofluorescent assay (IFA) was conducted to confirm the specificity of rabbit immune sera against VP1 antigens. Rabbit immune sera elicited by wt-VP1, tPA-VP1 and VP1-d DNA vaccines were able to recognize VP1 antigens transiently expressed in 293T cells (Fig. 3A). To further confirm that antibodies elicited by VP1 DNA vaccines are able to recognize actual EV71 virus, rabbit immune sera elicited by wt-VP1 was tested against EV71 virus-infected RD cells and showed strong positive staining while the pre-bleed was completely negative (Fig. 3B). As the positive control, only EV71 infected patient serum but not normal healthy human serum recognized EV71-infected target cells.

Pilot *in vitro* neutralizing antibody study was conducted in Vero cells against 10JA8-F5, a genotype C4 EV71 strain virus that was isolated from a Chinese patient infected with EV71 (Fig. 4A). Normal human sera at a 1:8 dilution did not protect cells from CPE while EV71 patient sera were able to protect at a 1:16 dilution (protective effect disappeared at 1:32 serum dilution) (Fig. 4B). Rabbit immune sera elicited by various VP1 DNA vaccines were

able to show low titer protective activities at ~1:4 serum dilutions. Control serum with empty DNA vaccine vector did not have any protective activity even at a 1:2 dilution (Fig. 4C).

4. Discussion

EV71 remains a major public health concern in certain regions of the world where a large population of children are living under the threat of this emerging infectious disease. Several inactivated EV71 vaccines have been developed and tested in animals [15,21] and some have advanced into various stages of human studies (China sFDA unpublished report). However, given the known low immunogenicity of inactivated vaccines and the potential safety issues of using the whole inactivated viruses, particularly when the exact mechanism of action for producing severe central neurologic diseases is not well understood, there is need to develop safer and potentially highly immunogenic vaccines as alternatives to inactivated vaccines.

Subunit vaccines provide a high safety profile but it is a challenge to develop such vaccines against EV71. The protective antigen, VP1 protein, is part of the polyprotein complex (VP1–VP4) when these proteins are expressed by the virus. Selective expression of VP1 alone, while maintaining its immunogenicity with proper conformation, is a technical challenge. In the current study, we attempted to design various modified VP1 antigens and to study their immunogenicity in small animals in order to produce a better designed VP1 antigen for more advanced study.

We used a DNA vaccine platform as it is a useful tool to test various antigen designs without the need to produce recombinant protein production *in vitro*. A previous report using VP1-based DNA vaccines confirmed that this vaccine delivery approach was capable of eliciting VP1-specific antibody responses [23].

One key issue related to both recombinant protein and DNA vaccines is improvement of the level of antigen expression. High level expression of VP1 protein in a natural antigen conformation is critical for the success of both approaches. In the current report, various novel designs of VP1 antigen inserts were produced to test both *in vitro* expression and *in vivo* immunogenicity of these modified VP1 antigens. Indeed, our data suggested that different designs of VP1 antigens showed different levels of potential to be secreted or to form higher molecular weight oligomers. Such structural differences may also affect the immunogenicity of these VP1 antigen designs. Two forms of VP1 designs achieved high level antigen secretion. All of these findings will be very useful to guide further modification of VP1 antigens. More significantly, we found that the tPA-VP1 antigen design was much more immunogenic than other designs and should be used as the leading candidate for future VP1-based EV71 vaccine development.

The overall neutralizing antibody titers are still low and similar to what was reported in the past [15,23,26]. It is not clear at this point what levels of protective antibodies are needed to protect young children from lethal EV71 infection. However, the positive control human serum also had a low titer which indicated that the sensitivity of *in vitro* assay used in our study is limited. Due to the limit on the availability of EV71 protection animal models, no animal protection study was conducted with the candidate VP1 vaccines described in this report. In summary, our study identified the feasibility of several novel VP1 designs. Their immunogenicity can be further improved if adjuvant or the more promising DNA prime-protein boost approach is used [27,28]. These approaches should be incorporated into future studies.

Acknowledgments

This study was partially funded by National Natural Science Foundation of China (Grant #81000725). Authors would like to thank Dr. Jill Serrano for critical reading and editing of the manuscript.

Appendix A. Supplementary data

Supplementary data associated with this article can be found, in the online version, at http://dx.doi.org/10.1016/j.bbrc.2012.03.067.

References

[1] G.D. Hsiung, J.R. Wang, Enterovirus infections with special reference to enterovirus 71, J. Microbiol. Immunol. Infect. 33 (2000) 1–8.
[2] P. McMinn, K. Lindsay, D. Perera, H.M. Chan, K.P. Chan, M.J. Cardosa, Phylogenetic analysis of enterovirus 71 strains isolated during linked epidemics in Malaysia, Singapore, and Western Australia, J. Virol. 75 (2001) 7732–7738.
[3] M.J. Cardosa, D. Perera, B.A. Brown, D. Cheon, H.M. Chan, K.P. Chan, H. Cho, P. McMinn, Molecular epidemiology of human enterovirus 71 strains and recent outbreaks in the Asia–Pacific region: comparative analysis of the VP1 and VP4 genes, Emerg. Infect. Dis. 9 (2003) 461–468.
[4] S. Ranganathan, S. Singh, C.L. Poh, V.T. Chow, The hand, foot and mouth disease virus capsid: sequence analysis and prediction of antigenic sites from homology modelling, Appl. Bioinformatics 1 (2002) 43–52.
[5] E. Hendry, H. Hatanaka, E. Fry, M. Smyth, J. Tate, G. Stanway, J. Santti, M. Maaronen, T. Hyypia, D. Stuart, The crystal structure of coxsackievirus A9: new insights into the uncoating mechanisms of enteroviruses, Structure 7 (1999) 1527–1538.
[6] B.A. Brown, M.A. Pallansch, Complete nucleotide sequence of enterovirus 71 is distinct from poliovirus, Virus Res. 39 (1995) 195–205.
[7] R.R. Rueckert, Picornaviruses and their replication, in: B.N. Fields (Ed.), Virology, Lippincott-Raven, New York, 1990, p. 507.
[8] S.H. Kung, S.F. Wang, C.W. Huang, C.C. Hsu, H.F. Liu, J.Y. Yang, Genetic and antigenic analyses of enterovirus 71 isolates in Taiwan during 1998–2005, Clin. Microbiol. Infect. 13 (2007) 782–787.
[9] V. Caro, S. Guillot, F. Delpeyroux, R. Crainic, Molecular strategy for 'serotyping' of human enteroviruses, J. Gen. Virol. 82 (2001) 79–91.
[10] B.A. Brown, M.S. Oberste, J.P. Alexander Jr., M.L. Kennett, M.A. Pallansch, Molecular epidemiology and evolution of enterovirus 71 strains isolated from 1970 to 1998, J. Virol. 73 (1999) 9969–9975.
[11] C. Li, H. Wang, S.R. Shih, T.C. Chen, M.L. Li, The efficacy of viral capsid inhibitors in human enterovirus infection and associated diseases, Curr. Med. Chem. 14 (2007) 847–856.
[12] B.H. Chua, P. Phuektes, S.A. Sanders, P.K. Nicholls, P.C. McMinn, The molecular basis of mouse adaptation by human enterovirus 71, J. Gen. Virol. 89 (2008) 1622–1632.
[13] S.R. Shih, M.C. Tsai, S.N. Tseng, K.F. Won, K.S. Shia, W.T. Li, J.H. Chern, G.W. Chen, C.C. Lee, Y.C. Lee, K.C. Peng, Y.S. Chao, Mutation in enterovirus 71 capsid protein VP1 confers resistance to the inhibitory effects of pyridyl imidazolidinone, Antimicrob. Agents Chemother. 48 (2004) 3523–3529.
[14] T.C. Chen, S.C. Liu, P.N. Huang, H.Y. Chang, J.H. Chern, S.R. Shih, Antiviral activity of pyridyl imidazolidinones against enterovirus 71 variants, J. Biomed. Sci. 15 (2008) 291–300.
[15] C.N. Wu, Y.C. Lin, C. Fann, N.S. Liao, S.R. Shih, M.S. Ho, Protection against lethal enterovirus 71 infection in newborn mice by passive immunization with subunit VP1 vaccines and inactivated virus, Vaccine 20 (2001) 895–904.
[16] M.G. Mateu, Antibody recognition of picornaviruses and escape from neutralization: a structural view, Virus Res. 38 (1995) 1–24.
[17] P.D. Minor, Antigenic structure of picornaviruses, Curr. Top. Microbiol. Immunol. 161 (1990) 121–154.
[18] C.S. Tan, M.J. Cardosa, High-titred neutralizing antibodies to human enterovirus 71 preferentially bind to the N-terminal portion of the capsid protein VP1, Arch. Virol. 152 (2007) 1069–1073.
[19] L.A. Sivasamugham, M.J. Cardosa, W.S. Tan, K. Yusoff, Recombinant Newcastle disease virus capsids displaying enterovirus 71 VP1 fragment induce a strong immune response in rabbits, J. Med. Virol. 78 (2006) 1096–1104.
[20] C.-C. Liu, W.-C. Lian, M. Butler, S.-C. Wu, High immunogenic enterovirus 71 strain and its production using serum-free microcarrier Vero cell culture, Vaccine 25 (2007) 19–24.
[21] K.C. Ong, S. Devi, M.J. Cardosa, K.T. Wong, Formaldehyde-inactivated whole-virus vaccine protects a murine model of enterovirus 71 encephalomyelitis against disease, J. Virol. 84 (2010) 661–665.
[22] Y.-C. Chung, M.-S. Ho, J.-C. Wu, W.-J. Chen, J.-H. Huang, S.-T. Chou, Y.-C. Hu, Immunization with virus-like particles of enterovirus 71 elicits potent immune responses and protects mice against lethal challenge, Vaccine 26 (2008) 1855–1862.
[23] W. Tung, S. Bakar, Z. Sekawi, R. Rosli, DNA vaccine constructs against enterovirus 71 elicit immune response in mice, Genet. Vaccines Ther. 5 (2007) 6.
[24] C.-H. Chiu, C. Chu, C.-C. He, T.-Y. Lin, Protection of neonatal mice from lethal enterovirus 71 infection by maternal immunization with attenuated *Salmonella enterica serovar Typhimurium* expressing VP1 of enterovirus 71, Microbes Infect. 8 (2006) 1671–1678.

[25] Y.-C. Lin, C.-N. Wu, S.-R. Shih, M.-S. Ho, Characterization of a vero cell-adapted virulent strain of enterovirus 71 suitable for use as a vaccine candidate, Vaccine 20 (2002) 2485–2493.
[26] D.G.W. Foo, S. Alonso, V.T.K. Chow, C.L. Poh, Passive protection against lethal enterovirus 71 infection in newborn mice by neutralizing antibodies elicited by a synthetic peptide, Microbes Infect. 9 (2007) 1299–1306.
[27] S. Lu, Heterologous prime-boost vaccination, Curr. Opin. Immunol. 21 (2009) 346–351.
[28] Z. Wang, S.X. Wang, S.Y. Liu, Immunogenicities of env glycoproteins from circulating HIV-1 isolates in China focusing on the strategy of "DNA prime plus protein boost", Chin. Med. J. (Engl.) 122 (2009) 2339–2345.

Biochemical and Biophysical Research Communications 420 (2012) 762–767

Contents lists available at SciVerse ScienceDirect

Biochemical and Biophysical Research Communications

journal homepage: www.elsevier.com/locate/ybbrc

TNFα and IL-1β are mediated by both TLR4 and Nod1 pathways in the cultured HAPI cells stimulated by LPS

Wenwen Zheng [a,b,1], Xuexing Zheng [a,b,1], Shue Liu [b], Hongsheng Ouyang [a], Roy C. Levitt [b], Keith A. Candiotti [b], Shuanglin Hao [b,*]

[a] College of Animal Science and Veterinary Medicine, Jilin University, Changchun 130062, Jilin Province, PR China
[b] Department of Anesthesiology, University of Miami Miller School of Medicine, Miami, FL 33136, USA

ARTICLE INFO

Article history:
Received 6 March 2012
Available online 17 March 2012

Keywords:
Microglia
TLR4
JNK
Nod1
NF-κB
Cytokines

ABSTRACT

A growing body of evidence recently suggests that glial cell activation plays an important role in several neurodegenerative diseases and neuropathic pain. Microglia in the central nervous system express toll-like receptor 4 (TLR4) that is traditionally accepted as the primary receptor of lipopolysaccharide (LPS). LPS activates TLR4 signaling pathways to induce the production of proinflammatory molecules. In the present studies, we verified the LPS signaling pathways using cultured highly aggressively proliferating immortalized (HAPI) microglial cells. We found that HAPI cells treated with LPS upregulated the expression of TLR4, phospho-JNK (pJNK) and phospho-NF-κB (pNF-κB), TNFα and IL-1β. Silencing TLR4 with siRNA reduced the expression of pJNK, TNFα and IL-1β, but not pNF-κB in the cells. Inhibition of JNK with SP600125 (a JNK inhibitor) decreased the expression of TNFα and IL-1β. Unexpectedly, we found that inhibition of Nod1 with ML130 significantly reduced the expression of pNF-κB. Inhibition of NF-κB also reduced the expression of TNFα and IL-1β. Nod1 ligand, DAP induced the upregulation of pNF-κB which was blocked by Nod1 inhibitor. These data indicate that LPS-induced pJNK is TLR4-dependent, and that pNF-κB is Nod1-dependent in HAPI cells treated with LPS. Either TLR4–JNK or Nod1–NF-κB pathways is involved in the expression of TNFα and IL-1β.

© 2012 Elsevier Inc. All rights reserved.

1. Introduction

Microglia, one of the resident immune cells, are activated in most pathological conditions of the central nervous system (CNS) and participate in the regulation of innate and adaptive immune responses [1]. Prolonged activation of microglia can cause neuroinflammation due to increased production of proinflammatory mediators, eventually leading to neuronal death [2], which is a common characteristic found in several neurodegenerative diseases and neuropathic pain [3,4].

The bacterial lipopolysaccharide (LPS) is responsible for its toxic properties, as well as a core polysaccharide and O-specific polysaccharide [5]. LPS stimulation has long been considered the gold standard for glial activation. It mimics infection of Gram-negative bacteria leading to a view of microglia as neurotoxic and proinflammatory cells [1].

Toll-like receptors (TLRs) are membrane-bound pattern-recognition receptors that sense a variety of microbial-specific motifs to trigger an innate immune response [6,7]. TLR4 is traditionally accepted as the primary LPS receptor [7–11] and has been reported as critical for the glial response to LPS [12–14]. Upon stimulation with LPS, TLR4 initiates a series of signaling cascades that result in the activation of nuclear factor kappa B (NF-κB) and mitogen-activated protein kinases (MAPKs) [15] to induce the release of proinflammatory cytokines. However, evidence shows that several other receptors have also been involved in the LPS-induced effects [16,17], and that LPS-induced superoxide production in microglia is independent of TLR4 [13].

Nucleotide-binding and oligomerization domain (Nod)-like receptors (NLRs) are a family of intracellular sensors that have key roles in innate immunity and inflammation. The Nod1 receptor is demonstrated to confer responsiveness to LPS in 293T cells [17]. Inohara et al. demonstrates that Nod1 binds to ^{3}H-LPS and activates NF-κB in a TLR4-independent fashion [17]. These data raise the possibility that Nod1 may act as an intracellular receptor for invasive bacterial pathogens and LPS in microglial cells. In the present study, we investigated whether the TLR4 and Nod1 pathways are involved in the JNK or NF-κB-mediated expression of proinflammatory cytokines in rat microglial cells activated by LPS.

* Corresponding author. Address: Department of Anesthesiology, University of Miami Miller School of Medicine, 1550 NW 10th Avenue, Fox BLDG, Rm 304C, Miami, FL 33136, USA. Fax: +1 305 243 9160.
E-mail address: shao@med.miami.edu (S. Hao).
[1] Authors contributed equally to the paper.

0006-291X/$ - see front matter © 2012 Elsevier Inc. All rights reserved.
http://dx.doi.org/10.1016/j.bbrc.2012.03.068

2. Materials and methods

2.1. Cell culture

Highly aggressively proliferating immortalized (HAPI) microglial cells derived from the neonatal brain of rats [18], and grown in Dulbecco's Modified Eagle's Medium supplemented with 5% fetal bovine serum (Fisher, Pittsburgh, PA) at 37 °C in 5% CO2, as previously described [19]. HAPI cells were seeded into six-well plates at 2×10^5 cells/well 24 h before treatment with drugs. The cells were stimulated by 1 μg/ml of LPS or 0.5 μg/ml of Nod1 ligand, C12-iE-DAP (DAP) for 6 h.

2.2. Preparation and transfection of siRNA

TLR4 siRNA duplexes targeting rat TLR4 and mismatch RNA were synthesized by Invitrogen (Invitrogen, Camarillo, CA). TLR4 siRNA (forward 5′-GGAUCUUUCUUAUAACUAUdTdT-3′, reverse-5′-AUAGUUAUAAGAAAGAUCCdTdT-3′) and mismatch RNA (forward-5′-GCCCGUAGAACACGUCGUAdTdT-3′, reverse-5′-UACGACGUGUUCUACGGGCdTdT-3′) were used. Transient transfection procedures were performed according to Lipofectamine RNAiMAX reagent instructions (Invitrogen). Briefly, HAPI cells were incubated with 100 pmol of siRNA and 6 μl of Lipofectamine RNAiMAX complexes, in Opti-MEM I reduced serum medium (Invitrogen). Twenty-four hours after siRNA application, the cells were stimulated by 1 μg/ml of LPS from *Escherichia coli* (Sigma, St. Louis, MO). Six hours after LPS, the cells were harvested.

2.3. RT-PCR analysis

Total RNA was isolated from HAPI cells via TRIzol (Invitrogen), treated with RNase-free DNase-I (Roche), and re-purified, and then quantified spectrophotometrically. First strand cDNA was produced with omniscript reverse transcriptase (Qiagen), then amplified using following primer sets: TLR-4-forward (5′-GACTCCATTCAAGCCCAAGCC-3′) and TLR-4-reverse (5′-GCAGAGCCAACTGACCAAAGC-3′); TNFα-forward (5′-TGCCTCAGCCTCTTCTCATTCC-3′) and TNFα-reverse (5′-GGGCAGCCTTGTCCCTTGAA-3′); IL-1β -forward (5′-GACTTGGGCTGTCCAGATGAGA-3′) and IL-1β -reverse (5′-GGAGAATACCACTTGTTGGCTTA-3′). The level of β-actin was determined by its specific primers: β-actin-forward (5′-CAGTTCGCCATGGATGACGATATC-3′) and β-actin-reverse (5′-CACGCTCGGTCAGGATCTTCATG-3′) for β-actin. All reactions involved initial denaturation at 95 °C for 15 min followed by 30 cycles for TLR4, 27 cycles for TNFα and IL-1β, 24 cycles for β-actin (94 °C for 30 s, 58 °C for 30 s, 72 °C for 1 min) and 1 cycle 72 °C for 10 min using a DNA Engine PCR (Bio-Rad).

2.4. Western-blot analysis

HAPI cells were lysed using protein lysis buffer (150 mM sodium chloride, 1.0% NP-40, 0.5% sodium deoxycholate, 0.1% SDS, 50 mM Tris) containing protease inhibitors and phosphatase inhibitors (Phosphatase Inhibitor Cocktail 1 and 2). After centrifugation at 18,000g for 20 min, the supernatant was harvested as the total protein extract. Equal amounts of protein were separated by 4–12% Tris–glycine SDS–PAGE gel electrophoresis, and electrophoretically transferred to PVDF membrane. The membrane was then blocked and then incubated with primary antibodies overnight at 4 °C, including rabbit anti-pNF-κB (1:2000, Cell Signaling, Danvers, MA), mouse anti-NF-κB (1:2000, Millipore, Billerica, MA), mouse anti-pJNK (1:2000, Cell Signaling), rabbit anti-JNK (1:2000, Cell Signaling), rabbit anti-TNFα (1:1000, Millipore, Billerica, MA), rabbit anti-IL-1β (1:1000, Santa Cruz Biotechnology, Santa Cruz, CA), rabbit anti-TLR-4 (1:1000, Santa Cruz Biotechnology, Santa Cruz, CA), and mouse anti-β-actin (1:10000, Santa Cruz Biotechnology). The blots were incubated with a secondary antibody, developed in a chemiluminescence solution. Quantification of Western blots was done from the obtained chemiluminescence values (Bio-Rad ChemiDoc, Hercules, CA). Targeted protein bands were normalized using the amount of β-actin as a standard.

2.5. Drug treatments and data analysis

HAPI cells were pretreated for 1 h with 10 μM of SP600125 (an antagonist of JNK, Sigma), 100 μM of pyrrolidine dithiocarbamate (PDTC, an inhibitor of NF-κB, Sigma), or for 14 h with 30 μM of ML130 (a new inhibitor of Nod1, ID# BAS07162070, ASINEX USA, Winston Salem, NC) and then the cells were stimulated by 1 μg/ml of LPS in 5% FBS DMEM for 6 h. After further cultivation for 6 h, cells were harvested. LPS and PDTC were dissolved in saline; SP600125 and ML130 dissolved in DMSO. For Nod1 experiment, HAPI cells were pretreated for 14 h with 30 μM of ML130 and then the cells were stimulated by 500 ng/ml of DAP (Invivogen, San Diego, CA) for 6 h. DAP was dissolved in DMSO. Statistical significance of the difference between drug-treated and control cells was determined by *t* test. Data are expressed as mean ± sem, with *p*-value less than 0.05 considered significant.

3. Results

3.1. LPS induces phosphorylation of JNK and NF-κB to release TNFα and IL-1β in HAPI cells

In LPS-stimulated macrophage, proinflammatory cytokines are produced, and these effects are at least partially mediated through suppression of the MAPK and NF-κB signaling pathways [20]. We have reported that HAPI cells treated with LPS release TNFα [21]. Microglia are activated by LPS to produce proinflammatory factors through TLR4 [13]. Here, HAPI cells were treated with LPS, and collected for Western blots. We observed that LPS significantly induced the upregulation of TLR4, phosphorylation of JNK (pJNK), phosphorylation of NF-κB (pNF-κB), TNFα and IL-1β (Fig. 1A–E), but total JNK and NF-κB did not change in HAPI cells. In a similar set of experiments, HAPI cells were collected for RT-PCR. We found that LPS also induced upregulation of mRNA of TLR4, TNFα and IL-1β (Fig. 1F–I).

3.2. TLR4 knockdown with siRNA decreased pJNK, TNFα and IL-1β in HAPI cells treated with LPS

Several newly discovered families of non-coding RNAs include microRNA, siRNA, are involved in gene expression regulation [22]. Small interfering RNA plays a variety of roles in biology. The most notable role of siRNA is its involvement in the RNA interference, where it interferes with the expression of a specific gene. We silenced TLR4 gene expression with siRNA in HAPI cells, and found that siRNA of TLR4 significantly reduced the synthesis of TLR4 protein compared to mismatch RNA (mmRNA) (Fig. 2A). And, treatment with siRNA to TLR4 simultaneously decreased pJNK (Fig. 2B), and downregulated TNFα and IL-1β (Fig. 2D–E). Unexpectedly, TLR4 knockdown did not reversed upregulation of pNF-κB induced by LPS (Fig. 2C). TLR4 siRNA did not change total JNK and NF-κB. In a separate set of the studies, HAPI cells were collected for RT-PCR; TLR4 knockdown also suppressed the mRNA expression of TLR4, TNFα, and IL-1β (Fig. 2F–I). Thus, we think that JNK, TNFα, and IL-1β were downstream signals of TLR4 in HAPI cells stimulated by LPS.

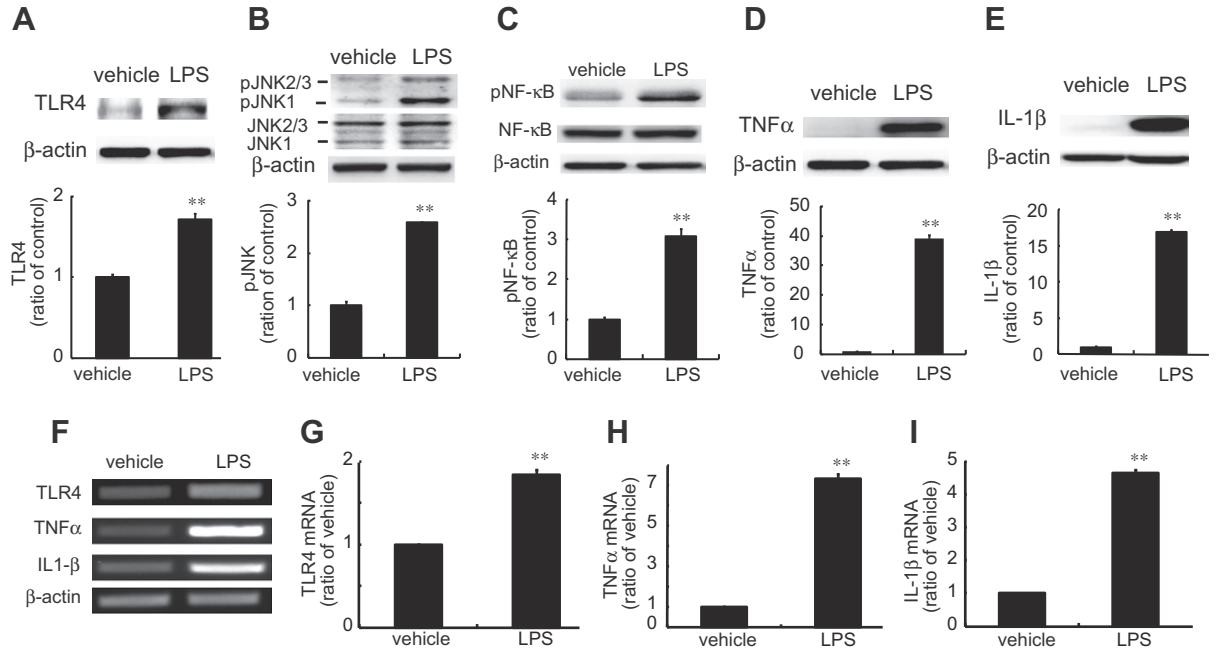


Fig. 1. The neurochemical effects of LPS on HAPI cells. The cultured HAPI cells were treated with LPS (1 μg/ml) for 6 h, and HAPI cells were collected for Western blots. LPS upregulated the expression of TLR4 (A), pJNK (B), pNF-κB (C), TNFα (D) and IL-1β (E), $^{**}p < 0.01$ *vs* vehicle, *t* test, $n = 3–4$. In a similar set of experiment, HAPI cells were collected for RT-PCR (F). LPS treatment increased the mRNA expression of TLR4 (G), TNFα (H), and IL-1β (I), $^{**}p < 0.01$ *vs* vehicle, *t* test, $n = 3–4$.

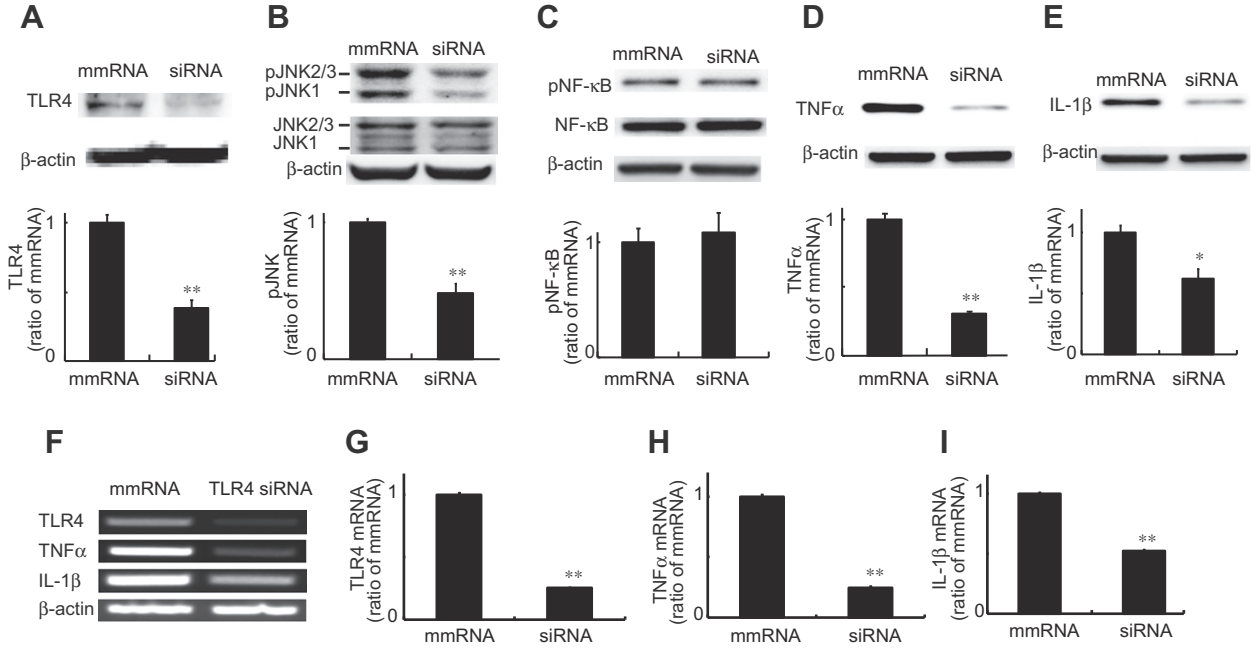


Fig. 2. The neurochemical effect of TLR4 knockdown with TLR4 siRNA on HAPI cells treated with LPS. Pretreatment with TLR4 siRNA, but not mismatch RNA (mmRNA) reversed the expression of TLR4 (A), pJNK (B), TNFα (D), and IL-1β (E), however, the treatment did not change pNF-κB (C) compared to mmRNA, $^{**}p < 0.01$ *vs* mmRNA, *t* test, $n = 3–4$. In a similar set of experiment, the effects of TLR4 knockdown on the expression of mRNA of TLR4, TNFα and IL-1β were carried out (F). TLR4 siRNA, but not mmRNA reversed the expression of mRNA of TLR4 (G), TNFα (H), and IL-1β (I), $^{**}p < 0.01$ *vs* mmRNA, *t* test, $n = 3–4$.

3.3. Inhibition of JNK reduced TNFα and IL-1β in HAPI cells treated with LPS

In traditional downstream signaling pathways of TLR4, the overexpression of many of proinflammatory cytokines is likely dependent on MAPK-dependent transcription factors [6]. Previous studies have shown that LPS activates glial cells releasing inflammatory cytokines through JNK [23]. To determine the involvement of JNK in the LPS-induced increase in cytokines, we gave SP600125 (a selective JNK inhibitor) to HAPI cells 1 h prior to LPS exposure. SP600125 significantly inhibited the expression of TNFα and IL-1β in the same samples (Fig. 3A and B). Thus, our data suggest that JNK is the upstream signal for TNFα and IL-1β. But SP600125 did not significantly change pNF-κB (data not shown),

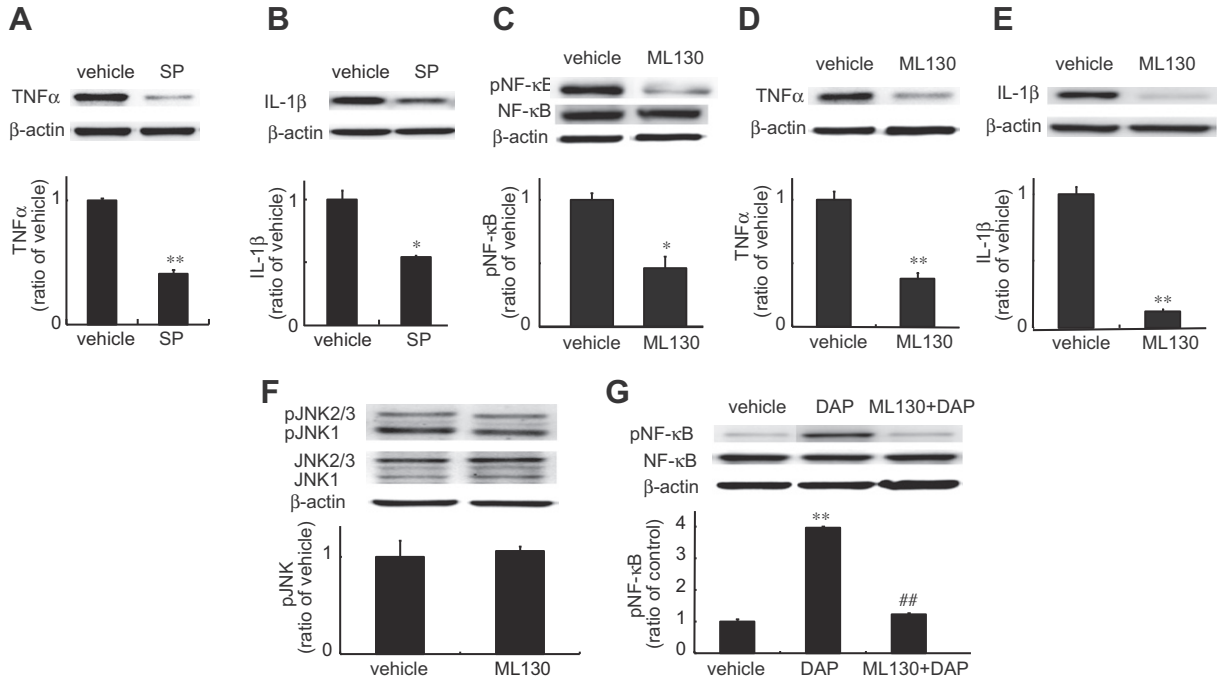


Fig. 3. The inhibition of JNK and Nod1 reduced the expression of TNFα and IL-1β in HAPI cells treated with LPS. HAPI cells were pretreated with SP600125 (SP, JNK inhibitor) for 1 h, then treated with LPS. SP600125 treatment reduced the expression of TNFα (A), and IL-1β (B), $^{**}p < 0.01$ *vs* vehicle, *t* test, $n = 3–4$. The effects of Nod1 on the pNF-κB in HAPI cells treated with LPS were examined (C–E). HAPI cells were treated with ML130 (a Nod1 inhibitor) for 14 h, followed by LPS. HAPI cells were collected, and pNF-κB was examined using Western blots. ML130 reduced the expression of pNF-κB (C). In the same sample, the expression of TNFα (D) and IL-1β (E) were suppressed by ML130. $^{*}p < 0.05$, $^{**}p < 0.01$ *vs* vehicle, *t* test, $n = 4$. However, ML130 did not affect the JNK (F). C12-iE-DAP (DAP, a Nod1 ligand) treated HAPI cells significantly induced upregulation of pNF-κB, which can be blocked by ML130 (G). $^{**}p < 0.01$ *vs* vehicle, $^{\#\#}p < 0.01$ *vs* DAP, *t* test, $n = 3–4$.

so we believe that JNK activation does not regulate pNF-κB. Overall these results underscored the important role of JNK in regulating the expression of proinflammatory genes after LPS.

3.4. Inhibition of Nod1 reduced NF-κB induced by LPS

Recently, Nod1-like receptor has been identified as key mediator of inflammatory and immune responses [17]. Upon activation, Nod1 initiates a proinflammatory response largely dependent on NF-κB activation [24,25], which might be important in HAPI cells treated with LPS. To understand whether Nod1 was involved in the expression of NF-κB, we treated HAPI cells with ML130 (a selective Nod1 inhibitor) 14 h prior to exposure of LPS. Unexpectedly, we found that ML130 significantly inhibited the expression of pNF-κB (Fig. 3C). Meanwhile, ML130 markedly decreased the expression of TNFα and IL-1β (Fig. 3D and E) either. But ML130 did not change pJNK in HAPI cells (Fig. 3F). We further treated HAPI cells with Nod1 ligand, DAP, and found that DAP significantly upregulated the expression of pNF-κB which was blocked by ML130 (Fig. 3G). These results indicated that pNF-κB was dependent on Nod1 in HAPI cells activated by LPS.

3.5. Inhibition of NF-κB reduced TNFα and IL-1β induced by LPS

It has been reported that LPS induced cellular inflammatory factors through NF-κB-target inflammatory genes in macrophages [26]. To understand whether NF-κB was involved in the expression of TNFα and IL-1β, we treated HAPI cells with PDTC (a selective NF-κB inhibitor) 1 h before LPS exposure. PDTC significantly inhibited the expression of TNFα and IL-1β in protein levels (Fig. 4A and B). In a separate set of studies, we found that PDTC reduced the mRNA expression of TNFα and IL-1β (Fig. 4C–E). These results indicated that pNF-κB was also an upstream signaling of both TNFα and IL-1β in HAPI cells activated by LPS.

4. Discussion

The current study showed (1) that HAPI cells treated with LPS, induced pJNK and pNF-κB, and released TNFα and IL-1β, (2) that pJNK induced by LPS was TLR4-dependent, and (3) that, unexpectedly, pNF-κB induced by LPS, is dependent on Nod1, but not TLR4, (4) that both JNK and NF-κB mediated the expression of TNFα and IL-1β.

Microglial cells are the main source of proinflammatory cytokines within the CNS [27]. Increased cytokines in the CNS have been observed especially after injury or ischemia, in bacterial and viral infections (e.g., HIV), as well as in multiple sclerosis and Alzheimer's disease; harmful outcomes of increased TNFα relate to its activity to promote inflammation and edema [28]. Microglial cytokines also seems to be critical in boosting chemokine-induced glutamate release from astrocytes [28].

TLRs signal via a common pathway leads to the expression of diverse inflammatory genes [6,7,29]. TLRs are expressed in various cell types in the CNS, including microglia, astrocytes, neurons, and cerebral vascular cells [30]. It has recently been discovered that TLR4 is capable of activation by endogenous 'danger signal' molecules released following cellular injury. Recent evidence supports that TLR4 is involved in neurodegenerative diseases [31].

TLR4 is traditionally accepted as the primary LPS receptor. LPS induced early activation of the transcription factor NF-κB and expression of TNFα in cultured astrocytes through TLR4; MAPKs (e.g., JNK) were also involved in TLR4-cytokine signaling [32]. LPS activates several intracellular signaling pathways in human monocytes that include NF-κB and MAPKs pathways. These signaling pathways in turn activate a variety of transcription factors that

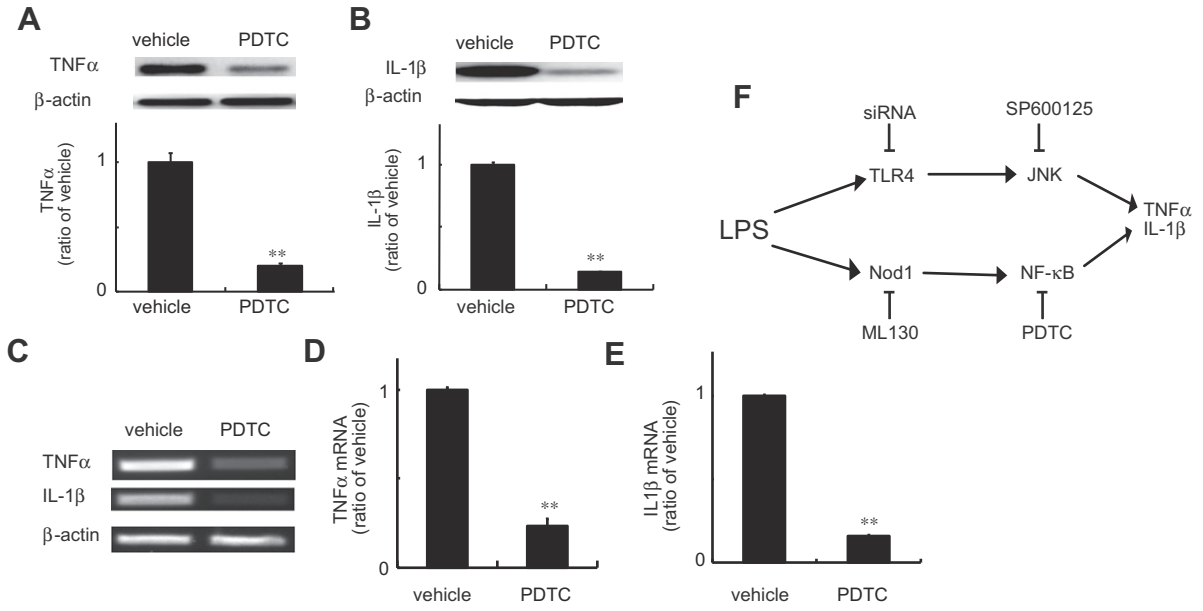


Fig. 4. The inhibition of NF-κB on HAPI cells treated with LPS. HAPI cells were treated with PDTC (a NF-κB inhibitor, 100 μM) for 1 h, followed by LPS. HAPI cells were collected and protein of TNFα (A) and IL-1β (B) was examined using Western blots. PDTC decreased the expression of TNFα and IL-1β. $^{**}p < 0.01$ *vs* vehicle, *t* test, $n = 3–4$. In a similar set of experiment, the inhibition of NF-κB on mRNA expression of TNFα and IL-1β on HAPI cells treated with LPS was examined (C–E). HAPI cells were collected and mRNA of TNFα (D) and IL-1β (E) was examined using RT-PCR. PDTC reduced the mRNA expression of TNFα and IL-1β. $^{**}p < 0.01$ *vs* vehicle, *t* test, $n = 3–4$. Schematic description of LPS signaling pathways (F). LPS binds to the TLR4 on the membrane of HAPI cells to activate pJNK to induce the release of TNFα and IL-1β. LPS can be internalized through an as yet unknown mechanism, and may bind to intracellular Nod1 and result in activation of NF-κB, and finally, induces the expression of TNFα/IL-1β in HAPI cells.

include NF-κB (p50/p65) and AP-1, which coordinate the induction of many genes encoding inflammatory mediators [33]. In the current studies, silencing TLR4 with siRNA reduced pJNK, TNFα and IL-1β induced by LPS, and inhibition of JNK reversed the release of TNFα and IL-1β. Thus, we think that LPS induced the release of TNFα and IL-1β through TLR4–JNK pathway, which is in line with previous report [32,33].

NF-κB is usually sequestered in the cytoplasm in an inactive form by molecules of the inhibitor of NF-κB family. Activation of NF-κB involves the phosphorylation and proteolysis of the IκB proteins and the concomitant release and nuclear translocation of the NF-κB factors [34]. LPS/TLR4 signaling can activate NF-κB by MyD88-dependent and MyD88-independent pathways, which mediate the activation of proinflammatory cytokine (see review [15]). However, studies shows other receptors may be involved in the LPS-induced effect either [16,17]. Certain LPS preparations exert TLR4-independent effects [35]. LPS-induced superoxide production in microglia is independent of TLR4 [13].

Nod1 plays a key role in innate immunity as a sensor of specific microbial components derived from bacterial peptidoglycans and induction of inflammatory responses [36,37]. Nod1 polymorphisms are associated with several human inflammatory disorders [38,39]. Recently, Nod1 has additionally been implicated in neuroinflammatory processes involved in the progression of multiple sclerosis [40]. Mutations in Nod proteins have been associated with various inflammatory diseases that affect NF-κB activity [36,37]. Inohara et al. demonstrated that Nod1 binds to LPS and activates NF-κB in a TLR4-independent fashion in HEK293T cells [17]. LPS can be internalized through an as yet unknown mechanism, and may bind to intracellular Nod1 and result in activation of NF-κB [41]. In the present studies, TLR4 knockdown did not reduce pNF-κB, which raises the possibility that Nod1 may act as a receptor for LPS. Nod1 inhibitor ML130 significantly reversed the pNF-κB and expression of TNFα and IL-1β induced by LPS in HAPI cells; Nod1 ligand induced pNF-κB. Inhibition of NF-κB decreased the expression of TNFα and IL-1β. Thus, we think that Nod1–NF-κB pathway may be involved in the production of cytokines in HAPI cells.

In summary, LPS is a common inflammagen to activate glia in animal models of inflammation-mediated neurodegeneration [42,43]. The current studies demonstrated that LPS activated cultured microglia to release proinflammatory cytokines through both TLR4–JNK and Nod1–NF-κB pathways. Our findings provide novel insights into the mechanisms by which microglia release proinflammatory cytokines.

Acknowledgments

Supported by NIH DA26734 (S.H.), DA25527 (S.H.), and NS66792 (S.H.), Department of Anesthesiology, University of Miami (S.H.), China Scholarship Council (X.Z.), Jilin University, China (W.Z.). HAPI cells were kindly provided by Drs. David Fink and Marina Mata (Neurology, University of Michigan). We acknowledge the support from Dr. David Lubarsky (Chair of Anesthesiology, University of Miami, FL).

References

[1] U.K. Hanisch, H. Kettenmann, Microglia: active sensor and versatile effector cells in the normal and pathologic brain, Nat. Neurosci. 10 (2007) 1387–1394.
[2] L.E. Rojo, J.A. Fernandez, A.A. Maccioni, J.M. Jimenez, R.B. Maccioni, Neuroinflammation: implications for the pathogenesis and molecular diagnosis of Alzheimer's disease, Arch. Med. Res. 39 (2008) 1–16.
[3] P.D. Drew, P.D. Storer, J. Xu, J.A. Chavis, Hormone regulation of microglial cell activation: relevance to multiple sclerosis, Brain Res. Rev. 48 (2005) 322–327.
[4] E.D. Milligan, L.R. Watkins, Pathological and protective roles of glia in chronic pain, Nat. Rev. Neurosci. 10 (2009) 23–36.
[5] H. Sasaki, S.H. White, Aggregation behavior of an ultra-pure lipopolysaccharide that stimulates TLR-4 receptors, Biophys. J. 95 (2008) 986–993.
[6] T. Kawai, S. Akira, TLR signaling, Semin. Immunol. 19 (2007) 24–32.
[7] T. Kawai, S. Akira, Pathogen recognition with Toll-like receptors, Curr. Opin. Immunol. 17 (2005) 338–344.
[8] K. Hoshino, O. Takeuchi, T. Kawai, H. Sanjo, T. Ogawa, Y. Takeda, K. Takeda, S. Akira, Cutting edge: Toll-like receptor 4 (TLR4)-deficient mice are hyporesponsive to lipopolysaccharide: evidence for TLR4 as the Lps gene product, J. Immunol. 162 (1999) 3749–3752.

[9] C.A. Byrd-Leifer, E.F. Block, K. Takeda, S. Akira, A. Ding, The role of MyD88 and TLR4 in the LPS-mimetic activity of Taxol, Eur. J. Immunol. 31 (2001) 2448–2457.
[10] A. Poltorak, I. Smirnova, X. He, M.Y. Liu, C. Van Huffel, O. McNally, D. Birdwell, E. Alejos, M. Silva, X. Du, P. Thompson, E.K. Chan, J. Ledesma, B. Roe, S. Clifton, S.N. Vogel, B. Beutler, Genetic and physical mapping of the Lps locus: identification of the toll-4 receptor as a candidate gene in the critical region, Blood Cells Mol. Dis. 24 (1998) 340–355.
[11] A. Poltorak, X. He, I. Smirnova, M.Y. Liu, C. Van Huffel, X. Du, D. Birdwell, E. Alejos, M. Silva, C. Galanos, M. Freudenberg, P. Ricciardi-Castagnoli, B. Layton, B. Beutler, Defective LPS signaling in C3H/HeJ and C57BL/10ScCr mice: mutations in Tlr4 gene, Science 282 (1998) 2085–2088.
[12] S. Lehnardt, L. Massillon, P. Follett, F.E. Jensen, R. Ratan, P.A. Rosenberg, J.J. Volpe, T. Vartanian, Activation of innate immunity in the CNS triggers neurodegeneration through a Toll-like receptor 4-dependent pathway, Proc. Natl. Acad. Sci. USA 100 (2003) 8514–8519.
[13] L. Qin, G. Li, X. Qian, Y. Liu, X. Wu, B. Liu, J.S. Hong, M.L. Block, Interactive role of the toll-like receptor 4 and reactive oxygen species in LPS-induced microglia activation, Glia 52 (2005) 78–84.
[14] O. Saito, C.I. Svensson, M.W. Buczynski, K. Wegner, X.Y. Hua, S. Codeluppi, R.H. Schaloske, R.A. Deems, E.A. Dennis, T.L. Yaksh, Spinal glial TLR4-mediated nociception and production of prostaglandin E(2) and TNF, Br. J. Pharmacol. 160 (2010) 1754–1764.
[15] Y.C. Lu, W.C. Yeh, P.S. Ohashi, LPS/TLR4 signal transduction pathway, Cytokine 42 (2008) 145–151.
[16] K. Triantafilou, M. Triantafilou, R.L. Dedrick, A CD14-independent LPS receptor cluster, Nat. Immunol. 2 (2001) 338–345.
[17] N. Inohara, Y. Ogura, F.F. Chen, A. Muto, G. Nunez, Human Nod1 confers responsiveness to bacterial lipopolysaccharides, J. Biol. Chem. 276 (2001) 2551–2554.
[18] P. Cheepsunthorn, L. Radov, S. Menzies, J. Reid, J.R. Connor, Characterization of a novel brain-derived microglial cell line isolated from neonatal rat brain, Glia 35 (2001) 53–62.
[19] Z. Zhou, X. Peng, J. Hagshenas, R. Insolera, D.J. Fink, M. Mata, A novel cell-cell signaling by microglial transmembrane TNFalpha with implications for neuropathic pain, Pain 151 (2010) 296–306.
[20] J.X. Wang, L.F. Hou, Y. Yang, W. Tang, Y. Li, J.P. Zuo, SM905, an artemisinin derivative, inhibited NO and pro-inflammatory cytokine production by suppressing MAPK and NF-kappaB pathways in RAW 264.7 macrophages, Acta Pharmacol. Sin. 30 (2009) 1428–1435.
[21] Z. Zhou, X. Peng, S. Hao, D.J. Fink, M. Mata, HSV-mediated transfer of interleukin-10 reduces inflammatory pain through modulation of membrane tumor necrosis factor alpha in spinal cord microglia, Gene Ther. 15 (2008) 183–190.
[22] P.D. Zamore, B. Haley, Ribo-gnome: the big world of small RNAs, Science 309 (2005) 1519–1524.
[23] R. Pangestuti, S.S. Bak, S.K. Kim, Attenuation of pro-inflammatory mediators in LPS-stimulated BV2 microglia by chitooligosaccharides via the MAPK signaling pathway, Int. J. Biol. Macromol. 49 (2011) 599–606.
[24] S.E. Girardin, R. Tournebize, M. Mavris, A.L. Page, X. Li, G.R. Stark, J. Bertin, P.S. DiStefano, M. Yaniv, P.J. Sansonetti, D.J. Philpott, CARD4/Nod1 mediates NF-kappaB and JNK activation by invasive *Shigella flexneri*, EMBO Rep. 2 (2001) 736–742.
[25] S.E. Girardin, I.G. Boneca, L.A. Carneiro, A. Antignac, M. Jehanno, J. Viala, K. Tedin, M.K. Taha, A. Labigne, U. Zahringer, A.J. Coyle, P.S. DiStefano, J. Bertin, P.J. Sansonetti, D.J. Philpott, Nod1 detects a unique muropeptide from Gram-negative bacterial peptidoglycan, Science 300 (2003) 1584–1587.
[26] E. Roh, H.S. Lee, J.A. Kwak, J.T. Hong, S.Y. Nam, S.H. Jung, J.Y. Lee, N.D. Kim, S.B. Han, Y. Kim, MD-2 as the target of nonlipid chalcone in the inhibition of endotoxin LPS-induced TLR4 activity, J. Infect. Dis. 203 (2011) 1012–1020.
[27] F. Correa, M. Hernangomez, L. Mestre, F. Loria, A. Spagnolo, F. Docagne, V. Di Marzo, C. Guaza, Anandamide enhances IL-10 production in activated microglia by targeting CB(2) receptors: roles of ERK1/2, JNK, and NF-kappaB, Glia 58 (2010) 135–147.
[28] U.K. Hanisch, Microglia as a source and target of cytokines, Glia 40 (2002) 140–155.
[29] M.A. Nahid, M. Satoh, E.K. Chan, MicroRNA in TLR signaling and endotoxin tolerance, Cell. Mol. Immunol. 8 (2011) 388–403.
[30] Y. Kong, Y. Le, Toll-like receptors in inflammation of the central nervous system, Int. Immunopharmacol. 11 (2011) 1407–1414.
[31] J.M. van Noort, M. Bsibsi, Toll-like receptors in the CNS: implications for neurodegeneration and repair, Prog. Brain Res. 175 (2009) 139–148.
[32] R. Gorina, M. Font-Nieves, L. Marquez-Kisinousky, T. Santalucia, A.M. Planas, Astrocyte TLR4 activation induces a proinflammatory environment through the interplay between MyD88-dependent NFkappaB signaling, MAPK, and Jak1/Stat1 pathways, Glia 59 (2011) 242–255.
[33] M. Guha, N. Mackman, LPS induction of gene expression in human monocytes, Cell Signal. 13 (2001) 85–94.
[34] S. Akira, K. Takeda, Toll-like receptor signalling, Nat. Rev. Immunol. 4 (2004) 499–511.
[35] R.B. Yang, M.R. Mark, A. Gray, A. Huang, M.H. Xie, M. Zhang, A. Goddard, W.I. Wood, A.L. Gurney, P.J. Godowski, Toll-like receptor-2 mediates lipopolysaccharide-induced cellular signalling, Nature 395 (1998) 284–288.
[36] P.M. Khan, R.G. Correa, D.B. Divlianska, S. Peddibhotla, E.H. Sessions, G. Magnuson, B. Brown, E. Suyama, H. Yuan, A. Mangravita-Novo, M. Vicchiarelli, Y. Su, S. Vasile, L.H. Smith, P.W. Diaz, J.C. Reed, G.P. Roth, Identification of Inhibitors of NOD1-Induced Nuclear Factor-kappaB Activation, ACS Med. Chem. Lett. 2 (2011) 780–785.
[37] R.G. Correa, P.M. Khan, N. Askari, D. Zhai, M. Gerlic, B. Brown, G. Magnuson, R. Spreafico, S. Albani, E. Sergienko, P.W. Diaz, G.P. Roth, J.C. Reed, Discovery and characterization of 2-aminobenzimidazole derivatives as selective NOD1 inhibitors, Chem. Biol. 18 (2011) 825–832.
[38] I. Tattoli, L.H. Travassos, L.A. Carneiro, J.G. Magalhaes, S.E. Girardin, The Nodosome: Nod1 and Nod2 control bacterial infections and inflammation, Semin. Immunopathol. 29 (2007) 289–301.
[39] L.A. Carneiro, J.G. Magalhaes, I. Tattoli, D.J. Philpott, L.H. Travassos, Nod-like proteins in inflammation and disease, J. Pathol. 214 (2008) 136–148.
[40] P.J. Shaw, M.J. Barr, J.R. Lukens, M.A. McGargill, H. Chi, T.W. Mak, T.D. Kanneganti, Signaling via the RIP2 adaptor protein in central nervous system-infiltrating dendritic cells promotes inflammation and autoimmunity, Immunity 34 (2011) 75–84.
[41] M.A. Dobrovolskaia, S.N. Vogel, Toll receptors, CD14, and macrophage activation and deactivation by LPS, Microbes Infect. 4 (2002) 903–914.
[42] H.M. Gao, J. Jiang, B. Wilson, W. Zhang, J.S. Hong, B. Liu, Microglial activation-mediated delayed and progressive degeneration of rat nigral dopaminergic neurons: relevance to Parkinson's disease, J. Neurochem. 81 (2002) 1285–1297.
[43] H.M. Gao, F. Zhang, H. Zhou, W. Kam, B. Wilson, J.S. Hong, Neuroinflammation and alpha-synuclein dysfunction potentiate each other, driving chronic progression of neurodegeneration in a mouse model of Parkinson's disease, Environ. Health Perspect. 119 (2011) 807–814.

Biochemical and Biophysical Research Communications 420 (2012) 768–774

Contents lists available at SciVerse ScienceDirect

Biochemical and Biophysical Research Communications

journal homepage: www.elsevier.com/locate/ybbrc

Stress granules contribute to α-globin homeostasis in differentiating erythroid cells

Laura Ghisolfi [a,1,2], Shilpee Dutt [b,1,3], Marie E. McConkey [b], Benjamin L. Ebert [b], Paul Anderson [a,*]

[a] Division of Rheumatology, Immunology and Allergy, Brigham and Women's Hospital, Harvard Medical School, One Jimmy Fund Way, Smith 652, Boston, MA 02115, USA
[b] Division of Hematology, Brigham and Women's Hospital, Harvard Medical School, 1 Blackfan Circle, Room 5211, Boston, MA 02115, USA

ARTICLE INFO

Article history:
Received 13 March 2012
Available online 20 March 2012

Keywords:
Erythroid cell
Stress granule
HRI/eIF2α
G3BP
α-Globin

ABSTRACT

Hemoglobin is the major biosynthetic product of developing erythroid cells. Assembly of hemoglobin requires the balanced production of globin proteins and the oxygen-carrying heme moiety. The heme-regulated inhibitor kinase (HRI) participates in this process by phosphorylating eIF2α and inhibiting the translation of globin proteins when levels of free heme are limiting. HRI is also activated in erythroid cells subjected to oxidative stress. Phospho-eIF2α-mediated translational repression induces the assembly of stress granules (SG), cytoplasmic foci that harbor untranslated mRNAs and promote the survival of cells subjected to adverse environmental conditions. We have found that differentiating erythroid, but not myelomonocytic or megakaryocytic, murine and human progenitor cells assemble SGs, *in vitro* and *in vivo*. Targeted knockdown of HRI or G3BP, a protein required for SG assembly, inhibits spontaneous and arsenite-induced assembly of SGs in erythroid progenitor cells. This is accompanied by reduced α-globin production and increased apoptosis suggesting that G3BP+ SGs facilitate the survival of developing erythroid cells.

© 2012 Elsevier Inc. All rights reserved.

1. Introduction

Globin proteins are synthesized throughout erythroid cell maturation. The translation of globin proteins is coordinated with the synthesis of heme moieties to ensure the efficient assembly of hemoglobin. This process requires the heme-regulated inhibitor (*HRI*), a kinase that phosphorylates eIF2α to inhibit the translation of globin proteins when intracellular free heme is limiting [1]. Dysregulation of this process leads to apoptotic cell death and anemia [1,2].

Sodium arsenite (SA), a pharmacological activator of HRI, induces the phosphorylation of eIF2α and the assembly of stress granules (SGs) [3]. SGs are discrete cytoplasmic foci at which untranslated mRNAs accumulate in a dynamic process that modulates the degradation, storage and translational re-initiation of mRNA to help re-program protein expression in cells exposed to adverse environmental conditions [4]. The assembly of SGs enhances the survival of stressed cells by poorly characterized mechanisms [4].

In addition to untranslated mRNAs, SGs harbor small, but not large, ribosomal subunits as well as an eclectic collection of translation factors, RNA binding proteins, and signaling molecules. The Ras GAP SH3 domain-binding protein (G3BP) is an essential component of stress granules whose overexpression nucleates SG assembly and whose knockdown inhibits SG assembly [5]. G3BP is a multifunctional RNA-binding protein [6], that has been implicated in various aspects of cell survival and proliferation [7,8].

Based on the known importance of translational control mechanisms in erythroid cell physiology, we investigated the role of cytoplasmic SGs in the regulation of α-globin mRNA stability and protein synthesis. We found that a subset of CD34+ murine and human bone marrow cells in the erythroid (but not myeloid or megakaryocytic) lineage assemble SGs. Lentivirus-delivered shRNAs targeting HRI or G3BP inhibit both spontaneous and arsenite-induced SG assembly, suggesting that formation of spontaneous SGs is HRI dependent. Inhibition of SGs through G3BP knockdown also reduces α-globin mRNA and protein levels as well as CD34+ cell viability. Our data provide evidence that G3BP and SGs promote α-globin transcript stability and survival of cells in the erythroid lineage.

2. Materials and methods

2.1. Cell culture and drug treatment

Primary normal human bone marrow CD34+ cells were cultured in a two-phase liquid culture system [9]. To screen for lineage specificity of SG formation, cells were cultured in media containing cytokines supporting erythroid, myeloid and megakaryocytic

* Corresponding author. Fax: +1 617 525 1310.
E-mail address: panderson@rics.bwh.harvard.edu (P. Anderson).
[1] These authors contributed equally to this work.
[2] Current address: Department of Gastroenterology, Beth Israel Deaconess Medical Center, Harvard Medical School, 330 Brookline Ave., Dana 534, Boston, MA 02215, USA.
[3] Current address: Tata Memorial Centre/ACTREC, Navi Mumbai 410210, India.

0006-291X/$ - see front matter © 2012 Elsevier Inc. All rights reserved.
http://dx.doi.org/10.1016/j.bbrc.2012.03.070

differentiation [10]. To support erythroid differentiation, 100 ng ml^{-1} stem cell factor, 10 ng ml^{-1} interleukin-3, 10 ng ml^{-1} interleukin-6 and 0.5 U ml^{-1} erythropoietin were added to Serum-Free Expansion Medium (Stem Cell Technologies). The concentration of erythropoietin was increased to 3 U ml^{-1} on day 7. To support megakaryocytic and granulocytic differentiation, 50 ng ml^{-1} thrombopoietin, 15 ng ml^{-1} granulocyte colony-stimulating factor (Neupogen) and 40 ng ml^{-1} FLT-3 ligand were added. In all other experiments, cells were cultured with cytokines supporting erythroid and myeloid differentiation (cytokine combination listed above, without thrombopoietin).

CD34+ cell samples for Western blot analysis of p-eIF2α/eIF2α or α-globin were cultured in media supporting erythroid differentiation.

To induce SGs, CD34+ cells were treated with SA (0.5 mM final concentration) for 45 min. To inhibit polysome disassembly, CD34+ cells were treated with 20 μM emetine alone for 60 min prior to culture in the absence or presence of SA for 45 min.

2.2. Antibodies

All antibodies used in this study are listed in Supplementary material, Table S1.

2.3. Lentiviral vectors and infection and knockdown effects

Primary CD34+ cells were infected with shRNA lentiviruses targeting non-overlapping regions in the 3′-UTR of HRI or G3BP mRNAs [9]. Four days after infection, cells were collected for further assays. Lentiviral shRNA target sequences for HRI or G3BP silencing are listed in Table S1.

Knockdown efficiencies were verified by real-time quantitative PCR following reverse transcription (RT-qPCR). Effects of HRI or G3BP silencing on p-eIF2α/eIF2α or α-globin expression were evaluated by Western blot on cells collected 4 days after lentivirus infection. Knockdown effects on SGs were assessed by quantifying the percentage of cells with SGs (>100 cells from different fields).

2.4. Cytospin

Bone marrow-derived CD34+ cells (>0.5 × 10^5) were collected, washed twice in cold PBS, resuspended in 200 μl of 4% paraformaldehyde, rocked at room temperature for 10 min, resuspended in 100 μl PBS and then cytospun onto round (12 mm) coverslips at 700 rpm for 4 min. Air-dried coverslips were placed in a 24-well plate and processed for immunofluorescence microscopy. For hematopoietic lineage detection, CD34+ were incubated for 60 min tumbling at 4 °C with the specific florochrome-labeled antibodies (listed in Table S1) in blocking solution, followed by 3 washings in PBS of 5 min each, and fixed with 4% paraformaldehyde before cytospin.

2.5. Whole murine and human bone marrow experiments

Total bone marrow cells from 6 month old wild type Balb/c male mice were harvested, washed twice in cold PBS and then processed for immunofluorescence with anti-mouse lineage specific florochrome-labeled antibodies (listed in Table S1) as described above.

Unprocessed human bone marrow from healthy donor patient (Lonza Walkersville, Inc.), containing 22.8 × 10^6 cells/ml, $V \geqslant 10$ ml, was delivered fresh at 4 °C and aliquoted in vials containing 2 × 10^6 cells/ml. Hematopoietic lineage marker staining and SGs detection was performed as described above.

2.6. Immunofluorescent microscopy

General immunofluorescence procedures were performed on cytospun CD34+ cells, mouse or human bone marrow cells, as described previously [11]. Images were captured by a Nikon Eclipse 800 microscope with CCD-SPOT RT digital camera (Diagnostic Instruments), using 100× magnification objective. The images were compiled with Adobe Photoshop CS3 (v.10.0.1) (Adobe Systems).

2.7. Western blot

Western blot assays on human hematopoietic CD34+ cell samples were performed under standard conditions as previously described [12], using antibodies listed in Table S1. Protein concentrations were determined using the Micro BCA Protein Assay (Fisher Scientific). Protein band densities were quantified using Image J software.

2.8. Flow cytometry

Primary human bone marrow CD34+ cells were infected with lentiviruses expressing shRNAs [9], selected with puromycin the following day and analyzed for hematopoietic differentiation by flow cytometry on day 7 of culture. Flow cytometry was performed using antibodies against antigens expressed on erythroid cells, glycophorin A (GlyA– FITC-conjugated antibody) and CD71 – PECy5-conjugated antibody (both BD Biosciences). Live/dead cell absolute numbers and apoptosis were assessed by flow cytometry on day 7 in culture using phycoerythrin labeled annexin V antibody (BD Pharmingen). Flow cytometry was performed on a FACS Calibur cytometer (BD Biosciences) and data was analyzed using FlowJo software (Tree star).

2.9. Statistics

Statistical significance was determined by two tailed Student's *t*-test. $^*P < 0.05$, $^{**}P < 0.005$, $^{***}P < 0.001$.

3. Results

Normal erythrocyte differentiation requires the balanced production of the hemoglobin precursors globin and heme. The translation of globin transcripts is controlled by HRI, an eIF2α kinase that is activated when heme concentrations are low. We hypothesized that HRI kinase would be activated during erythroid differentiation, and that phosphorylation of eIF2α would trigger SG assembly. First we investigated whether hematopoietic cells are capable of forming SGs under stress conditions. We used immunofluorescence microscopy to visualize SGs in normal bone marrow-derived CD34+ hematopoietic progenitor cells cultured in media containing cytokines supporting erythroid, myeloid and megakaryocytic differentiation [10]. After 4 days of normal differentiation, cells were cultured in the presence or absence of SA (SA, 500 μM) for 45 min, and stained using antibodies reactive with SGs (eIF3b, TIA-1, phospho-eIF2α and eIF4E) or processing bodies (PBs) (S6K1/Hedls and eIF4E) (Fig. 1). PBs are cytoplasmic mRNP aggregates that are distinct from, but dynamically linked to, SGs [4]. PBs are constitutive components of cycling cells, and are thought to play a role in mRNA degradation. Dynamic interactions between SGs and PBs suggest that mRNA may be transferred from SGs to PBs for decay [13]. We found that Hedls+ PBs are prominent components of unstressed CD34+ progenitor cells (Fig. 1, upper panels: red). Unexpectedly, small TIA-1+ SGs were also observed in the cytoplasm of these cells (Fig. 1C: green). When these cells are subjected to SA-induced

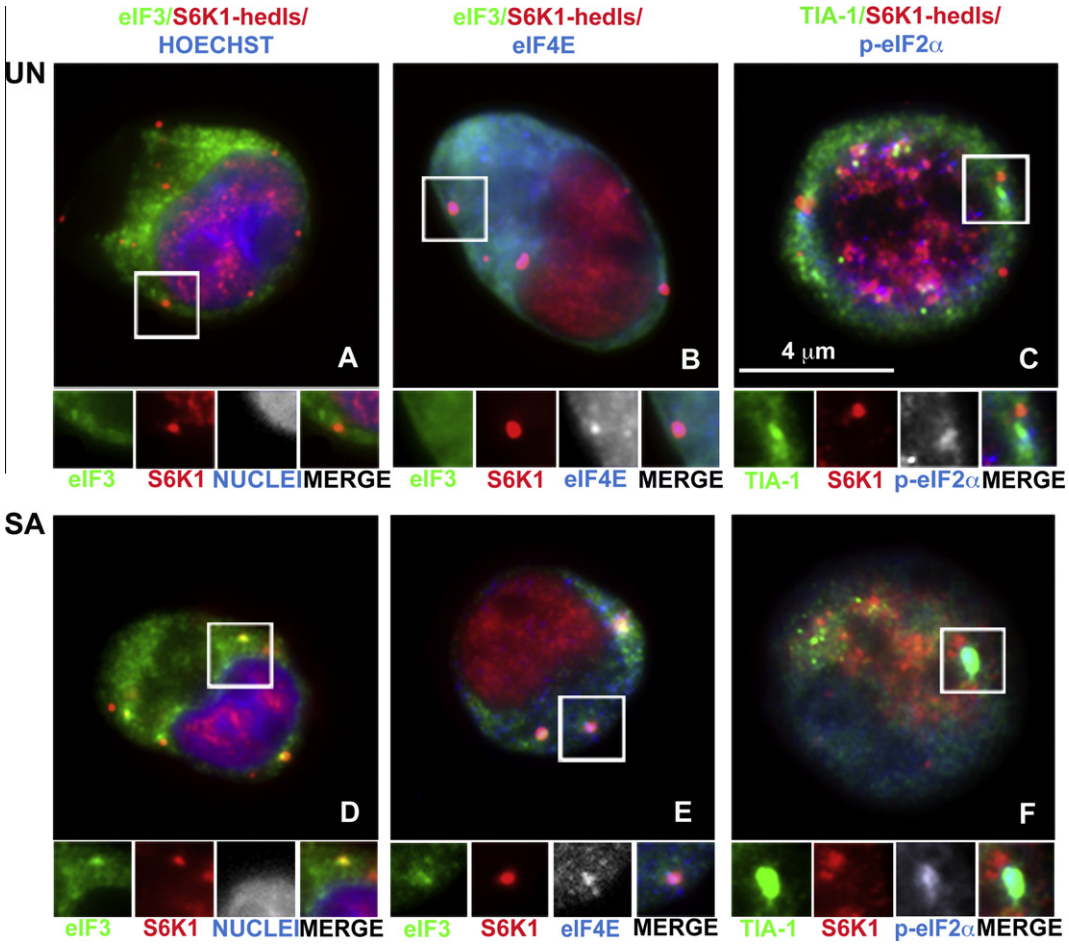


Fig. 1. Human bone marrow-derived CD34+ hematopoietic cells assemble cytoplasmic SGs and PBs. CD34+ cells, collected at day 4 of *in vitro* differentiation, were cultured in the absence (UN; A–C) or presence (SA; D–F) of SA for 45 min. Samples were stained for SG markers (eIF3b, green; TIA-1, green; p-eIF2α, blue), a PB specific marker (S6K1–Hedls, red) or SG/PB marker (eIF4E, blue). Cells were counterstained with Hoechst (A and D) to reveal nuclei. Enlarged views (1.8-fold) of boxed areas show separate channels and merged views.

oxidative stress (Fig. 1D–F), large TIA-1+ SGs and Hedls+ PBs were sometimes found in close physical apposition (Fig. 1F). In addition, granules containing both SG and PB markers were commonly observed (Fig. 1D and E: insets) suggesting that SGs and PBs can fuse together in these cells. These findings indicate that SGs assemble in differentiating primary human hematopoietic progenitor cells in the absence of exogenous stress.

To confirm that these cytoplasmic granules are indeed SGs, we treated differentiating hematopoietic cells with emetine (Fig. S1), a drug that freezes ribosomes onto polysomes and promotes SG disassembly [13]. In CD34+ cells treated with emetine (20 μM) for 120 min, both spontaneous (upper panel) and SA-induced (lower panel) SGs were disassembled. This result indicates that untranslated mRNAs found in these granules are in equilibrium with polysomes, an invariant property of normal SGs.

During the *in vitro* differentiation of human bone marrow CD34+ cells over the course of 2 weeks, spontaneous cytoplasmic SGs were observed in a fraction of CD34+ cells (Fig. 2A and B). The percentage of eIF3b/G3BP+ SGs peaked at day 6 (27%), then slowly decreased over time (Fig. 2B). No abnormal morphological changes were seen in these cells at various stages of differentiation, as assessed by May-Grünwald–Giemsa staining (Fig. S2A). Fluorescence microscopy using antibodies specific for erythroid (CD71± GlyA), megakaryocytic (CD41a), or myeloid (CD11b) cells revealed the expected maturation of each lineage (Fig. S2B) which ruled out a preferential overgrowth of the erythroid lineage under these culture conditions. Normal erythroid cell differentiation was also confirmed by hemoglobinization data, assessed at different time points, using 2,7-diaminofluorene (DAF) staining (Fig. S2C).

SGs are almost exclusively found in immature and mature erythroid cells. At early time points the majority of SGs are found in immature (CD71+ GlyA−) erythroid cells, while at later times, SGs are mainly found in mature (CD71+ GlyA+) erythroid cells (Fig. 2C). On day 6 of the *in vitro* differentiation, when the highest % of SGs is detected, an average of 28% erythroid precursor cells (CD71+ GlyA−) and approximately 4% of mature erythroid cells (CD71+ GlyA+) contained cytoplasmic SGs (Fig. S2D). These data suggest that cyclic assembly/disassembly of SGs in different subpopulations of erythroid cells may be a part of normal erythroid development.

To determine whether HRI contributes to SG assembly in developing erythroid cells, we infected CD34+ human bone marrow progenitor cells with lentiviral vectors expressing shRNAs targeting HRI transcripts. Three independent shRNAs significantly reduced the expression of HRI transcripts in these cultures (Fig. S2E). Knockdown of HRI inhibited eIF2α phosphorylation (Fig. 2D) and significantly reduced the spontaneous and SA-induced (Fig. 2E) assembly of SGs in these cultures. These results confirm that HRI is the eIF2α kinase that regulates SG assembly in developing erythroid cells.

To determine whether SGs are found in differentiating hematopoietic cells *in vivo* under normal physiological conditions, we harvested bone marrow from seven 6-month old healthy wild type Balb/c mice (Fig. S3A) and stained cells for erythroid (CD71 and Ter119), granulocytic (CD11b+) and megakaryocytic (CD41+)

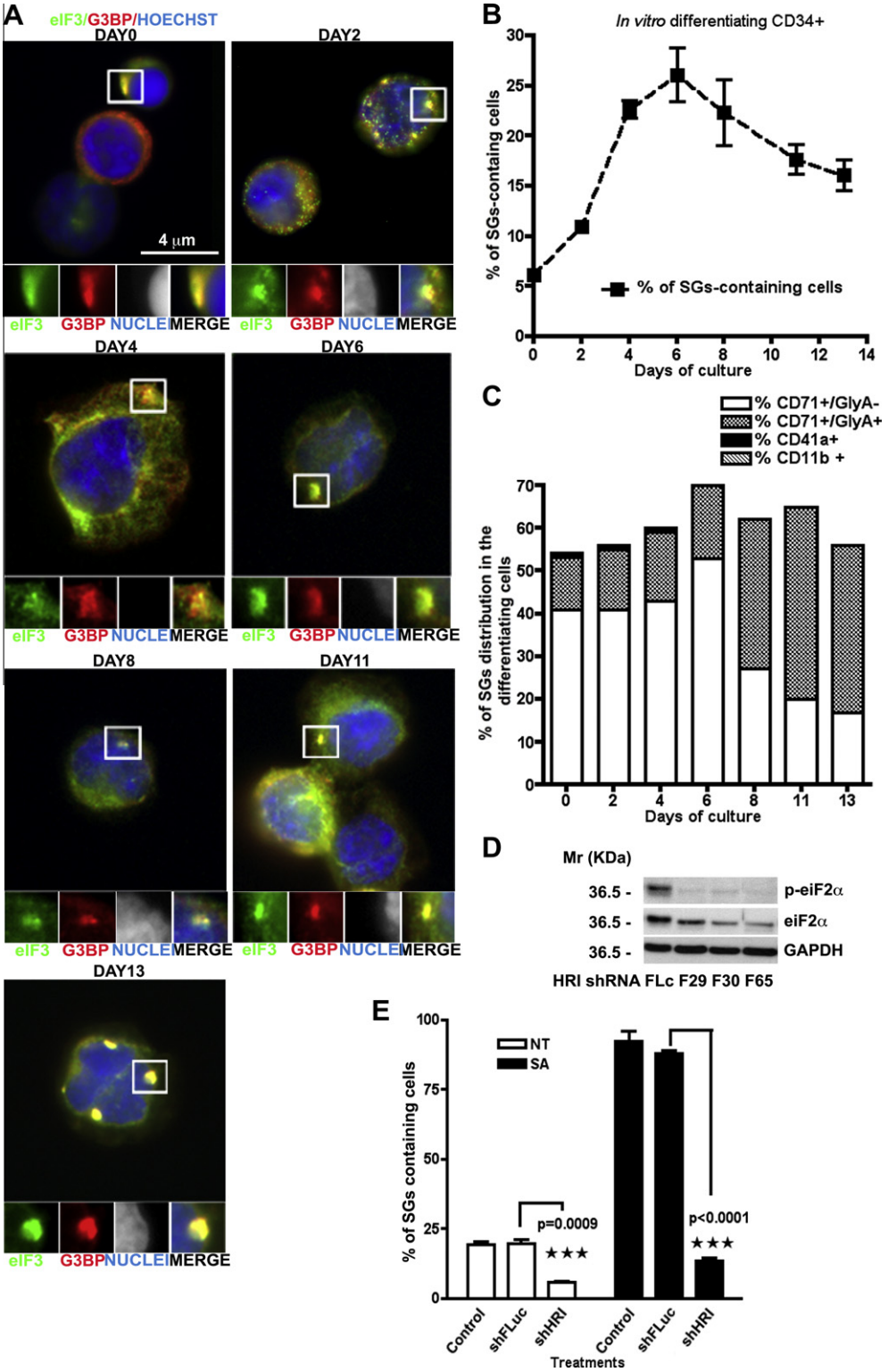


Fig. 2. CD34+ erythroid precursor cells assemble HRI/p-eIF2α-induced SGs during *in vitro* maturation. (A) CD34+ cells, collected at different days of *in vitro* differentiation were stained for SG markers eIF3b (eIF3, green) and G3BP (G3BP, red), in combination with Hoechst (blue) to reveal nuclei. Enlarged views (3.2-fold) of boxed areas depict separate channels and merged views of SGs. (B) The mean percentage ($n = 3$) of differentiating CD34+ cells with SGs (quantified by counting >100 cells per sample per experiment). (C) Lineage and maturation specific assembly of SGs. CD34+ cells were stained for the indicated differentiation markers as well as markers specific for immature erythroid precursors (CD71), in combination with SG markers. At the indicated times, cells were processed for immunofluorescence microscopy and the percentage of SGs in cells from each lineage was quantified. $n = 3 \pm$ SEM. (D) HRI knockdown reduces eIF2α phosphorylation. Representative Western blots are shown, with GAPDH as loading control. (E) Percentage of spontaneous and arsenite-induced SGs in CD34+ hematopoietic cells. CD34+ cells were infected with the indicated lentiviruses 4 days prior to culture with or without SA. Cells treated with each shRNA were pooled together before cytospin and SG quantification. $n = 3 \pm$ SEM.

surface markers as well as intracellular SG markers (Fig. 3A–C). Approximately 5–10% of the bone marrow cells contained SGs as assessed by G3BP and eIF3 staining (Fig. 3B). As also seen in our *in vitro* experiments, SGs were almost exclusively observed in

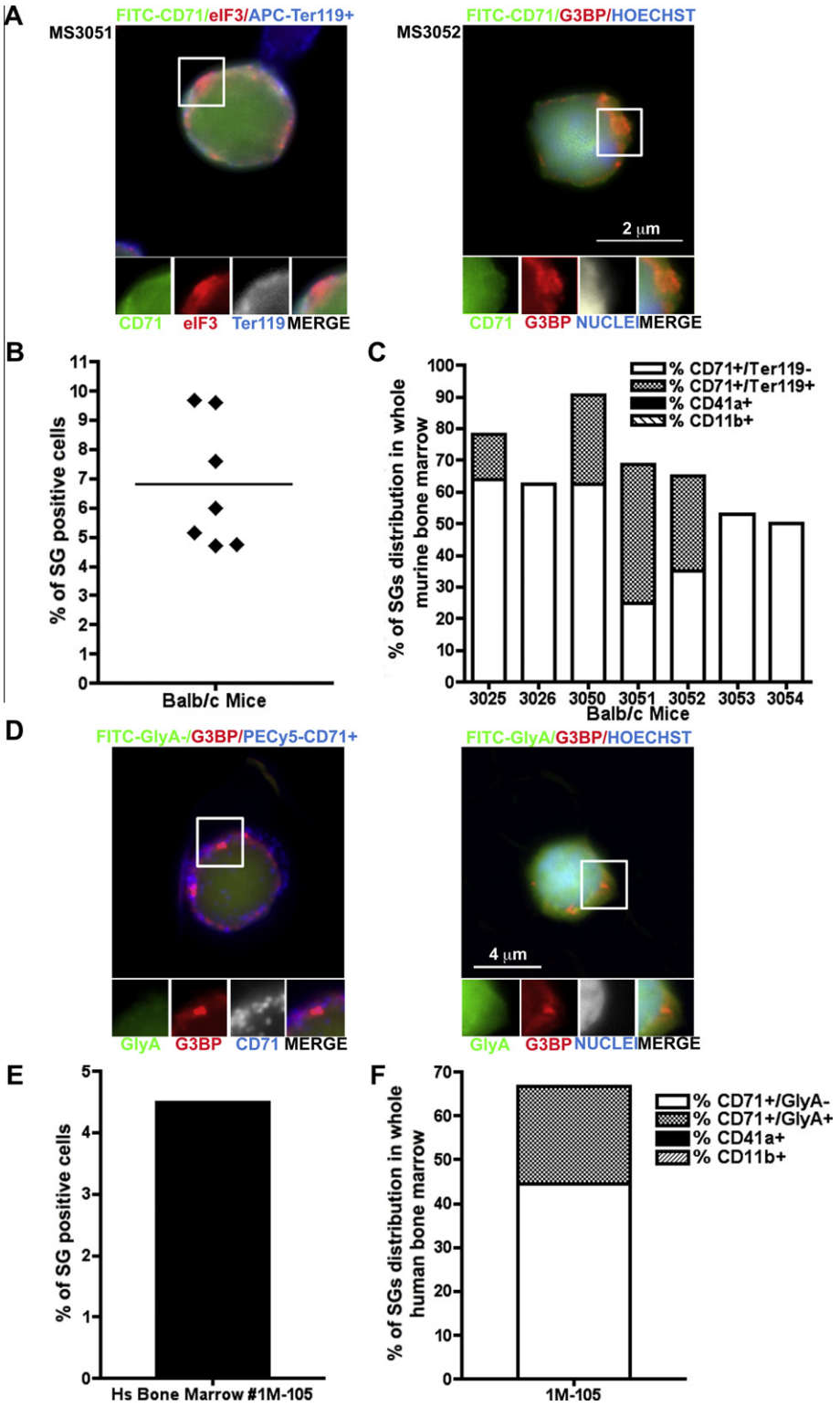


Fig. 3. Mouse and human bone marrow erythroid precursor cells assemble SGs during *in vivo* maturation. (A-C) Total bone marrow cells Balb/c male mice were stained for markers of lineage differentiation (CD71 – FITC, TER119 – APC, CD41 – FITC and CD11b – PECy5) and SGs (eIF3b and G3BP). (A) Left panel: A CD71+/Ter119+ erythroid cell (green/blue) containing eIF3b+ SGs (red) in bone marrow from sample MS3051. Right panel: A CD71+ erythroid cell (green) containing, G3BP+ SG (red) from sample MS3052. Enlarged views (1.7-fold) of boxed areas show separate channels and merged views of RNA granules. (B) The mean percentage of SGs containing cells was quantified by counting >100 cells from 3 independent fields per animal (seven mice). (C) Murine bone marrow cells were stained for the indicated differentiation markers, in combination with the SG markers eIF3 and G3BP. The percentage of SG positive cells from each lineage was quantified. Values are the means of 3 independent fields in which >100 cells were counted. (D–F) Total human fresh bone marrow collected from a healthy donor was stained for markers of lineage differentiation (CD71 – PECy5, GlyA – FITC, CD41 – FITC and CD11b – PECy5) and SGs (eIF3b and G3BP). (D) Left panel: A CD71+/GlyA– erythroid cell (blue) containing G3BP+ SGs (red). Right panel: A GlyA+ erythroid cell (green) containing, G3BP+ SG (red). (E) The mean percentage of SGs was quantified by counting >100 cells from 3 independent fields. (F) Total human bone marrow cells, stained for the indicated differentiation markers and the SG marker G3BP, showed that the majority of SG containing cells are erythroid cells. Values are the means of three independent fields in which at least 100 cells were counted. Enlarged views (1.6-fold) of boxed areas show separate channels and merged views of RNA granules.

erythroid cells (CD71± Ter119) (Fig. 3C). Approximately 8–15% of CD71+ Ter119− and 4% CD71+ Ter119+ cells show positive SGs staining (Fig. S3B).

To obtain further evidence that SGs are spontaneously assembled in differentiating hematopoietic cells *in vivo*, we analyzed whole fresh bone marrow collected from a healthy human donor. Bone marrow cells were stained for erythroid (CD71 and GlyA), megakaryocytic (CD41+), and granulocytic (CD11b+) surface markers as well as intracellular SG markers (Fig. 3D). Approximately 5% of freshly isolated human bone marrow cells contain G3BP+ SGs, the majority of which are erythroid cells (CD71± GlyA) (Fig. 3E and F). An average of 8.5% erythroid precursor cells (CD71+ GlyA−) and 4% mature erythroid cells (CD71+ GlyA+) contained cytoplasmic SGs (Fig. S3C). These results reveal that 5–10% of bone marrow erythroid cells form SGs *in vivo*, demonstrating for the first time that SGs can form in bone marrow erythroid cells under normal physiological conditions in both mice and humans.

To investigate the role of stress granules in erythroid differentiation, we determined whether reduced expression of G3BP, a protein that is essential for SG assembly [5], alters the production of globin mRNA and protein as well as cell survival. CD34+ bone marrow cultures were infected with shRNA vectors targeting G3BP transcripts. Three independent shRNAs significantly reduced the expression of G3BP mRNA (Fig. S4A) and protein (Fig. 4B). Partial knockdown of G3BP reduced the spontaneous and SA induced assembly of SGs in these cultures (Fig. 4A). Thus G3BP is required for the optimal assembly of spontaneous and arsenite-induced SGs in CD34+ erythroid progenitor cells.

We also quantified α-globin RNA and protein expression in CD34+ cells treated with control or G3BP-specific shRNAs. Knock down of G3BP significantly reduced the expression of α-globin RNA in these cultures (Fig. S4B). Although the knock down of G3BP protein was heterogeneous, α-globin protein levels were reduced in proportion to the reduction in G3BP protein expression (Fig. 4B). Thus, SGs may serve to protect α-globin transcripts from degradation during erythroid differentiation.

We also determined whether abrogation of SGs through decreased expression of G3BP affects erythroid differentiation *in vitro*. CD34+ hematopoietic progenitor cells were treated with control (Luc) or *G3BP*-specific lentiviral shRNAs prior to quantifying

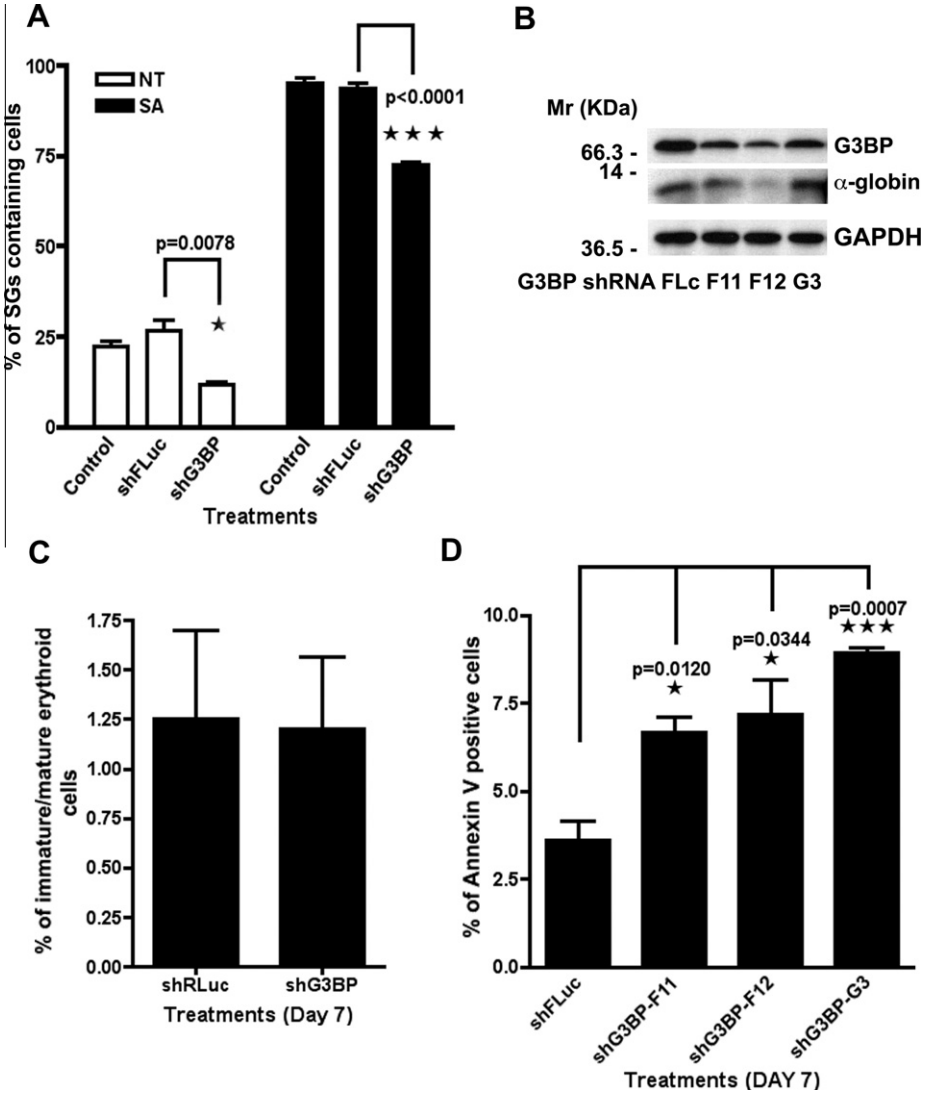


Fig. 4. Targeted knockdown of G3BP inhibits SGs formation and hampers expression of α-globin and erythroid cells survival. (A) G3BP knockdown significantly reduces spontaneous and SA-induced SG assembly in bone-marrow-derived CD34+ hematopoietic cells. The experiment was performed as previously described in Fig. 2E, relative to HRI silencing. $n = 3 \pm$ SEM. (B) Western blot of α-globin and G3BP with GAPDH as loading control. Representative blots are shown. (C) Effect of G3BP knockdown on the expression of erythroid maturation markers. *In vitro* cultured CD34+ cells were infected with shRNA, cultured for 7 days, and processed for FACS for erythroid surface molecules CD71 and GlyA. No significant differences in the ratio of CD71+ GlyA− immature to CD71+ GlyA+ mature erythroid cells are found. $n = 3 \pm$ SEM. (D) Human hematopoietic CD34+ cells treated with shG3BP lentivirus were harvested after 7 days for quantification of Annexin V positive cells $n = 3 \pm$ SEM.

the expression of GlyA and CD71 erythroid differentiation markers using flow cytometry. We monitored the ratio of CD71+ GlyA− (immature)/CD71+ GlyA+(mature) cells to assess erythroid differentiation in culture. Despite its ability to decrease expression of α-globin, reduced expression of G3BP and SGs did not significantly affect the expression of erythroid differentiation markers (Fig. 4C). However, when we investigated whether inhibition of SGs affects the survival of differentiating CD34+ progenitor cells, we found that after 7 days (Fig. 4D) of *in vitro* culture, G3BP downregulation significantly increases the percentage of annexin V+ apoptotic cells. Absolute numbers of live and dead cells after G3BP knock down are reported in Fig. S4C. These results suggest that spontaneous SGs may promote the survival of differentiating erythroid cells. SG assembly can promote the survival of cells exposed to adverse environmental conditions [3,14].

4. Discussion

In erythroid cells, post-transcriptional regulatory mechanisms play a major role in determining the expression of α-globin protein. In terminally differentiated anucleated erythrocytes, highly stable globin transcripts continue to synthesize globin protein to support the production of hemoglobin. The stability of α-globin transcripts is determined by the binding of α-complex to C-rich motifs located in the 3′-UTR [15,16]. The α-complex masks the binding site for an erythroid-enriched endoribonuclease, ErEN [17], to ensure that α-globin transcripts are available for translation. The translation of these transcripts is regulated by *HRI* [1]. When the concentration of intracellular heme is limiting, HRI phosphorylates eIF2α to inhibit the translation of α-globin [1,3,4,13]. In this study, we show that HRI-induced phosphorylation of eIF2α triggers the assembly of SGs in differentiating erythrocytes. Our results also implicate SGs in the regulation of α-globin mRNA stability and translation.

In cultures of differentiating CD34+ progenitor cells, spontaneous SGs are observed in the CD71+ erythroid lineage, but not in the CD11b+ myeloid or CD41+ megakaryocytic lineages. SGs are assembled in both CD71+/GlyA− immature erythroid cells and in more mature CD71+/GlyA+ erythroid cells (Fig. 2). Thus, SG assembly appears to occur throughout the erythroid differentiation process and may modulate gene expression in both early and late erythroid precursor cells.

In developing erythroid cells, HRI acts as a heme sensor and translational repressor. Our *in vitro* results suggest that HRI is activated to maintain hemoglobin homeostasis throughout erythroid development. This conclusion is supported by the appearance of SGs in murine (Figs. 3A–C and S2B) and human (Figs. 3D–F and S2C) bone marrow-derived erythroid cells. The further finding that targeted knock down of HRI inhibits phosphorylation of eIF2α, as well as spontaneous and oxidative stress-induced SG assembly (Fig. 2), identifies HRI as the eIF2α kinase in erythroid progenitor cells.

Finally, we demonstrate that knockdown of the essential SG component G3BP inhibits the spontaneous and arsenite-induced assembly of SGs in cultured CD34+ progenitor cells. G3BP knockdown is accompanied by decreased expression of α-globin transcripts (Fig. 4). SG inhibition may cause α-globin transcripts that normally reside in the cytoplasm to become more susceptible to degradation. Alternatively, this effect could be dependent on interactions between G3BP and Egr-1, an erythroid stimulator [18].

SG abrogation upon G3BP knockdown does not prevent erythroid differentiation despite α-globin downregulation, as assessed by expression of GlyA (Fig. 4E). It does, however, promote increasing apoptotic cell death (Fig. 4F and G) as assessed by expression of Annexin V. Since SGs are known to promote cell survival [3,14], it is likely that their assembly contributes to the viability of erythrocytes throughout differentiation.

In conclusion, our data reveal that differentiating erythroid cells assemble SGs. This is the first example of the *in vivo* assembly of SGs in primary cells that have not been subjected to exogenous stress. It is conceivable that reduced levels of heme encountered under *in vitro* culture conditions, contribute to the assembly of SGs in this system, as fluctuations in iron concentration *in vivo* can confer physiological stress. We also show that G3BP, a protein essential for SG assembly, regulates the expression of α-globin transcripts as well as the survival of differentiating erythroid progenitor cells. SG-mediated reprogramming of globin metabolism may therefore play a key role in globin production during erythroid differentiation.

Acknowledgments

We thank members of the Anderson Lab for helpful discussions and advice. We thank Dr. M. J. Weiss of The Children's Hospital of Philadelphia for kindly providing an aliquot of rabbit anti-human α-globin antibody and Johan Flygare for help with the DAF staining protocol. This work was supported by grants from the NIH and the American College of Rheumatology.

Appendix A. Supplementary data

Supplementary data associated with this article can be found, in the online version, at doi:10.1016/j.bbrc.2012.03.070.

References

[1] J.J. Chen, Regulation of protein synthesis by the heme-regulated eIF2α kinase: relevance to anemias, Blood 109 (2007) 2693–2699.
[2] C. Brugnara, Iron deficiency and erythropoiesis: new diagnostic approaches, Clin. Chem. 49 (2003) 1573–1578.
[3] E. McEwen, N. Kedersha, B. Song, et al., Heme-regulated inhibitor kinase-mediated phosphorylation of eukaryotic translation initiation factor 2 inhibits translation, induces stress granule formation, and mediates survival upon arsenite exposure, J. Biol. Chem. 280 (2005) 16925–16933.
[4] P. Anderson, N. Kedersha, Stress granules: the Tao of RNA triage, Trends Biochem. Sci. 33 (2008) 141–150.
[5] H. Tourriere, K. Chebli, L. Zekri, et al., The RasGAP-associated endoribonuclease G3BP assembles stress granules, J. Cell Biol. 160 (2003) 823–831.
[6] K. Irvine, R. Stirling, D. Hume, et al., Rasputin, more promiscuous than ever: a review of G3BP, Int. J. Dev. Biol. 48 (2004) 1065–1077.
[7] N. Kociok, P. Esser, K. Unfried, et al., Upregulation of the RAS-GTPase activating protein (GAP)-binding protein (G3BP) in proliferating RPE cells, J. Cell. Biochem. 74 (1999) 194–201.
[8] L. Zekri, K. Chebli, H. Tourriere, et al., Control of fetal growth and neonatal survival by the RasGAP-associated endoribonuclease G3BP, Mol. Cell. Biol. 25 (2005) 8703–8716.
[9] B.L. Ebert, J. Pretz, J. Bosco, et al., Identification of RPS14 as a 5q-syndrome gene by RNA interference screen, Nature 451 (2008) 335–339.
[10] B.L. Ebert, M.M. Lee, J.L. Pretz, et al., An RNA interference model of RPS19 deficiency in diamond-blackfan anemia recapitulates defective hematopoiesis and rescue by dexamethasone: identification of dexamethasone-responsive genes by microarray, Blood 105 (2005) 4620–4626.
[11] T. Ohn, N. Kedersha, T. Hickman, et al., A functional RNAi screen links O-GlcNAc modification of ribosomal proteins to stress granule and processing body assembly, Nat. Cell Biol. 10 (2008) 1224–1231.
[12] N. Gilks, N. Kedersha, M. Ayodele, et al., Stress granule assembly is mediated by prion-like aggregation of TIA-1, Mol. Biol. Cell 15 (2004) 5383–5398.
[13] N. Kedersha, G. Stoecklin, M. Ayodele, et al., Stress granules and processing bodies are dynamically linked sites of mRNP remodeling, J. Cell Biol. 169 (2005) 871–884.
[14] S. Yamasaki, P. Anderson, Reprogramming mRNA translation during stress, Curr. Opin. Cell Biol. 20 (2008) 222–226.
[15] I.M. Weiss, S.A. Liebhaber, Erythroid cell-specific determinants of alpha-globin mRNA stability, Mol. Cell. Biol. 14 (1994) 8123–8132.
[16] A.N. Chkheidze, D.L. Lyakhov, A.V. Makeyev, et al., Assembly of the alpha-globin mRNA stability complex reflects binary interaction between the pyrimidine-rich 3′ untranslated region determinant and poly(C) binding protein alphaCP, Mol. Cell. Biol. 19 (1999) 4572–4581.
[17] H. Liu, M. Kiledjian, An erythroid-enriched endoribonuclease (ErEN) involved in alpha-globin mRNA turnover, Protein Pept. Lett. 14 (2007) 131–136.
[18] C. Schulze, T. Buchse, S. Mikkat, et al., Erythropoietin receptor-mediated Egr-1 activation: structural requirements and functional implications, Cell. Signal. 20 (2008) 1848–1854.

Biochemical and Biophysical Research Communications 420 (2012) 775–781

Contents lists available at SciVerse ScienceDirect

Biochemical and Biophysical Research Communications

journal homepage: www.elsevier.com/locate/ybbrc

The differentiating and apoptotic effects of 2-aza-5′-deoxycytidine are dependent on the PU.1 expression level in PU.1-transgenic K562 cells

Sayuri Aoyama [a], Hiroko Nakano [b], Mikio Danbara [c], Masaaki Higashihara [c], Hideo Harigae [d], Shinichiro Takahashi [a,b,*]

[a] Division of Molecular Hematology, Kitasato University Graduate School of Medical Sciences, 1-15-1 Kitasato, Miniami-ku, Sagamihara, Kanagawa 252-0373, Japan
[b] Division of Hematology, Kitasato University School of Allied Health Sciences, 1-15-1 Kitasato, Miniami-ku, Sagamihara, Kanagawa 252-0373, Japan
[c] Division of Molecular Oncology, Kitasato University Graduate School of Medical Sciences, 1-15-1 Kitasato, Miniami-ku, Sagamihara, Kanagawa 252-0373, Japan
[d] Department of Hematology and Rheumatology, Tohoku University School of Medicine, 1-1 Seiryou-machi, Aoba-ku, Sendai 980-8574, Japan

ARTICLE INFO

Article history:
Available online 20 March 2012

Keywords:
PU.1
2-Aza-5′-deoxycytidine
K562
Erythroid differentiation
Apoptosis

ABSTRACT

The use of 5-aza-2′-deoxycytidine (5-azadc) for myelodysplastic syndrome, acute myeloid leukemia and chronic myeloid leukemia is becoming an effective and attractive option for these hematological malignancies. The PU.1 transcription factor is important for cellular differentiation through the control of its target genes not only in myeloid and B-lymphoid cells, but also in erythroid cells. Downregulation of PU.1 was reported to play a role in the pathogenesis of various hematological malignancies. In this study, we sought to identify the relationship between the effects of 5-azadc and PU.1. For this purpose, we employed PU.1-knockdown K562 (K562 PU.1KD) cells stably expressing PU.1 short inhibitory RNAs and PU.1-overexpressing K562 (K562 PU.1OE) cells. Therapeutic concentrations (0.1 and 0.5 μM) of 5-azadc resulted in growth arrest in the G2/M phase. Strikingly, however, K562 PU.1OE cells had significantly increased rates of G2/M and apoptotic sub-G1 phase cells. We observed the induction of cyclin B1, a regulator of the G2/M transition, after the addition of 5-azadc. This induction was abolished in K562 PU.1KD cells, but significantly induced in K562 PU.1OE cells. Further analyses revealed potent induction of hemoglobin A1 expression in K562 PU.1OE cells. Taken together, these findings suggest that the PU.1 expression level is tightly related to the differentiating and apoptotic effects of 5-azadc in K562 cells.

© 2012 Elsevier Inc. All rights reserved.

1. Introduction

PU.1 is a member of the Ezb transformation-specific sequence family of transcription factors and is expressed in granulocytic, monocytic and B-lymphoid cells [1]. PU.1 is also normally present in immature erythroid cells [2,3], and its downregulation is required for erythroid terminal differentiation [4]. However, a recent study by Wontakal et al. [5] demonstrated that PU.1 regulates an extensive network of genes that constitute major pathways for controlling the growth and survival of immature erythroid cells. They further revealed that fetal liver erythroid progenitors, the earliest erythroid-committed cells, are dramatically reduced *in vivo* in mice with low PU.1 expression [5]. Meanwhile, another group revealed that PU.1 expression is dramatically silenced in murine erythroleukemia (MEL) cells resistant to hexamethylene bisacetamide, which induces erythroid differentiation [6]. These two reports suggest that sufficient expression of PU.1 is necessary for erythroid differentiation. Collectively, PU.1 plays important roles in not only myeloid and B-lymphoid cells, but also immature erythroid cells, for proper differentiation.

The use of DNA methyltransferase (DNMT) inhibitors in myelodysplastic syndrome (MDS), acute myeloid leukemia (AML), chronic myeloid leukemia (CML) and sickle cell anemia is becoming an effective and attractive option for these diseases [9]. 5-Aza-2′-deoxycytidine (5-azadc) and 5-azacytidine are hypomethylating cytosine analogs with activity in leukemia [7,8]. A reanalysis of data from three sequential Cancer and Leukemia Group B trials of the DNMT inhibitor 5-azacytidine demonstrated that among 103 patients with AML at baseline (using World Health Organization criteria), 48% exhibited hematologic improvement or better responses [10,11]. However, there have been no reports

Abbreviations: MDS, myelodysplastic syndrome; AML, acute myeloid leukemia; CML, chronic myeloid leukemia; MEL, murine erythroleukemia; DNMT, DNA methyltransferase; 5-azadc, 5-aza-2′-deoxycytidine; HIFBS, heat-inactivated fetal bovine serum; HBA1, hemoglobin A1; GAPDH, glyceral dehyde 3-phosphate dehydrogenase; PBS, phosphate-buffered saline; TfR1, transferrin receptor 1.

* Corresponding author at: Division of Hematology, Kitasato University School of Allied Health Sciences, 1-15-1 Kitasato, Miniami-ku, Sagamihara, Kanagawa 252-0373, Japan. Fax: +81 42 778 8216.
E-mail address: shin@kitasato-u.ac.jp (S. Takahashi).

0006-291X/$ - see front matter © 2012 Elsevier Inc. All rights reserved.
http://dx.doi.org/10.1016/j.bbrc.2012.03.071

of useful and accurate markers for analyzing the efficacies and predicting the effects of these hypomethylating agents. For example, there is no clear correlation between the clinical response and loss of methylation of the p15INK4B gene after cycles of 5-azadc treatment [12].

Previously, it was reported that PU.1 interacts with DNMT3a and DNMT3b [8], and regulates its target genes through epigenetic modifications, such as DNA methylation [6,7]. Moreover, downregulation of PU.1 was reported to play a role in the pathogenesis of various hematological malignancies, including AML [13], multiple myeloma [14] and MDS [15]. In this study, we examined whether the effects of 5-azadc are correlated with PU.1 expression in CML PU.1-transgenic K562 cells. We report that therapeutic concentrations of 5-azadc induce erythroid differentiation of these cells, that PU.1 expression is tightly related to the effect of the agent, and that sufficient PU.1 expression accelerates erythroid differentiation and apoptosis induced by 5-azadc.

2. Materials and methods

2.1. Cell culture of PU.1-knockdown K562 (K562 PU.1KD) and PU.1-overexpressing K562 (K562 PU.1OE) cells

K562 PU.1KD and K562 PU.1OE cells were previously established in our laboratory [16,17] and were employed for this study. Specifically, we used 2–10 and 3–10 as K562 PU.1KD cells with vec 5 and vec 6 as their control cells, and H8 and A2 as K562 PU.1OE cells with V1 and V2 as their control cells [16,17]. The K562 PU.1KD cells were maintained in RPMI (Gibco BRL, Rockville, MD) containing 10% heat-inactivated fetal bovine serum (HIFBS) and 1 μg/ml puromycin. The K562 PU.1OE cells were grown in RPMI containing 10% HIFBS and 400 μg/ml neomycin. All cells were cultured under 5% CO_2 at 37 °C in a humidified atmosphere. For 5-azadc treatment, the cells were incubated with specified amounts of 5-azadc, and the media were changed in every 24 h in the presence of the same amounts of this agent.

2.2. Immunoblotting

Cells were collected, lysed in lysis buffer (50 mM Tris–HCl pH 8.0, 1.5 mM $MgCl_2$, 150 mM NaCl, 1 mM EDTA, 5% glycerol, 1% Triton X-100, 1× protease inhibitor cocktail [Roche, Indianapolis, IN]) and incubated on ice for 20 min. The lysates were subjected to ultrasonic sonication, followed by centrifugation to remove cellular debris. To examine the expression of cyclin A, cyclin B1, cyclin E2 and hemoglobin A1 (HBA1), mouse monoclonal anti-cyclin A (Cell Signaling Technology, Beverly, MA), rabbit polyclonal anti-cyclin B1 (Cell Signaling Technology), rabbit polyclonal anti-cyclin E2 (Cell Signaling Technology) and mouse monoclonal anti-HBA1 (Abnova, Taipei, Taiwan) antibodies were employed. Rabbit polyclonal glyceraldehyde 3-phosphate dehydrogenase (GAPDH) (Cell Signaling Technology) antibody was used to examine equal protein loading in each lane. Horseradish peroxidase-conjugated anti-rabbit IgG (Cell Signaling Technology) and anti-mouse IgG (Jackson ImmunoResearch, West Grove, PA) were used as the secondary antibodies. Finally, the membranes were developed by chemiluminescence (ECL; Amersham Pharmacia Biotech, Little Chalfont, United Kingdom).

2.3. Cell cycle analysis

Cell cycle profiles were determined by analyzing the DNA contents using propidium iodide (Dojindo, Kumamoto, Japan) staining and flow cytometry. PU.1-transgenic cells (3×10^6) were incubated with 5-azadc (0.1 or 0.5 μM) for 24, 48, 72 or 96 h. The cells were then washed with phosphate-buffered saline (PBS), fixed with ice-cold 70% ethanol and stored at −20 °C until analysis. The fixed cells were collected, suspended in 300 μl of RNase/PBS solution (100 μg/ml) and incubated at 37 °C for 30 min. The cells were then collected, resuspended in 300 μl of propidium iodide/PBS solution (5 μg/ml) and incubated in the dark at room temperature for 15 min. After filtration through a nylon mesh sheet, all samples were analyzed by flow cytometry using an Epics XL (Beckman Coulter, Nyon, Switzerland), as described previously [17]. To analyze the data, WinMDI2.9 (http://en.bio-soft.net/other/WinMDI.html) and MultiCycle AV for Windows (PHOENIX, San Diego, CA) were employed.

2.4. Analysis of DNA damage

After treatment with various amounts of 5-azadc, the cells were collected, washed with PBS, fixed with 3.7% formaldehyde at 37 °C for 10 min and placed on ice for 1 min. The cells were then collected, fixed with ice-cold 90% methanol and incubated on ice for 30 min. Subsequently the cells were collected, washed twice with incubation solution (0.5% albumin/PBS), resuspended to a final concentration of 1×10^6 cells/100 μl and incubated at room temperature for 10 min. After addition of 1 μg of a rabbit Alexa Fluor 488-conjugated anti-phospho-histone H2A.X (Ser139) polyclonal antibody (Cell Signaling Technology) or its isotype control rabbit IgG (Cell Signaling Technology), the cells were incubated at room temperature for 1 h. The cells were washed with incubation solution and Alexa Fluor 488-conjugated anti-rabbit IgG (H + L) F(ab′)2 Fragment (Cell Signaling Technology) was added. Then, these samples were analyzed by flow cytometry using an Epics XL (Beckman Coulter).

2.5. mRNA expression analysis

cDNAs were prepared from cells using reverse transcriptase (Transcriptor First Strand cDNA Synthesis Kit; Roche). Quantitative PCR was performed using Quantitect SYBR Green PCR Reagent (Qiagen, Miami, FL) according to the manufacturer's protocol and using an Opticon Mini Real-time PCR Instrument (Bio-Rad, Hercules, CA) as described [18]. The primers sequences were: α-globin forward, 5′- AAGGTCGGCGCGCACGCT-3′, reverse, 5′-CTCAGGTCGA AGTGCGGG-3′; human β-globin forward, 5′-CTCATGGCAAGAAAGT GCTCG-3′, reverse, 5′-AATTCTTTGCCAAAGTGATGGG-3′; GAPDH forward, 5′-GAAGGTGAAGGTCGGAGT-3′, reverse; 5′-GAAGATGGT-GATGGGATTTC-3′. The thermal cycling conditions for α-globin were incubation at 95 °C for 15 min, followed by 35 cycles of 95 °C for 15 s, 55 °C for 15 s and 72 °C for 15 s. The thermal cycling conditions for β-globin and GAPDH were incubation at 95 °C for 15 min, followed by 35 cycles of 95 °C for 30 s, 55 °C for 30 s and 72 °C for 45 s. The copy number of each sample was calculated as previously described [19].

3. Results

3.1. Effects of 5-azadc on the cell viability and cell cycle

First, we examined the effects of 5-azadc on the PU.1-transgenic cell viability and cell cycle dynamics. A previous study of therapy for solid tumors demonstrated that the therapeutic peak plasma concentration of 5-azadc is 0.01–0.4 μM when administered at doses of less than 60 mg/m^2 [20]. Therefore, in this study, we examined the effects of 5-azadc at concentrations of 0.1 and 0.5 μM. Although there was almost no difference in the proportions of viable cells incubated with 0.1 μM 5-azadc for 72 h (Fig. 1A), the viable cells among K562 PU.1KD cells were increased

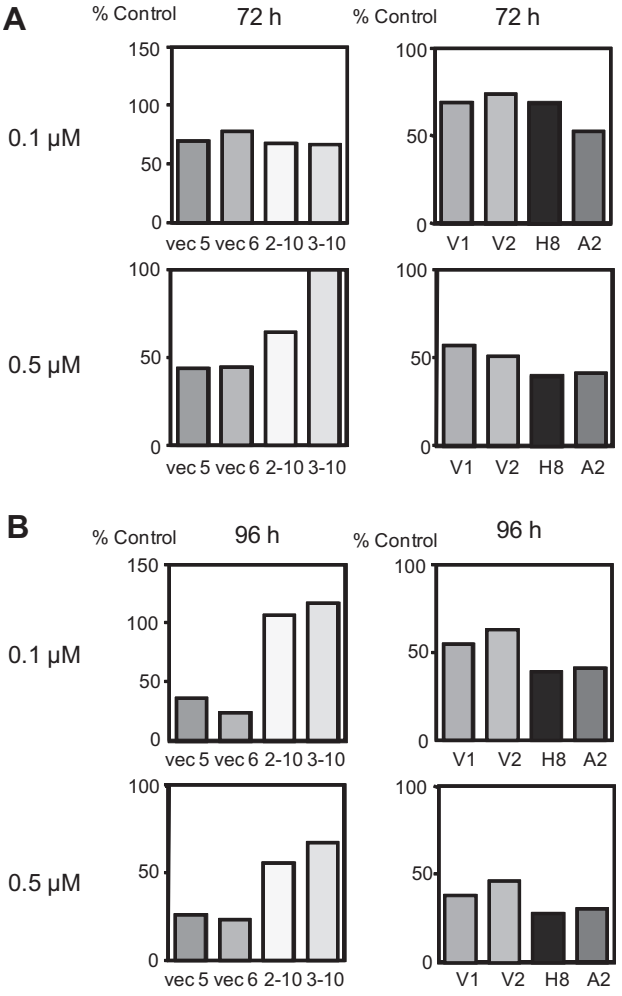


Fig. 1. Effects of 5-azadc on the cell growth of PU.1-transgenic K562 cells. We used 2–10, 3–10 as K562 PU.1KD cells with vec 5 and vec 6 as their control cells, and H8 and A2 as K562 PU.1OE cells with V1 and V2 as their control cells. The cells were incubated with 5-azadc for 72 h (A) or 96 h (B), and then analyzed by the Trypan blue dye exclusion method. The% control values shown in the X-axis were calculated as the number of live cells with 5-azadc treatment divided by the number of live cells without 5-azadc treatment. At least three independent experiments were performed with similar results, and representative data are shown.

compared with their controls at 96 h (Fig. 1B). In contrast, the viable cells were decreased among PU.1OE cells incubated with 5-azadc at 0.1 and 0.5 μM for 96 h (Fig. 1B). Cell cycle analyses revealed that the proportions of G2/M phase cells were slightly less in PU.1KD cells in the presence of 0.1 and 0.5 μM 5-azadc, compared with their controls (Figs. 2 and S1). In contrast, K562 PU.1OE cells showed a significant change to cell cycle arrest in the G2/M phase under the identical treatment conditions (Figs. 3 and S1). In addition, there were marked increases in sub-G1 phase cells (Fig. 3), indicating a profound increment in apoptotic cells among K562 PU.1OE cells. These findings suggest that 5-azadc has potent effects on the cell growth and apoptosis of K562 PU.1 OE cells.

3.2. Induction of cyclin B1 by 5-azadc is related to the PU.1 expression level

Since we observed specific effects of 5-azadc on the cell cycle, we examined the protein expression of cyclins in PU.1-transgenic cells in the presence or absence of 5-azadc. As shown in Fig. 4A, the expression levels of cyclin A remained constant. Cyclin E2 expression was induced by the addition of 5-azadc, but the inductions were unrelated to the PU.1 expression level. However, induction of the protein expression of cyclin B1, a critical regulator of the G2/M transition in the cell cycle [21], by 5-azadc was highest in clone H8, in which PU.1 expression is highest [17]. This induction was significantly abolished in K562 PU.1KD cells, especially clone 2–10, in which PU.1 expression is lowest [17] (Fig. 4A, upper panel). Collectively, these findings indicate that induction of cyclin B1, a critical regulator of the G2/M transition, by 5-azadc is related to the PU.1 expression level.

3.3. Analysis of the DNA damage marker γ-H2AX after treatment of PU.1-transgenic cells with 5-azadc

Since G2/M arrest is a hallmark of DNA damage and differentiation, we examined whether 5-azadc treatment caused induction of γ-H2AX, a well-known marker of DNA double-strand breaks. γ-H2AX is rapidly phosphorylated by ATM and other PI3 kinase members in response to DNA double-strand breaks caused by naturally occurring endogenous processes, such as VDJ recombination, or exposure to DNA-damaging agents in the environment [22]. Treatment of PU.1-transgenic cells with 0.5 μM 5-azadc for 96 h caused no significant changes in γ-H2AX in all cells (Fig. S2). These findings suggest that treatment with 5-azadc at this concentration has no effects on DNA damage in these cells.

3.4. β-Globin and HBA1 expression are dramatically induced in K562 PU.1OE cells after treatment with 5-azadc

It was recently reported that sustained exposure to 2.0 μM 5-azadc leads to apoptotic cell death in K562 cells by promoting erythroid differentiation [23]. Therefore, we examined whether 0.5 μM 5-azadc leads to the differentiation of K562 cells. For this purpose, we examined the expression of α-globin and β-globin by real-time PCR. Slight inductions of α-globin by 5-azadc were observed in both K562 PU.1KD and K562 PU.1OE cells (Fig. S3A). In contrast, β-globin was markedly induced by 5-azadc, and this effect was more prominent in K562 PU.1OE cells (Fig. S3B). We further examined the protein expression of HBA1, a marker of erythroid differentiation. Although there were no significant changes in the induction of HBA1 in K562 PU.1KD cells and their control cells, we observed potent induction of HBA1 in K562 PU.1OE cells (H8 and A2) in the presence of 5-azadc (Fig. 4B). These findings suggest that 5-azadc induces erythroid differentiation of K562 cells, and that this effect is augmented by overexpression of PU.1.

4. Discussion

The DNMT inhibitors 5-azacytidine and 5-azadc have activity in MDS as demonstrated in randomized studies [7,24,25], and both are approved by the United States Food and Drug Administration. The features of azacytidine and 5-azadc in MDS studies are delayed clearance of blasts, delayed myelosuppression, slow responses (median number of cycles to best response was more than three) and eventual cytogenetic responses. Similar phenomena were reported in patients with chronic myelogenous leukemia treated with 5-azadc [26]. These clinical studies suggest that the mechanism of action of these drugs does not involve cytotoxicity, because DNMT inhibitors generally induce gene expression at lower concentrations [27] and DNA damage at higher concentrations [28].

Early studies with 5-azadc reported that the compound can induce muscle cell differentiation [29], erythroid differentiation of MEL cells [30] and leukemic blasts from patients with AML [31]. However, the mechanism of the differentiation induced by 5-azadc

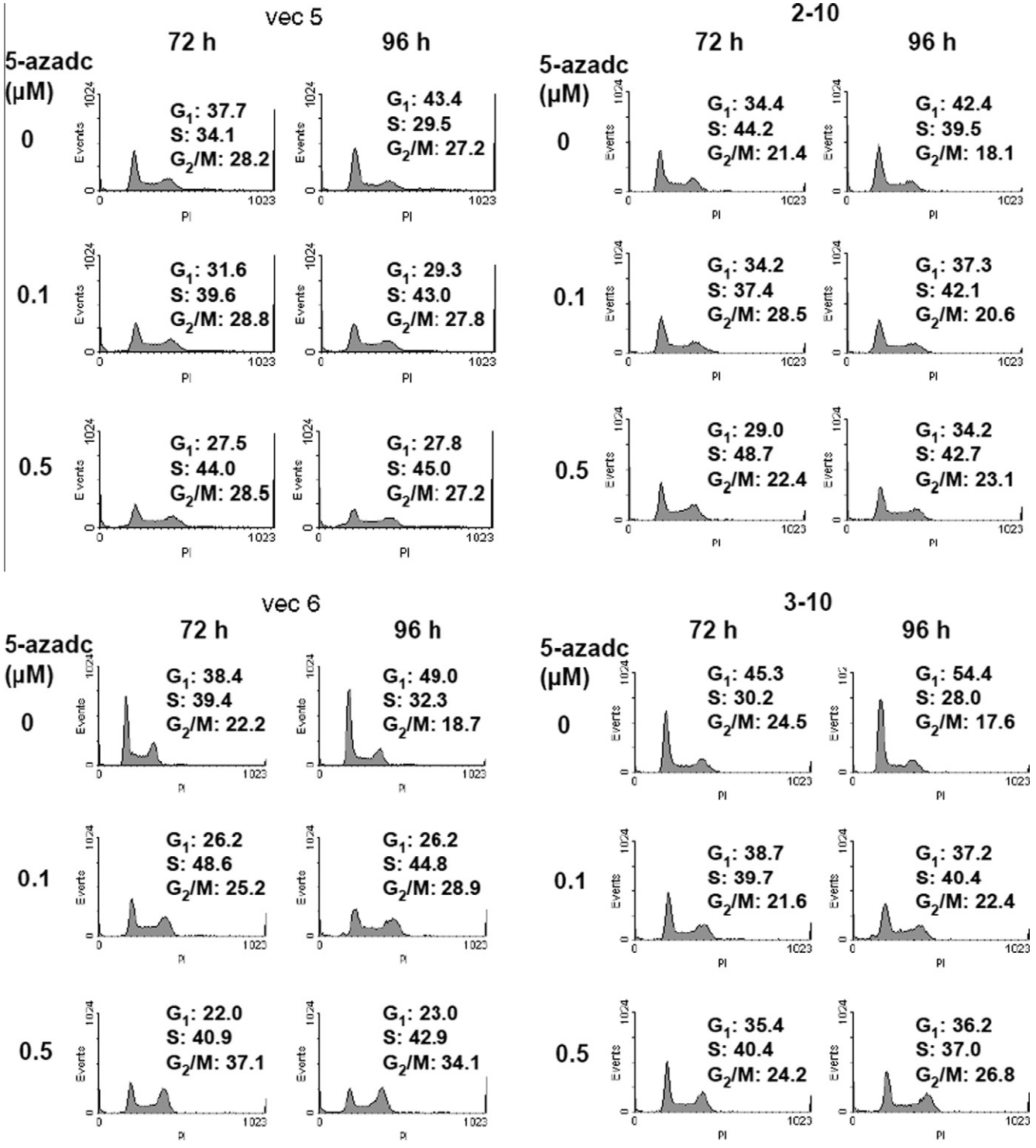


Fig. 2. Cell cycle profiles of K562 PU.1KD cells and their control cells, in the presence (0.1, 0.5 μM) or absence of 5-azadc. The data shown are representative of three independent experiments, and reproducibility was confirmed.

is not clear. Recent studies on the biological functions of 5-azadc have focused on its role in regulating transcription factors involved in the cell cycle [32]. In particular, c-myc has shown importance in its role as a 5-azadc target, because it can activate transferrin receptor 1 (TfR1), ferritin and iron regulatory protein 2 [33,34]. 5-Azadc activates iron uptake and heme biosynthesis by increasing c-myc nuclear localization and binding to the e-boxes of the TfR1 and ferrochelatase genes [33]. All of these proteins are important in cellular iron acquisition and therefore critical for erythroid differentiation, and may play pivotal roles in MDS and AML. Importantly, c-myc is epigenetically repressed by PU.1 through HDAC and Dnmt activities [35]. Therefore, we speculate that the effects of 5-azadc are prominent in PU.1OE cells because c-myc and/or related genes (max, etc.) may be potently induced by the inhibition

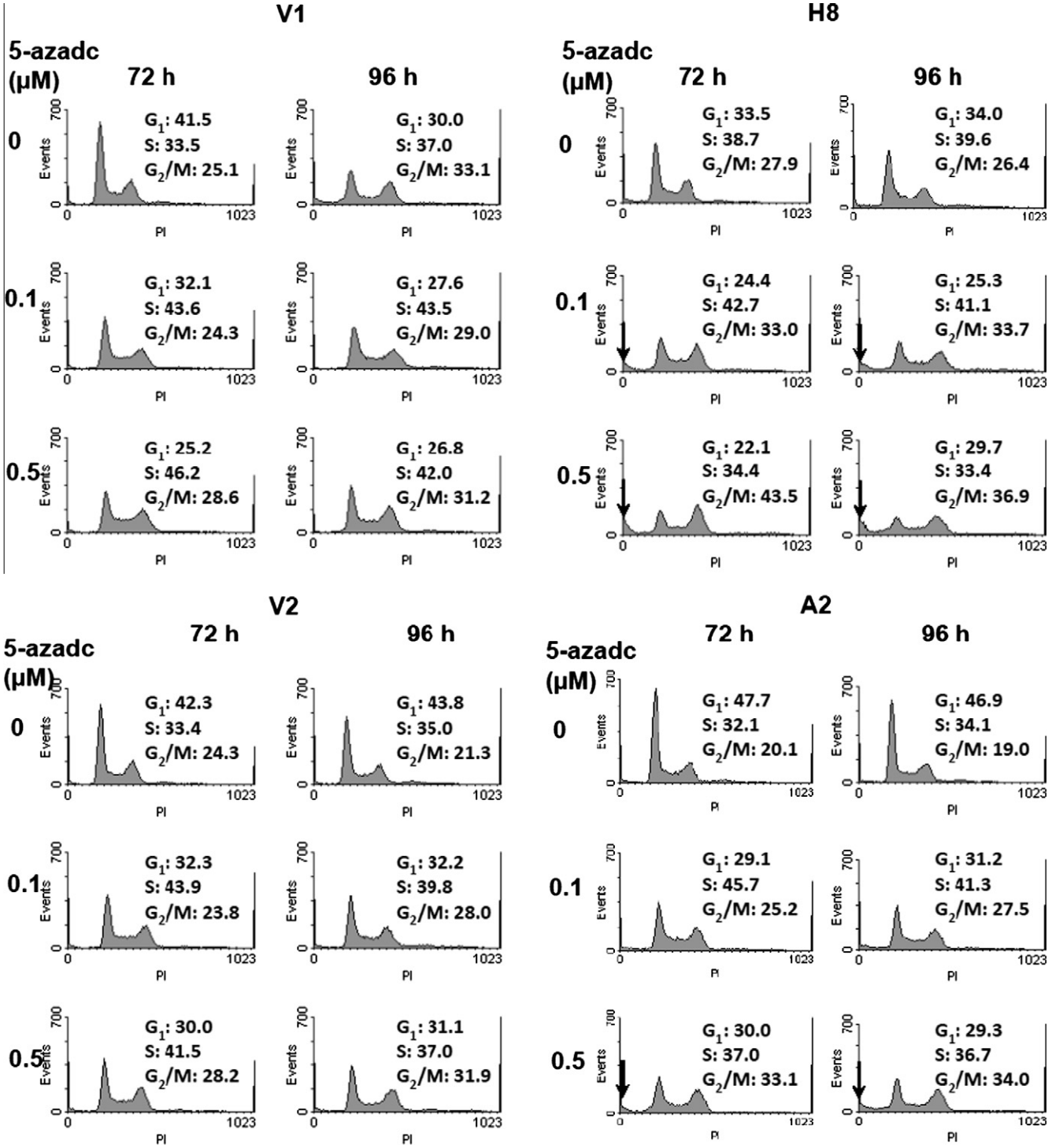


Fig. 3. Effects of 5-azadc on the cell cycle of K562 PU.1OE cells and their control cells. Similar to Fig. 2. The arrows in (B) indicate the detection of apoptotic cells as cells with fractional DNA contents (sub-G1 peaks). The data shown are representative of three independent experiments, and reproducibility was confirmed.

of DNMT activity. Therefore, high PU.1 expression is related to efficient effects of 5-azadc that lead to erythroid differentiation. We are now examining these mechanisms in detail.

Constitutive upregulation of PU.1 is believed to be the main cause for a blockade in the differentiation process of MEL cells [4,36]. However, the present findings and those of a previous study [5] indicate a requirement for PU.1 expression for erythroid differentiation. One possible explanation for this discrepancy is that K562 cells express the endogenous ε-globin and γ-globin genes, but not the adult stage-specific β-globin gene, and have therefore been considered as a model for the embryonic–fetal stages of erythroid development [37,38]. On the other hand, MEL cells are considered to be a model for fetal–adult development [38]. Therefore, the roles of PU.1 may differ during the erythroid differentiation stages. We speculate that, at least, proper expression of PU.1 is necessary for the differentiation of very immature erythroid cells. We are now working to analyze other lineages of PU.1-transgenic leukemia cell lines to examine the effects of 5-azadc.

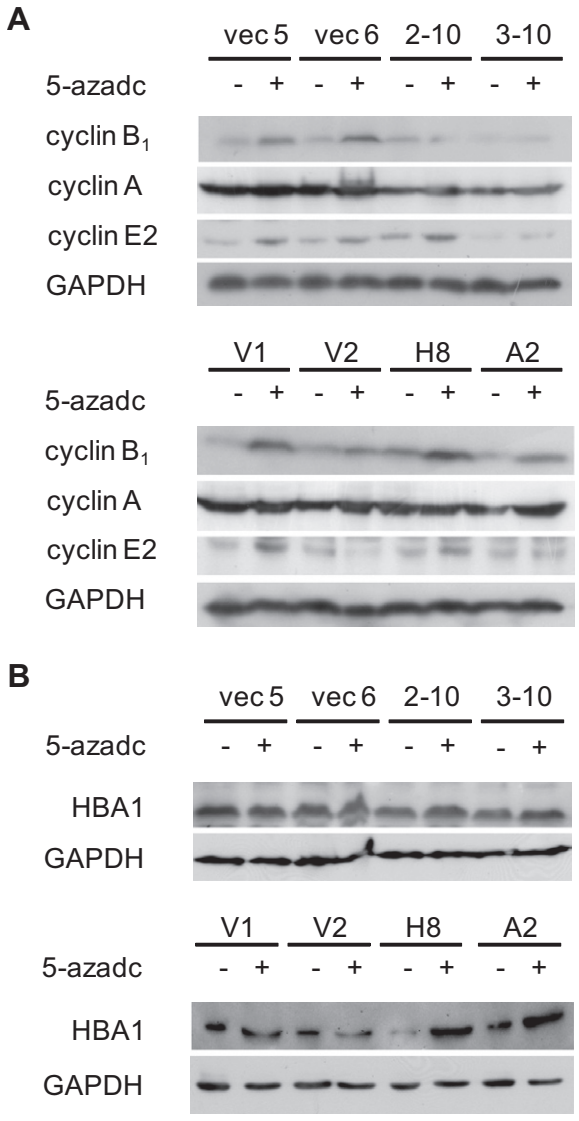


Fig. 4. Analyses of cyclin expressions and erythroid differentiation induced by 5-azadc in PU.1-transgenic cells. (A) Western blotting analysis of cyclin protein expressions in the presence or absence of 0.5 μM 5-azadc using K562 PU.1KD and K562 PU.1OE cells. The membranes were probed with anti-cyclin B1 and anti-cyclin A antibodies. The membranes were then stripped and reprobed with anti-cyclin E and anti-GAPDH antibodies. Equal loading of the protein was confirmed by the GAPDH expression. (B) Western blotting analyses of HBA1 in PU.1-transgenic cells with and without 0.5 μM 5-azadc. Equal loading of the protein was confirmed by GAPDH expression.

Collectively, our study findings shed light on the possibility of PU.1 as a novel biomarker to predict the differentiating and apoptotic effects of 5-azadc on hematological malignancies.

Competing interests

The authors declare no competing interests.

Acknowledgments

The authors thank Dr. Hirotaka Matui, Research Institute for Radiation Biology and Medicine, for valuable suggestions on the effect of 5-azadc for erythroid differentiation.

We also thank Ms Akemi Imoto for helping cell cycle analyses, Drs. Toshio Okazaki and Takashi Satoh for stimulating discussions.

This work was supported in part by the Takeda Science Foundation, Grants-in-Aid for Scientific Research (No. 23590687) from the MEXT, the Kanagawa Nanbyou Study Foundation, and a foundation from the Kitasato University School of Allied Health Sciences (Grants-in-Aid for Research Project, No 2011-1001).

Appendix A. Supplementary data

Supplementary data associated with this article can be found, in the online version, at http://dx.doi.org/10.1016/j.bbrc.2012.03.071.

References

[1] H.M. Chen, P. Zhang, M.T. Voso, S. Hohaus, D.A. Gonzalez, C.K. Glass, D.E. Zhang, D.G. Tenen, Neutrophils and monocytes express high levels of PU.1 (Spi-1) but not Spi-B, Blood 85 (1995) 2918–2928.
[2] J. Back, A. Dierich, C. Bronn, P. Kastner, S. Chan, PU.1 determines the self-renewal capacity of erythroid progenitor cells, Blood 103 (2004) 3615–3623.
[3] R. Pop, J.R. Shearstone, Q. Shen, Y. Liu, K. Hallstrom, M. Koulnis, J. Gribnau, M. Socolovsky, A key commitment step in erythropoiesis is synchronized with the cell cycle clock through mutual inhibition between PU.1 and S-phase progression, PLoS Biol. 8 (2010).
[4] G. Rao, N. Rekhtman, G. Cheng, T. Krasikov, A.I. Skoultchi, Deregulated expression of the PU.1 transcription factor blocks murine erythroleukemia cell terminal differentiation, Oncogene 14 (1997) 123–131.
[5] S.N. Wontakal, X. Guo, B. Will, M. Shi, D. Raha, M.C. Mahajan, S. Weissman, M. Snyder, U. Steidl, D. Zheng, A.I. Skoultchi, A large gene network in immature erythroid cells is controlled by the myeloid and B cell transcriptional regulator PU.1, PLoS Genet. 7 (2011) e1001392.
[6] M.J. Fernandez-Nestosa, P. Hernandez, J.B. Schvartzman, D.B. Krimer, PU.1 is dispensable to block erythroid differentiation in Friend erythroleukemia cells, Leuk. Res. 32 (2008) 121–130.
[7] G. Leone, L. Teofili, M.T. Voso, M. Lubbert, DNA methylation and demethylating drugs in myelodysplastic syndromes and secondary leukemias, Haematologica 87 (2002) 1324–1341.
[8] J.P. Issa, Epigenetic changes in the myelodysplastic syndrome, Hematol. Oncol. Clin. North Am. 24 (2010) 317–330.
[9] D. de Vos, W. van Overveld, Decitabine: a historical review of the development of an epigenetic drug, Ann. Hematol. 84 (Suppl. 1) (2005) 3–8.
[10] L.R. Silverman, D.R. McKenzie, B.L. Peterson, J.F. Holland, J.T. Backstrom, C.L. Beach, R.A. Larson, Further analysis of trials with azacytidine in patients with myelodysplastic syndrome: studies 8421, 8921, and 9221 by the Cancer and Leukemia Group B, J. Clin. Oncol. 24 (2006) 3895–3903.
[11] F. Ravandi, A.K. Burnett, E.D. Agura, H.M. Kantarjian, Progress in the treatment of acute myeloid leukemia, Cancer 110 (2007) 1900–1910.
[12] B. Hackanson, C. Robbel, P. Wijermans, M. Lubbert, In vivo effects of decitabine in myelodysplasia and acute myeloid leukemia: review of cytogenetic and molecular studies, Ann. Hematol. 84 (Suppl. 1) (2005) 32–38.
[13] F. Rosenbauer, K. Wagner, J.L. Kutok, H. Iwasaki, M.M. Le Beau, Y. Okuno, K. Akashi, S. Fiering, D.G. Tenen, Acute myeloid leukemia induced by graded reduction of a lineage-specific transcription factor, PU.1, Nat. Genet. 36 (2004) 624–630 (Epub 2004 May 2016).
[14] M. Pettersson, C. Sundstrom, K. Nilsson, L.G. Larsson, The hematopoietic transcription factor PU.1 is downregulated in human multiple myeloma cell lines, Blood 86 (1995) 2747–2753.
[15] H.J. Huh, S.L. Chae, M. Lee, K.S. Hong, Y.C. Mun, C.M. Seong, W.S. Chung, J.W. Huh, CD34, RAB20, PU.1 and GFI1 mRNA expression in myelodysplastic syndrome, Int. J. Lab. Hematol. 31 (2009) 344–351.
[16] A. Imoto, M. Okada, T. Okazaki, H. Kitasato, H. Harigae, S. Takahashi, Metallothionein-1 isoforms and vimentin are direct PU.1 downstream target genes in leukemia cells, J. Biol. Chem. 285 (2010) 10300–10309.
[17] Y. Iseki, A. Imoto, T. Okazaki, H. Harigae, S. Takahashi, Identification of annexin 1 as a PU.1 target gene in leukemia cells, Leuk. Res. 33 (2009) 1658–1663.
[18] Y. Iseki, M. Nakahara, M. Kubo, F. Obata, H. Harigae, S. Takahashi, Correlation of PU.1 and signal regulatory protein alpha1 expression in PU.1 transgenic K562 cells, Int. J. Mol. Med. 29 (2012) 319–323.
[19] S. Takahashi, H. Harigae, J. Kameoka, T. Sasaki, M. Kaku, AML1B transcriptional repressor function is impaired by the Flt3 internal tandem duplication, Br. J. Haematol. 130 (2005) 428–436.
[20] C.J. van Groeningen, A. Leyva, A.M. O'Brien, H.E. Gall, H.M. Pinedo, Phase I and pharmacokinetic study of 5-aza-2′-deoxycytidine (NSC 127716) in cancer patients, Cancer Res. 46 (1986) 4831–4836.
[21] L.A. Porter, D.J. Donoghue, Cyclin B1 and CDK1: nuclear localization and upstream regulators, Prog. Cell Cycle Res. 5 (2003) 335–347.
[22] C. Redon, D. Pilch, E. Rogakou, O. Sedelnikova, K. Newrock, W. Bonner, Histone H2A variants H2AX and H2AZ, Curr. Opin. Genet. Dev. 12 (2002) 162–169.
[23] M. Schnekenburger, C. Grandjenette, J. Ghelfi, T. Karius, B. Foliguet, M. Dicato, M. Diederich, Sustained exposure to the DNA demethylating agent, 2′-deoxy-5-azacytidine, leads to apoptotic cell death in chronic myeloid leukemia by promoting differentiation, senescence, and autophagy, Biochem. Pharmacol. 81 (2011) 364–378.

[24] M. Lubbert, P. Wijermans, R. Kunzmann, G. Verhoef, A. Bosly, C. Ravoet, M. Andre, A. Ferrant, Cytogenetic responses in high-risk myelodysplastic syndrome following low-dose treatment with the DNA methylation inhibitor 5-aza-2′-deoxycytidine, Br. J. Haematol. 114 (2001) 349–357.
[25] L.R. Silverman, E.P. Demakos, B.L. Peterson, A.B. Kornblith, J.C. Holland, R. Odchimar-Reissig, R.M. Stone, D. Nelson, B.L. Powell, C.M. DeCastro, J. Ellerton, R.A. Larson, C.A. Schiffer, J.F. Holland, Randomized controlled trial of azacitidine in patients with the myelodysplastic syndrome: a study of the cancer and leukemia group B, J. Clin. Oncol. 20 (2002) 2429–2440.
[26] H.M. Kantarjian, S. O'Brien, J. Cortes, F.J. Giles, S. Faderl, J.P. Issa, G. Garcia-Manero, M.B. Rios, J. Shan, M. Andreeff, M. Keating, M. Talpaz, Results of decitabine (5-aza-2′deoxycytidine) therapy in 130 patients with chronic myelogenous leukemia, Cancer 98 (2003) 522–528.
[27] J.G. Herman, S.B. Baylin, Gene silencing in cancer in association with promoter hypermethylation, N. Engl. J. Med. 349 (2003) 2042–2054.
[28] S.S. Palii, B.O. Van Emburgh, U.T. Sankpal, K.D. Brown, K.D. Robertson, DNA methylation inhibitor 5-aza-2′-deoxycytidine induces reversible genome-wide DNA damage that is distinctly influenced by DNA methyltransferases 1 and 3B, Mol. Cell. Biol. 28 (2008) 752–771.
[29] P.G. Constantinides, P.A. Jones, W. Gevers, Functional striated muscle cells from non-myoblast precursors following 5-azacytidine treatment, Nature 267 (1977) 364–366.
[30] F. Creusot, G. Acs, J.K. Christman, Inhibition of DNA methyltransferase and induction of Friend erythroleukemia cell differentiation by 5-azacytidine and 5-aza-2′-deoxycytidine, J. Biol. Chem. 257 (1982) 2041–2048.
[31] A. Pinto, V. Attadia, A. Fusco, F. Ferrara, O.A. Spada, P.P. Di Fiore, 5-Aza-2′-deoxycytidine induces terminal differentiation of leukemic blasts from patients with acute myeloid leukemias, Blood 64 (1984) 922–929.
[32] B.C. Valdez, Y. Li, D. Murray, P. Corn, R.E. Champlin, B.S. Andersson, 5-Aza-2′-deoxycytidine sensitizes busulfan-resistant myeloid leukemia cells by regulating expression of genes involved in cell cycle checkpoint and apoptosis, Leuk. Res. 34 (2010) 364–372.
[33] B. Ning, G. Liu, Y. Liu, X. Su, G.J. Anderson, X. Zheng, Y. Chang, M. Guo, Y. Liu, Y. Zhao, G. Nie, 5-Aza-2'-deoxycytidine activates iron uptake and heme biosynthesis by increasing c-Myc nuclear localization and binding to the E-boxes of transferrin receptor 1 (TfR1) and ferrochelatase (Fech) genes, J. Biol. Chem. 286 (2011) 37196–37206.
[34] K.J. Wu, A. Polack, R. Dalla-Favera, Coordinated regulation of iron-controlling genes, H-ferritin and IRP2, by c-MYC, Science 283 (1999) 676–679.
[35] F. Kihara-Negishi, H. Yamamoto, M. Suzuki, T. Yamada, T. Sakurai, T. Tamura, T. Oikawa, In vivo complex formation of PU.1 with HDAC1 associated with PU.1-mediated transcriptional repression, Oncogene 20 (2001) 6039–6047.
[36] T. Yamada, N. Kondoh, M. Matsumoto, M. Yoshida, A. Maekawa, T. Oikawa, Overexpression of PU.1 induces growth and differentiation inhibition and apoptotic cell death in murine erythroleukemia cells, Blood 89 (1997) 1383–1393.
[37] D. Donze, T.M. Townes, J.J. Bieker, Role of erythroid Kruppel-like factor in human gamma- to beta-globin gene switching, J. Biol. Chem. 270 (1995) 1955–1959.
[38] L. Wall, N. Destroismaisons, N. Delvoye, L.G. Guy, CAAT/enhancer-binding proteins are involved in beta-globin gene expression and are differentially expressed in murine erythroleukemia and K562 cells, J. Biol. Chem. 271 (1996) 16477–16484.

Biochemical and Biophysical Research Communications 420 (2012) 782–786

Contents lists available at SciVerse ScienceDirect

Biochemical and Biophysical Research Communications

journal homepage: www.elsevier.com/locate/ybbrc

Characterization of Dkk1 gene regulation by the osteoblast-specific transcription factor Osx

Chi Zhang [a,*], Hui Dai [b], Benoit de Crombrugghe [b]

[a] Bone Research Laboratory, Texas Scottish Rite Hospital for Children, University of Texas Southwestern Medical Center, 2222 Welborn St., Dallas, TX 75219, USA
[b] Department of Genetics, University of Texas M.D. Anderson Cancer Center, Houston, TX 77030, USA

ARTICLE INFO

Article history:
Received 4 March 2012
Available online 20 March 2012

Keywords:
Osx
Osterix
Dkk1
Osteoblast
Wnt signaling
Bone formation

ABSTRACT

Bone formation is a developmental process involving the differentiation of mesenchymal stem cells to osteoblasts. Osterix (Osx) is an osteoblast-specific transcription factor required for bone formation and osteoblast differentiation. Previous observation that Osx inhibits Wnt signaling pathway provides a novel concept of feedback control mechanisms involved in bone formation. Wnt antagonist Dickkopf-1 (Dkk1) plays an important role on skeletal development and bone remodeling. Osx has been shown to activate the *Dkk1* promoter; however, the detailed mechanism of Osx regulation on *Dkk1* expression is not fully understood. In this study, quantitative real-time RT-PCR results demonstrated that *Dkk1* expression was downregulated in *Osx*-null calvaria at two different points of E15.5 and E18.5 in mice embryos. Overexpression of Osx resulted in upregulation of *Dkk1* expression in Tet-off stable C2C12 cell line. Inhibition of Osx expression by siRNA led to downregulation of *Dkk1* in osteoblasts. These data suggest that Osx may target Dkk1 directly. To define minimal region of *Dkk1* promoter activated by Osx, we made a series of deletion mutants of *Dkk1* promoter constructs, and narrowed down the minimal region to the proximal 250 bp by transient transfection assay. It was shown that two GC-rich binding sites within this minimal region of *Dkk1* promoter were required for the *Dkk1* promoter activation by Osx. Importantly, quantitative chromatin immunoprecipitation (ChIP) assays were performed to show that endogenous Osx associated with native *Dkk1* promoter in primary osteoblasts. Taken together, these findings support our hypothesis that Dkk1 is a direct target of Osx.

© 2012 Elsevier Inc. All rights reserved.

1. Introduction

Bone formation takes place through two distinct processes: endochondral ossification involving a cartilage model and intramembranous ossification by which bones form directly from condensations of mesenchymal cells without a cartilage intermediate. Bone formation is a highly regulated process involving the differentiation from mesenchymal progenitor cells into preosteoblast, then into osteoblast lineage, and finally into osteocytes [1,2]. Osteoblast differentiation is regulated by different transcription factors and signaling proteins including Indian hedgehog, Runx2, Osterix (Osx) and Wnt signaling pathway. Ihh is required for endochondral but not for intramembranous bone formation [3] and is needed for the establishment of the osteogenic portion of the perichondrium/periosteum and for the initial activation of the gene for Runx2. Runx2 is needed for bone formation since no endochondral and no membranous bones are formed in *Runx2*-null mice [4]. *Runx2* is required for the differentiation of mesenchymal cells into preosteoblasts. As a downstream gene of *Runx2*, *Osx* is required for the differentiation of preosteoblasts into mature osteoblasts. Osx is specifically expressed in all osteoblasts. In *Osx*-null embryos, cartilage is formed normally, but the embryos completely lack bone formation [2]. *Osx* expression pattern in mice indicates that the presence of *Osx* transcript begins as early as the commitment time for mesenchymal cells to enter osteoblast lineage and its signal becomes stronger as osteoblast differentiation occurs. The C terminal region of Osx contains the DNA-binding domain which can bind to specific GC-rich sequences to control target gene expression, such as osteoblast differentiation markers type 1 collagen, bone sialoprotein, and osteocalcin (OC).

Wnt signaling has been studied for its broad range of activities in cell proliferation, differentiation and cell death during both embryonic development and the adult stage in a variety of tissue types including bone [5]. Wnts are secreted glycoproteins that bind to Frizzled family receptors and low-density lipoprotein receptor-related proteins (LRP) 5/6 coreceptors. In the absence of Wnt,

Abbreviations: Osx, osterix; Dkk1, Dickkopf 1; OC, osteocalcin; E15.5, embryonic day 15.5; E18.5, embryonic day 18.5; ChIP, chromatin immunoprecipitation; Dox, Doxycycline; LRP, low-density lipoprotein receptor-related protein.

* Corresponding author. Fax: +1 214 559 7872.
E-mail address: Chi5.Zhang@utsouthwestern.edu (C. Zhang).

0006-291X/$ - see front matter © 2012 Elsevier Inc. All rights reserved.
http://dx.doi.org/10.1016/j.bbrc.2012.03.073

β-catenin forms a complex with the APC, Axin and the kinases glycogen synthase kinase 3, which facilitates phosphorylation and proteosomal degradation of β-catenin. Stimulation of these receptors by Wnts leads to the intracellular molecule β-catenin to accumulate and translocate into the nucleus, where it interacts with TCF/Lef1 transcription factor to activate transcription of target genes. Wnt/β-catenin pathway has been known to play a crucial role in bone formation and bone metabolism [6]. Gain-of-function mutants of *Lrp5* cause high bone mass syndrome in patients [7] and in mice [8]. Conditional inactivation of *β-catenin* in either skeletal progenitor cells or at a later stage of osteoblast development in mouse embryos blocks osteoblast differentiation [9–12].

Inhibitors of Wnt signaling can bind to frizzled (serum frizzled-related proteins), Wnt (Wnt inhibitory factors) or LRP 5/6 (sclerostin and Dickkopf-1). These agonist proteins prevent Wnt from activating the frizzled LRP 5/6 receptor signaling pathway, leading to a decrease in signaling. The canonical Wnt pathway is regulated by a large number of antagonists, including the Dkk family and secreted frizzled-related proteins. Dickkopf (Dkk) is a Wnt antagonist. It binds to LRP5/6 receptor to form a complex with Kremen1 and 2 and inhibits Wnt signaling by reducing the availability of LRP5/6 [5]. To date, four Dkk proteins have been identified in mammals [13], among which Dkk1 and Dkk2 have been well characterized and found to act as antagonists to the canonical Wnt pathway by binding to LRP5/6 in combination with a second coreceptor designated as Kremen [14,15]. Transgenic overexpression of Dkk1 under the control of the ColA1 promoter leads to decreased bone mass [16]. In agreement with this observation, deletion of Dkk1 expression in osteoblasts results in an increase in bone formation and mass [17].

It has been discovered that in addition to its essential role in osteoblast differentiation, the osteoblast-specific transcription factor Osx also inhibits osteoblast proliferation and negatively regulates Wnt/β-catenin signaling [18]. Further data have indicated that Osx controls Wnt signaling by two different mechanisms (i) stimulates Wnt antagonist DKK1 expression and (ii) disrupts Tcf1 binding to DNA to inhibit the transcriptional activity of β-catenin/Tcf. Osx inhibition of Wnt signaling provides a feedback control mechanism involved in bone formation. Osx has been shown to activate the *Dkk1* promoter; however, the detailed mechanism of Osx regulation on Dkk1 expression is not fully understood.

In this study, our results from quantitative real time RT-PCR revealed that Dkk1 expression was downregulated at both E15.5 and E18.5 in the calvaria of *Osx*-null mouse embryos, suggesting Osx is essential for Dkk1 expression. Dkk1 gene regulation by Osx was further characterized. We provide evidences to demonstrate that Dkk1 is a direct target of Osx.

2. Materials and methods

2.1. Plasmid constructs and subcloning

The fragments of Dkk1 promoter region were generated by PCR using mouse genomic DNA as a template and subcloned into the XhoI and MluI sites of pGL-3 vector. Primers were obtained from Integrated DNA Technologies (IDT) (Coralville, IA), and the sequences were as follows: (1) Dkk1-Xho-3 5′TGG TGG AGT CTC TGG CTG CCA, (2) Dkk1-Mlu-2 k 5′GGC ATC TAT GCA AGG TTC AG, (3) Dkk1-Mlu-1 k 5′TAT TAA CCC ACC GCT GGG AAC, (4) Dkk1-Mlu-500 5′TTG ATG AAT GGC TGC TCG CA and (5) Dkk1-Mlu-250 5′TAG TGC TCT AGT GAC CCA CAC. A. Dkk1 point mutants were made with the QuickChange site-directed mutagenesis kit (Stratagene) using Dkk1-250 as a template by the following primers: (1) Dkk1-M1-1 5′GGG ACC ACA GTG CAA TTT ATT TTC GAG GGG AGA GTG TC, (2) Dkk1-M1-2 5′GA CAC TCT CCC CTC GAA AAT AAA TTG CAC TGT GGT CCC, (3) Dkk1-M2-1 5′CGA CAC ACA AAC ACT AAA AAT AAA AGC TCC TCC CAA AGC and (4) Dkk1-M2-2 5′GCT TTG GGA GGA GCT TTT ATT TTT AGT GTT TGT GTG TCG. All constructs including mutants were verified by DNA sequencing.

2.2. Cell culture and transient transfection assay

HEK293 cells (ATCC) were cultured in Dulbecco's modified Eagle's medium (Invitrogen, CA) with 10% fetal bovine serum and 100 units/ml penicillin plus 100 μg/ml streptomycin at 37 °C. HEK293 cells were plated in 12-well plates, cultured to 60–80% confluence and transfected with FuGENE 6 (Roche) according to the manufacture's instruction. Cells were cotransfected with 300 ng of Dkk1 promoter reporter, Osx expression plasmid as indicated and 25 ng of pSV2-beta-gal. After transfection, cells were incubated for 24 h before harvest. The reporter assays were analyzed with BD Monolight system (BD Biosciences). Luciferase activity was normalized by β-galactosidase activity. Every transfection experiment was done at least three times. Values were presented as the mean ± S.D. MC3T3 cells (ATCC) were cultured in Alpha Minimum Essential Medium with ribonucleosides, deoxyribonucleosides, 2 mM L-glutamine and 1 mM sodium pyruvate, but without ascorbic acid (GIBCO), and with 10% FBS and penicillin plus streptomycin. Stable C2C12 mesenchymal cells expressing Osx were generated with pTet-off Advanced Inducible Gene Expression System (Clontech) as previously used [18]. Osx expression was induced in the absence of tetracycline. C2C12 cells were cultured in ATCC described medium with additives G418, Hygromycine, and with or without Doxycycline (Dox), a member of the tetracycline antibiotics group.

2.3. siRNA interference

MC3T3 cells were transfected by siRNA against mouse Osx with Lipofectamine 2000. siRNA oligos were purchased from Thermo Scientific Dharmacon, and siGENOME Lamin A/C Control siRNA was used as a non-specific control. Cells were cultured in 6-well plates. One day before transfection, cells were plated in 1 ml of growth medium without antibiotics. Cells were 30–50% confluent at the time of transfection. For each sample, siRNA:Lipofectamine 2000 transfection complex was prepared as follows: (1) dilute 2 μl of 50 μM siRNA in 50 μl of Opti-MEM I Reduced Serum Medium without serum, (2) mix Lipofectamine 2000 gently, then dilute 3 μl in 50 μl of Opti-MEM I medium, (3) combine the diluted siRNA with the diluted Lipofectamine 2000 and (4) add 100 μl of siRNA:Lipofectamine 2000 complex to each well. After 4 h incubation, the growth medium was replaced. Cells were cultured at 37 °C in a CO_2 incubator for 24 h before harvest.

2.4. Chromatin immunoprecipitation (ChIP) assay

ChIP assay kit was from Millipore. ChIP assays were performed according to previously described protocol [19], provided in Supplementary materials.

3. Results

3.1. Dkk1 expression is down-regulated in the absence of Osx

Our recent studies have demonstrated that Osx can inhibit Wnt signaling, a possible mechanism for Osx to inhibit osteoblast proliferation [18], and that Osx activates Dkk1 expression. In this study, we further characterized Dkk1 regulation by Osx. We carried out quantitative real time RT-PCR to compare RNA levels of Dkk1 between *Osx* wild type and knockout mice at two different points

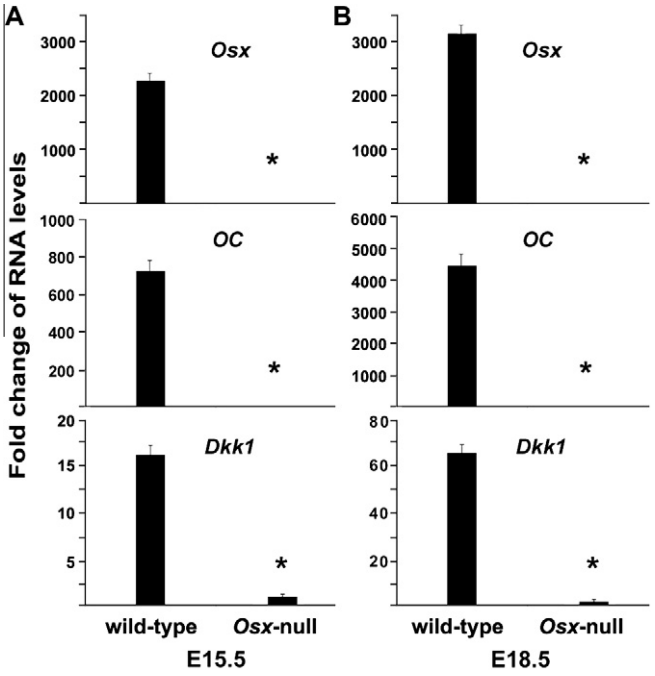


Fig. 1. Effect of Osx on Dkk1 expression. (A) Fold change in RNA levels from E15.5 wild-type and *Osx*-null mice embryos. Calvaria RNAs were isolated from E15.5 *Osx* wild-type and *Osx*-null embryos. (B) Fold change in RNA levels from E18.5 wild-type and *Osx*-null mice embryos. Calvaria RNAs were isolated from E18.5 *Osx* wild-type and *Osx*-null embryos. RNA levels for Osx, OC and Dkk1 were analyzed by quantitative real-time RT-PCR. The level of each RNA from *Osx*-null calvaria was normalized to a value of 1. ∗: a star indicates statistical significance compared to Osx wild type group.

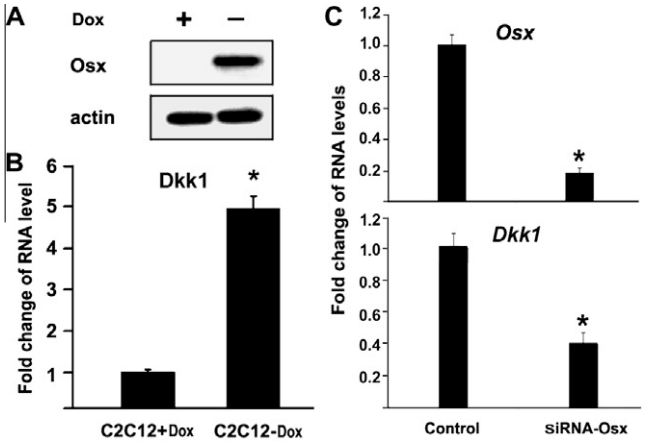


Fig. 2. Osx controls Dkk1 expression. (A) Western immunoblot analysis of the Dox-regulated Osx-expressing C2C12 cells. Osx expression was turned on in the absence of Dox. Beta-actin was used as a loading control. (B) Overexpression of Osx activates Dkk1 gene expression in C2C12 mesenchymal cells. Dkk1 mRNA levels in a stable, Tet-off C2C12 mesenchymal cell line. RNA was obtained from cultures treated with or without Dox. Osx expression was induced in the absence of Dox. Dkk1 mRNA levels were quantitated by real-time RT-PCR. The Dkk1 RNA level obtained from the cells cultured with Dox was normalized to a value of 1. Values are presented as the mean ± SD. A paired *t*-test was performed comparing Dox (−) and Dox (+) groups. ∗: A star indicates statistical significance compared to Dox (+) group. (C) siRNA-directed knockdown of Osx impairs Dkk1 gene expression in MC3T3 osteoblasts. MC3T3 osteoblasts were transfected with siRNA targeting mouse Osx. RNA was isolated 24 h post-transfection. RNA expression levels as determined by quantitative real-time RT-PCR. The RNA level from the control siRNA group was normalized to a value of 1. Values were presented as the mean ± SD. A paired *t*-test was performed comparing si-control group and si-Osx group. ∗: A star indicates statistical significance compared to control group.

of E15.5 and E18.5 in mice embryos. RNA was isolated from calvaria of both E15.5 and E18.5 mouse embryos. As shown in Fig. 1A, Osx expression was abolished at E15.5 in *Osx*-null calvaria. Osteoblast marker gene OC was at undetected level as expected. Interestingly, Wnt signaling antagonist Dkk1 expression was found downregulated by about 16 folds in *Osx*-null calvaria compared with that in wild type calvaria. As shown in Fig. 1B, both Osx and OC expression were abolished at E18.5 in *Osx*-null calvaria. Dkk1 expression was found downregulated by about 64 folds in *Osx*-null calvaria compared with that in wild type calvaria. The marked decrease in *Dkk1* RNA level in *Osx* knockout mice suggests that Osx controls *Dkk1* gene expression.

3.2. Overexpression of Osx activates Dkk1 expression

Next we asked whether Osx could positively regulate Dkk1 expression. To address this question, a C2C12 stable cell line was used in which the expression of Osx could be induced by using the tetracycline (Tet) system as previously described [18]. Osx expression was tuned on in the absence of Dox (Fig. 2A). Total RNA was isolated from C2C12 stable cell line in the presence or absence of Dox and measured by real time RT-PCR for Dkk1 expression. As shown in Fig. 2B, in the absence of Dox when Osx expression was induced, Dkk1 expression was upregulated by about 4.8 folds. This observation indicates that Osx activates Dkk1 expression.

3.3. Inhibition of Osx by siRNA led to repression of Dkk1 expression in osteoblasts

To further confirm the effect of Osx on Dkk1 expression, we used siRNA transfection to knockdown Osx expression in MC3T3 osteoblast cells to determine the possible change of Dkk1 expression. Real-time RT-PCR was performed to analyze mRNA expression level. As shown in Fig. 2C, when Osx RNA expression was decreased by 80% by siRNA against Osx, Dkk1 RNA expression was repressed by 60%. Therefore, these data suggest that Osx regulates Dkk1 positively in osteoblasts.

3.4. Identification of the Osx binding site in the promoter of Dkk1 gene

We have shown Osx can stimulate Dkk1 promoter activity, however it is still not clear which region within Dkk1 promoter is responsible for Osx activation. To address this question, the deletion analysis and transient transfection assay were carried out to narrow down responsible region within 2 kb Dkk1 promoter for Osx activation. Dkk1 luciferase reporter constructs driven by different lengths of Dkk1 promoter region were generated. As shown in Fig. 3A, Osx was able to activate Dkk1 promoter reporters of Dkk1-2 kb, Dkk1-1 kb, Dkk1-500 bp and Dkk1-250 bp in transient transfection assay. Previous study has shown that Osx is a zinc finger-containing transcription factor and belongs to the Sp/XKLF family [2]. This family of transcription factors tends to bind to GC-rich sequence in target gene promoter region to control target gene expression. According to the sequence analysis of the region within 250 bp of Dkk1 promoter, two tentative binding sites for Osx were identified as GC rich elements. To test which binding site is responsible for Dkk1 promoter activation by Osx, we generated two point mutants of Dkk1-250 promoter reporter by the QuickChange site-directed mutagenesis kit (Stratagene) using Dkk1-250 bp as a template. The two mutants were designated Dkk1-250-M1 and Dkk1-250-M2, in which the guanines (Gs) and the cytosine (Cs) in each element were replaced with thymine (Ts) and adenines (As) respectively. As shown in Fig. 3B, Osx activation of the Dkk1-250-M1 and Dkk1-250-M2 promoter mutants

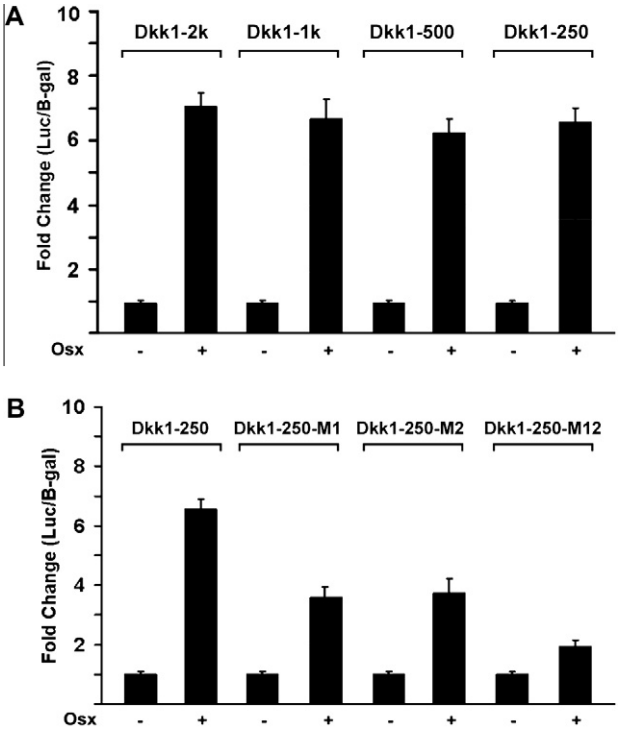


Fig. 3. Identification of the Osx binding site in the promoter of *Dkk1* gene. (A) Deletion analysis of *Dkk1* promoter reporter activated by Osx. Dkk1-2 k, Dkk1-1 k, Dkk1-500 bp and Dkk1-250 bp *Dkk1* promoter reporter plasmids were constructed. Each plasmid was cotransfected with Osx expression plasmid in HEK293 cells. Luciferase activity was normalized by β-galactosidase activity. (B) The two GC-rich elements are responsible for *Dkk1* promoter reporter activation by Osx. Dkk1-250-M1, Dkk1-250-M2 point mutants and double mutant Dkk1-250-M12 were constructed. Each plasmid was cotransfected with Osx expression plasmid in HEK293 cells. Luciferase activity was normalized by β-galactosidase activity.

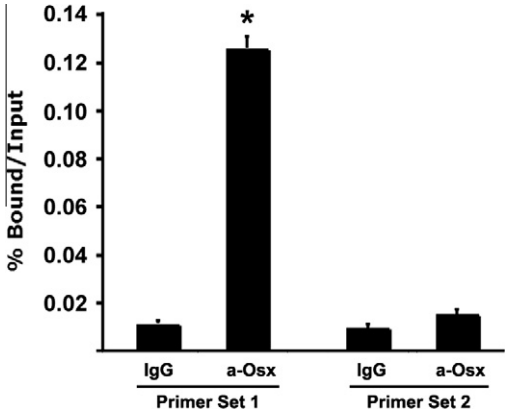


Fig. 4. Endogenous Osx in primary osteoblasts is associated with the native *Dkk1* promoter *in vivo*. Chromatin immunoprecipitation (ChIP) assays were conducted using primary calvarial osteoblasts isolated from new born wild-type mice. Anti-Osx antibody (a-Osx) was used for ChIP analysis, and IgG was used as a negative control. The precipitated chromatin was analyzed by quantitative real-time PCR. As described in the Methods, Primer set 1 corresponds to a segment covering two GC-rich elements within 250 bp the *Dkk1* promoter. As a negative control, Primer set 2 covers a distal 3 kb region of the *Dkk1* promoter, which does not contain GC-rich sequences. A paired *t*-test was performed comparing IgG and a-Osx group. ∗: A star indicates statistical significance compared to IgG control group.

was only 55% and 58% respectively, that of the wild-type Dkk1-250 bp promoter. Finally, we generated a double mutant in which both GC-rich elements were disrupted (Dkk1-250-M12). As shown in Fig. 3B, Dkk1-250-M12 mutant almost abolished Osx activation of the Dkk1-250 bp promoter reporter. Thus, these results revealed that two GC-rich sequences in Dkk1-250 bp region were responsible for *Dkk1* promoter activation by Osx.

3.5. Osx associates with native Dkk1 promoter in vivo

The studies above indicate that Osx can positively regulate Dkk1 expression and activate the *Dkk1* promoter *in vitro* through two GC-rich sequences in *Dkk1* promoter. Next we tested whether endogenous Osx can bind to the native *Dkk1* promoter *in vivo*. Therefore, ChIP assay was performed to determine whether Osx could associate with *Dkk1* promoter in primary calvarial cells isolated from new born wild-type mice. Two sets of primers were designed. Primer set 1 covered GC-rich element identified within 250 bp *Dkk1* promoter in Fig. 3. Primer set 2 covered a sequence without GC-rich region at the distal 3 kb of *Dkk1* promoter. Anti-Osx antibody was used as previously described for ChIP analysis [18]. The precipitated chromatin was analyzed by quantitative real-time PCR using Primer set 1 and 2. As shown in Fig. 4, Osx was found to associate with the *Dkk1* promoter region containing GC rich sequence (Primer set 1) compared with IgG control group. Osx did not associate with the distal *Dkk1* promoter region without GC rich sequence (Primer set 2), demonstrating that the observed Osx–DNA association was specific. The data suggest that Osx associates with *Dkk1* promoter *in vivo*.

4. Discussion

Osx is an osteoblast-specific transcription factor that controls the expression of essential genes needed for appropriate osteoblast differentiation and function. Osx inhibits Wnt pathway. In this study, we further characterized Osx regulation on Wnt antagonist Dkk1 expression. The findings presented here support our hypothesis that Dkk1 is a direct target of Osx.

First, we identified Dkk1 as an Osx target gene. This is supported by the Osx-directed gene expression studies in several *in vivo* and *in vitro* model systems. For example, *Osx*-null calvaria displayed defective *in vivo* expression of Dkk1 at E15.5 and E18.5 compared to wild-type calvaria in mice (Fig. 1). A Tet-off inducible C2C12 stable cell system revealed that ectopic expression of Osx resulted in an increase in Dkk1 transcript level (Fig. 2B) and MC3T3 osteoblast cultures also had markedly impaired *Dkk1* gene expression when Osx expression was knocked-down using siRNA targeting strategies (Fig. 2C). Moreover, a direct regulation of *Dkk1* gene transcription by Osx was evident in the ability of recombinant Osx to activate *Dkk1* promoter-reporter constructs (Fig. 3A), thus indicating that the RNA expression studies were likely due to the effects of Osx expression on *Dkk1* gene transcription.

In terms of mechanism, Osx is an SP/KLF family member that presumably functions by binding directly to DNA promoter elements via an SP1-like DNA-binding domain consisting of three C2H2-type zinc fingers located within its C-terminus [2]. They likely are GC-rich in nature based on the similarities of DNA-binding domains and elements among this family of transcription factors. Indeed, two GC-rich regions exist in the most proximal regions of the murine *Dkk1* promoter. Importantly, our studies define these two elements as critical for mediating the transcriptional activation of the *Dkk1* promoter by Osx. Mutation of each element (Dkk1-250-M1 or Dkk1-250-M2) reduced Osx-directed activation of the *Dkk1* promoter by approximately 50% and mutation of both elements Dkk1-250-M12 nearly abolished the response (Fig. 3B). Of course, limitations of this particular approach include the heterologous expression and somewhat artificial nature of the plasmid DNA constructs used as a measure of a biologically relevant transcriptional event. Thus, the chromatin immunoprecipitation approaches (Fig. 4) strongly support the reporter gene expression

data. These studies clearly demonstrated that endogenous Osx was associated with the GC-rich proximal region of the native *Dkk1* promoter in primary osteoblastic cells. These studies help establish Osx mechanisms involving direct binding of Osx to sequence specific, GC-rich promoter elements to activate the expression of genes in osteoblastic cells.

Wnt signaling is known to have the major impact at different stages of bone formation and bone metabolism [5,6]. Wnt signaling-mediated gene expression can promote osteoblast proliferation and differentiation. Some studies investigated the role of Wnt/β-catenin signaling in nonunion and osteoporosis, suggesting Wnt signaling could possibly have potential to become a target of pharmacological intervention to increase bone formation [20,21]. Dkk1 is one of the Wnt antagonists. Our observation that *Dkk1* expression is absent in *Osx*-null calvaria of at both E15.5 and E18.5 embryos parallels the previously reported finding that *Dkk1* expression was absent in tibia of E18.5 embryos in which β-catenin was inactivated using an *Osx-Cre* transgene [12]. This suggests that both Osx and β-catenin are required for *Dkk1* expression in osteoblasts. Thus, the *Dkk1* gene might be a common target of these transcription factors in these cells. Due to the important role of Wnt signaling during bone formation, it will be interesting to investigate regulations of Wnt signaling. Osx is required for osteoblast differentiation and bone formation [2]. Previous study has demonstrated that Osx inhibits Wnt signaling activity during bone formation, a possible mechanism for the inhibition by Osx of osteoblast proliferation [18]. The findings in this study that Osx controls *Dkk1* expression should further reinforce the feedback control effect that Dkk1 exerts on Wnt/β-catenin signaling.

In summary, we performed *in vitro* and *in vivo* experiments to demonstrate that the Wnt antagonist Dkk1 is a direct target of osteoblast-specific transcription factor Osx in osteoblasts.

Acknowledgments

Work in Bone Research Laboratory is supported by Research Grant from Arthritis Foundation (To C. Zhang) and RAP01 grant from Texas Scottish Rite Hospital for Children (To C. Zhang).

Appendix A. Supplementary data

Supplementary data associated with this article can be found, in the online version, at http://dx.doi.org/10.1016/j.bbrc.2012.03.073.

References

[1] R.T. Franceschi, C. Ge, G. Xiao, H. Roca, D. Jiang, Transcriptional regulation of osteoblasts, Cells Tissues Organs 189 (2009) 144–152.
[2] K. Nakashima, X. Zhou, G. Kunkel, Z. Zhang, J.M. Deng, R.R. Behringer, B. de Crombrugghe, The novel zinc finger-containing transcription factor osterix is required for osteoblast differentiation and bone formation, Cell 108 (2002) 17–29.
[3] B. St-Jacques, M. Hammerschmidt, A.P. McMahon, Indian hedgehog signaling regulates proliferation and differentiation of chondrocytes and is essential for bone formation, Genes Dev. 13 (1999) 2072–2086.
[4] T. Komori, H. Yagi, S. Nomura, A. Yamaguchi, K. Sasaki, K. Deguchi, Y. Shimizu, R.T. Bronson, Y.H. Gao, M. Inada, M. Sato, R. Okamoto, Y. Kitamura, S. Yoshiki, T. Kishimoto, Targeted disruption of Cbfa1 results in a complete lack of bone formation owing to maturational arrest of osteoblasts, Cell 89 (1997) 755–764.
[5] E. Piters, E. Boudin, W. Van Hul, Wnt signaling: a win for bone, Arch. Biochem. Biophys. 473 (2008) 112–116.
[6] R. Baron, G. Rawadi, S. Roman-Roman, Wnt signaling: a key regulator of bone mass, Curr. Top. Dev. Biol. 76 (2006) 103–127.
[7] R.D. Little, J.P. Carulli, R.G. Del Mastro, J. Dupuis, M. Osborne, C. Folz, S.P. Manning, P.M. Swain, S.C. Zhao, B. Eustace, M.M. Lappe, L. Spitzer, S. Zweier, K. Braunschweiger, Y. Benchekroun, X. Hu, R. Adair, L. Chee, M.G. FitzGerald, C. Tulig, A. Caruso, N. Tzellas, A. Bawa, B. Franklin, S. McGuire, X. Nogues, G. Gong, K.M. Allen, A. Anisowicz, A.J. Morales, P.T. Lomedico, S.M. Recker, P. Van Eerdewegh, R.R. Recker, M.L. Johnson, A mutation in the LDL receptor-related protein 5 gene results in the autosomal dominant high-bone-mass trait, Am. J. Hum. Genet. 70 (2002) 11–19.
[8] P. Babij, W. Zhao, C. Small, Y. Kharode, P.J. Yaworsky, M.L. Bouxsein, P.S. Reddy, P.V. Bodine, J.A. Robinson, B. Bhat, J. Marzolf, R.A. Moran, F. Bex, High bone mass in mice expressing a mutant LRP5 gene, J. Bone Miner. Res. 18 (2003) 960–974.
[9] T.F. Day, X. Guo, L. Garrett-Beal, Y. Yang, Wnt/beta-catenin signaling in mesenchymal progenitors controls osteoblast and chondrocyte differentiation during vertebrate skeletogenesis, Dev. Cell 8 (2005) 739–750.
[10] T.P. Hill, D. Spater, M.M. Taketo, W. Birchmeier, C. Hartmann, Canonical Wnt/beta-catenin signaling prevents osteoblasts from differentiating into chondrocytes, Dev. Cell 8 (2005) 727–738.
[11] H. Hu, M.J. Hilton, X. Tu, K. Yu, D.M. Ornitz, F. Long, Sequential roles of hedgehog and Wnt signaling in osteoblast development, Development 132 (2005) 49–60.
[12] S.J. Rodda, A.P. McMahon, Distinct roles for hedgehog and canonical Wnt signaling in specification, differentiation and maintenance of osteoblast progenitors, Development 133 (2006) 3231–3244.
[13] Y. Kawano, R. Kypta, Secreted antagonists of the Wnt signalling pathway, J. Cell Sci. 116 (2003) 2627–2634.
[14] B. Mao, W. Wu, Y. Li, D. Hoppe, P. Stannek, A. Glinka, C. Niehrs, LDL-receptor-related protein 6 is a receptor for Dickkopf proteins, Nature 411 (2001) 321–325.
[15] B. Mao, W. Wu, G. Davidson, J. Marhold, M. Li, B.M. Mechler, H. Delius, D. Hoppe, P. Stannek, C. Walter, A. Glinka, C. Niehrs, Kremen proteins are Dickkopf receptors that regulate Wnt/beta-catenin signalling, Nature 417 (2002) 664–667.
[16] J. Li, I. Sarosi, R.C. Cattley, J. Pretorius, F. Asuncion, M. Grisanti, S. Morony, S. Adamu, Z. Geng, W. Qiu, P. Kostenuik, D.L. Lacey, W.S. Simonet, B. Bolon, X. Qian, V. Shalhoub, M.S. Ominsky, H. Zhu Ke, X. Li, W.G. Richards, Dkk1-mediated inhibition of Wnt signaling in bone results in osteopenia, Bone 39 (2006) 754–766.
[17] F. Morvan, K. Boulukos, P. Clement-Lacroix, S. Roman Roman, I. Suc-Royer, B. Vayssiere, P. Ammann, P. Martin, S. Pinho, P. Pognonec, P. Mollat, C. Niehrs, R. Baron, G. Rawadi, Deletion of a single allele of the Dkk1 gene leads to an increase in bone formation and bone mass, J. Bone Miner. Res. 21 (2006) 934–945.
[18] C. Zhang, K. Cho, Y. Huang, J.P. Lyons, X. Zhou, K. Sinha, P.D. McCrea, B. de Crombrugghe, Inhibition of Wnt signaling by the osteoblast-specific transcription factor Osterix, Proc. Natl. Acad. Sci. USA 105 (2008) 6936–6941.
[19] C. Zhang, D.R. Dowd, A. Staal, C. Gu, J.B. Lian, A.J. van Wijnen, G.S. Stein, P.N. MacDonald, Nuclear coactivator-62 kDa/Ski-interacting protein is a nuclear matrix-associated coactivator that may couple vitamin D receptor-mediated transcription and RNA splicing, J. Biol. Chem. 278 (2003) 35325–35336.
[20] P.S. Issack, D.L. Helfet, J.M. Lane, Role of Wnt signaling in bone remodeling and repair, HSS J. 4 (2008) 66–70.
[21] V. Krishnan, H.U. Bryant, O.A. Macdougald, Regulation of bone mass by Wnt signaling, J. Clin. Invest. 116 (2006) 1202–1209.

Biochemical and Biophysical Research Communications 420 (2012) 787–792

Contents lists available at SciVerse ScienceDirect

Biochemical and Biophysical Research Communications

journal homepage: www.elsevier.com/locate/ybbrc

MicroRNA-320a suppresses human colon cancer cell proliferation by directly targeting β-catenin

Jian-Yong Sun [a,b,1], Yi Huang [c,1], Ji-Peng Li [b,1], Xiang Zhang [a], Lei Wang [a], Yan-Ling Meng [d], Bo Yan [a], Yong-Qian Bian [b], Jing Zhao [a], Wei-Zhong Wang [b,*], An-Gang Yang [a,d,*], Rui Zhang [a,*]

[a] State Key Laboratory of Cancer Biology, Department of Biochemistry and Molecular Biology, Fourth Military Medical University, 710032 Xi'an, China
[b] State Key Laboratory of Cancer Biology, Xijing Hospital of Digestive Diseases, Fourth Military Medical University, 710032 Xi'an, China
[c] Department of Anesthesiology, Xijing Hospital, Fourth Military Medical University, 710032 Xi'an, China
[d] Department of Immunology, Fourth Military Medical University, 710032 Xi'an, China

ARTICLE INFO

Article history:
Received 12 March 2012
Available online 20 March 2012

Keywords:
MicroRNA
Colorectal cancer
β-Catenin
Proliferation

ABSTRACT

Recent profile studies of microRNA (miRNA) expression have documented a deregulation of miRNA (miR-320a) in human colorectal carcinoma. However, its expression pattern and underlying mechanisms in the development and progression of colorectal carcinoma has not been elucidated clearly. Here, we performed real-time PCR to examine the expression levels of miR-320a in colon cancer cell lines and tumor tissues. And then, we investigated its biological functions in colon cancer cells by a gain of functional strategy. Further more, by the combinational approaches of bioinformatics and experimental validation, we confirmed target associations of miR-320a in colorectal carcinoma. Our results showed that miR-320a was frequently downregulated in cancer cell lines and colon cancer tissues. And we demonstrated that miR-320a restoration inhibited colon cancer cell proliferation and β-catenin, a functionally oncogenic molecule was a direct target gene of miR-320a. Finally, the data of real-time PCR showed the reciprocal relationship between miR-320a and β-catenin's downstream genes in colon cancer tissues. These findings indicate that miR-320a suppresses the growth of colon cancer cells by directly targeting β-catenin, suggesting its application in prognosis prediction and cancer treatment.

© 2012 Elsevier Inc. All rights reserved.

1. Introduction

Colorectal cancer is one of the major causes for cancer-associated death in the world [1]. With the development of advanced genomic technology, the global genomic landscape and critical gene mutations in colorectal cancer have been well documented [2–4]. Based on genetic animal models, it has been proposed that the development and progression of colorectal cancer is from cumulative stepwise genetic changes in key genes controlling cell proliferation, apoptosis and invasion [5]. Although abnormally high activation of multiple signaling pathways such as the WNT/APC/β-catenin pathway and RAS/RAF pathway have been demonstrated to be required for the initiation and progression of colorectal cancer, previous analyses of the genetic mutations still can not clearly define the underlying mechanism of human colorectal carcinoma [6].

MicroRNAs (miRNAs) are endogenous small non-coding RNA molecules capable of silencing protein coding genes by binding complementary sequences in 3′-untranslated regions (3′-UTR) of target mRNAs to induce their degradation or translational repression [7,8]. An increasing body of evidence has suggested that the aberrant expression of miRNAs may lead to the development and progression of malignant diseases. Based on their expression patterns in cancer tissues, miRNAs can be classified as oncomirs and tumor suppressive miRNAs. The high level expression of oncomirs or the low level expression of tumor suppressive miRNAs is frequently associated with poor prognosis for clinical patients, indicating that the forced expression of tumor suppressive miRNAs or the decreased expression of endogenous oncomirs could be a promising strategy for cancer therapeutics [9]. In recent years, functional studies have demonstrated that microRNA-mediated posttranscriptional regulation can coordinately target multiple genes to promote the development and progression of colorectal cancer [10]. Given the fundamental biological processes regulated by microRNAs and the knowledge that many of these processes are altered in colon cancers, it follows that we should investigate the

Abbreviations: CRC, colorectal cancer; miRNA, microRNA; qRT-PCR, quantitative real time polymerase chain reaction; MTT, 3-(4,5-dimethylthiazol-2-yl)-2,5-diphenyl tetrazolium bromide; FBS, fetal bovine serum; UTR, untranslated regions; WT, wild type; Mut, mutant; Lv, lentivirus; NC, nonsense control.

* Corresponding authors. Address: Department of Immunology, Fourth Military Medical University, 710032 Xi'an, China (A.-G. Yang). Fax: +86 29 83253816.
E-mail addresses: weichang@fmmu.edu.cn (W.-Z. Wang), agyang@fmmu.edu.cn (A.-G. Yang), ruizhang@fmmu.edu.cn (R. Zhang).

[1] These authors contributed equally.

0006-291X/$ - see front matter © 2012 Elsevier Inc. All rights reserved.
http://dx.doi.org/10.1016/j.bbrc.2012.03.075

biological function and underlying mechanism of microRNAs in these processes [11]. Recently, a clinical study reported that downregulation of miR-320a expression was associated with a poor prognosis for clinical patients with colon cancer in stage II [12]. However, until now, functional evidence of miR-320a in colon cancer has not been well documented.

In the present study, we investigated the potential involvement of miR-320a in colon cancer. We examined the expression level of miR-320a in human colon cancer cells and cancer tissues, and tested its effects on cell growth, cell-cycle distribution, and colony formation *in vitro*. Further more, we explored the proper underlying mechanism of miR-320a's function in colon cancer cells. And finally, we also analyzed the possible relationship between miR-320a and its downstream genes in collected colorectal cancer tissues. Our study would provide a better understanding of colon cancer pathogenesis.

2. Result

2.1. MiR-320a is downregulated in colon cancer tissues and colon cancers cell lines

The expression level of miR-320a in a panel of human colon cancers cell lines was first quantitatively analyzed. The result of qRT-PCR showed that the miR-320a expression was decreased in all three colon cancer cell lines examined compared with an immortalized non-tumorigenic cell line GES (Fig. 1A). We further examined the expression level of miR-320a in 40 colon cancer specimens and their paired adjacent normal tissues. Consistent with the data obtained from colon cancer cell lines, the average expression level of miR-320a was significantly lower in colon cancer specimens than in paired adjacent normal tissues (Fig. 1B). These results indicated that the expression of miR-320a is significantly decreased in human colorectal cancer specimens and cell lines.

2.2. MiR-320a induces growth inhibition in colon cancer cells

To explore the effect of miR-320a on cell growth, we used lentiviral vectors to stably restore the expression of miR-320a in SW480 and HCT116 colon cancer cells and examined cell growth rate and cell-cycle distribution. By using qRT-PCR, we found that the expression levels of miR-320a were increased to about 300 folds in both SW480 and HCT116 cells compared with them in the control cells (Fig. 2A). As shown in Fig. 2B, the results of MTT assay displayed that overexpression of miR-320a inhibited cell growth in SW480 and HCT116 colon cancer cells, whereas the control had no effect on cell growth. Further more, the colony formation assay was performed to determine the long-term impact of miR-320a on cell growth. As shown in Fig. 2C, LV-miR320a-infected SW480 and HCT116 cells displayed much fewer and smaller colonies than in LV-Luc-infected cells. We proposed that the reduced proliferation in miR-320a-overexpressing colon cancer cells may be due to altered cell cycle progression. The analysis of cell cycle distribution showed that miR-320a-overexpressing SW480 and HCT116 cells were blocked in the G1 phase, with a corresponding reduction in the percentage of S and G2/M phases (Fig. 2D). These results suggested that miR-320a may function as a negative regulator of cancer cell proliferation by arresting cell cycle progression in G1 phase.

2.3. β-catenin is a direct target gene of miR-320a in colon cancer cells

Since miR-320a had a profound impact on colon cancer cell proliferation, we reasoned that the specific genes suppressed by miR-320a should predominantly function in this process. According to the information in KEGG pathway, our interest focused on the functional molecules involved in the development and progression of colorectal carcinoma (Supplementary Fig. 1). Strikingly, by using computational prediction [13], we found that the 3′UTR of β-catenin mRNA contains one miR-320a binding site (Fig. 3A). It has been widely accepted that the abnormally high activation of β-catenin plays a critical role in unlimited proliferation of colon cancer cells. To assess miRNA binding to the 3′UTR, we constructed luciferase reporters with the β-catenin 3′UTR. Subsequently, the constructs were transiently transfected into 293 cells along with miR-320a or NC mimics and relative luciferase activity was measured at 48 h. The relative luciferase activity of the construct with wild-type 3′-UTR was significantly repressed by 40% following miR-320a transfection (Fig. 3B). However, site-directed mutagenesis of the miR-320a binding site within β-catenin's 3′ UTR completely abolished this suppression (Fig. 3B), suggesting that miR-320a directly binds to this site. Consistently, overexpression of miR-320a in colon cancer cells downregulated endogenous β-catenin in protein levels but not in mRNA levels (Fig. 3C and D). These findings indicated that miR-320a may negatively regulate the β-catenin expression via inhibiting the translation of β-catenin but do not have any impact on mRNA stability.

2.4. Overexpression of miR-320a inhibits β-catenin-mediated transcriptional activity in colon cancer cell lines

Given that β-catenin is a direct target of miR-320a, it is logical to speculate that downregulation of β-catenin's target genes such as c-myc, CCND1 and survivin might be a major cause for the inhibitory effect of miR-320a in colon cancer cell proliferation [14–16]. To test this hypothesis, we performed Western blot and

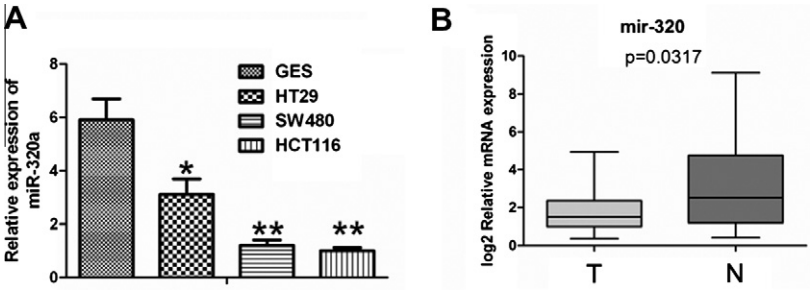


Fig. 1. The expression levels of miR-320a in CRC tissues and colon cancer cell lines. (A) Expression levels of miR-320a were examined by qRT-PCR in GES cells and three colon cancer cell lines. Experiments were performed three times. Data are presented as means ± SE (*$P < 0.05$, **$P < 0.01$, independent t test). (B) Expression levels of mature miR-320a in 40 paired CRC and adjacent non-tumor tissues. Alteration of expression was shown as box plot presentations, with the y axis indicating miR-320a expression. The mean level of miR-320a expression in CRCs was significantly lower than that in non-tumour tissues. ($P < 0.05$, independent t test). T: tumor tissues; N: adjacent normal tissues.

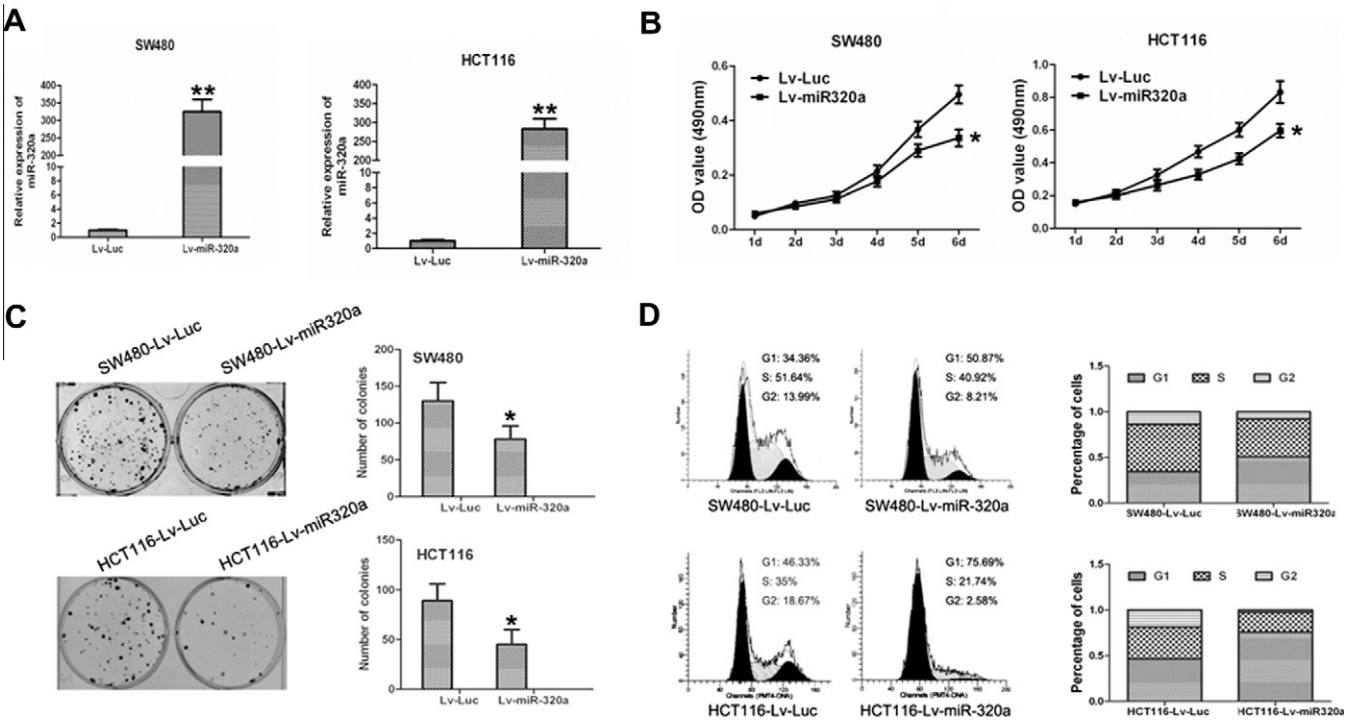


Fig. 2. Lentivirus-mediated expression of miR-320a inhibited cell proliferation and colony formation in colon cancer cell lines. (A) Analysis of qRT-PCR to show lentivirus-mediated expression of miR-320a in SW480 and HCT116 colon cancer cells (**$P < 0.01$, independent t test). (B) Analysis of MTT assay in colon cancer cells infected with Lv-Luc or Lv-miR-320a. Values at the indicated time points were provided as the mean absorbance with an SD of six wells (*$P < 0.05$, independent t test). (C) Colonies formed by Lv-Luc or Lv-miR-320a infected cancer cells were shown 2 weeks after plating. Right panel showed the quantification of the relative colony formation in Lv-Luc versus Lv-miR320a-infected cells (*$P < 0.05$, independent t test). (D) Impact of miR-320a on cell cycle of cancer cells. Cells were cultured in a serum-free condition for 24 h and were released by culturing in cell culture medium with 10% fetal bovine serum for another 16 h and were then collected for cell cycle profile analysis by flow cytometry. The percentage of cells in G1, S, and G2 phases is shown in the left panel. And the statistic analysis is also shown in the right panel.

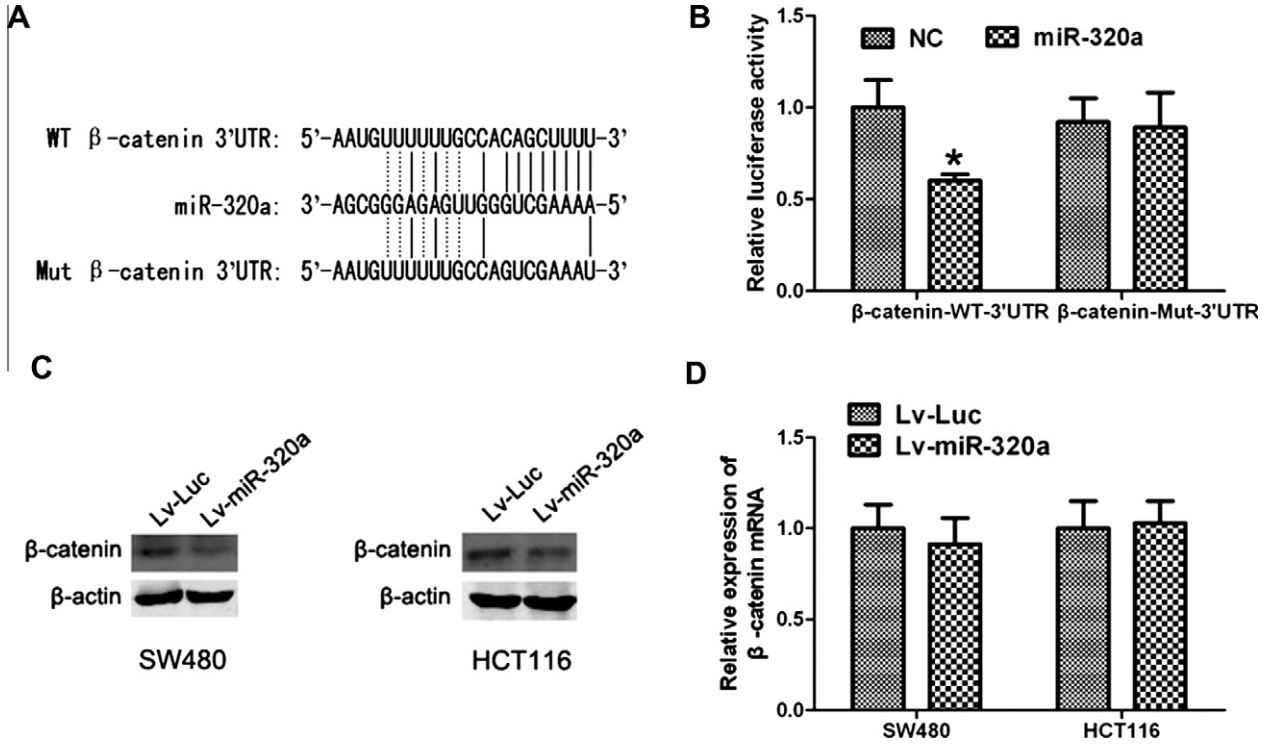


Fig. 3. β-Catenin is a direct target of miR-320a in colon cancer cells. (A) Putative miR-320a-binding sequence in the 3′-UTR of β-Catenin mRNA. Mutation was generated on the β-Catenin 3′-UTR sequence in the complementary site for the seed region of miR-320a, as indicated. (B) Analysis of luciferase activity. 293 cells were co-transfected with a control Renilla luciferase expression construct pRL-TK, firefly luciferase reporter plasmid containing either wild-type or mutant β-Catenin 3′-UTR (indicated as WT or MUT on the X-axis), and either the miR-320a mimics or NC mimics. Luciferase activity was assayed 48 h after transfection. Firefly luciferase activity of each sample was normalized by Renilla luciferase activity. The normalized luciferase activity for the NC-transfected cells was set as relative luciferase activity 1. Columns showed the mean of at least three independent experiments done in duplicate (*$P < 0.05$, independent t test). (C) Analysis of expression levels of endogenous β-catenin in colon cancer cells infected with Lv-Luc or Lv-miR-320a by using Western blot. (D) Analysis of expression levels of endogenous β-catenin in colon cancer cells infected with Lv-Luc or Lv-miR-320a by using qRT-PCR.

qRT-PCR to detect the expression patterns of c-myc, CCND1 and survivin in miR-320a-overexpressing colon cancer cells. As shown in Fig. 4A and B, exogenous expression of miR-320 downregulated the expression levels of c-myc, CCND1 and survivin in both mRNA and protein levels. Taken together, all these results demonstrate that β-catenin is a *bona fide* target gene of miR-320a in colon cancer cells and miR-320a suppresses colon cancer cell proliferation by inhibition of β-catenin-mediated transcriptional activity.

2.5. β-Catenin is a functional mediator for miR-320a in CRC cells

If β-catenin indeed acts as a functional target of miR-320a in CRC cells, reintroduction of β-catenin into miR-320a-expressing cells should be able to antagonize the effects of miR-320a on its target genes. To test the hypothesis, we stably transferred a vector-based β-catenin without the 3′-UTR into miR-320a-expressing CRC cells. As shown in Fig. 4C, the expression levels of CCND1, c-myc and survivin were recovered after exogenous expression of wild-type of β-catenin. These results indicate that β-catenin is a functional mediator for miR-320a in CRC cells.

2.6. miR-320a levels are inversely correlated with mRNA expression of β-catenin's target genes in colon cancer tissues

As reported previously, miR-320a is downregulated in several types of cancers including colon cancer and intrahepatic cholangiocarcinoma [17,18]. Analogously, a high transcriptional activation of β-catenin has been documented in more than 60% of colorectal carcinomas [6]. In light of our observation that miR-320a is capable of downregulating β-catenin expression, it is logical to postulate that the expression of miR-320a may be correlated with the expression levels of β-catenin's downstream genes in human colorectal carcinoma. To validate this hypothesis, the expression of mature miR-320a and β-catenin's downstream genes, including c-myc, CCND1 and survivin was analyzed by qRT-PCR in colorectal cancer tissues and paired adjacent normal tissues. As shown in Fig. 4D, the expression levels of endogenous miR-320a were negatively correlated with the mRNA expression levels of β-catenin's downstream genes, including c-myc, CCDN1 and survivin, whereas there was no obvious correlation between the mRNA expression of miR-320a and β-catenin's target genes in 40 paired adjacent normal tissue samples (Fig. 4E). These results further confirmed a functional link between miR-320a and β-catenin in human colorectal carcinoma.

3. Discussion

In the past one decade, emerging evidence has demonstrated an important role of miRNAs in pathogenesis of cancers [19]. Virtually, all tested tumor types are characterized by globally abnormal miRNA expression patterns, and miRNA profiles are highly informative for cancer classification, prognosis, and response to therapy [20,21]. Moreover, increasing studies demonstrate a functional contribution of specific miRNAs to cellular transformation and tumorigenesis. And functional studies have directly documented the potent pro- and anti-tumorigenic activity of specific miRNAs both *in vitro* and *in vivo* [22]. In a recent study, it has been reported that the clinical patients suffering from colorectal cancer in stage II had a favorable prognosis when they had a higher level expression of miR-320a. However, few studies are available on its functions

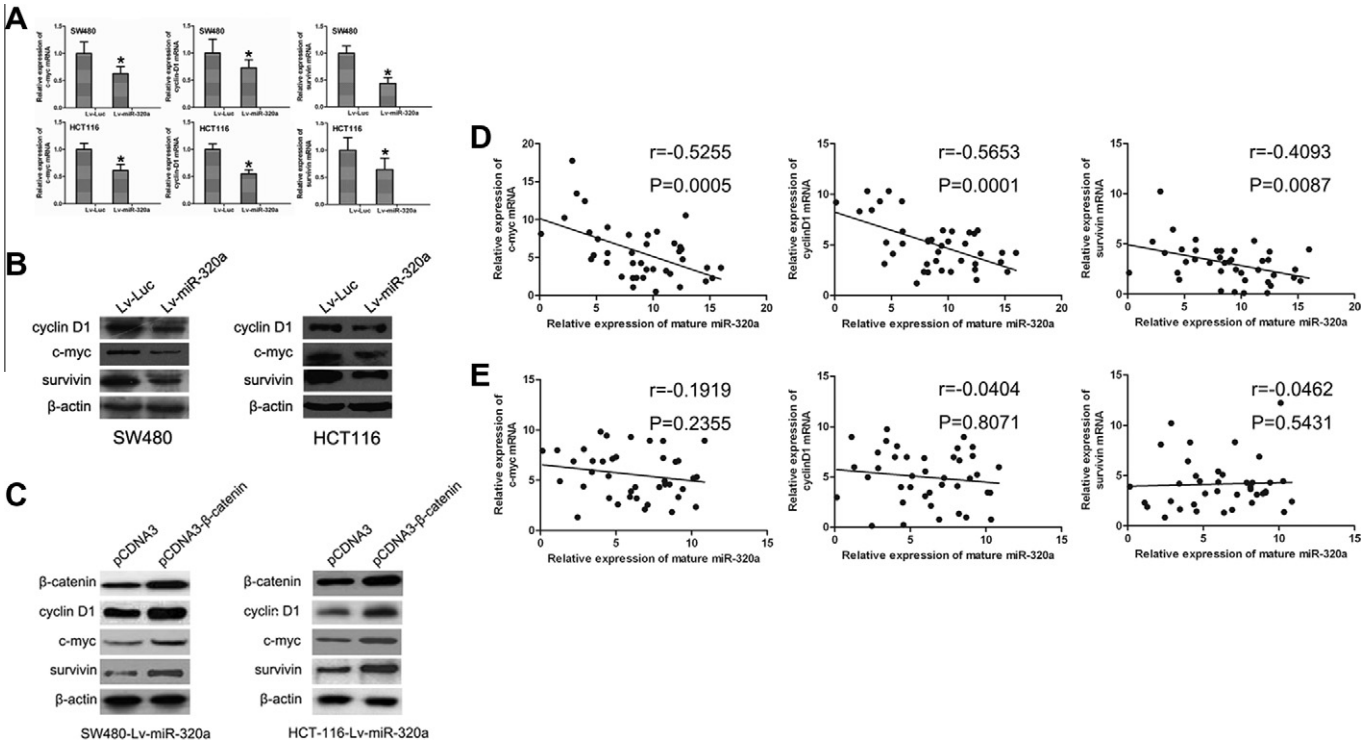


Fig. 4. β-Catenin is a functional mediator for miR-320a in CRC cells. (A) Analysis of expression levels of c-myc, CCND1 and survivin in colon cancer cells infection with Lv-Luc or Lv-miR-320a by using qRT-PCR (*$P < 0.05$, independent t test). (B) Analysis of expression levels of c-myc, CCND1 and survivin in colon cancer cells infection with Lv-Luc or Lv-miR-320a by using Western blot. (C) Western blot analysis of expression levels of c-myc, CCND1 and survivin in Lv-miR-320a-infected colon cancer cells after a stable transfection of wild-type of β-catenin without 3′-UTR. (D) Expression levels of miR-320a are negatively correlated with c-myc, CCND1 and survivin in human colorectal cancer tissues. Pearson's correlation analysis of the relative expression levels of miR-320a (normalized to U6) and the relative expression levels of c-myc, CCND1 and survivin mRNA (normalized to β-actin) determined using qRT-PCR in 40 human colorectal carcinoma tissue samples. (E) Expression levels of miR-320a are not obviously correlated with c-myc, CCND1 and survivin in paired adjacent normal tissues. Pearson's correlation analysis of the relative expression levels of miR-320a (normalized to U6) and the relative expression levels of c-myc, CCND1 and survivin mRNA (normalized to β-actin) determined using qRT-PCR in 40 paired adjacent normal tissue samples.

[12]. It is commonly accepted that colorectal cancer in stage II always has a high activation of proliferation but does not have invasive characteristics [6], so we hypothesized that miR-320a may function as a proliferation inhibitor. In the present, we found that downregulation of miR-320a was a frequent event in colorectal cancer tissues and cancer cell lines. In functional studies, reintroduction of miR-320a dramatically suppressed colon cancer cell proliferation and colony formation, and induced cell cycle arrest in G1 phase, indicating its potential tumor suppressive role in CRC cells.

In previous studies, it was reported that miR-320a expression was downregulated in human intrahepatic cholangiocarcinoma [17,18]. Overexpression of miR-320a can induce apoptosis of cancer cells by directly targeting Mcl-1, an anti-apoptotic molecule [18]. And recently, one report showed that the expression level of miR-320 family members decreased in colon cancer stem-like cells, indicating that miR-320 may function to prompt the differentiation of colon cancer cells [23]. A large number of evidence has demonstrated that β-catenin plays a critical role in the maintenance of colonospheres in colon cancer cells and β-catenin-targeting strategy could potentially inhibit self renewal of colon cancer stem cells [24–26]. Here, we identify that β-catenin is a direct target gene of miR-320a in colon cancer cells and miR-320a negatively regulated the β-catenin expression through translational inhibition. Additionally, our investigation in clinical CRC tissues further established a functional link between miR-320a and β-catenin in human colorectal carcinoma, because the expression levels of endogenous miR-320a were negatively correlated with the mRNA expression levels of β-catenin's downstream genes in cancer tissues (Fig. 4D). To common knowledge, one characteristics of microRNA is that one microRNA can directly target multiple downstream genes [8]. In previous studies, it has been reported that miR-320a regulated survivin expression in leukemia cells and downregulated ETS-1 in fibroblast cells [27,28]. These previously reported target genes may also partially explain the relationship between miR-320a and the detected genes. However, the defined target genes of a specific microRNA should be dependent on its biological functions in the different biological systems. For example, miR-26a functions as a tumor suppressor in human hepatocellular carcinoma by targeting cyclin-D2 and cyclin-E2 [29]. However, in malignant glioblastoma, miR-26a exerts its function as oncomiR by targeting PTEN [30]. Thus, to identify the proper target genes of one microRNA should be in a cell-context dependent manner. In the present study, we performed a rescue experiment to detect that if β-catenin is a functional mediator for miR-320a in CRC cells. The data showed that reintroduction of β-catenin into miR-320a-overexpressing CRC cells antagonized the effects of miR-320a on its target genes, including CCND1, c-myc and survivin (Fig. 4C). These results further confirmed our conclusion that β-catenin is a functional mediator for miR-320a in CRC cells.

The development and progression of colon cancer is a complicated process involving stepwise genetic alterations. The Wnt/β-catenin signaling pathway plays a central role in the pathogenesis of colorectal cancer. A large number of evidence demonstrates the Wnt/β-catenin cascade as the major driving force behind the proliferative potential of adenomas and adenocarcinomas of the colon. Colon cancers almost invariably carry activating mutations in the Wnt/β-catenin pathway, which target the tumor suppressors APC and Axin2 or the oncogene β-catenin. The common denominator of the Wnt pathway is the formation of Tcf/β-catenin complexes and the subsequent uncontrolled target gene's transcription, including c-myc, CCND1, survivin and etc. [6,31]. However, although the Wnt/β-catenin signaling is also one of the major causes of hepatocellular and gastric cancer development, unlike colon cancer, APC gene mutations are not common in these types of cancers, and β-catenin mutations are present in fewer than 30% of the Wnt/β-catenin-activated cancers [32,33]. Thus, other mechanism(s) may also contribute to the hyperactivation of Wnt/β-catenin signaling in cancer. Recently, one report showed that QKI, one RNA-binding protein can suppress β-catenin's transactivation by directly binding to the 3′UTR of its mRNA in colon cancer cells, indicating that posttranscriptional modification may also plays a critical role in the regulation of β-catenin's activation [34]. In the present study, we for the first time demonstrated that miR-320a was a negative regulator of β-catenin expression in a posttranscriptional level. Recent studies from other groups have also shown that several other microRNAs, including miR-200a, miR1826 and miR-483-3p can also directly bind to the β-catenin 3′UTR and inhibit its expression in different types of cancer, suggesting that microRNA-mediated post-transcriptional silencing mechanisms play a critical role in regulating the expression of β-catenin in cancer cells [35–37].

Taken together, our present study demonstrates miR-320a as a growth-suppressive miRNA in human colon cancer, at least, partially through repression of β-catenin. Our data provide further evidence of a pivotal role of miRNAs in colon cancer tumorigenesis. As miR-320a is downregulated in colon cancer, reintroduction of this mature miRNA into the tumor tissues may provide a therapeutic strategy by reducing the expression of its target genes. Although miRNA-based therapeutics is still in their infancy, our findings on miR-320a are encouraging and suggest that this miRNA could be a potential target for the treatment of colon cancer in future.

Acknowledgment

This work was supported by grants from The National Natural Scientific Foundation of China (81030045 and 30901771).

Appendix A. Supplementary data

Supplementary data associated with this article can be found, in the online version, at http://dx.doi.org/10.1016/j.bbrc.2012.03.075.

References

[1] A. Jemal, R. Siegel, E. Ward, et al., Cancer statistics, CA Cancer J. Clin. 57 (2007) (2007) 43–66.
[2] L.D. Wood, D.W. Parsons, S. Jones, et al., The genomic lscapes of human breast and colorectal cancers, Science 318 (2007) 1108–1113.
[3] I. Bozic, T. Antal, H. Ohtsuki, et al., Accumulation of driver passenger mutations during tumor progression, Proc. Natl. Acad. Sci. USA 107 (2010) 18545–18550.
[4] H. Carter, S. Chen, L. Isik, et al., Cancer-specific high-throughput annotation of somatic mutations computational prediction of driver missense mutations, Cancer Res. 69 (2009) 6660–6667.
[5] E.R. Fearon, B. Vogelstein, A genetic model for colorectal tumorigenesis, Cell 61 (1990) 759–767.
[6] S.D. Markowitz, M.M. Bertagnolli, Molecular origins of cancer: molecular basis of colorectal cancer, N. Engl. J. Med. 361 (2009) 2449–2460.
[7] D.P. Bartel, MicroRNAs target recognition regulatory functions, Cell 136 (2009) 215–233.
[8] D.P. Bartel, MicroRNAs: genomics, biogenesis, mechanism and function, Cell 116 (2004) 281–297.
[9] R. Garzon, G.A. Calin, C.M. Croce, MicroRNAs in Cancer, Annu. Rev. Med. 60 (2009) 167–179.
[10] A.J. Schetter, S.Y. Leung, J.J. Sohn, et al., MicroRNA expression profiles associated with prognosis therapeutic outcome in colon adenocarcinoma, JAMA 299 (2008) 425–436.
[11] J.M. Cummins, Y. He, R.J. Leary, et al., The colorectal microRNAome, Proc. Natl. Acad. Sci. USA 103 (2006) 3687–3692.
[12] T. Schepeler, J.T. Reinert, M.S. Ostenfeld, et al., Diagnostic and prognostic microRNAs in stage II colon cancer, Cancer Res. 68 (2008) 6416–6424.
[13] M. Thomas, J. Lieberman, A. Lal, Desperately seeking microRNA targets, Nat. Struct. Mol. Biol. 17 (2010) 1169–1174.
[14] T.C. He, A.B. Sparks, C. Rago, et al., Identification of c-MYC as a target of the APC pathway, Science 281 (1998) 1509–1512.
[15] O. Tetsu, F. McCormick, Beta-catenin regulates expression of cyclin D1 in colon carcinoma cells, Nature 398 (1999) 422–426.
[16] P.J. Kim, J. Plescia, H. Clevers, et al., Survivin and molecular pathogenesis of colorectal cancer, Lancet 362 (2003) 205–209.

[17] F. Meng, R. Henson, M. Lang, et al., Involvement of human micro-RNA in growth and response to chemotherapy in human cholangiocarcinoma cell lines, Gastroenterology 130 (2006) 2113–2129.
[18] L. Chen, H.X. Yan, W. Yang, et al., The role of microRNA expression pattern in human intrahepatic cholangiocarcinoma, J. Hepatol. 50 (2009) 358–369.
[19] G.A. Calin, C.D. Dumitru, M. Shimizu, et al., Frequent deletions and down-regulation of micro-RNA genes miR15 and miR16 at 13q14 in chronic lymphocytic leukemia, Proc. Natl. Acad. Sci. USA 99 (2002) 15524–15529.
[20] S. Volinia, G.A. Calin, C.G. Liu, et al., A microRNA expression signature of human solid tumors defines cancer gene targets, Proc. Natl. Acad. Sci. USA 103 (2006) 2257–2261.
[21] J. Lu, G. Getz, E.A. Miska, et al., MicroRNA expression profiles classify human cancers, Nature 435 (2005) 834–838.
[22] R. Garzon, G. Marcucci, C.M. Croce, Targeting microRNAs in cancer rationale, strategies and challenges, Nat. Rev. Drug. Discov. 9 (2010) 775–789.
[23] H. Zhang, W. Li, F. Nan, et al., MicroRNA expression profile of colon cancer stem-like cells in HT29 adenocarcinoma cell line, Biochem. Biophys. Res. Commun. 404 (2011) 273–278.
[24] T. Reya, H. Clevers, Wnt signalling in stem cells and cancer, Nature 434 (2005) 843–850.
[25] E.M. de Sousa, L. Vermeulen, D. Richel, et al., Targeting Wnt signaling in colon cancer stem cells, Clin. Cancer Res. 17 (2011) 647–653.
[26] S.S. Kanwar, Y. Yu, J. Nautiyal, et al., The Wnt/beta-catenin pathway regulates growth and maintenance of colonospheres, Mol. Cancer. 9 (2010) 212.
[27] C. Diakos, S. Zhong, Y. Xiao, et al., TEL-AML1 regulation of survivin and apoptosis via miRNA-494 and miRNA-320a, Blood 116 (2010) 4885–4893.
[28] A. Bronisz, J. Godlewski, J.A. Wallace, et al., Reprogramming of the tumour microenvironment by stromal PTEN-regulated miR-320, Nat. Cell Biol. 14 (2011) 159–167.
[29] J. Kota, R.R. Chivukula, K.A. O'Donnell, et al., Therapeutic microRNA delivery suppresses tumorigenesis in a murine liver cancer model, Cell 137 (2009) 1005–1017.
[30] J.T. Huse, C. Brennan, D. Hambardzumyan, et al., The PTEN-regulating microRNA miR-26a is amplified in high-grade glioma and facilitates gliomagenesis in vivo, Genes Dev. 23 (2009) 1327–1337.
[31] Y.Z. Deng, F. Yao, J.J. Li, et al. RACK1 Suppresses Gastric Tumorigenesis by Stabilizing the β-Catenin Destruction Complex, Gastroenterology. 2012.
[32] D.K. Woo, H.S. Kim, H.S. Lee, et al., Altered expression and mutation of beta-catenin gene in gastric carcinomas and cell lines, Int. J. Cancer. 95 (2001) 108–113.
[33] A. de La Coste, B. Romagnolo, P. Billuart, et al., Somatic mutations of the beta-catenin gene are frequent in mouse and human hepatocellular carcinomas, Proc. Natl. Acad. Sci. USA 95 (1998) 8847–8851.
[34] G. Yang, H. Fu, J. Zhang, et al., RNA-binding protein quaking, a critical regulator of colon epithelial differentiation and a suppressor of colon cancer, Gastroenterology 138 (2010) 231–240.
[35] H. Xia, W.K. Cheung, J. Sze, et al., MiR-200a regulates epithelial-mesenchymal to stem-like transition via ZEB2 and beta-catenin signaling, J. Biol. Chem. 285 (2010) 36995–37004.
[36] H. Hirata, Y. Hinoda, K. Ueno, et al. MicroRNA-1826 directly targets beta-catenin (CTNNB1) and MEK1 (MAP2K1) in VHL-inactivated renal cancer, Carcinogenesis. 2012 (Epub ahead of print).
[37] A. Veronese, R. Visone, J. Consiglio, et al., Mutated beta-catenin evades a microRNA-dependent regulatory loop, Proc. Natl. Acad. Sci. USA 108 (2011) 4840–4845.

Biochemical and Biophysical Research Communications 420 (2012) 793–798

Contents lists available at SciVerse ScienceDirect

Biochemical and Biophysical Research Communications

journal homepage: www.elsevier.com/locate/ybbrc

In vitro reprogramming of rat bone marrow-derived mesenchymal stem cells into insulin-producing cells by genetically manipulating negative and positive regulators

Hong-Tu Li [a,d,1], Fang-Xu Jiang [b,*,1], Ping Shi [c,1], Tao Zhang [a], Xiao-Yu Liu [a], Xue-Wen Lin [a], Xi-Ning Pang [a,*]

[a] Department of Stem Cells and Regenerative Medicine, Key Laboratory of Cell Biology of Ministry of Public Health, China Medical University, Shenyang 110001, China
[b] Centre for Diabetes Research, Western Australian Institute for Medical Research, and Centre for Medical Research, University of Western Australia, Perth 6000, Australia
[c] Department of General Practice, The First Affiliated Hospital, China Medical University, Shenyang 110001, China
[d] Liaoning Province Research Institute of Family Planning, Key Laboratory of Reproduction Health of Liaoning Province, Shenyang 110031, China

ARTICLE INFO

Article history:
Received 6 March 2012
Available online 21 March 2012

Keywords:
Mesenchymal stem cells
Reprogramming
Insulin-producing cells
Lentivirus vector

ABSTRACT

Islet cell replacement therapy represents the most promising approach for the cure of type 1 diabetes if autoimmunity to β cells is under control. However, this potential is limited by a shortage of pancreas donors. To address the donor shortage problem, we determined whether bone marrow-derived mesenchymal stem cells (bmMSCs) can be directly reprogrammed to islet lineages by simultaneously forced suppression and over-expression of key regulator genes that play critical roles during pancreas development. Here, we report that rat bmMSCs were converted *in vitro* into insulin-producing cells by suppressing two-repressor genes repressor element-1 silencing transcription factor/neuronal restrictive silencing factor (Rest/Nrsf) and sonic hedgehog (Shh) and by over-expressing pancreas and duodenal transcription factor 1 (Pdx1). The reprogrammed bmMSCs expressed both genes and proteins specific for islet cells. These converted cells were capable of releasing insulin in a glucose-responsive manner. Our study suggests that bmMSCs may ultimately be reprogrammed to functional insulin-secreting cells.

Crown Copyright © 2012 Published by Elsevier Inc. All rights reserved.

1. Introduction

Diabetes is a major public health problem worldwide with huge economical and social burdens. It currently affects approximately 200 million people, and this number is likely to increase to 400 million by 2030 [1]. Approximately 10% of these cases will have type 1 diabetes (T1D), caused by absolute deficiency of insulin-producing β cells. Therefore, a cellular therapy from stem/progenitor cells including those from other lineages is the best prospect for a cure of T1D, provided autoimmunity to β cells can be controlled and there is a sufficient supply of insulin-secreting β cells for transplantation.

The mesenchymal stem/stromal cells (MSCs) are mesoderm-derived and pluripotent [2]. These cells can be prepared with relatively ease from patients and are readily expanded *in vitro*. The bone marrow-derived MSCs (bmMSCs) have been shown to be able to differentiate *in vivo* into a variety of ectodermal, mesodermal, and endodermal tissues [3–6]. It was previously believed that during development cellular differentiation is unidirectional, but the recent creation of induced pluripotent stem cell from differentiated cells [7] has changed the paradigm, indicating that the differentiation state of a cell is rather plastic. Differentiation is a process of precise patterns of gene expression events characterized with temporal and spatial specificities. Namely, cell differentiation is governed by the internal programming of gene expression. The differentiation plasticity makes reprogramming of a different cell fate possible.

The repressor element-1 silencing transcription factor (Rest), also known as neuron-restrictive silencer factor (Nrsf) is a krüppel family zinc finger protein which binds specifically to a 21- to 23-base pair (bp) conserved DNA response element (neuron-restrictive silencer element/repressor element-1, Nrse/Re1) [8]. It has been reported that there are 1892 and 1894 Rest/Nrsf target genes that contain Nrse/Re1 sites in the human and mouse genomes, respectively [9]. Rest/Nrsf was first recognized for its ability to block the transcription of neuronal differentiation genes in non-neuronal cells or in neural stem/progenitor cells by binding to Nrse/Re1 [8]. And just like the neuronal cells, mature islet endocrine cells also do not express Rest/Nrsf [10]. Recently, target genes for Rest/Nrsf associated with islet cell development have

Abbreviations: bmMSCs, bone marrow-derived mesenchymal stem cells; Rest/Nrsf, repressor element-1 silencing transcription factor/neuronal restrictive silencing factor; Shh, sonic hedgehog; Pdx1, pancreas and duodenal transcription factor 1; GFP, green fluorescent protein; Gcg, glucagon; Sst, somatostatin.

* Corresponding authors. Addresses: 50 Murray St. (Rear), Perth, WA, Australia. Fax: +61 8 92240322 (F.-X. Jiang), 92 Beier Rd., Heping District, Shenyang, China. Fax: +86 24 23261091 (X.-N. Pang).

E-mail addresses: fangxu.jiang@uwa.edu.au (F.-X. Jiang), pxining@yahoo.com (X.-N. Pang).

[1] These authors contributed equally to this work.

0006-291X/$ - see front matter Crown Copyright © 2012 Published by Elsevier Inc. All rights reserved.
http://dx.doi.org/10.1016/j.bbrc.2012.03.076

been reported [11–13], including *Hnf4α* (*hepatocyte nuclear factor 4a*), *Pax4* (*paired homeobox 4*), *Ngn3* (*neurogenin-3*), *NeuroD1* (*neuronal differentiation 1*) and *connexin36*. These data suggest that the suppression of Rest/Nrsf plays a role in islet β cell development.

Sonic hedgehog (Shh) signaling exerts opposite roles in neuron and pancreas development. Whereas promoting neuronal development [14,15], the expression of Shh inhibits pancreas specification [16–18]. Pancreatic and duodenal homeobox 1 (Pdx1), a member of the homeodomain-containing transcription factor family, plays an important role in initiating the differentiation of pancreatic endocrine cells [19].

Application of bmMSCs has attracted a significant attention in recent years as a source for generation of insulin-producing cells for potentially future T1D regenerative medicine. In addition to treating with extracellular signaling molecules [20–25], forced expression of positive intracellular regulators in bmMSCs has induced gene expression for pancreas or islet progenitors [23,26–28]. Here we tested whether simultaneous suppression of negative regulator genes (*Rest/Nrsf* and *Shh*) and over-expression of a positive regulator gene (*Pdx1*) would allow us to generate islet-like cells from bmMSCs.

2. Materials and methods

2.1. Isolation, culture and phenotypic analysis of bmMSCs

Animal usage was approved by China Medical University. For bmMSC preparation, the thigh- and shin-bones were aseptically removed from Sprague–Dawley rats and then bone marrow was flushed out with serum-free low-glucose Dulbecco's modified Eagle's medium (LG-DMEM, Gibco). The bone marrow cells were cultured at a density of 2×10^6 cells/ml in a 25 cm^2 plastic culture flask in the LG-DMEM containing 10% fetal bovine serum (FBS, Hyclone), 100 U/ml penicillin and 100 μg/ml streptomycin. After 72 h, non-adherent cells were discarded and adherent cells were thoroughly washed twice with warm phosphate-buffer saline (PBS). Upon reaching near confluence, cells were detached using 0.25% trypsin and 0.02% ethylenediamine tetraacetic acid (EDTA, Gibco) for 1–2 min at 37 °C. After multi-round plastic-adherence selection, the pure cells were cultured for approximately 10–14 days and referred to as the first-passage bmMSCs. The dissociated bmMSCs were seeded at 50–100 cells per cm^2 and grown to ~80% confluence for further passaging.

For flow cytometry analysis, harvested cells were fixed in 100% methanol 10 min at 4 °C and stained for 30–60 min at 4 °C with antibodies against surface molecules including CD14, CD34, CD45, CD73, CD44 and CD90 (Santa Cruz), all conjugated to fluorescein isothiocyanate (FITC) followed by two washes. Mouse IgG conjugated to FITC was used as a negative control. All cells were washed twice with PBS and then analyzed on the FACS Calibur (Becton Dickson Labware) using the Cell Quest Pro software.

2.2. Plasmid construct

Lentivirus gene transfer vectors were constructed by Genechem Co., Ltd (Shanghai, China) for expression of small hairpin RNA (shRNA) of rat *Rest/Nrsf* and *Shh,* each fused with a green fluorescent protein (GFP) sequence. The targeting sequences for *Rest/Nrsf* (NM_031788) and *Shh*(NM_017221) were 5′-GAAGTGAGAGGCC TGTAAA-3′ and 5′-GAGGTGCAAAGACAAGTTA-3′ respectively. The DNA oligos containing the target sequences of shRest/Nrsf and shShh were each chemically synthesized, annealed and inserted into the pFU-GW-RNAi vector (Genechem) by double digestion with HpaI and XhoI. Their sequences were confirmed by PCR and sequencing analyses. PCR was performed using the primers of 5′-GCCCCGGTTAATTTGCATAT-3′ and 5′-GAGGCCAGATCTTGGG TG-3′. Rat Pdx1 cDNA was amplified by RT-PCR from rat cDNA library (Takara) using the primer pair 5′-GAGGATCCCCGGGTACC GGTCGCCACCATGAATAGTGAGGAGCAGTAC-3′ and 5′-TCACCATGG TGGCGACCGGCCGGGGTTCCTGCGGTCGCAG-3′. To construct the Pdx1 transgene, the pFU-FU vector (Genechem) was digested with BamHI and XhoI and the rat Pdx1 cDNA inserted in place of the GFP cDNA.

2.3. Lentivirus generation and infection

Lentiviruses were generated essentially as described [29]. Briefly, 20 μg of shRest/Nrsf, shShh and Pdx1 lentiviral vectors or scrambled control (GFP-lentiviral vector), 15 μg pHelper 1.0 and 10 μg pHelper 2.0 were co-transfected into 293T cells using the Lipofectamine 2000 reagent (Invitrogen). After 48 h culture, supernatant was harvested, filtered at 0.45 μm and pelleted by ultracentrifugation at 4000*g* for 10–15 min at 4 °C. After resuspension, serially diluted lentiviral particles were used to transduce 293T cells; 4 days later, the transfected 293T cells were counted to determine the viral titer. The recombinant lentiviruses for shRest/Nrsf, shShh, Pdx1 and the scrambled control were concentrated to 10^9 TU/ml. The bmMSCs were plated in 6-well plates (5×10^4 cells/well) overnight. The GFP expression efficiency in the bmMSCs was used to determine the multiplicity of infection (MOI). Initially, bmMSCs were infected with MOI 100, 80, 50, 30, 10 and 1 respectively. The bmMSCs were infected with shRest/Nrsf, shShh, Pdx1 and scrambled control lentiviruses respectively or in different combination at MOI 80 in the presence of polybrene. Twenty-four hr post-transfection, the medium was replaced with fresh LG-DMEM containing 10% FBS. Then cells were cultured for 10 days, with the culture medium refreshed every 3 days.

2.4. Quantitative real-time RT-PCR (qRT-PCR)

Total RNA was extracted using Trizol reagents (Invitrogen) as described by the manufacturer's protocol. The concentration of extracted RNA was determined with an ultraviolet spectrophotometer. 300 ng total RNA was then reverse-transcribed into cDNA by PrimeScript™ RT reagent (TaKaRa). The primers were listed in Table 1. qRT-PCR analysis was performed with an ABI7500 Sequence Detection System (Applied Biosystems) using the SYBR PrimeScript™ PCR (TaKaRa). Each experiment was preformed for three biological replicates. Target gene expression was normalized with the housekeeping gene GAPDH. Data were analyzed using the $2^{-\Delta\Delta Ct}$ method [30].

2.5. Immunohistochemical analysis

Mouse anti-insulin, rat anti-glucagon and mouse anti-somatostatin immunoglobulins were purchased from Santa Cruz.

Table 1
Primers for real time PCR analysis.

Gene	Forward primer	Reverse primer
Rest/Nrsf	ACTCGACACATGCGTACTCACTCA	CTTGCGTGTCGGGTCACTTC
Shh	GGCTGGATTCGACTGGGTCTACTA	AACTTGGTGCCACCCTGCTC
Pdx1	CGGCTGCCACCATGAATAG	ATGAATAGTGAGGAGCAGTACTACG
Ngn3	GCTGCCTCCAGACGCAATTTA	TGCGGGTGGTCAGAGTCAAG
Neurod1	AAAGGTTTGTCCCAGCCCACTAC	GCATGTCCGGATTCTGCTCA
Slc2a2	CCAGCCTGTGTATGCAACCATC	ACCAGTCCCAGCGACATGAAG
Nkx6.1	CCTTTGCGAGAACCATGAAATGTA	TGAGATCTCTGATGAGGCCAGGTA
MafA	CACATTCTGGAGAGCGAGAAG	TCTCGTATTTCTCCTTGTACAGGTC
Insulin 1	AAGCGTGGCATTGTGGATCA	GGAGTGGTGGACTCAGTTGCAGTA
Pax4	CAGACAGATGTTCCAGTGACACCA	GCCAGGCAAATTCCATGTATGAG
Gcg	ACCGTTTACATCGTGGCTGGA	TCTGATCAGGGTCTTCAAGTGGTTC
Sst	CCAGACTCCGTCAGTTTCTGC	GGGCATCGTTCTCTGTCTGG
GAPDH	GGCACAGTCAAGGCTGAGAATG	ATGGTGGTGAAGACGCCAGTA

Ten-day after culture, the bmMSCs were fixed with 4% paraformaldehyde for 20 min and permeablized with 0.1% Triton X-100/PBS for 10 min at room temperature. The fixed cells were treated in Protein Block (DAKO) for 10 min and then incubated with the primary antibodies overnight at 4 °C in a humid chamber and with the secondary antibody (TRITC-conjugated goat anti-mouse or anti-rabbit IgG; R&D Systems) for 1 h. DAPI (4′,6-diamidino-2-phenylindole) was used to counter-stain nuclear DNA. Images were captured using an Olympus BX51 phase contrast fluorescent microscope (Olympus).

2.6. Glucose-stimulated insulin-secretion assay

Glucose-stimulated insulin secretion assay was performed as described previously [31]. In brief, 1×10^5 cells were first washed twice with the Krebs–Ringer bicarbonate buffer (KRBB) containing 0.1% BSA (KRB-BSA). The cells were then incubated for 1 h at 37 °C in the KRB-BSA alone and subsequently for 2 h at 37 °C in the presence of 5, 30, 50 or 100 mM glucose. Supernatant was collected to determine the concentration of secreted insulin with an ultrasensitive (rat/mouse) insulin ELISA kit (Millipore), according to the manufacturer's instructions.

2.7. Statistical analysis

All experiments were repeated at least for three times. Data are shown as means ± SD and analyzed statistically by the Student's *t*-test. Difference was considered to be significant when $p < 0.05$.

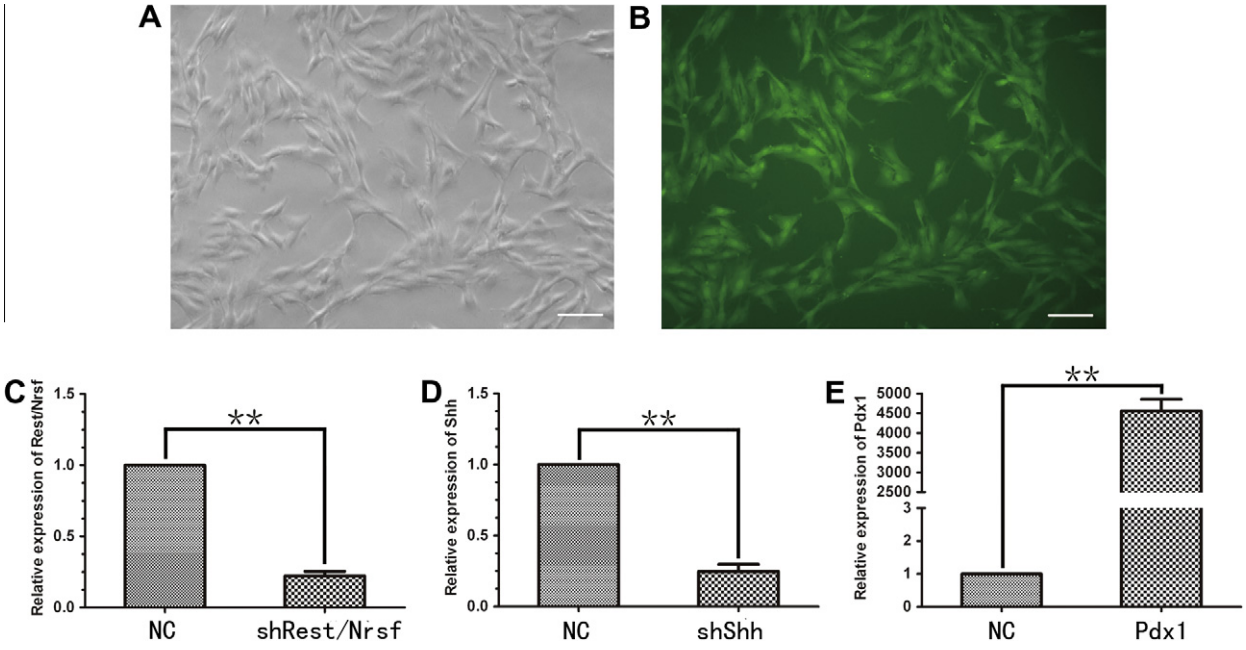


Fig. 1. Transfection of rat bone marrow-derived mesenchymal stem cells (bmMSCs) with sh*Rest/Nrsf*, sh*Shh* or *Pdx1* lentiviruses. (A) Morphology of the transfected bmMSCs. The phase contrast (A) and fluorescence images (B) were captured under a fluorescence microscope. Scale bar: 100 μm. Confirmation of suppression or up-regulation of targeted genes in the transfected bmMSCs. RNA was extracted from the transfected bmMSCs and reverse transcribed into cDNAs for real-time quantitative RT-PCR analysis of *Rest/Nrsf* (C), *Shh* (D) and *Pdx1* (E). $^{**}P$ value < 0.01.

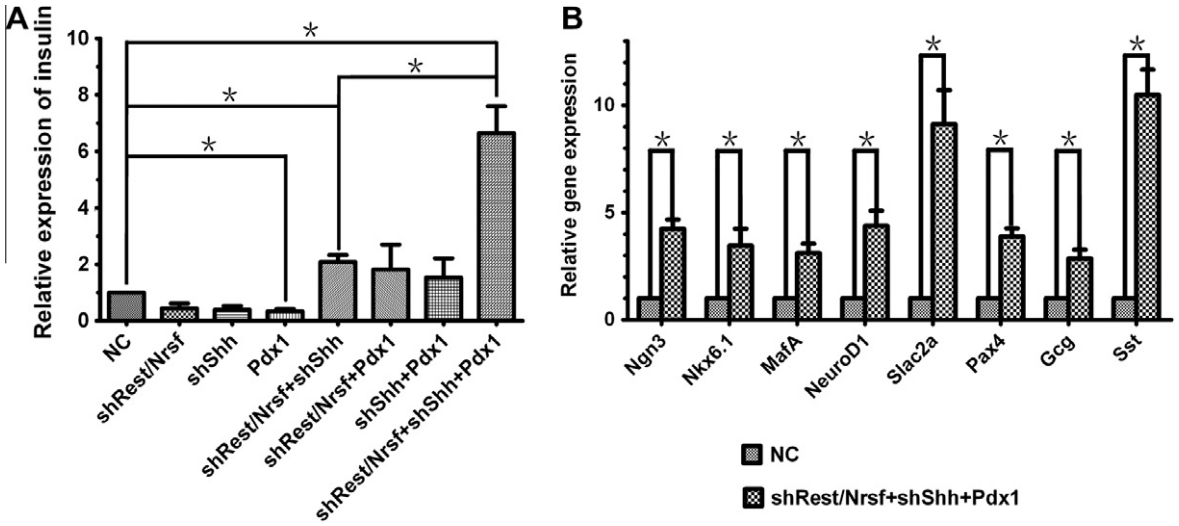


Fig. 2. Real-time quantitative RT-PCR analysis of genetically manipulated rat bone marrow-derived mesenchymal stem cells (bmMSCs). (A) Insulin gene expression. (B) Expression of genes specific for islet cell development. RNA was extracted from the transfected bmMSCs and reverse transcribed into cDNAs for real-time quantitative RT-PCR analysis. $^{*}P$ value < 0.05, $^{**}P$ value < 0.01.

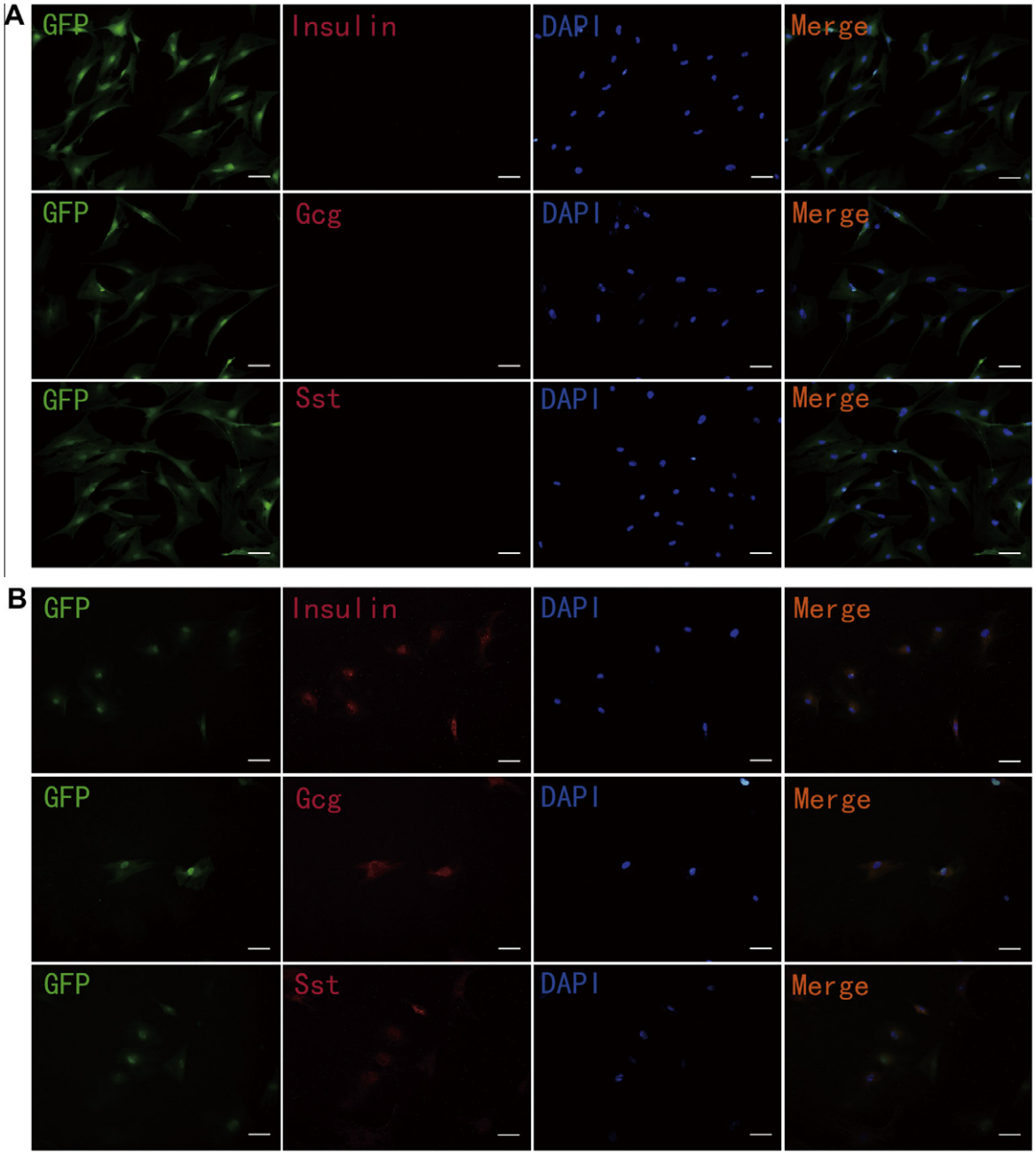


Fig. 3. Immunofluorescence analysis of genetically manipulated rat bone marrow-derived mesenchymal stem cells without (A) or with a combined transfection of all three negative and positive regulator genes. The manipulated cells at day 10 were fixed and stained with antibodies against insulin, glucagon and somatostatin and visualized with secondary antibody. 4′,6-diamidino-2-phenylindole (DAPI) was used to counter-stain DNA (blue). Microphotographs were taken with a fluorescence microscope. Scale bar: 100 μm. (For interpretation of the references to colour in this figure legend, the reader is referred to the web version of this article.)

3. Results

3.1. Isolation and identification of the bmMSCs

The primary culture of the isolated bone marrow cells contained a heterogeneous cell population with both round and fibroblast-like cells. After three selections with plastic adherences, the near homogeneous adherent spindle and fibroblast-like cells appeared whereas the round-shaped cells gradually disappeared (see Supplementary Fig. S1A). In order to confirm their phenotype, we performed flow cytometry analyses. Our results showed that these fibroblast-like cells were positive for CD73, CD44 and CD90 but negative for CD34, CD45 and CD14, characteristic of MSCs, termed here as bmMSCs (see Supplementary Fig. S1B).

3.2. Forced expression of ShRest/Nrsf, shShh and Pdx1 lentiviruses in bmMSCs

To identify key regulators that may reprogram the cells towards islet lineages, the bmMSCs were forced to express sh*Rest/Nrsf,* sh*Shh* and *Pdx1*. As the lentiviral constructs were tagged with the GFP reporter, the infection efficiency was first examined using fluorescence microscopy. Twenty-four hr after transfection, the bmMSCs first expressed weakly for GFP, suggesting that the lentivirus has integrated into the genome of the bmMSCs. The GFP

expression peaked around 96 h after transfection, and the infection efficiency was approximately 100% when the MOI was 80 (Fig. 1A and B).

To determine the efficiency of lentiviral-mediated suppression or over-expression of interested genes in the bmMSCs, qRT-PCR was used to quantify their expression levels 4 days after infection. The results showed that the expression of *Rest/Nrsf* and *Shh* was down-regulated approximately 80% (Fig. 1C and D), whereas that of *Pdx1* was up-regulated 5000-fold (Fig. 1E). These results indicated that our lentiviral vectors performed efficiently.

3.3. Genes specific for developing islet cells were expressed in the manipulated bmMSCs

To provide evidence which or which combination of gene manipulations could induce islet gene expression, RNA was extracted 10 days after infection for qRT-PCR analysis. Although neither single gene manipulation elicited transcription of insulin gene (Fig. 2A), a co-transfection of shRestNrsf and shShh up-regulated 3-fold of insulin gene expression (Fig. 2A). However, the combination of all three genes strongly up-regulated insulin transcripts for approximately 7-fold. Meanwhile, *Ngn3*, *Nkx6.1*, *Pax4* and *NeuroD1,* marker genes for islet progenitors, were also up-regulated approximately 4-, 3-, 3- and 4-fold, respectively (Fig. 2B). β-cell specific genes, *MafA* and *Slc2a2,* were elevated 3- and 9-fold, respectively. Genes for other islet cells, *glucagon* (*Gcg*) and *somatostatin (Sst)* were also increased 3- and 11-fold, respectively (Fig. 3B).

3.4. Characterization of manipulated bmMSCs

To further characterize these manipulated cells, we first performed immunofluorescence staining to detect protein expression. The results showed that in contrast to untransfected cells (Fig. 3A), co-transfected cells expressed insulin, glucagon and somatostatin (Fig. 3B). To test the functionality of the co-transfected cells, we then performed glucose stimulated insulin secretion after treatment with 5, 30, 50 or 100 mM glucose and insulin concentrations were measured with immunoassays. The insulin secretion appeared to be glucose dose-dependent (Fig. 4). Taken together, our results indicated that the gene-manipulated bmMSCs acquired characteristics of pancreatic islet cells.

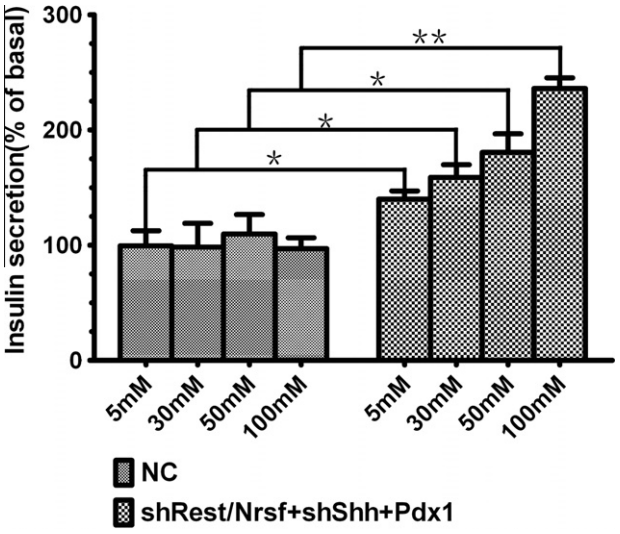


Fig. 4. Glucose stimulated insulin secretion analysis in the manipulated rat bone marrow-derived mesenchymal stem cells. Insulin concentrations were determined with an ultrasensitive insulin ELISA assay. Data expressed as the percentage increase in insulin release relative to cells incubated in buffer containing 5 mM glucose, $n = 3$. $^{*}P$ value < 0.05, $^{**}P$ value < 0.01.

4. Discussion

We have successfully manipulated simultaneously both negative and positive regulator genes in bmMSCs. We showed that the bmMSCs can be reprogrammed to a pancreatic islet fate by stable suppression of *Rest*/*Nrsf* and *Shh* whereas simultaneously up-regulation of *Pdx1*. These manipulated bmMSCs had an elevated glucose-stimulated insulin-secretion. The reprogramming of bmMSCs into pancreatic β-like cells may ultimately provide an alternative renewable source for a diabetes cell therapy.

Islet cells share many traits of neurons [10]. A recent report showed that after knocking down Rest/Nrsf, human amniotic fluid-derived stem cells differentiated into insulin-producing cells [32]. Others showed that forced expression *Pdx-1* in human and rat bmMSCs allows generation of insulin-positive cells [26,28]. However, we did not convert bmMSCs to insulin-expressing cells by suppression of *Rest*/*Nrsf* or up-regulation of *Pdx1* alone. The reason for this discrepancy is unknown, likely due to the differences in species and/or cell types used. Although Shh is not normally expressed in the pancreatic domain [17], suppression of *Shh* alone was unable to initiate insulin gene expression, consistent with the fact that additional extracellular signaling molecules are required for pancreas specification during early development [33].

To the best of our knowledge, this is the first demonstration that the suppression of both *Rest*/*Nrsf* and *Shh* in bmMSCs up-regulated approximately 3-fold expression of insulin gene, suggesting that in addition to Shh, Rest/Nrsf also is a key negative regulator of islet cell specification. Future studies are required to understand the mechanism of this synergistic action.

We further demonstrated that a simultaneous genetic manipulation of *Rest*/*Nrsf*, *Shh* and *Pdx1* in the bmMSCs worked synergistically to initiate the differentiation of insulin-producing cells *in vitro* without the addition of any extracellular inducers. Our immune fluorescence and glucose-stimulated insulin secretion analyses indicated that these manipulated bmMSCs had some features of islet cells (Fig. 4). These reprogrammed cells remain as single cells or small clusters and do not organize into islet structures. The lack of islet-like structure for those induced β-like cells may impair their function, as the signaling between β-cells inhibits basal insulin secretion but enhances glucose-stimulated insulin secretion [34]. Future strategies that promote aggregation of the induced β-like cells *in vitro* may enhance the glucose responsiveness.

In conclusion, our data provide valuable novel information on reprogram/conversion of endoderm-derived islet cells from mesoderm-derived bmMSCs. This approach may also be used to reprogram cells from other lineages to islet-like cells for an ultimate future replacement therapy in type 1 diabetes.

Funding source

This work was supported by the Science and Technology Plan Project of Liaoning Science and Technology Bureau (2010225034). In addition, this work was supported by the National Natural Science Foundation of China (81150018).

Acknowledgments

We thank Fanbiao Meng, Caihong Li of Department of Stem Cells and Regenerative Medicine for technical assistance, and Chunyang Song of Department of Development Biology of China Medical University for help with computational software.

Appendix A. Supplementary data

Supplementary data associated with this article can be found, in the online version, at http://dx.doi.org/10.1016/j.bbrc.2012.03.076.

References

[1] L.T. Lock, E.S. Tzanakakis, Stem/progenitor cell sources of insulin-producing cells for the treatment of diabetes, Tissue Eng. 13 (2007) 1399–1412.

[2] K. English, A. French, K.J. Wood, Mesenchymal stromal cells: facilitators of successful transplantation, Cell Stem Cell 7 (2010) 431–442.

[3] N.M. Caplice, T.J. Bunch, P.G. Stalboerger, S. Wang, D. Simper, D.V. Miller, S.J. Russell, M.R. Litzow, W.D. Edwards, Smooth muscle cells in human coronary atherosclerosis can originate from cells administered at marrow transplantation, Proc. Natl. Acad. Sci. USA 100 (2003) 4754–4759.

[4] Y. Jiang, B.N. Jahagirdar, R.L. Reinhardt, R.E. Schwartz, C.D. Keene, X.R. Ortiz-Gonzalez, M. Reyes, T. Lenvik, T. Lund, M. Blackstad, J. Du, S. Aldrich, A. Lisberg, W.C. Low, D.A. Largaespada, C.M. Verfaillie, Pluripotency of mesenchymal stem cells derived from adult marrow, Nature 418 (2002) 41–49.

[5] D.S. Krause, N.D. Theise, M.I. Collector, O. Henegariu, S. Hwang, R. Gardner, S. Neutzel, S.J. Sharkis, Multi-organ, multi-lineage engraftment by a single bone marrow-derived stem cell, Cell 105 (2001) 369–377.

[6] R. Okamoto, T. Yajima, M. Yamazaki, T. Kanai, M. Mukai, S. Okamoto, Y. Ikeda, T. Hibi, J. Inazawa, M. Watanabe, Damaged epithelia regenerated by bone marrow-derived cells in the human gastrointestinal tract, Nat. Med. 8 (2002) 1011–1017.

[7] K. Takahashi, S. Yamanaka, Induction of pluripotent stem cells from mouse embryonic and adult fibroblast cultures by defined factors, Cell 126 (2006) 663–676.

[8] C.J. Schoenherr, D.J. Anderson, The neuron-restrictive silencer factor (NRSF): a coordinate repressor of multiple neuron-specific genes, Science 267 (1995) 1360–1363.

[9] A.W. Bruce, I.J. Donaldson, I.C. Wood, S.A. Yerbury, M.I. Sadowski, M. Chapman, B. Gottgens, N.J. Buckley, Genome-wide analysis of repressor element 1 silencing transcription factor/neuron-restrictive silencing factor (REST/NRSF) target genes, Proc. Natl. Acad. Sci. USA 101 (2004) 10458–10463.

[10] F. Atouf, P. Czernichow, R. Scharfmann, Expression of neuronal traits in pancreatic beta cells. Implication of neuron-restrictive silencing factor/repressor element silencing transcription factor, a neuron-restrictive silencer, J. Biol. Chem. 272 (1997) 1929–1934.

[11] D.S. Johnson, A. Mortazavi, R.M. Myers, B. Wold, Genome-wide mapping of in vivo protein–DNA interactions, Science 316 (2007) 1497–1502.

[12] D.M. Kemp, J.C. Lin, J.F. Habener, Regulation of Pax4 paired homeodomain gene by neuron-restrictive silencer factor, J. Biol. Chem. 278 (2003) 35057–35062.

[13] D. Martin, T. Tawadros, L. Meylan, A. Abderrahmani, D.F. Condorelli, G. Waeber, J.A. Haefliger, Critical role of the transcriptional repressor neuron-restrictive silencer factor in the specific control of connexin36 in insulin-producing cell lines, J. Biol. Chem. 278 (2003) 53082–53089.

[14] J. Ericson, S. Morton, A. Kawakami, H. Roelink, T.M. Jessell, Two critical periods of Sonic Hedgehog signaling required for the specification of motor neuron identity, Cell 87 (1996) 661–673.

[15] M. Placzek, The role of the notochord and floor plate in inductive interactions, Curr. Opin. Genet. Dev. 5 (1995) 499–506.

[16] S. Cervantes, J. Lau, D.A. Cano, C. Borromeo-Austin, M. Hebrok, Primary cilia regulate Gli/Hedgehog activation in pancreas, Proc. Natl. Acad. Sci. USA 107 (2010) 10109–10114.

[17] H. Kawahira, N.H. Ma, E.S. Tzanakakis, A.P. McMahon, P.T. Chuang, M. Hebrok, Combined activities of hedgehog signaling inhibitors regulate pancreas development, Development 130 (2003) 4871–4879.

[18] J.K. Mfopou, L. Bouwens, Hedgehog signals in pancreatic differentiation from embryonic stem cells: revisiting the neglected, Differentiation 76 (2008) 107–117.

[19] V.M. Schwitzgebel, A. Mamin, T. Brun, B. Ritz-Laser, M. Zaiko, A. Maret, F.R. Jornayvaz, G.E. Theintz, O. Michielin, D. Melloul, J. Philippe, Agenesis of human pancreas due to decreased half-life of insulin promoter factor 1, J. Clin. Endocrinol. Metab. 88 (2003) 4398–4406.

[20] M. Banerjee, A. Kumar, R.R. Bhonde, Reversal of experimental diabetes by multiple bone marrow transplantation, Biochem. Biophys. Res. Commun. 328 (2005) 318–325.

[21] L.B. Chen, X.B. Jiang, L. Yang, Differentiation of rat marrow mesenchymal stem cells into pancreatic islet beta-cells, World J. Gastroenterol. 10 (2004) 3016–3020.

[22] A. Ianus, G.G. Holz, N.D. Theise, M.A. Hussain, In vivo derivation of glucose-competent pancreatic endocrine cells from bone marrow without evidence of cell fusion, J. Clin. Invest. 111 (2003) 843–850.

[23] C. Moriscot, M.J. Richard, M. Marchand, P. Savatier, D. Bosco, M. Favrot, P.Y. Benhamou, Human bone marrow mesenchymal stem cells can express insulin and key transcription factors of the endocrine pancreas developmental pathway upon genetic and/or microenvironmental manipulation in vitro, Stem Cells 23 (2005) 594–603.

[24] S. Sumi, Y. Gu, A. Hiura, K. Inoue, Stem cells and regenerative medicine for diabetes mellitus, Pancreas 29 (2004) e85–e89.

[25] D.Q. Tang, L.Z. Cao, B.R. Burkhardt, C.Q. Xia, S.A. Litherland, M.A. Atkinson, L.J. Yang, In vivo and in vitro characterization of insulin-producing cells obtained from murine bone marrow, Diabetes 53 (2004) 1721–1732.

[26] O. Karnieli, Y. Izhar-Prato, S. Bulvik, S. Efrat, Generation of insulin-producing cells from human bone marrow mesenchymal stem cells by genetic manipulation, Stem Cells 25 (2007) 2837–2844.

[27] L. Li, F. Li, H. Qi, G. Feng, K. Yuan, H. Deng, H. Zhou, Coexpression of Pdx1 and betacellulin in mesenchymal stem cells could promote the differentiation of nestin-positive epithelium-like progenitors and pancreatic islet-like spheroids, Stem Cells Dev. 17 (2008) 815–823.

[28] H. Yuan, J. Li, N. Xin, Z. Zhao, G. Qin, Expression of Pdx1 mediates differentiation from mesenchymal stem cells into insulin-producing cells, Mol. Biol. Rep. 37 (2010) 4023–4031.

[29] C. Lois, E.J. Hong, S. Pease, E.J. Brown, D. Baltimore, Germline transmission and tissue-specific expression of transgenes delivered by lentiviral vectors, Science 295 (2002) 868–872.

[30] K.J. Livak, T.D. Schmittgen, Analysis of relative gene expression data using real-time quantitative PCR and the 2(-Delta Delta C(T)) Method, Methods 25 (2001) 402–408.

[31] B.L. Le, A. Virsolvy, D. Manechez, J.J. Godfroid, B. Guardiola-Lemaitre, F.M. Gribble, F.M. Ashcroft, D. Bataille, In vitro mechanism of action on insulin release of S-22068, a new putative antidiabetic compound, Br. J. Pharmacol. 128 (1999) 1021–1026.

[32] B. Li, S. Wang, H. Liu, D. Liu, J. Zhang, B. Zhang, H. Yao, Y. Lv, R. Wang, L. Chen, W. Yue, Y. Li, X. Pei, Neuronal restrictive silencing factor silencing induces human amniotic fluid-derived stem cells differentiation into insulin-producing cells, Stem Cells Dev. 20 (2011) 1223–1231.

[33] F.C. Pan, C. Wright, Pancreas organogenesis: from bud to plexus to gland, Dev. Dyn. 240 (2011) 530–565.

[34] I. Konstantinova, G. Nikolova, M. Ohara-Imaizumi, P. Meda, T. Kucera, K. Zarbalis, W. Wurst, S. Nagamatsu, E. Lammert, EphA-Ephrin-A-mediated beta cell communication regulates insulin secretion from pancreatic islets, Cell 129 (2007) 359–370.

Biochemical and Biophysical Research Communications 420 (2012) 799–804

Contents lists available at SciVerse ScienceDirect

Biochemical and Biophysical Research Communications

journal homepage: www.elsevier.com/locate/ybbrc

Wnt3a promotes melanin synthesis of mouse hair follicle melanocytes

Haiying Guo, Ke Yang, Fang Deng, Jixing Ye, Yizhan Xing, Yuhong Li, Xiaohua Lian, Tian Yang *

Department of Cell Biology, Third Military Medical University, Chongqing 400038, PR China

ARTICLE INFO

Article history:
Received 26 February 2012
Available online 21 March 2012

Keywords:
Wnt3a
Wnt/β-catenin signaling
Hair follicle
Melanocyte
Melanin synthesis

ABSTRACT

Although the importance of Wnt3a in melanocyte development has been well recognized, the effect of Wnt3a in normal HF melanocytes has not been clearly elucidated yet. Thus, we sought to examine the presence and location of Wnt3a in HF during hair cycle. By using melanocyte-targeted Dct-LacZ transgenic mice, we found that Wnt3a signaling is activated in mouse HF melanocytes during anagen of hair cycle. To further explore the potential functions of Wnt3a in mouse melanocytes, we infected melan-a cells with AdWnt3a to serve as the production source of Wnt3a protein. We demonstrated that Wnt3a promoted melanogenesis through upregulation of MITF and its downstream genes, tyrosinase and TRP1, in melanocytes. *In vivo*, AdWnt3a rescued the effects of AdsimMITF on HF melanocytes and promoted melanin synthesis. Our results suggest that Wnt3a plays an important role in mouse HF melanocytes homeostasis.

© 2012 Elsevier Inc. All rights reserved.

1. Introduction

Melanocytes play important roles in skin and hair pigmentation by producing melanin [1,2]. Melanocytes originate from neural crest-derived melanoblasts. During embryogenesis, melanoblasts migrate through the dermis into the epidermis. In the hairy region of mammalian skin, melanoblasts further enter the newly developing hair follicles (HFs) where they finally become localized [3–5]. Henceforward, melanoblasts are separated into two subpopulations: differentiated melanocytes, localized in the hair bulb, expresses MITF, DCT, TRP1, and tyrosinase, responsible for hair pigmentation; and melanocyte stem cells (McSCs), localized in the bulge region, expresses only DCT, responsible for the repopulation of the melanocyte system in subsequent hair cycles [6,7]. Melanocytes in HFs repeatedly proliferate and differentiate during every hair cycle [8]. During active growth (anagen) of HFs, melanocytes that are located in the hair bulb proliferate and differentiate to produce pigment for the hair shaft [2,9]. Melanocytes begin to shut down melanogenesis in late anagen and regression phase (catagen), and die by apoptosis from the hair bulb in rest phase (telogen), but reappear at the same location when HFs reenter anagen [10–12].

Wnt3a has been reported to act through the canonical pathway and has important roles in the development of melanocytes. Mutant mice deficient in Wnt1 and Wnt3a are almost completely devoid of pigment cells [13]. *In vitro* studies found that neural crest cells depleted of Wnt1 and Wnt3a become neurons rather than melanocytes [14], while treatment with Wnt3a caused them to become pigment cells rather than neurons and glial cells [15]. Wnt3a acts on melanoblasts along with EDN3 and KITL to maintain MITF expression and promote melanoblasts to differentiate to become melanocytes [16].

Although the importance of Wnt3a in melanocyte development has been well recognized, the effect of Wnt3a in normal HF melanocytes has not been clearly elucidated yet. To address this issue, we used Dct-LacZ transgenic mice [17] to examine the expression of Wnt3a in HF melanocytes and adenoviral gene delivery of Wnt3a to investigate the effects of Wnt3a in mouse melanocyte cell line (melan-a) and primary cultured mouse melanocytes.

2. Materials and methods

2.1. Animals and skin samples

Dct-LacZ transgenic mice were kindly provided by Prof. Ian Jackson [17]. The generated colony was backcrossed with C57BL/6J. Mice were housed in the community cages at the animal facility of Third Military Medical University. All the animal-related procedures were in strict accordance with the approved institutional animal care and maintenance protocols.

2.2. X-gal staining and immunohistochemistry

The harvested skins were first fixated at 4 °C in 4% paraformaldehyde for 2 h, then stained with X-gal staining solution

Abbreviations: HF, hair follicle; X-gal, 5-bromo-4-chloro-3-indolyl-β-D-galactoside; IRS, inner root sheath; McSC, melanocyte stem cell; Ad, adenovirus; MITF, microphthalmia-associated transcription factor; DCT, dopachrome tautomerase; TRP1, tyrosinase-related protein 1; TPA, 12-*o*-tetradecanoyl phorbol-13-acetate.

* Corresponding author.
E-mail address: tiany@163.net (T. Yang).

0006-291X/$ - see front matter © 2012 Elsevier Inc. All rights reserved.
http://dx.doi.org/10.1016/j.bbrc.2012.03.077

(Beyotime, China) at room temperature for 24 h, and post-fixed overnight with 4% paraformaldehyde at 4 °C [6]. The skin specimens were embedded in paraffin and sliced into 5 μm sections for immunodetection. Sections were deparaffinized, rehydrated, and microwave heated for antigen retrieval. After blocking endogenous peroxidase and non-specific biotin binding, sections were incubated with rabbit anti-Wnt3a antibody (Abcam, USA), rabbit anti-β-catenin antibody (Abcam, USA), goat anti-Lef-1 antibody (Santa Cruz, USA), or goat anti-TRP1 antibody (Santa Cruz, USA) and rabbit anti-Wnt3a antibody co-staining at 4 °C overnight, and signals were detected using appropriate secondary antibodies conjugated with Cy3 (Beyotime, China), Alexa Fluor 488 (Invitrogen, USA) or with DAB (Tiangen, China). Finally, sections were counterstained with DAPI for cell nuclei visualization. All images were obtained using an Olympus microscope (BH2, Olympus, Japan).

2.3. Cell culture

An immortal line of mouse melanocytes, melan-a, were a kind gift of Dr. D.C. Bennett [18]. The cells were cultured in RPMI 1640 medium (Gibco, USA) with 10% FBS (Gibco, USA), 2 mM L-glutamine (Sigma, USA), 200 nM PTA (Sigma, USA), and grown in a humidified atmosphere containing 10% CO_2 in air at 37 °C. Primary melanocytes were isolated from trunk skin of C57BL/6J mice up to 24 h old, more or less as described previously for melanoblast cultures [19,20]. In short, the skin was removed and incubated in 0.25% trypsin (Invitrogen, USA) for 20 h at 4 °C, epidermal sheets were peeled mechanically with fine forceps from dermal tissues. The peeled epidermal sheets were cut finely and dissociated briefly with trypsin and EDTA, and the resulting cell suspension was plated on dishes coated with type IV collagen. The cells were cultured in RPMI 1640 medium with 5% FBS, 2.5 ng/mL FGF2 (R&D Systems, USA), 50 ng/mL SCF (PeproTech, USA), 2 mM L-glutamine, 20 nM TPA (Sigma, USA), 200 pM cholera toxin (Sigma, USA) in a 5% CO2 incubator at 37 °C [19].

2.4. Adenovirus amplification and infection

The adenoviruses expressing green fluorescent protein (AdGFP), Wnt3a protein (AdWnt3a), and SimMITF (AdSimMITF, a small interfering RNA of MITF mediated by adenovirus) were kindly provided by Dr. T.-C. He. The adenoviruses were propagated and purified as previously described [21]. Briefly, the adenoviruses were propagated in HEK 293 cells. Cell pellets were re-suspended in PBS and lysed by four freeze–thaw–vortex cycles. After being purified by cesium chloride (Amresco, USA) density gradient centrifugation, adenovirus was dialyzed into storage buffer, then their titers were determined and diluted with storage buffer to the ultimate titers of 10^8 plaque-forming unit (PFU)/mL.

2.5. Isolation of total RNA and RT-PCR

Total cellular RNA was isolated at the indicated time-points using TRIzol reagent (Invitrogen, USA). Single-stranded cDNA was synthesized by using ReverTra Ace reverse transcriptase (TOYOBO, Japan) and Oligo-dT primers according to the manufacturer's protocol. Semi-quantitative PCR was performed using primers for Wnt3a, MITF, TRP1, DCT, and tyrosinase (see Table 1 in Supplemental materials for primer sequences). PCR reaction was performed by using a touchdown protocol previously described [22]. Briefly, touchdown PCR was performed with the following program: 1 cycle at 94 °C for 2 min, 12 cycles at 92 °C for 20 s, 68 °C for 30 s, and 70 °C for 45 s with a decrease of one degree per cycle, and 25 cycles at 92 °C for 20 s, 55 °C for 30 s, and 70 °C for 45 s.

2.6. Melanin content assay

Melan-a cells were plated onto 6-well plates at a concentration of 1×10^5 cells/well. After 12 h of incubation, cells were infected with AdWnt3a or AdGFP for 72 h, then trypsinized and counted. The same number (1×10^5) of cells were collected and washed twice with ethanol–ether 1:1 (v/v) to remove opaque substances other than melanin. Then the pellets were dissolved in 1 mL of 1 M sodium hydroxide at 80 °C for 1 h. The sample was then vigorously vortexed to solubilize the melanin pigment. 200 μL of the cell extracts were transferred to 96-well plates and absorbance was measured at 405 nm. The experiments were performed at least three times.

2.7. Tyrosinase activity assay

Tyrosinase activity assays were performed according to the method previously reported [23]. Melan-a cells in 6-well plates were infected with AdWnt3a or AdGFP for 72 h, then trypsinized and counted. 1×10^5 cells were treated with 200 μL 1% TritonX-100/PBS at −80 °C for 30 min and thawed at 37 °C. Then, the extracts were clarified by centrifugation, 50 μL of the supernatant were transferred into 96-well plates and 10 μL 2 mg/mL L-Dopa (Sigma, USA) were added. After incubation for 2 h at 37 °C, absorbance was measured at 490 nm. The experiments were performed at least three times.

2.8. Intradermal administration of adenoviruses

To induce hair cycle, depilation of the dorsal skin of female Dct-LacZ transgenic mice (8-week-old) were performed as described previously [24]. Twenty-five microliters AdWnt3a, AdsimMITF, or AdGFP vehicle control were administered intracutaneously to dorsal skin after the depilation. For the histochemical analyses, dorsal skin were harvested for X-gal staining 4 days after administration. Three different experiments were done.

2.9. Statistical analysis

Data were presented as a mean ± SD of three independent experiments. Statistical differences were evaluated using a *t*-test and $p < 0.05$ was considered statistically significant.

3. Results

3.1. Wnt3a is expressed in melanocyte stem cells and melanocytes during anagen

By using Dct-LacZ transgenic mice, X-gal staining was used to label LacZ-positive melanocytes in HFs. The results showed that melanocyte stem cells (McSCs) were located in the bulge of the outer root sheath and melanocytes were located in the hair bulb and above the dermal papilla (Fig. S1).

In anagen, high expression of Wnt3a protein was detected in cells at the epidermis, bulge, inner root sheath (IRS) precursors and hair bulb, including melanocytes and McSCs (Fig. 1A). In catagen, the expression of Wnt3a was decreased gradually and detected only in the bulge (Fig. 1B). In telogen, no obvious Wnt3a protein was detected in the hair follicles (Fig. 1C). Interestingly, when HFs entered the next anagen, Wnt3a protein was expressed in the hair bulb and melanocytes again (Fig. 1D). Consistent with these data, Wnt3a mRNA was most strongly expressed in anagen, decreased in catagen, and lowest in telogen (Fig. 1E).

TRP1 is a marker of melanocytes, including differentiating melanocytes and pigment-producing melanocytes [7]. We also

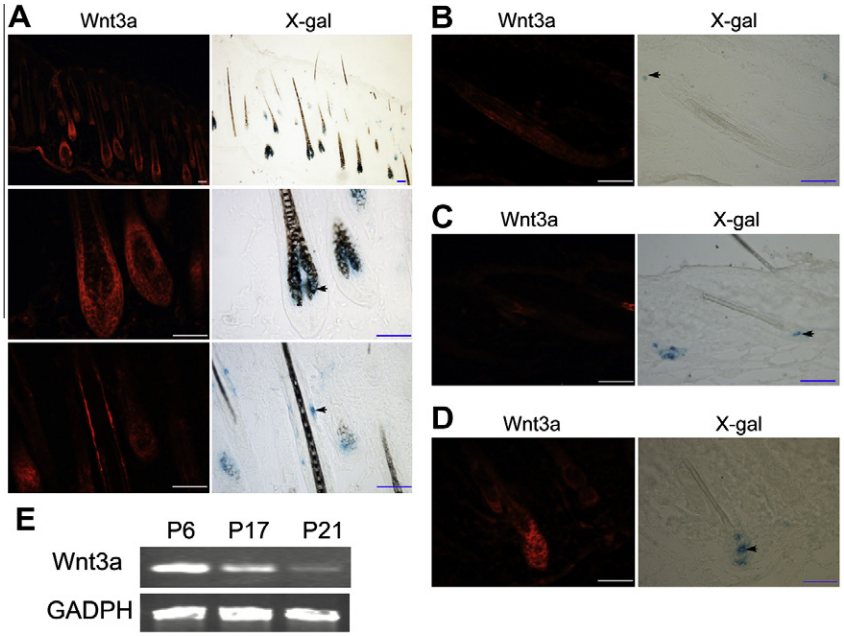


Fig. 1. Expression of Wnt3a in HF during the hair cycle. (A–D) Dorsal skin sections from Dct-LacZ mice were stained with both X-gal and anti-Wnt3a antibody. The same regions were shown by fluorescent-field and bright-field optics. (A) Postnatal day 6 (P6), in anagen, Wnt3a was expressed in the epidermis, bulge, IRS and hair bulb including some $LacZ^+$ melanocyte stem cells (arrows) and melanocytes (arrows). (B) P18, in catagen, Wnt3a was only detected in the bulge area. (C) P21, in telogen, little Wnt3a protein was detected in the hair follicle. (D) P26, in the next anagen onset, Wnt3a was expressed again in the hair follicle and including melanocytes (arrows). (E) RT-PCR for the expression of Wnt3a mRNA in the dorsal skin of Dct-LacZ transgenic mice. Scale bars represent 50 μm.

detected the co-expression patterns of Wnt3a and TRP1 in HF melanocytes of anagen hair follicles. In anagen, a number of TRP1-positive cells co-expressed Wnt3a (Fig. 2E).

3.2. Wnt/β-catenin signaling pathway is activated in melanocytes during anagen

We next analyzed the activity of Wnt/β-catenin signaling in anagen HF melanocytes. We examined the expression pattern of β-catenin, the key downstream mediator of Wnt signaling, and found that it was expressed in the cytomembrane or nucleus of the epidermis, bulge, IRS and hair matrix cells, as well as in the nucleus of melanocytes in anagen (Fig. 2A and B). We then examined the expression of Lef-1, an important transcription factor of Wnt signaling, and found that it was expressed in the IRS, hair bulb, as well as melanocytes during anagen (Fig. 2C and D). Expression of nuclear β-catenin and Lef-1 in hair bulb melanocytes indicated that Wnt/β-catenin signaling is activated in HF melanocytes. Unexpectedly, neither nuclear β-catenin nor Lef-1 was detected in McSCs (arrowheads in Fig. 2B and D), suggesting that Wnt/β-catenin signaling was suppressed in bulge McSCs in anagen HFs.

The results showed that both Wnt3a and active Wnt/β-catenin signaling were detected in HF melanocytes during anagen, which implied that Wnt3a and Wnt/β-catenin signaling may play important roles in HF melanocyte proliferation, differentiation and pigmentation.

3.3. Wnt3a promotes the melanogenesis of melanocytes in vitro

To further explore the potential role of Wnt3a in HF melanocytes, we used a mouse melanocyte cell line, melan-a [18], as an *in vitro* cell model. We infected melan-a cells with AdWnt3a at a pre-determined optimal titer. The expression of Wnt3a was

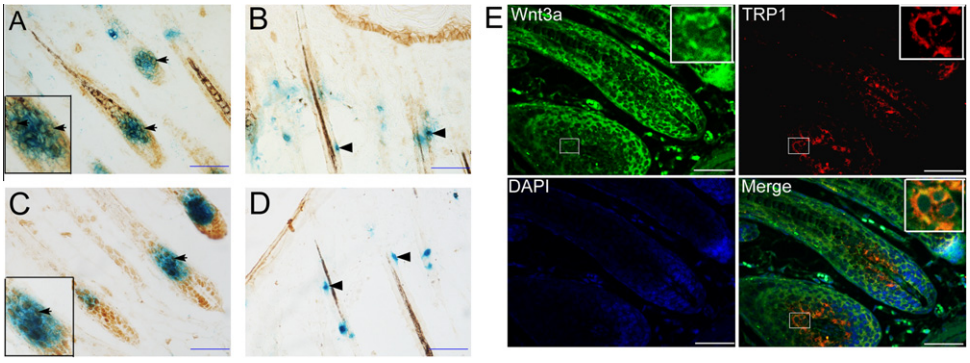


Fig. 2. Expression of β-catenin, Lef-1 and co-expression of Wnt3a and TRP1 in melanocytes of anagen HFs. (A–D) X-gal staining and immunohistochemistry of dorsal skin sections from P6 Dct-LacZ mice. (A and B) Nuclear β-catenin was detected in some hair bulb melanocytes (arrows) but not detected in bulge McSCs (arrowheads). (C and D) Lef-1 was expressed in hair bulb melanocytes (arrows) but not expressed in bulge McSCs (arrowheads). (E) Co-expression of Wnt3a and TRP1 in melanocytes of anagen HFs. Green, Wnt3a; Red, TRP1; Blue, DAPI. Scale bars represent 50 μm. (For interpretation of the references to color in this figure legend, the reader is referred to the web version of this article.)

confirmed by immunofluorescent staining and RT-PCR in AdWnt3a-infected cells but not in AdGFP-infected cells (Fig. 3A and B).

Tyrosinase is the key regulatory enzyme for melanin synthesis and, therefore, its activity is a marker for the pigmentation of melanocytes. Tyrosinase activity assay was utilized to analyze tyrosinase activity in melan-a cells infected with AdWnt3a or AdGFP control. As shown in Fig. 3D, a greatly significant increase of tyrosinase activity was detected in AdWnt3a-infected cells compared with AdGFP-infected cells. In conformity with the results of the tyrosinase activity assay, melanin content assay also revealed that AdWnt3a-infected cells increased melanin synthesis significantly (Fig. 3C).

To confirm that Wnt3a was responsible for production of melanin, we also cultured primary melanocytes isolated from neonatal mice skin and infected them with AdWnt3a or AdGFP. As shown in Fig. 3F, the immature melanocytes during development exhibited characteristic small and bipolar cell bodies but, after treatment with AdWnt3a, the cell size and melanin synthesis of the melanocytes increased noticeably.

To investigate how Wnt3a promotes melanin synthesis, we studied the expression of MITF, the transcriptional master regulator of melanocytes, and its downstream target genes, including tyrosinase, TRP1, as well DCT [25–27]. RT-PCR analyses showed that Wnt3a increased the expression levels of MITF, tyrosinase, and TRP1 in melan-a cells, but did not affect the expression of DCT (Fig. 3E). Then, we infected melan-a cells with AdSimMITF to reduce the endogenous MITF. RT-PCR analyses showed that AdSimMITF did remarkably decrease the expression of MITF and its downstream target genes. Next, we co-infected melan-a cells with AdSimMITF and AdWnt3a and found that Wnt3a rescued the expression of MITF, tyrosinase, TRP1 and DCT (Fig. 3E).

The data strongly suggested that Wnt3a contributed to increase the melanin synthesis and the functional activation of melanocytes while upregulating the expression of MITF and its downstream genes.

3.4. Wnt3a promotes the melanogenesis of melanocytes in vivo

To investigate whether the effects of Wnt3a on mouse HF melanocytes *in vivo* are consistent with those *in vitro*, we induced the hair cycle by depilation and intradermal administration of AdsimMITF, AdGFP vehicle control, or co-administration of AdsimMITF and AdWnt3a. The dorsal skin was analyzed at anagen III stage (i.e., 4 days after depilation) [24]. While the skin around administered of AdsimMITF was still pink, the skin around administered of co-administered of AdsimMITF and AdWnt3a were changed to gray (Fig. 4B). Histochemical analyses showed that AdsimMITF inhibited the melanin synthesis of HF melanocytes efficiently (Fig. 4D). However, when co-administered of AdWnt3a

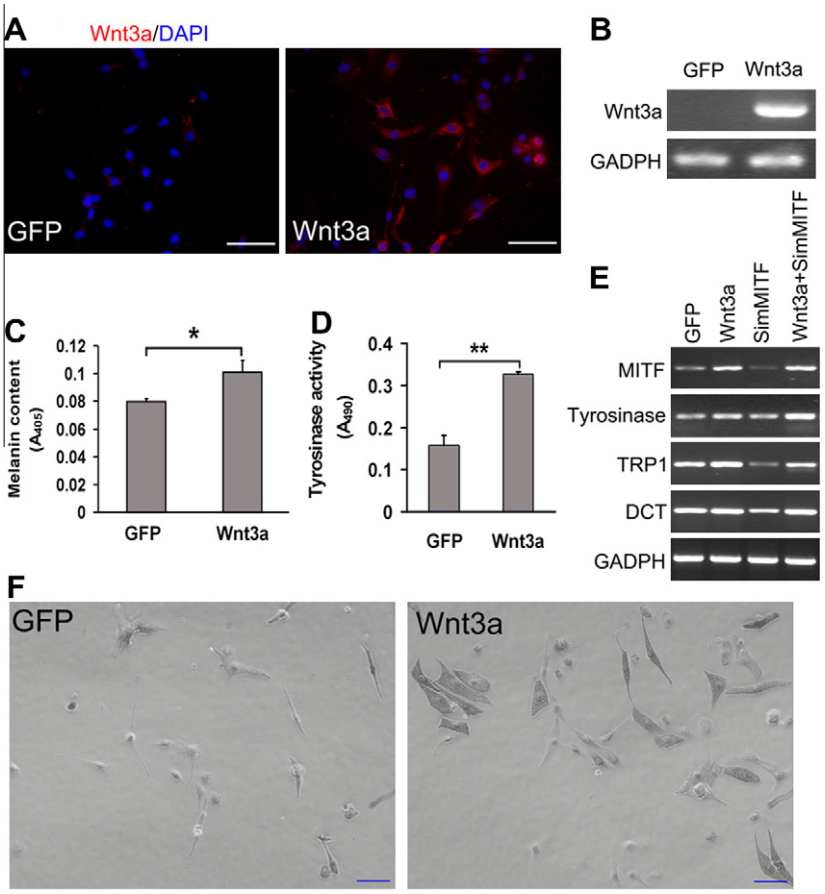


Fig. 3. Effects of Wnt3a on pigmentation of melan-a cells and primary cultured melanocytes. (A and B) AdWnt3a mediated efficient gene transfer in melan-a cells. Immunofluorescent staining (A) and RT-PCR analysis (B) of Wnt3a in melan-a cells after infection with AdWnt3a or AdGFP. Red, Wnt3a; Blue, DAPI. Scale bars represent 50 μm. (C) Melanin synthesis of melan-a cells infected with AdWnt3a or AdGFP detected. (D) Tyrosinase activity of melan-a cells infected with AdWnt3a or AdGFP. (E) Effect of Wnt3a on the expression of pigmentation-related mRNA in melan-a cells. Cells were infected with AdGFP, AdWnt3a, AdSimMITF, or co-infected with AdSimMITF and AdWnt3a, respectively. After 72 h, RT-PCR analyses were performed with primers specific for MITF, tyrosinase, TRP1, and DCT. (F) Phase contrast micrographs of primary cultured melanocytes infected with AdWnt3a or AdGFP. Melanocytes isolated from neonatal mice skin were cultured for 7 days. Then the cells were infected with AdWnt3a or AdGFP. Scale bars represent 100 μm. These data were representative results of three independent experiments. $^{*}p < 0.05$ and $^{**}p < 0.01$. $n = 3$. (For interpretation of the references to color in this figure legend, the reader is referred to the web version of this article.)

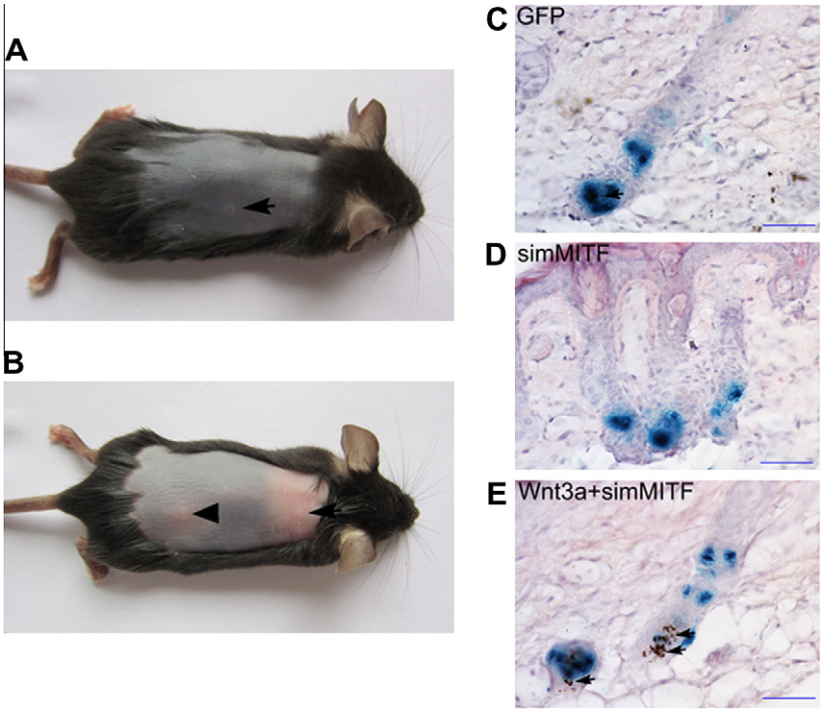


Fig. 4. Effects of Wnt3a on pigmentation of mouse HF melanocytes. (A) The skin color around the administered site of AdGFP was gray (arrow). (B) The skin color around the administered site of AdsimMITF was pink (arrow), and co-administered site of AdsimMITF and AdWnt3a was gray (arrowhead). (C–E) X-gal staining and eosin-hematoxylin counterstained of skin sections around the administered sites. (C and E) Pigmented melanocytes in the bulb (arrow). (D) Absent of melanin in the bulb. Scale bars represent 50 μm. (For interpretation of the references to color in this figure legend, the reader is referred to the web version of this article.)

and AdsimMITF, the melanocytes synthesized melanin visibly (Fig. 4E), suggesting that Wnt3a might rescued the expression of MITF and promoted melanogenesis of HF melanocytes.

4. Discussion

Despite the well-known role for Wnt3a in the development of melanocytes, the effect of Wnt3a signaling in HF melanocytes remains undetermined. Recent studies have shown that postnatally, Wnt3a mRNA and protein are expressed in the IRS precursors of HFs and basal keratinocytes of epidermis [28,29]. However, whether HF melanocytes express Wnt3a or whether Wnt3a expression correlates with HF melanocyte proliferation, differentiation, and apoptosis are unknown. To address these questions, we investigated the effect of Wnt3a in mouse HF melanocytes in this study.

First, we used Dct-LacZ transgenic mice [17] as a model to examine the *in situ* expression status of Wnt3a protein in mouse HF melanocytes during the hair cycle. X-gal staining, immunochemistry, and RT-PCR revealed that Wnt3a was expressed in the epidermis, bulge, IRS precursors and hair bulb in anagen, decreased in catagen, and was basically not expressed in telogen. Some melanocytes residing in the hair bulb also expressed Wnt3a in anagen. Previous research showed that melanocytes in the hair bulb proliferate and produce melanin during anagen, undergo apoptosis in catagen, and are absent throughout the telogen stage [2,9,10,12]. Our results showed that a number of melanocytes and adjacent keratinocytes in the hair bulb both expressed Wnt3a during anagen. Subsequently, when melanocytes ceased to produce melanin, the expression level of Wnt3a in the IRS and hair bulb was decreased and eventually lost. Thus, Wnt3a might exert its effects on melanocyte melanogenesis.

Reddy et al. demonstrated that Wnt3a RNA was expressed in the IRS cells adjacent to the hair shaft precursors [29]. In our study, the expression level of Wnt3a in the IRS precursors was higher than those in the hair bulb and melanocytes. Given that Wnt3a is a paracrine protein, it might exert its effects in a paracrine manner when secreted by the IRS cells to the adjacent keratinocytes and melanocytes in the hair bulb.

Rabbani et al. reported that melanocytes in the hair bulb showed nuclear β-catenin in anagen HFs, and the nuclear signal decreases by late anagen [30]. Osawa et al. showed that Lef-1 was detectable in melanocytes while undetectable in melanocyte stem cells in anagen HFs [7]. In our study, we found that both β-catenin and Lef-1 displayed nuclear positivity in hair bulb melanocytes in anagen HFs, suggesting that Wnt/β-catenin signaling was activated in HF melanocytes during anagen.

Interestingly, though Wnt3a was expressed in bulge region in anagen and catagen, neither nuclear β-catenin nor Lef-1 was detected in McSCs. It was reported that McSCs expressed a high level of Wnt inhibitors such as Wif1, Sfrp1, Dab2 and Dkk4 [31]. Thus, the expression of Wnt inhibitors may decrease the effectiveness of Wnt3a signaling. Although Wnt/β-catenin signaling was suppressed in bulge McSCs during hair cycle, it was activated at anagen onset in the secondary hair germ McSCs [30].

Tyrosinase is an enzyme uniquely expressed in melanocytes and catalyzes the rate-limiting initial events of melanogenesis. TRP1 and DCT are also critically important for melanogenesis, functioning as downstream enzymes in the melanin biosynthetic pathway. To investigate the influence of Wnt3a melanogenesis of mouse melanocytes, we analyzed tyrosinase activity and melanin content in melan-a cells. Our data showed that Wnt3a increased tyrosinase activity and melanin synthesis significantly in melan-a cells. Furthermore, Wnt3a acted on primary mouse melanocytes to increase melanin synthesis. In support of our findings, previous studies reported that inhibition of Wnt/β-catenin signaling strongly inhibited melanin synthesis [32,33].

It is well known that MITF is a transcription factor that regulates the expression of three major pigment enzymes: tyrosinase, TRP1, and Dct as well as other pigmentation factors [25]. In this

study, we detected the expression of MITF and its downstream target genes, tyrosinase, TRP1, and DCT, and demonstrated that Wnt3a up-regulated the expression of MITF, tyrosinase, and TRP1 in cultured melanocytes. Furthermore, Wnt3a rescued the expression of MITF and its downstream target genes following reduction of endogenous MITF in melan-a cells by AdSimMITF. With the same melan-a cells, Takeda et al. found that Wnt3a protein induced MITF mRNA expression and activated the MITF promoter by recruiting Lef-1 and β-catenin to the Lef-1-binding site [27]. Our data are consistent with the result of Takeda et al. that MITF is a target gene of Wnt3a signaling.

In our study, we also cultured primary mouse melanocytes and confirmed that Wnt3a promoted the melanogenesis of the primary melanocytes as well. And the effects of Wnt3a on mouse HF melanocytes melanogenesis *in vivo* were consistent with those *in vitro* in our intradermal administration studies.

In summary, we demonstrate that Wnt3a signaling is activated in mouse HF melanocytes during anagen. *In vitro*, Wnt3a promotes the melanin synthesis through the upregulation of MITF and its downstream genes. *In vivo*, AdWnt3a rescued the effects of AdsimMITF on HF melanocytes and promoted melanin synthesis.

Acknowledgments

This work was supported by the National Natural Science Foundation of China (No. 30872711). We thank Dr. T-C. He (Chicago University) for adenovirus production and technical assistance. We thank Prof. Dorothy C Bennett (University of London) and Dr. Zhixiu Lin (The Chinese University of Hong Kong) for providing melan-a cells; We thank Prof. Ian Jackson (MRC Human Genetics Unit) for the Dct-LacZ transgenic mice. We are also grateful to Cheng-Ming Chuong (University of Southern California) for carefully revising the manuscript.

Appendix A. Supplementary data

Supplementary data associated with this article can be found, in the online version, at doi:10.1016/j.bbrc.2012.03.077.

References

[1] Y. Yamaguchi, M. Brenner, V.J. Hearing, The regulation of skin pigmentation, J. Biol. Chem. 282 (2007) 27557–27561.
[2] A. Slominski, J. Wortsman, P.M. Plonka, K.U. Schallreuter, R. Paus, D.J. Tobin, Hair follicle pigmentation, J. Invest. Dermatol. 124 (2005) 13–21.
[3] T.C. Mayer, The migratory pathway of neural crest cells into the skin of mouse embryos, Dev. Biol. 34 (1973) 39–46.
[4] S.A. Jordan, I.J. Jackson, MGF (KIT ligand) is a chemokinetic factor for melanoblast migration into hair follicles, Dev. Biol. 225 (2000) 424–436.
[5] M. Osawa, Melanocyte stem cells, StemBook June 30. (2009) 1–23.
[6] E.K. Nishimura, S.A. Jordan, H. Oshima, et al., Dominant role of the niche in melanocyte stem-cell fate determination, Nature 416 (2002) 854–860.
[7] M. Osawa, G. Egawa, S.-S. Mak, et al., Molecular characterization of melanocyte stem cells in their niche, Development 132 (2005) 5589–5599.
[8] E.K. Nishimura, Melanocyte stem cells: a melanocyte reservoir in hair follicles for hair and skin pigmentation, Pigm. Cell Melanoma Res. 24 (2011) 401–410.
[9] A. Slominski, R. Paus, Melanogenesis is coupled to murine anagen: toward new concepts for the role of melanocyte and the regulation of melanogenesis in hair growth, J. Invest. Dermatol. (1993) 90S–97S.
[10] D.J. Tobin, E. Hagen, V.A. Botchkarev, et al., Do hair bulb melanocytes undergo apoptosis during hair follicle regression (catagen)?, J Invest. Dermatol. 111 (1998) 941–947.
[11] A. Slominski, R. Paus, P. Plonka, et al., Melanogenesis during the anagen–catagen–telogen transformation of the murine hair cycle, J. Invest. Dermatol. (1994) 862–869.
[12] D.J. Tobin, A. Slominski, V. Botchkarev, et al., The fate of hair follicle melanocytes during the hair growth cycle, J. Investig. Dermatol. Symp. Proc. 4 (1999) 323–332.
[13] M. Ikeya, S.M. Lee, J.E. Johnson, et al., Wnt signalling required for expansion of neural crest and CNS progenitors, Nature 389 (1997) 966–970.
[14] R.I. Dorsky, R.T. Moon, D.W. Raible, Control of neural crest cell fate by the Wnt signalling pathway, Nature 396 (1998) 370–373.
[15] E.J. Jin, C.A. Erickson, S. Takada, et al., Wnt and BMP signaling govern lineage segregation of melanocytes in the avian embryo, Dev. Biol. 233 (2001) 22–37.
[16] Karen Joyce Dunn, Matthew Brady, Christina Ochsenbauer-Jambor, Sara Snyder, Arturo Incao, W.J. Pavan, WNT1 and WNT3a promote expansion of melanocytes through distinct modes of action, Pigm. Cell Res. 18 (2005) 167–180.
[17] M.A. Mackenzie, S.A. Jordan, P.S. Budd, I.J. Jackson, Activation of the receptor tyrosine kinase kit is required for the proliferation of melanoblasts in the mouse embryo, Dev. Biol. 192 (1997) 99–107.
[18] D.C. Bennett, P.J. Cooper, I.R. Hart, A line of non-tumorigenic mouse melanocytes, syngeneic with the B16 melanoma and requiring a tumour promoter for growth, Int. J. Cancer. 39 (1987) 414–418.
[19] E.V. Sviderskaya, W.F. Wakeling, D.C. Bennett, A cloned, immortal line of murine melanoblasts inducible to differentiate to melanocytes, Development (1995) 1547–1557.
[20] S. Yonetani, M. Moriyama, C. Nishigori, et al., *In vitro* expansion of immature melanoblasts and their ability to repopulate melanocyte stem cells in the hair follicle, J. Invest. Dermatol. 128 (2007) 408–420.
[21] J. Luo, Z.L. Deng, X. Luo, et al., A protocol for rapid generation of recombinant adenoviruses using the AdEasy system, Nat. Protoc. 2 (2007) 1236–1247.
[22] Y. Peng, Q. Kang, H. Cheng, et al., Transcriptional characterization of bone morphogenetic proteins (BMPs)-mediated osteogenic signaling, J. Cell. Biochem. 90 (2003) 1149–1165.
[23] E.K. Nishimura, M. Suzuki, V. Igras, et al., Key roles for transforming growth factor Beta in melanocyte stem cell maintenance, Cell Stem Cell 6 (2010) 130–140.
[24] S. Muller-Rover, B. Handjiski, C. van der Veen, S. Eichmuller, K. Foitzik, I.A. McKay, K.S. Stenn, R. Paus, A comprehensive guide for the accurate classification of murine hair follicles in distinct hair cycle stages, J. Invest. Dermatol. 117 (2001) 3–15.
[25] H.R. Widlund, D.E. Fisher, Microphthalamia-associated transcription factor: a critical regulator of pigment cell development and survival, Oncogene 22 (2003) 3035–3041.
[26] E. Steingrimsson, N.G. Copeland, N.A. Jenkins, Melanocytes and the microphthalmia transcription factor network, Annu. Rev. Genet. 38 (2004) 365–411.
[27] K. Takeda, K. Yasumoto, R. Takada, et al., Induction of melanocyte-specific microphthalmia-associated transcription factor by Wnt-3a, J. Biol. Chem. 275 (2000) 14013–14016.
[28] L. Jia, J. Zhou, S. Peng, et al., Effects of Wnt3a on proliferation and differentiation of human epidermal stem cells, Biochem. Biophys. Res. Commun. 368 (2008) 483–488.
[29] S. Reddy, T. Andl, A. Bagasra, et al., Characterization of Wnt gene expression in developing and postnatal hair follicles and identification of Wnt5a as a target of sonic hedgehog in hair follicle morphogenesis, Mech. Dev. 107 (2001) 69–82.
[30] P. Rabbani, M. Takeo, W. Chou, et al., Coordinated activation of wnt in epithelial and melanocyte stem cells initiates pigmented hair regeneration, Cell 145 (2011) 941–955.
[31] S.I. Nishikawa, M. Osawa, Generating quiescent stem cells, Pigm. Cell Res. 20 (2007) 263–270.
[32] M. Cho, M. Ryu, Y. Jeong, et al., Cardamonin suppresses melanogenesis by inhibition of Wnt/beta-catenin signaling, Biochem. Biophys. Res. Commun. 390 (2009) 500–505.
[33] Y. Yamaguchi, T. Passeron, T. Hoashi, et al., Dickkopf 1 (DKK1) regulates skin pigmentation and thickness by affecting Wnt/beta-catenin signaling in keratinocytes, FASEB J. 22 (2008) 1009–1020.

Biochemical and Biophysical Research Communications 420 (2012) 805–810

Contents lists available at SciVerse ScienceDirect

Biochemical and Biophysical Research Communications

journal homepage: www.elsevier.com/locate/ybbrc

18β-Glycyrrhetinic acid inhibits adipogenic differentiation and stimulates lipolysis

Myung-Hee Moon, Jae-Kyo Jeong, You-Jin Lee, Jae-Won Seol, Dong-Choon Ahn, In-Shik Kim, Sang-Youel Park *

Center for Healthcare Technology Development, Biosafety Research Institute, College of Veterinary Medicine, Chonbuk National University, Jeonju, Jeonbuk 561-756, South Korea

ARTICLE INFO

Article history:
Received 12 March 2012
Available online 21 March 2012

Keywords:
18β-Glycyrrhetinic acid
3T3-L1 preadipocytes
Adipogenesis
Lipolysis

ABSTRACT

18β-Glycyrrhetinic acid (18β-GA) obtained from the herb liquorice has various pharmacological properties including anti-inflammatory and anti-bacterial activities. However, potential biological anti-obesity activities are unclear. In this study, novel biological activities of 18β-GA in the adipogenesis of 3T3-L1 preadipocytes and in lipolysis of differentiated adipocytes were identified. Mouse 3T3-L1 cells were used as an in vitro model of adipogenesis and lipolysis, using a mixture of insulin/dexamethasone/3-isobutyl-1-methylxanthine (IBMX) to induce differentiation. The amount of lipid droplet accumulation was determined by an AdipoRed assay. The expression of several adipogenic transcription factors and enzymes was investigated using real-time reverse transcriptase-polymerase chain reaction (RT-PCR) and Western blotting. 18β-GA dose-dependently (1–40 μM) significantly decreased lipid accumulation in maturing preadipocytes. In 3T3-L1 preadipocytes, 10 μM of 18β-GA down-regulated the transcriptional levels of the peroxisome proliferator-activated receptor γ, CCAAT/enhancer-binding protein α and adiponectin, which are markers of adipogenic differentiation via Akt phosphorylation. Also, in differentiated adipocytes, 18β-GA increased the level of glycerol release and up-regulated the mRNA of hormone-sensitive lipase, adipose TG lipase and perilipin, as well as the phosphorylation of hormone-sensitive lipase at Serine 563. The results indicate that 18β-GA alters fat mass by directly affecting adipogenesis in maturing preadipocytes and lipolysis in matured adipocytes. Thus, 18β-GA may be useful for the treatment of obesity.

© 2012 Elsevier Inc. All rights reserved.

1. Introduction

Obesity is the most common metabolic disease in developed nations and has become a global epidemic [1]. Obesity is associated with a variety of chronic diseases, including glucose intolerance, insulin resistance, dyslipidemia and hypertension. A combination of these abnormalities is termed metabolic syndrome [2]. Obesity is due to adipocyte hyperplasia and hypertrophy caused by intake of excess energy [3]. Increased adipocyte number during the aging process may contribute to the increase in the incidence and severity of obesity observed in older individuals [4]. Thus, hyperplasia of adipocytes might be an important factor in the development of obesity. Also, it is important for the prevention and improvement of obesity to maintain an adequate balance between energy accumulation and consumption.

Lipolysis is one of the most important metabolic pathways regulating adipose tissue weight and obesity. The two major enzymes that catabolize triglycerides (TGs) are hormone-sensitive lipase (HSL) and adipose TG lipase (ATGL) [5–7]. HSL is the most active enzyme against diglycerides (DG), which are hydrolyzed 10 times faster than TG. On the other hand, ATGL selectively performs the first step in TG hydrolysis resulting in the formation of DG and free fatty acids (FFAs). Its activity against TG is 10 times more specific than that against DG. Differences between these two lipases are also found in their localization. Whereas HSL is present in the cytosol, ATGL is localized in the cytosol and also on lipid droplets [6,8].

White adipose tissue (WAT) plays an important role in regulating whole body energy homeostasis [6]. One of its major roles is to release FAs under conditions of negative energy balance or prolonged exercise to provide energy for peripheral tissues. The molecular machinery involved in TG breakdown and FA release works in an orderly and regulated fashion, conferring to WAT the capacity to respond to various feeding conditions and to the energy demands of the body [9]. Importantly, conditions that lead to overeating and obesity disrupt the normal regulation of WAT lipolysis. In fact, basal lipolysis has repeatedly been reported as elevated, whereas catecholamine-induced lipolysis is suppressed in obese humans and rodents [6,10]. The classical mechanism to explain this condition centers on the fact that the largely expanded WAT of obese subjects becomes resistant to insulin, impairing the major lipogenic and antilipolytic effects of this hormone [6,9,11–13]. Although increased lipolysis in high fat diet feeding leads to release of FFA to serum, resulting in insulin resistance terminally, other mouse models with increased lipolysis and decreased adipose tissue mass have also reported unchanged or reduced serum

* Corresponding author. Fax: +82 63 270 3780.
E-mail address: sypark@chonbuk.ac.kr (S.-Y. Park),

0006-291X/$ - see front matter © 2012 Elsevier Inc. All rights reserved.
http://dx.doi.org/10.1016/j.bbrc.2012.03.078

non-esterified fatty acid (NEFA) [14–18]. Also, increased lipolysis results in ectopic TAG accumulation in the liver and skeletal muscle, increased oxygen consumption and increased Ucp1, Dio2 and Ppard mRNA expression in WAT, suggesting higher oxidation and thermogenesis in WAT [15].

Adipocytes are derived from mesenchymal stem cells, which have the potential to differentiate into myoblasts, chondroblasts, osteoblasts and adipocytes [19]. Adipogenesis has been investigated extensively using 3T3-L1 cells. Adipocyte differentiation involves an elaborate network of transcription factors that regulate the expression of numerous genes responsible for the phenotype of mature adipocytes [20]. Among the various transcription factors that promote preadipocyte differentiation and influence adipogenesis, peroxisome proliferator-activated receptor γ (PPARγ) is considered the "master regulator of adipogenesis" [21–23]. Other adipogenic transcription factors include the CCAAT/enhancer binding proteins (C/EBPα, C/EBPβ and C/EBPγ) [4,20,24]. They are necessary for the expression of adipocyte-specific genes (adiponectin) [25]. These transcription factors, especially PPARγ and C/EBPα, are regulated by Akt pathway during adipogenesis [26–28].

Elevated cortisol concentrations have been associated with metabolic diseases such as diabetes type 2 and obesity [29]. 18β-Glycyrrhetinic acid (18β-GA), a principal active ingredient of liquorice root, was recently reported to target 11 beta-hydroxysteroid dehydrogenase type 1 (11 HSD1), a regulator that controls the cortisol/cortisone shuttle, and which is involved in obesity [30,31]. However, the effect of 18β-GA on adipogenesis has not been studied, especially on adipogenesis and lipolysis, which are important on obesity development. Investigation of the direct effect of 18β-GA on adipocyte will provide some novel insights for additional inhibitory mechanism of 18β-GA on obesity. We report that 18β-GA inhibits adipogenesis via phosphorylation of Akt and increases lipolysis through HSL activation.

2. Materials and methods

2.1. Reagents

18β-GA was purchased from Sigma–Aldrich (St. Louis, MO, USA). 18β-GA was prepared as a 10 mM solution in dimethylsulfoxide and then further diluted in cell culture medium.

2.2. Cell culture and differentiation

3T3-L1 cells were maintained in Dulbecco's modified Eagle's medium (DMEM) containing 10% calf serum and antibiotics (100 μg mL^{-1} gentamycin and 100 μg·mL^{-1} penicillin–streptomycin). To induce differentiation, 2-day post confluent 3T3-L1 cells were incubated in MDI induction medium (DMEM containing 10% fetal bovine serum, 0.5 mM 3-isobutyl-1-methylxanthine (IBMX), 1 μm dexamethasone and 1 μg/ml of insulin) for 2 days. In some experiments, 18β-GA (1–40 μM) was added at the time of the induction of differentiation. Two days after MDI (day 2), the medium was changed to an insulin containing medium. The AdipoRed Assay and detection of glycerol release contents were performed on day 7.

2.3. Quantification of lipid content

Lipid content was quantified using a commercially available AdipoRed Assay Reagent (Lonza, Verviers, Belgium) according to the manufacturer's instructions. In brief, preadipocytes grown in 24-well plates were incubated with MDI medium alone or supplemented with test compounds during the adipogenic phase. On day 7, culture supernatant was removed and carefully washed with 500 μl phosphate-buffered saline (PBS). The wells were then filled with 300 μl PBS and 30 μl of AdipoRed reagent was added and incubated for 10 min at 37 °C. Fluorescence was measured with an excitation at 485 nm and emission at 572 nm.

2.4. Adipolysis assay

Glycerol release was measured using a commercially available Adipolysis Assay Kit (Cayman Chemical, Ann Arbor, MI, USA) according to the manufacturer's instructions. Briefly, the differentiated adipocytes in a 96-well plate were stimulated with 18β-GA or isoproterenol solution used as a positive control for 24 h. After stimulation, the cell culture supernatants were collected from each well and stored until use at −20 °C. One hundred microliters of free glycerol assay reagent was added to 25 μl of each supernatant. After incubation for 15 min at room temperature, the absorbance was measured at 540 nm.

2.5. Quantitative real-time polymerase chain reaction (qRT-PCR)

Total RNA was extracted from 3T3-L1 cells treated with 18β-GA using the Easy-spin™ total RNA extraction kit (iNtRON Biotechnology, Seoul, Korea). cDNA synthesis was carried out following the instructions of the TaKaRa Prime Script TM 1st strand cDNA synthesis kit (TaKaRa Bio, Tokyo, Japan). For qRT-PCR, 1 μl of gene primers with SYBR Green (Bio-Rad Laboratories, Hercules, CA, USA) in 20 μl of reaction volume was applied. The sequences of the primers used for the real-time PCR were as follows:

PPARγ (forward 5′CGGAAGCCCTTTGGTGACTTTATG3′, reverse 5′GCAGCAGGTTGTCTTGGATGTC3′),

C/EBP-α (forward 5′CGGGAACGCAACAACATCGC3′, reverse 5′TGTCCAGTTCACGGCTCAGC3′),

Adiponectin (forward 5′TGACGGCAGCACTGGCAAG3′, reverse 5′TGATACTGGTCGTAGGTGAAGAGAAC3′),

ATGL (forward 5′GAGCTTCGCGTCACCAAC3′, reverse 5′CACATCTCTCGGAGGACCA3′), HSL (forward 5′AGACCACATCGCCCACA3′, reverse 5′CCTTTATTGTCAGCTTCTTCAAGG3′), Perilipin (forward 5′CACTCTCTGGCCATGTGGA3′, reverse 5′AGAGGCTGCCAGGTTGTG 3′), and β-actin (forward 5′TGAGAGGGAAAT CGTGCGTGAC3′, reverse 5′GCTCGTTGCCAATA GTGATGACC3′)

All reactions with iTaq SYBR Green Supermix (Bio-Rad Laboratories) were performed on the CFX96 real-time PCR detection system (Bio-Rad Laboratories).

2.6. Western blot

The 3T3-L1 cells were lysed in a lysis buffer (25 mM HEPES; pH 7.4, 100 mM NaCl, 1 mM EDTA, 5 mM $MgCl_2$, 0.1 mM dithiothreitol and protease inhibitor mixture). Proteins were electrophoretically resolved using 8–15% sodium dodecyl sulfate–polyacrylamide gele electrophoresis, and immunoblotting was performed as previously described [32]. Images were captured using the Fusion FX7 acquisition system (VilbertLourmat, Eberhardzell, Germany). Densitometry of the signal bands was analyzed using Bio-1D (VilberLourmat) [33]. The antibodies used for immunoblotting were PPARγ (Santa Cruz Biotechnology, Santa Cruz, CA, USA), p-Akt (Ser 473) (Epitomics, Burlingame, CA, USA), p-HSL (Ser 563; Cell Signaling Technology, Beverly, CA, USA), p-HSL (Ser 565; Cell Signaling Technology) and ß-actin (Sigma–Aldrich).

2.7. Statistical evaluation

All data are expressed as the mean ± SEM, and the data were compared using the Student's *t*-test and the ANOVA Duncan test with the SAS statistical package (SAS Institute, Cary, NC, USA).

The results were considered significant for values of $^{*}P < 0.05$ or $^{**}P < 0.01$.

3. Results and discussion

3.1. 18β-GA inhibits lipid accumulation during the differentiation of 3T3-L1 preadipocytes

Some reports have indicated that increased adipocyte number during the aging process may contribute to the increase in the incidence and severity of obesity observed in older individuals [4]. Thus, hyperplasia of adipocytes might be an important factor in the development of obesity. 18β-GA effect on decreasing fat mass is pronounced [31], but there has been no study about the influence on adipogenesis. Therefore, we explored the influence of 18β-GA on adipocyte differentiation in 3T3-L1 cells. When 3T3-L1 cells differentiated over 6 days in the presence of increasing concentrations of 18β-GA in the adipogenic medium, a reduction in TG accumulation was observed (Figs. 1A and B). The effect of 18β-GA was significantly detected at 5 μM and was maximal at 40 μM. From these results, we elucidated that 18β-GA inhibited adipocyte differentiation in 3T3-L1 cells for the first time.

3.2. 18β-GA down-regulates the expression of biochemical markers of differentiation and up-regulates the expression of Pref-1 that inhibits adipogenesis

The adipogenesis process is tightly controlled by PPARγ and C/EBPα. PPARγ is the master regulator of adipogenesis. Forced expression of PPARγ is sufficient to induce adipocyte differentiation in fibroblasts, and no factor has been discovered that promotes adipogenesis in the absence of PPARγ [23]. In addition, C/EBPα induces many adipocyte genes directly [23]. They are necessary for the expression of adipocyte-specific genes (adiponectin) [25]. To confirm the anti-adipogenic differentiation of 18β-GA, the mRNA levels of biochemical markers of differentiation (PPARγ, C/EBPα, and adiponectin) were determined (Fig. 2). When the 3T3-L1 preadipocytes differentiated with MDI treatment, the mRNA levels of the biochemical markers of differentiation increased compared to the control. However, 18β-GA treatment led to a significant reduction; by increasing the dose of S1P in the mRNA level of PPARγ, C/EBPα, aP2 and adiponectin (Fig. 2). In the case of PPARγ, the protein expression was also decreased by 18β-GA (Fig. 3A). Another important factor influencing adipogenesis is Pref-1, a Preadipocyte Secreted Factor which is an inhibitor of adipogenesis [34–36]. In vivo, mice lacking Pref-1 show accelerated fat deposition; conversely, mice overexpressing soluble Pref-1 in adipose tissue show a decrease in fat mass [34]. Pref-1 is highly expressed in 3T3-L1 cells but is extinguished during adipocyte differentiation. 18β-GA increased the expression of Pref-1 mRNA in the dose-dependent manner (Fig. 2D). For these results, we confirmed that the 18β-GA has an anti-adipogenic activity in 3T3-L1 cells.

3.3. Anti-adipogenic effect of 18β-GA is caused by down-regulation of p-Akt (Ser473)

Akt phosphorylates and regulates a large number of substrates involved in a diverse array of biological processes [26], many of which could contribute to the role of Akt in driving adipocyte differentiation. Ultimately, the differentiation defect in mouse embryonic fibroblasts (MEFs) and 3T3-L1 preadipocytes lacking Akt1 stems from an inability to induce PPARγ expression at the initiation of the adipogenesis program [27,28,37]. The PPARγ transcription factor is the master regulator of adipocyte differentiation

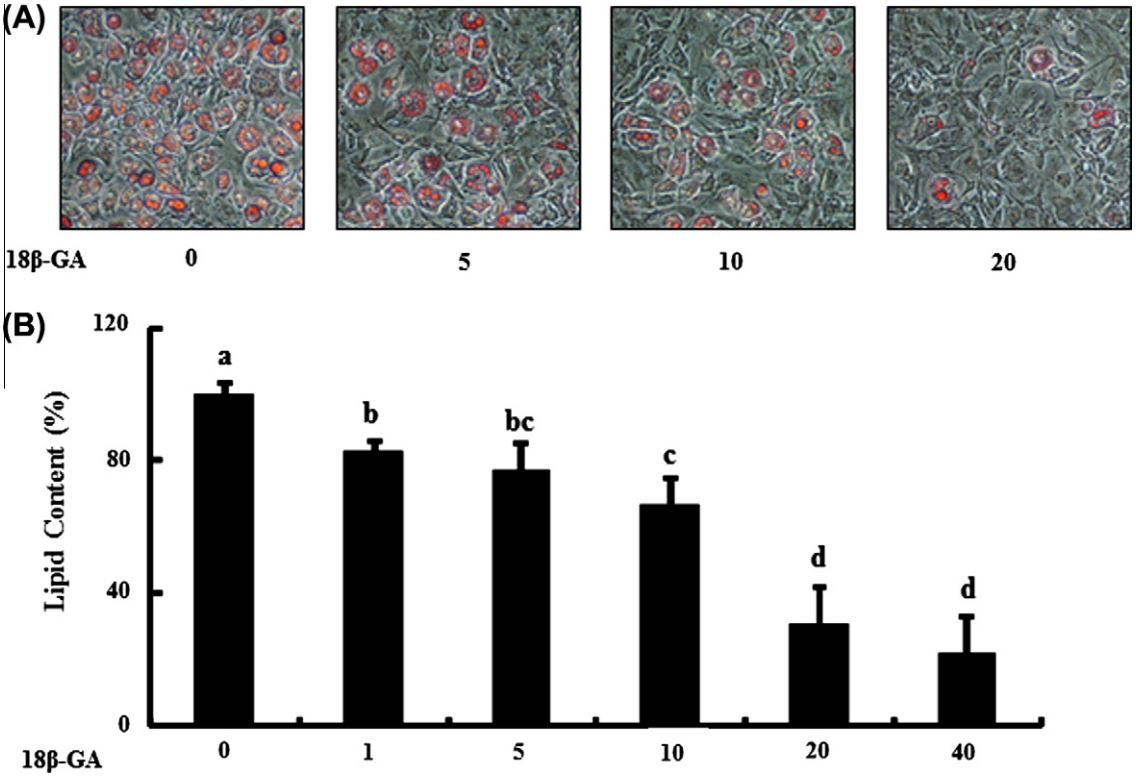


Fig. 1. 18β-GA inhibits lipid accumulation during the differentiation of 3T3-L1 preadipocytes. (A) Preadipocytes were induced to differentiate with 18β-GA of increasing concentrations for 6 days. The AdipoRed assays were performed on d6 and were photographed with a light microscope (200×). (B) Fluorescence was measured with excitation at 485 nm and emission at 572 nm. Bar graph indicates the mean ± S.E.M. ($n = 3$). The data were analyzed using analysis of variance (ANOVA) and Duncan multiple range test ($p < 0.05$). Means sharing a common alphabetical symbol do not differ significantly. Bars showing different letters indicate significant differences among each group of bars according to Duncan's test at $p < 0.05$.

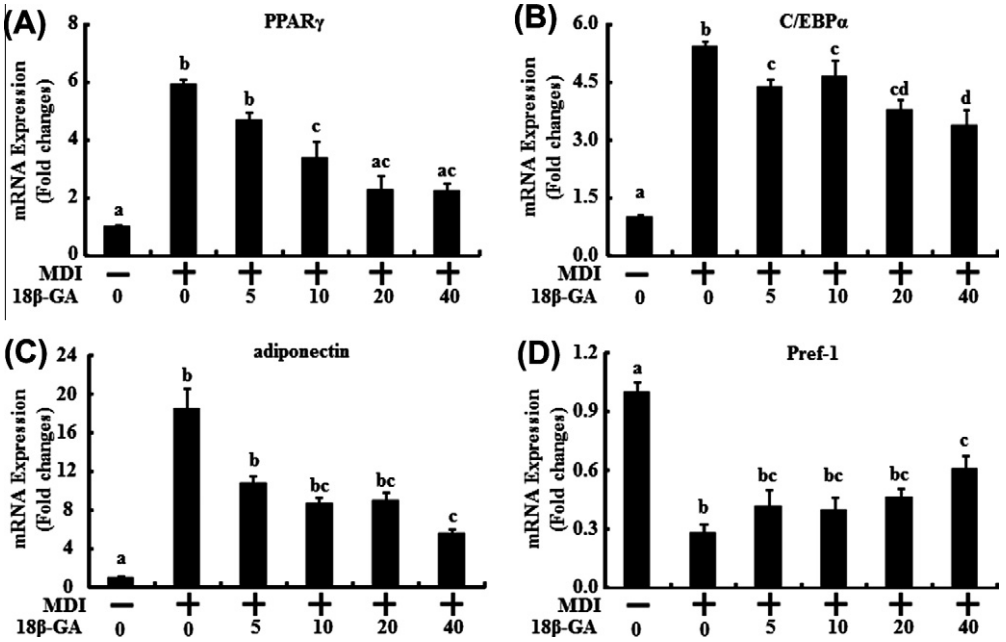


Fig. 2. 18β-GA down-regulates the expression of main transcriptional factors for adipogenesis and adipocyte-specific gene and increases the expression of Pref-1. (A) Preadipocytes were induced to differentiate with 18β-GA (from 5 to 40 μM) and harvested at d7 during the differentiation period. The mRNA expressions of PPARγ (A), C/EBPα (B), adiponectin (C) and Pref-1 (D) were analyzed by real-time RT-PCR. Values are mean ± S.D. of data from three separate experiments; each experiment was performed in triplicate. The experiments were repeatedly performed to confirm the results. The data were analyzed using analysis of variance (ANOVA) and Duncan multiple range test ($p < 0.05$).Means sharing a common alphabetical symbol do not differ significantly. Bars showing different letters indicate significant differences among each group of bars according to Duncan's test at $p < 0.05$.

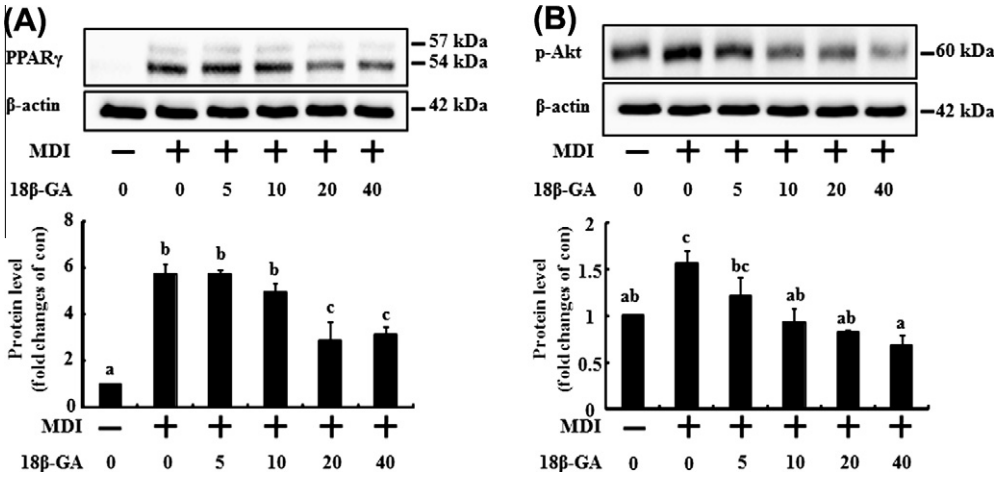


Fig. 3. 18β-GA down-regulates the expression of p-Akt (Ser473). (A and B) Preadipocytes were induced to differentiate with 18β-GA dose-dependently(from 5 to 40 μM) for 6 days. At d6, the protein levels of PPARγ(A) and p-Akt (B) were analyzed by western blot (Upper panel). Levels of PPARγ and p-Aktwere normalized to β-actin (Lower panel). The experiments were repeatedly performed to confirm the results. The data were analyzed using analysis of variance (ANOVA) and Duncan multiple range test ($p < 0.05$). Means sharing a common alphabetical symbol do not differ significantly. Bars showing different letters indicate significant differences among each group of bars according to Duncan's test at $p < 0.05$.

and, like Akt1, its activation is both necessary and sufficient for differentiation [21–23]. Supporting an essential role for PPARγ induction downstream of Akt1, forced expression of PPARγ in Akt-deficient MEFs rescues their severe adipogenesis defect [27,37]. 18β-GA treatment markedly abolishes the phosphorylation of Akt [38]. To gain insight into the molecular mechanisms responsible for the observed biological effects of 18β-GA, the ability of the 18β-GA to inactivate Akt was then examined. As illustrated in Fig. 3B, the MDI containing adipocyte differentiation cocktail increased phosphorylation of Ser 473 of Akt after MDI addition. However, from 5 to 20 μM of 18β-GA dose-dependently decreased the phosphorylation of Akt (Ser 473). These results are consistent with the ability of 18β-GA to regulate the phosphorylation of Akt, conferring an anti-adipogenic effect in vitro. From these data, we suggest that the anti-adipogenic effect of 18β-GA is caused by the phosphorylation of Akt.

3.4. 18β-GA enhances lipolysis in differentiated adipocytes through up-regulation of HSL, ATGL, perilipin and phosphorylation of HSL

To study the effect of 18β-GA on lipolysis, differentiated adipocytes were incubated with various concentrations of 18β-GA for 24 h, and the glycerol level was determined in the medium. 18β-GA treatment led to a significantly higher release of glycerol after 24 h was analyzed (Fig. 4A). Also, 18β-GA dose-dependently substantially increased lipolysis (Fig. 4A). To assess the effects of

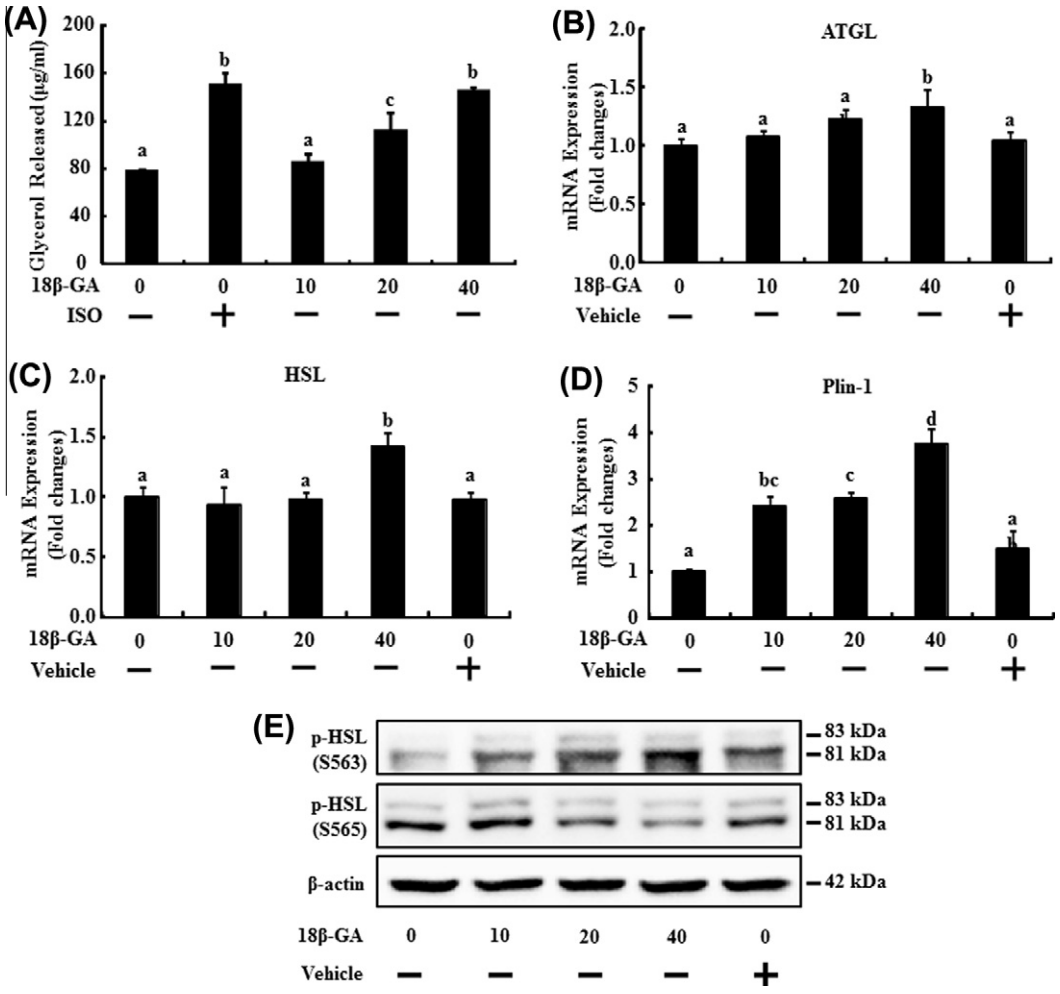


Fig. 4. 18β-GA increases glycerol release as well as ATGL, HSL and perilipin mRNA levels and enhances the activation of HSL through up-regulation of phosphorylation of HSL Ser 563 and down-regulation of phosphorylation of HSL Ser565 in differentiated adipocytes. (A) Differentiated adipocytes were stimulated with indicated concentrations (μM) 18β-GA for 24 h. The concentration of glycerol in the medium determined as described in Section 2. (B–D) Differentiated adipocytes were stimulated with indicated concentrations (μM) of 18β-GA for 24 h. Then, relative mRNA levels were measured by RT-qPCR for ATGL (B), HSL (C), and perilipin (D) genes. Bar graph indicates the mean ± S.E.M. ($n = 3$). The data were analyzed using analysis of variance (ANOVA) and Duncan multiple range test ($p < 0.05$). Means sharing a common alphabetical symbol do not differ significantly. Bars showing different letters indicate significant differences among each group of bars according to Duncan's test at $p < 0.05$. (E) Western blot analysis for p-HSL (Ser 563) (Upper panel) and p-HSL (Ser 565) (middle panel) protein in differentiated adipocytes treated with the increasing dose (from 10 to 40 μM) of FTY72018β-GA for 24 h. DMSO was used as vehicle control. The experiments were repeatedly performed to confirm the results.

18β-GA on major molecular mechanisms that regulate lipolysis in vitro, we examined the phosphorylation of HSL on key serine residues, as well as the mRNA content of ATGL, HSL and perilipin. When the differentiated adipocytes were incubated with various increasing dose of 18β-GA for 24 h, and the ATGL, HSL and perilipin mRNA levels were significantly increased (Figs. 4B–D). HSL induces lipolysis after phosphorylation of serine residues 563, 659, and 660 [11,39,40], leading to translocation of HSL to lipid droplets and markedly enhancing lipolysis. Phosphorylation of perilipin A, a protein associated with the lipid droplet, by protein kinase A (PKA) is necessary for activation of HSL and for catecholamine-induced lipolysis to occur [41]. Conversely, the cellular energy sensor AMP-activated protein kinase (AMPK) phosphorylates Ser565 of HSL, which prevents PKA-mediated phosphorylation of this enzyme and impairs catecholamine-stimulated lipolysis [42]. While presently the phosphorylation of HSL at Ser 563 was increased, phosphorylation of HSL at Ser 565 was dose-dependently decreased by 18β-GA (Figs. 4E and F). The effect of 18β-GA was significantly detected at 1 μM from 4 h and was prolonged to 48 h (Figs. 4E and F). These results revealed the pro-lipolytic activity of 18β-GA in vitro. Because conditions that lead to overeating and obesity disrupt normal regulation of WAT lipolysis, hormone-induced lipolysis is suppressed in obese humans and rodents. Therefore, we suggest that our novel findings that 18β-GA enhances lipolysis in adipocytes might be useful for obesity treatment.

In conclusion, the results of this study show that exposure of 18β-GA inhibits the process of adipocyte differentiation, as confirmed by a reduction in TG accumulation, a reduction in the expression of adipocyte specific genes and regulating Akt pathways. Also, 18β-GA enhanced lipolysis of differentiated adipocytes as confirmed by an increase in glycerol release. The mechanisms of 18β-GA to increase lipolysis are that up-regulation of lipolysis-associated gene expressions (HSL, ATGL and perilipin) and regulating HSL (Ser 563 and Ser 565). This is the first study to identify the anti-adipogenic and pro-lipolytic action of 18β-GA by modulating Akt and HSL phosphorylation, respectively. These results suggest that FTY720 might be a therapeutic for obesity.

Acknowledgments

This study was supported by the National Research Foundation of the Korea Grant funded by the Korean Government (2010-E00019).

References

[1] F. Lei, X.N. Zhang, W. Wang, D.M. Xing, W.D. Xie, H. Su, L.J. Du, Evidence of anti-obesity effects of the pomegranate leaf extract in high-fat diet induced obese mice, Int. J. Obes. (Lond.) 31 (2007) 1023–1029.

[2] K.B. Boyle, D. Hadaschik, S. Virtue, W.P. Cawthorn, S.H. Ridley, S. O'Rahilly, K. Siddle, The transcription factors Egr1 and Egr2 have opposing influences on adipocyte differentiation, Cell. Death Differ. 16 (2009) 782–789.

[3] J.-Y. Lee, H. Hashizaki, T. Goto, T. Sakamoto, N. Takahashi, T. Kawada, Activation of peroxisome proliferator-activated receptor-α enhances fatty acid oxidation in human adipocytes, Biochem. Biophys. Res. Commun. 407 (2011) 818–822.

[4] T. Yanagiya, A. Tanabe, K. Hotta, Gap-junctional communication is required for mitotic clonal expansion during adipogenesis, Obes. (Silver Spring) 15 (2007) 572–582.

[5] J.A. Villena, S. Roy, E. Sarkadi-Nagy, K.-H. Kim, H.S. Sul, Desnutrin, an adipocyte gene encoding a novel patatin domain-containing protein, is induced by fasting and glucocorticoids, J. Biol. Chem. 279 (2004) 47066–47075.

[6] R. Zimmermann, J.G. Strauss, G. Haemmerle, G. Schoiswohl, R. Birner-Gruenberger, M. Riederer, A. Lass, G. Neuberger, F. Eisenhaber, A. Hermetter, R. Zechner, Fat mobilization in adipose tissue is promoted by adipose triglyceride lipase, Science 306 (2004) 1383–1386.

[7] C.M. Jenkins, D.J. Mancuso, W. Yan, H.F. Sims, B. Gibson, R.W. Gross, Identification, cloning, expression, and purification of three novel human calcium-independent phospholipase A2 family members possessing triacylglycerol lipase and acylglycerol transacylase activities, J. Biol. Chem. 279 (2004) 48968–48975.

[8] A. Lasa, M. Schweiger, P. Kotzbeck, I. Churruca, E. Simón, R. Zechner, M.d.P. Portillo, Resveratrol regulates lipolysis via adipose triglyceride lipase, J. Nutr. Biochem. 23 (2012) 379–384.

[9] M.P. Gaidhu, N.M. Anthony, P. Patel, T.J. Hawke, R.B. Ceddia, Dysregulation of lipolysis and lipid metabolism in visceral and subcutaneous adipocytes by high-fat diet: role of ATGL, HSL, and AMPK, Am. J. Physiol. – Cell Physiol. 298 (2010) C961–C971.

[10] J.W. Jocken, E.E. Blaak, Catecholamine-induced lipolysis in adipose tissue and skeletal muscle in obesity, Physiol. Behav. 94 (2008) 219–230.

[11] P. Arner, Human fat cell lipolysis: biochemistry, regulation and clinical role, Best Pract. Res. Clin. Endocrinol. Metab. 19 (2005) 471–482.

[12] M. Stumvoll, B.J. Goldstein, T.W. van Haeften, Type 2 diabetes: principles of pathogenesis and therapy, Lancet 365 (2005) 1333–1346.

[13] M. Roden, How free fatty acids inhibit glucose utilization in human skeletal muscle, Physiology 19 (2004) 92–96.

[14] J. Martinez-Botas, J.B. Anderson, D. Tessier, A. Lapillonne, B.H. Chang, M.J. Quast, D. Gorenstein, K.H. Chen, L. Chan, Absence of perilipin results in leanness and reverses obesity in Lepr(db/db) mice, Nat. Genet. 26 (2000) 474–479.

[15] K. Jaworski, M. Ahmadian, R.E. Duncan, E. Sarkadi-Nagy, K.A. Varady, M.K. Hellerstein, H.Y. Lee, V.T. Samuel, G.I. Shulman, K.H. Kim, S. de Val, C. Kang, H.S. Sul, AdPLA ablation increases lipolysis and prevents obesity induced by high-fat feeding or leptin deficiency, Nat. Med. 15 (2009) 159–168.

[16] S. Lucas, G. Tavernier, C. Tiraby, A. Mairal, D. Langin, Expression of human hormone-sensitive lipase in white adipose tissue of transgenic mice increases lipase activity but does not enhance in vitro lipolysis, J. Lipid Res. 44 (2003) 154–163.

[17] A.V. Hertzel, L.A. Smith, A.H. Berg, G.W. Cline, G.I. Shulman, P.E. Scherer, D.A. Bernlohr, Lipid metabolism and adipokine levels in fatty acid-binding protein null and transgenic mice, Am. J. Physiol. Endocrinol. Metab. 290 (2006) E814–823.

[18] J.T. Tansey, C. Sztalryd, J. Gruia-Gray, D.L. Roush, J.V. Zee, O. Gavrilova, M.L. Reitman, C.X. Deng, C. Li, A.R. Kimmel, C. Londos, Perilipin ablation results in a lean mouse with aberrant adipocyte lipolysis, enhanced leptin production, and resistance to diet-induced obesity, Proc. Natl. Acad. Sci. USA 98 (2001) 6494–6499.

[19] S. Rayalam, M.A. Della-Fera, C.A. Baile, Phytochemicals and regulation of the adipocyte life cycle, J. Nutr. Biochem. 19 (2008) 717–726.

[20] H. Lee, Y.J. Lee, H. Choi, E.H. Ko, J.W. Kim, Reactive oxygen species facilitate adipocyte differentiation by accelerating mitotic clonal expansion, J. Biol. Chem. 284 (2009) 10601–10609.

[21] K. Wakabayashi, M. Okamura, S. Tsutsumi, N.S. Nishikawa, T. Tanaka, I. Sakakibara, J. Kitakami, S. Ihara, Y. Hashimoto, T. Hamakubo, T. Kodama, H. Aburatani, J. Sakai, The peroxisome proliferator-activated receptor gamma/retinoid X receptor alpha heterodimer targets the histone modification enzyme PR-Set7/Setd8 gene and regulates adipogenesis through a positive feedback loop, Mol. Cell Biol. 29 (2009) 3544–3555.

[22] P. Tontonoz, B.M. Spiegelman, Fat and beyond: the diverse biology of PPARgamma, Annu. Rev. Biochem. 77 (2008) 289–312.

[23] E.D. Rosen, O.A. MacDougald, Adipocyte differentiation from the inside out, Nat. Rev. Mol. Cell. Biol. 7 (2006) 885–896.

[24] P.V. Nerurkar, Y.K. Lee, V.R. Nerurkar, Momordica charantia (bitter melon) inhibits primary human adipocyte differentiation by modulating adipogenic genes, BMC Complement Altern. Med. 10 (2010) 34.

[25] Y. Xing, F. Yan, Y. Liu, Y. Zhao, Matrine inhibits 3T3-L1 preadipocyte differentiation associated with suppression of ERK1/2 phosphorylation, Biochem. Biophys. Res. Commun. 396 (2010) 691–695.

[26] B.D. Manning, L.C. Cantley, AKT/PKB signaling: navigating downstream, Cell 129 (2007) 1261–1274.

[27] H.H. Zhang, J. Huang, K. Düvel, B. Boback, S. Wu, R.M. Squillace, C.-L. Wu, B.D. Manning, Insulin stimulates adipogenesis through the Akt-TSC2-mTORC1 pathway, PLoS ONE 4 (2009) e6189.

[28] A. Baudry, Z.Z. Yang, B.A. Hemmings, PKBalpha is required for adipose differentiation of mouse embryonic fibroblasts, J. Cell. Sci. 119 (2006) 889–897.

[29] D. Classen-Houben, D. Schuster, T. Da Cunha, A. Odermatt, G. Wolber, U. Jordis, B. Kueenburg, Selective inhibition of 11beta-hydroxysteroid dehydrogenase 1 by 18alpha-glycyrrhetinic acid but not 18beta-glycyrrhetinic acid, J. Steroid. Biochem. Mol. Biol. 113 (2009) 248–252.

[30] R.H. Stimson, B.R. Walker, Glucocorticoids and 11beta-hydroxysteroid dehydrogenase type 1 in obesity and the metabolic syndrome, Minerva Endocrinol. 32 (2007) 141–159.

[31] D. Armanini, D. Nacamulli, F. Francini-Pesenti, G. Battagin, E. Ragazzi, C. Fiore, Glycyrrhetinic acid, the active principle of licorice, can reduce the thickness of subcutaneous thigh fat through topical application, Steroids 70 (2005) 538–542.

[32] M.H. Moon, J.K. Jeong, J.S. Seo, J.W. Seol, Y.J. Lee, M. Xue, C.J. Jackson, S.Y. Park, Bisphosphonate enhances TRAIL sensitivity to human osteosarcoma cells via death receptor 5 upregulation, Exp. Mol. Med. 43 (2011) 138–145.

[33] J.S. Seo, M.H. Moon, J.K. Jeong, J.W. Seol, Y.J. Lee, B.H. Park, S.Y. Park, SIRT1, a histone deacetylase, regulates prion protein-induced neuronal cell death, Neurobiol. Aging (2010), in press.

[34] Y. Wang, K.-A. Kim, J.-H. Kim, H.S. Sul, Pref-1, a preadipocyte secreted factor that inhibits adipogenesis, J. Nutr. 136 (2006) 2953–2956.

[35] H. Sul, C. Smas, B. Mei, L. Zhou, Function of pref-1 as an inhibitor of adipocyte differentiation, Int. J. Obes. 24 (2000) 15–19.

[36] C.M. Smas, L. Chen, H.S. Sul, Cleavage of membrane-associated pref-1 generates a soluble inhibitor of adipocyte differentiation, Mol. Cell. Biol. 17 (1997) 977.

[37] X.D. Peng, P.Z. Xu, M.L. Chen, A. Hahn-Windgassen, J. Skeen, J. Jacobs, D. Sundararajan, W.S. Chen, S.E. Crawford, K.G. Coleman, N. Hay, Dwarfism, impaired skin development, skeletal muscle atrophy, delayed bone development, and impeded adipogenesis in mice lacking Akt1 and Akt2, Genes Dev. 17 (2003) 1352–1365.

[38] G. Sharma, S. Kar, S. Palit, P.K. Das, 18beta-glycyrrhetinic acid (concur) induces apoptosis through modulation of Akt/FOXO3a/Bim pathway in human breast cancer MCF-7 cells, J. Cell. Physiol. 227 (2012) 1923–1931.

[39] W.J. Shen, S. Patel, V. Natu, F.B. Kraemer, Mutational analysis of structural features of rat hormone-sensitive lipase, Biochemistry 37 (1998) 8973–8979.

[40] M.W. Anthonsen, L. Rönnstrand, C. Wernstedt, E. Degerman, C. Holm, Identification of novel phosphorylation sites in hormone-sensitive lipase that are phosphorylated in response to isoproterenol and govern activation properties in vitro, J. Biol. Chem. 273 (1998) 215–221.

[41] H. Miyoshi, S.C. Souza, H.H. Zhang, K.J. Strissel, M.A. Christoffolete, J. Kovsan, A. Rudich, F.B. Kraemer, A.C. Bianco, M.S. Obin, A.S. Greenberg, Perilipin promotes hormone-sensitive lipase-mediated adipocyte lipolysis via phosphorylation-dependent and -independent mechanisms, J. Biol. Chem. 281 (2006) 15837–15844.

[42] A.J. Garton, D.G. Campbell, D. Carling, D.G. Hardie, R.J. Colbran, S.J. Yeaman, Phosphorylation of bovine hormone-sensitive lipase by the AMP-activated protein kinase, A possible antilipolytic mechanism, Eur. J. Biochem. 179 (1989) 249–254.

Biochemical and Biophysical Research Communications 420 (2012) 811–815

Contents lists available at SciVerse ScienceDirect

Biochemical and Biophysical Research Communications

journal homepage: www.elsevier.com/locate/ybbrc

Glucose and insulin induce Ca^{2+} signaling in nesfatin-1 neurons in the hypothalamic paraventricular nucleus

Darambazar Gantulga [a], Yuko Maejima [a], Masanori Nakata [a], Toshihiko Yada [a,b,*]

[a] Division of Integrative Physiology, Department of Physiology, Jichi Medical University School of Medicine, 3311-1 Shimotsuke, Tochigi 329-0498, Japan
[b] Department of Developmental Physiology, Division of Adaptation Development, National Institute for Physiological Sciences, Okazaki, Aichi 444-8585, Japan

ARTICLE INFO

Article history:
Received 14 March 2012
Available online 23 March 2012

Keywords:
Nesfatin-1
PVN
Glucose
Insulin
Satiety
Cytosolic Ca^{2+}

ABSTRACT

Nucleobindin-2 derived nesfatin-1 in the hypothalamic paraventricular nucleus (PVN) plays a role in inhibition of feeding. The neural pathways downstream of PVN nesfatin-1 have been extensively investigated. However, regulation of the PVN nesfatin-1 neurons remains unclear. Since starvation decreases and refeeding stimulates nesfatin-1 expression specifically in the PVN, this study aimed to clarify direct effects of meal-evoked metabolic factors, glucose and insulin, on PVN nesfatin-1 neurons. High glucose (10 mM) and insulin (10^{-13} M) increased cytosolic calcium concentration ($[Ca^{2+}]_i$) in 55 of 331 (16.6%) and 32 of 249 (12.9%) PVN neurons, respectively. Post $[Ca^{2+}]_i$ measurement immunocytochemistry identified that 58.2% of glucose-responsive and 62.5% of insulin-responsive neurons were immunoreactive to nesfatin-1. Furthermore, a fraction of the glucose-responsive nesfatin-1 neurons also responded to insulin, and *vice versa*. Some of the neurons that responded to neither glucose nor insulin were recruited to $[Ca^{2+}]_i$ increases by glucose and insulin in combination. Our data demonstrate that glucose and insulin directly interact with and increase $[Ca^{2+}]_i$ in nesfatin-1 neurons in the PVN, and that the nesfatin-1 neuron is the primary target for them in the PVN. The results suggest that high glucose- and insulin-induced activation of PVN nesfatin-1 neurons serves as a mechanism through which meal ingestion stimulates nesfatin-1 neurons in the PVN and thereby produces satiety.

© 2012 Elsevier Inc. All rights reserved.

1. Introduction

Food intake is regulated by the feeding center in the hypothalamus, whose activity is altered by nutritional and hormonal status of the body. Hypothalamic paraventricular nucleus (PVN) receives afferent inputs via the first order feeding centers, the arcuate nucleus (ARC) and nucleus tractus solitarius (NTS), communicates with other brain areas related to various functions including stress, circadian rhythm and reward, and integrates the peripheral and central signals to finally control feeding. Therefore, PVN is considered the second order or integrative feeding center [1–5]. The PVN is located bilaterally bordering the third ventricle and equipped with neurons synthesizing anorexigenic neuropeptides including corticotropin-releasing hormone (CRH), thyrotropin-releasing hormone (TRH) oxytocin, and newly discovered nesfatin-1 [6–8].

Nesfatin-1, a 82-amino-acid peptide derived from the nucleobindin2 (NUCB2) is an emerging new player in regulation of food intake [8,9] and is expressed in several nuclei including the hypothalamic PVN, ARC, and the brain stem NTS [8,10]. Acute intracerebroventricular (i.c.v) injection of nesfatin-1 decreases food intake in rats and mice [8,11,12]. Chronic infusion of nesfatin-1 into the third ventricle significantly decreases food intake and body weight gain in rats, while i.c.v injection of NUCB2 antisense oligonucleotide increases food intake and body weight [8]. Regarding the neural mechanisms downstream of the PVN nesfatin-1, central injection of nesfatin-1 reportedly evokes anorexia by activating the oxytocin neurons in the PVN which project to pro-opiomelanocortin (POMC) neurons in the NTS, thereby inducing melanocortin-dependent anorexia [13]. It has also been reported that CRH mediates the effects of central nesfatin-1 [11]. A physiologic role of central nesfatin-1 in food intake regulation is further supported by the finding that the expression of NUCB2/nesfatin-1 in the PVN is altered by nutritional states [8,14]. Altogether, these data have evidenced that nesfatin-1 is an anorectic molecule implicated in the physiologic regulation of food intake.

Although the neural pathways downstream of PVN nesfatin-1 have been extensively studied, the factors that regulate nesfatin-1

Abbreviations: PVN, paraventricular nucleus; ARC, arcuate nucleus; NTS, nucleus tractus solitarius; CRH, corticotropin-releasing hormone; TRH, thyrotropin releasing hormone; NUCB2, nucleobindin2; $[Ca^{2+}]_i$, cytosolic calcium concentration; POMC, pro-opiomelanocortin; BBB, blood-brain barrier; HKRB, Hepes-buffered Krebs-Ringer bicarbonate buffer; IR, immunoreactive; i.c.v, intracerebroventricular.

* Corresponding author at: Division of Integrative Physiology, Department of Physiology, Jichi Medical University School of Medicine, Shimotsuke, Tochigi 329 0498, Japan. Fax: +81 285 44 9962.

E-mail addresses: daram@jichi.ac.jp (D. Gantulga), maejimay@jichi.ac.jp (Y. Maejima), nakata@jichi.ac.jp (M. Nakata), tyada@jichi.ac.jp (T. Yada).

0006-291X/$ - see front matter © 2012 Elsevier Inc. All rights reserved.
http://dx.doi.org/10.1016/j.bbrc.2012.03.079

neurons in PVN remain unknown. By now, it has been shown that starvation for 24 h decreases the NUCB2 mRNA level and nesfatin-1 protein content selectively in the PVN [8]. Conversely, refeeding activates nesfatin-1 neurons in the PVN, as measured by c-Fos expression [14]. Hence, it is possible that the nesfatin-1 neuron in the PVN responds to the meal-evoked signals. Plasma glucose and insulin surge postprandially [15,16], and penetrate into the cerebrospinal fluid through the blood–brain barrier (BBB) [17,18]. The present study aimed to clarify whether high glucose and insulin could directly activate nesfatin-1 neurons in the PVN. We investigated the effects of glucose and insulin on cytosolic Ca^{2+} concentration ($[Ca^{2+}]_i$) in the neurons isolated from PVN of mice, followed by immunocytochemical identification of nesfatin-1 neurons. We found that high glucose and insulin directly interact with and increase $[Ca^{2+}]_i$ in PVN nesfatin-1 neurons, and that they cooperate to recruit some of unresponsive nesfatin-1 neurons to $[Ca^{2+}]_i$ increases.

2. Materials and methods

2.1. Animals

Male C57BL/6 mice (Nihon SLC, Hamamatsu, Japan) aged 5–6 weeks were used in the experiments. Animals were maintained on a 12 h light/dark cycle (19:30 lights off) and given conventional food (CE-2; Clea, Osaka, Japan) and water *ad libitum*. Experimental procedures and care of animals were carried out according to the Jichi Medical University Institute of Animal Care and Use Committee.

2.2. Preparation of single neurons from PVN

Single neurons were prepared according to procedures reported previously [19] with slight modifications. Briefly, brain slices containing the entire PVN were prepared and the PVN was excised from the left and right sides. The dissected tissues were washed with 10 mM HEPES-buffered Krebs–Ringer bicarbonate buffer (HKRB) containing 1 mM glucose. They were then incubated in the HKRB supplemented with 20 U/ml papain (Sigma Chemical Co., St. Louis, MO), 0.015 mg/ml deoxyribonuclease, 0.75 mg/ml BSA, and 1 mM cysteine for 15 min at 36 °C in a shaking water bath, followed by gentle mechanical trituration for 5–10 min. After trituration, the cell suspension was centrifuged at 100 g for 5 min. The pellet was resuspended in HKRB. The single neurons obtained were distributed onto coverslips and incubated in the humidified chamber at 30 °C for 30 min and then at 25 °C for up to 6 h until use.

2.3. Measurement of $[Ca^{2+}]_i$ in single PVN neurons

$[Ca^{2+}]_i$ was measured by ratiometric fura-2 fluorescence imaging as previously reported [13,19]. Briefly, single neurons on coverslips were incubated with 2 μmol/l fura-2/AM (Dojin chemical,

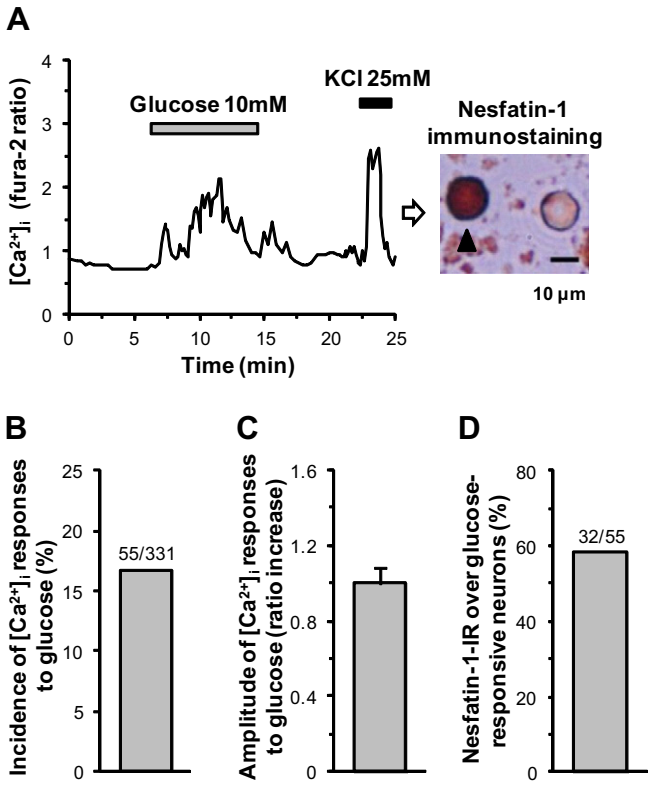


Fig. 1. Glucose increases $[Ca^{2+}]_i$ in PVN nesfatin-1 neurons. (A) Elevation of the glucose concentration to 10 mM from a basal level of 1 mM under superfusion conditions increased $[Ca^{2+}]_i$ in a single neuron isolated from PVN that subsequently responded to 25 mM KCl with an increase in $[Ca^{2+}]_i$ (left panel). Superfusate contained 1 mM glucose unless indicated by the bars. The bars above the tracing indicate the period of treatment specified. This neuron was proven to be nesfatin-1-immunoreactive (IR), as designated by arrow head, (right panel). Scale bar, 10 μm. (B) Percentage of PVN neurons that responded to glucose with $[Ca^{2+}]_i$ increases. The numbers above the bar indicate the number of PVN neurons that responded to 10 mM glucose over the number of PVN neurons examined. (C) Amplitude of glucose-induced $[Ca^{2+}]_i$ increases is expressed as the increment of ratio. Bar represents mean ± SE. (D) Percentage of nesfatin-1-IR over glucose-responsive neurons. The numbers above the bar indicate the number of PVN neurons IR to nesfatin-1 over that responded to 10 mM glucose.

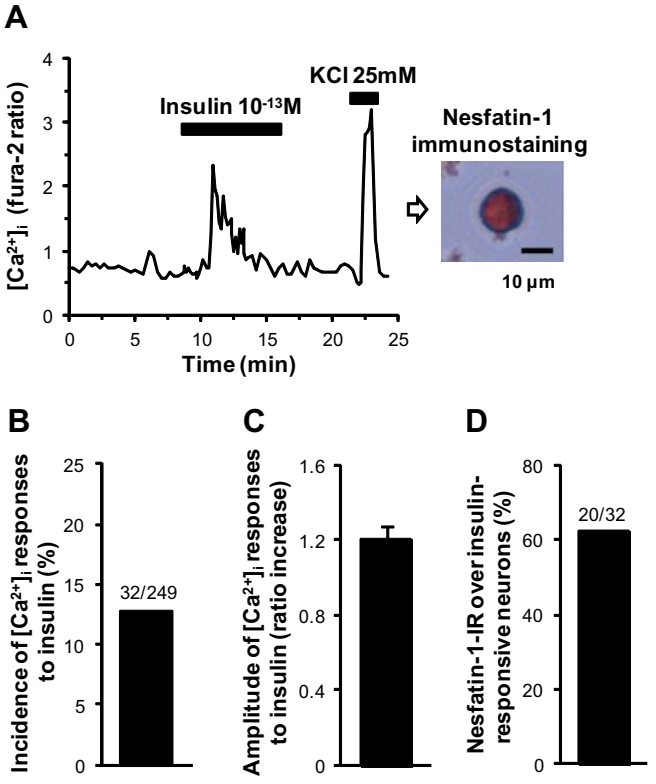


Fig. 2. Insulin increases $[Ca^{2+}]_i$ in PVN nesfatin-1 neurons. (A) Insulin at 10^{-13} M increased $[Ca^{2+}]_i$ (left panel) in a PVN neuron, which was shown to be immunoreactive to nesfatin-1 (right panel). (B) Incidence of $[Ca^{2+}]_i$ responses to insulin in PVN neurons, expressed by percentage. (C) Amplitude of $[Ca^{2+}]_i$ responses to insulin is expressed as delta ratio. Bar represents mean ± SE. (D) Twenty of 32 insulin-responsive neurons (62.5%) were nesfatin-1-immunoreactive.

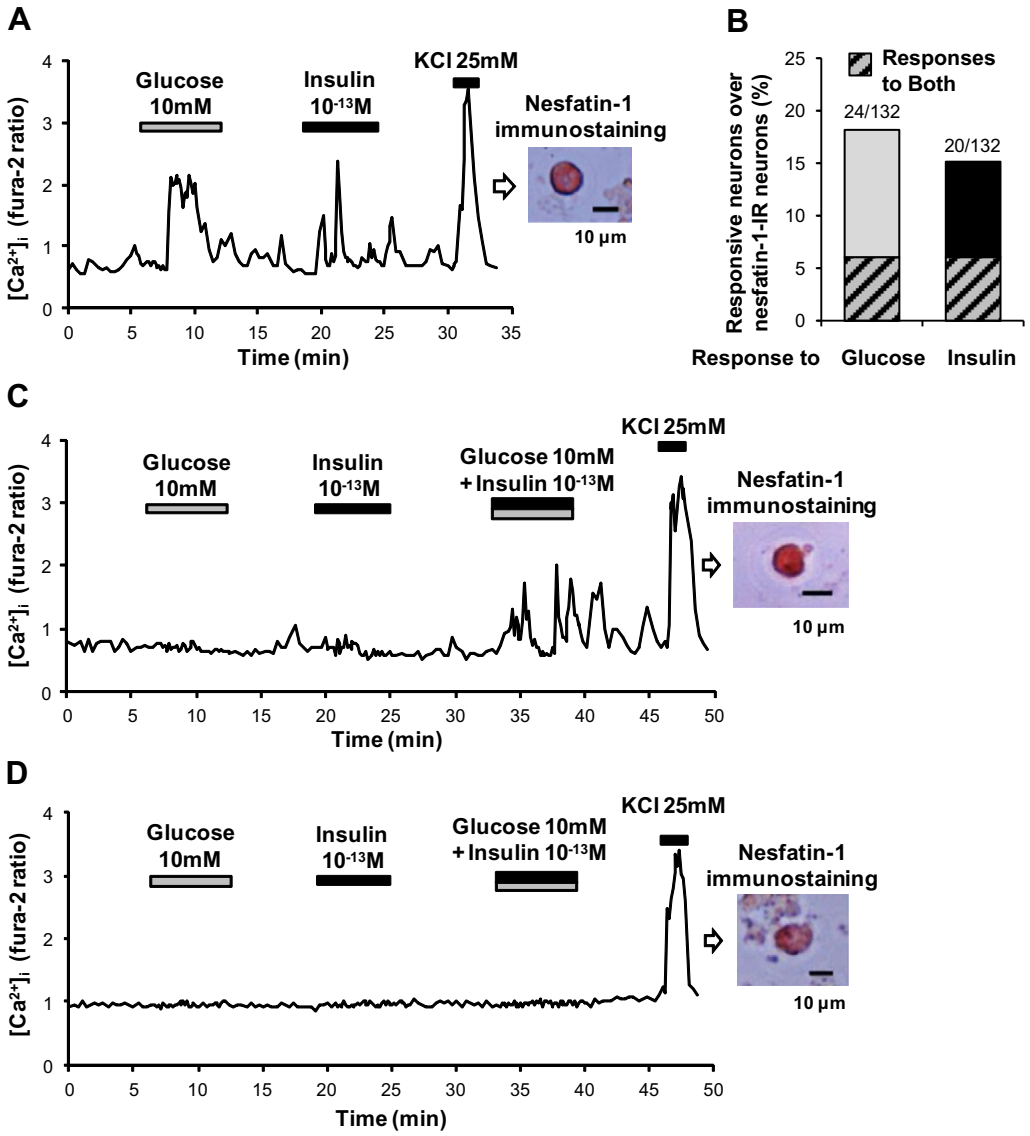


Fig. 3. Glucose and insulin target or synergistically activate the common PVN nesfatin-1 neurons. (A) Sequential administrations of 10 mM glucose and 10^{-13} M insulin induced increases in $[Ca^{2+}]_i$ (left panel) in a single PVN neuron that was subsequently shown to be nesfatin-1-IR (right panel). (B) Incidence of $[Ca^{2+}]_i$ responses to glucose and that to insulin in nesfatin-1 neurons are expressed by percentage. The areas with stripe represent the neurons that responded to both glucose and insulin. (C) Neither 10 mM glucose nor 10^{-13} M insulin increased $[Ca^{2+}]_i$, but the combination of the two increased $[Ca^{2+}]_i$ in a single PVN neuron that was subsequently shown to be nesfatin-1-IR. (D) Neither 10 mM glucose, nor 10^{-13} M insulin, nor the combination increased $[Ca^{2+}]_i$ in a PVN neuron IR to nesfatin-1. This neuron subsequently responded to 25 mM KCl with $[Ca^{2+}]_i$ increase.

Kumamoto, Japan) for 40 min at room temperature, mounted in chamber and superfused with HKRB at 1 ml/min at 33 °C. Fluorescence images due to excitation at 340 and 380 nm were captured and the ratio (F340/F380) images produced by an Argus-50 system (Hamamatsu Photonics, Hamamatsu, Japan). Criteria for $[Ca^{2+}]_i$ responses followed previous reports [13,19,20]. All data were shown as means ± SEM.

2.4. Immunocytochemistry for nesfatin-1 in single neurons

Post $[Ca^{2+}]_i$ immunostaining was performed with rabbit antiserum against nesfatin-1 (1:5000) as previously reported [13]. Correlation of $[Ca^{2+}]_i$ and immunocytochemical data were performed by comparing the images of the phase-contact photographs of the cells subjected to $[Ca^{2+}]_i$ measurements and the photographs of immunostained cells.

2.5. Solution and chemicals

Measurements were carried out in HKRB solution composed of 129 mmol/l NaCl, 5.0 mmol/l $NaHCO_3$, 4.7 mmol/l KCl, 1.2 mmol/l KH_2PO_4, 1.8 mmol/l $CaCl_2$, 1.2 mmol/l $MgSO_4$, and 10 mmol/l HEPES at pH 7.4. Insulin (porcine) was purchased from Sigma (Tokyo, Japan).

3. Results

3.1. Glucose increased $[Ca^{2+}]_i$ in PVN nesfatin-1 neurons

To determine the direct effect of glucose on PVN nesfatin-1 neurons, we used a method of $[Ca^{2+}]_i$ imaging in single neurons isolated from PVN followed by immunocytochemical identification of nesfatin-1 neurons. As depicted in Fig. 1A, a rise in the glucose

concentration to 10 mM from a basal level of 1 mM under superfusion conditions increased $[Ca^{2+}]_i$ in the single PVN neuron that was subsequently shown to be immunoreactive (IR) to nesfatin-1 (Fig. 1A, right panel). The elevated $[Ca^{2+}]_i$ returned to the basal level within several min after changing glucose concentration back to 1 mM. The neuron subsequently exhibited $[Ca^{2+}]_i$ response to 25 mM KCl, confirming the viability of the neuron. High glucose increased $[Ca^{2+}]_i$ in 55 of 331 PVN neurons (16.6%) with the average peak amplitude of about 1.0 ratio unit (Fig. 1B and C). Thirty-two of 55 glucose-responsive neurons (58.2%) were proved to be IR to nesfatin-1 (Fig. 1D).

3.2. Insulin increased $[Ca^{2+}]_i$ in PVN nesfatin-1 neurons

Administration of 10^{-13} M insulin increased $[Ca^{2+}]_i$ in the PVN neuron (Fig. 2A, left panel) that was subsequently proved to contain nesfatin-1 by immunocytochemistry (Fig. 2A, right panel). Among 249 PVN neurons examined, 32 neurons (12.9%) responded to insulin (Fig. 2B) with $[Ca^{2+}]_i$ increases, and their average amplitude was 1.2 ratio unit (Fig. 2C). Furthermore, 20 of 32 insulin-responsive neurons (62.5%) were nesfatin-1-IR neurons (Fig. 2D).

3.3. A subpopulation of PVN nesfatin-1 neurons responded to both glucose and insulin

To investigate whether the glucose-responsive neuron is distinct from or overlap with the insulin-responsive neuron, two agents were administered sequentially on the same neuron. In a neuron depicted in Fig. 3A, stimulation with 10 mM glucose increased $[Ca^{2+}]_i$, and after the glucose stimulation terminated and $[Ca^{2+}]_i$ returned to the basal level, the neuron was challenged with 10^{-13} M insulin. Insulin also increased $[Ca^{2+}]_i$ in a reversible manner (Fig. 3A, left panel). The neuron that responded to both high glucose and insulin was shown to be IR to nesfatin-1 (Fig. 3A, right panel). Among 132 nesfatin-1-IR cells, eight cells (6.1%) responded to both glucose and insulin, which corresponds to 33.3% of glucose-responsive and 40% of insulin-responsive nesfatin-1-IR neurons (Fig. 3B and Fig. 4).

3.4. Effect of co-administration of glucose and insulin

We investigated a possible interaction of glucose and insulin on PVN nesfatin-1 neurons by administrating glucose and insulin in combination. Interestingly, among 75 PVN nesfatin-1 neurons that responded neither 10 mM glucose nor 10^{-13} M insulin, 5 neurons (6.7%) were recruited to $[Ca^{2+}]_i$ increases by co-administration of the two (Fig. 3C, Fig. 4), while the rest of nesfatin-1 neurons (70 of 75, 93.3%) remained unresponsive to the combination (Fig. 3D).

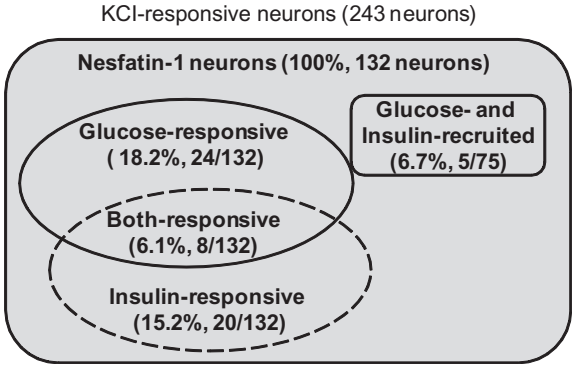


Fig. 4. Subpopulations of PVN nesfatin-1 neurons with regard to responsiveness to glucose and insulin. Among 243 neurons isolated from the PVN, 132 neurons were IR to nesfatin-1. Out of 132 nesfatin-1-IR neurons, 24 neurons (18.2%) responded to high glucose (10 mM), 20 neurons (15.2%) to insulin (10^{-13} M), and 8 neurons (6.1%) to both. Five of 75 (6.7%) nesfatin-1 neurons that did not respond to high glucose nor to insulin were recruited to $[Ca^{2+}]_i$ increases by high glucose plus insulin in combination.

4. Discussion

We used the method for analyzing species-specified single cells [21], and demonstrated that high glucose and insulin, the prominent meal-evoked metabolic signals, directly interact with and increase $[Ca^{2+}]_i$ in the nesfatin-1 neurons of the PVN. $[Ca^{2+}]_i$ is a principal regulator of neuronal activities including gene expression enzyme activity, synthesis and release of neurotransmitters/neuropeptides, and the increase in $[Ca^{2+}]_i$ is considered the appropriate marker reflecting the activation of neurons [22]. Therefore, our data indicate that high glucose and insulin activate the PVN nesfatin-1 neurons.

It has been reported that a fraction of PVN neurons are activated by high glucose [23]. However, the neurochemical identity of the glucose-responsive neurons has remained unclear. In the present study, we have demonstrated that as much as 58% of the PVN glucose-responsive neurons are nesfatin-1 neurons, revealing that nesfatin-1 neuron is the principal target of glucose in the PVN.

In this study, insulin at the concentration of 10^{-13} M increased $[Ca^{2+}]_i$ in nesfatin-1 neurons. Plasma insulin level surges postprandially by 7.3-fold, a level around 5×10^{-10} M [16]. Insulin passes through the BBB at a rate of 0.046% [24]. Accordingly, the calculated postprandial insulin concentration in the brain, as an estimate, is in a range around 2.3 x 10^{-13} M. Therefore, the $[Ca^{2+}]_i$ response to 10^{-13} M insulin in isolated nesfatin-1 neurons, observed in this study, could reflect the physiologic response. In this study, insulin increases $[Ca^{2+}]_i$ in 32 of 249 (12.9%) neurons of the PVN, which may fit with the report that insulin receptor is expressed substantially in the PVN [25]. Notably, 20 of 32 insulin-responsive neurons (62.5%) were proved to be nesfatin-1 neurons, revealing that the nesfatin-1 neuron is the major target of insulin in the PVN.

We found that substantial fraction of glucose-responsive nesfatin-1 neurons in the PVN also responded to insulin and *vice versa*. The nesfatin-1 neurons that responded to both glucose and insulin in the PVN could act as an effective sensor of the postprandial state by detecting the two representative meal-evoked factors. Conversely, some of PVN nesfatin-1 neurons responded to neither high glucose nor insulin alone. Among 75 of these apparently glucose-unresponsive, insulin-unresponsive neurons, 5 neurons (6.7%) were recruited to marked $[Ca^{2+}]_i$ increases by the combination of glucose and insulin. Although the significance of this subpopulation of neurons remains to be studied, the following role could be speculated. These neurons are not activated by conditions of high glucose alone, such as stress-induced hyperglycemia, nor by conditions of elevated insulin alone, such as the hyperglycemia associated with insulin resistance. However, they are activated by the postprandial conditions characteristic with elevated glucose and insulin together in the circulation, suggesting their specific role in producing meal-evoked satiety.

The significance of the nesfatin-1 neurons in the PVN that failed to respond to glucose, insulin and the combination is unclear. However, these nesfatin-1 neurons could be related to the documented functions of nesfatin-1 other than feeding, which include the regulation of water intake [3,26], stress responses [1,27], blood pressure [26], body temperature [3] and sympathetic nerve activity [9].

In summary, this study demonstrates that high glucose and insulin directly activate PVN nesfatin-1 neurons in the PVN, potentially contributing to meal-evoked satiety.

Acknowledgments

This work was supported by Grant-in-Aid for Scientific Research (B) (18390065, 20390061, 23390044), for Challenging Exploratory Research (22659044) and for Scientific Research on Innovative Areas (23115715) from JSPS, Strategic Research Program for Brain Sciences (10036069) by the Ministry of Education, Culture, Sports, Science and Technology of Japan, Support Programs for Strategic Research Platform for Private University from Ministry of Education, Culture, Sports, Science and Technology of Japan, Grants from Japan Diabetes Foundation, Takeda Science Foundation and Uehara Memorial Foundation, and Insulin Research Award from Novo Nordisk and Basic Science Research Award from Sumitomo Foundation to TY. This study was subsidized by JKA through its promotion funds from KEIRIN RACE to TY.

References

[1] N. Yoshida, Y. Maejima, U. Sedbazar, A. Ando, H. Kurita, B. Damdindorj, E. Takano, D. Gantulga, Y. Iwasaki, T. Kurashina, T. Onaka, K. Dezaki, M. Nakata, M. Mori, T. Yada, Stressor-responsive central nesfatin-1 activates corticotropin-releasing hormone, noradrenaline and serotonin neurons and evokes hypothalamic-pituitary-adrenal axis, Aging (Albany NY) 2 (2010) 775–784.

[2] J.G. Tasker, Rapid Glucocorticoid Actions in the Hypothalamus as a Mechanism of Homeostatic Integration, Obesity 14 (2006) 259S–265S.

[3] K. Konczol, O. Pinter, S. Ferenczi, J. Varga, K. Kovacs, M. Palkovits, D. Zelena, Z.E. Toth, Nesfatin-1 exerts long-term effect on food intake and body temperature, Int. J. Obes. (2012).

[4] G.J. Morton, D.E. Cummings, D.G. Baskin, G.S. Barsh, M.W. Schwartz, Central nervous system control of food intake and body weight, Nature 443 (2006) 289–295.

[5] M.W. Schwartz, S.C. Woods, D. Porte, R.J. Seeley, D.G. Baskin, Central nervous system control of food intake, Nature 404 (2000) 661–671.

[6] E. Valassi, M. Scacchi, F. Cavagnini, Neuroendocrine control of food intake, Nutr. Metab. Cardiovasc. Dis. 18 (2008) 158–168.

[7] G.C. Brailoiu, S.L. Dun, E. Brailoiu, S. Inan, J. Yang, J.K. Chang, N.J. Dun, Nesfatin-1: distribution and interaction with a G protein-coupled receptor in the rat brain, Endocrinology 148 (2007) 5088–5094.

[8] I.S. Oh, H. Shimizu, T. Satoh, S. Okada, S. Adachi, K. Inoue, H. Eguchi, M. Yamamoto, T. Imaki, K. Hashimoto, T. Tsuchiya, T. Monden, K. Horiguchi, M. Yamada, M. Mori, Identification of nesfatin-1 as a satiety molecule in the hypothalamus, Nature 443 (2006) 709–712.

[9] A. Stengel, Y. Tache, Minireview: nesfatin-1–an emerging new player in the brain-gut, endocrine, and metabolic axis, Endocrinology 152 (2011) 4033–4038.

[10] M. Goebel-Stengel, L. Wang, A. Stengel, Y. Tache, Localization of nesfatin-1 neurons in the mouse brain and functional implication, Brain Res. 1396 (2011) 20–34.

[11] A. Stengel, M. Goebel, L. Wang, J. Rivier, P. Kobelt, H. Monnikes, N.W. Lambrecht, Y. Tache, Central nesfatin-1 reduces dark-phase food intake and gastric emptying in rats: differential role of corticotropin-releasing factor2 receptor, Endocrinology 150 (2009) 4911–4919.

[12] M. Goebel, A. Stengel, L. Wang, Y. Taché, Central nesfatin-1 reduces the nocturnal food intake in mice by reducing meal size and increasing inter-meal intervals, Peptides 32 (2011) 36–43.

[13] Y. Maejima, U. Sedbazar, S. Suyama, D. Kohno, T. Onaka, E. Takano, N. Yoshida, M. Koike, Y. Uchiyama, K. Fujiwara, T. Yashiro, T.L. Horvath, M.O. Dietrich, S. Tanaka, K. Dezaki, I.S. Oh, K. Hashimoto, H. Shimizu, M. Nakata, M. Mori, T. Yada, Nesfatin-1-regulated oxytocinergic signaling in the paraventricular nucleus causes anorexia through a leptin-independent melanocortin pathway, Cell Metab. 10 (2009) 355–365.

[14] D. Kohno, M. Nakata, Y. Maejima, H. Shimizu, U. Sedbazar, N. Yoshida, K. Dezaki, T. Onaka, M. Mori, T. Yada, Nesfatin-1 neurons in paraventricular and supraoptic nuclei of the rat hypothalamus coexpress oxytocin and vasopressin and are activated by refeeding, Endocrinology 149 (2008) 1295–1301.

[15] F.Q. Nuttall, M.C. Gannon, J.L. Wald, M. Ahmed, Plasma glucose and insulin profiles in normal subjects ingesting diets of varying carbohydrate, fat, and protein content, J. Am. Coll. Nutr. 4 (1985) 437–450.

[16] D.E. Cummings, J.Q. Purnell, R.S. Frayo, K. Schmidova, B.E. Wisse, D.S. Weigle, A Preprandial Rise in Plasma Ghrelin Levels Suggests a Role in Meal Initiation in Humans, Diabetes 50 (2001) 1714–1719.

[17] W.A. Banks, J.B. Jaspan, W. Huang, A.J. Kastin, Transport of insulin across the blood-brain barrier: saturability at euglycemic doses of insulin, Peptides 18 (1997) 1423–1429.

[18] A.B. Steffens, A.J. Scheurink, D. Porte, S.C. Woods, Penetration of peripheral glucose and insulin into cerebrospinal fluid in rats, Am. J. Physiol.-Regul., Integr. Comp. Physiol. 255 (1988) R200–R204.

[19] D. Kohno, M. Nakata, F. Maekawa, K. Fujiwara, Y. Maejima, M. Kuramochi, T. Shimazaki, H. Okano, T. Onaka, T. Yada, Leptin suppresses ghrelin-induced activation of neuropeptide Y neurons in the arcuate nucleus via phosphatidylinositol 3-kinase- and phosphodiesterase 3-mediated pathway, Endocrinology 148 (2007) 2251–2263.

[20] Y. Maejima, D. Kohno, Y. Iwasaki, T. Yada, Insulin suppresses ghrelin-induced calcium signaling in neuropeptide Y neurons of the hypothalamic arcuate nucleus, Aging (Albany NY) 3 (2011) 1092–1097.

[21] T. Yada, S. Vigh, A. Arimura, Pituitary adenylate cyclase activating polypeptide (PACAP) increases cytosolic-free calcium concentration in folliculo-stellate cells and somatotropes of rat pituitary, Peptides 14 (1993) 235–239.

[22] C. Grienberger, A. Konnerth, Imaging Calcium in Neurons, Neuron 73 (2012) 862–885.

[23] A.A. Dunn-Meynell, E. Govek, B.E. Levin, Intracarotid glucose selectively increases Fos-like immunoreactivity in paraventricular, ventromedial and dorsomedial nuclei neurons, Brain Res. 748 (1997) 100–106.

[24] W.A. Banks, A.J. Kastin, Differential Permeability of the Blood–Brain Barrier to Two Pancreatic Peptides: Insulin and Amylin, Peptides 19 (1998) 883–889.

[25] G.A. Werther, A. Hogg, B.J. Oldfield, M.J. McKinley, R. Figdor, A.M. Allen, F.A. Mendelsohn, Localization and characterization of insulin receptors in rat brain and pituitary gland using in vitro autoradiography and computerized densitometry, Endocrinology 121 (1987) 1562–1570.

[26] G.L.C. Yosten, W.K. Samson, The anorexigenic and hypertensive effects of nesfatin-1 are reversed by pretreatment with an oxytocin receptor antagonist, Am. J. Physiol.-Regul., Integr. Comp. Physiol. 298 (2010) R1642–R1647.

[27] M. Goebel, A. Stengel, L. Wang, Y. Tache, Restraint stress activates nesfatin-1-immunoreactive brain nuclei in rats, Brain Res. 1300 (2009) 114–124.

Biochemical and Biophysical Research Communications 420 (2012) 816–821

Contents lists available at SciVerse ScienceDirect

Biochemical and Biophysical Research Communications

journal homepage: www.elsevier.com/locate/ybbrc

Chlamydia trachomatis Tarp cooperates with the Arp2/3 complex to increase the rate of actin polymerization

Shahanawaz Jiwani [a], Ryan J. Ohr [a], Elizabeth R. Fischer [b], Ted Hackstadt [b], Stephenie Alvarado [a], Adriana Romero [a], Travis J. Jewett [a,*]

[a] *Burnett School of Biomedical Sciences, College of Medicine, University of Central Florida, Orlando, FL 32827, USA*
[b] *Host-Parasite Interactions Section, Laboratory of Intracellular Parasites, Rocky Mountain Laboratories, National Institute of Allergy and Infectious Diseases, National Institutes of Health, Hamilton, MT 59840, USA*

ARTICLE INFO

Article history:
Received 22 February 2012
Available online 23 March 2012

Keywords:
Chlamydia trachomatis
Tarp
Arp2/3 complex
Actin

ABSTRACT

Actin polymerization is required for *Chlamydia trachomatis* entry into nonphagocytic host cells. Host and chlamydial actin nucleators are essential for internalization of chlamydiae by eukaryotic cells. The host cell Arp2/3 complex and the chlamydial translocated actin recruiting phosphoprotein (Tarp) are both required for entry. Tarp and the Arp2/3 complex exhibit unique actin polymerization kinetics individually, but the molecular details of how these two actin nucleators cooperate to promote bacterial entry is not understood. In this study we provide biochemical evidence that the two actin nucleators act synergistically by co-opting the unique attributes of each to enhance the dynamics of actin filament formation. This process is independent of Tarp phosphorylation. We further demonstrate that Tarp colocalization with actin filaments is independent of the Tarp phosphorylation domain. The results are consistent with a model in which chlamydial and host cell actin nucleators cooperate to increase the rate of actin filament formation.

© 2012 Elsevier Inc. All rights reserved.

1. Introduction

Chlamydia trachomatis is the most prevalent sexually transmitted bacterium in the United States [1]. Chlamydia can infect the genital tract of both men and women. A majority of infections in women are asymptomatic, which if not detected, can lead to pelvic inflammatory disease, ectopic pregnancy and infertility [2]. Worldwide, *C. trachomatis* infection of the eye (trachoma) is the leading cause of preventable blindness with an estimated 40 million active trachoma infections in 2009 [3].

Chlamydiae display a unique developmental cycle in which the extracellular infectious elementary bodies (EBs) invade human epithelial cells. Once internalized the EB differentiates into a reticulate body (RB) within a membrane bound vacuole called an inclusion and undergoes several rounds of replication before differentiating back to EBs, which are released from the infected cell and can initiate a new infection [4,5].

C. trachomatis entry into a human cell is dependent on host cytoskeletal rearrangements triggered by bacterial attachment to the host cell surface [6]. Host cells treated with drugs such as cytochalasin D that disrupt actin polymerization inhibit chlamydial entry [6]. In addition, chlamydial entry is inhibited by disruption of the host actin related proteins 2 and 3 nucleating (Arp2/3) complex [7,8]. A chlamydial type III secreted effector protein termed Tarp, for translocated actin recruiting phosphoprotein, has also been implicated in the bacterial induced cytoskeletal changes that permit EB entry [9]. Tarp harbors distinct actin binding and oligomerization domains which allow for the clustering of multiple actin monomers to nucleate a new actin filament [10]. Antibodies with specificity to the Tarp actin binding domain, when microinjected into host cells prior to *C. trachomatis* infection, inhibited bacterial entry [11]. Taken together, these findings implicate both host and bacterial actin nucleation complexes in driving cytoskeletal changes required for *C. trachomatis* entry. The molecular details of Tarp and Arp2/3 complex interactions are unknown.

Each of these two independent actin nucleators employs unique strategies for the generation of new actin filaments. The host cell Arp2/3 complex is comprised of seven proteins including the actin related proteins 2 and 3 polypeptides which share homology with actin [12–14]. The Arp2/3 complex is regulated by host cell machinery such as those members of the Wiskott–Aldrich syndrome family proteins (WASP) whose members are themselves regulated by signal transduction cascades [15,16]. The Arp2/3 complex associates with existing actin filaments to nucleate a new actin filament forming a branch at an angle of approx. 70°

* Corresponding author. Address: Burnett School of Biomedical Sciences, College of Medicine, University of Central Florida, 6900 Lake Nona Blvd., Orlando, FL 32827, USA. Fax: +1 407 266 7002.
E-mail address: travis.jewett@ucf.edu (T.J. Jewett).

0006-291X/$ - see front matter © 2012 Elsevier Inc. All rights reserved.
http://dx.doi.org/10.1016/j.bbrc.2012.03.080

[12]. Conversely, Tarp is a single chlamydial polypeptide of 1005 amino acids, which harbors distinct phosphorylation, oligomerization and actin binding domains [9,10,17]. Tarp is able to associate with globular actin to nucleate the formation of linear actin filaments without activation from a nucleation promoting factor [10].

C. trachomatis Tarp is rapidly phosphorylated by host tyrosine kinases such as Abl, Syk and Src family members following translocation into the host cell [18,19]. Phosphorylated Tarp has been shown to associate with phosphoinositide 3-kinase (PI3K) and Src homology 2 (SH2) domain containing transforming protein 1 (SCH-1) via their respective SH2 domains [20]. Additionally, phosphorylated Tarp had been suggested to be implicated in the GTPase mediated activation of the host cell Arp2/3 complex [20]. Consequently, a role for Tarp phosphorylation in bacterial entry is controversial as chemical inhibitors which prevent Tarp phosphorylation do not inhibit chlamydial entry [18]. Furthermore, Tarp orthologs from other chlamydial species are not phosphorylated suggesting they have evolved mechanisms to circumvent any requirement for Tarp phosphorylation [11,17,21].

We demonstrate here that Tarp and the Arp2/3 complex cooperate to increase the rate of actin polymerization and were accompanied by a concomitant increase in branched actin filaments observed by scanning electron microscopy. We show that Tarp phosphorylation does not alter the cooperation between Tarp and the Arp2/3 complex. Furthermore, Tarp colocalization with actin filaments is independent of the Tarp phosphorylation domain. Taken together our results indicate that bacterial and host cell derived actin nucleators work cooperatively to increase the rate of actin filament formation and promote chlamydial entry.

2. Materials and methods

2.1. SDS–PAGE and immunoblotting

Proteins were separated on SDS-10% polyacrylamide gels and stained with coomassie R-250 (Pierce) or transferred to 0.45 μm pure nitrocellulose transfer and immobilization membrane (Schleicher & Schuell, Keene, NH). Immunoblotting employed peroxidase conjugated secondary antibodies (Chemicon International, Temecula, CA) and Supersignal West Pico chemiluminescent substrate (Pierce, Rockford, IL). The anti-phosphotyrosine 4G10 monoclonal antibody was purchased from Upstate (Millipore). Polyclonal rabbit antibodies directed towards *C. trachomatis* L2 LGV 434 Tarp was developed at Rocky Mountain Laboratories as previously described [9].

2.2. Cloning, protein expression and purification

An in frame glutathione-S-transferase (GST) and polyhistidine *C. trachomatis* L2 LGV 434 Tarp fusion protein was generated by PCR amplifying the corresponding coding regions from *C. trachomatis* genomic DNA (QIAGEN genomic purification kit, Valencia CA) using custom synthesized oligonucleotide primers (Integrated DNA Technologies, Coralville, IA) engineered with SalI, SacI or NotI linkers. PCR products were purified (QIAGEN), digested with restriction enzymes (New England Biolabs, Beverly, MA) and subcloned into linearized pGEX-6P-1 to generate translational fusions with GST at the N-terminus and polyhistidine at the C-terminus. The PCR fragments described above harboring *tarP* were also cloned into pEGFP-C3 (BD Biosciences Clontech) to allow for the ectopic expression of eGFP-Tarp in HeLa cells.

pGEX-6P-1 plasmids were transformed into BL21 strain of *Escherichia coli* (Novagen, Madison WI). Protein expression and purification were performed according to the procedures outlined for Ni Sepharose 6 Fast Flow and Glutathione Sepharose 4B in the Bulk GST Purification Module (GE health sciences, Piscataway, NY).

2.3. Pyrene assay

The rate of actin polymerization in the presence of Tarp and the Arp2/3 complex was monitored according to the methods outlined in the Actin Polymerization Biochem Kit BK003 (Cytoskeleton, Denver CO). Briefly, monomeric pyrene labeled actin was prepared by diluting 500 μg of lyophilized pyrene actin into 5 mls of 5 mM Tris (pH 8.0), 0.2 mM $CaCl_2$, and 0.2 mM ATP (G-buffer) and incubating for 1 h at room temperature followed by an additional hour of incubation at 4 °C. Monomeric pyrene actin was obtained by collecting the supernatant following a 2 h, 100,000 rcf, 4 °C spin in a Beckman Optima TLX Ultracentrifuge using a TLA 100.3 rotor (Beckman Colter Inc., Fullerton, CA). Approximately 40 μg of pyrene labeled actin was gently mixed with 2–5 μg of test proteins in a volume of 500 μl for 5 min prior to the addition of 1/20th volume of polymerization buffer (500 mM KCl, 20 mM $MgCl_2$, and 10 mM ATP). The reaction was monitored over one hour with an LS 55 Luminescence spectrophotometer equipped with a biokinetics accessory and directed by FL WinLab software version 4.0 (Perkin Elmer, Beaconsfield, BUCKS, UK) with 2.5 nm bandwidth at 365 nm excitation wavelength and 2.5 nm bandwidth at 407 nm emission wavelength.

2.4. Scanning electron microscopy

Actin filaments were added to an SEM type 3 mount and sputter coated with 8–10 nm chromium. Coated filaments were examined in a Hitachi S5200 scanning electron microscope at 30 kV accelerating voltage.

2.5. Transfection of HeLa cells and indirect immunofluorescence microscopy

Hela cells (2×10^5) were seeded in 6 well plates with coverslips and grown for 24 h in DMEM containing 10% FBS. Cells were then transfected with transfection mixture containing 8 μl of Fugene HD (promega) and 2.5 mg of respective plasmid. Following 24 h, cells were fixed by adding 4% paraformaldehyde and incubating at 4 °C for 15 min. Cells were then treated with ice cold 0.4% Triton-X for 10 min, followed by blocking with 5% BSA for 45 min. To visualize tyrosine phosphorylated protein, cells were first incubated with anti-phosphotyrosine primary antibody (upstate) at 1:1000 dilutions in 0.5% BSA at RT for 45 min followed by incubation with anti-mouse secondary antibody conjugated to Alexa 350 (invitrogen). To simultaneously visualize actin, phalloidin conjugated to Alexa 568 (invitrogen) was added to the above mixture containing secondary antibodies. To stain for Arp2/3 complex, cells were first incubated with anti-Arp3 primary antibody (upstate) at 1:100 dilutions in 0.5% BSA at RT for 45 min followed by incubation with anti-rabbit secondary antibody conjugated to Alexa 594 (invitrogen). Coverslips were rinsed and mounted in Prolong Gold antifade reagent (invitrogen). Cells were examined with a Zeiss Axio Observer A1 microscope equipped with phase contrast and epifluorescence optics. Images were obtained using an AxioCam MRm camera controlled by AxioVision 4.8.2 and further processed using Adobe Photoshop CS2.

3. Results

3.1. Tarp and activated Arp2/3 cooperate to polymerize actin

We have previously shown that the actin filaments produced by chlamydial Tarp are linear [10], whereas actin filaments produced via activated Arp2/3 complex from existing filaments result in branched actin filaments [13]. To test whether the chlamydial

and host cell actin nucleators cooperate, we examined the rate of actin polymerization in a pyrene actin polymerization assay following the addition of each purified actin nucleator singularly and together (Fig. 1). Chlamydial Tarp and activated Arp2/3 complex (Arp2/3 complex and the nucleation promoting factor verprolin, cofilin, acidic (VCA) domain of the Wiskott–Aldrich Syndrome protein (WASp)) were able to polymerize actin at a greater rate than actin alone controls (Fig. 1B) [10,16]. Arp2/3 mediated actin nucleation, similar to actin alone controls, exhibits a lag phase in which actin monomers assemble to form a nucleus from which linear actin filament formation proceeds. As the concentration of small linear actin filaments increases, the activated Arp2/3 complex is able to associate to the linear filaments and initiate the formation of a new filament (branched actin) from the existing filament [22–24]. Conversely, a lag phase is not observed when chlamydial Tarp is added to the pyrene assay indicating that there is no requirement for existing actin filaments to promote Tarp mediated actin nucleation. The rate of actin filament formation increased when Tarp and the activated Arp2/3 complex were added in the same actin polymerization reaction indicating the two actin nucleators cooperate (Fig. 1B). To test whether phosphorylation of Tarp altered its cooperation with the Arp2/3 complex to polymerize actin, recombinant Tarp was phosphorylated with purified Fyn kinase (Fig. 1C) and examined in the pyrene actin polymerization assay (Fig. 1D). Phosphorylated Tarp did not alter the kinetics of actin polymerization as compared to that of nonphosphorylated Tarp, nor did it alter cooperation with the Arp2/3 complex. To examine whether Tarp might activate the Arp2/3 complex directly by serving as a nucleation-promoting factor (NPF) *in vitro*, pyrene actin polymerization assays were performed in the presence of Tarp or phosphorylated Tarp (Tarp-PO4) and the Arp2/3 complex in the absence of the VCA peptide, which activates the Arp2/3 complex.

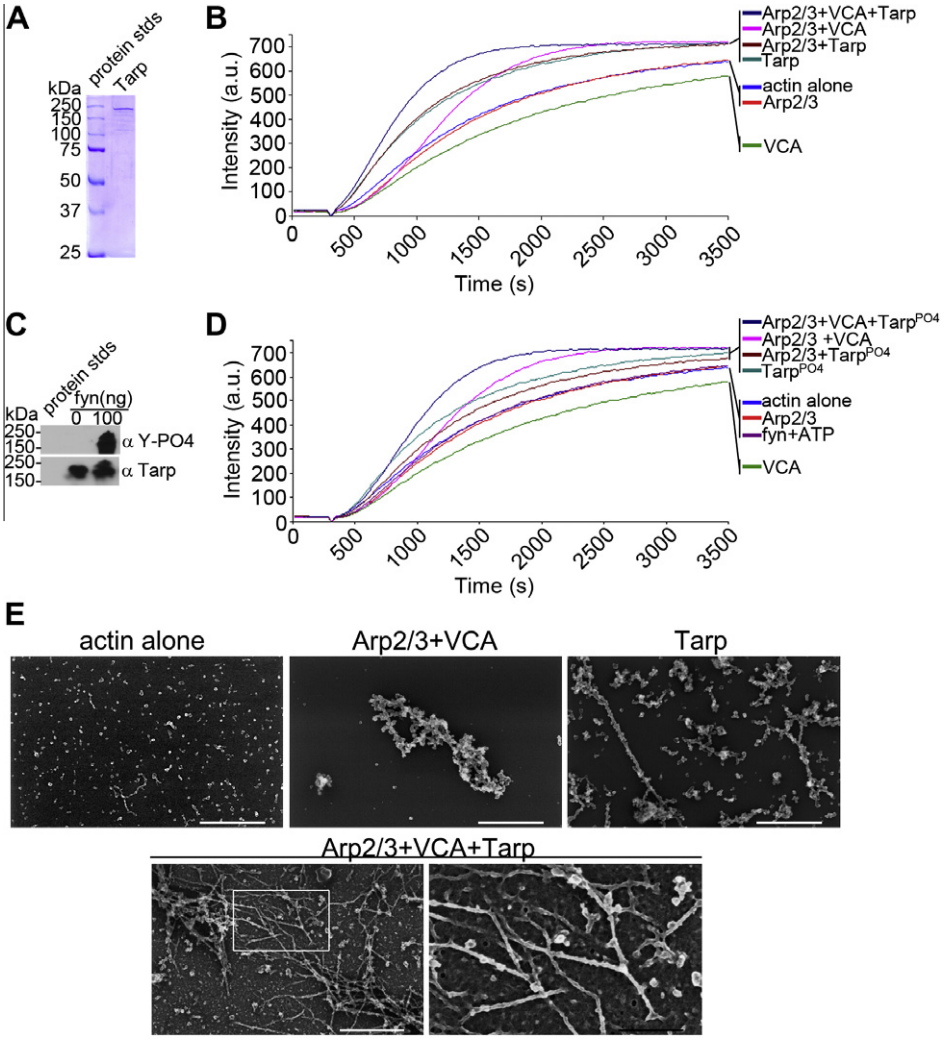


Fig. 1. Tarp and Arp2/3 complex cooperate to polymerize actin. (A) Purified recombinant Tarp employed for these studies was resolved by SDS–PAGE and visualized by Coomassie blue staining. (B) Pyrene actin polymerization in the presence of Tarp and activated Arp2/3 complex (Arp2/3 + VCA + Tarp) was compare to actin polymerization kinetics initiated by Tarp alone (Tarp), activated Arp2/3 complex alone (Arp2/3 + VCA) and Tarp with an inactive Arp2/3 complex (Arp2/3 + Tarp). Actin alone (actin), inactive Arp2/3 complex (Arp2/3) and the Verprolin, Cofilin, Acidic (VCA) domain of N-WASP served as additional controls. Bacterial and host cell nucleators were incubated with pyrene conjugated actin and actin polymerization was measured by an increase in fluorescence of pyrenyl-actin incorporated into actin filaments (Intensity (a.u.)) over approximately 1 h (Time (s)) following the addition of polymerization buffer at 300 s. (C) Purified recombinant Tarp was phosphorylated by the Src family kinase member fyn. Tarp proteins were incubated with 100 ng of purified fyn kinase and ATP and following a short incubation were suspended in protein sample buffer and resolved by SDS–PAGE followed by transfer to nitrocellulose. Immunoblots were performed with Tarp (α Tarp) and phosphotyrosine (α Y-PO4) specific antisera. (D) Pyrene actin polymerization assays as B but with phosphorylated Tarp. Additional controls include actin polymerization assays performed in the presence of fyn kinase and phosphorylation buffer containing ATP (fyn + ATP). (E) Electron micrographs of actin filaments nucleated by Tarp and the Arp2/3 complex. Protein samples were removed from actin polymerization experiments similar to those shown in B at 900 s (10 min after the addition of polymerization buffer) and actin filaments were visualized by scanning electron microscopy. White scale bar represents 400 nm and black scale bar represents 150 nm.

The rate of actin polymerization did not change relative to Tarp alone (with or without phosphorylation) suggesting that Tarp does not activate the Arp2/3 complex directly (Fig. 1B and D). Actin filaments removed from a pyrene actin polymerization assay at 10 min post-delivery of the actin polymerization buffer were analyzed by scanning electron microscopy (Fig 1E). Electron micrography revealed an increase in the amount of branched actin filaments observed in the presence of both the Arp2/3 complex and Tarp compared to activated Arp2/3 complex alone suggesting that the two actin nucleators cooperate to increase the local concentration of branched actin.

3.2. Ectopically expressed eGFP-Tarp colocalizes with actin filaments but not the Arp2/3 complex

Previous studies have examined actin colocalization with ectopically expressed eGFP-Tarp fusion proteins [9–17]. Tarp fusion proteins aggregate in the host cell cytosol and colocalize with actin filaments. The actin colocalization is clearly observed with fusion proteins containing the entire Tarp protein sequence as well as the C-terminal half of Tarp [17]. Subsequent studies have specifically identified the actin binding alpha helix present between amino acids 748–758 as responsible for Tarp mediated actin binding [10]. Conversely, the ectopically expressed N-terminus and repeat region (phosphorylation domain) of Tarp do not aggregate in the cytosol and appear to localize to the host cell nucleus [17]. A new eGFP-Tarp fusion protein was engineered which harbors the phosphorylation domain and the proline rich domain, responsible for Tarp aggregation, but lacks the actin binding domain (Fig. 2A). Host cells expressing this eGFP fusion protein (Tarp$^{1\text{-}747}$) displayed small discrete aggregates in the host cell cytosol that were phosphorylated and did not localize with actin filaments (Fig. 2B), whereas eGFP-Tarp lacking the phosphorylation domain but harboring the actin binding domain (Tarp$^{624\text{-}1005}$) did localize with actin filaments. Interestingly neither the ectopically expressed full length nor mutant eGFP-Tarp proteins colocalized with the Arp2/3 complex which is consistent with previous reports in which the Arp2/3 complex was not detected in Tarp binding studies (Supplemental Fig. 2) [10]. Taken together, these data demonstrate that the Tarp phosphorylation domain is not required for colocalization with actin and suggests the phosphorylation domain alone is not sufficient to drive the cytoskeletal changes observed surrounding the ectopically expressed full length Tarp but that the proline-rich oligomerization domain may play a prominent role in aggregation of ectopically expressed Tarp.

4. Discussion

We have previously hypothesized that chlamydial entry relies upon the coordinated efforts of Tarp and the Arp2/3 complex

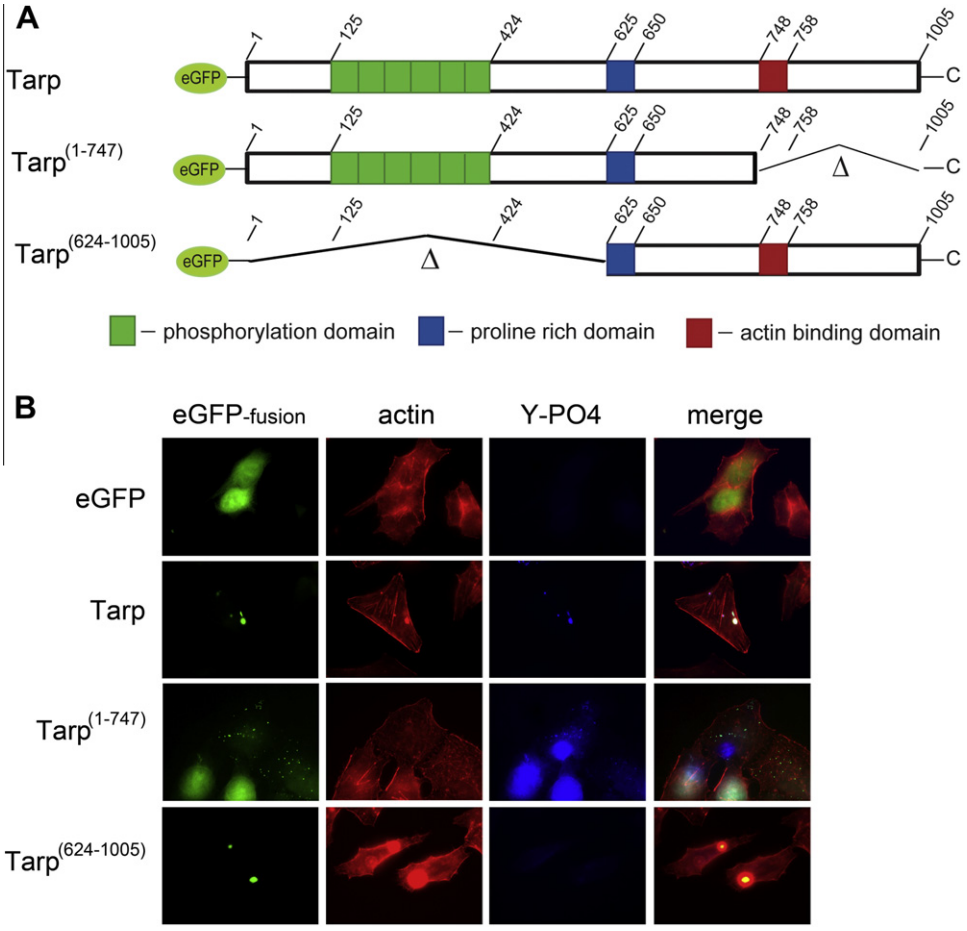


Fig. 2. Actin filaments co-localize with ectopically expressed Tarp in a phosphorylation domain independent manner. Tarp proteins ectopically expressed as enhanced green fluorescence protein fusions were examined for their ability to localize with actin filaments. (A) Schematic of the eGFP-Tarp fusion proteins indicating the location of the actin binding domain (red box), the proline rich domain (blue box) and the tyrosine rich phosphorylation domain (green boxes). Δ indicates amino acids deleted in the mutant eGFP-Tarp fusion proteins and numbers indicate amino acid positions encoded within the *C. trachomatis* tarP gene. (B) Host cells expressing eGFP (eGFP) alone or eGFP fusions (eGFP-fusion) of full length Tarp (Tarp), or deletion mutants lacking the phosphorylation domain (Tarp$^{624\text{-}1005}$) or actin binding domain (Tarp$^{1\text{-}747}$) but harboring the proline rich domain (PRD) required for protein aggregation were fixed and stained with Alexa fluor 568 conjugated phalloidin (actin), phosphotyrosine specific antisera (Y-PO4) and goat anti-mouse conjugated to Alexa 350. (For interpretation of the references to colour in this figure legend, the reader is referred to the web version of this article.)

acting cooperatively to alter the host cell cytoskeleton and promote chlamydial entry [10]. The Arp2/3 complex is highly regulated by host cell proteins called nucleation promoting factors (NPFs) such as those members of the Wiskott–Aldrich syndrome family proteins (WASP) whose members are themselves regulated by Rho family of GTPases [16,25]. Nucleation promoting factors are not restricted to eukaryotic origins and in some cases are derived from pathogens such as *Listeria monocytogenes* (ActA) and *Rickettsia conorii* (RickA) [26–28]. Although Tarp alone is capable of directly nucleating actin filaments, a role for Tarp as a NPF for the Arp2/3 complex had not been investigated. The addition of Tarp (with or without phosphorylation) to the Arp2/3 complex in the absence of known NPFs produced no changes to the rate of actin polymerization detected by pyrene actin polymerization assays compared to that of Tarp alone. Conversely, when Tarp and activated Arp2/3 were added together the rate of actin polymerization increased relative to Tarp alone (Fig. 1B). Our results suggest that Tarp's ability to rapidly initiate the formation of linear actin filaments provided substrate for the Arp2/3 complex to form branched actin. These results were supported by visualization of the actin filaments by scanning electron microscopy. Furthermore, the Tarp and Arp2/3 complex cooperation was not dependent on Tarp phosphorylation as Tarp proteins phosphorylated by Fyn kinase were also able to cooperate with the Arp2/3 complex.

A comparison of Tarp orthologs from different species and serovars of Chlamydia has shed light on the conserved nature of the characterized Tarp protein domains [11,17,21]. Interestingly, it appears that different Tarp orthologs can employ different mechanisms to nucleate actin depending on their respective number of actin binding domains [11]. Conversely, the phosphorylation domain is restricted to serovarsof *C. trachomatis*, suggesting Tarp phosphorylation may initiate signal transduction cascades not utilized by other chlamydial species. Phosphorylated Tarp has been shown to associate with the host cell adapter protein SHC-1 and this association is implicated in altering expression of host cell genes pertinent to cell growth and host cell survival [21]. Phosphorylated Tarp peptides have also been shown to immunoprecipitate a complex of proteins containing Sos1 and Vav2, two Rac guanine nucleotide exchange factors thought to participate in WAVE2 and Arp2/3 complex recruitment [20]. To examine whether Tarp was capable of recruiting actin in the absence of an actin binding domain, via the Tarp phosphorylation domain, eGFP-Tarp fusion proteins were expressed in HeLa cells that were missing the actin binding domain, but still harbored the proline rich domain required for Tarp aggregation. eGFP-Tarp proteins were phosphorylated and did not colocalize with filamentous actin consistent with the belief that Tarp/actin colocalization is a function of the C-terminal actin binding domain and does not require the phosphorylation domain.

Collectively, the data demonstrate that the Arp2/3 complex and Tarp actin nucleators cooperate to increase the rate of actin filament formation, however, Tarp does not directly activate the Arp2/3 complex. While an indirect role for phosphorylated Tarp mediated Arp2/3 complex activation is possible, the eGFP-Tarp mutant proteins harboring the phosphorylation domain alone were unable to recruit actin filaments *in vivo*. Our data advocates that Tarp signaling alone is insufficient to activate the Arp2/3 complex. Arp2/3 complex activation during chlamydial entry is likely to be multifactorial as multiple signals converge on the host actin nucleating complex. Arp2/3 complex activation might be accomplished in part via EB binding to host cell receptors. Fibroblast Growth Factor Receptors (FGFRs) were recently implicated in EB entry and are known to activate the Arp2/3 complex by association with Ras GTPase activating-like protein 1 (IQGAP1) [29–31]. Presently, a role for IQGAP1 in chlamydial entry has not been examined and requires further investigation. Although Arp2/3 complex activation during EB entry remains unclear, our results indicate that bacterial and host actin nucleators cooperate biochemically to increase the local concentration of actin filaments required for invasion.

Acknowledgments

The authors wish to recognize members of Mollie W. Jewett laboratory for helpful discussions as well as acknowledge the technical assistance of Talia Chavez and Brenda Nguyen. This work was supported by the NIAID, NIH K award 5K22AI81729-2 and the University of Central Florida to T.J.J. and the intramural research program of the NIAID, NIH to T.H.

Appendix A. Supplementary data

Supplementary data associated with this article can be found, in the online version, at http://dx.doi.org/10.1016/j.bbrc.2012.03.080.

References

[1] CDC Grand Rounds: Chlamydia prevention: challenges and strategies for reducing disease burden and sequelae. MMWR Morb Mortal Wkly Rep 60 370–373.
[2] J. Schachter, Infection and disease epidemiology, in: R.S. Stephens (Ed.), Chlamydia; Intracellular biology, pathogenesis, and immunity, ASM Press, Washington, D.C., 1999, pp. 139–169.
[3] S.P. Mariotti, D. Pascolini, J. Rose-Nussbaumer, Trachoma: global magnitude of a preventable cause of blindness, Br. J. Ophthalmol. 93 (2009) 563–568.
[4] K. Hybiske, R.S. Stephens, Mechanisms of host cell exit by the intracellular bacterium Chlamydia, Proc. Natl. Acad. Sci. USA 104 (2007) 11430–11435.
[5] J.W. Moulder, Interaction of chlamydiae and host cells in vitro, Microbiol. Rev. 55 (1991) 143–190.
[6] R.A. Carabeo, S.S. Grieshaber, E. Fischer, T. Hackstadt, Chlamydia trachomatis induces remodeling of the actin cytoskeleton during attachment and entry into HeLa cells, Infect. Immun. 70 (2002) 3793–3803.
[7] R.A. Carabeo, C.A. Dooley, S.S. Grieshaber, T. Hackstadt, Rac interacts with Abi-1 and WAVE2 to promote an Arp2/3-dependent actin recruitment during chlamydial invasion, Cell Microbiol. 9 (2007) 2278–2288.
[8] K. Hybiske, R.S. Stephens, Mechanisms of Chlamydia trachomatis entry into nonphagocytic cells, Infect. Immun. 75 (2007) 3925–3934.
[9] D.R. Clifton, K.A. Fields, S.S. Grieshaber, C.A. Dooley, E.R. Fischer, D.J. Mead, R.A. Carabeo, T. Hackstadt, A chlamydial type III translocated protein is tyrosine-phosphorylated at the site of entry and associated with recruitment of actin, Proc. Natl. Acad. Sci. USA 101 (2004) 10166–10171.
[10] T.J. Jewett, E.R. Fischer, D.J. Mead, T. Hackstadt, Chlamydial TARP is a bacterial nucleator of actin, Proc. Natl. Acad. Sci. USA 103 (2006) 15599–15604.
[11] T.J. Jewett, N.J. Miller, C.A. Dooley, T. Hackstadt, The conserved Tarp actin binding domain is important for chlamydial invasion, PLoS Pathog. 6 (2010) e1000997.
[12] R.D. Mullins, J.A. Heuser, T.D. Pollard, The interaction of Arp2/3 complex with actin: nucleation, high affinity pointed end capping, and formation of branching networks of filaments, Proc. Natl. Acad. Sci. USA 95 (1998) 6181–6186.
[13] R.D. Mullins, W.F. Stafford, T.D. Pollard, Structure, subunit topology, and actin-binding activity of the Arp2/3 complex from Acanthamoeba, J. Cell. Biol. 136 (1997) 331–343.
[14] M.D. Welch, A.H. DePace, S. Verma, A. Iwamatsu, T.J. Mitchison, The human Arp2/3 complex is composed of evolutionarily conserved subunits and is localized to cellular regions of dynamic actin filament assembly, J. Cell. Biol. 138 (1997) 375–384.
[15] H.N. Higgs, T.D. Pollard, Regulation of actin polymerization by Arp2/3 complex and WASp/Scar proteins, J. Biol. Chem. 274 (1999) 32531–32534.
[16] H. Yamaguchi, H. Miki, S. Suetsugu, L. Ma, M.W. Kirschner, T. Takenawa, Two tandem verprolin homology domains are necessary for a strong activation of Arp2/3 complex-induced actin polymerization and induction of microspike formation by N-WASP, Proc. Natl. Acad. Sci. USA 97 (2000) 12631–12636.
[17] D.R. Clifton, C.A. Dooley, S.S. Grieshaber, R.A. Carabeo, K.A. Fields, T. Hackstadt, Tyrosine phosphorylation of the chlamydial effector protein Tarp is species specific and not required for recruitment of actin, Infect. Immun. 73 (2005) 3860–3868.
[18] T.J. Jewett, C.A. Dooley, D.J. Mead, T. Hackstadt, Chlamydia trachomatis tarp is phosphorylated by src family tyrosine kinases, Biochem. Biophys. Res. Commun. 371 (2008) 339–344.
[19] A. Mehlitz, S. Banhart, S. Hess, M. Selbach, T.F. Meyer, Complex kinase requirements for Chlamydia trachomatis Tarp phosphorylation, FEMS Microbiol. Lett. 289 (2008) 233–240.

[20] B.J. Lane, C. Mutchler, S. Al Khodor, S.S. Grieshaber, R.A. Carabeo, Chlamydial entry involves TARP binding of guanine nucleotide exchange factors, PLoS Pathog. 4 (2008) e1000014.
[21] A. Mehlitz, S. Banhart, A.P. Maurer, A. Kaushansky, A.G. Gordus, J. Zielecki, G. Macbeath, T.F. Meyer, Tarp regulates early Chlamydia-induced host cell survival through interactions with the human adaptor protein SHC1, J. Cell. Biol. 190 (2010) 143–157.
[22] E.I. Lutter, C. Bonner, M.J. Holland, R.J. Suchland, W.E. Stamm, T.J. Jewett, G. McClarty, T. Hackstadt, Phylogenetic analysis of Chlamydia trachomatis Tarp and correlation with clinical phenotype, Infect. Immun. 78 (2010) 3678–3688.
[23] K.J. Amann, T.D. Pollard, Direct real-time observation of actin filament branching mediated by Arp2/3 complex using total internal reflection fluorescence microscopy, Proc. Natl. Acad. Sci. USA 98 (2001) 15009–15013.
[24] K.J. Amann, T.D. Pollard, The Arp2/3 complex nucleates actin filament branches from the sides of pre-existing filaments, Nat. Cell. Biol. 3 (2001) 306–310.
[25] N. Volkmann, K.J. Amann, S. Stoilova-McPhie, C. Egile, D.C. Winter, L. Hazelwood, J.E. Heuser, R. Li, T.D. Pollard, D. Hanein, Structure of Arp2/3 complex in its activated state and in actin filament branch junctions, Science 293 (2001) 2456–2459.
[26] H. Miki, K. Miura, T. Takenawa, N-WASP, a novel actin-depolymerizing protein, regulates the cortical cytoskeletal rearrangement in a PIP2-dependent manner downstream of tyrosine kinases, EMBO J. 15 (1996) 5326–5335.
[27] E. Gouin, C. Egile, P. Dehoux, V. Villiers, J. Adams, F. Gertler, R. Li, P. Cossart, The RickA protein of Rickettsia conorii activates the Arp2/3 complex, Nature 427 (2004) 457–461.
[28] M.D. Welch, J. Rosenblatt, J. Skoble, D.A. Portnoy, T.J. Mitchison, Interaction of human Arp2/3 complex and the Listeria monocytogenes ActA protein in actin filament nucleation, Science 281 (1998) 105–108.
[29] D. Vingadassalom, K.G. Campellone, M.J. Brady, B. Skehan, S.E. Battle, D. Robbins, A. Kapoor, G. Hecht, S.B. Snapper, J.M. Leong, Enterohemorrhagic E. coli requires N-WASP for efficient type III translocation but not for EspFU-mediated actin pedestal formation, PLoS Pathog. 6 (2010) e1001056.
[30] L.B. Bensenor, H.M. Kan, N. Wang, H. Wallrabe, L.A. Davidson, Y. Cai, D.A. Schafer, G.S. Bloom, IQGAP1 regulates cell motility by linking growth factor signaling to actin assembly, J. Cell Sci. 120 (2007) 658–669.
[31] J.H. Kim, S. Jiang, C.A. Elwell, J.N. Engel, Chlamydia trachomatis Co-opts the FGF2 signaling pathway to enhance infection. PLoS Pathog 7 e1002285.

Biochemical and Biophysical Research Communications 420 (2012) 822–827

Contents lists available at SciVerse ScienceDirect

Biochemical and Biophysical Research Communications

journal homepage: www.elsevier.com/locate/ybbrc

Cyclin A regulates a cell-cycle-dependent expression of CKAP2 through phosphorylation of Sp1

Du-Seock Kang [a], Kyeong-Man Hong [b], Joobae Park [a], Chang-Dae Bae [a,*]

[a] Department of Molecular Cell Biology and Samsung Biomedical Research Institute, Sungkyunkwan University School of Medicine, 300 Chunchundong, Jangangu, Suwon 440-746, Republic of Korea
[b] Research Institute, National Cancer Center, 323 Ilsan-ro, Ilsandong-gu, Goyang 410-769, Republic of Korea

ARTICLE INFO

Article history:
Received 12 March 2012
Available online 23 March 2012

Keywords:
CKAP2
Promoter
Sp1
Cyclin A

ABSTRACT

CKAP2 plays crucial roles in proper chromosome segregation and maintaining genomic stability. CKAP2 protein showed cell-cycle-dependent expression, which reached a maximum level at the G2/M phase and disappeared at the onset of G1 phase. To elucidate the mechanisms underlying cell cycle-dependent expression of CKAP2, we cloned and analyzed the human CKAP2 promoter. The upstream 115-bp region from the transcription start site was sufficient for minimal CKAP2 promoter activity. We identified 2 regulatory sequences; a CHR (−110 to −104 bp) and a GC box (−41 to −32 bp). We confirmed Sp1 bound to the GC box using a supershift assay and a ChIP assay. Mutation in the GC box resulted in a near complete loss of CKAP2 promoter activity while mutation in the CHR decreased the promoter activity by 50%. The CHR mutation showed enhanced activity at the G1/S phase, but still retained cyclic activity. The Chromatin IP revealed that the amount of Sp1 bound to the GC box gradually increased and reached a maximum level at the G2/M phase. The amount of Sp1 bound to the GC box was greatly reduced when Cyclin A was depleted, which was restored by adding Cyclin A/Cdk2 complex back into the nuclear extracts. Together, we concluded that the GC box was responsible for the cyclic activity of human CKAP2 promoter through the phosphorylation of Sp1, possibly by Cyclin A/Cdk complex.

© 2012 Elsevier Inc. All rights reserved.

1. Introduction

The cell-cycle-dependent genes can be clustered by their expression peak time at the cell cycle. For example, Cyclin E1 and E2F1 reach the peak time at the G1/S phase and belong to G1/S cluster while Cyclin A2 and Plk1 reach the peak time at the G2/M phase and belong to G2/M cluster [1]. Most G2/M clustered genes lack the TATA box in their promoter, and instead have other regulatory sequences such as a GC box, CCAAT box or cell cycle dependent element (CDE)–cell cycle dependent genes homology region (CHR) [2–4]. The transcription factors specific for such regulatory sequences are also well studied. Sp1, a GC box binding factor, is phosphorylated by several kinases including DNA dependent kinase, MAP kinase, Cdk2 [2,5,6] and regulates the DNA binding affinity of Sp1 in many genes including Cyclin A2, Cyclin B1, Cdc2, and Cdc25C [7–9]. NF-Y, a CCAAT box binding factor, plays an important role in the cyclic expressions of Cdc25B, Cdc25C, Cyclin B2, Cyclin B1, and Cdc2 [10,11]. The CDE–CHR elements are involved in the cyclic expression of Cyclin A2, Cyclin B1, Cdc25C, Cdc2, Aurora kinase, and Plk1. The expression of those genes is repressed through occupied CDE–CHR at the G0/G1 phases and activated by released CDE–CHR later in the cell cycle [9,12–15]. Recently, several transcriptional regulators including E2F4 and Lin54 have been reported to bind to the CDE–CHR of the cdc2 promoter [16] but the specific transcription factors are still not clear.

CKAP2 gene belongs to G2/M clustered gene. It begins to express at the late G1/S phase, reaches the peak time during the G2/M phase, and then degrades through the APC/Cdh1-mediated ubiquitin proteasomal pathway [17,18]. Upregulation of CKAP2 has been reported in gastric cancers [19] and large B-cell lymphoma [20]. Recently, we reported the possible relationship between CKAP2 expression and prognosis of breast cancers [21].

In this study, we performed the promoter analysis to elucidate the regulation mechanism of cell-cycle-dependent expression of the human CKAP2.

2. Materials and methods

2.1. Preparation of nuclear extracts

Nuclear proteins were extracted from HeLa cells maintained in DMEM with 10% FBS (Gibco, Grand Island, NY, USA) by incubating

Abbreviation: CKAP2, cytoskeleton-associated protein 2.

* Corresponding author. Fax: +82 31 299 6149.
E-mail address: cdbae@skku.edu (C.-D. Bae).

0006-291X/$ - see front matter © 2012 Elsevier Inc. All rights reserved.
http://dx.doi.org/10.1016/j.bbrc.2012.03.081

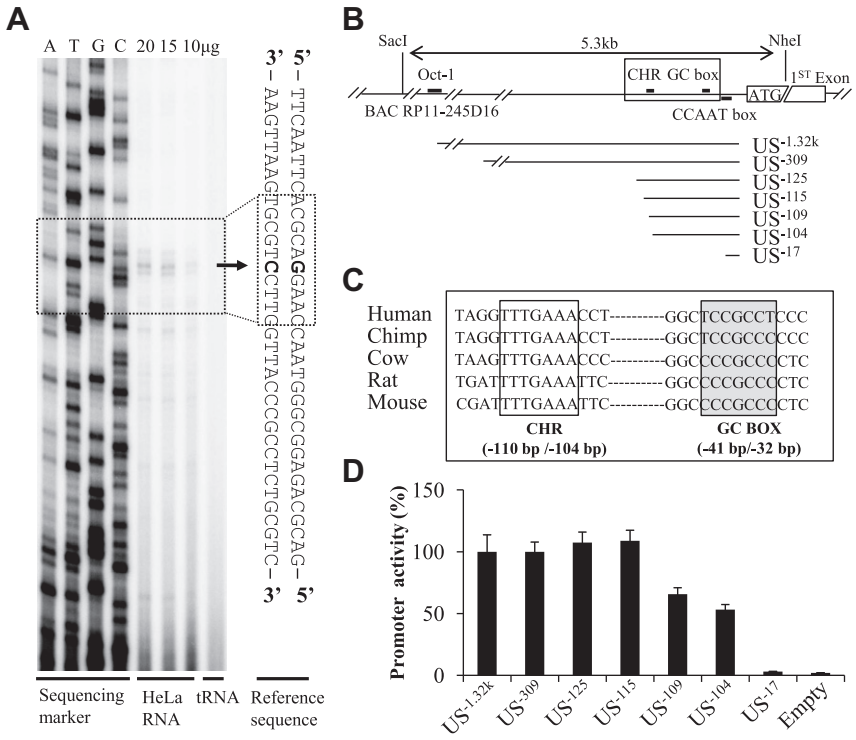


Fig. 1. Determination of minimal promoter region of human CKAP2 gene (A) Primer extension was performed to determine transcription start site. The DNA sequencing ladder generated with the same primer was run in parallel. (B) Each deletion construct was subcloned into pGL3-basic vector by PCR using a SacI/NheI (5.3 kb) fragment from BAC RP11-245D16 as the PCR template (see Section 2). Each deletion construct was named as US (upstream) with a superscript number meaning the length from the transcription start site. (C) Comparison of CKAP2 promoter regions of a human, chimp, cow, rat, and mouse. (D) The relative promoter activity of each deletion construct was presented as a percentage the promoter activity of each construct of that of the control $US^{-1.32k}$. Results are presented as the means ± SDs of triplicate assays.

the nuclear fractions in high-salt buffer (40 mM HEPES-KOH pH 7.9, 0.4 M KCl, 1 mM dithiothreitol, 10% glycerol, 0.1 mM phenylmethylsulfonyl fluoride, and 0.1% aprotinin) and subsequent centrifugation at 103,900*g* for 20 min at 4 °C.

2.2. CKAP2 promoter activity assay

RP11-245D16 BAC clone (GenBank Accession AL359513.12) containing from 33918920 to 34025349 on the chromosome 13 genomic contig primary assembly (NT_024524.14) was purchased from Children's Hospital Oakland Research Institute (Oakland, CA, USA). A 7.7 kb NotI-BamHI fragment containing a 5.3 kb (5319 bp) upstream sequence from the translation initiation site and part of the 1st exon of human CKAP2 was subcloned into pGL3 basic vector (Promega, Madison, WC, USA). Deletion fragments of the upstream sequence of CKAP2 gene were amplified by PCR and subcloned into pGL3 basic vector. Each construct was transfected along with control pRL vector (Promega, Madison, WC, USA) into HeLa cells using Lipofectamine Plus (Invitrogen, Carlsbad, CA, USA). The promoter activity of each deletion construct was calculated as a ratio of the firefly luciferase activity to the Renilla luciferase activity. Primer sets used for amplifying each deletion fragment are followings:

$US^{-1.32k}$: 5′-TGAGCTCTATGTAACTTTTCATATATTAC-3′,
US^{-309}: 5′-AGAGCTCGCGATGTTTAATAAGAAGG-3′,
US^{-125}: 5′-AGAGCTCGCGCTGTTTAGGTTTGAAA-3′,
US^{-115}: 5′-AGAGCTCAGGTTTGAAACCTGCAGAC-3′,
US^{-109}: 5′-AAAAGCTCAAACCTGCAGACTCAGTCC-3′,
US^{-104}: 5′-AAGAGCTAATGCAGACTCAGTCCCAA-3′,
US^{-17}:5′-5′-AAGAGCTCCTTATTCAATTCACGCAGGAA-3′,
Downstream primer: 5′-AGCTAGCAAGATAGAACTTCCTCAGA CCA-3′.

2.3. Primer extension and DNase I footprinting

Primer extension was performed MMLV reverse transcriptase (Invitrogen, Carlsbad, CA, USA) according to the manufacturer's instructions. The oligonucleotide complementary to the sequence spanning −39 to −65 bp from the human CKAP2 translation start codon was used as a gene-specific primer. Nuclear extracts were incubated with the 3′-end-labled DNA fragment spanning −309 to +91 from the CKAP2 translation start codon and digested with DNase I (Promega, Madison, WC, USA) at RT for 1 min. Reaction products were resolved through denaturing polyacrylamide gel electrophoresis and exposed to a BAS-IR SR 2040 imaging plate (Fujifilm, Tokyo, Japan).

2.4. Electrophoretic mobility shift assay

The double-stranded oligonucleotides containing putative CHR motif (5′-GAAGAGCGC TGTTTAGGTTTGAAACCTGCAGACTCAGTCC-3′), GC box motif (5′-CAGTCCAGG CTCCGCCTCCCTACGCCCATTGGC -3′), and NF-Y motif (5′-GCCTCCCTACGCCCA TTGGCTTATTCAATTCACG-3′) were used for mobility shift assays. The siRNA sequences for targeting Cyclin A1 and Cyclin A2 were 5′-GGUCCCUCUUGAUUAUCCA(dTdT)-3′, 5′-CUCAAGUCAGACCUGCACU(dTdT)-3, respectively. Transfection of the siRNA duplex was carried out using DharmaFect (Thermo, IL, USA) according to the manufacturer's instructions. Nuclear extract was incubated with each labeled oligonucleotide in the binding buffer (50 mM NaCl, 10 mM Tris–HCl, pH 7.5, 0.5 mM EDTA, 0.5 mM DTT, 1 mM $MgCl_2$, 4% glycerol, and 2.5 μg of poly(dI·dC)·poly(dI·dC)) for 20 min at room temperature. For the supershift assay, anti-Sp1 antibody (Santa Cruz, CA, USA) was pre-incubated before addition of oligonucleotides. Binding mixtures were analyzed using a 4% polyacrylamide gel and exposed to a BAS-IP SR 2040 imaging plate (Fujifilm, Tokyo, Japan).

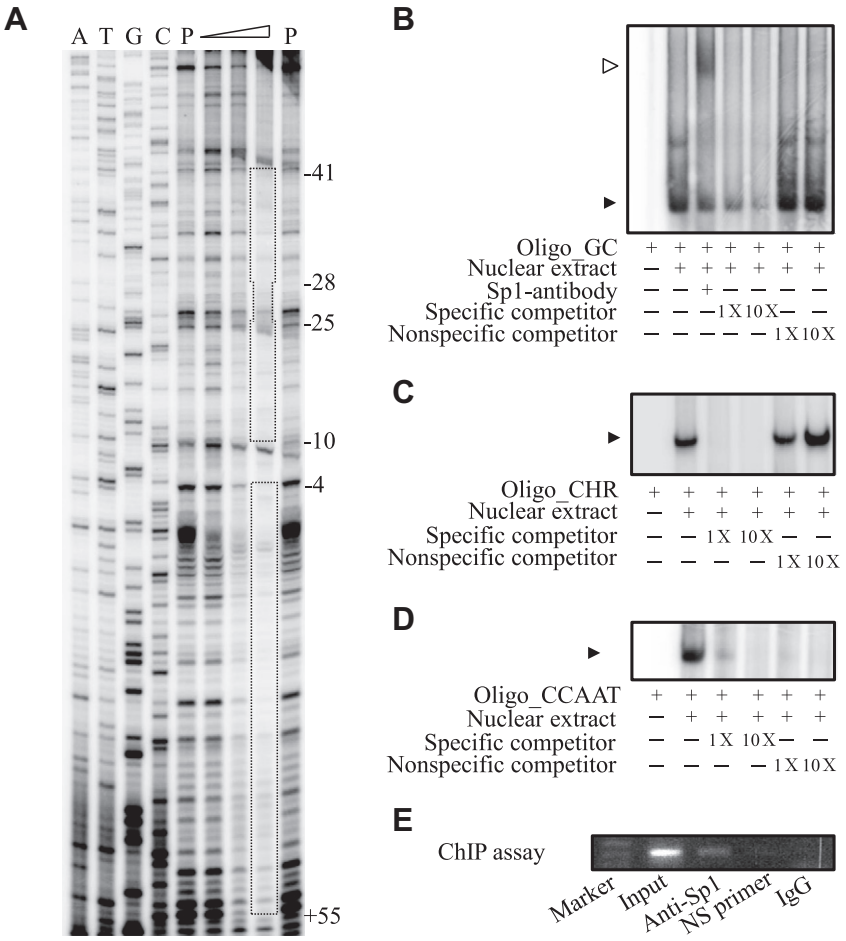


Fig. 2. Transcription regulatory elements in human CKAP2 minimal promoter (A) The [γ-^{32} P] ATP-labeled probe (−100 bp/+91 bp) was incubated with 1, 2 and 4 μg of nuclear extract (lanes 6–8) or without nuclear extracts (lanes 5 and 9) and digested with DNase I. The boxes indicated the protected regions from DNase I digestion. The sequencing ladder was run alongside to determine the position of the protected regions. (B) EMSA was performed using an oligonucleotide containing the GC box (Oligo_GC). The shift band (black arrow head) was reduced dose-dependently in the presence of unlabeled probe (lanes 4 and 5) but unaffected in the presence of an oligonucleotide containing mutated GC box (lanes 6 and 7). This specific interaction was further confirmed by the supershift band (white arrow head) observed in the presence of Sp1 antibody (lane 3). (C and D) EMSA was performed using (C) oligonucleotide containing the CHR element (Oligo_CHR) or (D) oligonucletoide containing CCAAT (Oligo_CCAAT). Unlabeled probes were included in lanes 3 and 4, and the oligonucleotides with mutated CHR or mutated CCAAT sequence were included in lanes 5 and 6 at each panel. Black arrow head represents the shift band. (E) ChIP assay of the human CKAP2 promoter containing a GC box. The input lane represents 0.5% of the total chromatin used in the ChIP assays. Anti-IgG and a nonspecific (NS) primer were used as negative controls.

2.5. Immunoprecipitation assay

HeLa cells were transfected with siRNA mixture targeting both Cyclin A1 and Cyclin A2. The nuclear extracts were incubated with a polyclonal Sp1 antibody for 2 h at 4 °C, followed by incubation for 1 h with protein A-agarose beads (Thermo, IL, USA). Immunoprecipitates were subjected to western blot analysis using a monoclonal phosphor-serine antibody (1:200) (Abcam, Cambridge, UK) and a polyclonal Sp1 antibody (1:1000).

2.6. Chromatin immunoprecipitation assay (ChIP)

ChIP was performed as previously described (http://dx.doi.org/10.1101/pdb.prot5279, Michel et al., 2009, Cold Spring Harb Protocol). Briefly, Cells were sonicated after cross-linked in 1% formaldehyde. The cell lysates were precleared by incubating with salmon sperm DNA and incubated with anti-Sp1 antibody (sc-59) or rabbit IgG along with 100 μL of proteinA-agarose beads for 2 h at 4 °C. DNA fragments were extracted with 500 μL of phenol–chloroform and amplified by PCR reactions. The region spanning −309 to +91 bp was amplified for GC box motif and a region downstream to GC box (−17 bp/+391 bp) was amplified for non-specific precipitation.

3. Results

3.1. Identification of minimal promoter region of human CKAP2 gene

To define the minimal promoter region, we performed a primer extension experiment using the oligonucleotide spanning −39 to −65 bp upstream from the translation start codon. As shown in Fig. 1A, major extension product with the highest intensity started at −132 bp upstream from the translation start. Next, we compared the promoter activities of varying length of upstream sequences with that of 5.3 kb upstream sequence subcloned from BAC clone (Fig. 1B). The region spanning −1.32 kb to +91 bp retained full activity compared to the promoter activity of 5.3 kb upstream sequence (data not shown, Fig. 1B, US$^{-1.32k}$). We made a series of deleted fragments of this upstream region using PCR (see Section 2) and cloned them into a pGL3 firefly luciferase vector (Fig. 1B). The promoter activity of each construct was calculated as a percentage of that of US$^{-1.32k}$. As shown in Fig. 1D, the promoter

activities of 115 bp or longer upstream sequences were similar to that of $US^{-1.32k}$ while the promoter activities of the shorter upstream sequences remained <60% of the activity of $US^{-1.32k}$. The promoter activity of US^{-17} was totally abolished. These results indicated that the upstream 115 bp region retained the essential regulatory regions for transcription of the human CKAP2. Next, we compared genomic sequence of the minimal promoter from some of vertebrate species. When we compared those of mammals, two sites were revealed as likely candidates: a CHR and a GC box (Fig. 1C). Notably, the TATA box was not found in this region.

3.2. Characterization of transcription factors binding to CKAP2 promoter

We explored in vitro binding of transcription factors to the minimal promoter region near the transcription start site using DNase I footprinting. As shown in Figs. 2A and 3 distinct regions were protected from DNase I digestion: +55 bp to −4 bp containing the putative TFCP2 motif, −10 to −25 bp containing the putative CCAAT box, and −28 to −41 bp containing the putative GC box. Next, we performed a gel shift assay using double stranded oligonucleotide containing two motifs in the protected regions, a GC box (oligo_GC, −41/−32) and a CCAAT box (oligo_CCAAT, −25/−10). We also performed a gel shift assay using the oligonucleotide containing a putative CHR (oligo_CHR, −110/−104) which is well conserved among mammalian CKAP2 genes. As shown in Fig. 2B–D, all 3 oligonucleotides were retarded when incubated with HeLa nuclear extracts (Fig. 2, black arrows). However, retarded oligo_CCAAT was disappeared when either specific or nonspecific competitor was added, which indicated nonspecific binding (Fig. 2D). On the other hand, either retarded oligo_GC (Fig. 2B) or retarded oligo_CHR (Fig. 2C) was unaffected by non-specific competitors but disappeared dose-dependently with each specific competitor. Moreover, the supershift assay using anti-Sp1 antibody showed an up-shifted band (Fig. 2B, lane 3, white arrow head), which disappeared dose-dependently by a specific competitor (Fig. 2B, lanes 4 and 5) but was not affected with a nonspecific competitor (Fig. 2B, lanes 6 and 7). Finally, we performed a ChIP assay to make sure Sp1 bound to the GC box in the human CKAP2 promoter in vivo. As shown in Fig. 2E, DNA fragments were detected in the immunoprecipitate with Sp1 antibody, but not with control IgG. Taken together, we concluded that the GC box, the CHR, but not the CCAAT box, served as a transcription factor binding sites in the minimal promoter of human CKAP2.

3.3. Sp1 is essential for cyclic expression of human CKAP2

To elucidate the functional importance of the GC box and the CHR, we made 4 site-directed mutants; $US^{\Delta GC}$ where the GC box was destroyed, $US^{\Delta CHR}$ where CHR was destroyed, $US^{\Delta GC\Delta CHR}$ where both the GC box and CHR were destroyed, and $US^{\Delta NFY}$, a nonspecific control where the NF-Y binding sequence was destroyed. As shown in Fig. 3A, the promoter activity of $US^{\Delta GC}$ was only 20% of that of US^{-309} or $US^{\Delta NFY}$. $US^{\Delta CHR}$ also showed decreased promoter activity but still retained >50% of US^{-309} or $US^{\Delta NFY}$ activity. $US^{\Delta GC\Delta CHR}$ showed promoter activity similar to that of $US^{\Delta GC}$, which indicated the GC box and the CHR did not work synergistically.

Our next question was whether either the GC box or the CHR was responsible for the cyclic expression of CKAP2. We measured the promoter activities of the mutants at the G1/S phase or at the G2/M phase. We performed a single thymidine block 4 h after transfection to ensure HeLa cells were arrested at the G1/S phase of the first cell cycle after transfection. For the G2/M phase, HeLa cells were treated for 16 h with nocodazole 4 h after transfection in order to minimize the influence of the promoter activity during the G1/S phase. As shown in Fig. 3B, US^{-309} showed much higher activity at the G2/M

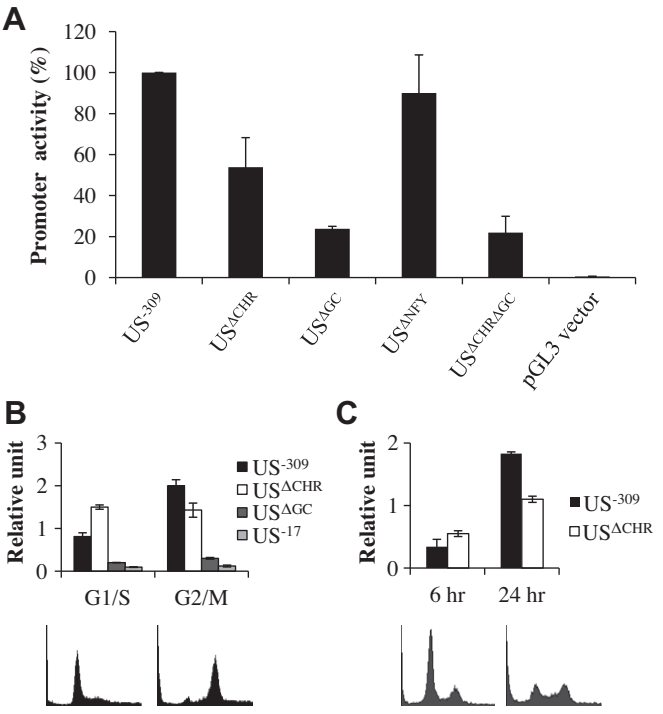


Fig. 3. Sp1 plays a crucial role in human CKAP2 transcription. (A) The GC box and the CHR were mutated using wild-type construct (US^{-309}) as a PCR template. $US^{\Delta GC}$ and $US^{\Delta CHR}$ retained 20% or about 50% of promoter activity of US^{-309}, respectively while the construct containing mutant CCAAT ($US^{\Delta NFY}$) was unaffected. (B) Promoter activities of mutant constructs were measured in HeLa cells arrested at G1/S by thymidine block or G2/M by nocodazole. (C) Promoter activities of mutant constructs were measured at the designated time points in HeLa cells released from G1/S arrest induced by thymidine block. The promoter activities of both US^{-309} and $US^{\Delta CHR}$ kept increased along with G2/M progression.

phase reflecting its cyclic activity. The promoter activities of US^{-17} and $US^{\Delta GC}$ were almost undetectable throughout the cell cycle, which showed again the GC box was essential for the promoter activity. Interestingly, $US^{\Delta CHR}$ showed almost a 2-fold higher activity than that of US^{-309} at the G1/S phase, which suggested the repression through the CHR. We chased the promoter activity of $US^{\Delta CHR}$ during the cell cycle because the role of the CHR in the cyclic expression was unclear. Most HeLa cells were at the G1/S phase 6 h after releasing from nocodazole arrest, and ~50% of HeLa cells entered the G2/M phase 24 h after being released from nocodazole arrest (see FACS profile in Fig. 3C). The promoter activity of $US^{\Delta CHR}$ was increased ~1.8-fold from 6 h to 24 h after released from nocodazole arrest while the US^{-309} was increased >4-fold from 6 h to 24 h after released from nocodazole arrest. Taken together, we concluded that the GC box was essential for CKAP2 minimal promoter activity and CHR might be responsible for the repression of CKAP2 during the G1/S phase.

3.4. Cyclin A regulates Sp1-binding to human CKAP2 promoter and thereby inducing periodic expression during cell cycle

Because mutation of the GC box almost totally abolished promoter activity, it was hard to tell whether the GC box was responsible for the cyclic activity. We investigated the temporal profile of Sp1 binding to the GC box in HeLa cells released from nocodazole-induced G2/M arrest status. As shown in Fig. 4A, most HeLa cells were at the G1/S phase at 12 h, at the G2/M phase between 18 h and 22 h, and had completed one cell cycle at 24 h after release. The amount of Sp1 bound to the GC box, measured by Chip assay, was gradually increased from 12 h to 22 h after release and decreased thereafter (Fig. 4A). CKAP2 transcription was also fluctuating accordingly in the same cells where we measured the Sp1

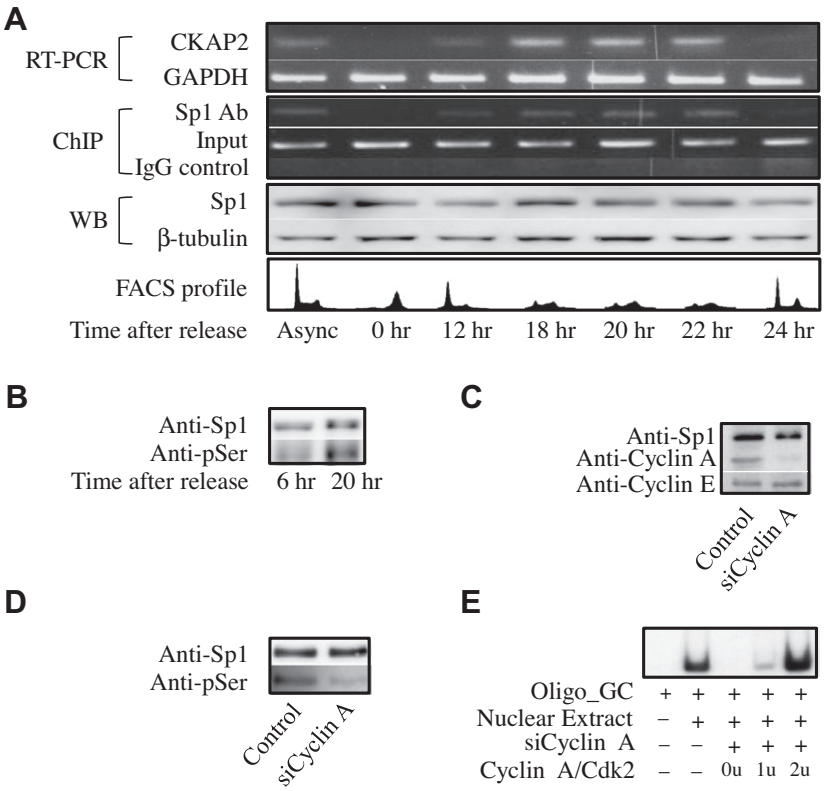


Fig. 4. Cyclin A regulates Sp1-binding to human CKAP2 promoter and cell-cycle-dependent expression of human CKAP2. (A) The human CKAP2 mRNA level, immunoprecipitated chromatin by Sp1 antibody, the amount of Sp1, and the FACS profile were monitored in HeLa cells released from nocodazole arrest. All measurements were performed using the same cell populations at the designated releasing time. (B) Sp1 was immunoprecipitated and probed with anti-phosphoserine antibody from HeLa cells at 6 h or 20 h after released from nocodazole arrest. (C) Cyclin A was greatly knock-downed in HeLa cells transfected with siRNAs targeting Cyclin A1 and Cyclin A2 (siCyclin A). (D) Sp1 was immunoprecipitated and probed with anti-phosphoserine antibody from HeLa cells transfected with siCyclin A. (E) EMSA was performed using the Cyclin A-depleted HeLa nuclear extracts in the absence (lane 3) or in the presence (lanes 4 and 5) of Cyclin A/Cdk2 complex.

amount. The amount of Sp1 was not changed significantly throughout the cell cycle. Taken together, we concluded the temporal change of GC box-binding affinity of Sp1 was responsible for the cyclic expression of human CKAP2.

Since Sp1 amount itself was not changed during cell cycle and cyclin A-CDK complex has been reported to phosphorylate Sp1 [6], we explored whether the phosphorylation status of Sp1 was changed during cell cycle progression in HeLa cells released from nocodazole arrest. As shown in Fig. 4B, serine-phosphorylation of Sp1 was increased at 20 h after release from nocodazole arrest. Next we prepared Cyclin A-depleted nuclear extracts by transfecting siRNA mixture targeting Cyclin A1 and Cyclin A2 in order to check whether Cyclin A might be responsible for the phosphorylation of Sp1. As shown in Fig. 4C, Cyclin A was efficiently knock-downed while Cyclin E, another mitotic cyclin, was unaffected upon Cyclin A-targeting siRNA treatment. Depletion of Cyclin A greatly reduced Sp1 phosphorylation (Fig. 4D) and almost completely abolished Sp1-DNA binding (Fig. 4E lane 3). When we added active Cyclin A/Cdk2 complex back to the Cyclin A-depleted nuclear extracts, the Sp1-DNA binding was completely restored to the control level (Fig. 4E lanes 4 and 5).

Taken together, we concluded that Sp1 is a major regulator of periodic expression of CKAP2, and cell-cycle-dependent phosphorylation of Sp1 mediated by Cyclin A can regulate the DNA-binding affinity of Sp1.

4. Discussion

In this study, we identified the GC box and CHR element as the essential *cis*-acting elements for the cyclic expression of human CKAP2. These *cis*-acting elements were also well conserved among other mammalian CKAP2 genes and frequently found in promoters of the G2/M clustered genes. Disruption of GC box almost completely blocked the promoter activity, indicating that Sp1 was the major transcriptional activator. We postulated that the binding affinity of Sp1 to would be changed during cell cycle, if Sp1 regulated the cyclic expression. We examined the amount of the immunoprecipitated chromatin by anti-Sp1 antibody which was gradually increased along with the cell cycle progression (Fig. 4A). The peak of Sp1 bound to CKAP2 promoter was observed at 20 h after release from nocodazole arrest, which corresponded to the G2/M phase according to a FACS profile of the same cell population (Fig. 4A). We also found that serine phosphorylation of Sp1 was increased at 20 h after release from nocodazole (Fig. 4B). These data indicated that the DNA-binding affinity of Sp1 was changed during cell cycle progression, possibly by phosphorylation.

CyclinA/Cdk2 induces the cyclic transcriptional activity of Sp1 acting through phosphorylation of the Ser59 [6,22]. When we inhibited Cdks using Roscovitine at the concentration of in order to check the possible involvement of Cyclin A/Cdk2, both Sp1 phosphorylation and Sp1-DNA binding were greatly reduced (data not shown). Although we used the concentration of Roscovitine at which other cell cycle regulatory kinases such as Plk and Aurora kinases were barely inhibited [23], we could not eliminate the possible involvement of other kinases including ERK, MEK, which retained a half of their activities at 1 μM of Roscovitine [23]. To further clarify the role of Cyclin A in Sp1 phosphorylation, we prepared HeLa cell nuclear extracts depleted in Cyclin A using siRNAs. Cyclin A depletion reduced Sp1 phosphorylation greatly and also abolished Sp1-DNA binding near completely. Such Cylcin A depletion effects were completely restored by active Cyclin A/Cdk2 complex (Fig. 4C–E). These results strongly supported that

Cyclin A and possibly Cdks were responsible for Sp1 phosphorylation and subsequent cyclic expression of human CKAP2.

The CHR has been reported to be a regulator for cell-cycle-dependent expression of G2/M clustered genes in concert with CDE. G2/M clustered genes such as cdc25C, cyclin A, and cyclin B2 are repressed at the G0/G1 phase by occupied CDE/CHR. Typical CDE/CHR containing promoters usually lack a TATA box and have a CDE 4-base upstream to a CHR. The CKAP2 minimal promoter also lacks a TATA box and has a single CHR sequence without CDE. The CKAP2 promoter with a mutated CHR still showed periodic activity (see Fig. 3) but almost 2-fold higher activity at the G1/S phase, which suggests that the CHR alone might repress the promoter activity of CKAP2. Promoters regulated by a single CHR element have also been reported. Mouse Cdc25C promoter without functional CDE are repressed by a single CHR element and derepressed at the S or G2/M phase by NF-Y [9,24]. Unlike mouse Cdc25C, the GC box was located downstream to the CHR element, and no E2F site was found in CKAP2. Because the CKAP2 promoter lacks a CCAAT motif, derepression by NF-Y cannot occur. How the activity of a CKAP2 minimal promoter is enhanced in a CHR mutant remains to be elucidated.

In this report, we showed that the GC box and the CHR are necessary for the proper cyclic expression of CKAP2. The CHR might repress promoter activity at the G1/S phase, similar to other CDE/CHR. Sp1 is in charge of not only transcription of CKAP2, but also cell-cycle-dependent expression of CKAP2 through phosphorylation-dependent DNA-binding affinity changes of Sp1. We also showed Cyclin A was responsible for the cell-cycle-dependent Ser-phosphorylation of Sp1 and concluded Cyclin A was the master regulator of the cyclic expression of the CKAP2.

Acknowledgments

This research was supported by a Grant (07203703) from the National R&D Program for Cancer Control, Ministry of Health and Welfare, Republic of Korea.

References

[1] M.L. Whitfield, G. Sherlock, A.J. Saldanha, et al., Identification of genes periodically expressed in the human cell cycle and their expression in tumors, Mol. Biol. Cell 13 (2002) 1977–2000.
[2] S.P. Jackson, J.J. MacDonald, S. Lees-Miller, R. Tjian, GC box binding induces phosphorylation of Sp1 by a DNA-dependent protein kinase, Cell 63 (1990) 155–165.
[3] R. Muller, Transcriptional regulation during the mammalian cell cycle, Trends Genet. 11 (1995) 173–178.
[4] R.J. Cho, M.J. Campbell, E.A. Winzeler, et al., A genome-wide transcriptional analysis of the mitotic cell cycle, Mol. Cell. 2 (1998) 65–73.
[5] J.A. Lee, D.C. Suh, J.E. Kang, et al., Transcriptional activity of Sp1 is regulated by molecular interactions between the zinc finger DNA binding domain and the inhibitory domain with corepressors, and this interaction is modulated by MEK, J. Biol. Chem. 280 (2005) 28061–28071.
[6] P. Fojas de Borja, N.K. Collins, P. Du, et al., Cyclin A-CDK phosphorylates Sp1 and enhances Sp1-mediated transcription, EMBO J. 20 (2001) 5737–5747.
[7] J. Zwicker, F.C. Lucibello, L.A. Wolfraim, et al., Cell cycle regulation of the cyclin A, cdc25C and cdc2 genes is based on a common mechanism of transcriptional repression, EMBO J. 14 (1995) 4514–4522.
[8] K.S. Katula, A. Fields, P. Apple, T. Rotruck, Cell cycle specific changes in the human cyclin B1 gene regulatory region as revealed by response to trichostatin A, Arch. Biochem. Biophys. 401 (2002) 271–276.
[9] U. Haugwitz, M. Wasner, M. Wiedmann, et al., A single cell cycle genes homology region (CHR) controls cell cycle-dependent transcription of the cdc25C phosphatase gene and is able to cooperate with E2F or Sp1/3 sites, Nucleic Acids Res. 30 (2002) 1967–1976.
[10] H.D. Chae, J. Kim, D.Y. Shin, NF-Y binds to both G1- and G2-specific cyclin promoters; a possible role in linking CDK2/Cyclin A to CDK1/Cyclin B, BMB Rep. 44 (2011) 553–557.
[11] J. Yun, H.D. Chae, T.S. Choi, et al., Cdk2-dependent phosphorylation of the NF-Y transcription factor and its involvement in the p53–p21 signaling pathway, J. Biol. Chem. 278 (2003) 36966–39672.
[12] W. Zhu, P.H. Giangrande, J.R. Nevins, E2Fs link the control of G1/S and G2/M transcription, EMBO J. 23 (2004) 4615–4626.
[13] T. Uchiumi, D.L. Longo, D.K. Ferris, Cell cycle regulation of the human polo-like kinase (PLK) promoter, J. Biol. Chem. 272 (1997) 9166–9174.
[14] M. Tanaka, A. Ueda, H. Kanamori, et al., Cell-cycle-dependent regulation of human aurora A transcription is mediated by periodic repression of E4TF1, J. Biol. Chem. 277 (2002) 10719–10726.
[15] M. Kimura, C. Uchida, Y. Takano, et al., Cell cycle-dependent regulation of the human aurora B promoter, Biochem. Biophys. Res. Commun. 316 (2004) 930–936.
[16] F. Schmit, S. Cremer, S. Gaubatz, LIN54 is an essential core subunit of the DREAM/LINC complex that binds to the cdc2 promoter in a sequence-specific manner, FEBS J. 276 (2009) 5703–5716.
[17] S.M. Jeon, B. Choi, K.U. Hong, et al., A cytoskeleton-associated protein, CKAP2, is involved in the proliferation of human foreskin fibroblasts, Biochem. Biophys. Res. Commun. 348 (2006) 222–228.
[18] K.U. Hong, Y.S. Park, Y.S. Seong, et al., Functional importance of the anaphase-promoting complex-Cdh1-mediated degradation of CKAP2 in regulation of spindle function and cytokinesis, Mol. Cell. Biol. 27 (2007) 3667–3681.
[19] C.D. Bae, Y.S. Sung, S.M. Jeon, et al., Up-regulation of cytoskeletal-associated protein 2 in primary human gastric adenocarcinomas, J. Cancer Res. Clin. Oncol. 129 (2003) 621–630.
[20] L. Maouche-Chretien, N. Deleu, C. Badoual, et al., Identification of a novel cDNA, encoding a cytoskeletal associated protein, differentially expressed in diffuse large B cell lymphomas, Oncogene 17 (1998) 1245–1251.
[21] H.S. Kim, Y.B. Choi, J.H. Lee, et al., Condensed chromatin staining of CKAP2 as surrogate marker for mitotic figures, J. Cancer Res. Clin. Oncol. 138 (2011) 95–102.
[22] E. Haidweger, M. Novy, H. Rotheneder, Modulation of Sp1 activity by a cyclin A/CDK complex, J. Mol. Biol. 306 (2001) 201–212.
[23] S. Bach, M. Knockaert, J. Reinhardt, et al., Roscovitine targets, protein kinases and pyridoxal kinase, J. Biol. Chem. 280 (2005) 31208–31219.
[24] M. Wasner, U. Haugwitz, W. Reinhard, et al., Three CCAAT-boxes and a single cell cycle genes homology region (CHR) are the major regulating sites for transcription from the human cyclin B2 promoter, Gene 312 (2003) 225–237.

Biochemical and Biophysical Research Communications 420 (2012) 828–833

Contents lists available at SciVerse ScienceDirect

Biochemical and Biophysical Research Communications

journal homepage: www.elsevier.com/locate/ybbrc

Divergent effects of 17-β-estradiol on human vascular smooth muscle and endothelial cell function diminishes TNF-α-induced neointima formation

Rungrat Nintasen [a,b,c], Kirsten Riches [a,b], Romana S. Mughal [a,b], Parnpen Viriyavejakul [c], Urai Chaisri [c], Yaowapa Maneerat [c], Neil A. Turner [a,b], Karen E. Porter [a,b,*]

[a] Division of Cardiovascular Medicine, Leeds Institute of Genetics, Health and Therapeutics, University of Leeds, Leeds LS2 9JT, UK
[b] Multidisciplinary Cardiovascular Research Center (MCRC), University of Leeds, Leeds LS2 9JT, UK
[c] Department of Tropical Pathology, Faculty of Tropical Medicine, Mahidol University, Thailand

ARTICLE INFO

Article history:
Received 20 February 2012
Available online 23 March 2012

Keywords:
Human
Neointima
Smooth muscle cell
Endothelial cell
TNF-α
17-β-estradiol

ABSTRACT

Coronary heart disease (CHD) is a condition characterized by increased levels of proinflammatory cytokines, including tumor necrosis factor-α (TNF-α). TNF-α can induce vascular endothelial cell (EC) and smooth muscle cell (SMC) dysfunction, central events in development of neointimal lesions. The reduced incidence of CHD in young women is believed to be due to the protective effects of estradiol (E2). We therefore investigated the effects of TNF-α on human neointima formation and SMC/EC functions and any modulatory effects of E2.

Saphenous vein (SV) segments were cultured in the presence of TNF-α (10 ng/ml), E2 (2.5 nM) or both in combination.

Neointimal thickening was augmented by incubation with TNF-α, an effect that was abolished by co-culture with E2. TNF-α increased SV–SMC proliferation in a concentration-dependent manner that was optimal at 10 ng/ml (1.5-fold increase), and abolished by E2 at all concentrations studied (1–50 nM). Surprisingly, E2 itself at low concentrations (1 and 5 nM) stimulated SV–SMC proliferation to a level comparable to that of TNF-α alone. SV–EC migration was significantly impaired by TNF-α (42% of control), and co-culture with E2 partially restored the ability of SV–EC to migrate and repair the wound. In contrast, TNF-α increased SV–SMC migration by 1.7-fold, an effect that was completely reversed by co-incubation with E2. Finally, TNF-α potently induced ICAM-1 and VCAM-1 expression in both SV–EC and SV–SMC. However there was no modulation by E2 in either cell-type.

In conclusion, TNF-α induced SV neointima formation, increased SMC proliferation and migration, impaired SV–EC migration and increased expression of adhesion molecules. E2 exerted distinct cell-type and function-specific modulation, the mechanisms underlying which are worthy of further detailed study.

© 2012 Elsevier Inc. All rights reserved.

1. Introduction

Vascular pathologies such as atherosclerosis, restenosis and vein bypass graft occlusion are characterized by endothelial cell (EC) dysfunction and an increase in proliferation and migration of smooth muscle cells (SMC) within vessel walls [1]. Dysfunction of the cellular components of the vasculature occurs as a complex response to environmental stimuli in which EC and SMC play key roles. Damage to EC by physical (e.g. hemodynamic forces [2]) or inflammatory stimuli (e.g. the proinflammatory cytokine tumor necrosis factor-α (TNF-α) [3]), provokes EC dysfunction which in turn promotes critical features of vascular inflammation [4]. TNF-α, acting via its cell surface receptors TNFRI and TNFRII, can influence a variety of cellular and molecular functions that contribute to chronic inflammatory disease states (reviewed in [5]), for example by inducing expression of endothelial adhesion molecules such as intercellular adhesion molecule-1 (ICAM-1) and vascular cell adhesion molecule-1 (VCAM-1) [6]. Promotion of an inflammatory response in the arterial wall by TNF-α is therefore likely to be a consequence of EC injury initially, and subsequent detrimental effects on underlying SMC, particularly stimulation of proliferation and migration [7,8]. Changes in both these functions are key cellular processes that contribute to neointimal formation, the underlying lesion of many cardiovascular pathologies including atherosclerosis and vein bypass graft failure.

Epidemiological studies suggest that young females are largely protected from coronary heart disease (CHD) compared with males

* Corresponding author at. Division of Cardiovascular Medicine, Leeds Institute of Genetics, Health and Therapeutics, University of Leeds, Leeds LS2 9JT, UK. Fax: +44 113 3434803.
E-mail address: medkep@leeds.ac.uk (K.E. Porter).

0006-291X/$ - see front matter © 2012 Elsevier Inc. All rights reserved.
http://dx.doi.org/10.1016/j.bbrc.2012.03.082

of similar age [9]; a phenomenon that is gradually lost after menopause. The protection of premenopausal women from pathologies such as myocardial infarction and stroke has been attributed to the cardioprotective effects of the hormone estrogen (17-β-estradiol, E2) [9,10]. In animal models of vascular injury, administration of E2 is reported to have vasoprotective effects and can alleviate the development of intimal hyperplasia [11–13]. However, *in vitro* data are contentious; whilst most studies concur that E2 inhibits SMC proliferation and migration [11–14], some claim that E2 augments SMC proliferation [15,16]. The applicability of these variable outcomes to human macrovasculature is not clear, hence the use of clinically relevant tissues and cells to study etiology of cardiovascular disease is important in this regard. The aim of this study was to determine the effect of TNF-α and E2, alone and in combination, on human saphenous vein (SV) neointima formation and EC and SMC function related to this pathology.

2. Materials and methods

2.1. Reagents

Cell culture reagents were purchased from Invitrogen (Paisley, UK). All experiments were carried out in phenol red-free medium, as phenol red itself is known to possess estrogenic properties [17,18]. Fetal bovine serum (FBS) was from LabTech International (Ringmer, East Sussex, UK). 17-β-estradiol (E2) and human recombinant TNF-α were obtained from Sigma–Aldrich (Poole, Dorset, UK). Migration assay chambers were from BD Biosciences (Oxford, UK). ICAM-1 and VCAM-1 antibodies were purchased from Santa Cruz Biotechnology Inc. (Santa Cruz, USA), β-actin antibody from AbCam (Cambridge, UK), and α-smooth muscle actin (α-SMA) antibody from Sigma–Aldrich.

2.2. Human saphenous vein organ culture

SV segments were obtained from patients undergoing coronary bypass grafting at the Leeds General Infirmary. Local ethical committee approval was granted and patients gave informed, written consent. The study was carried out in accordance with the principle of the Declaration of Helsinki as revised in 2000. Organ cultures were performed using undistended SV as we have described previously, in phenol red-free Dulbecco's modified eagle medium (DMEM) supplemented with 30% FBS, 1% L-glutamine and 1% penicillin / streptomycin [19], in the absence or presence of TNF-α (10 ng/ml), E2 (2.5 nM) or in combination, for 14 days. Segments were fixed, processed and sectioned to 6 μm. Neointimal thickness was determined using computational analysis on high field magnification at 100 μm intervals along each section by two independent observers.

2.3. Cell culture

EC were harvested from SV by collagenase digestion and cultured as described previously [20]. SMC were isolated by an explant technique as described previously [21]. All cells were maintained in phenol red-free medium in a humidified atmosphere of 5% CO_2 in air at 37 °C. Experiments were performed on cells of *passage* number 2–6 from different patients.

2.4. Proliferation assays

SV–SMC were seeded at a density of $1x10^4$ cells per well and incubated overnight before being quiesced in serum-free media for 72 h. Cells were then cultured in minimal growth promoting media (2.5% FBS) containing E2 (0–50 nM), TNF-α (0–50 ng/ml) or TNF-α (10 ng/ml) with E2 (2.5 nM) in combination for 4–7 days. Culture medium and treatments were replaced every 2 days and viable cell counts were taken on days 2, 4 and/or 7 using Trypan Blue and a hemocytometer.

2.5. Migration assays

EC migration was investigated using a scratch wound assay as previously described [22]. Confluent monolayers of EC were wounded using a sterile 1 ml pipette tip. Reference points were marked and microscopic images captured at x40 magnification (0 h). Cells were then exposed to control media containing 1% FBS and appropriate stimuli (10 ng/ml TNF-α, 2.5 nM E2 or

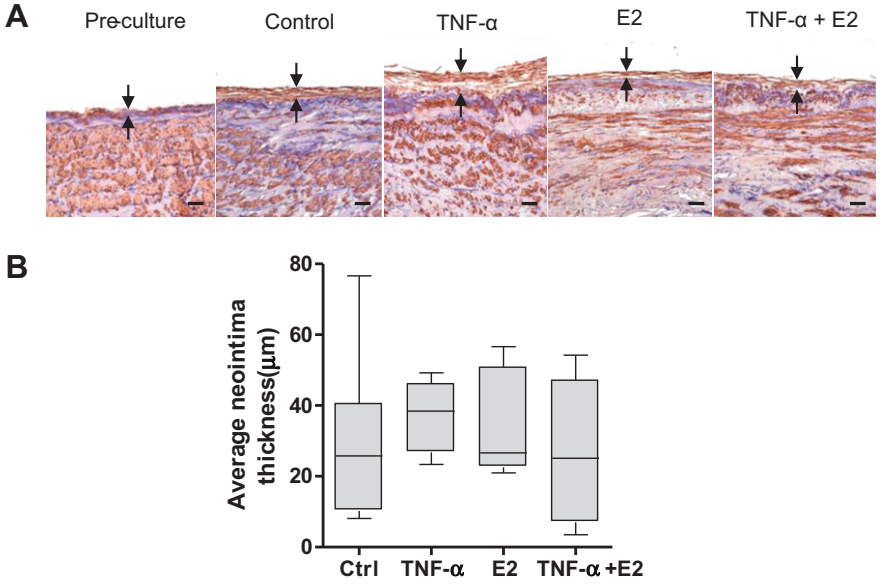


Fig. 1. Effect of TNF-α and E2 on human SV neointima formation. Fragments of SV were cultured for 14 days in media containing 30% FBS (control) before fixing and staining with α-SMA antibody and Miller's elastic stain. (A) Representative images of transverse sections, scale bar = 50 μm. Arrows define neointima. (B) Box and whisker plot of average neointima thickness of full length sections in response to TNF-α (10 ng/ml), E2 (2.5 nM) and both in combination. Box defines 25^{th}–75^{th} interquartile range, whiskers depict full range, and horizontal line is median ($n = 9$).

TNF-α + E2) for an additional 48 h. Further images were captured by aligning the dishes with the reference point identified at time 0 h. The number of cells migrated to or beyond a fixed distance 200 μm from the wound edge was counted.

SMC migration was performed using modified Boyden chambers [21]. Cells were quiesced for 72 h in medium containing 0.5% FBS prior to loading into the upper chamber at a density $1x10^5$ in control media (DMEM containing 0.5% FBS). The lower chamber was supplemented with or without TNF-α (10 ng/ml), E2 (2.5 nM) or both in combination. Following 6 h incubation at 37 °C, duplicate membranes were fixed, stained with hematoxylin and eosin and evaluated by counting cell nuclei on the underside of the membrane in 10 random fields under high power (x400) light microscopy [21].

2.6. Western blotting

Confluent EC and SMC were quiesced for 72 h and treated with 0.5% FBS (control) or supplemented with TNF-α (10 ng/ml), E2 (2.5 nM) alone and in combination for the indicated times before preparing whole cell homogenates and immunoblotting for ICAM-1, VCAM-1 and β-actin as described previously [23]. Densitometric analysis was performed using MagiScan and ImageQuant software (Amersham Biosciences).

2.7. Statistical analysis

Neointima data are expressed as median and range. All other data are expressed as mean ± SEM with *n* representing the number of different patients. Data were analyzed using one-way ANOVA with Newman–Keuls Multiple post–hoc test using GraphPad Prism software (www.graphpad.com). $P < 0.05$ was considered statistically significant.

3. Results

3.1. E2 abolishes TNF-α-induced neointimal thickening in human saphenous vein

The effects of TNF-α and E2 on neointimal formation were investigated using organ-cultured SV segments from 9 different patients (Fig. 1). After 14 days in culture, control vein segments developed a neointima comprising several layers of SMC beneath the luminal endothelium (Fig. 1A). Median neointimal thickness in control segments was 25.8 μm (Fig. 1B). This was increased in the presence of TNF-α to 38.4 μm. Median neointimal thickness in the presence of E2 alone was similar to control (26.7 μm). When segments were cultured with TNF-α and E2 in combination, E2 attenuated the increase in TNF-α-induced neointimal thickness

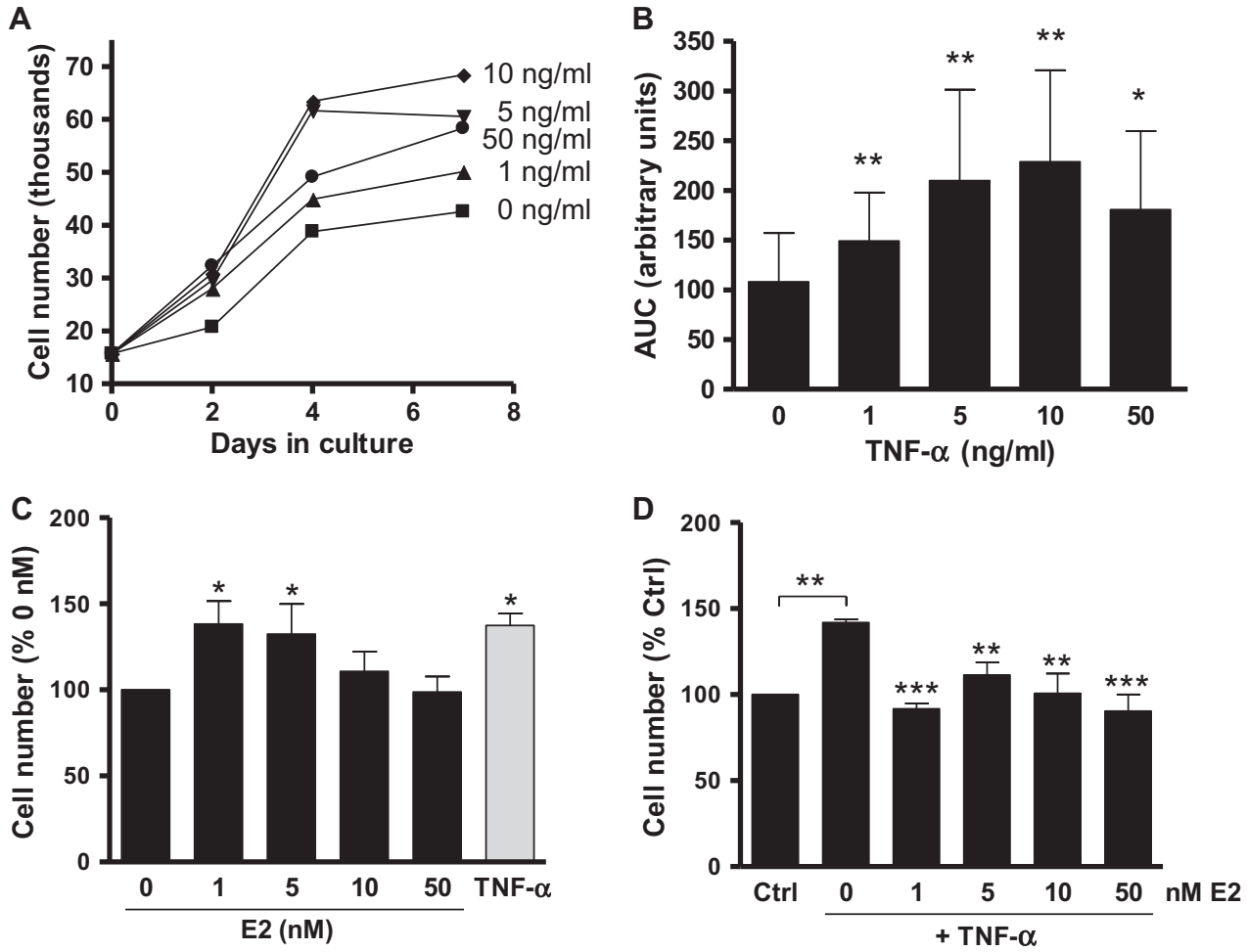


Fig. 2. Effect of TNF-α and E2 on human SV–SMC proliferation. Cells were seeded at a density of 10,000 per ml, quiesced for 72 h and then cultured for the specified time points before cell counts were taken. (A) SV–SMC were cultured with increasing concentrations of TNF-α (1–50 ng/ml) for 7 days with cells counted on days 2, 4 and 7 ($n = 3$). (B) Areas under the curves (AUC) were calculated from A ($n = 3$, $^{**}P < 0.01$, $^{*}P < 0.05$ vs. 0 ng/ml). (C) SV–SMC were treated with increasing concentrations of E2 (1–50 nM) alone for 4 days ($n = 5$, $^{*}P < 0.05$ vs. 0 nM). (D) SV–SMC were cultured with TNF-α (10 ng/ml) and increasing concentrations of E2 (1–50 nM) for 4 days ($n = 5$, $^{***}P < 0.001$, $^{**}P < 0.01$ vs. 0 nM).

resulting in a median thickness comparable to control segments (25.1 μm) (Fig. 1B).

3.2. Effects of E2 on SV-SMC proliferation

SV–SMC were cultured for up to 7 days in minimal growth promoting medium (2.5% FBS) containing 1–50 ng/ml TNF-α and growth curves constructed (Fig. 2A). TNF-α significantly induced SMC proliferation in a concentration-dependent manner with maximal stimulation observed in response to 10 ng/ml (Fig. 2A and B). All subsequent experiments were conducted over a 4-day interval.

In response to low concentrations of E2 alone (1–5 nM), an increase in SMC proliferation was observed that was equivalent to that of 10 ng/ml TNF-α alone (Fig. 2C). This mitogenic effect of E2 was not apparent at higher concentrations ($\geqslant$10 nM) (Fig. 2C). However, when E2 was added together with TNF-α, the TNF-α-induced proliferation was abolished at all concentrations of E2 (1–50 nM) (Fig. 2D).

3.3. E2 attenuates TNF-α-induced effects on SV–EC and SV–SMC migration

In the scratch wound migration assay, SV–EC migrate to repopulate the denuded area, as demonstrated in Fig. 3B. TNF-α significantly impaired EC migration by 60% compared to control. Co-culture with TNF-α and E2 significantly increased the ability of EC to migrate and repair the wound, compared to TNF-α alone (Fig. 3A).

SV–SMC migration was analyzed using a Boyden chamber technique. A representative high power field of cells migrating to the underside of the membrane under each incubation condition is shown in Fig. 3D. TNF-α significantly increased SV–SMC migration by 1.7-fold (Fig. 3C). E2 alone did not affect basal cell migration, but it fully prevented the increase in migration observed with TNF-α (Fig. 3C).

3.4. E2 does not modulate TNF-α-induced VCAM-1 and ICAM-1 expression in EC or SMC

TNF-α induced marked expression of ICAM-1 and VCAM-1 in both SV–EC (Fig. 4A and B) and SV–SMC (Fig. 4C and D) over 6 h. Expression was not modulated by co-incubation with E2 in SV–EC (Fig. 4A and B), or SV–SMC (Fig. 4C and D).

4. Discussion

TNF-α has been implicated in the pathogenesis of atherosclerosis [8], in response to arterial injury [24] and in vein graft stenosis [7] in animal models. Its role in human vascular pathology is also well documented (reviewed recently in [5]), but the mechanisms involved are unclear. Here, we observed a clear trend towards increased human SV neointimal formation with TNF-α, and this was ameliorated by co-incubation with E2. These activated "synthetic" SMC can migrate and proliferate from the media to the intima leading to neointimal hyperplasia [19], a condition that can be augmented by proinflammatory cytokines, including TNF-α [25]. E2 reduces neointimal formation after vascular injury in animal models [12,13,26,27]. Ours is the first study to investigate the effects of E2 on neointimal formation in clinically relevant human tissue, and concurs with these animal studies.

In vitro cell cultures were established to demonstrate the separate cellular processes involved in neointimal formation including SMC proliferation and migration, and EC migration. Our results demonstrated that TNF-α stimulated SV–SMC proliferation and migration and importantly, co-incubation with E2 abolished both of these effects. SMC express predominantly ERα compared with ERβ [26,28,29] and further, Nakamura et al. reported that the SMC growth-inhibiting effect of E2 was mediated specifically via the estrogen receptor-alpha (ERα) subtype [30]. It is likely therefore that the effect of E2 on TNF-α-induced SV–SMC proliferation that we observed was mediated via ERα. Whilst the majority of

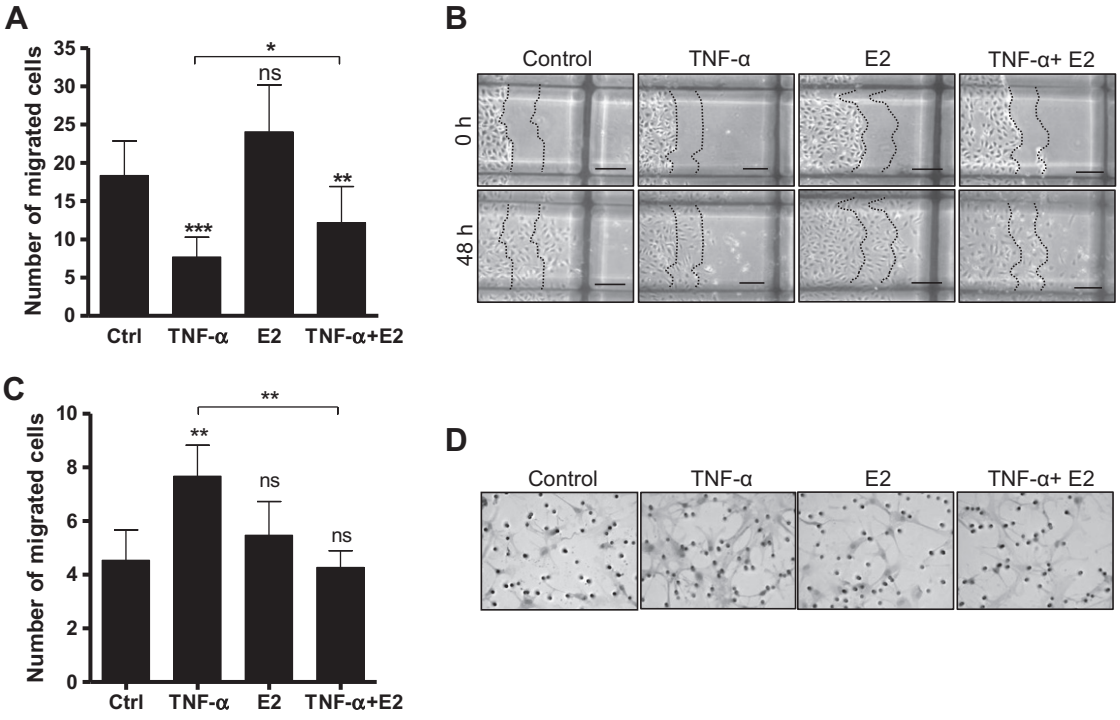


Fig. 3. Effect of TNF-α and E2 on SV–EC and SV–SMC migration. (A) Confluent SV–EC monolayers were wounded and imaged. The migratory response to TNF-α (10 ng/ml), E2 (2.5 nM) and both in combination was quantified by counting the number of cells that had migrated more than 200 μm from the wound edge (dotted line) per mm wound width within a 48 h period (n = 7, $^{***}P < 0.001$, $^{**}P < 0.01$, ns = non-significant vs. Ctrl). (B) Representative images from EC scratch wound assay. Scale bar = 200 μm. (C) SV–SMC migration was analyzed using modified Boyden chambers (n = 5, $^{**}P < 0.01$, ns = non-significant vs. Ctrl). (D) Representative images from SMC migration assays.

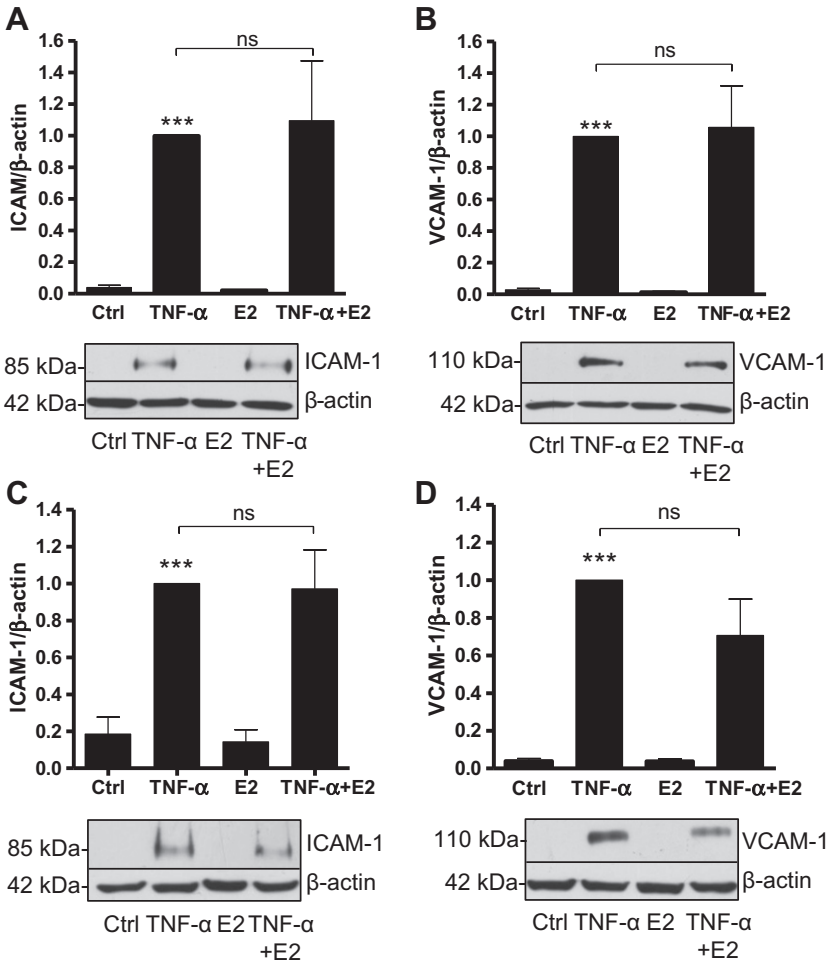


Fig. 4. Effect of TNF-α and E2 on ICAM-1 and VCAM-1 expression in human SV–EC and SV–SMC. Confluent cells were treated with TNF-α (10 ng/ml), E2 (2.5 nM) and both in combination for 6 h before whole cell homogenates were prepared and blotted for ICAM-1, VCAM-1 and β-actin as a loading control. (A) Densitometry and representative image for ICAM-1 and (B) VCAM-1 in SV–EC (both $n = 4$, $^{***}P < 0.001$ vs. Ctrl, ns = non-significant). (C) Densitometry and representative image for ICAM-1 and (D) VCAM-1 in SV–SMC (both $n = 6$, $^{***}P < 0.001$ vs. Ctrl, ns = non-significant).

studies concur that E2-mediated effects on SMC are ER-dependent, it has been reported that inhibition of inflammatory responses in rat aortic SMC is an ERβ-mediated event [31]. However, consistent with the majority of studies, we observed ERα, but no evidence of ERβ expression in SV–SMC (data not shown).

Unexpectedly, E2 itself at low concentrations of 1–5 nM (~280–1400 pg/ml) significantly stimulated SV–SMC proliferation to a level comparable with that observed with TNF-α alone. These data are compatible with a clinical study reporting that the use of hormone replacement therapy may be harmful. Normally, in premenopausal women E2 levels range from 10 to 80 pg/ml during the follicular phase and reach a level of 600 pg/ml at midcycle, but after menopause the concentration of E2 falls to 5–30 pg/ml [10]. Interestingly, a recent study reported dual effects of E2 on vascular SMC; observing increased proliferation at low concentrations (10 nM), gradually reversing to a concentration-dependent inhibitory action at concentrations up to 10 μM [16]. Although the growth stimulatory effect was compatible with our own data (we used 1–5 nM E2), we saw no effect of E2 alone above these concentrations, instead E2 specifically *inhibited* TNF-α-induced proliferation. It appears therefore that the mechanism(s) underlying the effect of E2 on SMC proliferation is complex and more detailed studies are needed.

At the level of the EC, TNF-α impaired migration, and co-incubation of TNF-α-treated EC with E2 partly restored the observed anti-migratory effect. These data suggest that re-endothelialisation of injured vessels may be augmented by E2 through improved EC migration, in agreement with a study performed in HUVEC [32]. Whether higher concentrations of E2 may be capable of fully reversing the effect of TNF-α is unknown and further study is necessary.

Using Western blot analysis, TNF-α robustly induced ICAM-1 and VCAM-1 expression within 6 h in EC and SMC, but unpredictably E2 was without any modulatory effects. Adhesion molecule expression has been well characterized in EC and SMC and is induced in response to inflammatory cytokines (reviewed in [33]). VCAM-1 and ICAM-1 play pivotal roles in adhesion of inflammatory cells at the luminal surface of damaged vascular walls, being expressed at sites that are prone to developing atherosclerotic lesions [34,35]. Both are induced by cytokine (including TNF-α) stimulation in human SV [36] and also in isolated SV-SMC [37,38]. A critical role for ICAM-1 in vein graft neointima formation is supported by a study showing that in SMC from ICAM-1 knockout mice, inflammatory cell adhesion was attenuated and accompanied by ~50% reduction in neointima formation [39]. Our data suggest that any potential beneficial effects of E2 in vascular wall cells are not at the level of VCAM-1 and ICAM-1 expression, at least under our *in vitro* conditions.

In conclusion, TNF-α induced neointimal formation, increased SV–SMC proliferation and migration, impaired SV–EC migration and induced adhesion molecule expression in EC and SMC, all of which are key events in the development of vascular lesions. Some

effects, but not all were attenuated by co-incubation with E2. The reduced incidence of CHD in premenopausal women compared with men of a similar age is beyond question. Experimental data have shown beneficial vascular effects of estrogen therapy, yet have mostly failed to translate into improved vascular protection with hormone replacement therapy (reviewed in [40]). Clinical studies have revealed concerns relating to the vascular effects of estrogen that are difficult to address in human subjects *in vivo*. Our data in clinically relevant human tissue and cells reveal particular cell-type and functional effects of E2, the underlying mechanisms of which are worthy of further study. In the long-term this may reveal pathways that are potentially exploitable to provide improved translational benefits of hormonal therapy.

5. Role of the funding source

This work was supported financially by Royal Golden Jubilee Scholarship, Thailand Research Fund through the Royal Golden Jubilee Ph.D. Program and Faculty of Tropical Medicine, Mahidol University, Thailand. The funding sources were not involved in study design; in the collection, analysis, and interpretation of data; in the writing of the report; or the decision to submit the paper for publication.

Acknowledgments

We are grateful to Philip Warburton and Jean Kaye for excellent technical assistance.

References

[1] A. Rudijanto, The role of vascular smooth muscle cells on the pathogenesis of atherosclerosis, Acta Med. Indones. 39 (2007) 86–93.
[2] J.J. Chiu, S. Chien, Effects of disturbed flow on vascular endothelium: pathophysiological basis and clinical perspectives, Physiol Rev. 91 (2011) 327–387.
[3] D.S. Van, G. McColl, I.P. Wicks, Accelerated atherosclerosis: an extraarticular feature of rheumatoid arthritis?, Arthritis Rheum 46 (2002) 862–873.
[4] J.S. Pober, W. Min, Endothelial dysfunction cell injury and death, Handb. Exp. Pharmacol. (2006) 135–156.
[5] G.E. McKellar, D.W. McCarey, N. Sattar, I.B. McInnes, Role for TNF in atherosclerosis? Lessons from autoimmune disease, Nat. Rev. Cardiol. 6 (2009) 410–417.
[6] L.A. Madge, J.S. Pober, TNF signaling in vascular endothelial cells, Exp. Mol. Pathol. 70 (2001) 317–325.
[7] L. Zhang, K. Peppel, L. Brian, L. Chien, N.J. Freedman, Vein graft neointimal hyperplasia is exacerbated by tumor necrosis factor receptor-1 signaling in graft-intrinsic cells, Arterioscler. Thromb. Vasc. Biol. 24 (2004) 2277–2283.
[8] L. Zhang, K. Peppel, P. Sivashanmugam, E.S. Orman, L. Brian, S.T. Exum, N.J. Freedman, Expression of tumor necrosis factor receptor-1 in arterial wall cells promotes atherosclerosis, Arterioscler. Thromb. Vasc. Biol. 27 (2007) 1087–1094.
[9] J.M. Sullivan, L.P. Fowlkes, The clinical aspects of estrogen and the cardiovascular system, Obstet. Gynecol. 87 (1996) 36S–43S.
[10] L. Gouva, A. Tsatsoulis, The role of estrogens in cardiovascular disease in the aftermath of clinical trials, Hormones. (Athens.) 3 (2004) 171–183.
[11] M. Akishita, Y. Ouchi, H. Miyoshi, K. Kozaki, S. Inoue, M. Ishikawa, M. Eto, K. Toba, H. Orimo, Estrogen inhibits cuff-induced intimal thickening of rat femoral artery: effects on migration and proliferation of vascular smooth muscle cells, Atherosclerosis 130 (1997) 1–10.
[12] M.L. Foegh, S. Asotra, M.H. Howell, P.W. Ramwell, Estradiol inhibition of arterial neointimal hyperplasia after balloon injury, J. Vasc. Surg. 19 (1994) 722–726.
[13] T.R. Sullivan Jr., R.H. Karas, M. Aronovitz, G.T. Faller, J.P. Ziar, J.J. Smith, T.F. O'Donnell Jr., M.E. Mendelsohn, Estrogen inhibits the response-to-injury in a mouse carotid artery model, J. Clin. Invest 96 (1995) 2482–2488.
[14] D. Dai-Do, E. Espinosa, G. Liu, T.J. Rabelink, F. Julmy, Z. Yang, F. Mahler, T.F. Luscher, 17 beta-estradiol inhibits proliferation and migration of human vascular smooth muscle cells: similar effects in cells from postmenopausal females and in males, Cardiovasc. Res. 32 (1996) 980–985.
[15] L.E. Keyes, L.G. Moore, S.J. Walchak, E.C. Dempsey, Pregnancy-stimulated growth of vascular smooth muscle cells: importance of protein kinase C-dependent synergy between estrogen and platelet-derived growth factor, J. Cell Physiol 166 (1996) 22–32.
[16] L. Zhang, C. Zhu, X. Zhang, Y. Wan, J. Song, Dual effects of estrogen on vascular smooth muscle cells: receptor-mediated proliferative vs. metabolite-induced pro-senescent actions, Steroids 76 (2011) 309–316.
[17] L.J. Hofland, K.P. van, J.W. Koper, H.A. den, S.W. Lamberts, Weak estrogenic activity of phenol red in the culture medium: its role in the study of the regulation of prolactin release in vitro, Mol. Cell Endocrinol. 54 (1987) 43–50.
[18] J. Wesierska-Gadek, T. Schreiner, M. Maurer, A. Waringer, C. Ranftler, Phenol red in the culture medium strongly affects the susceptibility of human MCF-7 cells to roscovitine, Cell Mol. Biol. Lett. 12 (2007) 280–293.
[19] K.E. Porter, K. Varty, L. Jones, P.R. Bell, N.J. London, Human saphenous vein organ culture: a useful model of intimal hyperplasia?, Eur J. Vasc. Endovasc. Surg. 11 (1996) 48–58.
[20] P.K. Aley, K.E. Porter, J.P. Boyle, P.J. Kemp, C. Peers, Hypoxic modulation of Ca^{2+} signaling in human venous endothelial cells. Multiple roles for reactive oxygen species, J. Biol. Chem. 280 (2005) 13349–13354.
[21] K.E. Porter, J. Naik, N.A. Turner, T. Dickinson, M.M. Thompson, N.J. London, Simvastatin inhibits human saphenous vein neointima formation via inhibition of smooth muscle cell proliferation and migration, J. Vasc. Surg. 36 (2002) 150–157.
[22] R.S. Mughal, J.L. Scragg, P. Lister, P. Warburton, K. Riches, D.J. O'Regan, S.G. Ball, N.A. Turner, K.E. Porter, Cellular mechanisms by which proinsulin C-peptide prevents insulin-induced neointima formation in human saphenous vein, Diabetologia 53 (2010) 1761–1771.
[23] N.A. Turner, S.G. Ball, A.J. Balmforth, The mechanism of angiotensin II-induced extracellular signal-regulated kinase-1/2 activation is independent of angiotensin AT_{1A} receptor internalisation, Cell Signal. 13 (2001) 269–277.
[24] M.A. Zimmerman, C.H. Selzman, L.L. Reznikov, S.A. Miller, C.D. Raeburn, J. Emmick, X. Meng, A.H. Harken, Lack of TNF-alpha attenuates intimal hyperplasia after mouse carotid artery injury, Am. J. Physiol Regul. Integr. Comp Physiol 283 (2002) R505–R512.
[25] C.M. Lambert, M. Roy, J. Meloche, G.A. Robitaille, M. Agharazii, D.E. Richard, S. Bonnet, Tumor necrosis factor inhibitors as novel therapeutic tools for vascular remodeling diseases, Am. J. Physiol Heart Circ. Physiol 299 (2010) H995–1001.
[26] D. Sivritas, M.U. Becher, T. Ebrahimian, O. Arfa, S. Rapp, A. Bohner, C.F. Mueller, T. Umemura, S. Wassmann, G. Nickenig, K. Wassmann, Antiproliferative effect of estrogen in vascular smooth muscle cells is mediated by Kruppel-like factor-4 and manganese superoxide dismutase, Basic Res. Cardiol. 106 (2011) 563–575.
[27] T. Watanabe, Y. Miyahara, M. Akishita, T. Nakaoka, N. Yamashita, K. Iijima, H. Kim, K. Kozaki, Y. Ouchi, Inhibitory effect of low-dose estrogen on neointimal formation after balloon injury of rat carotid artery, Eur. J. Pharmacol. 502 (2004) 265–270.
[28] J.F. Arnal, P.Y. Scarabin, F. Tremollieres, H. Laurell, P. Gourdy, Estrogens in vascular biology and disease: where do we stand today?, Curr Opin. Lipidol. 18 (2007) 554–560.
[29] D.W. Losordo, M. Kearney, E.A. Kim, J. Jekanowski, J.M. Isner, Variable expression of the estrogen receptor in normal and atherosclerotic coronary arteries of premenopausal women, Circulation 89 (1994) 1501–1510.
[30] Y. Nakamura, T. Suzuki, Y. Miki, C. Tazawa, K. Senzaki, T. Moriya, H. Saito, T. Ishibashi, S. Takahashi, S. Yamada, H. Sasano, Estrogen receptors in atherosclerotic human aorta: inhibition of human vascular smooth muscle cell proliferation by estrogens, Mol. Cell Endocrinol. 219 (2004) 17–26.
[31] D. Xing, W. Feng, A.P. Miller, N.M. Weathington, Y.F. Chen, L. Novak, J.E. Blalock, S. Oparil, Estrogen modulates TNF-alpha-induced inflammatory responses in rat aortic smooth muscle cells through estrogen receptor-beta activation, Am. J. Physiol Heart Circ. Physiol 292 (2007) H2607–H2612.
[32] P.J. Oviedo, A. Sobrino, A. Laguna-Fernandez, S. Novella, J.J. Tarin, M.A. Garcia-Perez, J. Sanchis, A. Cano, C. Hermenegildo, Estradiol induces endothelial cell migration and proliferation through estrogen receptor-enhanced RhoA/ROCK pathway, Mol. Cell Endocrinol. 335 (2011) 96–103.
[33] Y. Huo, K. Ley, Adhesion molecules and atherogenesis, Acta Physiol Scand. 173 (2001) 35–43.
[34] S. Blankenberg, S. Barbaux, L. Tiret, Adhesion molecules and atherosclerosis, Atherosclerosis 170 (2003) 191–203.
[35] E. Galkina, K. Ley, Vascular adhesion molecules in atherosclerosis, Arterioscler. Thromb. Vasc. Biol. 27 (2007) 2292–2301.
[36] M.F. Crook, A.C. Newby, K.M. Southgate, Expression of intercellular adhesion molecules in human saphenous veins: effects of inflammatory cytokines and neointima formation in culture, Atherosclerosis 150 (2000) 33–41.
[37] M. Braun, P. Pietsch, A. Zepp, K. Schror, G. Baumann, S.B. Felix, Regulation of tumor necrosis factor alpha- and interleukin-1-beta-induced induced adhesion molecule expression in human vascular smooth muscle cells by cAMP, Arterioscler. Thromb. Vasc. Biol. 17 (1997) 2568–2575.
[38] J.R. Gamble, S. Bradley, L. Noack, M.A. Vadas, TGF-beta and endothelial cells inhibit VCAM-1 expression on human vascular smooth muscle cells, Arterioscler. Thromb. Vasc. Biol. 15 (1995) 949–955.
[39] Y. Zou, Y. Hu, M. Mayr, H. Dietrich, G. Wick, Q. Xu, Reduced neointima hyperplasia of vein bypass grafts in intercellular adhesion molecule-1-deficient mice, Circ. Res. 86 (2000) 434–440.
[40] D. Xing, S. Nozell, Y.F. Chen, F. Hage, S. Oparil, Estrogen and mechanisms of vascular protection, Arterioscler. Thromb. Vasc. Biol. 29 (2009) 289–295.

Biochemical and Biophysical Research Communications 420 (2012) 834–838

Contents lists available at SciVerse ScienceDirect

Biochemical and Biophysical Research Communications

journal homepage: www.elsevier.com/locate/ybbrc

Xanthorrhizol induced DNA fragmentation in HepG2 cells involving Bcl-2 family proteins

Thiam-Tsui Tee [a,*], Yew-Hoong Cheah [a,b], Meenakshii Nallappan [c], Mohd Sharom Mohd Yusof [a], Azimahtol Hawariah Lope Pihie [a]

[a] School of Biosciences & Biotechnology, Faculty of Science & Technology, Universiti Kebangsaan Malaysia, 43600 Bangi, Selangor, Malaysia
[b] Bioassay Unit, Herbal Medicine Research Center, Institute for Medical Research, Jalan Pahang, Kuala Lumpur, Malaysia
[c] Biology Department, Faculty of Science, Universiti Putra Malaysia, 43400 Serdang, Selangor, Malaysia

ARTICLE INFO

Article history:
Received 8 March 2012
Available online 23 March 2012

Keywords:
Curcuma xanthorrhiza
Xanthorrhizol
HepG2 human hepatoma cell
Apoptosis
DNA fragmentation

ABSTRACT

Xanthorrhizol is a plant-derived pharmacologically active sesquiterpenoid compound isolated from *Curcuma xanthorrhiza*. Previously, we have reported that xanthorrhizol inhibited the proliferation of HepG2 human hepatoma cells by inducing apoptotic cell death via caspase activation. Here, we attempt to further elucidate the mode of action of xanthorrhizol. Apoptosis in xanthorrhizol-treated HepG2 cells as observed by scanning electron microscopy was accompanied by truncation of BID; reduction of both anti-apoptotic Bcl-2 and Bcl-X_L expression; cleavage of PARP and DFF45/ICAD proteins and DNA fragmentation. Taken together, these results suggest xanthorrhizol as a potent antiproliferative agent on HepG2 cells by inducing apoptosis via Bcl-2 family members. Hence we proposed that xanthorrhizol could be used as an anti-liver cancer drug for future studies.

© 2012 Elsevier Inc. All rights reserved.

1. Introduction

Hepatocellular carcinoma (HCC) is one of the most common primary malignant tumors of the liver worldwide with the highest prevalence in South East Asia [1] and the 2nd leading cause of cancer-related death in men [2]. Despite extensive researches have been made in chemotherapy regimen for HCC, the efficacy of drugs is often hampered by a range of adverse side-effects imposed on patients and inherent chemoresistance of HCC [3]. Cancer cells which are resistant to chemotherapy will eventually dominate the cell population and caused mortality [4]. Therefore, development of new anti-cancer drug from medicinal plant is a key issue for cancer chemotherapy for HCC.

Xanthorrhizol is a sesquiterpenoid compound isolated form the rhizome of *Curcuma xanthorrhiza* Roxburgh of the Zingiberaceae family which is known as temu lawak in Malaysia. *C. xanthorrhiza* is a medicinal plant widely spread in South East Asia and it is commonly used not only for food but also as folk medicine, such as cholagogues, aromatic stomachics, analgesics, rheumatic remedy, anti-diabetes, anti-cancer, anti-hypertension and particularly for the treatment of viral hepatitis in Indonesia [5,6]. Previous studies on xanthorrhizol suggest this bioactive compound exhibits various biological activities including anti-bacterial effect [7,8], anti-fungal effect [9,10], anti-inflammatory effect [11], preventive effects against cisplatin-induced hepatotoxicity [12] and nephrotoxicity [13]. In various studies on anti-carcinogenesis, xanthorrhizol exhibited anti-metastasis activity in a mouse spontaneous lung metastasis model [14] and exhibited antiproliferation effects on various cell lines such as HCT116 human colon cancer cells [15], MDA-MB-231 human breast cancer cells [16], MCF-7 human breast cancer cells [17], and HeLa human cervix cancer cells [18]. However, the mechanism of action for xanthorrhizol on HepG2 cells remains to be clarified.

Anticancer chemotherapy regimen triggers tumor cell death through the induction of apoptosis. Alteration in the apoptotic pathways may determine tumor resistance to current therapeutic strategies [19]. Hence, identification and targeting of the disabled pathway might be the most successful approach for chemotherapy in the future [20]. Therefore, it is vital to understand the mechanisms of action of xanthorrhizol induced apoptosis in HepG2 cells enabling more rational approaches to anti-tumor therapy.

In this study, we extracted xanthorrhizol from the rhizome of *C. xanthorrhiza* and the apoptotic effects on HepG2 cells were detected by scanning electron microscopy. Our experiments demonstrated that xanthorrhizol could dose-dependently induced HepG2 cell apoptosis with the characteristic of DNA fragmentation, truncation of BID; reduction of both anti-apoptotic Bcl-2 and Bcl-X_L expression; cleavage of PARP-1 and DFF45/ICAD proteins.

* Corresponding author. Fax: +60 389252698.
E-mail address: thiamtsu@yahoo.com (T.-T. Tee).

0006-291X/$ - see front matter © 2012 Elsevier Inc. All rights reserved.
http://dx.doi.org/10.1016/j.bbrc.2012.03.083

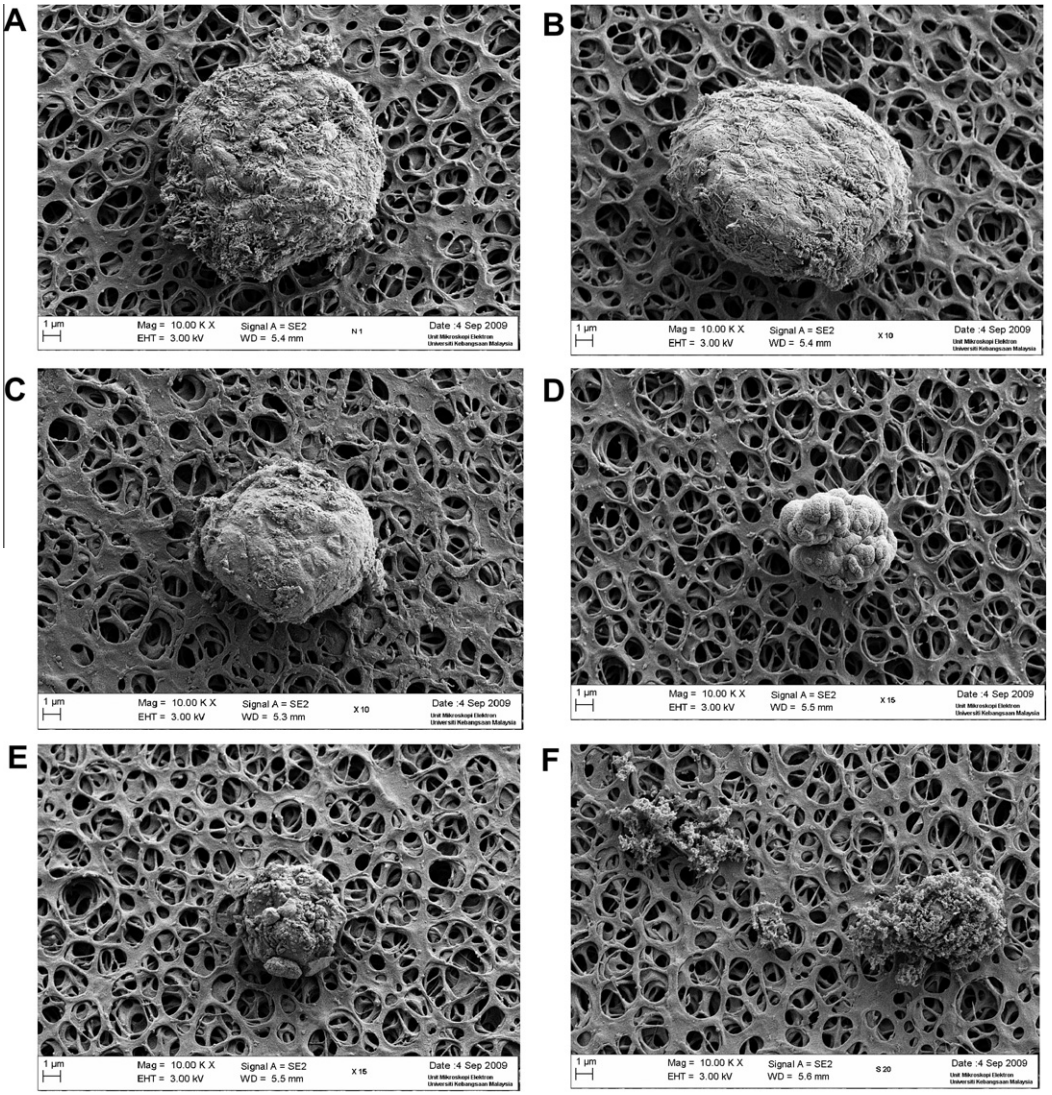


Fig. 1. SEM micrographs of surface ultrastructural characteristic of HepG2 cells treated with xanthorrhizol in dose-dependent manner (0, 20, 40, 60, 80, 100 μM). (A) The characteristic of untreated HepG2 cells surface showing typical morphological feature of a cancer cell with numerous mirovilli. (B–F) Xanthorrhizol-treated HepG2 cells (20, 40, 60, 80, 100 μM) showed distinct morphological changes corresponding to typical apoptosis, including disappearance or reduction of microvilli, cell membrane blebbing, overall cell shrinkage, and formation of apoptotic bodies (×10,000).

2. Materials and methods

2.1. Extraction and isolation of xanthorrhizol

Xanthorrhizol was isolated from the rhizomes of *C. xanthorrhiza* as previously described [21]. The identification of xanthorrhizol was accomplished by spectroscopic methods (GCMS and ^{1}H NMR), and comparison with those of published data and reference compounds.

2.2. Cell line and culture conditions

HepG2 cell line was obtained from the American Type Culture Collection (ATCC, Manassas, VA). HepG2 cells were cultured in DMEM medium (Invitrogen Co., Carlsbad, CA) supplemented with 10% FBS (Invitrogen Co., Carlsbad, CA) in a humidified atmosphere of 5% CO_2 in air at 37 °C. Cells were kept in the logarithmic growth phase by routinely passage every 2–3 days using 0.025% trypsin–EDTA treatment (Invitrogen Co., Carlsbad, CA).

2.3. Scanning electron microscopy (SEM)

The treated and non-treated HepG2 cells were trypsinized and centrifuged for 10 min at 3000 rpm. The pellets were fixed in 3% (v/v) glutaraldehyde in PBS for overnight at 4 °C. The fixed cells were washed in three changes of PBS for 10 min each then dehydrated in ascending grades of ethanol (50%, 75%, 95%, and 100%), and brought to critical point of drying by the critical point drier for 30 min. The cells were affixed to a metal SEM stub and sputter coated in gold by using SEM coating unit. The coated specimens were viewed using scanning electron microscopy.

2.4. DNA fragmentation assay

DNA fragmentation assay is a definitive assay to confirm apoptotic cell death has taken place in the cultures. DNA fragmentation assay was conducted using the Suicide Track™ DNA Ladder Isolation Kit (Calbiochem), according to manufacturer's instructions. Briefly, HepG2 cells were cultured in a T-25 flask and treated with xanthorrhizol for 24 h. Floating and trypsinized-adherent of

treated and untreated cells were collected by centrifuging at 900×*g* for 5 min. Cell pellets were then resuspended in 250 μl of extraction buffer following incubation on 4 °C for 30 min. The suspensions were then centrifuged at 16,000×*g* for 5 min at room temperature. The resulting supernatant were transferred to a clean tube, followed by the addition of 10 μl of RNase A solution and incubated at 37 °C for 1 h. DNA isolation buffer was added and further incubated at 50 °C for overnight. During the DNA precipitation step, 2 μl of Pellet Paint® Co-precipitant was added to the suspension together with 30 μl of 3 M sodium acetate and 311 μl of 2-propanol. Samples were mixed by inversion and then centrifuged at 16,000×*g* for 5 min. The resulting pellets were washed with 70% and 100% ethanol. The DNA samples were then air-dried and resuspended in 50 μl of resuspension buffer (10 mM Tris, 1 mM EDTA). Finally, the DNA fragmentation pattern was determined with an Agilent 2100 bioanalyzer using the Agilent DNA 7500 kit.

2.5. Antibodies and reagents

Antibodies to Bid, Bcl-2, Bcl-X_L, Bax, Bak, PARP, and DFF45/ICAD were obtained from Pharmingen (USA). Anti-actin antibody was obtained from Sigma (St. Louis, MO). Secondary horseradish-peroxidase-conjugated sheep anti-mouse antibodies were purchased from Pharmingen (USA).

2.6. Western blot analysis

Cells were lysed in buffer (50 mM Tris–HCl (pH 8.0), 150 mM NaCl, 5 mM EDTA, 5 mM EGTA, 1% (v/v) Triton-X, 1 mM phenylmethylsulfonyl fluoride, 10 mM glycerophosphate, 1 mM Na_3VO_4, 10 μg/ml pepstatin A, 10 μg/ml aprotinin, 20 μg/ml leupeptin, and 5 mM DTT) and put on ice for 45 min. Cells were then submitted to 3 freeze–thaw cycles and centrifuged at 10,000 rpm for 20 min at 4 °C to remove cellular debris. The supernatant extracts were quantified for protein using Bradford procedures. Equivalent amounts of proteins (20 μg) were mixed with an equal volume of 2× Laemmli sample buffer, boiled, and resolved by electrophoresis in 12% sodium dodecyl sulfate–polyacrylamide gels (SDS–PAGE). The proteins were then transferred from the gel to a polyvinyldenefluoride (PVDF) membranes (PolyScreen, NEN Life Sciences, USA) using an electroblotting apparatus. Membranes were incubated in blocking solution containing 5% non-fat dried milk in phosphate buffered saline overnight to inhibit non-specific binding. The membranes were then incubated with specific antibody for 2 h. After washing in Tris/0.1% Tween-20 for 30 min, membranes were incubated for another 1 h with horseradish peroxidase-conjugated secondary antibody. The membranes were then washed and developed with Renaissance Western blot Chemiluminescence reagent Plus. Expression of actin was used to control equal protein loading.

2.7. Statistical analysis

The results obtained were expressed as mean ± standard deviation (SD) for the number of experiments. The Student's *t*-test was used to make a statistical comparison between the groups. Results with $p < 0.05$ were considered statistically significant.

3. Results and discussion

Searching for new anti-tumor drugs and studying their medical value are of paramount importance to reduce the morbidity and mortality of HCC. Furthermore, induction of apoptosis is the main key and efficient strategy for cancer therapy. Apoptotic cells are usually characterized by several distinctive morphological changes, including cell shrinkage, membrane blebbing, chromatin condensation, DNA fragmentation, and fragmentation of the cell into membrane-bound apoptotic bodies [22].

In this work we found that xanthorrhizol from *C. xanthorrhiza*, a herbal medicine in Malaysia, induced HepG2 cells apoptosis using scanning electron microscopy. As displayed by electron micrographs (Fig. 1), control cells showed integrated plasma membrane and extensive membrane interdigitations and microvilli. However, xanthorrhizol treated HepG2 cells exhibited membrane blebbing, disappearance or reduction of membrane microvilli, overall cell shrinkage and formation of apoptotic bodies. All the changes indicated the apoptosis of xanthorrhizol-treated HepG2 cells. These distinctive morphological features form the basis of some of the most widely used techniques for the identification and quantification of apoptosis, and thus morphologic description using electron microscopy remains one of the best ways to define apoptosis and contrast it with necrosis [23].

One of the main regulators of the apoptosis signalling is the Bcl-2 family members. Three subfamilies of Bcl-2 protein have been identified as playing important roles in the apoptotic response. The Bcl-2 subfamily (e.g., Bcl-2 and Bcl-X_L) functions to inhibit apoptosis, whereas the Bax subfamily (e.g., Bax and Bak) and the BH3-only subfamily (e.g., Bid) promote apoptosis [24]. Most of the cancerous cells have overexpression of the pro-survival Bcl-2 family members leading to tumor formation and chemoresistance to chemotherapeutic drug. Therefore, we further evaluate the effect of xanthorrhizol on the protein expression patterns of Bcl-2 family members. Fig. 2 demonstrates that the expression level of both the anti-apoptotic protein Bcl-2 and Bcl-X_L were markedly diminished in HepG2 cells treated with xanthorrhizol. Both the Bcl-2 and Bcl-X_L are integral membrane proteins that prevent apoptosis in numerous biological systems. The expression of these anti-apoptotic proteins are inversely correlated with the susceptibility of cells to apoptosis [25]. Notwithstanding, the protein expression of both pro-apoptotic protein Bax and Bak remained almost unchanged throughout the experiments. Both Bax and Bak have been observed to translocate from the cytoplasm to the outer mitochondrial membrane, where they oligomerize to form pores and mediate cytochrome *c* release [26]. In addition, we found that the protein expression of Bid decreased significantly after treatment with xanthorrhizol. Activated tBID results in an allosteric

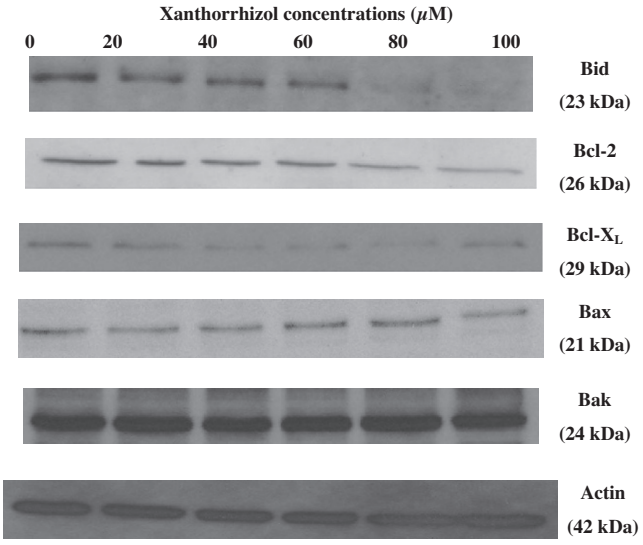


Fig. 2. Expression of Bid, Bcl-2, Bcl-X_L, Bax, and Bak proteins were examined by Western blotting analysis in xanthorrhizol-treated human hepatoma HepG2 cells. Expression of actin was used to control equal protein loading.

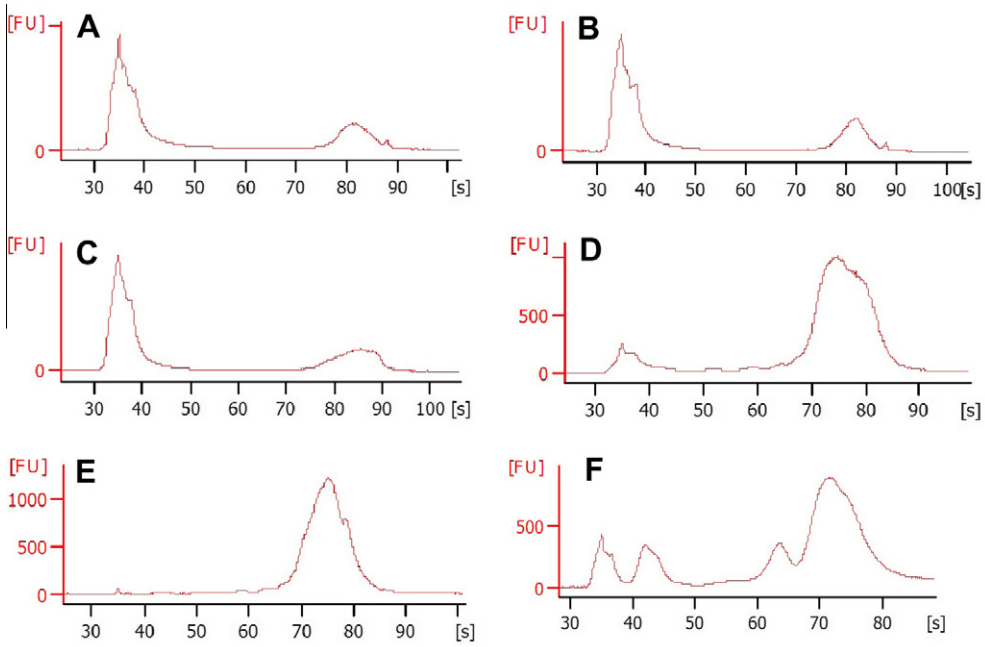


Fig. 3. DNA fragmentation in HepG2 cells treated with xanthorrhizol in dose-dependent manner. (A) Control cell cultures received solvent solution (DMSO) only. (B–E) DNA fragmentation in cell cultures with different concentration of xanthorrhizol (20, 40, 60, 80 μM). (F) Cell cultures treated with 0.1 μM of doxorubicin as positive control.

activation of Bax and Bak, inducing its intramembranous oligomerization into a proposed pore for cytochrome *c* efflux [27]. Taken together, alterations of the expression levels of these proteins would dispose the cells to apoptosis.

In addition, we determined the effect of xanthorrhizol treatment on DNA fragmentation in HepG2 cells. DNA fragmentation is the typical biochemical index of cell apoptosis [28]. As shown in Fig. 3, the electrophoresis pattern was typical for apoptotic, where major fragments detected had sizes of ~1000, ~1400 bp. The first signs of nucleosomal DNA fragmentation appeared after the addition of 60 μM of xanthorrhizol and the appearance became obvious when treated with 80 μM of xanthorrhizol, thus confirming apoptosis but not necrosis had taken place. The same pattern of DNA fragmentation was observed in DNA sample from doxorubicin-treated HepG2 cells as positive control. However, treatments at lower doses do not marked any DNA fragmentation as compared to control culture.

Several endonucleases have been implicated in the DNA fragmentation associated with apoptosis including poly-ADP-ribose polymerase (PARP) and DFF45 (inhibitor of caspase-activated DNase) proteins [29]. Therefore, we evaluated expression of both the PARP and DFF45/ICAD proteins accountable for characteristic DNA fragmentation. We observed that xanthorrhizol induced proteolytic cleavage of both the PARP and DFF45/ICAD proteins in HepG2 cells (Fig. 4). On the basis of these results, we proposed that the generation of DNA fragments, together with cleavage of PARP and DFF45/ICAD, and Bcl-2 family proteins contributes to an amplification phase of apoptosis in xanthorrhizol-treated HepG2 cells.

Our results provide important insights for the comprehensive understanding of the drug action mechanism of xanthorrhizol in HepG2 cells. Hence we proposed that xanthorrhizol could be used as an anti-liver cancer drug for future studies. Further studies are being performed to uncover the underlying apoptosis mechanism.

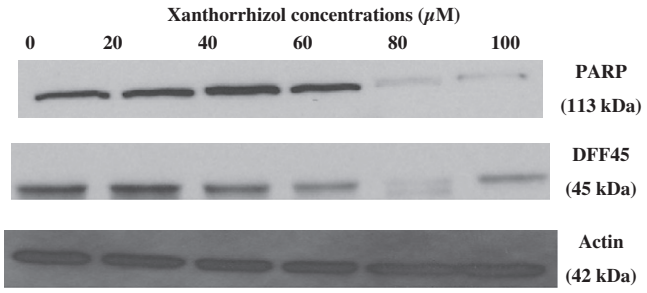


Fig. 4. Expression of PARP and DFF45/ICAD proteins were examined by Western blotting analysis in xanthorrhizol-treated human hepatoma HepG2 cells. Expression of actin was used to control equal protein loading.

Acknowledgment

This work was supported by the Ministry of Higher Education of Malaysia Grant UKM-ST-03-FRGS0015-2006.

References

[1] L.B. Seeff, J.H. Hoofnagle, Epidemiology of hepatocellular carcinoma in areas of low hepatitis B and hepatitis C endemicity, Oncogene 25 (2006) 3771–3777.
[2] A. Jemal, F. Bray, M.M. Center, J. Ferlay, E. Ward, D. Forman, Global cancer statistics, CA Cancer Journal for Clinicians 61 (2011) 69–90.
[3] J.L. Giglia, S.J. Antonia, L.B. Berk, S. Bruno, S. Dessureault, S.E. Finkelstein, Systemic therapy for advanced hepatocellular carcinoma: past, present, and future, Cancer Control 17 (2010) 120–129.
[4] S.A. Kang, H.J. Park, M.J. Kim, S.Y. Lee, S.W. Han, K.H. Leem, Citri Reticulatae Viride Pericarpium extract induced apoptosis in SNU-C4, human colon cancer cells, Journal of Ethnopharmacology 97 (2005) 231–235.
[5] S. Devaraj, A.Z. Esfahani, S. Ismail, S. Ramanathan, M.F. Yam, Evaluation of the antinociceptive activity and acute oral toxicity of standardized extract of the rhizome of *Curcuma xanthorrhiza* Roxb, Molecules 15 (2010) 2925–2934.
[6] Y. Ozaki, Antiinflammatory effect of *Curcuma xanthorrhiza* Roxb, and its active principles, Chemical and Pharmaceutical Bulletin (Tokyo) 38 (1990) 1045–1048.
[7] Y. Rukayadi, J.K. Hwang, *In vitro* activity of xanthorrhizol against *Streptococcus mutans* biofilms, Letters in Applied Microbiology 42 (2006) 400–404.
[8] J.K. Hwang, J.S. Shim, Y.R. Pyun, Antibacterial activity of xanthorrhizol from *Curcuma xanthorrhiza* against oral pathogens, Fitoterapia 71 (2000) 321–323.
[9] Y. Rukayadi, J.K. Hwang, *In vitro* antimycotic activity of xanthorrhizol isolated from *Curcuma xanthorrhiza* Roxb. against opportunistic filamentous fungi, Phytotherapy Research 21 (2007) 434–438.

[10] Y. Rukayadi, D. Yong, J.K. Hwang, *In vitro* anticandidal activity of xanthorrhizol isolated from *Curcuma xanthorrhiza* Roxb, Journal of Antimicrobial Chemotherapy 57 (2006) 1231–1234.

[11] C.S. Lim, D.Q. Jin, H. Mok, S.J. Oh, J.U. Lee, J.K. Hwang, I. Ha, J.S. Han, Antioxidant and anti-inflammatory activities of xanthorrhizol in hippocampal neurons and primary cultured microglia, Journal of Neuroscience Research 82 (2005) 831–838.

[12] S.H. Kim, K.O. Hong, W.Y. Chung, J.K. Hwang, K.K. Park, Abrogation of cisplatin-induced hepatotoxicity in mice by xanthorrhizol is related to its effect on the regulation of gene transcription, Toxicology and Applied Pharmacology 196 (2004) 346–355.

[13] S.H. Kim, K.O. Hong, J.K. Hwang, K.K. Park, Xanthorrhizol has a potential to attenuate the high dose cisplatin-induced nephrotoxicity in mice, Food and Chemical Toxicology 43 (2005) 117–122.

[14] M.A. Choi, S.H. Kim, W.Y. Chung, J.K. Hwang, K.K. Park, Xanthorrhizol, a natural sesquiterpenoid from *Curcuma xanthorrhiza*, has an anti-metastatic potential in experimental mouse lung metastasis model, Biochemical and Biophysical Research Communications 326 (2005) 210–217.

[15] Y.J. Kang, K.K. Park, W.Y. Chung, J.K. Hwang, S.K. Lee, Xanthorrhizol, a natural sesquiterpenoid, induces apoptosis and growth arrest in HCT116 human colon cancer cells, Journal of Pharmacological Sciences 111 (2009) 276–284.

[16] Y.H. Cheah, N. Fariza Juliana, T.T. Tee, L.P. Azimahtol Hawariah, A. Noor Rain, I. Zakiah, Antiproliferative property and apoptotic effect of xanthorrhizol on MDA-MB-231 breast cancer cells, Anticancer Research 28 (2008) 3677–3689.

[17] Y.H. Cheah, L.P. Azimahtol Hawariah, A. Noor Rain, Xanthorrhizol exhibits antiproliferative activity on MCF-7 breast cancer cells via apoptosis induction, Anticancer Research 26 (2006) 4527–4534.

[18] I. Norzila, L.P. Azimahtol Hawariah, N. Meenakshi, Xanthorrhizol induces apoptosis via the up-regulation of Bax and p53 in HeLa cells, Anticancer Research 25 (2005) 2221–2228.

[19] K. Yamaguchi, R. Uzzo, N. Dulin, J.H. Finke, V. Kolenko, Renal carcinoma cells undergo apoptosis without oligonucleosomal DNA fragmentation, Biochemical and Biophysical Research Communications 318 (2004) 710–713.

[20] S. Rodriguez-Nieto, B. Zhivotovsky, Role of alterations in the apoptotic machinery in sensitivity of cancer cells to treatment, Current Pharmaceutical Design 12 (2006) 4411–4425.

[21] Y.H. Cheah, N. Fariza Juliana, S. Rozie, T.T. Tee, L.P. Azimahtol Hawariah, M.S. Hasnah, A.R. Badrul Amini, A. Noor Rain, I. Zakiah, Combined xanthorrhizol-curcumin exhibits synergistic growth inhibitory activity via apoptosis induction in human breast cancer cells MDA-MB-231, Cancer Cell International 9 (2009) 1–12.

[22] J.F.R. Kerr, A.H. Wyllie, A.R. Currie, Apoptosis: a basic biological phenomenon with wide-ranging implications in tissue kinetics, British Journal of Cancer 26 (1972) 239–257.

[23] F. Doonan, T.G. Cotter, Morphological assessment of apoptosis, Methods 44 (2008) 200–204.

[24] M.H. Harris, C.B. Thompson, The role of the Bcl-2 family in the regulation of outer mitochondrial membrane permeability, Cell Death and Differentiation 7 (2000) 1182–1191.

[25] H.J. Lee, C.J. Wang, H.C. Kuo, F.P. Chou, L.F. Jean, T.H. Tseng, Induction apoptosis of luteolin in human hepatoma HepG2 cells involving mitochondria translocation of Bax/Bak and activation of JNK, Toxicology and Applied Pharmacology 203 (2005) 124–131.

[26] A. Nechushtan, C.L. Smith, Y.T. Hsu, R.J. Youle, Conformation of the Bax C-terminus regulates subcellular location and cell death, EMBO Journal 18 (1999) 2330–2341.

[27] S.J. Korsmeyer, M.C. Wei, M. Saito, S. Weiler, K.J. Oh, P.H. Schlesinger, Pro-apoptotic cascade activates BID, which oligomerizes BAK or BAX into pores that result in the release of cytochrome c, Cell Death and Differentiation 7 (2000) 1166–1173.

[28] W. Bao, H. Pan, M. Lu, Y. Ni, R. Zhang, X. Gong, The apoptotic effect of sarsasapogenin from *Anemarrhena asphodeloides* on HepG2 human hepatoma cells, Cell Biology International 31 (2007) 887–892.

[29] A.H. Boulares, A.J. Zoltoski, F.J. Contreras, A.G. Yakovlev, K. Yoshihara, M.E. Smulson, Regulation of DNAS1L3 endonuclease activity by poly(ADP-ribosyl)ation during etoposide-induced apoptosis. Role of poly(ADP-ribose) polymerase-1 cleavage in endonuclease activation, Journal of Biological Chemistry 277 (2002) 372–378.

Biochemical and Biophysical Research Communications 420 (2012) 839–844

Contents lists available at SciVerse ScienceDirect

Biochemical and Biophysical Research Communications

journal homepage: www.elsevier.com/locate/ybbrc

Ligand structural motifs can decouple glucocorticoid receptor transcriptional activation from target promoter occupancy

Raymond D. Blind [a,*], Inés Pineda-Torra [b,1], Yong Xu [d], H. Eric Xu [d], Michael J. Garabedian [b,c]

[a] Department of Pharmacology, New York University School of Medicine, New York, NY 10016, USA
[b] Department of Microbiology, New York University School of Medicine, New York, NY 10016, USA
[c] Department of Urology, New York University School of Medicine, New York, NY 10016, USA
[d] Laboratory of Structural Sciences, Van Andel Research Institute, Grand Rapids, MI 49503, USA

ARTICLE INFO

Article history:
Received 10 March 2012
Available online 23 March 2012

Keywords:
Glucocorticoid receptor
Anti-inflammatory
Steroids
Chromatin immunoprecipitation
Gene expression

ABSTRACT

Glucocorticoid (GC) induction of the tyrosine aminotransferase (TAT) gene by the glucocorticoid receptor (GR) is a classic model used to investigate steroid-regulated gene expression. Classic studies analyzing GC-induction of the TAT gene demonstrated that despite having very high affinity for GR, some steroids cannot induce maximal TAT enzyme activity, but the molecular basis for this phenomenon is unknown. Here, we used RT-PCR and chromatin immunoprecipitation to determine TAT mRNA accumulation and GR recruitment to the TAT promoter (TAT–GRE) in rat hepatoma cells induced by seven GR ligands: dexamethasone (DEX), cortisol (CRT), corticosterone (CCS), 11-deoxycorticosterone (DOC), aldosterone (ALD), progesterone (PRG) and 17-hydroxyprogesterone (17P). As expected, DEX, CRT, CCS and ALD all induced both TAT mRNA and GR recruitment to the TAT–GRE, while PRG and 17P did not. However, while DOC could not induce significant TAT mRNA, it did induce robust GR occupancy of the TAT–GRE. DOC also induced recruitment of the histone acetyltransferase p300 to the TAT–GRE as efficiently as DEX. These DOC-induced effects recapitulated at another GR target gene (sulfonyltransferase 1A1), and DOC also failed to promote the multiple changes in gene expression required for glucocorticoid-dependent 3T3-L1 adipocyte differentiation. Structural simulations and protease sensitivity assays suggest that DOC and DEX induce different conformations in GR. Thus, although steroids that bind GR with high affinity can induce GR and p300 occupancy of target promoters, they may not induce a conformation of GR capable of activating transcription.

© 2012 Elsevier Inc. All rights reserved.

1. Introduction

Glucocorticoids (GCs) are steroid hormones that regulate development, metabolism and the stress response [1]. GCs are also used therapeutically as potent anti-inflammatory agents for the treatment of arthritis, asthma and leukemia [2]. Problems arise when GCs are administered chronically, which can result in bone and muscle atrophy, stunted growth, and increased susceptibility to diabetes [3]. Developing GCs and non-steroidal analogs that minimize these harmful side effects while maintaining anti-inflammatory activity remains an important goal of pharmaceutical research [4].

Glucocorticoids elicit their physiological responses via the glucocorticoid receptor (GR), a ligand activated transcription factor [5]. Upon ligand binding, GR translocates into the cell nucleus where it can bind glucocorticoid-response elements (GREs) in the regulatory regions of target genes, enhancing transcription by interacting with coactivators that attract chromatin remodeling factors, such as p300, which in turn facilitate the recruitment of the RNA polymerase II transcription initiation complex [6,7]. GR also regulates gene expression independent of DNA-binding through protein–protein interactions, exemplified by GR repression of NFκB and AP-1 stimulated genes, two pathways associated with the anti-inflammatory activities of GCs [8,9].

Tyrosine aminotransferase (TAT) is an enzyme expressed in the parenchymal cells of liver where it is involved with the transamination of xenobiotics to aid in excretion and in the metabolism of several classes of drugs [10,11]. GCs induce the TAT gene, which is

Abbreviations: GC, glucocorticoid; GR, glucocorticoid receptor; TAT, tyrosine aminotransferase; DEX, dexamethasone; CRT, cortisol; CCS, corticosterone; DOC, 11-deoxycorticosterone; ALD, aldosterone; PRG, progesterone; 17P, 17-hydroxyprogesterone; GRE, glucocorticoid response element; GRU, glucocorticoid responsive unit.

* Corresponding author. Present address: Department of Cellular and Molecular Pharmacology, University of California San Francisco, San Francisco, CA 94158, USA. Fax: +1 415 626 4056.
E-mail address: ray.blind@gmail.com (R.D. Blind).
[1] Present address: University College of London, Division of Medicine, Centre for Clinical Pharmacology, 5 University Street, London WC1E6JJ, UK.

0006-291X/$ - see front matter © 2012 Elsevier Inc. All rights reserved.
http://dx.doi.org/10.1016/j.bbrc.2012.03.084

controlled by a regulatory region located ~2.5 kb upstream of the start site of transcription [12,13]. This region consists of two clusters of GRE's referred to as GC-responsive units I and II (GRU I, GRU II). Mutagenesis studies *in vitro* and GR recruitment *in vivo* have demonstrated that GC-mediated TAT induction occurs mainly through the GRU I regulatory region [13,14].

TAT was one of the first gene products ever shown to be stimulated by GCs in cultured cells [15] and has become a model for GC-regulated transcriptional regulation. Classic studies by Samuels and Tomkins established a hierarchy of the efficacy and potency of the induction of TAT enzyme activity by various steroids [16]. These studies and others showed that there was no clear correlation between the affinity of a particular steroid for GR and its ability to activate maximal TAT enzyme activity [16,17]. For example, despite corticosterone and 11-deoxycorticosterone having similar affinities for GR (Kd = 7.0 and 9.1 nM, respectively), deoxycorticosterone is only capable of inducing 50% of TAT activity relative to DEX, whereas corticosterone can induce 100% DEX TAT activity [16]. These results suggested that mechanisms apart from ligand binding to receptor were modulating TAT induction by different steroids. To gain further insight into the general mechanism of gene induction by steroids, we determined the mRNA induction, GR and p300 recruitment induced by seven representative steroids.

2. Materials and methods

2.1. Cell culture

GRH2 rat hepatoma cells stably expressing rat GR (clone G10) [18] were maintained in Dulbecco's modification of Eagle's media (DMEM) with 2 mM L-glutamine (Mediatech/Cellgro, Herndon, VA) supplemented with 10% fetal bovine serum (FBS; HyClone, Logan, UT), and 50 units/ml penicillin and streptomycin (Mediatech/Cellgro). 3T3-L1 pre-adipocytes (ATCC) were cultured in DMEM with 10% FBS at low density. Confluent cultures were differentiated by the addition of 1 μg/ml insulin, 0.5 mM isobutyl-L-methylzanthin, and 10 or 100 nM dexamethasone, or deoxycorticosterone and cells were maintained in this medium until processing for analysis.

2.2. Ligand treatments

Rat hepatoma cells in 15 cm plates containing 25 ml DMEM with 10% FBS were cultured until they reached ~95% confluence and were then treated with indicated ligand concentrations. For ligand treatments that represent the EC_{50} for induction of TAT enzyme activity [16]: Dexamethasone 8 nM; Cortisol 50 nM; Corticosterone 25 nM; Deoxycorticosterone 600 nM; Aldosterone 400 nM; Progesterone 4000 nM; 17-Hydroxyprogesterone 4000 nM.

2.3. Reverse transcriptase PCR

The *C. therm.* one-step RT-PCR kit (Roche Diagnostics, Inc.) was used for all RT-PCR reactions. Total RNA from hepatoma cells was isolated using the RNAeasy kit (Qiagen), and eluted from RNA purification columns. RNA concentration was determined by optical density and diluted to 0.25 ng/μl. RT-PCR reactions for *tat, sult1a1* and *gapdh* were performed on 0.05 ng total RNA. The PCR products were separated on a 3% agarose gel, visualized by ethidium bromide staining and photographed under UV light. Images of the *tat* and *sult1a1* expression products were scanned and quantitated using NIH Image (http://rsb.info.nih.gov/nih-image/), and normalized to *gapdh* signals.

2.4. Chromatin immunoprecipitation (ChIP) assays

Performed precisely as previously described [19], sequences of each primer pair are: *tat* GRE forward 5′-CCC ATA AAT AAC AGG AAG CCC AAG-3′; *tat* GRE reverse 5′-ATA CCA CCA CAC CCA GAA ACC GAC-3′; *tat* downstream forward 5′-TGT TCT AGC AGG ATT TGT CTG TG-3′; *tat* downstream reverse 5′-TCT GAG CCT GTT GTT GGC CCA-3′; *sult1a1* GRE forward 5′-CGT GTG AAT GCT CTG TCC CAT C-3′; *sult1a1* GRE reverse 5′-GCT GAA GAT TTT GTG TCC CAA GTG-3′; *sult1a1* upstream forward 5′-GTC TTC TCC TAA TCC ACA AAT CCG-3′; *sult1a1* upstream reverse 5′-GGG GTG CTG AAA ACA AAT AAC CAC-3′.

2.5. Oil red O staining

3T3-L1 cells were washed three times with PBS and fixed in 10% formalin in PBS for 1 h. After washing the cells twice with PBS, cells were stained with oil red staining solution (0.5% oil red [Sigma] in isopropanol, diluted 3:2 in water and filtered with a 0.22 μm filter). After staining, cells were washed three times with water and photographed.

2.6. Molecular modeling of GR–DOC

The initial structure [pdb code: 1M2Z.pdb] [20] of human GR–Dexamethasone (DEX) and human MR–deoxycorticosterone (DOC) [pdb code: 2AA7.pdb] [21] complexes were retrieved from the Protein Databank (PDB, http://www.rcsb.org/pdb). The ICM program was used for protein and ligand docking (Molsoft LLC, San Diego, CA). The coordinates of the GR structure were converted into an ICM project. The molecular structure of DOC was extracted from the MR–DOC complex. Atom and bond types of DOC were corrected in ICM interface. The geometry of DOC was optimized with MMFF94 force field [22]. The DOC molecule was docked into the ligand-binding pocket with default parameter implemented in ICM.

2.7. Protease sensitivity assays

Rat GR was synthesized *in vitro* using with TnT T7 quick-coupled transcription/translation system (Promega Corp., Madison, WI) in the presence of ^{35}S-methionine as described by the manufacture. Translation mix (10 μl) was diluted into 40 μl of 50 mM Tris–HCl pH 7.5 containing 100 nM Dex, 100 nM DOC or ethanol. The samples incubated overnight at 4 °C. Serial 10-fold dilutions of 1 mg/ml porcine pancreatic elastase (Sigma, E7885) were added to 4 μl of the sample diluted into 36 μl of 50 mM Tris–HCl pH 7.5 and incubated for 4 min at room temperature and terminated by the addition of 7.5 μl of 5× SDS sample buffer, boiled and resolved by 10% SDS–PAGE. Gels were fixed (25% Methanol, 10% acetic acid), dried and radiolabel polypeptide fragments visualized by autoradiography.

3. Results

We selected seven representative steroids to characterize, based on previously determined pharmacological properties [16,17] Fig. S1 shows the structures of these seven compounds and lists the previously determined values for their dissociation constants for GR binding (Kd), the EC_{50}s for TAT enzyme induction (EC_{50}), and their intrinsic activity to activate TAT enzyme relative to Dexamethasone (TAT IA), the standard synthetic GR agonist. We noted that there is no clear correlation between GR binding, EC_{50} or TAT IA for these compounds, which led us to further characterize how these steroids induce the TAT gene.

Using a rat hepatoma cell line, we examined induction of TAT mRNA by these steroids. Cells were treated 3 h at the EC_{50} of TAT induction determined previously for each steroid [16]: 17P (4 μM), PRG (4 μM), DOC (600 nM), CCS (25 nM), CRT (50 nM), ALD (400 nM) or DEX (8 nM). Total RNA was isolated and subjected to RT-PCR and the products separated by agarose gel electrophoresis. As expected ETH, 17P, PRG and DOC did not induce significant accumulation of TAT mRNA, while CCS, CRT, ALD and DEX all increased TAT mRNA levels (Fig. 1A). These results are largely consistent with the induction of TAT enzymatic activity by these steroids [16], however the lack of significant DOC-induced TAT mRNA lead us to repeat these experiments using saturating concentrations for all the compounds, which yielded similar results (data not shown). To determine whether GR is specifically recruited to the TAT promoter upon steroid treatment, ChIP assays were performed (Fig. 1B) after treating rat hepatoma cells with steroids identically as in Fig. 1A. Consistent with the TAT mRNA expression data, we observed that ETH, 17P and PRG failed to induce significant recruitment of GR, while CCS, CRT, ALD and DEX all induced GR recruitment to the TAT–GRE (Fig. 2B). However, DOC induced robust recruitment of GR to the TAT–GRE, equal to CCS and DEX, yet TAT mRNA induction by DOC was almost undetectable (refer to Fig. 1A). We observed similar results using saturating concentrations for all compounds (data not shown). The lack of DOC-induced TAT mRNA accumulation was not due simply to variations in the kinetics of TAT induction by DOC *vs.* DEX, since we did not detect significant levels of TAT mRNA accumulation upon DOC treatment throughout a 72-hour treatment regimen (Fig. 1C).

We next determined if there were any changes in the recruitment of the transcriptional cofactor p300 induced by DOC and DEX to the TAT–GRE. p300 is a cofactor central to transcription initiation that functions in histone acetylation [23]. We treated rat hepatoma cells with DOC or DEX, and examined p300 occupancy by ChIP. Surprisingly, recruitment of p300 to the TAT–GRE was very similar between DOC and DEX treatments at 1 and 3 h of treatment (Fig. 1D). Taken together, these data demonstrate that although DOC induces GR to occupy the TAT–GRE, GR is not competent to induce TAT mRNA, despite the presence of p300 at the TAT promoter.

We next asked if the effect of DOC on p300 recruitment and RNA induction were specific to the TAT gene, or if this phenomenon is observable at another GC-inducible GR target gene, Sulfonyltransferase 1A1 (*sulta1a1*) [19]. Indeed, DOC fails to induce *sult1a1* mRNA over a range of concentrations (Fig. 2A), yet p300 is recruited to the GRE of the *sult1a1* promoter in response to DOC as efficiently as DEX (Fig. 2B). These data demonstrate that our observations at the TAT promoter are not particular only to the TAT gene, at least in rat hepatoma cells.

We then asked if DOC could drive GR-dependent adipocyte differentiation, which is a more complex physiological readout reflecting multiple changes in gene expression driven by GR. Using mouse 3T3-L1 pre-adipocytes, where DEX, insulin, and 3-isobutyl-1-methylxanthine (IBMX) act together to drive adipocyte differentiation, we assessed the ability of DOC to replace DEX in the differentiation cocktail. DEX induced adipocyte differentiation, as assayed by oil red O staining (a measure of intracellular fat

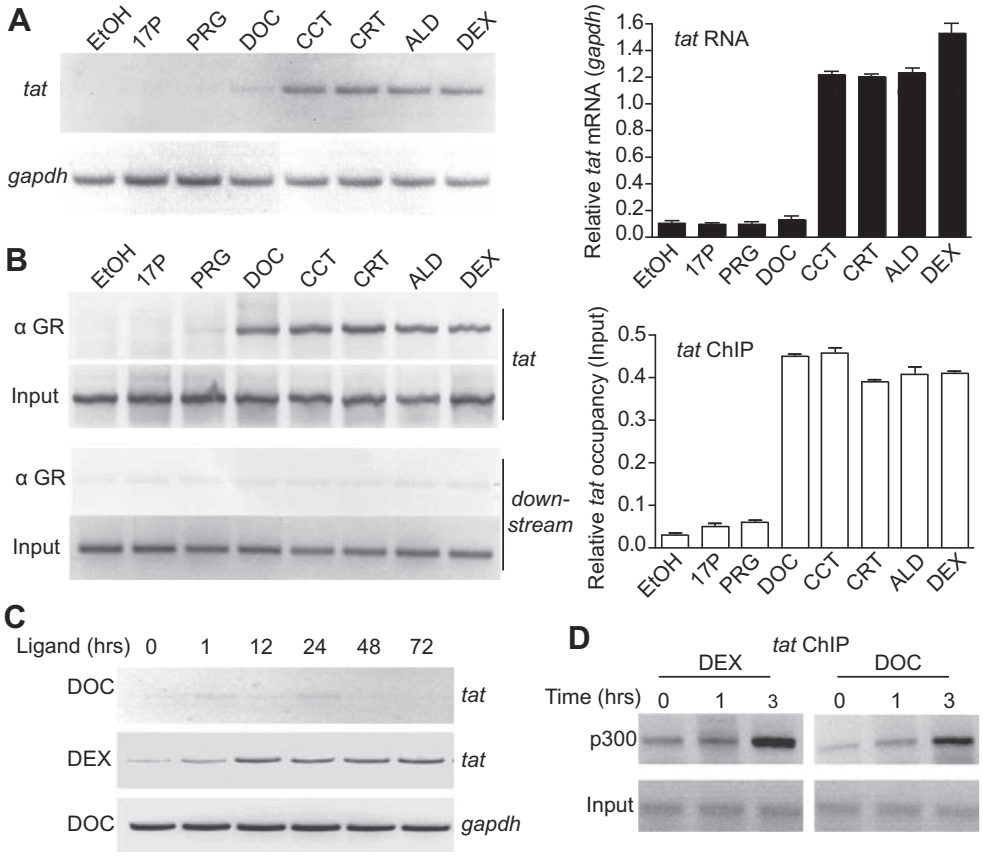


Fig. 1. DOC induces GR recruitment to TAT without inducing mRNA. (A) Rat hepatoma cells were treated with ethanol or indicated steroid for 3 h at the EC_{50} of TAT activation [16], total RNA isolated and subjected to RT-PCR with primers specific for the TAT and GAPDH mRNAs, quantitation on right. (B) Cells treated with steroids identically as in (A), then subjected to ChIP using a polyclonal anti-GR antibody. Precipitates were amplified using primers flanking the GRE necessary for TAT activation by GCs (TAT–GRE), or to a region ~5 kb downstream of the TAT promoter (control), quantitation on right. (C) Rat hepatoma cells were treated with 600 nM DOC or 8 nM DEX for 0, 1, 12, 24, 48 or 72 h. Total RNA isolated and subjected to RT-PCR as in (A). (D) Rat hepatoma cells treated with 600 nM DOC or 8 nM DEX over indicated time course subjected to ChIP using polyclonal anti-p300 antibodies, precipitates then amplified using primers flanking TAT–GRE. Input represents 0.5% of the total chromatin. All experiments repeated three times with similar results, error bars in this and all figures represent standard error of the mean.

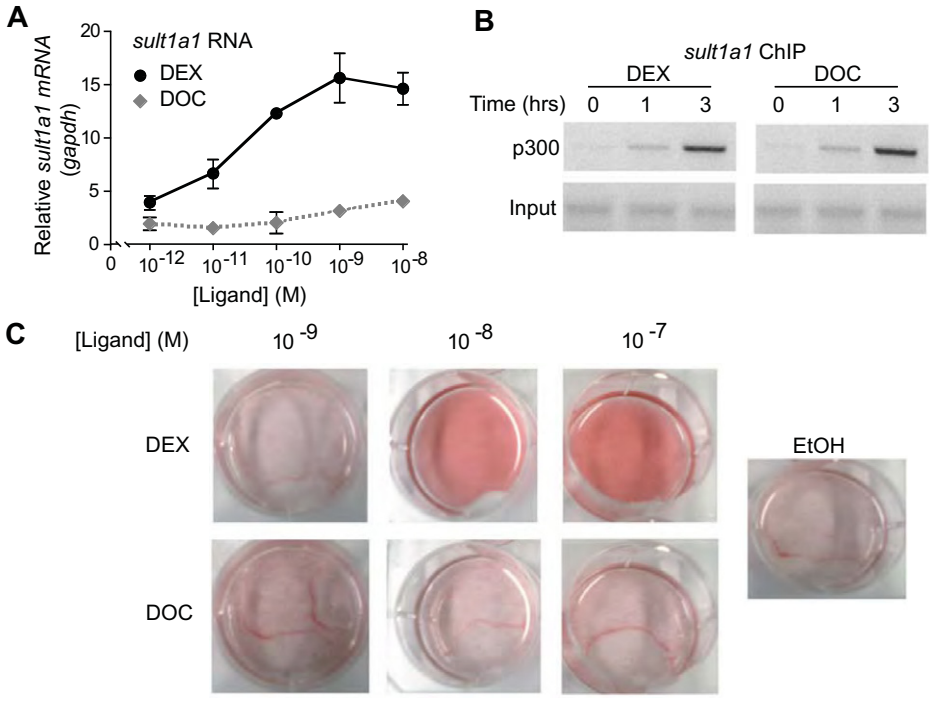


Fig. 2. DOC effects on GR are not specific to TAT. (A) Rat hepatoma cells treated with indicated concentrations of DOC or DEX for 24 h, total RNA isolated and subjected to RT-PCR with primers for *sult1a1* and *gapdh* mRNA, results quantitated relative to *gapdh*, repeated twice with similar results. (B) Rat hepatoma cells were treated with 10 nM DEX or DOC over 3 h, fixed with formaldehyde and subjected to ChIP using polyclonal anti-p300 antibodies. Precipitates were amplified using primers flanking the GRE in the *sult1a1* promoter. Input represents 0.5% of the total chromatin, experiment repeated three times with similar results. (C) Confluent cultures of 3T3-L1 cells were placed in differentiation medium that contained IBMX, insulin with DMSO (CTRL), DEX, and DOC at indicated concentrations and stained with oil red.

accumulation), whereas DOC failed to induce differentiation (Fig. 2C). Other steroids that induce TAT transcription were also able to promote differentiation similar to DEX (data not shown). These data demonstrate that DOC is unable to induce GR-dependent adipocyte differentiation in 3T3-L1 cells.

Phosphorylation of GR has been shown to modulate GR transcriptional activity [24]. However, we did not observe any significant differences in DOC *vs.* DEX-induced GR phosphorylation at serines 203, 211 and 226 (Fig. 3A), nor are there any differences in the chromatin recruitment of specific GR phospho-isoforms to the TAT–GRE by ChIP (Fig. 3B). These data suggest that DOC and DEX do not induce different phosphorylations on GR, and so phosphorylation of GR is not likely the mechanism accounting for differences in target gene induction.

Molecular docking was then performed to determine how DOC binds to GR. Comparison of the GR–DEX structure (Fig. 4A) and our GR–DOC model (Fig. 4B) reveals that both ligands make similar interactions with GR, and DOC fits well within the GR ligand-binding pocket. The most significant difference lies in the hydroxyl group at the C-11 position of the steroid C-ring, which is absent in DOC relative to DEX. In the GR–DEX structure, the amide side chain of N564 in helix 3 simultaneously forms hydrogen bonds with C-11 hydroxyl group of DEX and backbone carbonyl of E748, which is present in a loop preceding the C-terminal activation function 2 (AF-2) helix. This hydrogen bond network induced by DEX stabilizes helix 3 and positions the AF-2 helix in an "active" conformation. The GR–DOC model predicts that this hydrogen bond network will not form, altering the induced structure of GR. Based on this model, we hypothesize that DOC induces a GR conformation that is distinct from the DEX-bound form, which correlates with reduced GR transcriptional activation.

We next probed protease sensitivity differences between GR–DEX *vs.* GR–DOC. Radiolabeled GR was synthesized *in vitro*, bound with 100 nM DEX, DOC or left unbound (EtOH), then digested with

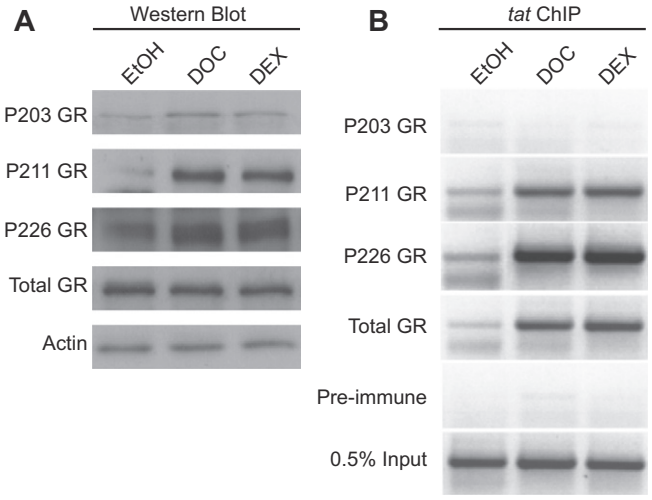


Fig. 3. DOC and DEX induce similar phosphorylation and TAT recruitment of GR-phospho-isoforms. (A) Western blots of rat hepatoma whole cell extracts after 3 h of treatment with EtOH, 600 nM DOC or 8 nM DEX, probed as indicated on the left. (B) Rat hepatoma cells treated as in (A), subjected to ChIP using antibodies indicated on the left.

increasing amounts of elastase. DEX produced a distinct digestion pattern of GR relative to the unbound control (Fig 4B; compare lanes 2–5 to 10–13), with a prominent protected fragment at the highest elastase concentration. When bound to DOC, GR showed an increase in protection from proteolytic degradation compare to control, but less than that observed with DEX (compare lanes 3–5 and 7–9). Additionally, the stable fragment in the GR–DEX complex at the highest elastase concentration is not observed in DOC bound GR (arrowhead, compare lanes 5 and 9). Thus, these

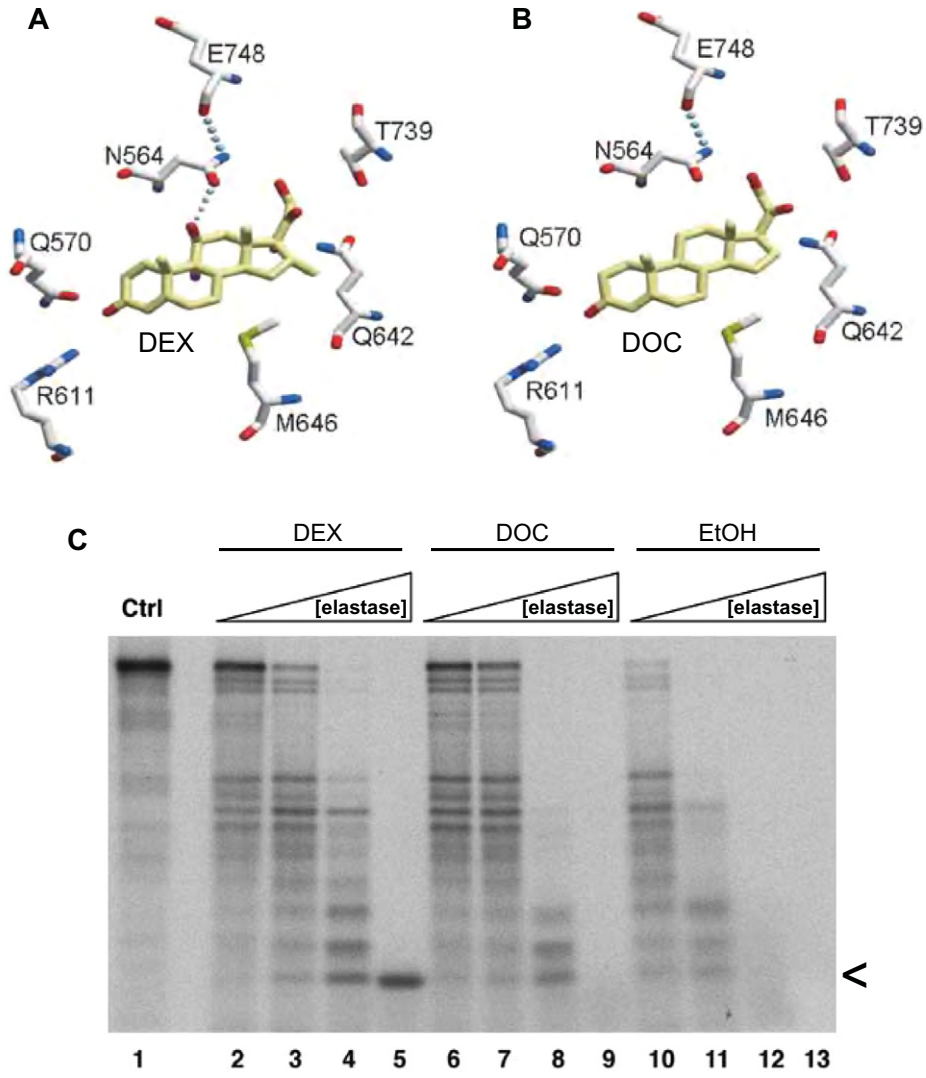


Fig. 4. Changes in GR conformation induced by DOC and DEX. (A) DEX (X-ray structure, 1M2Z.pdb) and (B) DOC (docked molecular simulation) are shown with yellow-color carbon atoms. Dashed lines show critical hydrogen bond networks. (C) 35S-methionine-labeled rat GR was synthesized in an *in vitro* transcription/translation system in the presence of ethanol or 100 nM DEX or DOC and incubated with increasing amounts of elastase. The polypeptide fragments were separated by SDS–PAGE, fixed, dried and exposed to X-ray film. (For interpretation of the references to color in this figure legend, the reader is referred to the web version of this article.)

data demonstrate that DOC-bound GR induces an elastase digestion pattern between that of DEX and the no-hormone receptor, suggesting that DOC and DEX induce distinct GR conformations.

4. Discussion

The regulation of TAT activity by steroids has been extensively studied, and is a paradigm for steroid-induced gene expression. Our findings indicate that TAT mRNA induction and GR recruitment to the TAT–GRE largely parallels the induction of TAT enzyme activity by the steroids examined. Surprisingly, DOC induces GR and p300 recruitment to the TAT–GRE as efficiently as DEX, but fails to induce significant TAT mRNA expression. Homology modeling and protease digestion experiments suggest that DOC and DEX induce different conformations in GR. Thus, DOC binding changes the transcriptional regulatory activity of GR at a step downstream of receptor and p300 recruitment, perhaps through different GR conformations induced by DOC *vs.* DEX.

How DOC induces GR and p300 recruitment to TAT–GRE to the same extent as DEX, yet does not cause mRNA induction, remains an unanswered question. DOC differs from DEX at five chemical positions on the steroid ring, including the lack of a hydroxyl at the C-11 position of the steroid C-ring in DOC (Fig. S1). In the GR–DEX crystal structure, this particular hydroxyl group makes a critical contact with N564 of GR [20]. Mutation of N564 to alanine in GR results in a substantial decrease in DEX-induced receptor transcriptional activity, suggesting that the C-11 hydroxyl interaction with N564 contributes to stabilization of the activated conformation of GR [25]. These observations of GR–DEX are consistent with our structural simulations of GR–DOC (Fig. 4A), however the other chemical differences between DOC and DEX could also contribute to alter GR activity.

GRIP1 is a known GR coactivator, but it has also been shown that GRIP1 can function as a GR corepressor at certain GREs [26] though a domain distinct from the GRIP1 activation domain [27,28]. It is tempting to speculate that the conformation of GR–DOC at the TAT–GRE may facilitate the GRIP1 corepressor conformation. This might help explain why GR–DOC has a dominant-inhibitory effect on TAT gene expression, despite the presence of GR and p300 at the TAT–GRE.

There have been several reports of nuclear receptor ligands being capable of inducing receptor recruitment while being

transcriptionally silent [29–32]. Dissociation of GR recruitment and activation has also been observed for aryl pyrazole compounds, which can induce GR occupancy at target genes, but were inactive in transcription [33]. It is interesting to note that a synthetic GR ligand (AL-438) that retains anti-inflammatory efficacy without affecting bone and glucose metabolism reduces the interaction between GR and peroxisomal proliferator-activated receptor coactivator-1(PGC-1), while maintaining GRIP1 interaction [34].

Our data suggest that lead anti-inflammatory compounds could be designed to occupy the promoter of GR target genes without activating transcription. This activity could enhance anti-inflammatory efficacy by competing with "transcriptionally active" GR for these promoters. It is very important to note that progesterone, despite having reasonable affinity for GR (Kd = 50 nM) and only differing from DOC by a single atom (Fig. S1), cannot induce GR recruitment to TAT–GRE (Fig. 1B). It therefore seems possible to define structure–activity relationships that result in high-affinity binding to GR, yet a receptor that is transcriptionally silent. Given that many of the deleterious side affects of GCs manifest through DNA-binding dependent GR activation of target genes containing classic GREs in their promoters [4], this type of structure activity analysis could help focus anti-inflammatory lead development into active, but transcriptionally silent compounds. This could aid in minimizing the side affects of anti-inflammatory compounds currently under development.

Acknowledgments

We thank Holly A. Ingraham, Keith Yamamoto, Herb Samuels and Susan Logan for critically reading the manuscript. This work was supported by NIGMS K12 IRACDA postdoctoral fellowship (RDB) and by Philip Morris USA Inc. and Philip Morris International (MJG).

Appendix A. Supplementary data

Supplementary data associated with this article can be found, in the online version, at doi:10.1016/j.bbrc.2012.03.084.

References

[1] A. Munck, P.M. Guyre, Glucocorticoid physiology, pharmacology and stress, Adv. Exp. Med. Biol. 196 (1986) 81–96.
[2] P.J. Barnes, Anti-inflammatory actions of glucocorticoids: molecular mechanisms, Clin. Sci. (Lond.) 94 (1998) 557–572.
[3] H. Schacke, W.D. Docke, K. Asadullah, Mechanisms involved in the side effects of glucocorticoids, Pharmacol. Ther. 96 (2002) 23–43.
[4] J.N. Miner, Designer glucocorticoids, Biochem. Pharmacol. 64 (2002) 355–361.
[5] M.R. Yudt, J.A. Cidlowski, The glucocorticoid receptor: coding a diversity of proteins and responses through a single gene, Mol. Endocrinol. 16 (2002) 1719–1726.
[6] B.D. Jenkins, C.B. Pullen, B.D. Darimont, Novel glucocorticoid receptor coactivator effector mechanisms, Trends Endocrinol. Metab. 12 (2001) 122–126.
[7] K.R. Yamamoto, Multilayered control of intracellular receptor function, Harvey Lect. 91 (1995) 1–19.
[8] R.M. Nissen, K.R. Yamamoto, The glucocorticoid receptor inhibits NFkappaB by interfering with serine-2 phosphorylation of the RNA polymerase II carboxy-terminal domain, Genes Dev. 14 (2000) 2314–2329.
[9] K.R. Yamamoto, B.D. Darimont, R.L. Wagner, J.A. Iniguez-Lluhi, Building transcriptional regulatory complexes: signals and surfaces, Cold Spring Harbor Symp. Quant. Biol. 63 (1998) 587–598.
[10] D.K. Granner, J.L. Hargrove, Regulation of the synthesis of tyrosine aminotransferase: the relationship to mRNA TAT, Mol. Cell. Biochem. 53–54 (1983) 113–128.
[11] J.B. Dietrich, Tyrosine aminotransferase: a transaminase among others?, Cell Mol. Biol. 38 (1992) 95–114.
[12] T. Grange, L. Cappabianca, M. Flavin, H. Sassi, H. Thomassin, *In vivo* analysis of the model tyrosine aminotransferase gene reveals multiple sequential steps in glucocorticoid receptor action, Oncogene 20 (2001) 3028–3038.
[13] T. Grange, J. Roux, G. Rigaud, R. Pictet, Two remote glucocorticoid responsive units interact cooperatively to promote glucocorticoid induction of rat tyrosine aminotransferase gene expression, Nucleic Acids Res. 17 (1989) 8695–8709.
[14] H.M. Jantzen, U. Strahle, B. Gloss, F. Stewart, W. Schmid, M. Boshart, R. Miksicek, G. Schutz, Cooperativity of glucocorticoid response elements located far upstream of the tyrosine aminotransferase gene, Cell 49 (1987) 29–38.
[15] D.K. Granner, S. Hayashi, E.B. Thompson, G.M. Tomkins, Stimulation of tyrosine aminotransferase synthesis by dexamethasone phosphate in cell culture, J. Mol. Biol. 35 (1968) 291–301.
[16] H.H. Samuels, G.M. Tomkins, Relation of steroid structure to enzyme induction in hepatoma tissue culture cells, J. Mol. Biol. 52 (1970) 57–74.
[17] G.G. Rousseau, J.D. Baxter, G.M. Tomkins, Glucocorticoid receptors: relations between steroid binding and biological effects, J. Mol. Biol. 67 (1972) 99–115.
[18] J.N. Vanderbilt, R. Miesfeld, B.A. Maler, K.R. Yamamoto, Intracellular receptor concentration limits glucocorticoid-dependent enhancer activity, Mol. Endocrinol. 1 (1987) 68–74.
[19] R.D. Blind, M.J. Garabedian, Differential recruitment of glucocorticoid receptor phospho-isoforms to glucocorticoid-induced genes, J. Steroid Biochem. Mol. Biol. 109 (2008) 150–157.
[20] R.K. Bledsoe, V.G. Montana, T.B. Stanley, C.J. Delves, C.J. Apolito, D.D. McKee, T.G. Consler, D.J. Parks, E.L. Stewart, T.M. Willson, M.H. Lambert, J.T. Moore, K.H. Pearce, H.E. Xu, Crystal structure of the glucocorticoid receptor ligand binding domain reveals a novel mode of receptor dimerization and coactivator recognition, Cell 110 (2002) 93–105.
[21] R.K. Bledsoe, K.P. Madauss, J.A. Holt, C.J. Apolito, M.H. Lambert, K.H. Pearce, T.B. Stanley, E.L. Stewart, R.P. Trump, T.M. Willson, S.P. Williams, A ligand-mediated hydrogen bond network required for the activation of the mineralocorticoid receptor, J. Biol. Chem. 280 (2005) 31283–31293.
[22] T.A. Halgren, Characterization of MMFF94, MMFF94s, and other widely available force fields for conformational energies and for intermolecular-interaction energies and geometries, J. Comp. Chem. 20 (1999) 730–748.
[23] H.M. Chan, N.B. La Thangue, P300/CBP proteins: HATs for transcriptional bridges and scaffolds, J. Cell Sci. 114 (2001) 2363–2373.
[24] N. Ismaili, M.J. Garabedian, Modulation of glucocorticoid receptor function via phosphorylation, Ann. N.Y. Acad. Sci. 1024 (2004) 86–101.
[25] R.K. Bledsoe, E.L. Stewart, K.H. Pearce, Structure and function of the glucocorticoid receptor ligand binding domain, Vitam. Horm. (N.Y.) 68 (2004) 49–91.
[26] I. Rogatsky, K.A. Zarember, K.R. Yamamoto, Factor recruitment and TIF2/GRIP1 corepressor activity at a collagenase-3 response element that mediates regulation by phorbol esters and hormones, EMBO J. 20 (2001) 6071–6083.
[27] I. Rogatsky, H.F. Luecke, D.C. Leitman, K.R. Yamamoto, Alternate surfaces of transcriptional coregulator GRIP1 function in different glucocorticoid receptor activation and repression contexts, Proc. Nat. Acad. Sci. U.S.A. 99 (2002) 16701–16706.
[28] Y. He, S.S. Simons Jr., STAMP, a novel predicted factor assisting TIF2 actions in glucocorticoid receptor-mediated induction and repression, Mol. Cell. Biol. 27 (2007) 1467–1485.
[29] P. Zhu, S.H. Baek, E.M. Bourk, K.A. Ohgi, I. Garcia-Bassets, H. Sanjo, S. Akira, P.F. Kotol, C.K. Glass, M.G. Rosenfeld, D.W. Rose, Macrophage/cancer cell interactions mediate hormone resistance by a nuclear receptor derepression pathway, Cell 124 (2006) 615–629.
[30] D. Masiello, S. Cheng, G.J. Bubley, M.L. Lu, S.P. Balk, Bicalutamide functions as an androgen receptor antagonist by assembly of a transcriptionally inactive receptor, J. Biol. Chem. 277 (2002) 26321–26326.
[31] Y. Shang, M. Myers, M. Brown, Formation of the androgen receptor transcription complex, Mol. Cell 9 (2002) 601–610.
[32] Y. Shang, X. Hu, J. DiRenzo, M.A. Lazar, M. Brown, Cofactor dynamics and sufficiency in estrogen receptor-regulated transcription, Cell 103 (2000) 843–852.
[33] J.C. Wang, N. Shah, C. Pantoja, S.H. Meijsing, J.D. Ho, T.S. Scanlan, K.R. Yamamoto, Novel arylpyrazole compounds selectively modulate glucocorticoid receptor regulatory activity, Genes Dev. 20 (2006) 689–699.
[34] M.J. Coghlan, P.B. Jacobson, B. Lane, M. Nakane, C.W. Lin, S.W. Elmore, P.R. Kym, J.R. Luly, G.W. Carter, R. Turner, C.M. Tyree, J. Hu, M. Elgort, J. Rosen, J.N. Miner, A novel antiinflammatory maintains glucocorticoid efficacy with reduced side effects, Mol. Endocrinol. 17 (2003) 860–869.

Biochemical and Biophysical Research Communications 420 (2012) 845–850

Contents lists available at SciVerse ScienceDirect

Biochemical and Biophysical Research Communications

journal homepage: www.elsevier.com/locate/ybbrc

Gene expression profile in the liver of *Rana catesbeiana* tadpoles exposed to low temperature in the presence of thyroid hormone

Kazuki Mochizuki [a], Toshinao Goda [a], Kiyoshi Yamauchi [b,*]

[a] Laboratory of Nutritional Physiology, School of Food and Nutritional Sciences, The University of Shizuoka, Shizuoka 422-8526, Japan
[b] Department of Biological Science, Faculty of Science, Shizuoka University, Shizuoka 422-8529, Japan

ARTICLE INFO

Article history:
Received 6 March 2012
Available online 23 March 2012

Keywords:
Amphibian metamorphosis
Gene activation
Liver
Low temperature
Rana catesbeiana

ABSTRACT

Amphibian metamorphosis, which is controlled by thyroid hormone (TH), is highly temperature-sensitive. Using real-time PCR, we investigated the gene expression profile in the liver of *Rana catesbeiana* tadpoles kept at 28 and 4 °C and treated with 5 nM 3,3′,5-triiodothyronine (T3). Out of the 48 genes tested, 12 were up-regulated at 4 °C in T3-treated or untreated tadpoles. These included genes involved in energy metabolism, transcription, and translation. Four TH-response genes, including TH receptor β (TRβ) gene, showed no response to T3 at 4 °C. Deiodinase III was the only gene down-regulated at 4 °C. Chromatin immunoprecipitation assays showed that CCAAT/enhancer-binding protein 2 gene activation by cold exposure was associated with an increase in the acetylation of histone H3 at lysine 9, whereas TRβ gene activation by T3 at 28 °C was associated with an increase in the methylation of histone H3 at lysine 36 with no T3-dependent changes in methylation states on cold exposure. Our results suggest that the transfer of TH signal to chromatin modifications on a primary early TH response gene was specifically blocked by exposure to cold.
© 2012 Elsevier Inc. All rights reserved.

1. Introduction

The environmental temperature influences many biological activities in ectotherms. Amphibian metamorphosis is highly sensitive to temperature. Although amphibian metamorphosis is controlled by thyroid hormone (TH), the TH response is abolished at 5 °C even if tadpoles are treated with the active form of TH, 3,3′,5-triiodothyronine (T3) [1]. In natural environments, *Rana catesbeiana* tadpoles hatch in spring or early summer, then grow and differentiate until autumn. In relatively higher latitudes or mountain ranges in the northern hemisphere, most tadpoles, especially those from late-spawning frogs, do not metamorphose during winter, but do transform into froglets in the following spring or summer [2].

Amphibian metamorphosis is a postembryonic developmental process governed by a hierarchy of TH-target genes that consist of primary early and secondary late response genes [3]. Tissue-specific activation or suppression of primary early response genes may affect gene regulation cascades responsible for tissue-specific transformation during metamorphosis. Thyroid hormone receptors (TRs) α and β bind to specific *cis*-acting DNA sequences, known as TH response elements (TREs), in the regulatory regions of primary early response genes [3]. The binding of TH to TRs recruits coactivators and chromatin modifiers to the TRE regions and with histone modifications, such as acetylation and methylation, results in a transcriptionally active state [4]. Changes in histone modification are thought to influence RNA polymerase II activity [5].

Findings from studies assessing the molecular mechanisms of the low temperature arrest of metamorphosis have shown that there are several temperature-sensitive processes in the TH-signaling pathway [6–10]. Although there are some discrepancies among the reported findings, these findings suggest that TH binds to TRs in the nucleus at 4 °C [8–10]. However, little is known about how TH signaling and gene expression is affected when tadpole metamorphosis is arrested by exposure to cold temperatures.

The objective of this study was to determine the effect of exposure to cold temperatures on TH-dependent morphological development, TH-dependent and overall gene expression, and the acetylation and methylation of histone H3 during tadpole metamorphosis. To do this we analyzed the gene expression profile and the acetylation and methylation states of histone H3 in the liver of *R. catesbeiana* tadpoles either treated with or not treated with T3 at 4 and 28 °C for 3 days.

2. Materials and methods

2.1. Animals and treatment

Premetamorphic *R. catesbeiana* tadpoles (TK stages X–XI [11]) were obtained from Saitama Amphibian Institute, Saitama, Japan.

* Corresponding author at: Department of Biological Science, Faculty of Science, Shizuoka University, Ohya 836, Suruga-ku, Shizuoka 422-8529, Japan. Fax: +81 54 238 0986.
E-mail address: sbkyama@ipc.shizuoka.ac.jp (K. Yamauchi).

0006-291X/$ - see front matter © 2012 Elsevier Inc. All rights reserved.
http://dx.doi.org/10.1016/j.bbrc.2012.03.085

The tadpoles were kept in 4 L of aerated and dechlorinated tap water at 28 °C and fed boiled spinach three times a week. After 7 days of acclimation, 2 aquaria (6 tadpoles/aquarium) were moved into a cold room (4 °C) the evening before T3 treatment and 2 aquaria were kept at 28 °C. 3,3′,5-Triiodothyronine treatment began the following day: 1 aquarium at 4 °C and 1 aquarium at 28 °C were treated with 5 nM T3 (Sigma–Aldrich, St. Louis, MI, USA) for 3 days. T3 treatment was renewed every day by changing the dechlorinated tap water containing T3. Tadpoles were not fed during the 3-day treatment period. After the 3-day treatment period, the tadpoles were anesthetized with 0.02% 3-aminobenzoic acid ethyl ester (Sigma–Aldrich), their body length and tail height measured, and their liver dissected, in accordance with the code of ethics on the Animal Welfare Committee of Shizuoka University.

2.2. Total RNA extraction and real-time PCR analysis of gene expression

We used the acid guanidinium–thiocyanate–phenol–chloroform method [12] to extract total RNA from the liver samples. After extraction, RNA was resuspended in diethylpyrocarbonate-treated water and quantified by UV absorption. Samples of RNA (1 μg) were treated with reverse transcriptase (SuperScript™ III RT, Invitrogen, Tokyo, Japan) as per the manufacturer's instructions. Sequence data of *R. catesbeiana* nuclear protein-coding genes, including TH response genes, were arbitrarily collected from public databases. The names of genes investigated and primer sequences for PCR were listed in Supplementary Table 1. Specific RNA species were amplified by real-time PCR using the LightCycler® 480 SYBR Green I Master (Roche Molecular Biochemicals, Tokyo), a LightCycler® 480 Real-Time PCR System (Roche). The PCR System program included denaturation at 95 (5 min) then 50 cycles of 95 (10 s), 60 (10 s), and 72 °C (6 s). The amounts of specific RNA species were quantified using the formula 2^{-Ct}, where the endpoint, Ct, was defined as the PCR cycle number that crossed an arbitrarily placed signal threshold. To standardize each experiment, the amount of a specific transcript was divided by the amount of β-actin transcript.

2.3. Preparation of nuclei and the chromatin immunoprecipitation (ChIP) assay

To make chromatin solution, proteins were cross-linked with DNA by homogenizing liver samples (~0.5 g) in 10 mL of fixation solution (1% formaldehyde, 4.5 mM HEPES, pH 8.0, 9 mM NaCl, 0.09 mM EDTA, and 0.04 mM EGTA) and incubating this mixture for 30 min at 37 °C [13]. The reaction was stopped after 30 min by adding 1 mL of 1.5 M glycine to the reaction mixture. The mixture was then washed with FACS solution (1 × PBS, 2% bovine serum and 0.05% sodium azide) and centrifuged twice for15 min at 1600×*g* at 4 °C. The pellet was vortexed in 1 mL of SDS lysis buffer (50 mM Tris, pH 8.0, 10 mM EDTA, 1% SDS) then incubated for 2 h on ice to solubilize the cells. The lysate was sonicated (12 × 30-second pulses; Sonifier, Branson Ultrasonics Corp., CT, USA) to obtain chromatin fragments between 200 and 500 bp in length. The resulting solution was centrifuged for 15 min at 20,000×*g* at 6–8 °C to remove debris. The protein concentration of the supernatant was quantified using the Lowry method [14] then adjusted to 3.24 mg/mL to make a chromatin solution. For each ChIP assay [15], 28 μL of chromatin solution was added with 0.6 μg of antibody. The antibodies were anti-acetylayted histone H3 lysine (K) 9 (Millipore), anti-mono-, anti-di-, and anti-tri-methylated histone H3-K4 (Abcam Japan, Tokyo, Japan), anti-mono-, anti-di-, and anti-tri-methylated histone H3-K9 (Millipore), anti-mono-, anti-di-, and anti-tri-methylated histone H3-K36 (Abcam Japan), and normal rabbit IgG (Sigma). Real-time PCR was done using the following primers (i) TRβ coding region +200 to +400: forward 5′-atttggttttggacgacagc-3′ and reverse 5′-ctggtgtcggttctggtttt-3′; (ii) CCAAT/enhancer-binding protein 1 (C/EBP-1) coding region +200 to +400: forward 5′-catagacatcagcgcctacatc-3′ and reverse 5′-gtcct gcttgctgttatggaa-3′ and (iii) C/EBP-2 coding region +200 to +400: forward 5′-atgagagcgccatagacttca-3′ and reverse 5′-cgttcttgct gttgaagaggt-3′. The amounts of specific RNA species were quantified using the formula 2^{-Ct}. The Ct values of the ChIP signals were expressed as percentages of the ChIP signals for the input DNA.

2.4. Statistical analysis

All data are expressed as mean ± standard error of the mean (SEM). Differences between two groups for multiple comparisons were analyzed by the Steel–Dwass test following the Kruskal–Wallis test. $P < 0.05$ was considered to be significantly different.

3. Results

3.1. T3-induced tadpole metamorphosis arrested by exposure to cold

The 3-day exposure of tadpoles to low temperature arrested the progress of T3-induced metamorphosis; the T3-dependent morphologic and transcriptional changes detected at 28 °C were completely abolished at 4 °C. Treatment with T3 significantly decreased the tail height/body length ratio of tadpoles at 28 °C [16] but not at 4 °C (Fig. 1). Treatment with T3 at 28 °C also significantly increased the amount of four TH response gene transcripts in the liver. These included genes for TRβ [16] (Fig. 2A), the urea cycle enzymes, carbamoyl phosphate synthetase 1 and ornithine transcarbamoylase (Fig 2C and D), and C/EBP-1 (Fig. 2N). However at 4 °C, T3 treatment had little effect on the transcription of these genes (Fig 2A, C, D, and N). No genes down-regulated by T3 at 28 °C were detected. The expression of all other genes tested was not affected by the addition of T3 at 28 or 4 °C.

3.2. Transcriptional changes in the liver of tadpoles induced by exposure to cold

Transcriptional changes were evident in some, but not all, of the genes in the liver of tadpoles exposed to 4 °C. When comparing the control tadpoles, the amount of transcript for the arginase (Fig. 2E) was significantly greater and for 5-deiodinase type III (Fig. 2B) significantly lower at 4 °C than at 28 °C. When comparing

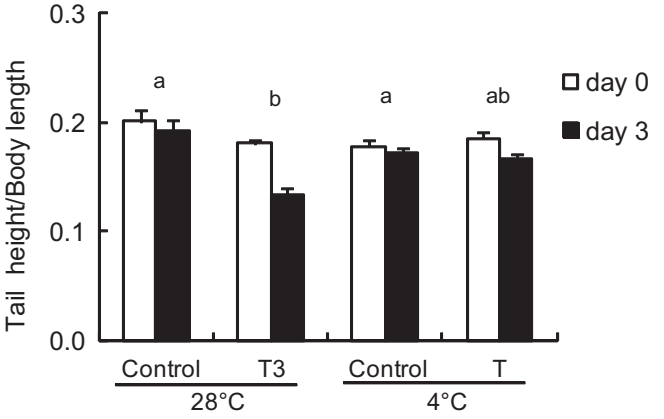


Fig. 1. The effect of cold temperature on the T3-induced change in tail height/body length ratio of *R. catesbeiana* tadpoles. Premetamorphic tadpoles kept at 28 or 4 °C in dechlorinated water were either treated or not treated with T3 for 3 days. The data are mean ± SEM ($n = 6$). The differences in the ratio between day 0 and day 3 were compared. Data for 28 °C have been reported previously [16].

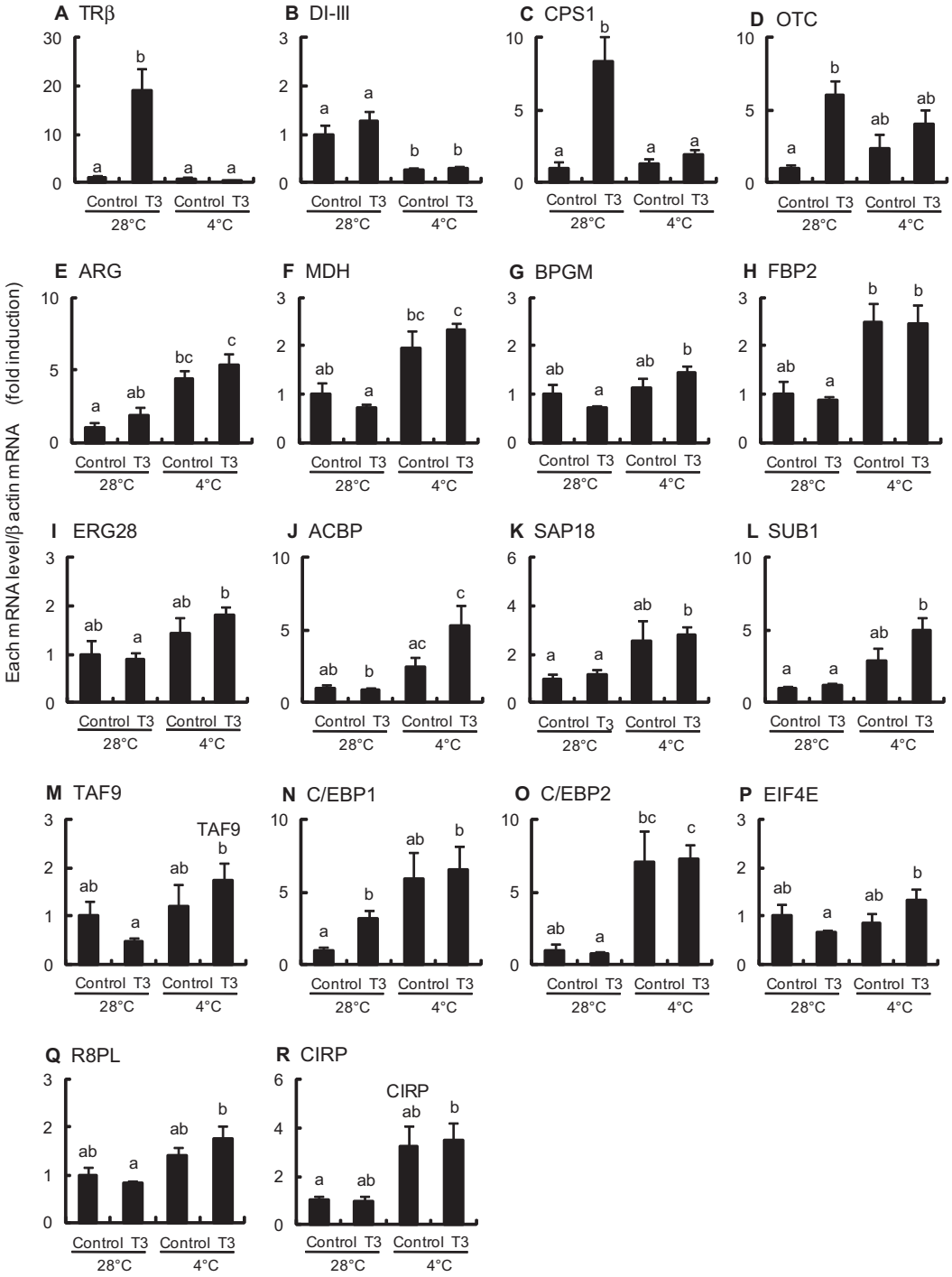


Fig. 2. Quantitative real-time PCR analyses of gene expression in the liver of *R. catesbeiana* tadpoles exposed to cold and T3. The results for each sample were normalized by the corresponding β-actin mRNA abundance. Livers were dissected from premetamorphic tadpoles either not treated (control) or treated (T3) with T3 in dechlorinated water at 4 and 28 °C. Transcript names investigated (A to R) are: TRβ, thyroid hormone receptor β; DI-III, 5-deiodinase type III; CPS1, carbamoyl phosphate synthetase 1; OTC, ornithine transcarbamoylase; ARG, arginase; MDH, malate dehydrogenase; BPGM, bisphosphoglycerate mutase; FBP2, 6-phosphofructo-2-kinase/fructose 2,6-bisphosphatase; ERG28, ergosterol biosynthetic protein 28; ACBP, acyl-CoA-binding protein; SAP18, histone deacetylase complex subunit SAP18; SUB1, RNA polymerase II transcriptional coactivator p15; TAF9, transcription initiation factor TFIID subunit 9; C/EBP, CCAAT/enhancer-binding protein; IF4E, eukaryotic translation initiation factor 4E; RPL8, ribosomal protein L8; CIRP, cold induced RNA-binding protein. The data are mean ± SEM ($n = 6$). Data for TRβ gene at 28 °C have been reported previously [16].

the tadpoles treated with T3, the amounts of 12 gene transcripts were significantly greater at 4 °C than at 28 °C. These included genes for a urea cycle enzyme (arginase, Fig. 2E), energy metabolism (malate dehydrogenase, Fig. 2F; bisphosphoglycerate mutase, Fig. 2G; 6-phosphofructo-2-kinase/fructose 2,6-bisphosphatase, Fig. 2H; ergosterol biosynthetic protein 28, Fig. 2I and acyl-CoA-binding protein, Fig. 2J), methylation/acetylation (histone deacetylase complex subunit SAP18, Fig. 2K), transcription (RNA polymerase II transcriptional coactivator p15, Fig. 2L; transcription initiation factor TFIID subunit 9, Fig. 2M and C/EBP-2, Fig. 2O), and translation (eukaryotic translation initiation factor 4E, Fig. 2P and ribosomal protein L8, Fig. 2Q). In particular, C/

EBP-2 was ninefold greater at 4 °C in tadpoles treated with T3. In contrast, the amounts of three gene transcripts, TRβ (Fig. 2A), 5-deiodinase type III (Fig. 2B) and carbamoyl phosphate synthetase I (Fig. 2C) were significantly lower at 4 °C than at 28 °C. The amounts of transcripts of other 35 genes were not significantly affected by cold exposure (data not shown).

3.3. Changes in acetylation and methylation states of histone H3 on TRβ and C/EBP genes in the liver of tadpoles induced by exposure to cold

Exposure to cold affected the acetylation and methylation states of histone H3 on the coding region (+200 bp to +400 bp) of the TRβ and C/EBP-2 genes. At 28 °C, treatment with T3 significantly increased the amount of di-and tri-methylated histone H3-K36 on the TRβ gene (Fig. 3C and D). The amount of di-methylated histone H3-K36 on the TRβ gene at 4 °C for both control and T3-treated tadpoles was similar to that for T3-treated tadpoles at 28 °C (Fig. 3C), whereas the fourfold increase in the amount of tri-methylated histone H3-K36 on the TRβ gene was abolished at 4 °C (Fig. 3D). At 4 °C, the amount of acetylated histone H3-K9 (Fig. 3I) on the C/EBP-2 gene was increased threefold in control tadpoles; T3 treatment had little effect on this increase. Among these changes, those for tri-methylated histone H3-K36 on the TRβ gene and acetylated histone H3-K9 on the C/EBP2 gene were associated with the transcriptional activation of the genes. We also detected significant decreases with T3 treatment in the amount of mono-methylated histone H3-K36 on the TRβ (Fig. 3B) and C/EBP-1 (Fig. 3F) genes at 4 °C; however, these changes were not associated with the transcriptional activation of the genes. The other histone modifications states tested, mono-, di-and tri-methylated histone H3-K4 and H3-K9, were not affected by T3 treatment or exposure to cold (data not shown).

4. Discussion

Our findings show that short-term exposure to cold arrested T3-induced metamorphosis of *R. catesbeiana* tadpoles and affected the gene expression profile in the liver. The transcription of almost all of the genes investigated was increased or did not change with

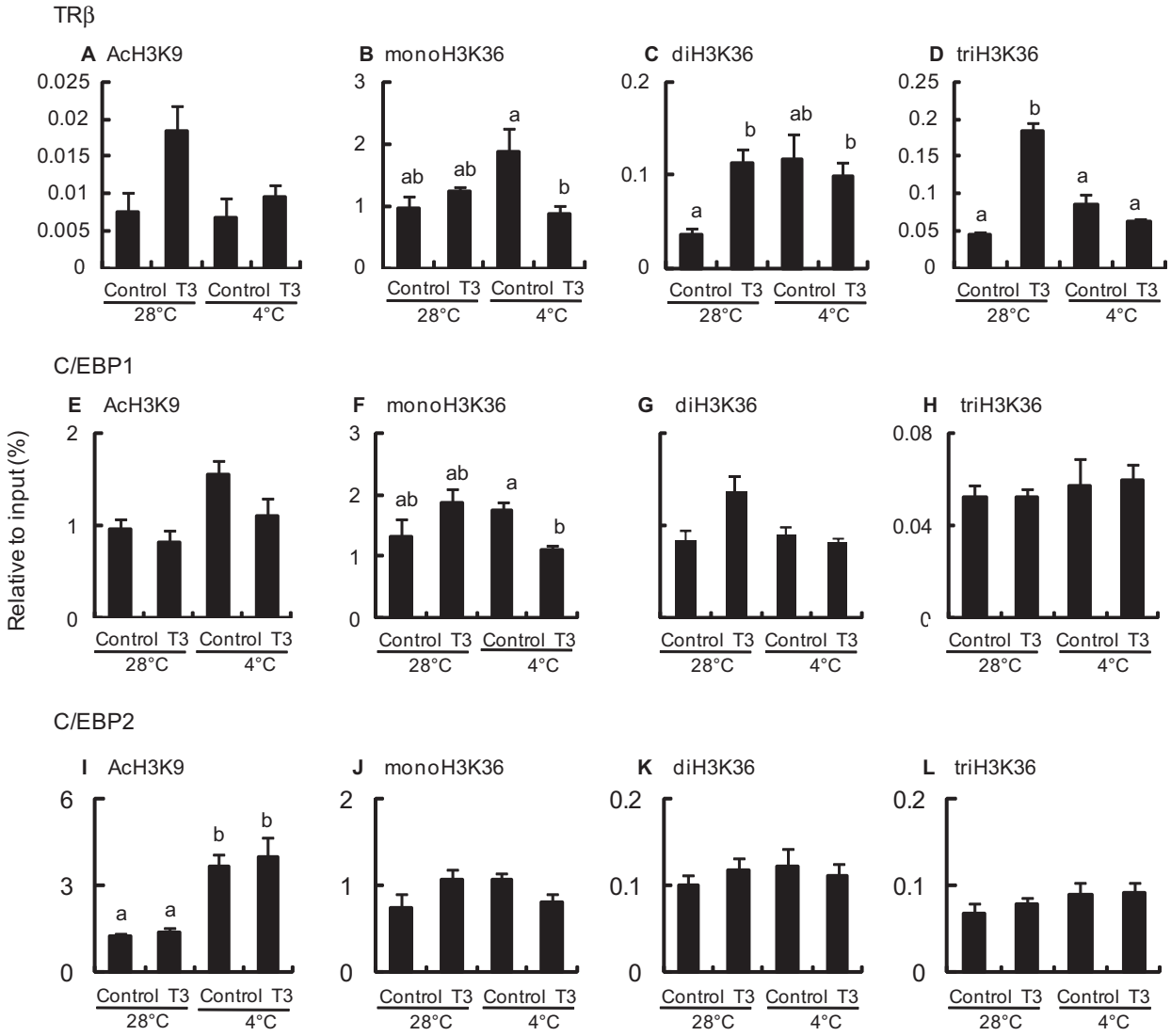


Fig. 3. Histone modification induced by exposure to cold in the liver of *R. catesbeiana* tadpoles. Acetylation of histone H3 at K9 (AcH3K9) and methylation of histone H3 at K36 (mono-, di- and tri-H3K36) were investigated within the +200 bp to +400 bp region of TRβ, C/EBP-1 and C/EBP-2 genes. ChIP signals were detected by quantitative real-time PCR following immunoprecipitation of acetylated histones H3K9 (A, E and I), and mono- (B, F and J), di- (C, G and K), and tri-methylated (D, H and L) H3K36. The data are mean ± SEM (n = 6 animals).

exposure to cold. In contrast to these responses, the T3-dependent transcriptional activation of TRβ gene was completely abolished by exposure to cold. Furthermore, the T3-dependent increase in the amount of tri-methylated H3-K36 on TRβ gene was also lost at 4 °C. These results suggest that a temperature-sensitive mechanism exists by which the transfer of the TH signal to the histones on TRβ gene is blocked at 4 °C.

4.1. An overview of gene expression in the liver of cold-exposed tadpoles

The exposure of *R. catesbeiana* tadpoles to cold for 3 days is unlikely to lead to the transcriptional suppression in the liver, as one quarter of the genes investigated in our study were up-regulated by exposure to cold. These genes include those involved in energy metabolism, transcription, and translation.

In general, temperatures lower than those considered optimal for metabolic activity decrease the activity of enzymes and other functional proteins, resulting in metabolic suppression. This phenomenon has been explained as the Q_{10} rule [17]. However, our gene expression profile in the liver did not obey the Q_{10} rule, suggesting that at least the transcriptional system in *R. catesbeiana* tadpoles is refractory to metabolic suppression by exposure to cold. This finding is in agreement with those from previous biochemical studies showing that temperature has little or no effect on the incorporation of ^{14}C-phenylalanine into proteins and ^{3}H-adenine into RNA [18]. To escape from simple Q_{10} relationships, ectotherms, including amphibians, would have to adapt to different temperatures to sustain relatively similar rates of metabolic activity [19]. In particular, up-regulation of genes for components of general transcription factors (RNA polymerase II transcriptional coactivator p15 and transcription initiation factor TFIID subunit 9), a translation factor (eukaryotic translation initiation factor 4E), and ribosome (ribosomal protein L8) would potentiate widely the synthesis of many proteins at transcriptional and translational levels.

Out of the 12 genes that were up-regulated by exposure to cold in our study, six are involved in energy metabolism. As glycogen in the liver and lipid in the body are the only fuel sources in no-feeding and tadpoles exposed to cold, the activation of genes for enzymes of amino acid metabolism (arginase), TCA cycle (malate dehydrogenase), glycolysis/glyconeogenesis (bisphosphoglycerate mutase and 6-phosphofructo-2-kinase/fructose 2,6-bisphosphatase), and lipid metabolism (ergosterol biosynthetic protein 28 and acyl-CoA-binding protein) may be important to drive temperature compensation of metabolism.

4.2. Genes exhibiting unique expression in the liver of cold-exposed tadpoles

4.2.1. Stress response genes

The changes in gene expression induced by short-term exposure to cold may in part reflect a stress response. The most remarkable induction was found in the gene for C/EBP-2, a homolog of mammalian C/EBP-δ [20]. The gene for C/EBP-1, a homolog of mammalian C/EBP-α [20], showed T3-dependent up-regulation at 28 °C that was abolished at 4 °C. These proteins are transcription factors belonging to C/EBP family members, and are known to play an essential role in cell cycle, hematopoiesis, differentiation, and host immune response in mammals [21]. Findings from our study, together with those from previous studies in fish and invertebrates, raise the possibility that genes for several types of C/EBP operate as general stress response genes in ectotherms. Recently, the gene for C/EBP-δ was found to be inducible by acute heat stress (18–32 °C for 4–8 h) and thermal acclimation (15–25 °C for 4 weeks) in the gill, white muscle and liver of the eurythermal estuarine goby *Gillichthys mirabilis* [22]. In a tropical species of damselfish *Pomacentrus moluccensis*, heat stress (26–34 °C for 3 h) repressed C/EBP-δ gene expression [23]. Interestingly, the goby C/EBP-δ gene had acute phase response element and hypoxia response elements in the 5′-untranslated region [22]. Similar heat stress responses were detected in C/EBP-α and -β genes of the symbiotic anemone *Anthopleura elegantissima* [24], and in C/EBP-β gene of the coral *Montastraea faveolata* [25].

4.2.2. TH response genes

The T3-response was abolished by exposure to cold in most of the TH-response genes investigated, with some individual variation. These genes include those for TRβ as a primary early response gene [10], 5-deiodinase type III and C/EBP-1, which are likely to be early response genes [3,26,27], and the urea cycle enzymes, carbamoyl phosphate synthetase 1, ornithine transcarbamoylase, argininosuccinate lyase, and arginase, as secondary late response genes [3,27]. The variation of the cold response may reflect what transcription factors besides TRs control directly or indirectly the expression of these genes.

A temperature-sensitive step may exist in the intracellular TH signaling pathway between T3-binding to TR and the phosphorylation of RNA polymerase II at serine 2 on primary early TH response genes in the tadpole liver. Recently, we found that the T3-signal is transferred to the histone H3 by increasing the amounts of tri-methylated K36 and acetylated K9 on the coding region of the TRβ gene through the phosphorylation of RNA polymerase II at serine 2, resulting in effective transcriptional elongation [16]. However, cold exposure did not enhance the amount of tri-methylated H3-K36 on TRβ gene in T3-treated tadpoles. This result reinforced the previous finding that the T3-signal does not reach the transcriptional machinery on primary early TH genes [10]. As T3 is thought to bind to TRs in the nuclei of tadpole tissues even at 4–5 °C [8–10], the T3 signal must be blocked by an unknown process after the binding of T3 to TR but before the phosphorylation of RNA polymerase II at serine 2. Our ChIP results also suggest that the C/EBP-2 gene activation induced by cold exposure is mechanically distinct from the T3-dependent TRβ gene activation.

In conclusion, we found that the short-term exposure to cold induced transcriptional changes to some genes in the liver of *R. catesbeiana* tadpoles. The amounts of transcripts in one-quarter of the genes investigated were increased by metabolic temperature compensation and/or by cold stress. However, the intracellular T3-signaling pathway was specifically interrupted by exposure to cold at a site after T3 binding to TR but before histone modifications on the primary early TH response genes.

Acknowledgments

We are grateful to Dr J. Monk for a thorough and critical reading of the manuscript.

Appendix A. Supplementary data

Supplementary data associated with this article can be found, in the online version, at doi:10.1016/j.bbrc.2012.03.085.

References

[1] E. Frieden, A. Wahlborg, E. Howard, Temperature control of the response of tadpoles to triiodothyronine, Nature 205 (1965) 1173–1176.
[2] S. Voparina, J.J. Just, The life period, growth and differentiation of *Rana catesbeiana* larvae occurring in nature, Copeia 1975 (1975) 103–109.
[3] Y.B. Shi, Amphibian Metamorphosis, from Morphology to Molecular Biology, Wiley-Liss, NY, USA, 2000 pp. 102–122.
[4] D.R. Buchholz, B.D. Paul, L. Fu, Y.B. Shi, Molecular and developmental analyses of thyroid hormone receptor function in *Xenopus laevis*, the African clawed frog, Gen. Comp. Endocrinol. 145 (2006) 1–19.

[5] R.J. Sims III, R. Belotserkovskaya, D. Reinberg, Elongation by RNA polymerase II: the short and long of it, Genes Dev. 18 (2004) 2437–2468.
[6] J.R. Tata, Simultaneous acquisition of metamorphic response and hormone binding in *Xenopus* larvae, Nature 227 (1970) 686–689.
[7] M.D. Griswold, M.S. Fischer, P.P. Cohen, Temperature-dependent intracellular distribution of thyroxine in amphibian liver, Proc. Natl. Acad. Sci. USA 69 (1972) 1486–1489.
[8] A. Kistler, K. Yoshizato, E. Frieden, Binding of thyroxine and triiodothyronine by nuclei of isolated tadpole liver cells, Endocrinology 97 (1975) 1036–1042.
[9] E. Toth, M. Tabachnick, Effect of temperature on the transport of triiodothyronine (T3) into liver nuclei of *Rana catesbeiana* tadpoles in vivo, Gen. Comp. Endocrinol. 42 (1980) 57–62.
[10] T. Murata, K. Yamauchi, Low-temperature arrest of the triiodothyronine-dependent transcription in *Rana catesbeiana* red blood cells, Endocrinology 146 (2005) 256–264.
[11] A.C. Taylor, J.J. Kollros, Stages in the normal development of *Rana pipiens* larvae, Anat. Rec. 94 (1946) 7–23.
[12] P. Chomczynski, N. Sacchi, Single-step method of RNA isolation by acid guanidinium thiocyanate–phenol–chloroform extraction, Anal. Biochem. 162 (1987) 156–159.
[13] S. Fujimoto, T. Goda, K. Mochizuki, In vivo evidence of enhanced di-methylation of histone H3 K4 on upregulated genes in adipose tissue of diabetic *db*/*db* mice, Biochem. Biophys. Res. Commun. 404 (2011) 223–227.
[14] O.H. Lowry, N.J. Rosebrough, A.L. Farr, R.J. Randall, Protein measurement with the folin phenol reagent, J. Biol. Chem. 193 (1951) 265–275.
[15] K. Honma, K. Mochizuki, T. Goda, Carbohydrate/fat ratio in the diet alters histone acetylation on the sucrase–isomaltase gene and its expression in mouse small intestine, Biochem. Biophys. Res. Commun. 357 (2007) 1124–1129.
[16] K. Mochizuki, A. Ishihara, T. Goda, K. Yamauchi, RNA polymerase II phosphorylation at serine 2 and histone H3 tri-methylation at lysine 36 are key steps for thyroid hormone receptor β gene activation by thyroid hormone in *Rana catesbeiana* tadpole liver, Biochem. Biophys. Res. Commun. 417 (2012) 1069–1073.
[17] W.S. Hoar, General and Comparative Physiology, second ed., Prentice-Hall, Inc., NJ. USA, 1975 pp. 329–362.
[18] E. Frieden, Thyroid hormones and the biochemistry of amphibian metamorphosis, Recent Prog. Horm. Res. 23 (1967) 139–186.
[19] G.N. Somero, Adaptation of enzymes to temperature: searching for basic "strategies", Comp. Biochem. Physiol. Part B: Biochem. Mol. Biol. 139 (2004) 321–333.
[20] Y. Chen, H. Hu, B.G. Atkinson, Characterization and expression of C/EPB-like genes in the liver of *Rana catesbeiana* tadpoles during spontaneous and thyroid hormone-induced metamorphosis, Dev. Genet. 15 (1994) 366–377.
[21] J. Tsukada, Y. Yoshida, Y. Kominato, P.E. Auron, The CCAAT/enhancer (C/EBP) family of basic-leucine zipper (bZIP) transcription factors is a multifaceted highly-regulated system for gene regulation, Cytokine 54 (2011) 6–19.
[22] B.A. Buckley, Acute heat stress and thermal acclimation induce CCAAT/enhancer-binding protein delta in the goby *Gillichthys mirabilis*, J. Comp. Physiol. B 181 (2011) 773–780.
[23] K.S. Kassahn, M.J. Caley, A.C. Ward, A.R. Connolly, G. Stone, R.H. Crozier, Heterologous microarray experiments used to identify the early gene response to heat stress in a coral reef fish, Mol. Ecol. 16 (2007) 1749–1763.
[24] S. Richier, M. Rodriguez-Lanetty, C.E. Schnitzler, V.M. Weis, Response of the symbiotic cnidarian *Anthopleura elegantissima* transcriptome to temperature and UV increase, Comp. Biochem. Physiol. Part D: Genomics Proteomics 3 (2008) 283–289.
[25] M.K. DeSalvo, C.R. Voolstra, S. Sunagawa, J.A. Schwarz, J.H. Stillman, M.A. Coffroth, A.M. Szmant, M. Medina, Differential gene expression during thermal stress and bleaching in the Caribbean coral *Montastraea faveolata*, Mol. Ecol. 17 (2008) 3952–3971.
[26] K.B. Becker, M.J. Schneider, J.C. Davey, V.A. Galton, The type III 5-deiodinase in *Rana catesbeiana* tadpoles is encoded by a thyroid hormone-responsive gene, Endocrinology 136 (1995) 4424–4431.
[27] Y. Chen, B.G. Atkinson, Role for the *Rana catesbeiana* homologue of C/EBP α in the reprogramming of gene expression in the liver of metamorphosing tadpoles, Dev. Genet. 20 (1997) 152–162.

Biochemical and Biophysical Research Communications 420 (2012) 851–856

Contents lists available at SciVerse ScienceDirect

Biochemical and Biophysical Research Communications

journal homepage: www.elsevier.com/locate/ybbrc

Over-expression of human clusterin increases stress resistance and extends lifespan in *Drosophila melanogaster*

Young-Nam Lee [a,1], Young-Jun Shim [a,1], Byeong-Ho Kang [a], Joong-Jean Park [b,*], Bon-Hong Min [a,*]

[a] Department of Pharmacology, College of Medicine, Korea University, 126-1 Anam-Dong 5 Ga, Seongbuk-Gu, Seoul 136-705, Republic of Korea
[b] Department of Physiology, College of Medicine, Korea University, 126-1 Anam-Dong 5 Ga, Seongbuk-Gu, Seoul 136-705, Republic of Korea

ARTICLE INFO

Article history:
Available online 24 March 2012

Keywords:
Clusterin
Drosophila
Lifespan
Motoneuron,
Reactive oxygen species
Antioxidant

ABSTRACT

Clusterin is a disulfide-linked heterodimeric glycoprotein that has been implicated in a variety of biological processes. Its expression has been shown to be elevated during cellular senescence and normal aging, but it is uncertain whether clusterin protects against aging or whether its expression is a consequence of aging. To investigate the functions of clusterin during organismal aging, we established transgenic *Drosophila* alleles to induce the expression of the secretory form of human clusterin ($hClu^S$) using the Gal4/UAS system. $hClu^S$ protein (~60 kDa) was detected in both adult homogenates and larval hemolymphs of flies ubiquitously overexpressing $hClu^S$ (*da*-Gal4 > UAS-$hClu^S$) and in motoneurons (*D42*-Gal4 > UAS-$hClu^S$). Interestingly, the mean lifespans of these $hClu^S$-overexpressing flies were significantly greater than those of control flies that exhibited no $hClu^S$ induction. $hClu^S$-overexpressing flies also showed significantly greater tolerance to heat shock, wet starvation, and oxidative stress. Furthermore, amounts of reactive oxygen species (ROS) in whole bodies were significantly lower in $hClu^S$-overexpressing flies. In addition, clusterin was found to prevent the inactivation of glutamine synthetase (GS) by metal-catalyzed oxidation (MCO) *in vitro*, and this protection was only supported by thiol-reducing equivalents, such as, DTT or GSH, and not by ascorbate (a non-thiol MCO system). Furthermore, this protection against GS inactivation by clusterin was abolished by reacting clusterin with *N*-ethylmaleimide, a sulfhydryl group-modifying agent. Taken together, these results suggest that a disulfide-linked form of clusterin functions as an antioxidant protein via its cysteine sulfhydryl groups to reduce ROS levels and delay the organismal aging in fruit flies.

© 2012 Elsevier Inc. All rights reserved.

1. Introduction

Human clusterin is a secreted heterodimeric glycoprotein of 75–80 kDa that consists of two ~40 kDa subunits (α and β) joined in an antiparallel manner by five disulfide bonds [1]. It is up-regulated in various tissues subject to severe physiological disturbances, such as those affected by, neurodegenerative diseases, ischemic conditions, atherosclerosis, renal disease, or cancer progression [2,3]. Its sequence conservation and ubiquitous expression imply that clusterin performs an important protective role in fundamental biological processes. Furthermore, recent studies on clusterin knockout mice suggest that clusterin protects animals from the pathological consequences of autoimmune myocardial damage [4], progressive glomerulopathy during ageing [5], and heat shock-mediated cell death [6]. Interestingly, the majority of diseases and severe physiological disturbances characterized by clusterin up-regulation represent states of increased oxidative stress [3]. Although minor variant intracellular isoforms with pro-apoptotic functionality have been reported in mammalian cells [7], a secretory disulfide-linked form of clusterin has been most extensively studied and this form probably functions as an extracellular chaperone that stabilizes stressed proteins in a folding-competent state [8]. In addition, several studies have demonstrated that clusterin mediates resistance to the cell death induced by heat shock or oxidative stress, which suggest an antioxidant function that reduces cellular ROS [3,9]. This suggested is supported by the finding that the clusterin gene promoter contains a conserved 14-bp clusterin-specific element (CLE), which is recognized by heat shock transcription factor 1 (HSF1) and can mediate oxidative stress-induced transcription[10].

It is generally accepted that oxidative stress is a major contributor to the effects of aging [11]. Interestingly, clusterin mRNA and protein levels were found to be elevated *in vitro* during the replicative- or stress-induced premature senescence of primary human cells and *in vivo* during normal aging [12,13]. Furthermore, clusterin serum levels increase with age in man [14], and thus, clusterin appears to be an important modulator of oxidative stress in the contexts of aging and age-related disease. However, it

* Corresponding authors. Fax: +82 2 925 5492 (J.-J. Park), +82 2 927 9289 (B.-H. Min).
E-mail addresses: parkjj@korea.ac.kr (J.-J. Park), bhmin@korea.ac.kr (B.-H. Min).
[1] These authors contributed equally to this work.

0006-291X/$ - see front matter © 2012 Elsevier Inc. All rights reserved.
http://dx.doi.org/10.1016/j.bbrc.2012.03.087

remains to be elucidated whether clusterin has a protective effect against aging, or whether its up-regulation is a consequence of the normal aging processes in *in vivo*.

In the present study, to investigate the function of clusterin during aging, we established transgenic *Drosophila* alleles carrying the secretory form of human clusterin (hClu^S; UAS-hClu^S) using the Gal4/UAS system [15] to induce the ectopic overexpression of hClu^S in fruit flies.

2. Materials and methods

2.1. Drosophila strains

The fly strains used in this study were; *CS10* (the wild-type; generously donated by Dr. Minoru Saitoe (Tokyo Metropolitan Institute of Medical Science), *da*-Gal4 and *D42*-Gal4 from the Bloomington *Drosophila* Stock Center, and the UAS-hClu^S lines established as described (Supplementary Materials and methods). In order to make isogenic stocks, UAS-hClu^S lines and Gal4 lines were back crossed 6 times into *CS10*, respectively. All flies were cultured at 25 °C on a medium containing 6% cornmeal, 3% yeast, 3% sugar, 6% glucose, and 0.6% agar.

2.2. Ectopic overexpression of the secretory form of human clusterin in Drosophila

Ectopic overexpression of hClu^S was achieved using the Gal4/UAS system. Three UAS-hClu^S lines were selected based on hClu^S protein levels, that is, UAS-hClu^{S4} on the second chromosome and UAS-hClu^{S7} and UAS-hClu^{S10} on the third chromosome, and were crossed with homozygotes of *da*-Gal4 and *D42*-Gal4 to obtain ubiquitous and motoneuron-specific expression of hClu^S, respectively.

2.3. Western blotting

See Supplementary Materials and methods.

2.4. Lifespan measurements

One hundred and twenty male flies were cultured in a plastic chamber ($7 \times 7 \times 10$ cm) with an adaptor for regular *Drosophila* vials. Every 2–3 days when food vials containing fresh food were replaced, dead flies were counted. The lifespans of genotypes were measured at least in three separate chambers. Flies were raised at 25 °C at a relative humidity of 50% under a 12:12 h light/dark cycle.

2.5. Stress resistance tests

Heat shock, wet starvation, and oxidative stress were performed as described in Supplementary Materials and methods.

2.6. ROS measurements in adult flies

The amount of ROS in flies was quantified using a ferric-xylenol orange assay [16] (see Supplementary Materials and methods).

2.7. Determination of thiol-specific antioxidant activity of clusterin

Thiol-specific antioxidant activity of clusterin was determined by measuring its ability to inhibit the GS inactivation by a metal catalyzed thiol MCO system [17] (see Supplementary Materials and methods).

2.8. Statistical analysis

Mean lifespan measurements and stress resistance study results were analyzed using the survival test. Comparisons among groups were conducted using Gehan's Wilcoxon test. ROS measurements were analyzed by two-way analysis of variance (ANOVA) using age and genotype as main effects. The *post hoc* testing of group means was done using Duncan's multiple comparison and statistical significance was accepted for p values of <0.05.

3. Results

3.1. The secretory form of human clusterin was synthesized and secreted into hemolymph in Drosophila

We examined the expression patterns of some of the newly established UAS-hClu^S lines under *da*-Gal4 or *D42*-Gal4 drivers. hClu^S protein (~60 kDa) was detected in the homogenate of adult whole body and in larval hemolymph (Supplementary Fig. S1). The size of clusterin in plasma is ~80 kDa, and in man, clusterin is synthesized as a 449 amino acid polypeptide. Proteolytic removal of the ER-targeting signal peptide and disulfide bond formation results in the 50–60 kDa pre-secretory form. As this precursor moves through to Golgi cisternae, it is further glycosylated and cleaved at Arg^{227}–Ser^{228} residues to render two ~40 kDa subunits joined by disulfide bonds [1]. Similarly, human clusterin seemed to be expressed in *Drosophila* as an internally cleaved heterodimer with disulfide bonds, since hClu^S was detected as a ~30 kDa band under reduced conditions, but as ~60 kDa band under non-reduced conditions. It is plausible that the size difference between secreted clusterin in man and *Drosophila*is due to different posttranslational modifications, such as, glycosylation. When hClu^S is reduced, the α- and β-subunits of clusterin are generated, but only the latter is detected as a ~30 kDa band since the epitope of 2G12 monoclonal clusterin antibody is mapped at the C-terminal of the β-subunit. In whole body homogenates, two bands of ~60 and ~30 kDa were visualized even under reduced conditions, suggesting both the pre-secretory form with no internal cleavage and the mature internally cleaved secretory form (Supplementary Fig. S1A). However, only one band of 30 kDa was observed in hemolymph, which contained only the secretory mature form (Supplementary Fig. S1B). In addition, ubiquitous (*da*-Gal4 > UAS-hClu^S) or motorneuron-specific over-expression (*D42*-Gal4 > UAS-hClu^S) of human clusterin produced the same expression patterns in hemolymph (data of *D42*-Gal4 > UAS-hClu^S lines not shown), suggesting that hClu^S is well processed through the secretory pathway in *Drosophila*, regardless of cell type.

3.2. The over-expression of hClu^S extends the lifespan of Drosophila

To understand the effects of hClu^S on *Drosophila* aging, we measured the survivals of hClu^S-overexpressing flies and their isogenic controls. Three UAS-hClu^S alleles (UAS-hClu^{S4}, UAS-hClu^{S7}, and UAS-hClu^{S10}) were tested to investigate positional effects associated with genomic integration of the pUAST construct. Over-expression of hClu^S that was induced by *da*-Gal4 or *D42*-Gal4 drivers significantly extended *Drosophila* lifespan ($P < 0.001$; Fig. 1A and B and Table 1). As compared with transgenic flies without Gal4, we found 15% and 22.5% increases in mean lifespans for flies overexpressing clusterin transgene on the second (UAS-hClu^{S4}/+) and third chromosomes (UAS-hClu^{S7}/+ and UAS-hClu^{S10}/+) under *da*-Gal4 driver, respectively. In an additional experiment, an extension in lifespan (34%) was also observed for hClu^S transgenic flies along with *D42*-Gal4-activated expression in motorneurons. Interestingly, the

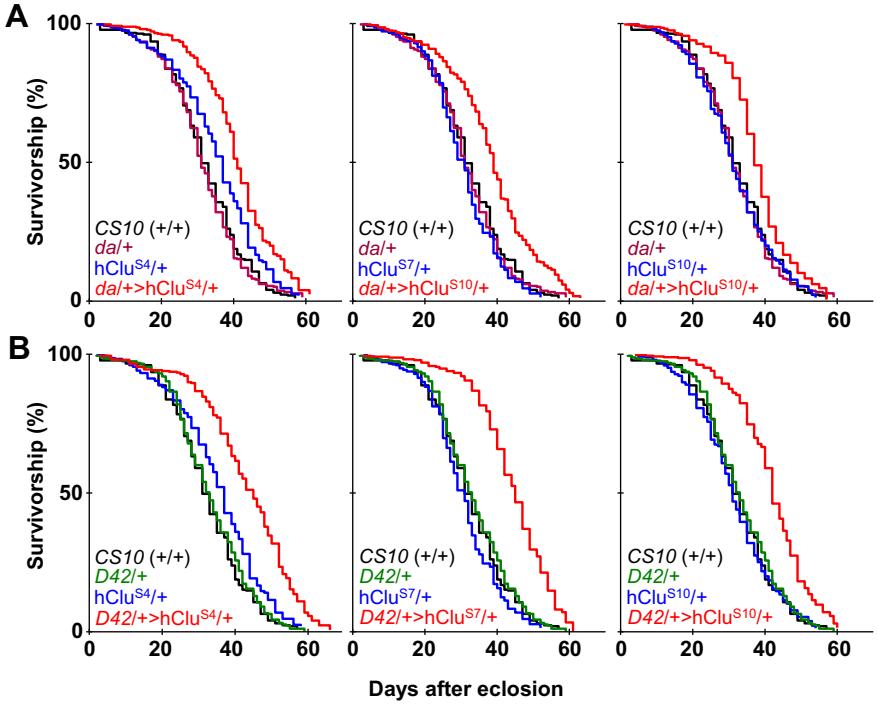


Fig. 1. Lifespans of hClu^S-overexpressing flies. The lifespans of three UAS-hClu^S lines (S4, S7, and S10) whose hClu^S was over-expressed in the whole body (A) and motorneurons (B) by *da*-Gal4 and *D42*-Gal4 driver lines, respectively, were measured as described in Section 2. Both ubiquitous and motoneuron-specific over-expression of hClu^S significantly extended *Drosophila* lifespan for all three alleles. Abbreviations: *da*-Gal4, *da*; UAS-hClu^S, hClu^S; *da*-Gal4 > UAS-hClu^S, da > hClu^S; *D42*-Gal4, *D42*; *D42*-Gal4 > UAS-hClu^S, *D42* > hClu^S.

overall increase of mean lifespan (34% vs. 20%) was even greater when hClu^S over-expression was restricted within motorneurons.

3.3. Over-expression of hClu^S enhanced tolerance against heat shock, starvation, and oxidative stress

Since clusterin is known to have a chaperone effect and an antioxidant function, we hypothesized that hClu^S could make animals more durable under stressful conditions. First, heat tolerance was tested in flies with different genotypes at 37 °C. At this high temperature, misfoldings of proteins occur and the animal's metabolism is altered [18]. The mean survival time (11.5 h) of flies over-expressing human clusterin under motorneuron-specific Gal4 driver (*D42*-Gal4 > UAS-hClu^{S4}, *D42*-Gal4 > UAS-hClu^{S7}, or *D42*-Gal4 > UAS-hClu^{S10}) was found to be significantly greater than that of other control flies, that is,*CS10*+/+(9.6 h), *D42*-Gal4/+ (9.8 h), and three control lines UAS-hClu^{S4}, UAS-hClu^{S7}, or UAS-hClu^{S10} (average of 9.7 h) ($P < 0.001$; Fig. 2A). Second, tolerance to wet starvation was examined. During starvation, metabolic energy sources stored in flies are promptly mobilized, which leads to enhanced ROS production [19]. Overexpression of hClu^S significantly increased mean survival time versus controls (66.6 h vs. 55.2 h, $P < 0.001$; Fig. 2B). Third, tolerance against oxidative stress induced by paraquat, which increases cellular oxygen radical levels, was tested. Similarly, human clusterin-over-expressing flies were also found to be significantly more resistant to oxidative stress than control flies (40.5 h vs. 29.5 h, $P < 0.001$; Fig. 2C).

3.4. Over-expression of hClu^S reduced whole body ROS contents

Elevated ROS levels are known to be linked to *in vivo* aging [20], and clusterin has a protective effect on the cellular ROS-induced oxidative stress [3,21]. Thus, we measured whole body ROS quantities to confirm the antioxidant effects of hClu^S under normal and stressful (18 mM paraquat) conditions. ANOVA indicated significant genotype ($F_{(7135)} = 85.6$, $P < 0.001$), treatment ($F_{(1135)} = 1810.0$, $P < 0.001$), and interaction effects ($F_{(1135)} = 19546.9$, $P < 0.001$). Under normal conditions, the average amount of ROS in flies over-expressing the human clusterin (*D42*-Gal4 > UAS-hClu^{S4}, *D42*-Gal4 > UAS-hClu^{S7}, or *D42*-Gal4 > UAS-hClu^{S10}) was significantly lower than in controls ($P < 0.001$; Fig. 3, open bars). Feeding paraquat significantly increased whole body ROS levels ($P < 0.001$), and of the flies fed paraquat, ROS levels of the clusterin over-expressing flies were significantly lower than in controls ($P < 0.001$; Fig. 3, closed bars).

3.5. In vitro thiol-specific antioxidant activity of clusterin

Mixed-function oxidation systems comprised of Fe^{3+}, O_2, and electron donors, such as thiol compounds or ascorbate, catalyze the inactivation of many enzymes including GS from *Escherichia coli* and yeast. This specific inactivation of GS is believed to be the result of nonenzymatic cleavage by ROS generated by DTT and iron [22,23]. Some proteins that are capable of removing ROS, such as, human serum albumin or thiol-dependent antioxidant proteins in red blood cells exhibit protective effects against the GS inactivation by the Fe^{3+}/DTT system [24,25]. Since ROS level of clusterin-overexpressing flies is lower than that of control, we examined the antioxidant activity of clusterin by monitoring its ability to inhibit the GS inactivation. Clusterin exerted a dose-dependent protective effect on the inactivation of GS by metal catalyzed thiol MCO systems (DTT or GSH, Fe^{3+}, O_2) (Fig. 4A and B). However, when a thiol reducing equivalent was replaced with another non-thiol electron donor, such as, ascorbate, clusterin no longer prevented the inactivation of GS by the ascorbate MCO system (Fig. 4C). Furthermore, when clusterin was reacted with *N*-ethylmaleimide (a cysteine-specific modifying reagent) in the presence of DTT, its protective activity against GS inactivation

Table 1
Increased lifespan of transgenic flies overexpressing human clusterin under *da*-Gal4 or *D42*-Gal4 drivers.

Genotype	*CS10* (+/+, A)			/*da*-Gal4 (B)			/*D42*-Gal4 (C)			ILS (b/a)	ILS (c/a)	*p* Value by Wilcoxon test (A vs. B)	*p* Value by Wilcoxon test (A vs. C)
	MLS (a)	MaxLS	(n)	MLS (b)	MaxLS	(n)	MLS(c)	MaxLS	(n)				
CS10 (+/+)	32.2	57.0	(356)	31.2	59.0	(355)	32.9	59.0	(350)	0.97	1.02	0.3166	0.2732
UAS-hClu^{S4}	35.1	58.0	(356)	40.3	61.0	(354)	42.9	61.0	(349)	1.15	1.22	<0.0001	<0.0001
UAS-hClu^{S7}	29.8	52.0	(355)	38.3	63.0	(342)	43.6	66.0	(331)	1.29	1.46	<0.0001	<0.0001
UAS-hClu^{S10}	31.2	54.0	(347)	36.2	57.0	(327)	41.8	60.0	(370)	1.16	1.34	<0.0001	<0.0001

MLS, mean lifespan; MaxLS, maximum lifespan; ILS, lifespan; *n*, is the total number of flies in three independent experiments.

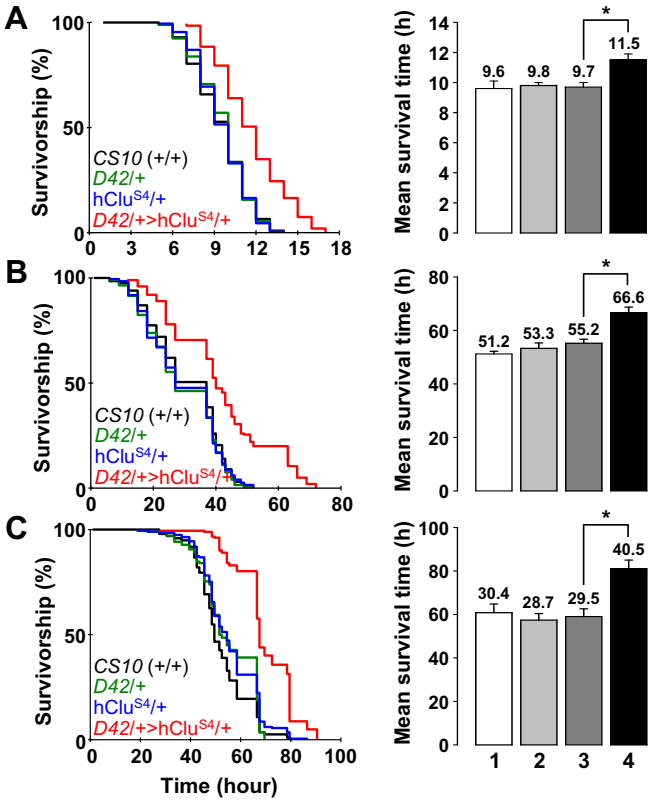


Fig. 2. Stress tolerance of hClu^{S}-overexpressing flies. Survivorship of 10-day-old male flies with motorneuron-specific overexpression of hClu^{S} was analyzed under heat shock (A), wet starvation (B), and paraquat-induced oxidative stress (C) as described (Supplementary Materials and methods). The average of mean survival time of the three independent hClu^{S}-overexpressing lines (*D42*-Gal4 > UAS-hClu^{S4}, *D42*-Gal4 > UAS-hClu^{S7}, *D42*-Gal4 > UAS-hClu^{S10}) was significantly greater than those of the age-matched driver controls (UAS-hClu^{S4}, UAS-hClu^{S7}, UAS-hClu^{S10}) in all three conditions tested (right panel, $^{*}P < 0.001$). Only the survivorship of *D42*-Gal4 > UAS-hClu^{S4} line is presented (left panel in A, B, and C). Arabic numerals at the bottom of right panel denotes as follows: lane 1 (*CS10*), lane 2 (*D42*/+), lane 3 (UAS-hClu^{S4}, UAS-hClu^{S7}, UAS-hClu^{S10}), lane 4 (*D42*-Gal4 > UAS-hClu^{S4}, *D42*-Gal4 > UAS-hClu^{S7}, *D42*-Gal4 > UAS-hClu^{S10}).

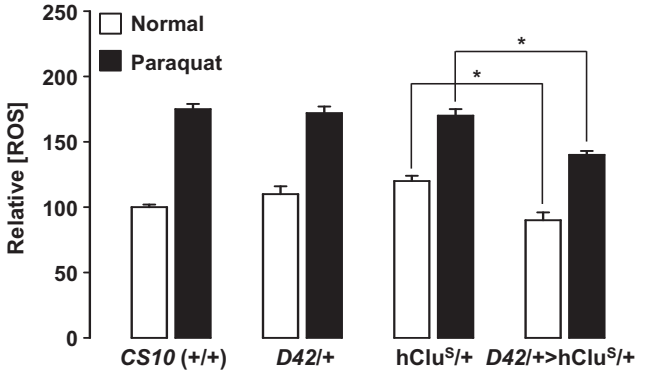


Fig. 3. Levels of whole body ROS in flies over-expressing hClu^{S}. Total ROS levels were quantified in flies fed normal food orparaquat as described (Supplementary Materials and methods). ROS levels were significantly higher in flies exposed to paraquat, regardless of genotype. In both under normal conditions (open bars) and paraquat feeding (closed bars), average amount of ROS in *D42*-Gal4 > UAS-hClu^{S4}, *D42*-Gal4 > UAS-hClu^{S7}, *D42*-Gal4 > UAS-hClu^{S10} was significantly lower than those of controls (UAS-hClu^{S4}, UAS-hClu^{S7}, UAS-hClu^{S10}). $^{*}P < 0.001$.

was abolished (Fig. 4D). These results suggest the antioxidant activity of clusterin is specific for mixed-function oxidation systems containing thiols, and that this activity depends on the sulfhydryl groups of cysteines.

4. Discussion

In this study, we present a novel role for the secretory form of clusterin in the extension of *Drosophila* lifespan, and show that tolerance to heat shock, wet starvation, and oxidative stress is higher and whole body ROS levels are significantly lower in clusterin-expressing flies than in isogenic controls. We also show clusterin purified from human plasma can exert thiol specific-antioxidant activity by preventing the GS inactivation, which is catalyzed by a mixed-function oxidation system. These data support the hypotheses that disulfide-linked clusterin functions to reduce ROS via cysteine sulfhydryl groups and that it increases tolerance to oxidative stress, which increases the lifespan of clusterin-expressing *Drosophila*.

Two types of isoforms of clusterin protein have been observed in mammalian cells, a major conventional secreted isoform and intracellular isoforms. The intracellular form of clusterin has been suggested to be involved in pro-apoptotic cell death pathways, whereas it is generally accepted that a conventional secreted isoform of clusterin probably functions as an extracellular chaperone that stabilizes misfolded-proteins under conditions of increased oxidative stress [8,26]. In addition, we and others have suggested that clusterin might function as an antioxidant protein by protecting cells from ROS [3,21]. Thus, it seems that a secretory form of clusterin has protective activity, whether it functions as a chaperone or as an antioxidant. In the present study, we found that only flies overexpressing a secretory form of clusterin exhibited lifespan extension and increased tolerance to oxidative stress, and in particular, that transgenic flies with an intracellular truncated form of clusterin did not (data not shown).

A secretory form of human clusterin seemed to be expressed in *Drosophila* as a heterodimeric internally cleaved clusterin with disulfide bonds, since a protein sized ~60 kDa was detected in transgenic flies under non-reduced conditions, but a ~30 kDa band was observed under reduced conditions (Supplementary Fig. S1). In humans, clusterin is synthesized as a 449 amino acid polypeptide and it is co-translationally transported in the lumen of endoplasmic reticulum, which results the productions of a 50–60 kDa

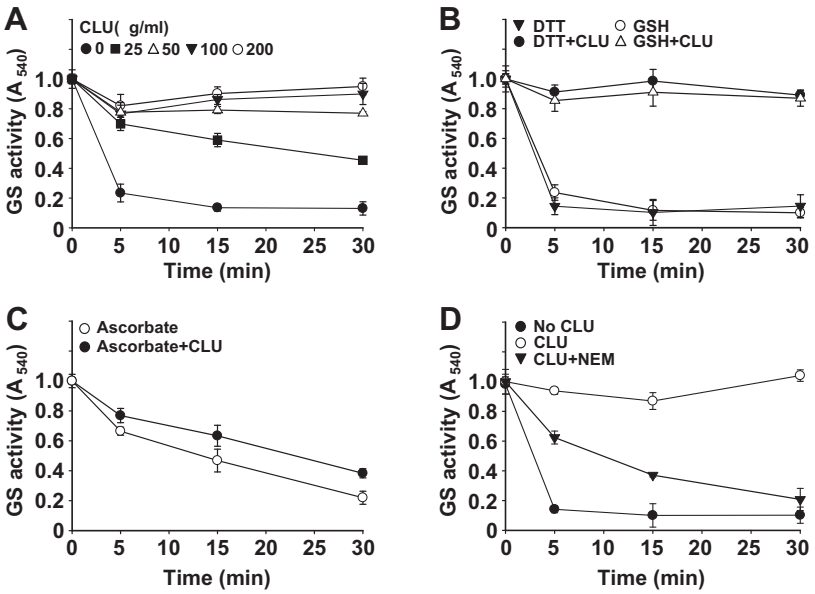


Fig. 4. Protection of human clusterin against the glutamine synthetase (GS) caused by metal-catalyzed oxidation (MCO) systems. Inactivation assays were performed in a 25 μl reaction mixture containing 2 μg of GS, 3 μM $FeCl_3$, 50 mMH epes, pH 7.0, 10 mM DTT. At the indicated times, aliquots (5 μl) were assayed for remaining GS activity as described (Supplementary Materials and methods). (A) Clusterin (25–200 μg/ml was added to reaction mixtures to examine its protective effect against GS inactivation caused by the DTT-MCO system. (B) GS inactivation was performed in a MCO system in which 10 mM DTT was replaced by 20 mM GSH. (C) Thiol reducing equivalents were replaced with a non-thiol electron donor, ascorbate (10 mM). (D) Clusterin was reacted with *N*-ethylmaleimide (a cysteine-specific modifying reagent) in the presence of DTT.

pre-secretory form and the secretion of a ~80 kDa disulfide-linked heterodimeric glycoprotein after further glycosylation and proteolytic cleavage to yield α and β subunits in the Golgi apparatus [1,27]. In whole body homogenates, two bands of ~60 and ~30 kDa were visualized even under reduced conditions, whereas only one band of ~60 kDa was detected under non-reduced conditions. However, this band was thicker and was suspected of being a doublet, which suggested that it was composed of a smaller pre-secretory form with no internal cleavage and an internally cleaved mature secretory form. The mature internally cleaved secretory form was detected as ~30 kDa under reduced and at ~60 kDa under non-reduced conditions, but the non-internally cleaved pre-secretory form presented as a ~60 kDa protein under both conditions. These observations suggest that glycosylations of human clusterin in the Golgi apparatus of *Drosophila* are significantly less frequent than in man, which is consistent with the finding that most *N*-glycans in recombinant glycoproteins expressed in *Drosophila* S2 cells are substantially different from those expressed in mammalian cells [28]. It is worth noting that variations in clusterin molecular mass are due to glycosylation variability in different species or tissues in same species [29].

The disulfide linkages of human clusterin expressed in *Drosophila* might be involved in the reduction of total ROS levels and in increased stress tolerance, since the antioxidant activity of clusterin was abolished when the sulfhydryl groups of cysteines were blocked with *N*-ethylmaleimide. Similarly, when DTT was replaced with a non-thiol electron donor, such as, ascorbate, clusterin no longer exerted its antioxidant activity in an ascorbate MCO system. Clusterin contains five cysteine residues in each of α- and β-subunits, the numbers and locations of which are completely conserved from mammals to zebra fish [30]. Choi-Miura et al. [31] found only four disulfide bridges in human clusterin and suggested one potential disulfide bond. Thus, we hypothesized that a local thiol-reducing species, such as, GSH might reduce disulfide bonds to scavenge ROS. To examine which sulfhydryl group among the 5-disulfide bridges acts as a functional nucleophile and reacts with ROS, we generated a series of clusterin mutants with different cysteine residues replaced with serine. However, clusterin protein was not synthesized in the mutants, indicating that the highly conserved cysteine residues are important for the structure and function of clusterin. Further study is required to determine whether clusterin acts as an extracellular antioxidant protein with thiol-specific peroxidase activity or as a sacrificial antioxidant protein that protects against oxidative damage associated with elevated ROS levels.

In the present study, transgenic *Drosophila* harboring human clusterin cDNA was induced using a ubiquitous driver (*da*-Gal4) or a motor neuron-specific driver (*D42*-Gal4). Although we observed the same expression patterns of human clusterin in hemolymph, the overall increase in mean lifespan was greater when the clusterin expression was restricted within motor neurons (Table 1). We have no explanation for the difference. However, it has been reported that the overexpression of human Cu/Zn superoxide dismutase (SOD1) in motor neurons can extend lifespan by up to 40% in *Drosophila* [32]. Interestingly, SOD1 overexpression under heatshock-Gal4, which drives expression broadly at all stages of development, did not extend lifespan. In addition, mutations in SOD1 gene and loss of motor neurons are known to be associated with familial amyotrophic lateral sclerosis, a lifespan-shortening paralytic disease [33]. These results suggest chronic oxidative damage occurring specifically in motor neurons could be a critical aging factor and that oxygen radical metabolizing enzymes, such as, SOD1 and clusterin, play important roles in the extension of *Drosophila* lifespan.

Collectively, our data suggest that a disulfide-linked form of clusterin functions as a thiol-specific antioxidant protein that uses its cysteine sulfhydryl groups to reduce ROS levels and delay organismal aging in fruit flies.

Acknowledgment

This work was supported by a Korea Science and Engineering Foundation (KOSEF) grant funded by the Korea Government (MEST) (No. 2011-002-8200).

Appendix A. Supplementary data

Supplementary data associated with this article can be found, in the online version, at doi:10.1016/j.bbrc.2012.03.087.

References

[1] S.E. Jones, C. Jomary, Clusterin, Int. J. Biochem. Cell Biol. 34 (2002) 427–431.
[2] M.E. Rosenberg, J. Silkensen, Clusterin: physiologic and pathophysiologic considerations, Int. J. Biochem. Cell Biol. 27 (1995) 633–645.
[3] I.P. Trougakos, E.S. Gonos, Regulation of clusterin/apolipoprotein J, a functional homologue to the small heat shock proteins, by oxidative stress in ageing and age-related diseases, Free Radic. Res. 40 (2006) 1324–1334.
[4] L. McLaughlin, G. Zhu, M. Mistry, C. Ley-Ebert, W.D. Stuart, C.J. Florio, P.A. Groen, S.A. Witt, T.R. Kimball, D.P. Witte, J.A. Harmony, B.J. Aronow, Apolipoprotein J/clusterin limits the severity of murine autoimmune myocarditis, J. Clin. Invest. 106 (2000) 1105–1113.
[5] M.E. Rosenberg, R. Girton, D. Finkel, D. Chmielewski, A. Barrie III, D.P. Witte, G. Zhu, J.J. Bissler, J.A. Harmony, B.J. Aronow, Apolipoprotein J/clusterin prevents a progressive glomerulopathy of aging, Mol. Cell Biol. 22 (2002) 1893–1902.
[6] R.W. Bailey, B. Aronow, J.A. Harmony, M.D. Griswold, Heat shock-initiated apoptosis is accelerated and removal of damaged cells is delayed in the testis of clusterin/ApoJ knock-out mice, Biol. Reprod. 66 (2002) 1042–1053.
[7] K.S. Leskov, D.Y. Klokov, J. Li, T.J. Kinsella, D.A. Boothman, Synthesis and functional analyses of nuclear clusterin, a cell death protein, J. Biol. Chem. 278 (2003) 11590–11600.
[8] A. Wyatt, J. Yerbury, S. Poon, R. Dabbs, M. Wilson, Chapter 6: The chaperone action of Clusterin and its putative role in quality control of extracellular protein folding, Adv. Cancer Res. 104 (2009) 89–114.
[9] I. Viard, P. Wehrli, L. Jornot, R. Bullani, J.L. Vechietti, J.A. Schifferli, J. Tschopp, L.E. French, Clusterin gene expression mediates resistance to apoptotic cell death induced by heat shock and oxidative stress, J. Invest. Dermatol. 112 (1999) 290–296.
[10] D. Michel, G. Chatelain, S. North, G. Brun, Stress-induced transcription of the clusterin/apoJ gene, Biochem. J. 328 (Pt 1) (1997) 45–50.
[11] T. Finkel, N.J. Holbrook, Oxidants, oxidative stress and the biology of ageing, Nature 408 (2000) 239–247.
[12] E.S. Gonos, A. Derventzi, M. Kveiborg, G. Agiostratidou, M. Kassem, B.F. Clark, P.S. Jat, S.I. Rattan, Cloning and identification of genes that associate with mammalian replicative senescence, Exp. Cell Res. 240 (1998) 66–74.
[13] P. Dumont, F. Chainiaux, F. Eliaers, C. Petropoulou, J. Remacle, C. Koch-Brandt, E.S. Gonos, O. Toussaint, Overexpression of apolipoprotein J in human fibroblasts protects against cytotoxicity and premature senescence induced by ethanol and *tert*-butylhydroperoxide, Cell Stress Chaperones 7 (2002) 23–35.
[14] I.P. Trougakos, M. Poulakou, M. Stathatos, A. Chalikia, A. Melidonis, E.S. Gonos, Serum levels of the senescence biomarker clusterin/apolipoprotein J increase significantly in diabetes type II and during development of coronary heart disease or at myocardial infarction, Exp. Gerontol. 37 (2002) 1175–1187.
[15] P. Rorth, K. Szabo, A. Bailey, T. Laverty, J. Rehm, G.M. Rubin, K. Weigmann, M. Milan, V. Benes, W. Ansorge, S.M. Cohen, Systematic gain-of-function genetics in *Drosophila*, Development 125 (1998) 1049–1057.
[16] D. Yamazaki, J. Horiuchi, Y. Nakagami, S. Nagano, T. Tamura, M. Saitoe, The *Drosophila* DCO mutation suppresses age-related memory impairment without affecting lifespan, Nat. Neurosci. 10 (2007) 478–484.
[17] E.R. Stadtman, C.N. Oliver, Metal-catalyzed oxidation of proteins. Physiological consequences, J. Biol. Chem. 266 (1991) 2005–2008.
[18] E.W. Trotter, L. Berenfeld, S.A. Krause, G.A. Petsko, J.V. Gray, Protein misfolding and temperature up-shift cause G1 arrest via a common mechanism dependent on heat shock factor in *Saccharomyces cerevisiae*, Proc. Natl. Acad. Sci. USA 98 (2001) 7313–7318.
[19] M.T. Marron, T.A. Markow, K.J. Kain, A.G. Gibbs, Effects of starvation and desiccation on energy metabolism in desert and mesic *Drosophila*, J. Insect. Physiol. 49 (2003) 261–270.
[20] K.B. Beckman, B.N. Ames, The free radical theory of aging matures, Physiol. Rev. 78 (1998) 547–581.
[21] J.H. Kim, H.O. Jun, Y.S. Yu, B.H. Min, K.H. Park, K.W. Kim, Protective effect of clusterin from oxidative stress-induced apoptosis in human retinal pigment epithelial cells, Invest. Ophthalmol. Vis. Sci. 51 (2010) 561–566.
[22] K. Kim, S.G. Rhee, E.R. Stadtman, Nonenzymatic cleavage of proteins by reactive oxygen species generated by dithiothreitol and iron, J. Biol. Chem. 260 (1985) 15394–15397.
[23] K. Kim, I.H. Kim, K.Y. Lee, S.G. Rhee, E.R. Stadtman, The isolation and purification of a specific "protector" protein which inhibits enzyme inactivation by a thiol/Fe(III)/O_2 mixed-function oxidation system, J. Biol. Chem. 263 (1988) 4704–4711.
[24] M.K. Cha, I.H. Kim, Glutathione-linked thiol peroxidase activity of human serum albumin: a possible antioxidant role of serum albumin in blood plasma, Biochem. Biophys. Res. Commun. 222 (1996) 619–625.
[25] M.K. Cha, I.H. Kim, Thioredoxin-linked peroxidase from human red blood cell: evidence for the existence of thioredoxin and thioredoxin reductase in human red blood cell, Biochem. Biophys. Res. Commun. 217 (1995) 900–907.
[26] S. Poon, S.B. Easterbrook-Smith, M.S. Rybchyn, J.A. Carver, M.R. Wilson, Clusterin is an ATP-independent chaperone with very broad substrate specificity that stabilizes stressed proteins in a folding-competent state, Biochemistry 39 (2000) 15953–15960.
[27] J. Lakins, S.A. Bennett, J.H. Chen, J.M. Arnold, C. Morrissey, P. Wong, J. O'Sullivan, M. Tenniswood, Clusterin biogenesis is altered during apoptosis in the regressing rat ventral prostate, J. Biol. Chem. 273 (1998) 27887–27895.
[28] Y.K. Kim, K.R. Kim, D.G. Kang, S.Y. Jang, Y.H. Kim, H.J. Cha, Suppression of beta-*N*-acetylglucosaminidase in the *N*-glycosylation pathway for complex glycoprotein formation in *Drosophila* S2 cells, Glycobiology 19 (2009) 301–308.
[29] D.E. Jenne, J. Tschopp, Clusterin: the intriguing guises of a widely expressed glycoprotein, Trends Biochem. Sci. 17 (1992) 154–159.
[30] S. Jiao, W. Dai, L. Lu, Y. Liu, J. Zhou, Y. Li, V. Korzh, C. Duan, The conserved clusterin gene is expressed in the developing choroid plexus under the regulation of notch but not IGF signaling in zebrafish, Endocrinology 152 (2011) 1860–1871.
[31] N.H. Choi-Miura, Y. Takahashi, Y. Nakano, T. Tobe, M. Tomita, Identification of the disulfide bonds in human plasma protein SP-40,40 (apolipoprotein-J), J. Biochem. 112 (1992) 557–561.
[32] T.L. Parkes, A.J. Elia, D. Dickinson, A.J. Hilliker, J.P. Phillips, G.L. Boulianne, Extension of *Drosophila* lifespan by overexpression of human SOD1 in motorneurons, Nat. Genet. 19 (1998) 171–174.
[33] D.R. Rosen, Mutations in Cu/Zn superoxide dismutase gene are associated with familial amyotrophic lateral sclerosis, Nature 364 (1993) 362.

Biochemical and Biophysical Research Communications 420 (2012) 857–861

Contents lists available at SciVerse ScienceDirect

Biochemical and Biophysical Research Communications

journal homepage: www.elsevier.com/locate/ybbrc

Sirtuin inhibition attenuates the production of inflammatory cytokines in lipopolysaccharide-stimulated macrophages

Cláudia A. Fernandes [a], Laurence Fievez [b], Audrey M. Neyrinck [c], Nathalie M. Delzenne [c], Fabrice Bureau [b], Rita Vanbever [a,*]

[a] Université catholique de Louvain, Louvain Drug Research Institute (LDRI), Pharmaceutics and Drug Delivery Research Group, Brussels B-1200, Belgium
[b] University of Liège, GIGA-Research, Laboratory of Cellular and Molecular Immunology, Liège B-4000, Belgium
[c] Université catholique de Louvain, LDRI, Metabolism and Nutrition Research Group, Brussels B-1200, Belgium

ARTICLE INFO

Article history:
Received 13 March 2012
Available online 24 March 2012

Keywords:
Inflammation
NAD-dependent enzymes
Cambinol
Sirtinol
Lipopolysaccharide
Macrophages
Sirtuins
Nuclear factor kappa B

ABSTRACT

In several inflammatory conditions such as rheumatoid arthritis or sepsis, the regulatory mechanisms of inflammation are inefficient and the excessive inflammatory response leads to damage to the host. Sirtuins are class III histone deacetylases that modulate the activity of several transcription factors that are implicated in immune responses. In this study, we evaluated the impact of sirtuin inhibition on the activation of lipopolysaccharide (LPS)-stimulated J774 macrophages by assessing the production of inflammatory cytokines. The pharmacologic inhibition of sirtuins decreased the production of tumour necrosis factor-alpha (TNF-α) interleukin 6 (IL-6) and Rantes. The reduction of cytokine production was associated with decreased nuclear factor kappa B (NF-κB) activity and inhibitor kappa B alpha (IκBα) phosphorylation while no impact was observed on the phosphorylation status of p38 mitogen-activated kinase (p38 MAPK). This work shows that sirtuin pharmacologic inhibitors are a promising tool for the treatment of inflammatory conditions.

© 2012 Elsevier Inc. All rights reserved.

1. Introduction

Macrophages are fundamental cells in cell-mediated innate immune responses with sentinel and clearance functions and the capacity to initiate acute inflammatory response [7]. Innate immune cells express pattern recognition receptors (PRRs) such as Toll-like receptors (TLRs) that recognise conserved structures from microorganisms called pathogen-associated molecular patterns (PAMPs) [22]. The recognition of PAMPs by PRRs triggers the activation of a cascade of enzymes and transcription factors that culminates in the production of inflammatory cytokines and chemokines with the aim to eliminate the signal of danger [22]. Macrophages express several TLRs including TLR4 which recognises lipopolysaccharide (LPS), a cell wall component of gram-negative bacteria. The recognition of LPS is a complex process that starts in the bloodstream via its binding to the lipopolysaccharide-binding protein (LBP). This complex is then recognised by the CD14 from the membrane cell and afterwards by TLR4 [15]. TLR4 activation triggers transcription factors such as the nuclear factor (NF)-κB and the mitogen-activated kinases (MAPKs), which leads to the expression of several inflammatory mediators. Thus, TLR4 activation induces the expression of several inflammatory proteins responsible for the activation and recruitment of inflammatory cells namely adhesion proteins such as intercellular adhesion molecule (ICAM)-1, cytokines and chemokines including tumour necrosis factor (TNF)-α and interleukin (IL)-8 [3,21]. The activation of this pathway is a double edged sword because, upon intense or prolonged activation, it leads to important tissue damage as observed in autoimmune diseases (e.g., rheumatoid arthritis [4]) or to excessive response to infectious agents as observed in sepsis [20]. Thus, the modulation of macrophage activity is a fundamental approach for the treatment of inflammatory conditions.

Sirtuins are a family of enzymes that belong to the family of class III histone deacetylases (HDACs). In mammals, sirtuins comprise seven proteins (SIRT1-7) with different subcellular localisation: SIRT 1 and SIRT2 are present both in the nucleus and cytoplasm, SIRT3-5 are in the mitochondria, and SIRT6-7 in the nucleus [23]. In contrast to class I and II HDACs that require zinc as a co-factor, sirtuins are nicotinamide adenine dinucleotide (NAD)-dependent enzymes. Sirtuins deacetylate the lysine residues of histone proteins but they also deacetylate nonhistone substrates such as several transcription factors including NF-κB, activator protein (AP)-1, forkhead box class O (FOXO) and tumor suppressor p53 [5,6,10,26]. Therefore, sirtuins participate in numerous cellular

* Corresponding author. Address: Université catholique de Louvain, LDRI, Pharmaceutics and Drug Delivery Research Group, Avenue E. Mounier, 73 bte B1.73.12, Brussels B-1200, Belgium. Fax. +32 2 764 73 98.
E-mail address: rita.vanbever@uclouvain.be (R. Vanbever).

0006-291X/$ - see front matter © 2012 Elsevier Inc. All rights reserved.
http://dx.doi.org/10.1016/j.bbrc.2012.03.088

processes such as metabolism, apoptosis, cell division, ageing and inflammation [23].

In the lungs of smokers and chronic obstructive pulmonary disease (COPD) patients, the expression of SIRT1 is decreased as compared to healthy lungs and this correlates with the acetylation and activation of RelA/p65, a sub-unit of NF-κB [16]. Thus, SIRT1 modulates NF-κB activity through the deacetylation of RelA/p65 on lysine 310, a crucial site for the transcriptional activity of NF-κB, and prevents the expression of inflammatory mediators [26]. In addition, SIRT6 deacetylates the H3 lysine 9 on NF-κB target gene promoter with the consequent repression of gene expression [11]. Yet, the role of sirtuins in immune responses is not straightforward and recent reports have described SIRT1 and SIRT6 as positive regulators of inflammatory mediators [1,13,24].

In view of these contradictory effects, we were interested in investigating whether two sirtuin inhibitors, cambinol and sirtinol, could modulate the production of inflammatory cytokines in LPS-stimulated macrophages. Both sirtuin inhibitors decreased the production of inflammatory cytokines in a concentration-dependent manner but cambinol showed a stronger effect. Therefore, we assessed the impact of sirtuin inhibition by cambinol on NF-κB and MAPK pathways.

2. Materials and methods

2.1. Cells

J774 macrophages were kindly given by Professor Marie-Paule Mingeot-Leclercq, Université catholique de Louvain, LDRI, Belgium. Unless specified, all cell culture media and reagents were bought from Gibco Invitrogen Corporation, Belgium. J774 were maintained in RPMI medium 1640 with L-glutamine supplemented with 10% (v/v) foetal bovine serum, 100 IU/ml of Penicillin G sodium and 100 μg/ml of streptomycin sulphate. Cells were maintained in a humidified 5% CO_2 atmosphere at 37 °C.

2.2. In vitro toxicity assay

The toxicity of cambinol (Otava, Toronto, Canada) and sirtinol (Sigma–Aldrich, St. Louis, USA) was evaluated through the reduction of MTT (3-(4,5-dimethylthiazol-2-yl)-2,5-diphenyl tetrazolium bromide, Sigma–Aldrich, St. Louis, USA) by metabolically active cells [25]. J774 macrophages were cultured at 6×10^4/ml in a 96-well plate and pre-incubated for 8 h in order to allow cell adherence. Medium was replaced by increasing concentrations of cambinol or sirtinol (0–250 μM) in medium. Cells were incubated at 37 °C in a humidified 5% CO_2 atmosphere overnight. Afterwards, the medium was replaced by MTT (0.5 mg/ml) in medium and cells were incubated for 3 h. The MTT medium was removed and the formazan crystals were dissolved with the addition of DMSO. Absorbance was measured at 560 nm in a microplate reader. Untreated cells were considered as the control with 100% viability. Triton X-100 at 1% was used as positive control of cytotoxicity.

2.3. Cytokine quantification

J774 macrophages cultured in 48-well plates (Corning incorporated, Belgium) were stimulated with lipopolysaccharide 1 μg/ml (LPS, Escherichia coli O111:B4, Sigma) and were simultaneously treated with increasing concentrations of cambinol (12.5, 25 and 50 μM) or sirtinol (6.25, 12.5 and 25 μM) overnight. Cell-free supernatants were harvested and stored at −20 °C for later cytokine quantification. TNF-α, IL-6 (BD Biosciences, San Diego, USA) and Rantes (PeproTech, United Kingdom) were assayed using commercial ELISA kits according to the recommendations of the manufacturers.

2.4. Preparation of whole-cell extracts and nuclear extracts

J774 macrophages were seeded into 75 cm^2 flasks and treated with increasing concentrations of cambinol for 2 h. Afterwards, LPS was added and cells were incubated for 30 min. Then, whole-cell extracts were prepared using RIPA buffer supplemented with phosphatase and protease inhibitors (Roche Diagnostics, Brussels, Belgium). For the preparation of nuclear extracts, J774 macrophages were seeded into 75 cm^2 flasks and stimulated with LPS (1 μg/ml) and simultaneously treated with increasing concentrations of cambinol. Cells were incubated overnight and nuclear protein extracts were prepared as previously described [2]. Protein amounts were quantified with the BCA protein assay reagent kit in order to normalize results (Pierce, Rockford, IL).

2.5. Electrophoretic mobility shift assay (EMSA)

Electrophoretic mobility shift experiments were performed using 5 μg nuclear proteins as described elsewhere [2]. The sequences of the probes used in this work were as follows: wild-type palindromic B probe, 5'-TTGGCAACGGCAGGGGAATTCCCCTCTCCTTAGGTT-3'; and mutated palindromic B probe, 5'-TTGGCAACGGCAGATCTATTCCCCTCTCCTTAGGTT-3'. The specificity was confirmed by a competition assay with a 50-fold excess of unlabelled wild-type and mutated probes. Images were scanned and were imported to ImageJ software, an image analyser, for semi-quantitative densitometry analysis.

2.6. Phosphoprotein assay

Phosphoproteins were measured in whole-cell extracts using Luminex technology (Bioplex, Bio-Rad, Belgium) according to the manufacturer instructions. Results were expressed as the ratio of fluorescence intensity of phosphorylated target to total target (IκBα, JNK, ERK and p38 MAPK).

2.7. Statistics

Results are expressed as means ± the standard error of the mean. Data were analysed by using the JMP version 4.0.2 and GraphPad & Prism version 5.00 software programs. Statistical analysis was made by one-way ANOVA with Dunnett's multiple comparison post-test. Comparison of p-38 MAPK phosphorylation status was made by a Student *t*-test (Fig. 4). A value of $p < 0.05$ was considered significant.

3. Results

3.1. In vitro toxicity assessment

In order to select non-toxic concentrations of sirtuin inhibitors, we evaluated the impact of cambinol and sirtinol at increasing concentrations on J774 macrophages viability using the MTT assay. Cambinol at a concentration of 250 μM and sirtinol at a concentrations of 50 μM showed significant cytotoxicity whereas lower concentrations had no impact on cell viability (Fig. 1A and B). Thus, in order to exclude a non-specific cellular toxicity as a possible reason for the observed effects, we decided to use cambinol concentrations ranging from 12.5 to 50 μM while sirtinol concentrations varied between 6.25 and 25 μM.

3.2. Sirtuin inhibition decreased the production of TNF-α, IL-6 and Rantes induced by LPS in J774 macrophages

In order to evaluate the impact of sirtuin inhibitors on the production of inflammatory cytokines, J774 macrophages were incubated in presence of LPS with or without cambinol or sirtinol overnight. The treatment of J774 macrophages with LPS induced a marked production of the inflammatory cytokines TNF-α, IL-6 and Rantes in cell supernatants. Both cambinol and sirtinol significantly reduced the production of TNF-α, IL-6 and Rantes in a concentration-dependent manner (Fig. 2A–F). Yet, cambinol showed stronger effects than sirtinol. Therefore, we used cambinol to further investigate the mechanism by which sirtuin inhibitors acted.

3.3. Cambinol reduced LPS-induced NF-κB activation in J774 macrophages

In activated macrophages, the transcription factor NF-κB, plays a fundamental role in the transcription of inflammatory mediators such as cytokines. Therefore, we assessed the impact of cambinol on the activity of NF-κB by electrophoretic mobility shift assay in LPS-stimulated J774 macrophages. NF-κB activity was significantly increased upon LPS stimulation. Cambinol reduced NF-κB activity in a concentration-dependent manner in LPS-treated J774 macrophages (Fig. 3A and B). The phosphorylation of inhibitor kappa B alpha (IκBα) and its subsequent degradation allows NF-κB migration from the cytoplasm into the nucleus where it induces gene transcription [3]. Therefore, we assessed the phosphorylation status of IκBα and we observed that cambinol decreased IκBα phosphorylation in a concentration-dependent manner as well (Fig. 3C).

3.4. Cambinol did not affect MAPK phosphorylation

Because cambinol can also affect cytokine production by modulating the phosphorylation of MAPKs, we evaluated JNK, ERK and p38 MAPK phosphorylation status in whole-cell extracts. Cellular extracts of LPS-treated cells showed increased p38 MAPK phosphorylation but no effect of cambinol was observed on p38 MAPK phosphorylation level in LPS-treated J774 macrophages (Fig. 4). In our model, we did not observe increased phosphorylation of JNK or ERK in J774 macrophages following stimulation with LPS and the treatment with cambinol did not modify the phosphorylation status of these proteins (data not shown).

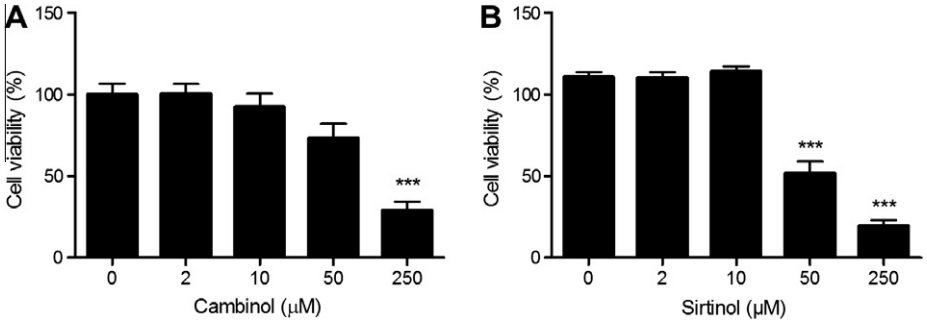


Fig. 1. Effect of sirtuin inhibitors on cell viability. Cell viability was evaluated by the MTT assay after overnight incubation of J774 macrophages with increasing concentrations of cambinol or sirtinol. Results are presented as mean ± SEM of three independent experiments. *indicates groups that are significantly different from vehicle-treated cells. ***$p < 0.001$ vs vehicle.

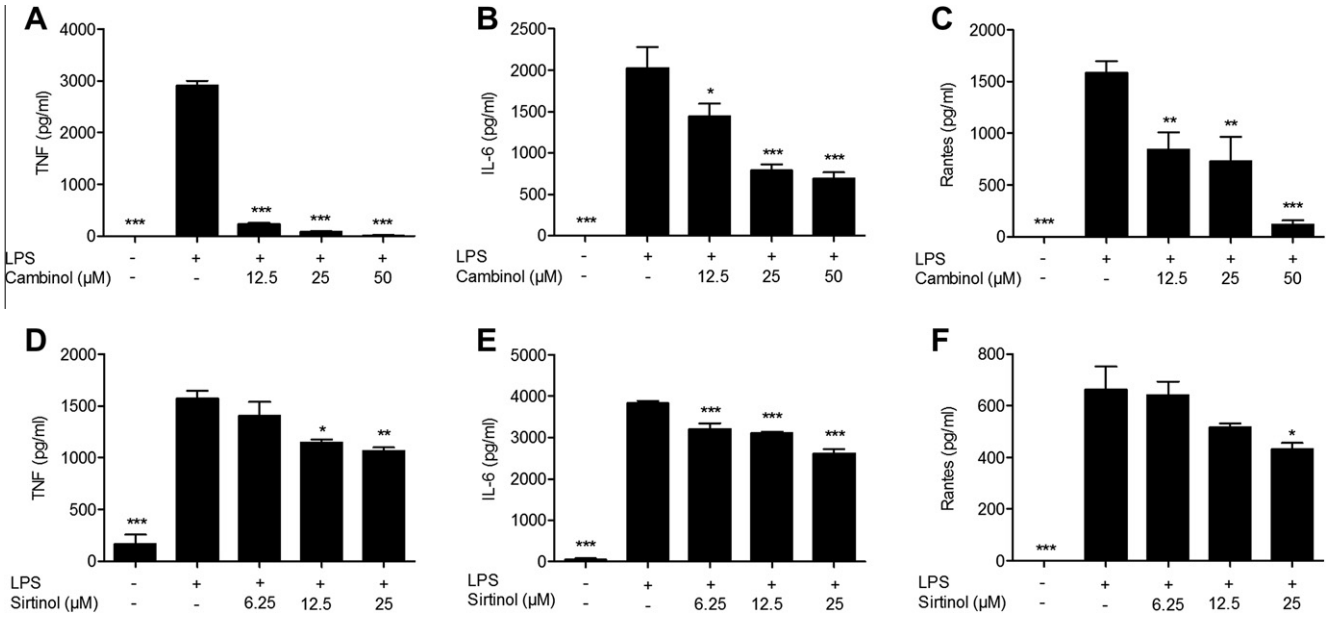


Fig. 2. Effect of sirtuin inhibitors on the production of inflammatory cytokines TNF α (A, D), IL-6 (B, E) and Rantes (C, F). J774 macrophages were stimulated with LPS and treated with increasing doses of cambinol or sirtinol overnight. Cell supernatants were recovered and used for cytokine quantification by ELISA. Results are presented as mean ± SEM and are representative of at least three independent experiments. *$p < 0.05$ vs LPS group, **$p < 0.01$ vs LPS group and ***$p < 0.001$ vs LPS group.

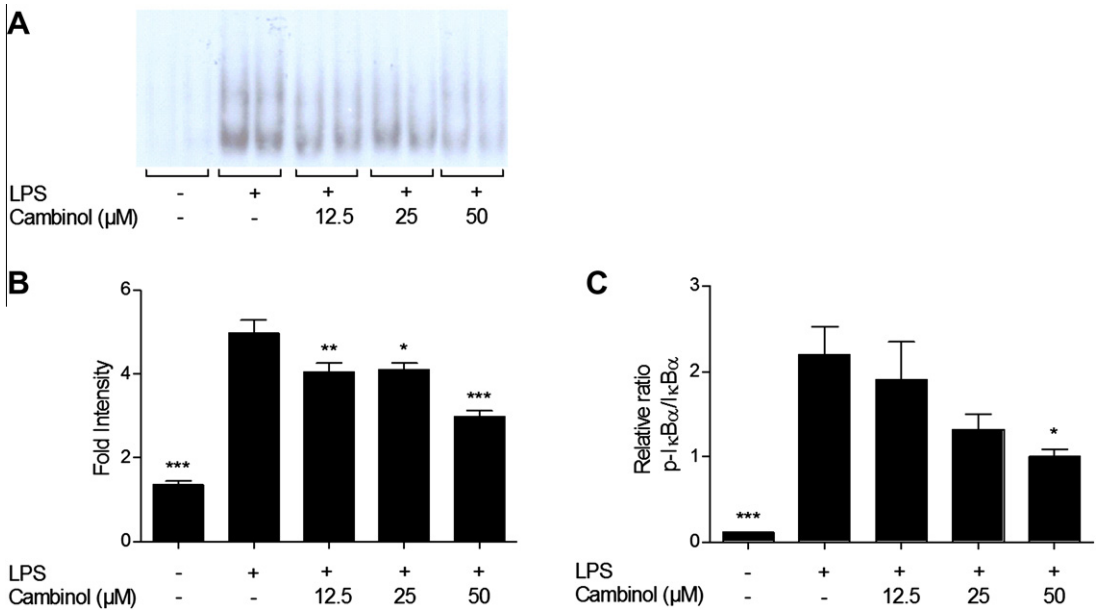


Fig. 3. Effect of cambinol on NF-κB activity. J774 macrophages were stimulated with LPS and treated with increasing concentrations of cambinol overnight. Nuclear extracts were analysed by electrophoretic mobility shift assay to assess NF-κB binding to DNA (A). The semi-quantification of band intensity (B) shows that cambinol significantly inhibited NF-κB activity. J774 macrophages were pre-treated with cambinol for 2 h and afterwards stimulated with LPS for 30 min. Cells were harvested and whole-cell extracts were used for analysis of phosphorylation status of IκBα (C). Results are presented as mean ± SEM of three independent experiments. *indicates significant differences from LPS group. $^{*}p < 0.05$ vs LPS group and $^{***}p < 0.001$ vs LPS group.

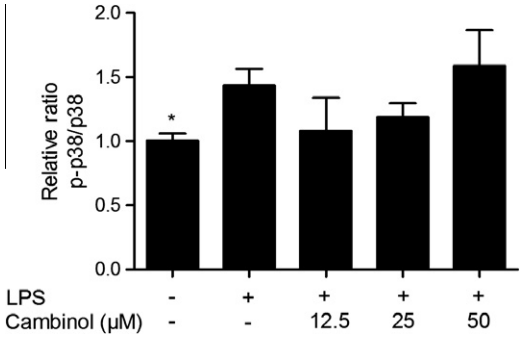


Fig. 4. Effect of cambinol on the phosphorylation status of p38 MAPK. J774 macrophages were pre-treated with cambinol for 2 h and then stimulated with LPS for 30 min. Cells were harvested and cell extracts were used for analysis of the phosphorylation status of p38 MAPK. Results are presented as mean ± SEM of three independent experiments. $^{*}p < 0.05$ vs LPS group.

4. Discussion

This study was designed to evaluate whether the pharmacological inhibition of sirtuins by cambinol and sirtinol could modulate the inflammatory response of macrophages. Our data show that sirtuin inhibitors attenuated the production of the inflammatory cytokines TNF-α, IL-6 and Rantes in a concentration-dependent manner (Fig. 2). Sirtuin pharmacologic inhibition was associated with decreased NF-κB activity and IκBα phosphorylation (Fig. 3) while no effect was observed on p38 MAPK pathway (Fig. 4).

Although both cambinol and sirtinol decreased the production of LPS-induced cytokines, cambinol showed a stronger effect. This can be related to the sirtuin selectivity of these two molecules. Indeed, sirtinol inhibits SIRT2 and in a lower extent SIRT1 while cambinol was shown to equally inhibit SIRT1 and SIRT2 *in vitro* without affecting SIRT3, SIRT5 or zinc-dependent histone deacetylases [8,9]. The impact of cambinol and sirtinol on SIRT4, SIRT6 and SIRT7 is not known because these sirtuins do not possess *in vitro* deacetylase activity [14]. Cambinol selectively inhibits sirtuins because it competes with the histone substrate but not with the co-substrate NAD+ [8]. Therefore, cambinol does not inhibit other NAD-dependent enzymes, while sirtinol was shown to inhibit several classes of enzymes *in vitro* by aggregation or precipitation [9].

Initial studies on the role of sirtuins in inflammation suggested that the pharmacological inhibition of sirtuins, in particular SIRT1, could accentuate the inflammatory response. Indeed, SIRT1 levels were decreased in COPD patients and in cigarette smoke- or in LPS-stimulated macrophages [16,19]. In addition, the reestablishment of SIRT1 activity decreased inflammatory cytokine production whereas SIRT1 silencing in myeloid cells increased pro-inflammatory signalling in response to environmental stress [16,18,19]. Yet, in this work, we observed that sirtuin pharmacological inhibitors decreased LPS-induced production of cytokines in J774 macrophages. These findings are in agreement with recent studies that pointed out a positive effect of SIRT6 on the production of inflammatory cytokines. In these recent studies, pharmacological inhibitors of sirtuins reduced the production of TNF, IL-6 or IFNγ, similarly to our results [1,24]. In addition, SIRT1 inhibition was found to dampen adaptative Th2 responses in a mouse model of airway allergy [13]. Further studies should be performed in order to determine which sirtuin or sirtuins are affected in our model.

The activation of the transcription factor NF-κB and the subsequent expression of inflammatory mediators can be regulated by the acetylation/deacetylation of its subunit p65. Yeung and colleagues showed that SIRT1 directly interacted with the RelA/p65 subunit of NF- κB and deacetylates the lysine 310, an important site for NF-κB activity [26]. SIRT6 was also found to limit NF-κB activity via histone deacetylation. SIRT6 interacts with the subunit RelA of NF-κB and it is carried to NF-κB target gene promoters where it deacetylates the histone H3 lysine 9 [11]. In contrast, our data describe for the first time that the inhibition of sirtuins by a pharmacological inhibitor, cambinol, is associated with decreased NF-κB activation and IκBα phosphorylation. In inactive cells, NF-κB is restricted to the cytoplasm in association with IκBα. After cell stimulation, IκBα is phosphorylated and degraded by the

proteasome allowing NF-κB migration to the nucleus where it binds to DNA and activates gene transcription [3]. The inhibition of IκBα phosphorylation by cambinol led to NF-κB retention in the cytoplasm and consequently inhibited the transcription of inflammatory genes. This result is consistent with the decreased production of inflammatory cytokines observed in cambinol-treated cells (Fig. 2).

In addition to NF-κB activation and nuclear translocation, the activation of TLR4 triggers a phosphorylation cascade and consequently the activation of the MAPK pathway. The activation of p38 MAPK increases the expression of inflammatory cytokines through the activation of the transcription factor NF-κB and by increasing cytokine mRNA translation and stability [12,17]. In this study, p38 MAPK activity was not affected by sirtuin inhibition showing that the modulation of cytokine production was not mediated by p38 MAPK pathway. These results are in line with a recent work from Schug and colleagues which used a myeloid cell-specific SIRT1 knockout mouse model and showed that SIRT1 did not interfere with the MAPK pathway [18].

In summary, our study shows that the pharmacologic inhibition of sirtuins inhibited the activation of the NF-κB pathway and decreased the production of LPS-induced cytokines in J774 macrophages *in vitro*. Further studies are needed in order to identify the sirtuin that positively regulates NF-κB activity and the production of inflammatory cytokines. Yet, our study provides a new therapeutic potential for inflammatory diseases such as rheumatoid arthritis and sepsis through sirtuin inhibition.

Acknowledgments

This work was supported by the Réseaux programme of the Walloon Region (Grant no. 415695; Belgium), by a Patrimoine research Grant from the Université catholique de Louvain and by the Fonds National de la Recherche Scientifique (FNRS, Belgium). Rita Vanbever is Senior research associate of the FNRS.

References

[1] S. Bruzzone, F. Fruscione, S. Morando, T. Ferrando, A. Poggi, A. Garuti, A. D'Urso, M. Selmo, F. Benvenuto, M. Cea, G. Zoppoli, E. Moran, D. Soncini, A. Ballestrero, B. Sordat, F. Patrone, R. Mostoslavsky, A. Uccelli, A. Nencioni, Catastrophic NAD+ depletion in activated T lymphocytes through Nampt inhibition reduces demyelination and disability in EAE, PLoS One 4 (2009) e7897.

[2] F. Bureau, A. Vanderplasschen, F. Jaspar, F. Minner, P.P. Pastoret, M.P. Merville, V. Bours, P. Lekeux, Constitutive nuclear factor-kappaB activity preserves homeostasis of quiescent mature lymphocytes and granulocytes by controlling the expression of distinct Bcl-2 family proteins, Blood 99 (2002) 3683–3691.

[3] L.F. Chen, W.C. Greene, Shaping the nuclear action of NF-kappaB, Nat. Rev. Mol. Cell Biol. 5 (2004) 392–401.

[4] S.K. Drexler, P.L. Kong, J. Wales, B.M. Foxwell, Cell signalling in macrophages, the principal innate immune effector cells of rheumatoid arthritis, Arthritis Res. Ther. 10 (2008) 216.

[5] D. Frescas, L. Valenti, D. Accili, Nuclear trapping of the forkhead transcription factor FoxO1 via Sirt-dependent deacetylation promotes expression of glucogenetic genes, J. Biol. Chem. 280 (2005) 20589–20595.

[6] Z. Gao, J. Ye, Inhibition of transcriptional activity of c-JUN by SIRT1, Biochem. Biophys. Res. Commun. 376 (2008) 793–796.

[7] S. Gordon, The macrophage: past, present and future, Eur. J. Immunol. 37 (Suppl. 1) (2007) S9–S17.

[8] B. Heltweg, T. Gatbonton, A.D. Schuler, J. Posakony, H. Li, S. Goehle, R. Kollipara, R.A. Depinho, Y. Gu, J.A. Simon, A. Bedalov, Antitumor activity of a small-molecule inhibitor of human silent information regulator 2 enzymes, Cancer Res. 66 (2006) 4368–4377.

[9] B. Heltweg, M. Jung, A microplate reader-based nonisotopic histone deacetylase activity assay, Anal. Biochem. 302 (2002) 175–183.

[10] B. Jung-Hynes, N. Ahmad, Role of p53 in the anti-proliferative effects of Sirt1 inhibition in prostate cancer cells, Cell Cycle 8 (2009) 1478–1483.

[11] T.L. Kawahara, E. Michishita, A.S. Adler, M. Damian, E. Berber, M. Lin, R.A. McCord, K.C. Ongaigui, L.D. Boxer, H.Y. Chang, K.F. Chua, SIRT6 links histone H3 lysine 9 deacetylation to NF-kappaB-dependent gene expression and organismal life span, Cell 136 (2009) 62–74.

[12] A. Kotlyarov, A. Neininger, C. Schubert, R. Eckert, C. Birchmeier, H.D. Volk, M. Gaestel, MAPKAP kinase 2 is essential for LPS-induced TNF-alpha biosynthesis, Nat. Cell Biol. 1 (1999) 94–97.

[13] A. Legutko, T. Marichal, L. Fievez, D. Bedoret, A. Mayer, V.H. de, L. Klotz, P.V. Drion, C. Heirman, D. Cataldo, R. Louis, K. Thielemans, F. Andris, O. Leo, P. Lekeux, C.J. Desmet, F. Bureau, Sirtuin 1 promotes Th2 responses and airway allergy by repressing peroxisome proliferator-activated receptor-{gamma} activity in dendritic cells, J. Immunol. 187 (2011) 4517–4529.

[14] B.J. North, B.L. Marshall, M.T. Borra, J.M. Denu, E. Verdin, The human Sir2 ortholog, SIRT2, is an NAD+-dependent tubulin deacetylase, Mol. Cell 11 (2003) 437–444.

[15] E.M. Palsson-McDermott, L.A. O'Neill, Signal transduction by the lipopolysaccharide receptor, Toll-like receptor-4, Immunology 113 (2004) 153–162.

[16] S. Rajendrasozhan, S.R. Yang, V.L. Kinnula, I. Rahman, SIRT1, an antiinflammatory and antiaging protein, is decreased in lungs of patients with chronic obstructive pulmonary disease, Am. J. Respir. Crit. Care Med. 177 (2008) 861–870.

[17] S. Saccani, S. Pantano, G. Natoli, P38-Dependent marking of inflammatory genes for increased NF-kappa B recruitment, Nat. Immunol. 3 (2002) 69–75.

[18] T.T. Schug, Q. Xu, H. Gao, A. Peres-da-Silva, D.W. Draper, M.B. Fessler, A. Purushotham, X. Li, Myeloid deletion of SIRT1 induces inflammatory signaling in response to environmental stress, Mol. Cell Biol. 30 (2010) 4712–4721.

[19] Z. Shen, J.M. Ajmo, C.Q. Rogers, X. Liang, L. Le, M.M. Murr, Y. Peng, M. You, Role of SIRT1 in regulation of LPS- or two ethanol metabolites-induced TNF-alpha production in cultured macrophage cell lines, Am. J. Physiol. Gastrointest. Liver Physiol. 296 (2009) G1047–G1053.

[20] J.W. Smith, R.L. Gamelli, S.B. Jones, R. Shankar, Immunologic responses to critical injury and sepsis, J. Intensive Care Med. 21 (2006) 160–172.

[21] A. Symons, S. Beinke, S.C. Ley, MAP kinase kinase kinases and innate immunity, Trends Immunol. 27 (2006) 40–48.

[22] O. Takeuchi, S. Akira, Pattern recognition receptors and inflammation, Cell 140 (2010) 805–820.

[23] D.M. Taylor, M.M. Maxwell, R. Luthi-Carter, A.G. Kazantsev, Biological and potential therapeutic roles of sirtuin deacetylases, Cell Mol. Life Sci. 65 (2008) 4000–4018.

[24] F. Van Gool, M. Galli, C. Gueydan, V. Kruys, P.P. Prevot, A. Bedalov, R. Mostoslavsky, F.W. Alt, S.T. De, O. Leo, Intracellular NAD levels regulate tumor necrosis factor protein synthesis in a sirtuin-dependent manner, Nat. Med. 15 (2009) 206–210.

[25] B. Vroman, M. Mazza, M.R. Fernandez, R. Jerome, V. Preat, Copolymers of epsilon-caprolactone and quaternized epsilon-caprolactone as gene carriers, J. Control Release 118 (2007) 136–144.

[26] F. Yeung, J.E. Hoberg, C.S. Ramsey, M.D. Keller, D.R. Jones, R.A. Frye, M.W. Mayo, Modulation of NF-kappaB-dependent transcription and cell survival by the SIRT1 deacetylase, EMBO J. 23 (2004) 2369–2380.

Biochemical and Biophysical Research Communications 420 (2012) 862–868

Contents lists available at SciVerse ScienceDirect

Biochemical and Biophysical Research Communications

journal homepage: www.elsevier.com/locate/ybbrc

A structurally novel hemopexin fold protein of rice plays role in chlorophyll degradation

Tirthartha Chattopadhyay [a], Sudipta Bhattacharyya [b], Amit K. Das [b], Mrinal K. Maiti [a,b,*]

[a] Adv. Lab. for Plant Genetic Engineering, Advanced Technology Development Center, Indian Institute of Technology Kharagpur, Kharagpur 721302, India
[b] Department of Biotechnology, Indian Institute of Technology Kharagpur, Kharagpur 721302, India

ARTICLE INFO

Article history:
Received 13 March 2012
Available online 23 March 2012

Keywords:
Chlorophyll degradation
Hemopexin fold protein
Hemin
OsHFP
Rice anther

ABSTRACT

Proteins containing hemopexin fold domain are suggested to have diverse functions in various living organisms. In order to investigate the structure and function of this type of protein in rice plant (*Oryza sativa*), the gene encoding a hemopexin fold protein (OsHFP) was cloned, analyzed *in silico* and characterized. Molecular modeling revealed that the OsHFP is closely related to other hemopexin fold proteins, but is unique with a cylindrical central tunnel as well as extended N- and C-terminal domains. The recombinant OsHFP was found to bind hemin, the oxidized form of heme *in vitro*. The expression of the single copy *OsHFP* gene was detected in rice flower buds. Heterologous expression of OsHFP in green leaf tissues resulted in chlorophyll degradation; however, stable expression of OsHFP was observed in transgenic hairy roots, a non-green tissue. The possible role of OsHFP in regulating programmed cell death in anther green tissues of rice is proposed.

© 2012 Elsevier Inc. All rights reserved.

1. Introduction

Heme (iron protoporphyrin IX) is an important component in living system for its biological activity in association with several proteins involved in cellular metabolism. Heme is present as prosthetic group in hemoglobin, in other hemoproteins like myoglobin and as an essential component of chlorophyll, some peroxidases, cytochromes and catalases. However, free heme is potentially toxic for the living system as it has the capability of generating oxidative stress by spontaneous auto-oxidation [1] and potentiality of intercalation into lipid membrane [2]. Moreover, free heme serves as an iron source for pathogenic invasive microorganisms [3]. In plant system, free heme is highly cytotoxic due to their capacity of producing potent radicals in presence of light [4]. In human system, hemopexin, a plasma glycoprotein of 60 kDa provides a line of defense as free heme scavenger by binding free heme with a very high affinity [5].

Interestingly, more than 500 proteins from various sources including virus, eukaryotes and prokaryotes have been reported to contain hemopexin fold domain with structural and/or functional resemblance. They constitute the hemopexin superfamily [6]. Among them, pea (*Pisum sativum*) albumin 2 (pa2) is the first reported plant protein, containing four hemopexin folds and thus advocates for the possibility that hemopexin repeats originated before the plant and animal kingdom diverged [7]. Later, the protein has been linked to the polyamine biosynthesis pathway in developing pea seeds [8]. Orthologous pa2 protein from chickpea (*Cicer arietinum*) has been purified and shown to bind hemin, oxidized form of heme, *in vitro* [9]. A heme binding membrane protein (At-TSPO) from Arabidopsis has been characterized recently [10]. It has been established that though At-TSPO plays a protective role during porphyrin toxicity, plant cells degrade At-TSPO through an autophagy-dependent mechanism. Possible adverse effect of At-TSPO on heme homeostasis has been advocated as the reason behind its degradation by plant cells.

Recently, crystal structure of LS-24, a hemopexin fold seed protein from lathyrus (*Lathyrus sativus*) has been elucidated, and a role of LS-24 in oxidative stress has been forwarded on the basis of the heme and spermine binding to the different oligomeric states of this protein [11]. Interestingly, crystal structure of CP4, another hemopexin fold protein from cowpea (*Vigna unguiculata*) has been solved; and biochemical characterization established that the CP4 binds spermine (like LS-24) but not hemin [12]. All these observations suggest that the heme–hemopexin interaction has significant biochemical and physiological implications also in plant system.

In the present study, we have identified and cloned the gene encoding a novel hemopexin fold protein (annotated hereafter as OsHFP; *Oryza sativa* hemopexin fold protein) from rice genome. Through *in silico* analysis, we have established the uniqueness of

* Corresponding author at: Department of Biotechnology & Adv. Lab. for Plant Genetic Engineering, Advanced Technology Development Center, Indian Institute of Technology Kharagpur, Kharagpur 721302, India. Fax: +91 3222 278707.
E-mail addresses: mrinalkmaiti@gmail.com, maitimk@hijli.iitkgp.ernet.in (M.K. Maiti).

0006-291X/$ - see front matter © 2012 Elsevier Inc. All rights reserved.
http://dx.doi.org/10.1016/j.bbrc.2012.03.089

the OsHFP compared to other reported hemopexin fold proteins. Biochemical and physiological functions of the OsHFP have been characterized by heterologous expression in bacterial and plant systems. To the best of our knowledge this is the first report of characterizing a hemopexin fold protein from rice plant, at structural and functional levels.

2. Materials and methods

2.1. Cloning of the OsHFP gene from rice

Sequence information of the coding DNA sequence (CDS) of *OsHFP* was obtained from a hypothetical protein reported in public database NCBI (GenBank ID: CAE03710). As the gene was predicted to have no intron, it was amplified through PCR from genomic DNA isolated from the local cultivar IR64 of rice. Specific forward primer (*OsHFP* FP 5′-GCGC*GGATCC*ATGGATGAAAACAATCAGAG-3′) and reverse primer (*OsHFP* RP 5′-AATT*GAGCTC*CTAGTCATCCTGGTC-GCGC-3′) were designed to incorporate *Bam*HI and *Sac*I restriction sites (underlined italics) to facilitate directional cloning. Sequence analysis of the cloned amplicon revealed 100% identity with the reported sequence in public database.

2.2. OsHFP sequence analysis and homology modeling

Amino acid sequence alignment was carried out in ClustalW [13]. *In silico* model building was performed using MODELLER 8v2 [14] taking crystal structure of LS-24 (PDB ID: 3LP9) as the template. Energy minimization of the resulting model was carried out by Insight II (version 2000.1, 2000; Accelrys), and the best model was stereo-chemically evaluated by PROCHECK [http://www.ebi.ac.uk/thornton-srv/software/PROCHECK] and VERIFY 3D [http://nihserver.mbi.ucla.edu/Verify_3D]. All the pictorial representations were prepared using PyMol [http://www.pymol.org].

2.3. Bacterial expression of the OsHFP

The *OsHFP* CDS was sub-cloned in *Bam*HI/*Sac*I sites of bacterial expression vector pRSET-A (Invitrogen) to have in-frame fusion with the N-terminal 6× His tag of the vector. The recombinant plasmid, mentioned hereafter as pRSET:OsHFP, was transformed into *E. coli* BL21 (DE3)/pLysE competent cells and recombinant clones were selected on LB agar plates supplemented with 200 mg l^{-1} ampicillin and 34 mg l^{-1} chloramphenicol. Bacterial expression of the recombinant OsHFP, designated as rOsHFP, was carried out as described in Supplementary information (Si. 1).

2.4. Purification, refolding and in vitro hemin binding assay of the recombinant OsHFP

Purification and on-column refolding of the rOsHFP was carried out as described in Supplementary information (Si. 2). Purified rOsHFP was used for custom production of anti-OsHFP polyclonal antibody in rabbit.

In-gel hemin binding assay was carried out based on the reported protocol [15] with minor modification. Briefly, the rOsHFP was subjected to SDS–PAGE. After electrophoresis, the gel was rinsed with Tris-buffered saline (TBS; 10 mM Tris, 150 mM NaCl, pH 8.0) containing 0.1% Tween 20 (v/v) followed by incubation for 1.5 h with TBS containing hemin (10 μg ml^{-1}), the oxidized form of heme. After that the gel was washed thoroughly in TBS and stained for detecting bound hemin using tetramethylbenzidine (TMB)–H_2O_2 as described previously [9].

2.5. Construction of recombinant plasmid bearing OsHFP gene expression cassette and plant transformation

The *OsHFP* CDS was sub-cloned in *Bam*HI/*Sac*I sites of the plant transformation vector pCAMBIA 1300, under the transcriptional regulation of enhanced (2×) CaMV 35S promoter and NOS terminator (Supplementary Fig. Sf1). The construct was verified through characteristic restriction digestion analysis to assure proper orientation of the genetic elements. The *OsHFP* gene construct was introduced separately into *A. tumefaciens* strain LBA4404 and strain EHA105 for transformation of tobacco and rice, respectively. *Agrobacterium*-mediated plant transformation was carried out as described earlier [16].

The *OsHFP* gene construct was also transferred into *Agrobacterium rhizogenes* strain LBA1334 for expressing OsHFP in a suitable transgenic non-green tissue, i.e., hairy roots of jute (*Corchorus* spp.). Transformation of jute cotyledonary leaves to raise transgenic hairy roots was performed as described elsewhere [17]. At the same time LBA1334 strain carrying the pCAM::2X35S::*gusA* construct [17] was used to develop GUS (β-glucuronidase) expressing transgenic hairy roots.

2.6. Plant protein extraction and immunobloting

Plant protein extraction and immunobloting were performed as described in Supplementary information (Si. 3). Protein quantity was measured by standard Bradford method [18].

3. Results

3.1. The OsHFP contains a central hemopexin fold flanked by N- and C-terminal domains

Analysis of the amino acid sequence (295 amino acids) derived from the cloned *OsHFP* CDS revealed that the OsHFP is predicted to have a molecular mass of ~34 kDa. The OsHFP shares ~33% and 32% sequence identity with the two recently reported hemopexin fold proteins from plant, namely, LS-24 of lathyrus and CP4 of cowpea, respectively (Supplementary Fig. Sf2). The *in silico* modeling yielded the model of the central hemopexin domain of OsHFP, whereas, the N-terminal (M1-V40) and C-terminal (I271-D295) domains remained unmodeled, due to the lack of sequence similarity (Fig. 1A). However, in order to ascertain the putative physicochemical properties of OsHFP as a function of hemopexin fold bearing protein, the structural detail of the central hemopexin domain was taken into account. The quality of the model showed 92.3% residues in the core region and 4.7% residues in the allowed region.

Interestingly, the *in silico* model of OsHFP with four symmetrically oriented β blades around a hollow central shaft, resembles the structural hierarchy of well documented four-bladed β propeller structure of the ubiquitous hemopexin fold. Each of the blades of the model consists of three or four anti-parallel β sheets oriented almost perpendicularly to the principal axis of the central tunnel (Fig. 1B). Though each blade of the β propeller model seems to exhibit the similar kind of three dimensional organizations, however, the structural superimposition indicated, Blade 1, Blade 3 and Blade 4 are highly similar whilst Blade 2 is a bit different. The relative twist of the anti-parallel β sheets of Blade 2 is responsible for such disparity. The whole structural motif of OsHFP with an inherent pseudo fourfold symmetry (of which the symmetry axis passes through the central tunnel), is arranged in such a way that the Blade 1 comes in close proximity with Blade 4 (Fig. 1B). However, similar to other orthologs, the central tunnel of OsHFP formed by the juxtaposition of four β sheets (β1, β5, β9 and β12) from each blade (Blade 1, Blade 2, Blade 3 and Blade 4, respectively, Fig. 1C)

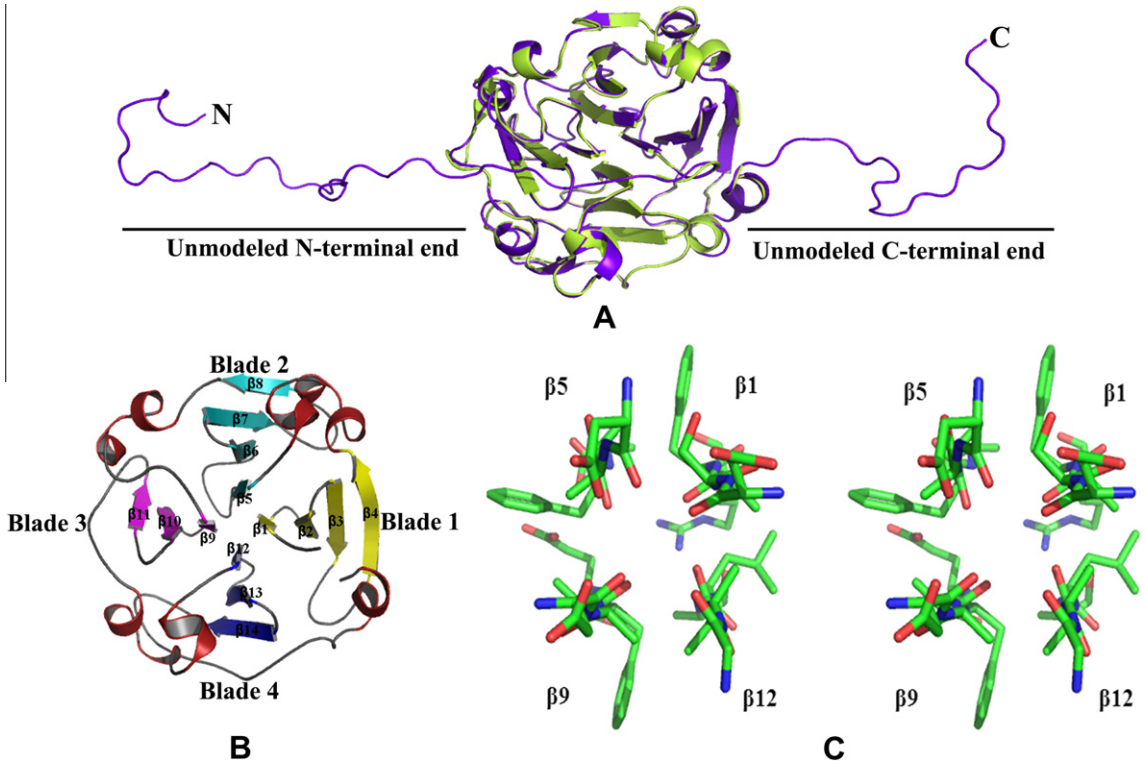


Fig. 1. Homology modeling of OsHFP. (A) Superimposition of OsHFP model structure (purple) with its template LS-24 (green). (B) A ribbon diagram showing the central hemopexin fold of OsHFP depicting the four-bladed β propeller model. Each blade of the propeller is colored differentially while the interconnecting α helices and loops are colored red and grey, respectively. (C) Wall eyed stereo view of the central tunnel of OsHFP hemopexin fold showing the close proximity of the backbone carbonyl groups of the constituent β sheets (for interpretation of the references to colour in this figure legend, the reader is referred to the web version of this article.).

is supposed to be populated by negatively or positively charged ions. The inward projection of the peptide carbonyl and amide groups coming from each constituent β sheets makes the tunnel ideal for the binding of charged species like metals and other anions. Unlike the funnel shaped tunnels found in other hemopexin folds, the central tunnel of OsHFP is roughly uniform in diameter (N-terminal diameter ~6.6 Å and C-terminal diameter ~7.2 Å), which is well adapted for the binding of the divalent and monovalent metals as well as other negatively charged anions. However unlike most of the mammalian hemopexin fold bearing protein, the central tunnel of plant ortholog is much more selective for the binding of anions. In OsHFP and in other plant orthologs, the presence of a conserved arginine (R49), at one end of the central tunnel may be crucial for steric exclusion of the large incoming anions like PO_4^{3-}. The root mean square deviations (r.m.s.d. C^{α}) of OsHFP with the hemopexin domain of human matrix metalloproteinase MMP12 (PDB ID: 3BA0), N-terminal domain of bilobal human blood serum hemopexin (PDB ID: 1QJS) and cowpea CP4 (PDB ID: 3OYO) are found to be 2.073, 7.937 and 0.762 Å, respectively, hence showing the structural reminiscence of OsHFP with plant hemopexins. Intriguingly, despite showing a high degree of sequence-structural resemblance with plant hemopexins, especially with its template LS-24 (root mean square deviation 0.236 Å), the OsHFP essentially lacks two of the three spermine binding residues (E80 and S118 of LS24 are replaced by A126 and K164 in OsHFP).

3.2. Bacterially expressed refolded recombinant OsHFP binds hemin

The recombinant OsHFP (rOsHFP) with N-terminal 6X His-tag was expressed in *E. coli* cells (Fig. 2A). The rOsHFP was found predominantly in the inclusion body fraction; lowering the growth temperature and/or IPTG concentration did not improve the solubility of rOsHFP (unpublished result). Urea solubilized rOsHFP was purified by Ni–NTA affinity chromatography (Fig. 2B) and confirmed by immunodetection using anti-His antibody (Fig. 2C).

Urea solubilized rOsHFP was further subjected to on-column refolding and was eluted at >90% purity (Supplementary Fig. Sf3). However, when the refolded protein was subjected to 10% native PAGE, its migration was highly restricted, indicating the possible formation of multimer (Fig. 2D). This observation was further supported by the gel-filtration chromatography where refolded rOsHFP was eluted from the column at a position corresponding to ~440 kDa (Fig. 2E).

Hemin binding activity of the OsHFP was verified by in-gel assay. To avoid the migration anomaly, hemin binding property of the refolded rOsHFP was checked after SDS–PAGE followed by activity staining to visualize the bound hemin. It was found that the refolded rOsHFP binds hemin even after SDS–PAGE, at all the three concentrations tested (Fig. 2F, right).

3.3. Single copy OsHFP gene is expressed in rice flower bud tissue

Genomic organization of the *OsHFP* was examined through Southern hybridization using radio-labeled *OsHFP* CDS as probe. Restriction fragment lengths generated by four different enzymes suggest the presence of a single locus of *OsHFP* in rice genome, as revealed by autoradiogram (Fig. 3A).

Immunodetection was performed to verify the expression pattern of OsHFP protein in different plant parts of rice. The immunoblot analysis revealed that the endogenous OsHFP of ~34 kDa is expressed in the flower bud, but not in the leaf and stem tissues of rice plant (Fig. 3B).

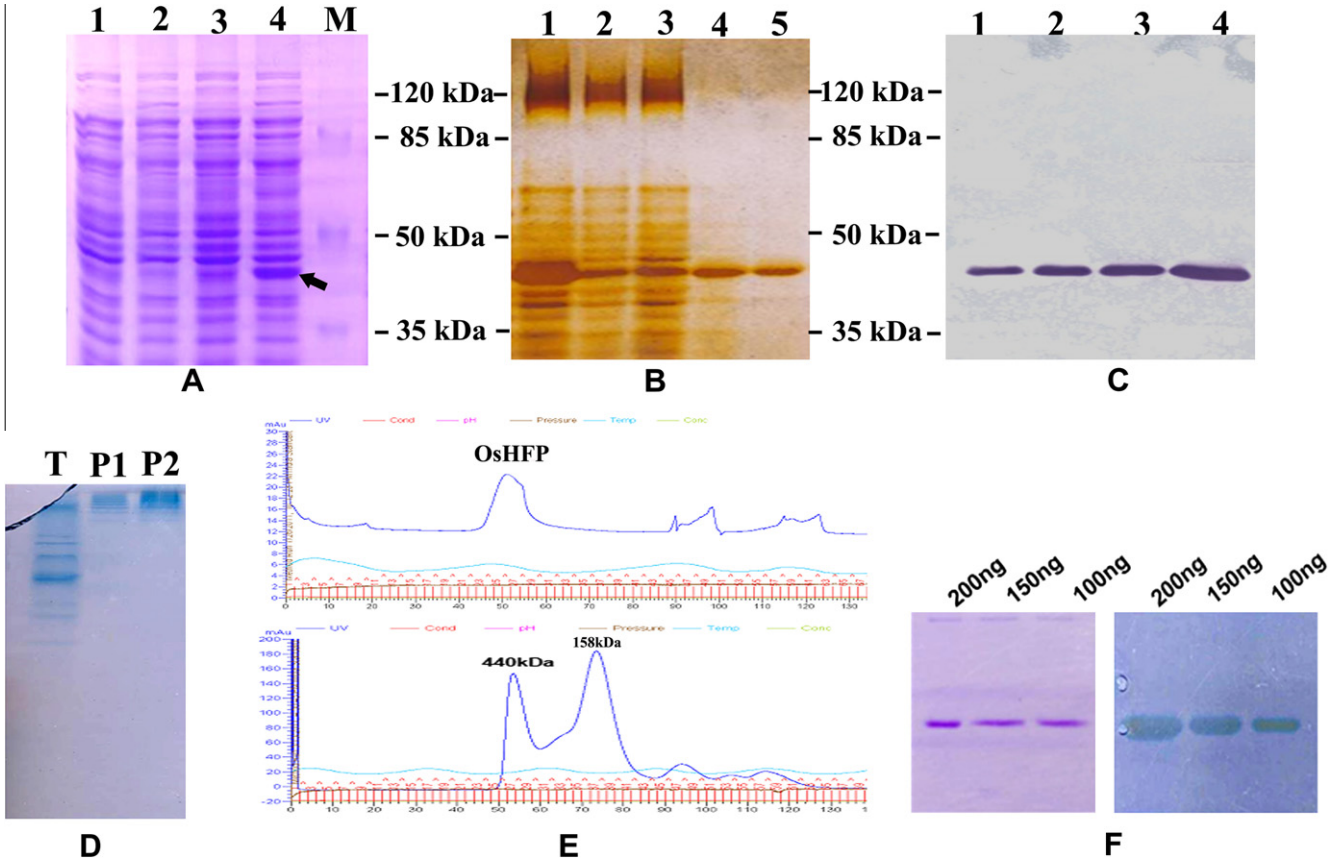


Fig. 2. Bacterial expression and hemin binding property of rOsHFP. (A) Coomassie blue stained 12% SDS–PAGE. Lanes 1–4 represent total protein from uninduced cells containing pRSET-A vector, induced cells containing pRSET-A vector, uninduced cells containing pRSET:OsHFP, and induced cells containing pRSET:OsHFP, respectively. Lane M represents protein molecular weight marker. Black arrow indicates expressed rOsHFP. (B) Silver stained 12% SDS–PAGE showing Ni–NTA based purification of the rOsHFP. Lanes 1–5 represent total protein from induced cells, unbound fraction, wash fraction, wash with 50 mM imidazole and eluted protein fraction, respectively. (C) Immunodetection of purified rOsHFP using anti-His antibody. Lanes 1–4 represent 50, 100, 150 and 200 ng of purified rOsHFP. (D) Migration of the refolded rOsHFP in 10% native PAGE. Lanes T, P1, P2 represent total protein solubilized in 8 M urea buffer, 250 ng refolded rOsHFP and 500 ng refolded rOsHFP, respectively. (E) Gel filtration chromatography of the refolded rOsHFP (top) in comparison to calibration (bottom) obtained with proteins of known molecular weights. (F) In-gel hemin binding activity of the refolded rOsHFP showing Coomassie blue stained part (left) and activity stained part (right) (for interpretation of the references to colour in this figure legend, the reader is referred to the web version of this article.).

3.4. OsHFP plays a role in chlorophyll degradation

In order to investigate the biochemical and physiological functions of OsHFP in plant system, attempts have been made to raise transgenic tobacco plants with the *OsHFP* gene construct through *A. tumefaciens*-mediated transformation. Surprisingly, within 10 days of infection, all the explants developed complete necrosis and no transformants could be recovered (Fig. 4A, left). In a parallel experiment, the same *OsHFP* gene construct was used to transform embryogenic rice calli to observe the effect of OsHFP over-expression in its native host, i.e., rice. In this case, several putative transformed calli (non-green) were obtained, which exhibited hygromycin resistance (as the Hyg^R gene is the selection marker in the *OsHFP* gene construct for screening plant transformants), but failed to develop into mature green plantlets in the regeneration medium (Fig. 4A, right). Similar tobacco leaf discs and rice calli transformed with a different gene construct, however, regenerated properly to develop transformed plantlets under the same culture conditions (Fig. 4A, controls). Both the experimental events were replicated thrice with identical results, indicating a possible antagonistic effect of OsHFP on green plant tissues, leading to the failure of plantlet development.

To study the effect of OsHFP heterologous expression on chlorophyll content of green plant tissues, normal leaf discs of tobacco were further transformed with *A. tumefaciens* cells harboring the same *OsHFP* gene construct. Chlorophyll a and chlorophyll b contents of the transformed leaf discs were measured 1, 4 and 7 days after co-cultivation. Leaf discs of tobacco transformed with the blank vector (without the *OsHFP* gene) were used as control. Analysis revealed that both chlorophyll a and chlorophyll b contents reduced rapidly in the leaf discs transformed with the OsHFP gene expression construct, compared to the control (Fig. 4B).

The effect of localized over-expression of OsHFP on the green leaf tissues of heterologous plant system, i.e. tobacco was evaluated through agroinfiltration of the *OsHFP* gene construct, taking blank vector (without the *OsHFP* gene) as control. Agroinfiltration of the *OsHFP* gene construct resulted in the development of dechlorophyllized regions surrounding the sites of infiltration on the tobacco leaves after 3 days, and became highly prominent after 6 days of infiltration (Fig. 4C).

To further clarify these observations, the OsHFP was expressed in a non-green plant expression system. To achieve it, the same *OsHFP* gene construct was used through *A. rhizogenes*-mediated transformation to develop transgenic hairy roots of jute plant. In this case, successful transgenic hairy roots were developed without any noticeable adverse phenotype (Fig. 4D). Transgenic hairy roots over-expressing the OsHFP had a similar growth pattern in comparison to the transgenic hairy roots expressing the *gusA* reporter gene under the same transcriptional regulation as *OsHFP* gene. Stable expression of OsHFP in non-green transgenic hairy root lines

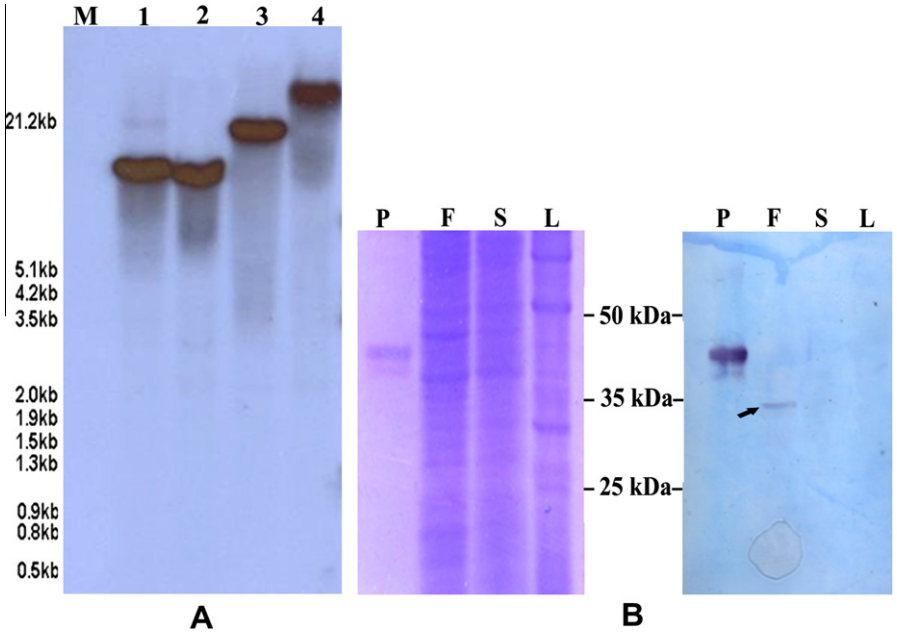


Fig. 3. Genomic organization of *OsHFP* gene locus and expression profiling of OsHFP in rice plant. (A) Southern hybridization of the rice genomic DNA with radio-labeled *OsHFP* CDS as probe. Lanes 1–4 represent 10 μg of genomic DNA digested with *Hin*dIII, *Bam*HI, *Sac*I and *Kpn*I, respectively. Lane M represents λ DNA digested with *Eco*RI + *Hin*dIII. (B) Endogenous OsHFP expression profiling in different parts of rice plant. Lanes P, F, S, L represent purified rOsHFP, and total proteins from flower bud, stem and leaf tissue of rice plant, respectively; Coomassie blue stained gel (left) and respective immunodetection with anti-OsHFP antibody (right). Black arrow indicates detected native OsHFP (for interpretation of the references to colour in this figure legend, the reader is referred to the web version of this article.).

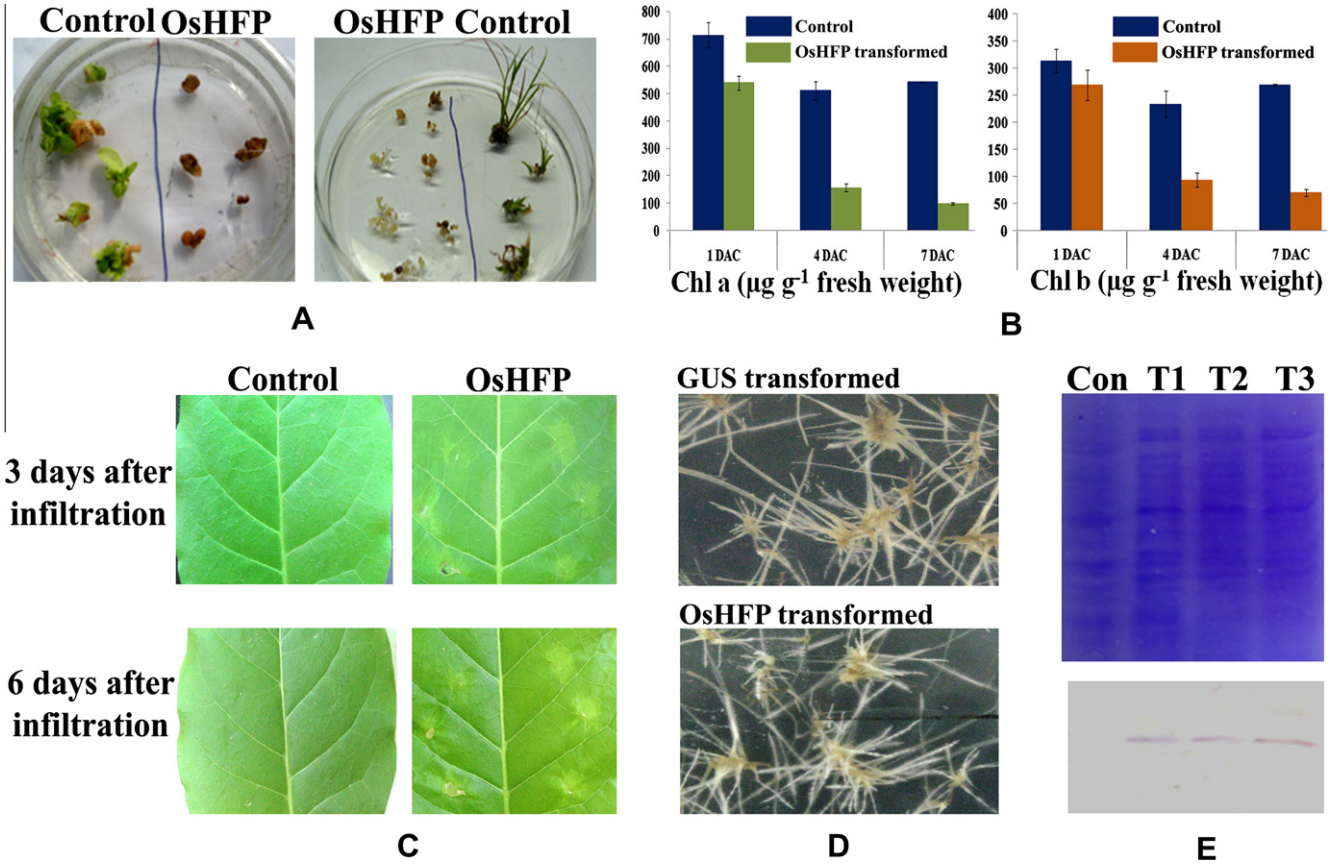


Fig. 4. Chlorophyll degradation property of OsHFP. (A) Effect of OsHFP expression on green leaf discs of tobacco (left) and non-green embryogenic calli of rice (right). Controls indicate similar explants transformed with a different gene construct. (B) Rapid reduction in chlorophyll a (Chl a) and chlorophyll b (Chl b) content in transformed tobacco leaf discs after OsHFP expression. DAC represents days after co-cultivation. Control indicates transformation with blank vector without the *OsHFP* gene. (C) Localized chlorophyll degradation by agroinfiltration of *OsHFP* in tobacco leaves. Control indicates agroinfiltration with the blank vector without the *OsHFP* gene. (D) OsHFP expressing transgenic hairy roots of jute plant (bottom) showing no distinguishable features in comparison to those expressing reporter gene *gusA* (top). (E) Immunodetection of OsHFP in transgenic hairy roots. Lanes Con, T1, T2, T3 represent total protein from a GUS expressing and three OsHFP expressing transgenic hairy root lines, respectively; Coomassie blue stained gel (top) and respective immunodetection with anti-OsHFP antibody (bottom) (for interpretation of the references to colour in this figure legend, the reader is referred to the web version of this article.).

was confirmed by immunodetection using anti-OsHFP polyclonal antibody (Fig. 4E).

4. Discussion

Results of the present study document cloning of the gene encoding a novel hemopexin fold protein (OsHFP) from rice, and characterization of the OsHFP at structural and functional level. Homology modeling based structural analysis of OsHFP establishes close resemblance of the central domain with a few plant hemopexin fold proteins, but not at the N- and C-terminal domains. Presence of unique cylindrical tunnel in the core of the hemopexin fold and extended termini at both the ends of the OsHFP may signify additional role of this protein in rice plant. Unlike mammalian hemopexin motif, where formation of intra-molecular disulfide bonds plays a crucial role in structural integrity [19]; no such intra-molecular disulfide bonds are found to be present in plant hemopexins [11]. Hence, just like other plant hemopexin orthologs, the gross structural organization of OsHFP is supposed to rely on the hydrophobic clustering caused by the β sandwich of the central hemopexin fold. Unique feature of the central core region of OsHFP advocates that binding of the positively and negatively charged ions to the central tunnel should play a crucial structural role by neutralizing the peptide backbone charges, which would otherwise disrupt the protein structure by repulsive forces. In our preliminary study, indicative observation has been obtained on the role of calcium in solubility of rOsHFP in bacterial system (unpublished result). Moreover, definite dipole moment resulting from the differential distribution of the positively and negatively charged amino acid residues at the two termini of the central tunnel may play a pivotal role in ligand specificity. However, the subtle ligand binding chemistry of hemopexin fold proteins, which is generally endowed by the interface residues of two interacting monomers, cannot be precisely discussed in the glimpse of *in silico* model of OsHFP and awaits future crystallization experiments.

In-gel hemin binding assay revealed that the recombinant OsHFP is capable of binding hemin (the oxidized form of heme). Hemin binding property of OsHFP is similar to that of HbpA, a membrane-associated hemin binding protein from *Bartonella*, which retains its hemin binding capacity even after SDS–PAGE and electrophoretic transfer to nitrocellulose membrane [15]. Hemin binding property of OsHFP is biologically significant, as the turnover of heme is very important in plant system from various biochemical and physiological aspects, including the biogenesis of protoporphyrin and chlorophyll. Very recently, it has been documented that the At-TSPO, a hemin binding protein of Arabidopsis is having a protective role against porphyrin toxicity [10].

The single copy *OsHFP* gene is found to be expressed in the flower bud tissues of rice plant. In our on-going studies, we have already observed that the putative promoter region of the *OsHFP* gene drives predominant expression in the anther connective tissues of transgenic tobacco lines (unpublished result). Connective tissues of anther contain chlorophyll [20] and are degenerated in a developmentally regulated manner to facilitate anther dehiscence for successful pollen release from the anther. The programmed cell death (PCD) of the connective tissue in anther is highly coordinated and still requires extensive study to decipher the regulation at the molecular level. Interestingly, involvement of chlorophyll breakdown products in plant PCD has been postulated [21].

The expression of OsHFP causes chlorophyll degradation in tobacco green leaves, and prevents plantlet regeneration from transformed rice calli. However, the stable expression of OsHFP is observed in non-green transgenic hairy roots of jute plant, the system that we have established earlier using *gusA* reporter gene expression [17]. Results of the present study establish a clear role of OsHFP in chlorophyll degradation, though the actual mechanism of action remains to be elucidated. On the basis of our findings and analyses on the OsHFP structure, its hemin binding activity, expression in the flower bud and chlorophyll degradation property, we hypothesize that the OsHFP plays a critical role in the PCD of anther for successful pollen formation in rice.

Acknowledgments

Authors sincerely thank Prof. S.K. Sen and Dr. A. Basu for their cooperation. TC and SB acknowledge Indian Institute of Technology Kharagpur, India for providing research scholarship. Financial supports from the DBT and DST, Government of India are acknowledged.

Appendix A. Supplementary data

Supplementary data associated with this article can be found, in the online version, at http://dx.doi.org/10.1016/j.bbrc.2012.03.089.

References

[1] H. Piccard, P.E. Van den Steen, G. Opdenakker, Hemopexin domains as multifunctional liganding modules in matrix metalloproteinases and other proteins, J. Leukoc. Biol. 81 (2007) 870–892.
[2] E. Tolosano, F. Altruda, Hemopexin: structure, function, and regulation, DNA Cell Biol. 21 (2002) 297–306.
[3] P. Ascenzi, A. Bocedi, P. Visca, F. Altruda, E. Tolosano, T. Beringhelli, M. Fasano, Hemoglobin and heme scavenging, IUBMB Life 57 (2005) 749–759.
[4] N. Mochizuki, R. Tanaka, B. Grimm, T. Masuda, M. Moulin, A.G. Smith, A. Tanaka, M.J. Terry, The cell biology of tetrapyrroles: a life and death struggle, Trends Plant Sci. 15 (2010) 488–498.
[5] Y.I. Miller, A. Smith, W.T. Morgan, N. Shaklai, Role of hemopexin in protection of low-density lipoprotein against hemoglobin-induced oxidation, Biochemistry 35 (1996) 13112–13117.
[6] D. Jenne, K.K. Stanley, Nucleotide sequence and organization of the human S-protein gene: repeating peptide motifs in the "pexin" family and a model for their evolution, Biochemistry 26 (1987) 6735–6742.
[7] D. Jenne, Homology of placental protein 11 and pea seed albumin 2 with vitronectin, Biochem. Biophys. Res. Commun. 176 (1991) 1000–1006.
[8] H. Vigeolas, C. Chinoy, E. Zuther, B. Blessington, P. Geigenberger, C. Domoney, Combined metabolomic and genetic approaches reveal a link between the polyamine pathway and albumin 2 in developing pea seeds, Plant Physiol. 146 (2008) 74–82.
[9] J. Pedroche, M. Yust, H. Lqari, C. Megías, J. Girón-Calle, M. Alaiz, F. Millán, J. Vioque, Chickpea pa2 albumin binds hemin, Plant Sci. 168 (2005) 1109–1114.
[10] C. Vanhee, G. Zapotoczny, D. Masquelier, M. Ghislain, H. Batoko, The *Arabidopsis* multistress regulator TSPO is a heme binding membrane protein and a potential scavenger of porphyrins via an autophagy-dependent degradation mechanism, Plant Cell 23 (2011) 785–805.
[11] V. Gaur, I.A. Qureshi, A. Singh, V. Chanana, D.M. Salunke, Crystal structure and functional insights of hemopexin fold protein from grass pea, Plant Physiol. 152 (2010) 1842–1850.
[12] V. Gaur, V. Chanana, A. Jain, D.M. Salunke, The structure of a haemopexin-fold protein from cow pea (*Vigna unguiculata*) suggests functional diversity of haemopexins in plants, Acta Crystallogr. Sect. F Struct. Biol. Cryst. Commun. 67 (2011) 193–200.
[13] J.D. Thompson, D.G. Higgins, T.J. Gibson, CLUSTAL W: improving the sensitivity of progressive multiple sequence alignment through sequence weighting, positions-specific gap penalties and weight matrix choice, Nucleic Acids Res. 22 (1994) 4673–4680.
[14] A. Sali, T.L. Blundell, Comparative protein modelling by satisfaction of spatial restrains, J. Mol. Biol. 234 (1993) 779–815.
[15] J.A. Carroll, S.A. Coleman, L.S. Smitherman, M.F. Minnick, Hemin-binding surface protein from *Bartonella quintana*, Infect. Immun. 68 (2000) 6750–6757.
[16] J. Banerjee, M.K. Maiti, Functional role of rice germin-like protein1 in regulation of plant height and disease resistance, Biochem. Biophys. Res. Commun. 394 (2010) 178–183.
[17] T. Chattopadhyay, S. Roy, A. Mitra, M.K. Maiti, Development of a transgenic hairy root system in jute (*Corchorus capsularis* L.) with *gusA* reporter gene through *Agrobacterium rhizogenes* mediated co-transformation, Plant Cell Rep. 30 (2011) 485–493.
[18] M.M. Bradford, A rapid and sensitive method for the quantification of microgram quantity of protein utilizing the principle of protein–dye binding, Anal. Biochem. 72 (1976) 248–254.

[19] M. Paoli, B.F. Anderson, H.M. Baker, W.T. Morgan, A. Smith, E.N. Baker, Crystal structure of hemopexin reveals a novel high-affinity heme site formed between two beta-propeller domains, Nat. Struct. Biol. 6 (1999) 926–931.
[20] C. Clément, P. Mischler, M. Burrus, J.C. Audran, Characteristics of the photosynthetic apparatus and CO_2-fixaton in the flower bud of *Lilium*. II. anther, Int. J. Plant Sci. 158 (1997) 801–810.
[21] J.M. Mach, A.R. Castillo, R. Hoogstraten, J.T. Greenberg, The *Arabidopsis*-accelerated cell death gene ACD2 encodes red chlorophyll catabolite reductase and suppresses the spread of disease symptoms, Proc. Natl. Acad. Sci. USA 98 (2001) 771–776.

Biochemical and Biophysical Research Communications 420 (2012) 869–874

Contents lists available at SciVerse ScienceDirect

Biochemical and Biophysical Research Communications

journal homepage: www.elsevier.com/locate/ybbrc

PI3-kinase and mTOR inhibitors differently modulate the function of the ABCG2 multidrug transporter

Csilla Hegedüs [a,1], Krisztina Truta-Feles [a,1], Géza Antalffy [a], Anna Brózik [b], Ildikó Kasza [a], Katalin Német [a], Tamás I. Orbán [a], Csilla Özvegy-Laczka [a], András Váradi [b], Balázs Sarkadi [a,c,*]

[a] Membrane Research Group of the Hungarian Academy of Sciences, Department of Biophysics, Semmelweis University and National Blood Center, Budapest, Hungary
[b] Research Centre for Natural Sciences, Institute of Enzymology, Hungarian Academy of Sciences, Budapest, Hungary
[c] Research Centre for Natural Sciences, Institute of Molecular Pharmacology, Hungarian Academy of Sciences, Budapest, Hungary

ARTICLE INFO

Article history:
Received 13 March 2012
Available online 24 March 2012

Keywords:
ABCG2
PI3-kinase/Akt/mTOR signaling
LY294002
Wortmannin
Rapamycin

ABSTRACT

The ATP-binding cassette (ABC) transporter ABCG2 plays an important role in tissue detoxification and confers multidrug resistance to cancer cells. Identification of expressional and functional cellular regulators of this multidrug transporter is therefore intensively pursued. The PI3-kinase/Akt signaling axis has been implicated as a key element in regulating various cellular functions, including the expression and plasma membrane localization of ABCG2. Here we demonstrate that besides inhibiting their respective target kinases, the pharmacological PI3-kinase inhibitor LY294002 and the downstream mTOR kinase inhibitor rapamycin also directly inhibit ABCG2 function. In contrast, wortmannin, another commonly used pharmacological inhibitor of PI3-kinase does not interact with the transporter. We suggest that direct functional modulation of ABCG2 should be taken into consideration when pharmacological agents are applied to dissect the specific role of PI3-kinase/Akt/mTOR signaling in cellular functions.

© 2012 Elsevier Inc. All rights reserved.

1. Introduction

The ABCG2 membrane glycoprotein belongs to the ATP-binding cassette transporter superfamily. ABCG2 eliminates various endogenous and environmental toxins from the cells by active efflux, and it plays a pivotal role in physiologic tissue protection against xenobiotics [1]. Exploiting the protective function of the transporter, cancer cells overexpressing ABCG2 become cross-resistant against a wide spectrum of chemically and target-wise unrelated drugs, a phenomenon known as multidrug resistance (MDR) [1,2]. Being a key multidrug transporter involved in both physiologic and pathological processes, identification of cellular factors regulating expression and function of ABCG2 is intensively studied.

The phosphatidylinositol 3-kinase/Akt signaling axis has been implicated in the regulation of a number of cellular functions, including that of ABCG2. Upon growth factor receptor phosphorylation, phosphatidylinositol 3-kinase (PI3-kinase, PI3K) is activated and generates phosphatidylinositol (3,4,5) trisphosphate, which results in subsequent plasma membrane recruitment and activation of Akt kinase [3]. Downstream targets of activated Akt include the mammalian target of rapamycin (mTOR) kinase [4]. Inhibition of Akt signaling has been shown to provoke rapid translocation of ABCG2 from the plasma membrane to intracellular compartments in mouse bone marrow cells [5], in polarized ABCG2-overexpressing porcine LLC-PK1 cells [6], in glioma-derived cells [7], in human gallbladder epithelial cells [8], in hepatocellular carcinoma-derived cells [9], and also in ABCG2-expressing extracellular vesicles formed between MCF-7/MR breast cancer cells [10]. Nevertheless, opposing results have also been published, showing that inhibition of Akt signaling in human leukemia cells down-regulated overall ABCG2 protein levels rather than affecting only its plasma membrane localization [11]. Involvement of the downstream mTOR kinase in regulating plasma membrane insertion of ABCG2 is also controversial [7,12]. The PI3K/Akt-mediated decrease in ABCG2 plasma membrane levels has also been associated with attenuated transporter function [5,7,9,10] resulting in reversal of ABCG2-mediated drug resistance [9,10].

In these studies, pharmacological inhibitors of the PI3K/Akt/mTOR pathway, such as the PI3K inhibitors wortmannin and LY294002 [13] and the mTOR inhibitor rapamycin [13] were also applied to manipulate cellular signal transduction. Given the multispecific drug recognition capability of ABCG2 [1], however, it is

Abbreviations: ABC, ATP-binding cassette; PI3K, phosphatidylinositol 3-kinase; mTOR, mammalian target of rapamycin; MDR, multidrug resistance.

* Corresponding author at: Membrane Research Group of the Hungarian Academy of Sciences and Semmelweis University, Department of Biophysics, H-1113, Diószegi u. 64, Budapest, Hungary. Fax: +36 1 372 4353.
E-mail address: sarkadi@biomembrane.hu (B. Sarkadi).

[1] These authors contributed equally to this work.

0006-291X/$ - see front matter © 2012 Elsevier Inc. All rights reserved.
http://dx.doi.org/10.1016/j.bbrc.2012.03.090

reasonable to assume that these compounds might also directly interact with the transporter. Such a direct drug-transporter interaction would also allow for different interpretation of the experimental results, especially those concerning ABCG2 function. Indeed, data regarding interaction of ABCG2 and rapamycin have already been published [12,14], however the issue of susceptibility of rapamycin to ABCG2-mediated transport was conflicting. LY294002 has been shown to be a competitive inhibitor of another multidrug transporter MRP1 [15], but interaction of this compound and the other PI3K inhibitor wortmannin with ABCG2 has not yet been characterized. In this work, we aimed to give a detailed biochemical characterization regarding the interaction between the aforementioned pharmacological PI3K/Akt/mTOR inhibitors and ABCG2. Additionally, we also studied the presently controversial role of PI3K/Akt/mTOR signaling in the rapid regulation of the subcellular distribution of ABCG2.

2. Materials and methods

2.1. Materials

Unless otherwise stated, all reagents were obtained from Sigma–Aldrich. Alexa-Fluor-conjugated antibodies, wheat germ agglutinin (WGA), TOPRO-3 and DAPI were obtained from Invitrogen. Ko143 was obtained from Tocris Bioscience. Phycoerythrin-conjugated secondary antibodies were purchased from Beckman Coulter.

2.2. Cell lines

A431 and PLB985 (PLB) cells stably expressing human wild-type ABCG2 were generated previously [16], [17]. MDCKII cells stably expressing the N-terminally GFP-tagged wild-type ABCG2 (GFP-ABCG2) variant [18] were generated by transposon-based gene delivery. Total ABCG2 protein expression of the cell lines was measured by Western blot using the anti-ABCG2 BXP-21 antibody [19].

2.3. Membrane ABCG2-ATPase activity measurements

Membranes were isolated from insect (Sf9) cells expressing ABCG2wt or GFP-ABCG2wt [18,20]. Cholesterol-loading of the membranes was achieved as described previously [21]. ABCG2 protein content of the membranes was determined by Western blot using the anti-ABCG2 BXP-21 antibody [19]. Vanadate-sensitive ABCG2-ATPase activity was measured by a colorimetric reaction [19], experiments were performed in duplicates.

2.4. Western blot analysis of kinase phosphorylation

Cells were dispersed in serum-free or complete media and were let to adhere. The following day, serum-starved cells were stimulated with 20 ng/mL human recombinant Epidermal Growth Factor (hEGF, Cell Signaling Technology) for 15 min and then were exposed to drugs for additional 15 min. To check phosphorylation status of Akt kinase for the ABCG2 localization experiments, cells were treated with wortmannin for 90 min. Cells were then washed and scraped in lysis buffer (50 mM TRIS–HCl, 150 mM NaCl, 1 mM EDTA-Na, 1 mM EGTA-Na, 1% Nonidet-P40) containing various inhibitors of phosphatase and protease enzyme activities [22]. Twenty micrograms of cellular proteins were resolved and analyzed by Western blot using the following antibodies: p-Akt 1/2/3 (Ser 473) and p-p70S6 kinase alpha (Thr 389) (Santa Cruz Biotechnology). Beta-actin staining was used to check sample loading.

2.5. 5D3 labeling of ABCG2

Cell surface ABCG2 expression was followed by flow cytometry using the anti-ABCG2 5D3 antibody which recognizes an extracellular epitope of the protein [23], [24]. 5D3 labeling was performed as described previously [24], using 1 μg/mL 5D3 or mouse IgG2b (isotype control) and 3 μg/mL phycoerythrin (PE) – or 200× diluted Alexa-Fluor-647-conjugated secondary antibodies. For the ABCG2 localization experiments, cells were fixed with 1% paraformaldehyde (PFA) for 10 min at 37 °C before the labeling procedure. Effect of drugs on the 5D3 binding affinity of ABCG2 [24] was investigated using the same labeling protocol, except that following a 5 min pre-incubation, drugs were present throughout labeling with the primary antibodies. Except for PFA-fixed samples, TO-PRO-3 or propidium iodide staining was also performed to allow exclusion of dead cells.

2.6. Inhibition of ABCG2-mediated efflux of Hoechst 33342 and mitoxantrone

Inhibitory effect of drugs on Hoechst 33342 or mitoxantrone efflux from intact ABCG2-expressing cells were measured and calculated as described previously [16], with minor modifications. One micromolar of Ko143 was used to achieve maximum inhibition of ABCG2.

2.7. MTT assay

MTT (3-[4,5-dimethylthiazol-2-yl]-2,5-diphenyltetrazolium) assay was applied to determine cellular viability. 4×10^3 cells were seeded in 96-well plates and were let to adhere overnight. Following exposure to drugs for 72 h, cells were stained with 0.5 mg/mL MTT for 4 h at 37 °C in 5% CO_2. The formed formazan crystals were solubilized by 9:1 isopropanol-hydrochloric acid solution. Absorbance was measured at 540 nm using a Perkin Elmer Victor X3 2030 Multilabel Plate Reader. Experiments were carried out in quadruplicates.

2.8. GFP-ABCG2 localization studies with confocal microscopy

To study subcellular distribution of GFP-ABCG2 in polarized cells, 2×10^4 MDCKII/GFP-ABCG2 cells/well were seeded onto Lab-Tek II chambered coverglass (Nalge Nunc International) and were grown for 5 days. Following drug treatment, cells were fixed with 4% PFA and were stained with 5 μg/mL Alexa-Fluor-633-conjugated WGA and 1 μM DAPI for 10 min at room temperature. Images were captured with an Olympus IX-81/FV500 laser scanning confocal microscope and analyzed by the FluoView 4.7 software.

3. Results and discussion

3.1. Effect of wortmannin, LY294002 and rapamycin on membrane ABCG2-ATPase

In order to pre-screen potential interaction between the pharmacological PI3K/Akt/mTOR inhibitors and ABCG2, we measured whether the inhibitors can influence the basal and the stimulated ATPase activity of the transporter (Fig. 1). Since GFP-tagged ABCG2 was also applied in further experiments, we also characterized the potential interaction between this protein and the pharmacological PI3K/Akt/mTOR inhibitors. Human wild-type ABCG2 or its GFP-tagged variant was expressed in Sf9 insect cells from which membrane fractions were isolated as described previously [20]. ABCG2 protein content of the isolated membrane fragments was measured by Western blot (Supplementary Fig. 1A). Since membrane

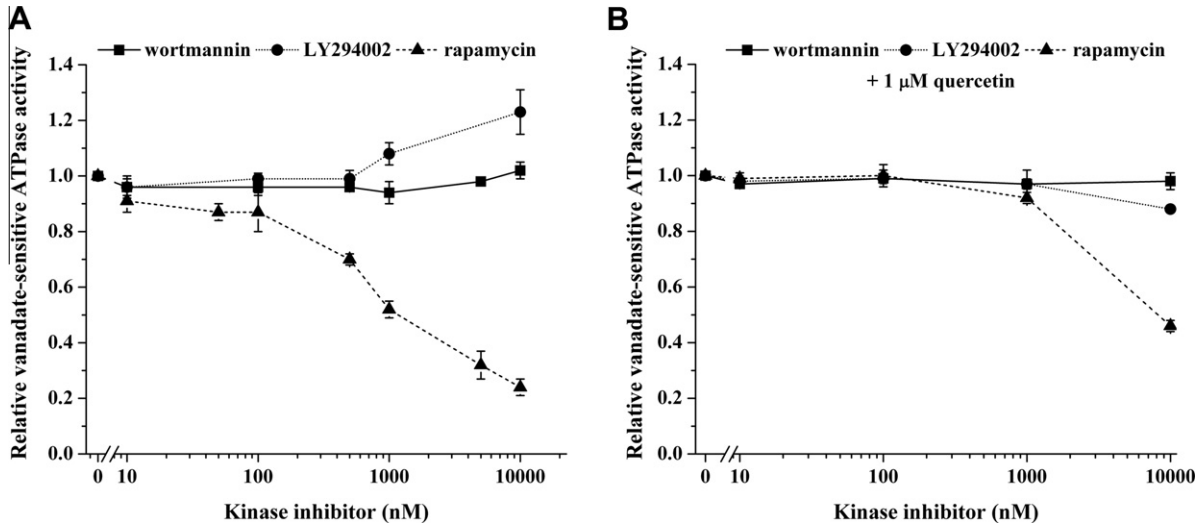


Fig. 1. Modulation of the ABCG2-ATPase activity by pharmacological PI3K/Akt/mTOR inhibitors. Modulatory effect of the PI3K/Akt/mTOR inhibitors on the (A) basal and (B) quercetin-stimulated ABCG2-ATPase was measured using isolated ABCG2-expressing Sf9 membranes. Data were normalized to the ABCG2-ATPase activities measured in the absence of PI3K/Akt/mTOR inhibitors. Mean ± SE values of at least three independent experiments are shown.

cholesterol has been shown to selectively modulate ABCG2 function thereby increasing sensitivity of the ATPase assay [21,25], we loaded the Sf9 membranes with cholesterol during the membrane preparation procedure [21].

The basal ABCG2-ATPase could be only slightly stimulated with LY294002 at the experimentally relevant 10 μM concentration (Fig. 1A). Rapamycin decreased the basal ABCG2-ATPase in a concentration-dependent manner and produced a pronounced inhibitory effect when applied at 10 μM (Fig. 1A). Wortmannin did not significantly influence the basal ABCG2-ATPase at any applied concentrations (Fig. 1A).

We also measured drug effects on the substrate-stimulated ABCG2-ATPase activity (Fig. 1B). In this setup, high turnover of the ABCG2-ATPase was triggered by administration of the high affinity ABCG2 substrate quercetin (1 μM) [26], and we expected that ABCG2-interacting drugs could decrease this stimulated ABCG2-ATPase activity [27]. This was indeed the case for 10 μM rapamycin (Fig. 1B). In contrast, 10 μM LY294002 only slightly decreased the stimulated ABCG2-ATPase, whereas wortmannin displayed no effect at all (Fig. 1B). Importantly, we obtained similar results in case of both the basal and the stimulated ATPase activity of GFP-ABCG2 as well (Supplementary Fig. 2).

Collectively, these data suggest that in contrast to wortmannin, LY294002 and rapamycin interact with ABCG2. Nevertheless, substrates transported at higher or lower rates can both stimulate and inhibit the high basal ABCG2-ATPase activity [20], respectively. Moreover, in certain cases ABCG2-interacting compounds produce no ABCG2-ATPase modulatory effect at all [27], [28]. Furthermore, LY294002 only slightly modified both the basal and the stimulated ABCG2-ATPase. Therefore, based on these results we could not determine the nature of the interaction between ABCG2 and rapamycin, and could not exclude a potential interaction of wortmannin with ABCG2 either. Also, it remained to be determined whether the potential interaction between LY294002 or rapamycin and ABCG2 is relevant in a cellular context.

3.2. The presence of ABCG2 does not influence target kinase inhibition by the investigated PI3K/Akt/mTOR inhibitors

Next, we studied whether a potential interaction between the studied pharmacological PI3K/Akt/mTOR inhibitors and ABCG2 resulted in decreased drug efficiency at the cellular level, which would suggest active ABCG2-mediated transport of the drugs. To this end, we followed phosphorylation of Akt and p70S6 kinases (a downstream target of mTOR) in drug-treated parental and ABCG2-overexpressing A431 cells (Supplementary Fig. 1B, C) (Fig. 2). A431 epidermoid carcinoma cells overexpress the Epidermal Growth Factor Receptor (EGFR) [17], and phosphorylation of kinase cascades downstream of EGFR, including the PI3K/Akt axis, can therefore be stimulated by EGF [3]. We used experimentally relevant concentrations of wortmannin, LY294002 and rapamycin. In addition, we tested 10 μM rapamycin, since it showed modulation of the ABCG2-ATPase at this concentration.

Stimulation of serum-starved A431 and A431/ABCG2 cells with 20 ng/mL hEGF resulted in elevated pAkt (Fig. 2A) and pp70S6K (Fig. 2B) levels. In A431 cells, the hEGF-mediated enhanced phosphorylation of Akt could be fully abolished by wortmannin (Fig. 2A). LY294002 also decreased pAkt levels, however, its effect was less pronounced than that of wortmannin (Fig. 2A). Rapamycin at 10 nM did not affect pAkt levels; however, when applied at 10 μM, it also resulted in a slight decrease (Fig. 2A). The hEGF-stimulated phoshorylation of p70S6K was inhibited similarly by wortmannin and LY294002, and was completely abolished by both applied concentrations of rapamycin (Fig. 2B). As we obtained similar phosphorylation patterns of both Akt (Fig. 2A) and p70S6 (Fig. 2B) kinases in inhibitor-treated A431/ABCG2 cells to those in A431 cells, we concluded that intracellular efficiencies of wortmannin, LY294002 and rapamycin are unaltered by the presence of ABCG2. These findings render it unlikely that any of these compounds at the experimentally relevant concentrations is transported by ABCG2 efficiently enough to decrease drug concentrations below the intracellular drug efficacy threshold.

3.3. LY294002 and rapamycin directly inhibit ABCG2 function

Our next aim was to study whether cellular administration of the investigated pharmacological PI3K/Akt/mTOR inhibitors blocks ABCG2 function. For these experiments, in order to exclude any potential cell line-specific effects, we applied various cell lines expressing human ABCG2wt with or without a GFP-tag (Supplementary Fig. 1B, C).

It has been shown previously, that fixation with paraformaldehyde or incubation with the ABCG2 specific inhibitors Ko143 or FTC results in a conformational change in the ABCG2 protein,

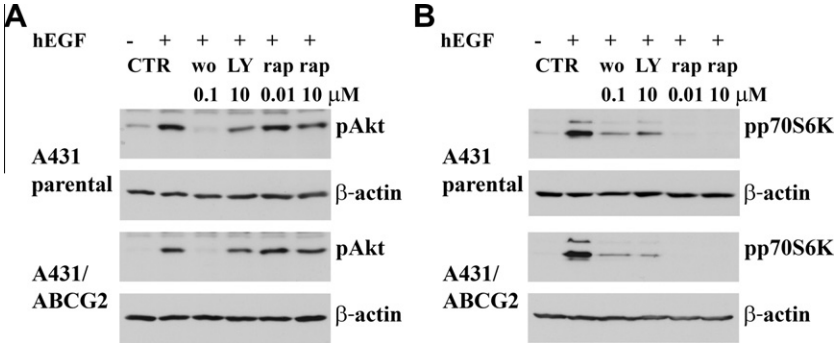


Fig. 2. Effect of pharmacological PI3K/Akt/mTOR inhibitors on phosphorylation of Akt or p70S6 kinases. A431 and A431/ABCG2 cells were stimulated with 20 ng/mL hEGF for 15 min then were exposed to wortmannin, LY294002 or rapamycin at the indicated concentrations for additional 15 min. Cell lysates were prepared and 20 μg proteins were analyzed by Western blot. Levels of (A) phosphorylated Akt (at Ser473) and (B) phosphorylated p70S6 (at Thr389) kinases were measured. Beta-actin was used as a loading control. Representative blots of three independent experiments are shown.

Table 1
Modulation of the 5D3 binding and Hoechst 33342 efflux capacity of ABCG2 by pharmacological PI3K/Akt/mTOR inhibitors.

	Wortmannin	LY294002	Rapamycin
Aliases	–	–	Sirolimus
Target	PI3K	PI3K	mTOR
5D3 binding in A431/ABCG2 cells (% relative to Ko143; mean ± SD)	No effect	63.2 ± 4.2	61.9 ± 10.6
EC50 of inhibition of Hoechst 33342 efflux in PLB/ABCG2 cells (μM; mean ± SD)	No effect	11.2 ± 2.0	1.6 ± 0.2

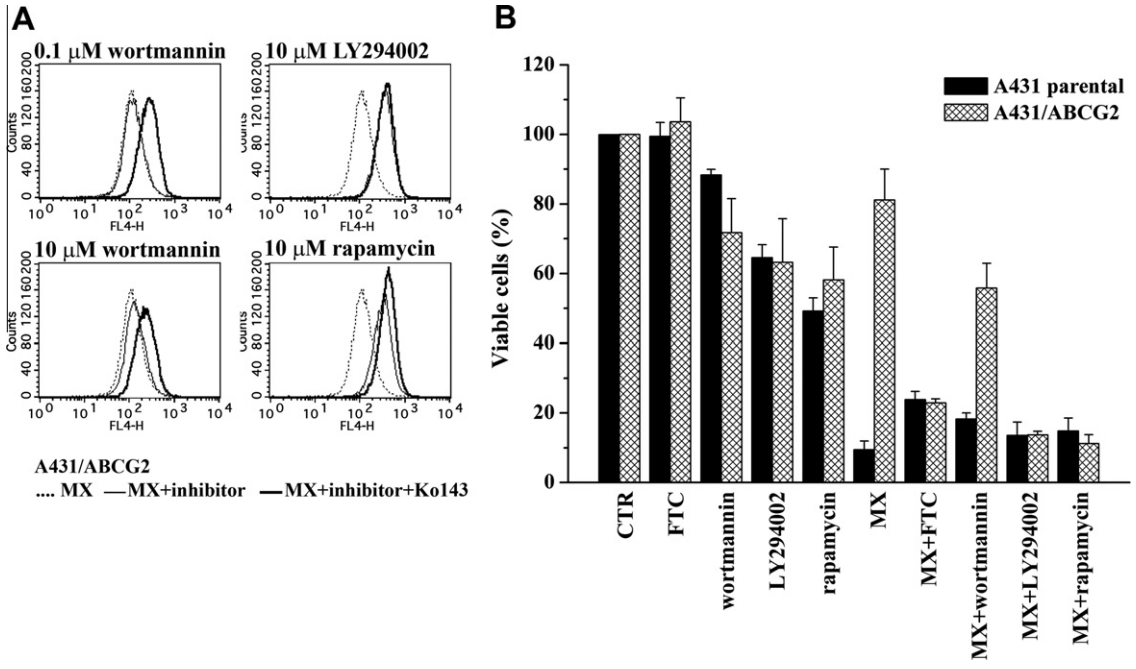


Fig. 3. Inhibition of ABCG2-mediated mitoxantrone (MX) efflux and restoration of MX-sensitivity by pharmacological PI3K/Akt/mTOR inhibitors. (A) Inhibition of MX efflux in A431/ABCG2 cells. Cells were incubated with 5 μM MX (*dotted line*), 5 μM MX with PI3K/Akt/mTOR inhibitors at the indicated concentrations (*solid line*) or 5 μM MX with inhibitors and 1 μM Ko143 (*solid, bold line*) at 37 °C for 30 min. MX fluorescence in live cells was measured by flow cytometry; representative histograms of three independent experiments are shown. (B) Viability of A431 and A431/ABCG2 cells treated with 5 μM FTC, 10 μM wortmannin, 10 μM LY294002, 10 μM rapamycin and 50 nM MX, administered either as single agents or in combination. Cells were exposed to drugs for 72 h and viability was assessed by MTT assay. Mean ± SE values of three independent experiments are shown.

which is thereby able to bind the conformation-sensitive monoclonal anti-ABCG2 5D3 antibody with significantly increased affinity [23,24]. Based on these observations, we have recently suggested that drug-mediated increase in the 5D3 binding affinity of ABCG2-expressing intact cells can be exploited to rapid screening of ABCG2 inhibitory compounds [26]. To test the investigated pharmacological PI3K/Akt/mTOR inhibitors in this regard, we measured the 5D3 binding of various ABCG2-overexpressing cells in the presence of increasing concentrations of wortmannin, LY294002 or rapamycin. Specific 5D3 binding was corrected with the corresponding labeling obtained in the presence of the isotype control antibody, and 1 μM Ko143 was used as a reference for maximum 5D3 binding. None of the investigated agents induced remarkable increase in 5D3 binding at 0.1 μM or 1 μM concentrations (data

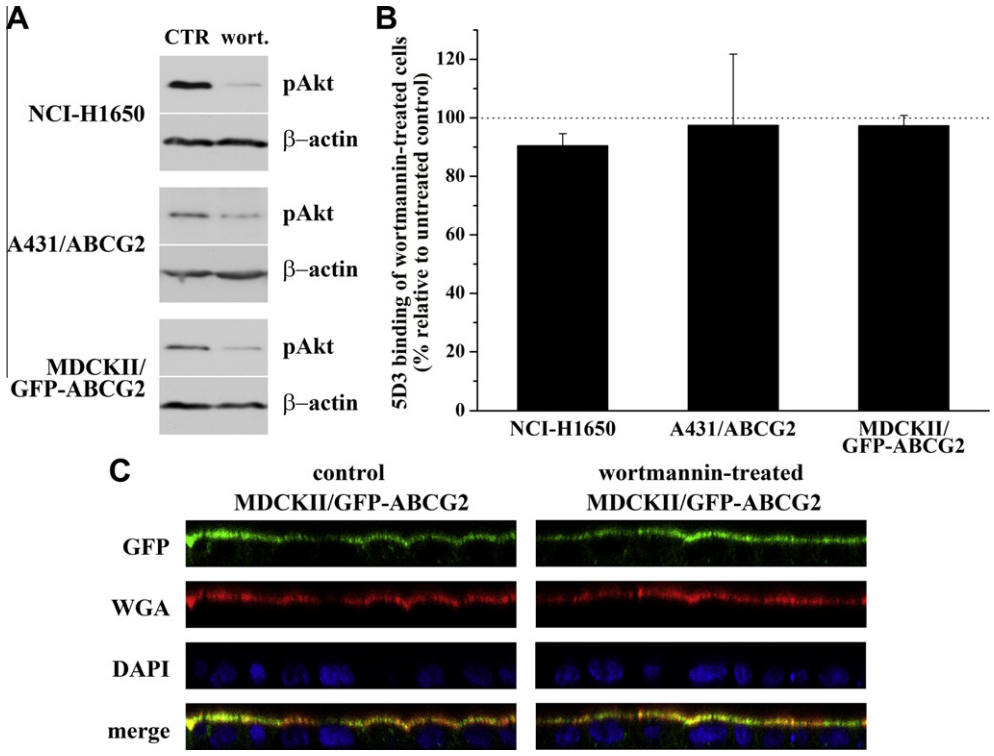


Fig. 4. Localization of ABCG2 in NCI-H1650, A431/ABCG2 and MDCKII/GFP-ABCG2 cells. Cells were treated with 100 nM wortmannin for 90 min at 37 °C. (A) Phosphorylation of Akt (at Ser473) was probed by Western blot. Beta-actin was used as a loading control. (B) Untreated control and wortmannin-treated cells were fixed with PFA, and were labeled with 5D3 or IgG2b and Alexa-Fluor-647-conjugated secondary antibodies. Using flow cytometry, geometric mean values of histograms representing 5D3-labeled cells were corrected with those of IgG2b-labeled cells, and data were plotted as percentage of 5D3 binding of untreated cells (100%). Mean ± SD values of three independent experiments are shown. (C) Control and wortmannin-treated polarized MDCKII/GFP-ABCG2wt cells were fixed with PFA and were stained with the apical marker Alexa-Fluor-633-conjugated WGA and the nuclear stain DAPI. Subcellular distribution of GFP-ABCG2 was evaluated by confocal microscopy. A representative image of three independent experiments is shown.

not shown). Wortmannin did not affect the 5D3 immunoreactivity of ABCG2 at 10 μM concentration either (Table 1). In contrast, 10 μM LY294002 and 10 μM rapamycin highly increased 5D3 binding of A431/ABCG2 cells (Table 1), and also of MDCKII/GFP-ABCG2 and PLB/ABCG2 cells (data not shown).

The 5D3 binding experiments indicated that in contrast to wortmannin, LY294002 and rapamycin may efficiently inhibit ABCG2 transport function. Therefore, we measured the inhibitory potential of the investigated drugs on the ABCG2-mediated transport of two fluorescent ABCG2 substrates, Hoechst 33342 and mitoxantrone (MX) [16]. In correlation with the 5D3 binding results, we observed an inhibition of Hoechst 33342 efflux by increasing concentrations of LY294002 or rapamycin in PLB/ABCG2 cells (Table 1) and also in A431/ABCG2 cells (data not shown). In contrast, wortmannin did not modify the Hoechst 33342 transport capacity of ABCG2 in any of the cell lines tested. LY294002 and rapamycin at 10 μM concentrations also completely abrogated ABCG2-mediated transport of MX in A431/ABCG2 cells, similarly to the specific ABCG2 inhibitor Ko143 (Fig. 3A). In contrast, wortmannin showed no inhibitory effect even when applied at a 100-fold excess to its experimentally used 0.1 μM concentration (Fig. 3A). Collectively, these results indicate that 10 μM LY294002 and 10 μM rapamycin directly inhibit the transport function of ABCG2, whereas wortmannin does not interact with the transporter.

In order to elucidate whether inhibition of ABCG2 function by LY294002 and rapamycin also results in reversal of ABCG2-mediated drug resistance, we measured the toxicity of MX in A431 and A431/ABCG2 cells, in the absence or presence of drugs, as indicated in Fig. 3B. Cells were treated with the drugs for 72 h and cellular viability was determined by the MTT assay. In contrast to FTC, administration of wortmannin, LY294002 or rapamycin alone reduced the viability of both A431 and A431/ABCG2 cells. A431/ABCG2 cells displayed resistance to MX, which could be fully reversed by the specific ABCG2 inhibitor FTC. Co-administration of MX with either LY294002 or rapamycin also resulted in re-sensitization of A431/ABCG2 cells towards MX, supporting the capability of these agents of long-term functional inhibition of ABCG2 thereby reversing multidrug resistance. MX resistance of A431/ABCG2 cells was not reverted by wortmannin, indicating that, in agreement with results of the 5D3 binding and dye transport inhibition experiments, this compound does not inhibit ABCG2 function. Importantly, the percentage of viable cells in the case of wortmannin, LY294002 and rapamycin treatment was similar in both A431 and A431/ABCG2 samples, further supporting that ABCG2 is not capable of hindering intracellular action of these PI3K/Akt/mTOR inhibitors by active efflux at the applied drug concentrations. Moreover, as wortmannin and LY294002, which both inhibit PI3K and thereby prevent phosphorylation of Akt and the downstream p70S6 kinase (Fig. 2), produced distinct effects on reversing ABCG2-mediated MX resistance (Fig. 3B), we concluded that the observed effects correlated with direct inhibition of ABCG2 function rather than with alterations in PI3K/Akt/mTOR signaling and subsequent potential changes in functional ABCG2 protein levels.

3.4. Inhibition of the PI3K/Akt cascade does not lead to rapid internalization of ABCG2

Involvement of the PI3K/Akt/mTOR axis in regulating plasma membrane localization of ABCG2 is controversial [5–12]. In order to investigate this phenomenon, NCI-H1650 cells showing endoge-

nous ABCG2 expression (unpublished results), or A431/ABCG2 cells engineered to overexpress ABCG2 and MDCKII/GFP-ABCG2 were exposed to wortmannin for 90 min at 37 °C. We chose wortmannin because it does not interact with ABCG2; therefore, PI3K/Akt signaling could be manipulated without direct functional modulation of the transporter. Under these conditions, wortmannin could efficiently prevent phosphorylation of Akt (Fig. 4A). Cells were fixed with PFA, and were labeled with the 5D3 antibody that recognizes ABCG2 only when it is in the plasma membrane. As shown in Fig. 4B, wortmannin treatment did not significantly decrease 5D3 binding, therefore cell surface expression of ABCG2 in any of the cell lines tested, as compared to the untreated cells (100%).

As a second approach, subcellular distribution of GFP-ABCG2 was followed in polarized MDCKII/GFP-ABCG2 cells by confocal microscopy (Fig. 4C). As expected [1], GFP-ABCG2 co-localized with the apical marker WGA in untreated cells. The major apical localization and subcellular distribution of GFP-ABCG2 was not altered by wortmannin treatment. Brief exposure of MDCKII/GFP-ABCG2 cells to the downstream mTOR inhibitor rapamycin applied at the experimentally relevant 10 nM concentration (which does not inhibit ABCG2) or 10 μM concentration (which inhibits ABCG2) did not alter subcellular distribution of GFP-ABCG2 either (Supplementary Fig. 3).

In summary, we found no impact of pharmacological PI3K/Akt/mTOR inhibitor treatment on plasma membrane localization of ABCG2. Nevertheless, we cannot rule out the possibility that regulation of ABCG2 by the PI3K/Akt/mTOR cascade is interspecies or cell-type dependent. The ABCG2-regulatory role of PI3K/Akt/mTOR signaling therefore remains an interesting aspect for future studies. Importantly, in this study we provide biochemical evidence that ABCG2 is directly inhibited by LY294002 and rapamycin; whereas wortmannin does not interact with the transporter. We suggest that direct functional modulation of the transporter by LY294002 and rapamycin should be taken into consideration when regulation of ABCG2 and a subsequent reversal of MDR by PI3K/Akt/mTOR signaling is investigated using these pharmacological signal transduction inhibitors.

Acknowledgments

The technical help of Gyöngyi Bézsenyi, Éva Krizsán and Zsuzsanna Andrási is greatly appreciated. The authors thank Drs. George Scheffer and Rik Scheper for the BXP-21 antibody and Brian P. Sorrentino for the 5D3 antibody. This work has been supported by grants from OTKA NK83533, KMOP-1.1.2-07/1-2008-0003, and NKTH-Stemkill. Csilla Özvegy-Laczka and Tamás I. Orbán are recipients of the János Bolyai Scholarship of the Hungarian Academy of Sciences. The authors declare no potential conflicts of interest.

Appendix A. Supplementary data

Supplementary data associated with this article can be found, in the online version, at http://dx.doi.org/10.1016/j.bbrc.2012.03.090.

References

[1] B. Sarkadi, L. Homolya, G. Szakacs, et al., Human multidrug resistance ABCB and ABCG transporters: participation in a chemoimmunity defense system, Physiol. Rev. 86 (2006) 1179–1236.
[2] K. Natarajan, Y. Xie, M.R. Baer, et al., Role of breast cancer resistance protein (BCRP/ABCG2) in cancer drug resistance, Biochem. Pharmacol. 83 (2012) 1084–1103.
[3] D.P. Brazil, B.A. Hemmings, Ten years of protein kinase B signalling: a hard Akt to follow, Trends Biochem. Sci. 26 (2001) 657–664.
[4] S. Faivre, G. Kroemer, E. Raymond, Current development of mTOR inhibitors as anticancer agents, Nat. Rev. Drug Discov. 5 (2006) 671–688.
[5] M. Mogi, J. Yang, J.F. Lambert, et al., Akt signaling regulates side population cell phenotype via Bcrp1 translocation, J. Biol. Chem. 278 (2003) 39068–39075.
[6] T. Takada, H. Suzuki, Y. Gotoh, et al., Regulation of the cell surface expression of human BCRP/ABCG2 by the phosphorylation state of Akt in polarized cells, Drug Metab. Dispos. 33 (2005) 905–909.
[7] A.M. Bleau, D. Hambardzumyan, T. Ozawa, et al., PTEN/PI3K/Akt pathway regulates the side population phenotype and ABCG2 activity in glioma tumor stem-like cells, Cell Stem Cell 4 (2009) 226–235.
[8] S. Aust, P. Obrist, W. Jaeger, et al., Subcellular localization of the ABCG2 transporter in normal and malignant human gallbladder epithelium, Lab Invest. 84 (2004) 1024–1036.
[9] C. Hu, H. Li, J. Li, et al., Analysis of ABCG2 expression and side population identifies intrinsic drug efflux in the HCC cell line MHCC-97L and its modulation by Akt signaling, Carcinogenesis 29 (2008) 2289–2297.
[10] V. Goler-Baron, I. Sladkevich, Y.G. Assaraf, Inhibition of the PI3K-Akt signaling pathway disrupts ABCG2-rich extracellular vesicles and overcomes multidrug resistance in breast cancer cells, Biochem. Pharmacol. 83 (2012) 1340–1348.
[11] T. Nakanishi, K. Shiozawa, B.A. Hassel, et al., Complex interaction of BCRP/ABCG2 and imatinib in BCR-ABL-expressing cells: BCRP-mediated resistance to imatinib is attenuated by imatinib-induced reduction of BCRP expression, Blood 108 (2006) 678–684.
[12] A. Pawarode, S. Shukla, H. Minderman, et al., Differential effects of the immunosuppressive agents cyclosporin A, tacrolimus and sirolimus on drug transport by multidrug resistance proteins, Cancer Chemother. Pharmacol. 60 (2007) 179–188.
[13] S.P. Davies, H. Reddy, M. Caivano, et al., Specificity and mechanism of action of some commonly used protein kinase inhibitors, Biochem. J. 351 (2000) 95–105.
[14] A. Gupta, Y. Dai, R.R. Vethanayagam, et al., Cyclosporin A, tacrolimus and sirolimus are potent inhibitors of the human breast cancer resistance protein (ABCG2) and reverse resistance to mitoxantrone and topotecan, Cancer Chemother. Pharmacol. 58 (2006) 374–383.
[15] R. Abdul-Ghani, V. Serra, B. Gyorffy, et al., The PI3K inhibitor LY294002 blocks drug export from resistant colon carcinoma cells overexpressing MRP1, Oncogene 25 (2006) 1743–1752.
[16] C. Ozvegy-Laczka, T. Hegedus, G. Varady, et al., High-affinity interaction of tyrosine kinase inhibitors with the ABCG2 multidrug transporter, Mol. Pharmacol. 65 (2004) 1485–1495.
[17] N.B. Elkind, Z. Szentpetery, A. Apati, et al., Multidrug transporter ABCG2 prevents tumor cell death induced by the epidermal growth factor receptor inhibitor Iressa ZD1839, Gefitinib, Cancer Res. 65 (2005) 1770–1777.
[18] T.I. Orban, L. Seres, C. Ozvegy-Laczka, et al., Combined localization and real-time functional studies using a GFP-tagged ABCG2 multidrug transporter, Biochem. Biophys. Res. Commun. 367 (2008) 667–673.
[19] C. Ozvegy, A. Varadi, B. Sarkadi, Characterization of drug transport, ATP hydrolysis, and nucleotide trapping by the human ABCG2 multidrug transporter Modulation of substrate specificity by a point mutation, J. Biol. Chem. 277 (2002) 47980–47990.
[20] C. Ozvegy, T. Litman, G. Szakacs, et al., Functional characterization of the human multidrug transporter, ABCG2, expressed in insect cells, Biochem. Biophys. Res. Commun. 285 (2001) 111–117.
[21] A. Telbisz, M. Muller, C. Ozvegy-Laczka, et al., Membrane cholesterol selectively modulates the activity of the human ABCG2 multidrug transporter, Biochim. Biophys. Acta 1768 (2007) 2698–2713.
[22] A. Kolonics, A. Apati, J. Janossy, et al., Activation of Raf/ERK1/2 MAP kinase pathway is involved in GM-CSF-induced proliferation and survival but not in erythropoietin-induced differentiation of TF-1 cells, Cell Signal. 13 (2001) 743–754.
[23] S. Zhou, J.D. Schuetz, K.D. Bunting, et al., The ABC transporter Bcrp1/ABCG2 is expressed in a wide variety of stem cells and is a molecular determinant of the side-population phenotype, Nat. Med. 7 (2001) 1028–1034.
[24] C. Ozvegy-Laczka, G. Varady, G. Koblos, et al., Function-dependent conformational changes of the ABCG2 multidrug transporter modify its interaction with a monoclonal antibody on the cell surface, J. Biol. Chem. 280 (2005) 4219–4227.
[25] A. Pal, D. Mehn, E. Molnar, et al., Cholesterol potentiates ABCG2 activity in a heterologous expression system: improved in vitro model to study function of human ABCG2, J. Pharmacol. Exp. Ther. 321 (2007) 1085–1094.
[26] A. Telbisz, C. Hegedus, C. Ozvegy-Laczka, et al., Antibody binding shift assay for rapid screening of drug interactions with the human ABCG2 multidrug transporter European journal of pharmaceutical sciences: official journal of the Eur, J. Pharm. Sci. 45 (2012) 101–109.
[27] C. Hegedus, G. Szakacs, L. Homolya, et al., Ins and outs of the ABCG2 multidrug transporter: an update on in vitro functional assays, Adv. Drug Deliv. Rev. 61 (2009) 47–56.
[28] G. Szakacs, A. Varadi, C. Ozvegy-Laczka, et al., The role of ABC transporters in drug absorption, distribution, metabolism, excretion and toxicity (ADME-Tox), Drug Discov. Today 13 (2008) 379–393.

Biochemical and Biophysical Research Communications 420 (2012) 875–881

Contents lists available at SciVerse ScienceDirect

Biochemical and Biophysical Research Communications

journal homepage: www.elsevier.com/locate/ybbrc

MiR-499 induces cardiac differentiation of rat mesenchymal stem cells through wnt/β-catenin signaling pathway

Lu-lu Zhang, Jing-jin Liu, Fang Liu, Wen-hua Liu, Yong-shun Wang, Bin Zhu, Bo Yu *

Department of Cardiology, The Second Affiliated Hospital of Harbin Medical University, Key Laboratory of Myocardial Ischemia Mechanism and Treatment (Harbin Medical University), Ministry of Education, Baojian Road, Harbin, Heilongjiang Province 150081, PR China

ARTICLE INFO

Article history:
Received 3 March 2012
Available online 23 March 2012

Keywords:
MiR-499
Mesenchymal stem cells
Cardiac differentiation
wnt/β-catenin signaling pathway

ABSTRACT

Objective: To test the hypothesis that over-expressing miR-499 in rat bone marrow-derived mesenchymal stem cells (BM-MSCs) induces them to differentiate into cardiomyocyte-like cells through the wnt/β-catenin signaling pathway.
Methods: Rat BM-MSCs were infected with lentiviral vectors bearing miR-499. The expression of cardiac-specific markers, NKx2.5, GATA4, MEF2C, and cTnI in these cells were examined by rtPCR or Western blot analysis and the activity of the wnt/β-catenin signaling pathway was evaluated by measuring the phosphorylation status of β-catenin.
Results: Over-expression of miR-499 in rat BM-MSCs increased the expression of cardiac-specific genes, such as NKx2.5, GATA4, MEF2C, and cTnI and decreased the ratio of phosphorylated/dephosphorylated β-catenin in the wnt/β-catenin signaling pathway, thus activating the pathway. Knocking down the expression of Dvl, an adaptor molecule in the wnt/β-catenin signaling, partially blocked the role of the miR-499 and decreased those cardiac-specific genes.
Conclusion: Over-expression of miR-499 in rat BM-MSCs induces them toward cardiac differentiation through the activating the wnt/β-catenin signal pathway.
© 2012 Elsevier Inc. All rights reserved.

1. Introduction

Mesenchymal stem cells (MSCs), which are referred to as multipotent stromal cells, have been isolated from various adult tissues since 1991 [1]. MSCs are capable of self-renewing and differentiating into multiple cell lineages [2,3]. In past years, MSCs have gained extensive interest in regenerative medicine. This is mostly because of their ease of isolating and expanding, their ability to differentiate to various specialized cells, their immuno-suppressive properties, and their lack of ethic concerns caused by using embryonic stem cells (ESCs). *In vitro*, treating MSCs with 5-azacytine induces them to differentiate to cardiomyocyte-like cells [4]. Transplantation of MSCs to damaged hearts benefits heart repair although there is no apparent evidence showing that MSCs differentiate to cardiomyocytes [5,6]. Cytokines, such as VEGF and FGF. paracrined by MSCs may play a major role in the repair of damaged hearts [7], however, other studies suggest that MSCs can differentiate to cardiomyocytes once they home damaged hearts. The reason why there are no apparent evidences showing that MSCs differentiate to cardiomyocytes might be that MSCs cannot survive long enough to allow their cardiac differentiation [5,6]. Therefore, shortening the cardiac differentiation process of MSCs may improve the therapeutic benefits of MSC transplantation on treating damaged hearts. Developing strategies to promote cardiac differentiation of MSCs requires us to elucidate the molecular mechanisms by which MSCs differentiate to cardiomyocytes.

MicroRNAs (miRNAs or miRs) are a group of endogenous small non-coding RNAs of approximately 22 nucleotides. They regulate gene expression post-transcriptionally [8,9]. Numerous evidences suggest that miRNAs play critical roles on controlling cellular processes, such as cell proliferation, apoptosis, and differentiation [10,11]. The miRNAs are also able to induce cardiac differentiation of MSCs [12]. For instance, microRNA-1 [13], 206 [14], 24 [15], 181 [16] can induce mouse and human MSCs toward cardiac differentiation. Conversely, microRNA-133 blocks the cardiac differentiation of mouse and human MSCs [13,17].

Another microRNA, microRNA-499 (miR-499) was identified in studies to get the global microRNA expression profile in zebrafish, porcine, and human hearts [18–21]. The miR-499 is transcribed from an intron of the myosin heavy chain 7B gene and is highly enriched in the cardiac ventricles. MiR-499 regulates myosin gene expression in mouse and human hearts [22–24] and is highly conserved among many species, suggesting its importance in heart development.

The miR-499 may regulate the cardiac differentiation in human. In cardiomyocyte progenitor cells, increased miR-499 expression

* Corresponding author. Fax: +86 451 86605180.
E-mail address: yubohmu@163.com (B. Yu).

0006-291X/$ - see front matter © 2012 Elsevier Inc. All rights reserved.
http://dx.doi.org/10.1016/j.bbrc.2012.03.092

promotes the cardiac muscle differentiation by targeting sex determining region Y-box 6 (Sox6) and regulator of differentiation 1 (Rod1) *in vitro* [22]. In embryonic stem cells or cardiac stem cells, over-expressing miR-499 increases the expression of cardiac-specific genes, such as Nkx2.5, GATA4, MEF2C, et al. [25–27].

The miR-499 may promote cardiac differentiation process through the wnt/β-catenin signaling pathway. First, the wnt/β-catenin pathway plays a primary and pivotal role in initiating cardiac differentiation of mammalian stem cells. In human embryonic stem cells, activating the wnt/β-catenin increases the protein levels of Cx43 and Nkx2.5, which are required for cardiac differentiation. In mouse embryonic stem cells, activating the wnt/β-catenin by wnt3a induces cardiac differentiation, whereas inhibiting the pathway reduces the cardiac differentiation as indicated by measuring cardiac-specific genes, such as β-myosin heavy chain (β-MHC), cardiac troponin T (cTnT), Nkx2.5, and sarcomeric myosin heavy chain (sMHC) [28]. In a mouse pluripotent cell line (P19CL6), either chemical, DMSO or lithium chloride, induces cardiac differentiation via activating wnt/β-catenin signaling pathway [29,30]. Second, the miR-499 shares target genes with the wnt/β-catenin pathway in the cardiac differentiation of human embryonic stem cells. A study aiming to find the targeting genes of miR-499 in the cardiac differentiation of human embryonic stem cells shows that the miR-499 regulates at least 10 genes that the wnt/β-catenin signaling pathway regulates in the same cellular process [26]. These results suggest that the role of miR-499 in mammalian cardiac differentiation may be related with the activity of the wnt/β-catenin signaling pathway.

In the wnt/β-catenin signaling pathway, Dvl [31] is a key component to regulate the pathway activity. Upon pathway activation by Wnt, Dvl inhibits the activity of GSK3β, which is required for the phosphorylation of β-catenin at its Ser3, Ser7 and Thr41 [32]. Dephosphorylated β-catenin is then translocated from cytoplasm to nucleus where β-catenin interacts with transcription coregulators, T cell factor (Tcf), and lymphocyte enhancer factor (Lef) to form a β-catenin/Lef/Tcf complex to regulate the expression of pathway target genes [33]. Thus, knocking down the expression of Dvl will block the pathway activation by wnt.

Although miR-499 has been shown to be involved in cardiac differentiation of mammalian embryonic stem cells, cardiac stem cells, and cardiac progenitor cells, few is known regarding its potential role in cardiac differentiation of MSCs. We hypothesize that over-expression of miR-499 in mammalian MSCs can induce their cardiac differentiation through wnt/β-catenin signaing pathway. To test this hypothesis, we over-expressed miR-499 in the MSCs isolated from rat bone marrow and examined the expression of cardiac-specific markers and the activity of the wnt/β-catenin signaling pathway in these cells.

2. Materials and methods

2.1. Isolation and expansion of rat mesenchymal stem cells

Bone marrow mesenchymal stem cells (BM-MSCs) were isolated from femurs and tibias of Wistar rats as described previously [34,35]. Briefly, bone marrow cells were flushed with 5 ml DMEM/F12 from femurs and tibias. After red blood cells were lysed and removed, five million cells were grown in a 25 cm^2 flask with 5 ml DMEM/F12 (Hyclone, Logan, UT) supplemented with 10% fetal calf serum (FCS; Hyclone, Logan, UT) and 1% Penicillin/streptomycin at 37 °C with 5% CO_2. After 3 days of culture, media and non-adherent cells were removed and fresh medium was added every 2–3 days. When reaching 80–90% confluence, adherent cells were trypsinized and expanded at 1:3 or 1:4 dilution. Before cells were used in the experiments, they were cultured for at least three passages to deplete monocytes and macrophages.

2.2. FACS analysis

All cells were analyzed by FACS for the expression of CD29, CD90, CD44, CD45, and CD34. To analyze these surface markers, cells were trypsinized, washed twice with phosphate buffered saline (PBS), and incubated with following mAbs, respectively: phycoerythrin (PE)-labeled anti-CD45, anti-CD90; Fluorescein Isothiocyanate (FITC)-labeled anti-CD44, anti-CD29 (BD Pharmingen, USA) and anti-CD34 (eBioscience, San Diego, CA). Mouse IgG1 isotype antibodies were used as a negative control. FACS was carried out using FACScan™ (BD Biosciences, Franklin, NJ, USA) and data were analyzed with CellQuest Analysis (BD Biosciences).

2.3. Viral infection and plasmid transfection

Lentiviral vector bearing miR-499 driven by U6 promoter (LV-miR-499) and plasmid bearing Dvl-1 shRNA driven by H1 promoter (P-Dvl shRNA) were purchased from Shanghai Chuangyi Co. Ltd. (China). Lentiviral infection of MSCs was carried out according to manufacturer's instruction. Briefly, MSCs were incubated in growth medium with LV-miR-499 at MOI of 200 in the presence of 2 μg/ml polybrene (Gibco) for 16 h before fresh growth medium was changed. The expression of miR-499 was analyzed by using real time PCR at day 3 post viral infections. Plasmid transfection of MSCs was carried out with Lipofectamine Kit (*in vitro* gene) according to manufacturer's instruction. Briefly, 5×10^5 MSCs were plated in a well of 6-well plate and grown in complete medium for overnight. After discarding the medium, we pretreated cells for 25 min in 125 μl Opti-MEM mixed with 5 μl Lipofectamine™2000. Cells were then transfected with 2 μg P-Dvl shRNA suspended in 1.5 ml PBS-free Opti-MEM for 4–6 h. Transfected cells were grown in DMEM/HG with 10% FBS for 48 h before subjected to analysis of gene expression. The expression of Dvl was also analyzed by using real time PCR.

2.4. Real time Polymerase Chain Reaction

To examine the expression of miRNA-499, Dvl, Nkx 2.5, GATA 4, and MEF2C, we used quantitative real time polymerase chain reaction (rt-PCR) to measure their mRNA levels. Briefly, total RNAs were isolated and reverse transcribed to cDNA by using the RevertAid TMFirst strand cDNA Synthesei Kit (Fermentans) according to the manufacturer's instructions. qPCR was carried out with SYBRPremix Ex Taq™ (TakaRa) and fluorescence quantitative PCR

Table 1
List of primers for real time PCR.

Genes	Forward	Reverse
Nkx 2.5	5′-CCACCTGGCGCTGTGAGACC-3′	5′-GAAGCGCCGCTCCAGCTCAT-3′
GATA 4	5′-GCCAACCCTGCGAGACACCC-3′	5'-TCAGCGTTACGGCGCCACAG -3'
MEF2C	5′-AGCAGGTGCTGACGGGAACAA-3′	5′-TCACAGTCGCACAGCACGCTC-3′
MiR499	5′-CTCAACTGGTGTCGTGGAGT-3′	5′-ACACTCCAGCTGGGTTAAGACTTGC-3′
GAPDH	5′-GGCTCTCTGCTCCTCCCTGTT-3′	5′-GCGGGATCTCGCTCCTGGAAG -3′

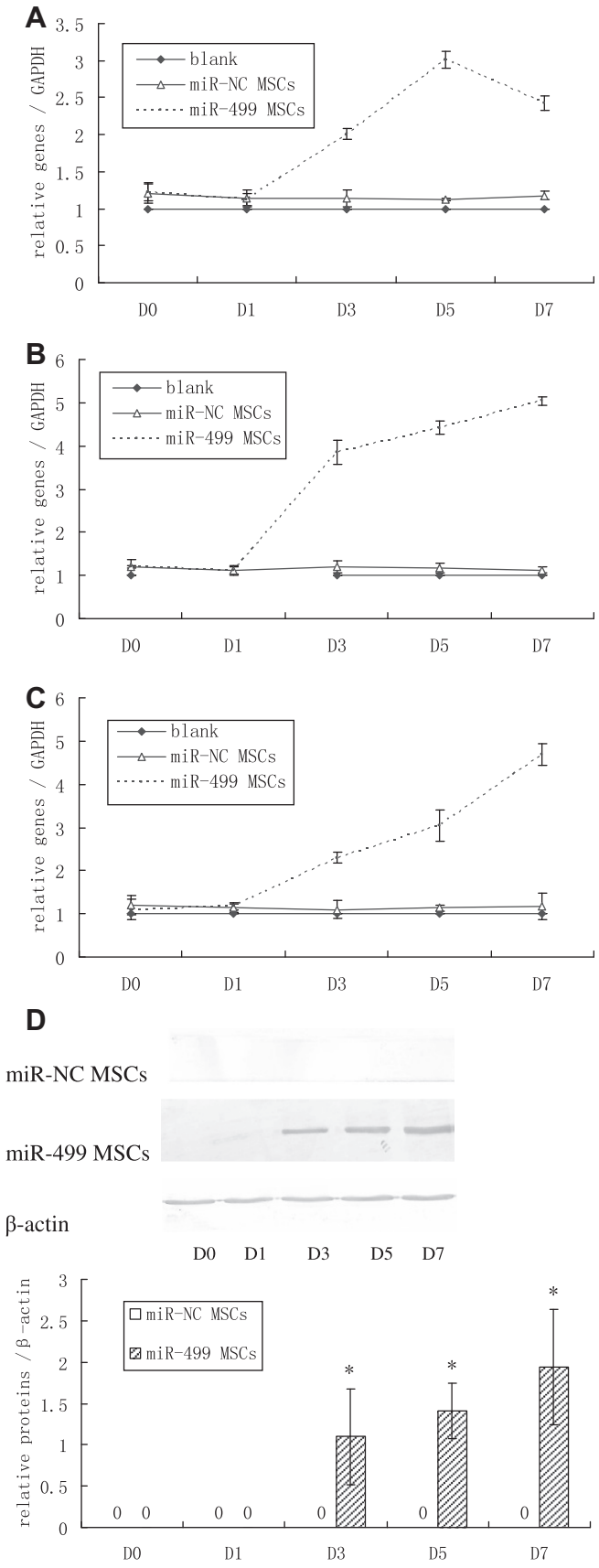


Fig. 1. Expression of cardiac-specific genes induced by over-expression of miR-499 in rat MSCs. Rat MSCs were infected with L-miR-499 and empty lentiviral vectors, respectively, at MOI of 200. Cells were harvested at different time points post viral infection and analyzed for the mRNA levels of NKx2.5 (A), GATA4 (B), and MEF2C (C) by using rt-PCR as well as the protein levels of cTnI (D) by using Western blotting.

system (ABI). The threshold cycle (Ct) was set within the exponential phase of the PCR. The relative gene expression was calculated by comparing cycle times for each target PCR. The target PCR *Ct* values were normalized by subtracting the GAPDH *Ct* value, which provided the ΔCt value. The relative expression level between treatments was then calculated using the following equation: relative gene expression = $2^{-(\Delta Ct \text{ sample} - \Delta Ct \text{ control})}$. The primer pairs used to detect the mRNA levels of above-mentioned genes were listed in Table 1.

2.5. Western blot analysis

The protein levels of cTnI, Phospho-β-catenin (Ser33/37/Thr41), and Non-phospho-β-catenin (Ser33/37/Thr41) in cells were analyzed with Western blotting as described before [36]. Antibodies against Cardiac Troponin I (Abcam, ab19615), Phospho-β-Catenin (Ser33/37/Thr41) (Cell Signaling Technology, #9561), Non-phospho-β-catenin (Ser33/37/Thr41) (Cell Signaling Technology, #4270), β-actin (Zhongshan Goldenbridge Biotechnolog Co. Ltd. #TA-09), Peroxidase-Conjugated AffiniPure Goat Anti-Mouse IgG (H+L) (Zhongshan Goldenbridge Biotechnolog Co. Ltd. #ZB2305) and Peroxidase-Conjugated AffiniPure Goat Anti-Rabbit IgG (H+L) (Zhongshan Goldenbridge Biotechnolog Co. Ltd. #ZB2301) were used. All the gels were analyzed by Tanon Gel Imaging System (Shanghai Tanon Co. Ltd., China).

2.6. Statistical analysis

Statistical analysis was performed with the SPSS (version 18.0; Chicago, IL) software package. Values for all measurements are presented as mean ± SD. Comparisons for all pairs were performed by Student's *t*-test or least significant difference (LSD) test. The value of $p < 0.05$ was considered statistically significant.

3. Results

3.1. Cells isolated from rat bone marrow show MSC characteristic

MSCs were uniformed spindle-like. FACS analysis showed that most cells from passage 3 expressed common surface markers for MSCs: they were positive for CD29 (99.0%), CD90 (88.3%), and CD44 (35.7%), but negative for CD34 (0.8%) and CD45 (2.1%) (shown in Supplementary Fig. 1). Therefore, only cells cultured *in vitro* for 3–5 passages were used for the following experiments.

3.2. Over-expressing miR-499 induces expression of cardiac-specific genes in MSCs

We firstly asked whether over-expressing miR-499 in MSCs could induce them toward cardiogenic differentiation. To over-express miR-499 in MSCs, we infected MSCs with the LV-miR-499. At day 3 post infection, the mRNA of miR-499 in MSCs was increased by 16.5-fold when compared with cells infected with empty lentiviral vectors (18.20 ± 0.60 *vs.* 1.10 ± 0.07), indicating that LV-miR-499 efficiently mediated miR-499 expression in MSCs (shown in Supplementary Fig. 2).

We thus investigated in these MSCs over-expressing miR-499 whether the expressions of several cardiac-specific genes, NKx2.5, GATA4, MEF2C, and cTnI, were increased by using real time PCR or Western blot analysis. We found that the mRNA levels of NKx2.5, GATA4, or MEF2C were increased gradually up to day 7 with a significant increase at day 3 post viral infection, respectively (Fig. 1A–C), and the cTnI protein levels was detected at day 3 and 5 with a significant increase at day 7 post viral infection (Fig. 1D). The cTnI protein

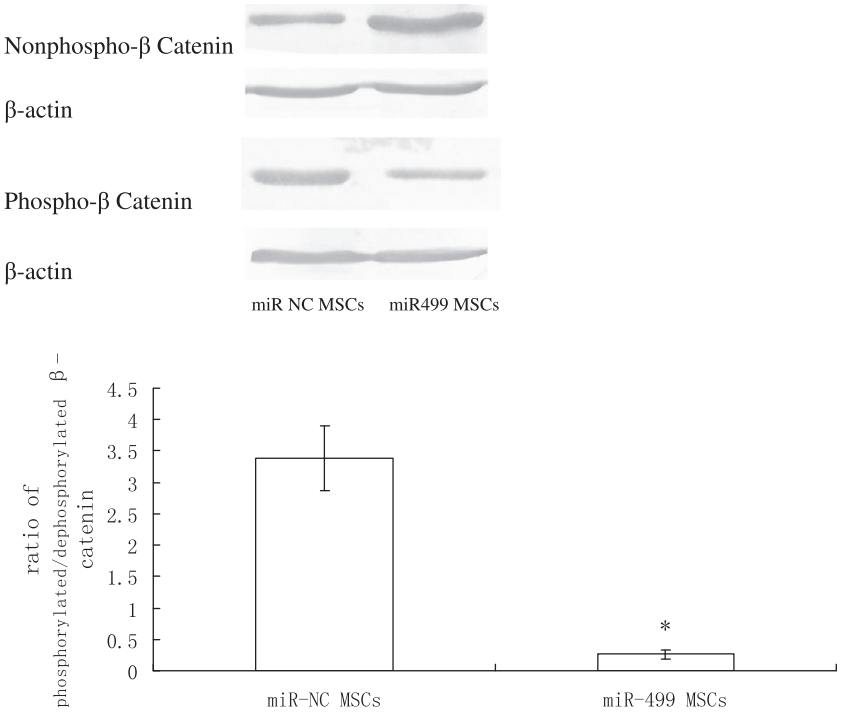


Fig. 2. Over-expression of miR-499 increases the β-catenin activity in rat MSCs. Rat MSCs were infected with L-miR-499 and empty lentiviral vectors, respectively, at MOI of 200. Cells were harvested at day x post viral infection and analyzed for the levels of both phosphorylated and dephosphorylated β-catenin by using Western blotting. The β-actin expression was used as an internal loading control.

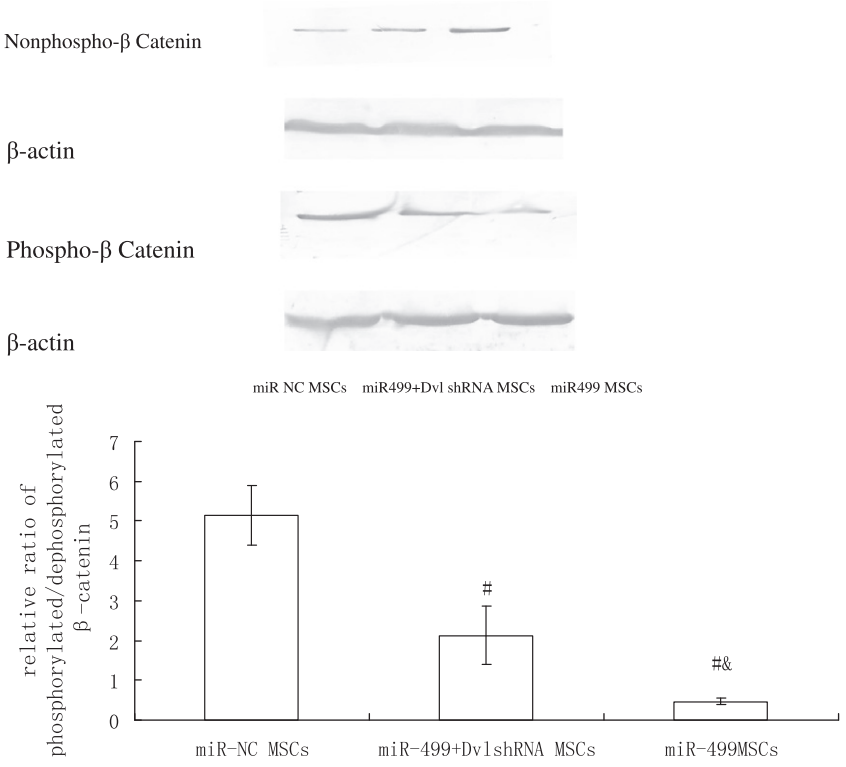


Fig. 3. Dvl is partially required for increased β-catenin activity induced by the over-expression of miR-499 in rat MSCs. L-miR-499 transduced rat MSCs were transfected with P-Dvl-shRNA and empty plasmid, respectively. Two four hours later, cells were harvested and analyzed for the levels of both phosphorylated and dephosphorylated β-catenin by using Western blotting. The β-actin expression was used as an internal loading control.

levels were not detected in the cells at day 1 post L-miR-499 viral infection and at any time point post empty lentiviral infection (Fig. 1D). Taken together, these results show that over-expression of miR-499 up-regulates expression of cardiac-specific genes at transcription or protein level in MSCs, indicating that over-expression of miR-499 induces cardiac differentiation of MSCs.

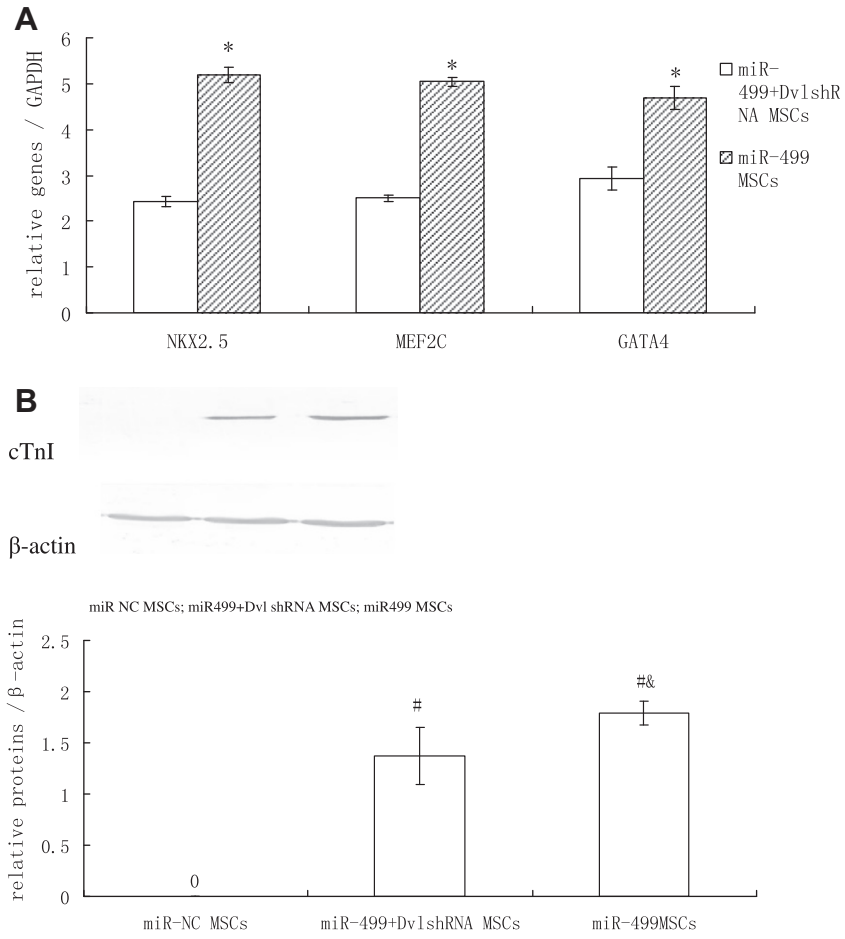


Fig. 4. Dvl is partially required for miR-499-induced expression of cardiac-specific genes in rat MSCs. L-miR-499 transduced rat MSCs were transfected with P-Dvl-shRNA and empty plasmid, respectively. Two four hours later, cells were harvested and analyzed for the mRNA levels of NKx2.5, GATA4, and MEF2C by using qPCR (A) as well as the protein levels of cTnI by using Western blotting (B). All mRNA levels were expressed as relative numbers to the mRNA levels of GAPDH gene; and the protein levels were relative numbers to the protein levels of β-actin.

3.3. Over-expression of miR-499 activates β-catenin signaling pathway

Previous studies strongly imply that miR-499 promoted cardiac differentiation in human embryonic stem cells, cardiac stem cells, or cardiac progenitor cells via regulating the activity of the wnt/β-catenin signaling pathway. We therefore asked whether the over-expression of miR-499 induces cardiac differentiation of rat MSCs through the wnt/β-catenin signaling pathway. For this purpose, we first compared the phosphorylation status of β-catenin in LV-miR-499 and empty lentiviral vector transduced MSCs. The lower the ratio of phosphorylated/dephosphorylated β-catenin (Ser33/37/Thr41) is, the higher the β-catenin pathway activity is. We found that the pathway activity was significantly higher in the MSCs transduced with LV-miR-499 than those with empty lentiviral vectors (0.26 ± 0.08 *vs.* 3.38 ± 0.52) of the ratio of phosphorylated/dephosphorylated β-catenin (Fig. 2).

3.4. MiR-499 induces cardiac differentiation through wnt/β-catenin signaling activating

We then asked whether increased activity of the β-catenin induced by the overexpression of miR-499 is through the wnt signaling. For this purpose, we knock-downed the expression of Dvl, a molecule essential for the wnt signaling to β-catenin, by expressing Dvl shRNA in the MSCs over-expressing miR-499 and investigated the potential changes of pathway activity by measuring the ratio of phosphorylated/dephosphorylated β-catenin (Ser33/37/Thr41). In order to knock down Dvl expression, we transfected the MSCs overexpressing miR-499 with P-Dvl-shRNA or empty plasmid. After transfection, the Dvl mRNA levels were decreased by 69.4%, from 1.08 ± 0.03 in the MSCs transfected with empty plasmid to 0.33 ± 0.03 in those with P-Dvl-shRNA (shown in Supplementary Fig. 3), suggesting that Dvl-shRNA partially reduced the Dvl expression in the cells overexpressing miR-499. Furthermore, we observed that β-catenin activity was partially inhibited in the cells transfecting with P-Dvl-shRNA when compared with the cells transfected with empty plasmid (2.13 ± 0.72 *vs.* 0.47 ± 0.07) of the ratio of phosphorylated/dephosphorylated β-catenin) (Fig. 3). Similarly, we observed that induced expressions of NKx2.5, GATA4, MEF2C, and cTnI in the cells transfected with P-Dvl-shRNA were partially decreased when compared with those with LV-miR-499 (Fig. 4A, B).

4. Discussion

In this study, we found that the over-expression of miR-499 in rat BM-MSCs induced their cardiac differentiation *in vitro*. The over-expression of miR-499 was achieved by infecting MSCs isolated from rat bone marrow aspirates with a lentiviral vector bearing miR-499. From day 3 to 7 post viral infection, the expressions of cardiac-specific transcription factors, Nkx2.5, GATA4, and

MEF2C, were gradually increased in LV-miR-499 transduced MSCs. Another cardiac-specific protein, cTnI, was also detected at day 3 with a significant increase at day 7 post viral infection. Over-expression of miR-499 has been shown to induce cardiac differentiation of human embryonic stem cells [26,27], cardiac stem cells [22], and cardiac stem cells [25]. The capability of MSCs to differentiate to cardiomyocytes has been observed [4]. In this study, we demonstrated that miR-499 is another molecule which can induce MSCs toward cardiac differentiation.

Our studies also demonstrated that the miR-499 induced cardiac differentiation of rat MSCs through the wnt/β-catenin signaling pathway. Several evidences in our study support our conclusion. First, we found that the over-expression of miR-499 activated β-catenin as shown lower ratio of phosphorylated/dephosphorylated (Ser33/37/Thr41) β-catenin in the cells infected with LV-miR-499 than those with empty viral vectors (Fig. 2). Second, blocking the wnt/β-catenin signaling by knocking down the expression levels of Dvl partially inhibited the activity of the wnt/β-catenin signaling pathway activated by over-expressing miR-499 (Fig. 3). Third, knock-down of the Dvl in the wnt/β-catenin signaling also partially blocked the effect of miR-499 on induced expression of cardiac-specific genes in MSCs (Fig. 4). In this study, we provided the direct evidences demonstrating that miR-499 promoted cardiac differentiation of rat MSCs by regulating the activity of the wnt/β-catenin signaling pathway. For the explanations, we consider the reasons below: First, as the previous study of bioinformatics, wnt/β-catenin signaling pathway shared as many as 10 genes with miR-499 [26], so miR-499 have the ability to regulate it and make it take part in some effection. Sox 6 is one of the target genes in miR-499 promoted cardiac differentiation, at the same time, it can regulate wnt/β-catenin signaling pathway. Sox 6 suppreses β-catenin activity by decreasing the acetylation of histones H3 and H4 [37]. So it may be the corresponding of them. Second, wnt/β-catenin signaling pathway itself has the ability of inducing differentiation of stem cells [28–30]. So it can be regulated by miR-499 and also take part in the inducing cardiac differentiation effection of miR-499.

In our study, we only observed partial blocking of miR-499-induced cardiac differentiation and partial inhibiting the activity of wnt/β-catenin pathway in rat MSCs when the expression of Dvl in these cells was reduced by Dvl-shRNA. This may be explained as the incomplete blocking of the pathway caused by limited plasmid transfection efficiency and/or the incomplete interference efficiency of Dvl-shRNA. In fact, in our study, the Dvl expression in MSCs transduced with P-Dvl-shRNA was only decreased by 69.4% when compared with one in MSCs transduced with empty plasmid. Other explanations are also possible. First, miR-499 may induce cardiac differentiation of MSCs through other pathways in addition to the wnt/β-catenin pathway. Previous studies have suggested that miR-499 may function through many signaling pathways, such as axonal guidance signaling, protein kinase A signaling, tight junction signaling, etc. [26]. Second, miR-499 may activate β-catenin through other factors that regulate the β-catenin activity without Dvl. For example, casein kinase Ia (CKIa) can regulate wnt/β-catenin pathway without the involvement of Dvl [38]. Besides, the effection of miR-499 is a complicated net, as the previous study indicated, there are many signal pathway involved, such as axonal guidance signaling, protein kinase A signaling, Tight junction signaling et al. [26]. So the role of wnt/β-catenin pathway might be partly. Further studies are needed to elucidate the mechanisms by which miR-499 induces cardiac differentiation of rat MSCs.

Although in our study MSCs over-expressing miR-499 expressed cardiac-specific genes, these cells still lacked the morphology of cardiomyocytes and did not beat by themselves, which are observed in studies with embryonic stem cells [27]. In addition, whether these cells can differentiate into cardiomyocytes *in vivo* to treat damaged hearts remains unknown. Furthermore, whether the over-expression of miR-499 in MSCs from the species other than rat can induce cardiac differentiation is needed to be addressed.

In summary, our study demonstrated that the over-expression of miR-499 in rat bone marrow-derived MSCs induced them toward cardiac differentiation through activating wnt/β-catenin signaling pathway. This finding opens an avenue for scientists to develop new strategies to explore MSC transplantation for treating damaged hearts.

Acknowledgments

We thank Prof. Hulun Li for his expertise assistance on experimental design, Dr. Wei Liu for her excellent technical assistance, and Jingbo Li for his help on FACS analysis. Prof. Hulun Li and Dr. Wei Liu are members of the Key Laboratory of Myocardial Ischemia Mechanism and Treatment (Harbin Medical University), Ministry of Education. This work was supported by grants from Key Laboratory of Myocardial Ischemia Mechanism and Treatment (Harbin Medical University), Ministry of Education (#KF20100).

Appendix A. Supplementary data

Supplementary data associated with this article can be found, in the online version, at http://dx.doi.org/10.1016/j.bbrc.2012.03.092.

References

[1] A.I. Caplan, Mesenchymal stem cells, J. Orthop. Res. 9 (1991) 641–650.
[2] D.J. Prockop, Marrow stromal cells as stem cells for nonhematopoietic tissues, Science 276 (1997) 71–74.
[3] B.E. Petersen, W.C. Bowen, K.D. Patrene, et al., Bone marrow as a potential source of hepatic oval cells, Science 284 (1999) 1168–1170.
[4] S. Makino, K. Fukuda, S. Miyoshi, et al., Cardiomyocytes can be generated from marrow stromal cells *in vitro*, J. Clin. Invest. 103 (1999 Mar) 697–705.
[5] Y.L. Tang, Q. Zhao, X. Qin, et al., Paracrine action enhances the effects of autologous mesenchymal stem cell transplantation on vascular regeneration in rat model of myocardial infarction, Ann. Thorac. Surg. 80 (2005) 229–236; discussion 236–7.
[6] O. Agbulut, M.L. Menot, Z. Li, et al., Temporal patterns of bone marrow cell differentiation following transplantation in doxorubicin-induced cardiomyopathy, Cardiovasc. Res. 58 (2003) 451–459.
[7] M. Gnecchi, Z. Zhang, A. Ni, V.J. Dzau, Paracrine mechanisms in adult stem cell signaling and therapy, Circ. Res. 103 (2008) 1204–1219.
[8] R.S. Pillai, MicroRNA function: multiple mechanisms for a tiny RNA?, RNA 11 (2005) 1753–1761
[9] P.D. Zamore, B. Haley, Ribo-gnome: the big world of small RNAs, Science 309 (2005) 1519–1524.
[10] A.M. Cheng, M.W. Byrom, J. Shelton, L.P. Ford, Antisense inhibition of human miRNAs and indications for an involvement of miRNA in cell growth and apoptosis, Nucleic Acids Res. 33 (2005) 1290–1297.
[11] C.Z. Chen, L. Li, H.F. Lodish, D.P. Bartel, MicroRNAs modulate hematopoietic lineage differentiation, Science 303 (2004) 83–86.
[12] L. Guo, R.C. Zhao, Y. Wu, The role of microRNAs in self-renewal and differentiation of mesenchymal stem cells, Exp. Hematol. 39 (2011) 608–616.
[13] J.F. Chen, E.M. Mandel, J.M. Thomson, et al., The role of microRNA-1 and microRNA-133 in skeletal muscle proliferation and differentiation, Nat. Genet. 38 (2006) 228–233.
[14] C. Anderson, H. Catoe, R. Werner, MIR-206 regulates connexin43 expression during skeletal muscle development, Nucleic Acids Res. 34 (2006) 5863–5871.
[15] Q. Sun, Y. Zhang, G. Yang, et al., Transforming growth factor-beta regulated miR-24 promotes skeletal muscle differentiation, Nucleic Acids Res. 36 (2008) 2690–2699.
[16] I. Naguibneva, M. Ameyar-Zazoua, A. Polesskaya, et al., The microRNA miR-181 targets the homeobox protein Hox-A11 during mammalian myoblast differentiation, Nat. Cell Biol. 8 (2006) 278–284.
[17] P.L. Boutz, G. Chawla, P. Stoilov, D.L. Black, MicroRNAs regulate the expression of the alternative splicing factor nPTB during muscle development, Genes Dev. 21 (2007) 71–84.
[18] W.P. Kloosterman, F.A. Steiner, E. Berezikov, et al., Cloning and expression of new microRNAs from zebrafish, Nucleic Acids Res. 34 (2006) 2558–2569.
[19] P. Landgraf, M. Rusu, R. Sheridan, et al., A mammalian microRNA expression atlas based on small RNA library sequencing, Cell 129 (2007) 1401–1414.
[20] Y. Liang, D. Ridzon, L. Wong, C. Chen, Characterization of microRNA expression profiles in normal human tissues, BMC Genom. 8 (2007) 166.
[21] A.M. Reddy, Y. Zheng, G. Jagadeeswaran, et al., Cloning, characterization and expression analysis of porcine microRNAs, BMC Genom. 10 (2009) 65.

[22] J.P. Sluijter, A. van Mil, P. van Vliet, et al., MicroRNA-1 and -499 regulate differentiation and proliferation in human-derived cardiomyocyte progenitor cells, Arterioscler. Thromb. Vasc. Biol. 30 (2010) 859–868.
[23] E. van Rooij, D. Quiat, B.A. Johnson, et al., A family of microRNAs encoded by myosin genes governs myosin expression and muscle performance, Dev. Cell. 17 (2009) 662–673.
[24] M.L. Bell, M. Buvoli, L.A. Leinwand, Uncoupling of expression of an intronic microRNA and its myosin host gene by exon skipping, Mol. Cell Biol. 30 (2010) 1937–1945.
[25] T. Hosoda, H. Zheng, M. Cabral-da-Silva, et al., Human cardiac stem cell differentiation is regulated by a mircrine mechanism, Circulation 123 (2011 Mar) 1287–1296.
[26] K.D. Wilson, S. Hu, S. Venkatasubrahmanyam, et al., Dynamic microRNA expression programs during cardiac differentiation of human embryonic stem cells: role for miR-499, Circ. Cardiovasc. Genet. 3 (2010) 426–435.
[27] J.D. Fu, S.N. Rushing, D.K. Lieu, et al., Distinct roles of microRNA-1 and -499 in ventricular specification and functional maturation of human embryonic stem cell-derived cardiomyocytes, PLoS One 6 (2011) e27417.
[28] S.L. Paige, T. Osugi, O.K. Afanasiev, et al., Endogenous wnt/b-catenin signaling is required for cardiac differentiation in human embryonic stem cells, PLoS One 5 (2010) e11134.
[29] T. Nakamura, M. Sano, Z. Songyang, M.D. Schneider, A Wnt and beta-catenin-dependent pathway for mammalian cardiac myogenesis, Proc. Natl. Acad. Sci. USA 100 (2003) 5834–5839.
[30] A.T. Naito, H. Akazawa, H. Takano, et al., Phosphatidylinositol 3-kinase–Akt pathway plays a critical role in early cardiomyogenesis by regulating canonical wnt signaling, Circ. Res. 97 (2005) 144–151.
[31] C.C. Malbon, H.Y. Wang, Dishevelled: a mobile scaffold catalyzing development, Curr. Top Dev. Biol. 72 (2006) 153–166.
[32] C. Yost, M. Torres, J.R. Miller, et al., The axis-inducing activity, stability, and subcellular distribution of beta-catenin is regulated in Xenopus embryos by glycogen synthase kinase 3, Genes Dev. 10 (1996) 1443–1454.
[33] D. Kimelman, W. Xu, Beta-catenin destruction complex: insights and questions from a structural perspective, Oncogene 25 (2006) 7482–7491.
[34] S.E. Haynesworth, J. Goshima, V.M. Goldberg, A.I. Caplan, Characterization of cells with osteogenic potential from human marrow, Bone 13 (1992) 81–88.
[35] M.F. Pittenger, A.M. Mackay, S.C. Beck, et al., Multilineage potential of adult human mesenchymal stem cells, Science 284 (1999) 143–147.
[36] P. Mundel, H.W. Heid, T.M. Mundel, et al., Synaptopodin: an actin-associated protein in telencephalic dendrites and renal podocytes, J. Cell Biol. 139 (1997) 193–204.
[37] H. Iguchi, Y. Urashima, Y. Inagaki, et al., SOX6 suppresses cyclin D1 promoter activity by interacting with beta-catenin and histone deacetylase 1, and its down-regulation induces pancreatic beta-cell proliferation, J. Biol. Chem. 282 (2007) 19052–19061.
[38] C. Liu, Y. Li, M. Semenov, et al., Control of beta-catenin phosphorylation/degradation by a dual-kinase mechanism, Cell 108 (2002) 837–847.

Biochemical and Biophysical Research Communications xxx (2012) xxx–xxx

Contents lists available at SciVerse ScienceDirect

Biochemical and Biophysical Research Communications

journal homepage: www.elsevier.com/locate/ybbrc

Inhibition of enterovirus 71 entry by transcription factor XBP1

Jia-Rong Jheng [1], Chiou-Yan Lin [1], Jim-Tong Horng *,[1], Kean Seng Lau

Department of Biochemistry and Research Center for Emerging Viral Infections, Chang Gung University, 259 Wen-Hwa First Road, Kweishan, Taoyuan 333, Taiwan

ARTICLE INFO

Article history:
Received 6 March 2012
Available online xxxx

Keywords:
Enterovirus 71
Endoplasmic reticulum stress
Inositol-requiring enzyme 1
Unfolded protein response
Translational attenuation
X-box-binding protein 1

ABSTRACT

Inositol-requiring enzyme 1 (IRE1) plays an important role in the endoplasmic reticulum (ER), or unfolded protein, stress response by activating its downstream transcription factor X-box-binding protein 1 (XBP1). We demonstrated previously that enterovirus 71 (EV71) upregulated XBP1 mRNA levels but did not activate spliced XBP1 (XBP1s) mRNA or its downstream target genes, EDEM and chaperones. In this study, we investigated further this regulatory mechanism and found that IRE1 was phosphorylated and activated after EV71 infection, whereas its downstream XBP1s protein level decreased. We also found that XBP1s was not cleaved directly by $2A^{pro}$, but that cleavage of eukaryotic translation initiation factor 4G by the EV71 $2A^{pro}$ protein may contribute to the decrease in XBP1s expression. Knockdown of XBP1 increased viral protein expression, and the synthesis of EV71 viral protein and the production of EV71 viral particles were inhibited in XBP1-overexpressing RD cells. When incubated with replication-deficient and UV-irradiated EV71, XBP1-overexpressing RD cells exhibited reduced viral RNA levels, suggesting that the inhibition of XBP1s by viral infection may underlie viral entry, which is required for viral replication. Our findings are the first indication of the ability of XBP1 to inhibit viral entry, possibly via its transcriptional activity in regulating molecules in the endocytic machinery.

© 2012 Elsevier Inc. All rights reserved.

1. Introduction

Three major transmembrane ER stress sensor proteins have been identified and characterized comprehensively: PKR-like ER kinase (PERK), activating transcription factor 6 (ATF6), and IRE1. These proteins manage three arms of the unfolded protein response (UPR) signaling pathway and activate different subsets of genes to manage stress. Activation of PERK initiates the phosphorylation of eukaryotic initiation factor 2α (eIF2α), which causes the inhibition of global translation [1]. ATF6 belongs to a highly conserved family of regulated intramembrane proteolysis transcription factors, which are cleaved to release cytosolic domains that transit to the nucleus to regulate the transcription of a collection of ER stress target genes, including BiP, by binding to a consensus ER stress response element (ERSE) sequence in the promoter region of these proteins [2,3].

IRE1 undergoes oligomerization to activate its kinase and endoribonuclease (RNase) activities to transmit the UPR signals [4]. The RNase of IRE1 splices mRNA encoding the transcription factor XBP1, leading to a frameshift splicing and subsequent translation of the active spliced XBP1 protein (XBP1s) [5]. XBP1 was originally identified as a basic leucine zipper transcription factor in B cells and is required for plasma cell differentiation [6]. By binding the ERSE promoter region, the spliced transcription factor XBP1s can sequentially stimulate chaperones to promote the folding capacity in the ER [7,8]. The clearing of incorrectly folded proteins retained in the ER is now known to occur through their retrotranslocation into the cytosol in a process involving ER-associated degradation (ERAD), which is also induced by XBP1 [4].

EV71 is a positive-stranded RNA virus that belongs to the group of human enteroviruses whose members include poliovirus and coxsackievirus. EV71 has a genome of about 7.5 kb comprising an open reading frame flanked by a 5′untranslated region (UTR) and a 3′poly(A) tail. The 5′UTR of the viral genome is an internal ribosome entry site (IRES), which directs translation of the viral RNA in a cap-independent fashion to synthesize a polyprotein that can be cleaved by viral proteases $2A^{pro}$ and $3C^{pro}$ to produce mature and functional structural and nonstructural proteins [9]. $2A^{pro}$ is also responsible for the cleavage of eukaryotic translation initial factor G (eIF4G), which in turn inhibits the cap-dependent translational inhibition of global cellular proteins [10]. Numerous studies suggest a relationship between the ER stress response and viral infection, and many viruses can regulate UPR to benefit their replication or to trigger an immune response [11]. We showed previously that EV71 infection activates and modifies the UPR signaling pathways to benefit viral replication [12]. XBP1 mRNA was upregulated, but no IRE1-mediated splicing was detected. In the present study, we examined further the role of IRE–XBP1 of UPR during EV71 replication.

* Corresponding author. Fax: +886 3 211 8407.
E-mail address: jimtong@mail.cgu.edu.tw (J.-T. Horng).
[1] These authors contributed equally to this project.

0006-291X/$ - see front matter © 2012 Elsevier Inc. All rights reserved.
http://dx.doi.org/10.1016/j.bbrc.2012.03.094

2. Materials and methods

2.1. Cell culture and viral infection

Rhabdomyosarcoma (RD) cells were cultured in Dulbecco's modified Eagle's medium (DMEM) supplemented with 10% fetal bovine serum (FBS) under humidified 5% CO_2 in air. EV71 BrCr was obtained from the ATCC (accession no. VR 784). Viral propagation and titer determination by plaque assay were performed in RD cells, and the titer was recorded as the number of plaque-forming units per milliliter [13].

2.2. Antibodies and reagents

Rabbit polyclonal antibodies to 3A were raised against GST-3A [14]. Rabbit polyclonal antibodies against eIF4G and lamin A/C, and mouse monoclonal anti-GST were from Santa Cruz Biotechnology (Santa Cruz, CA, USA). Rabbit polyclonal anti-phospho-IRE1 and anti-XBP1 were from Abcam (Ab48187, Cambridge, UK) and Anaspec (#54578, San Jose, CA, USA), respectively. Antibody to GAPDH was from Abnova (Taoyuan, Taiwan). Anti-His tag was from Serotec (#MCA1396B, Oxford, UK). Plasmids encoding XBP1s, $2A^{pro}$, $3C^{pro}$, and $2A^{pro}$(C110A) were cloned into pcDNA3.1-mycHis(−) (Invitrogen, Carlsbad, CA). GST-$2A^{pro}$ and GST-$2A^{pro}$ (C110A) were cloned into pGEX-2T and pGEX-5X-1 (GE Healthcare Bio-Sciences AB, Uppsala, Sweden), respectively. EV71 5′UTR and 5× ERSE were cloned into pcDNA3.1-mycHis-B(+)-Fluc, in which Fluc was PCR amplified from pGL3 and inserted into pcDNA3.1/myc-His-B(+) to generate pCMV-5′UTR-Fluc (4643-IRES-Fluc) and pCMV-5×ERSE-Fluc, respectively. Stealth RNAi™ siRNA of XBP1 (siXBP1, #HSS111391) and scrambled negative controls Lo GC (#12935200) were from Invitrogen.

2.3. UV irradiation and viral RNA determination

UV irradiation of EV71 was performed as described previously, and the remaining titer was measured by plaque assay [15]. RD cells transfected with XPB1 plasmid or its vector control were incubated with UV-treated virus (UV-EV71), the cells were collected after 0, 0.5, and 1 h, and the viral RNA was quantified using quantitative real-time PCR (qPCR). To quantify the changes in gene expression, the ΔCt method was used to calculate relative fold changes normalized against the GAPDH control.

2.4. Western blotting and nucleus/cytoplasm fractionation assays

The cells were harvested at the times indicated, and lysates were prepared with lysis buffer (10 mM Tris, pH 7.4, 10 mM NaCl, and 1 mM $MgCl_2$) containing protease inhibitor cocktail (Roche). Equal amounts of cellular protein were analyzed by SDS–PAGE, the bands were transferred to a polyvinylidene fluoride membrane, and the proteins on the membrane were detected with enhanced chemiluminescence reagents (Millipore). RD cells were mock infected or infected with EV71 at a multiplicity of infection (MOI) of 10. The cells were harvested at the times indicated, and the nuclei and cytoplasm were separated as described [12].

2.5. In vitro protease cleavage assay

Wild-type and the catalytic-inactive mutant (C110A: cysteine mutated to alanine at amino acid 110) of $2A^{pro}$ of EV71 were cloned into pGEX vectors, and these GST-fusion proteins were purified according to the manufacturer's instruction (GE Healthcare Bio-Sciences AB). The purified GST-fusion proteins were dialyzed in buffer (25 mM Tris–HCl, pH 7.5, 50 mM NaCl, 5 mM DTT, 0.5 mM EDTA, and 25% glycerol) before use. RD cells were treated with or without 2 μg of thapsigargin (Tg) for 4 h and were lysed with lysis buffer without proteinase inhibitors. The cell lysates were centrifuged at 17,900*g* for 10 min at 4 °C, and the supernatant was collected for the cleavage assay. Thirty micrograms of supernatant was incubated with 30 μg of GST-2A or GST-$2A^{pro}$(C110A) in a total volume of 100 μl, at 37 °C for 4 h, and then analyzed by SDS–PAGE and Western blotting.

2.6. Reporter assays

Each well containing 3×10^4 RD cells in a 48-well plate was transfected with Lipofectamine with 0.4 μg of firefly luciferase reporter gene and 0.04 μg of pTK-Rluc encoding *Renilla* luciferase as an internal control. The luciferase activities were measured using a dual-luciferase reporter kit (Promega, Madison, WI, USA). The results were normalized to the *Renilla* luciferase activity of the internal control.

2.7. Data analysis

The data were analyzed using two-tailed Student's *t* test and are expressed as the mean ± SEM. $P < 0.05$ was considered significant.

3. Results

To understand better the regulatory mechanism of the EV71-induced IRE1-XBP1 signaling pathway, we examined whether the upstream IRE was activated by EV71. RD cells were infected with EV71, and the cells were harvested at the designated times postinfection (p.i.). EV71 phosphorylated IRE1 from 7 h p.i., and the phosphorylation level correlated with the viral translation, as indicated by the level of viral 3A protein, from 5 h p.i. (Fig. 1A).

In response to ER stress, the RNase function of IRE1 is activated to initiate the nonconventional splicing of transcription factor XBP-1 mRNA to produce XBP1s, which then increases the folding capacity for targeting misfolded proteins for degradation [5,16]. We demonstrated previously that EV71 increases the XBP1 mRNA level but that spliced XBP1 mRNA and downstream target genes, EDEM and chaperones, are not produced [12]. We next asked whether the regulation of XBP1 is responsible for the decrease in XBP1 expression. In a time-course experiment, the expression of XBP1s did not increase in the nucleus where it occurs normally, but was reduced by viral infection (lanes 2, 4, and 6, Fig. 1B). Nuclear XBP1s expression was increased by DTT treatment, indicating that the reduction in XBP1s was specific to EV71 infection (lane 7, Fig. 1B).

To understand whether the reduced XBP1 expression resulted from viral replication, we used UV inactivation of EV71 to inhibit viral replication but not viral entry [17]. RD cells were infected with UV-irradiated virus, which abolished the titer completely (data not shown); cells were harvested at 6 h p.i. and analyzed by immunoblotting analysis (Fig. 1C). Similar to the mock-infected cells, UV-treated EV71 showed similar intensity of XBP1s expression compared with the mock-treated virus, indicating that the reduction in XBP1s required viral replication (lanes 2 and 3, Fig. 1C).

Enterovirus infection attenuates cellular protein synthesis [10]. We could not exclude the possibility that the reduction in XBP1s expression was mediated by virally encoded proteases $2A^{pro}$ and $3C^{pro}$. We transfected plasmids encoding EV71 $2A^{pro}$ and $3C^{pro}$ into RD cells and examined their effects on endogenous XBP1s induced by Tg (Fig. 2A). EV71 infection reduced the level of endogenous XBP1s in cells treated with or without Tg (lanes 3 and 4, Fig. 2A). Cells transfected with plasmids encoding $2A^{pro}$ but not $3C^{pro}$ showed a reduced level of XBP1s, although this reduction was less than that induced by the virus (lanes 5 and 6, Fig. 2A).

Please cite this article in press as: J.-R. Jheng et al., Inhibition of enterovirus 71 entry by transcription factor XBP1, Biochem. Biophys. Res. Commun. (2012), http://dx.doi.org/10.1016/j.bbrc.2012.03.094

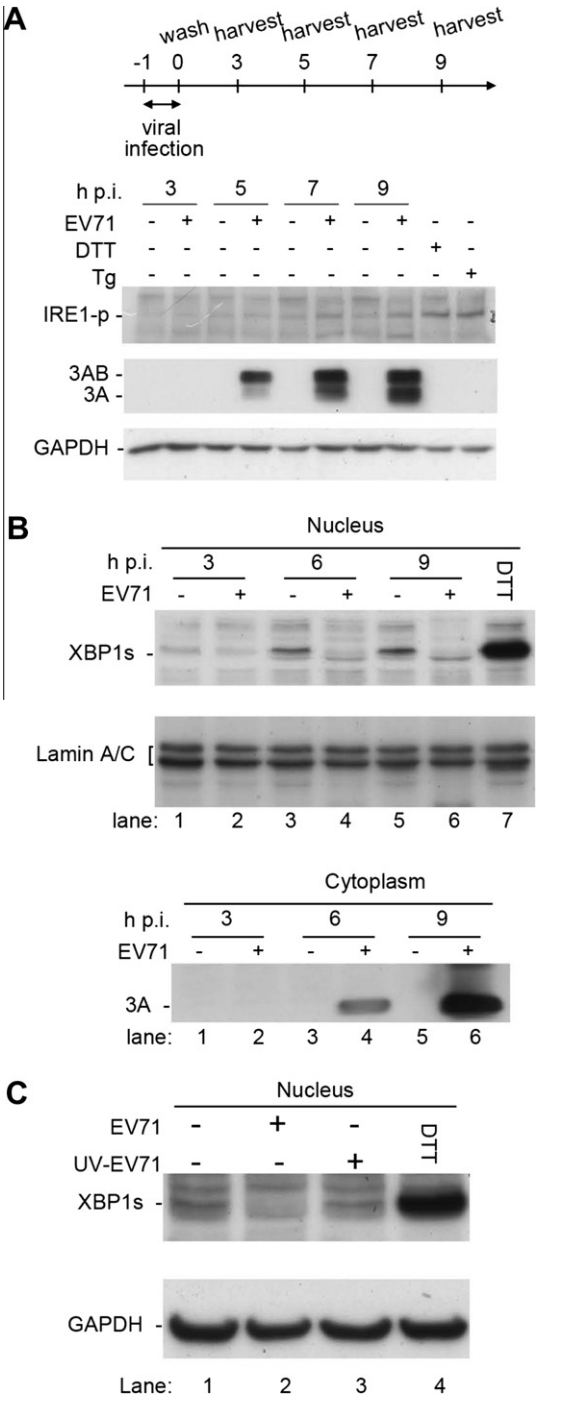


Fig. 1. EV71 induces phosphorylation of IRE1 and reduction of XBP1s. (A) RD cells were preadsorbed with EV71 (MOI10) on ice between −1 and 0 h p.i. The medium containing the unbound virus was replaced with DMEM containing 2% FBS and the temperature was increased to 37 °C. The infection protocol is sketched in the upper panel. The cells were harvested at the times indicated for western blotting using specific antibodies against p-IRE1 and 3A. The 3A antibodies recognized 3A and its precursor protein 3AB. Membranes were also probed with an antibody against GAPDH to control the loading of lanes. DTT (5 mM)- and Tg (2 μM)-treated cell lysates were used as a positive control for IRE1 phosphorylation under conditions of definitive UPR induction. These are representative of three independent assays. (B) RD cells were infected with EV71 (MOI 10) and the cells were collected to produce nuclear and cytoplasm fractions at 3, 6, and 6 h p.i. Equal amounts of lysate of the nuclear or cytosolic fraction were subjected to Western blotting. The nuclear fraction of cells treated with 2.5 mM DTT for 6 h were used as a control for the expression of XBP1s. Lamin A/C was a loading control for the nuclear fraction. (C) RD cells were infected with either mock-treated or UV-inactivated virus. Six hours after infection, the nuclear fraction was analyzed by Western blotting.

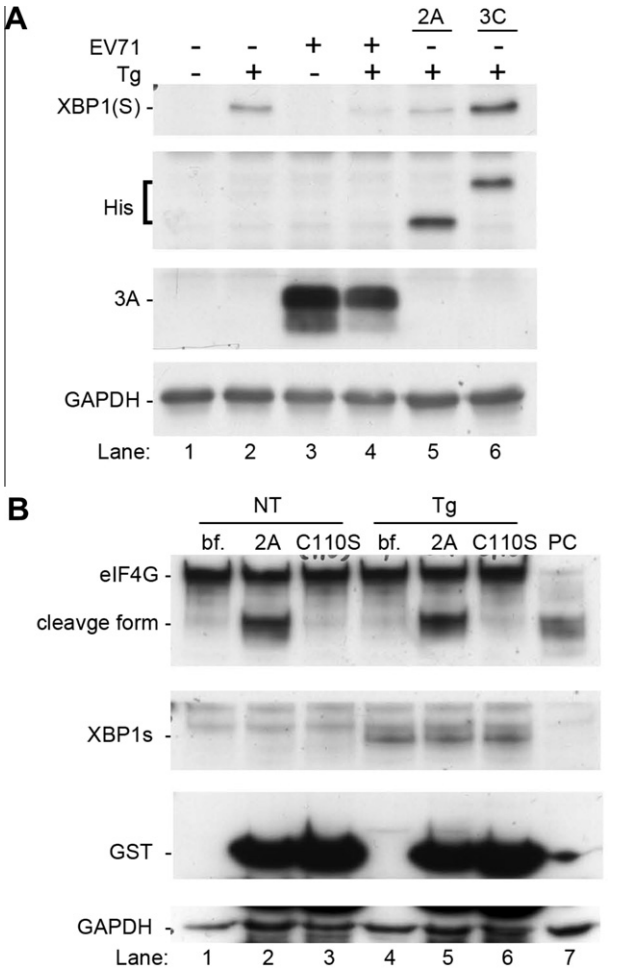


Fig. 2. The reduction in XBP1s is not caused by direct cleavage by 2A but by translational shutoff mediated by eIF4G cleavage. (A) RD cells were transfected with plasmids encoding viral proteases 2A and 3C for 24 h or infected with EV71 for 5 h. Anti-His tag and anti-3A antibodies were used to monitor the expression of 2A-his and 3C-his and viral infection, respectively. (B) Cell lysates prepared from RD cells pretreated with or without Tg were incubated with 30 μg of recombinant wild-type or mutant 2A for 4 h at 37 °C. "bf" is the dialysis buffer that was used as a negative control, and "PC" is the positive control, which comprised lysates prepared from RD cells transfected with 2A.

We next determined whether XBP1is the direct substrate of $2A^{pro}$ protease by incubating recombinant wild-type or mutant GST-$2A^{pro}$ with cell lysates obtained from cells treated with or without Tg (Fig. 2B). Mutation of C110S in $2A^{pro}$ causes defected autocleavage catalytic activity of $2A^{pro}$ released from viral polyprotein in *cis* and complete loss of proteolytic activity toward eIF4G in *trans* [18]. Catalytic cleavage of eIF4G by wild-type$2A^{pro}$, but not its catalytic mutant variant C110A, was detected, suggesting specificity of $2A^{pro}$ (upper panel, Fig. 2B). XBP1s was upregulated in Tg-treated cells (lanes 4–6, Fig. 2B). Parallel examination of its cleavage by $2A^{pro}$ and its mutant showed that XBP1s was not the direct substrate of $2A^{pro}$ (lanes 4–6, Fig. 2B). Together, these data suggest that the inhibition of XBP1s expression level is mediated by translational attenuation induced by proteolytic cleavage of eIF4G, but not of XBP1s by viral proteases.

To test the hypothesis that IRE-XBP1-mediated ER stress inhibits viral replication, we measured viral replication in XBP1-transfected cells. We constructed a chimeric protein in which the transcriptionally active XBP1s was cloned into pcDNA3.1-mycHis. This chimeric protein has the characteristic of the wild-type protein because it is expressed correctly and can activate a luciferase reporter plasmid

Please cite this article in press as: J.-R. Jheng et al., Inhibition of enterovirus 71 entry by transcription factor XBP1, Biochem. Biophys. Res. Commun. (2012), http://dx.doi.org/10.1016/j.bbrc.2012.03.094

driven by the ERSE promoter (Fig. S1). RD cells were transfected with the XBP1s overnight and then infected with EV71, and the cells were collected at times p.i. for western blotting. The viral protein expression as indicated by 3A became visible from 7 h p.i.; at this time, less viral protein was translated in XBP1s-transfected compared with the vector control-transfected cells (lane 8 versus 9, Fig. 3A). However, this inhibition disappeared at 9 h p.i., suggesting that XBP1s had been compensated or the viral translation reached a plateau (lanes 11 and 12, Fig. 3A). The viral titer in XBP1s-overexpressing cells decreased significantly (Fig. 3B).

We also analyzed viral replication using RNA interference to knock down XBP1s. siRNA targeting XBP1s (siXBP1) was transfected into RD cells (Fig. 3C and D). Compared with mock-transfected cells, cells transfected with siXBP1s showed a marked reduction in XBP1 level (Fig. 3D). By contrast, the GAPDH level was not affected under the same conditions. Viral protein synthesis increased in XBP1s-knockdown cells at 5 h p.i. (lanes 1 and 2), although the viral protein level reached a plateau afterward (Fig. 3C). These data suggest that the virus caused XBP1 disappearance, which facilitated its replication.

To examine if the possible inhibitory effect of XBP1 on viral translation was associated with viral IRES activity, IRES activity of EV71 was measured by luciferase driven by IRES. The reporter plasmid (CMV-EV71 5′UTR-Fluc) containing the EV71 4643IRES was placed upstream of the Fluc open reading frames (upper panel, Fig. S2). At 24 h after transfection with XBP1s or the corresponding vector control, the reporter containing EV71 IRES was then transfected alone with the internal control plasmid pTK-Rluc, and the cells were harvested for dual-luciferase reporter assay 8 h post-transfection. The transfection of XBP1 showed little effect on EV71 IRES activity, as indicated by the luciferase activity in the cells (bottom panel, Fig. S2), suggesting that XBP1 did not target viral IRES activity. To examine whether XBP1 inhibits viral entry, we used UV-irradiated EV71, which lack replication activity but can bind to and enter host cells [17]. EV71 at an MOI of 100 was inactivated by UV irradiation, and the remaining titers of UV-EV71 were inhibited completely as detected by plaque assay (data not shown). UV-EV71 was added to control vector-transfected or XBP1-transfected RD cells, and the cells were harvested after 0, 0.5, and 1 h. The viral RNA was measured as an index of viral uptake (Fig. 4). The XBP1-transfected cells showed no signal of viral uptake; the vector-transfected cells showed a significant increase in virus uptake in a time-dependent manner, suggesting that XBP1 inhibits viral entry (Fig. 4).

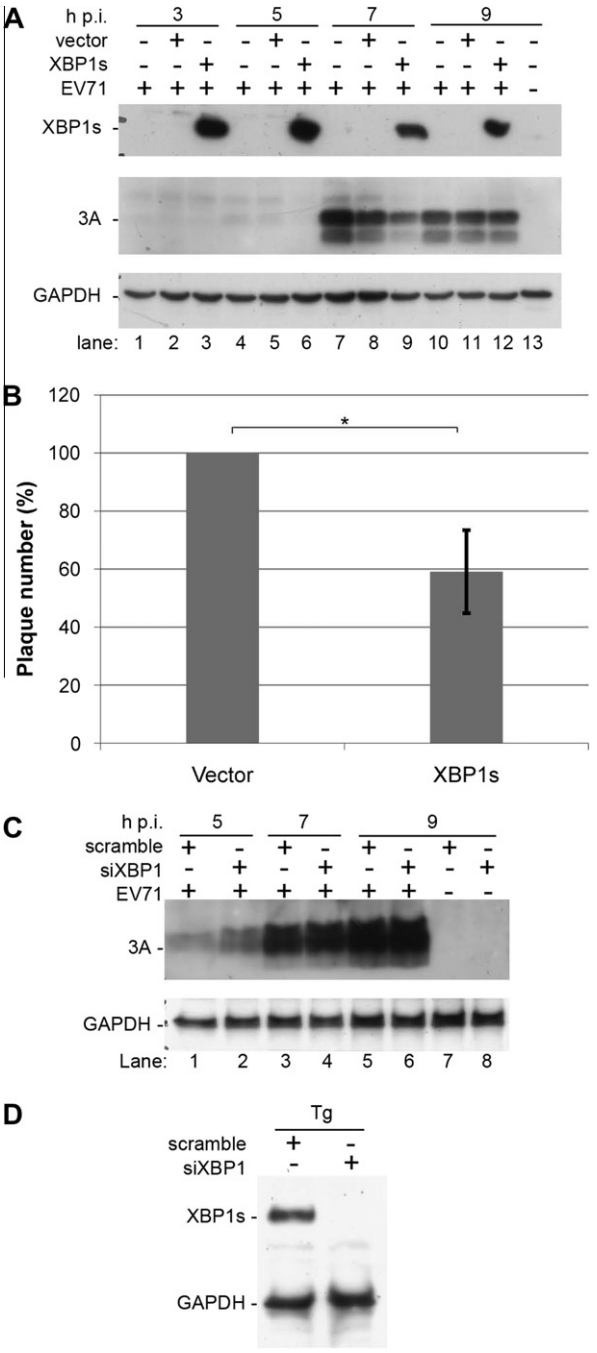


Fig. 3. Expression of XBP1s inhibits viral replication. (A) Viral protein synthesis was inhibited by the overexpression of XBP1s. RD cells were transfected with XBP1s or a control vector (4 μg each) for 24 h. The cells were infected with EV71 (MOI 10) and were harvested at the times indicated and subjected to Western blotting using specific antibodies against 3A. (B) Viral titer in RD cells transiently transfected with XBP1s plasmids was measured by plaque assay. After transfection for 24 h, the cells were infected with EV71 (MOI 10), and the amount of virus present in the cells and culture medium was measured by plaque assay. The average plaque numbers of cells transfected with XBP1s plasmid were normalized to that of vector control, arbitrarily set to 1. This is an average of three independent experiments. $^{*}p < 0.005$. (C and D) Time-course analysis of viral protein expression in siXBP1-transfected RD cells. Cells were transfected with scrambled siRNA or siXBP1 for 3 days. The cells were infected with EV71 (MOI 10) and harvested at the times indicated, and 50 μg aliquots of each cell lysate were used for Western blotting. The silencing effect by siXBP1by immunoblotting is shown in (D).

4. Discussion

In this study, we examined the role of the IRE1-XBP1 pathway in viral replication, and we conclude that XBP1 plays a critical role in EV71 replication at the entry step based on the following findings: (1) IRE1 was activated but no XBP1 splicing was detected during infection; (2) expression of XBP1 downregulated viral replication; (3) XBP1 was subject to translational shutoff by EV71-induced eIF4G cleavage; and (4) the uptake of UV-irradiated virus decreased in XBP1-overexpressed cells. We demonstrated previously that EV71 does not change the EDEM mRNA level driven by unfolded protein response element during the course of infection [12]. The resulting inhibition of the expression of genes such as EDEM may be beneficial to viral infection by inhibiting viral protein degradation by the ERAD mechanism. The gene for XBP1 contains an ERSE element and can be transactivated by ATF6 and XBP1 itself [5,19]. However, using a reporter assay, we reported that the EV71 did not activate the ERSE of XBP1 [12]. In our current study, we found further evidence that the translation of XBP1s is inhibited by attenuation of EV71-induced eIF4G-cleavage (Fig. 2).

Picornaviral proteinases catalyze the degradation of cellular targets, which shuts off global host protein synthesis. However, viral RNA undergoes cap-independent IRES translation, which is

Please cite this article in press as: J.-R. Jheng et al., Inhibition of enterovirus 71 entry by transcription factor XBP1, Biochem. Biophys. Res. Commun. (2012), http://dx.doi.org/10.1016/j.bbrc.2012.03.094

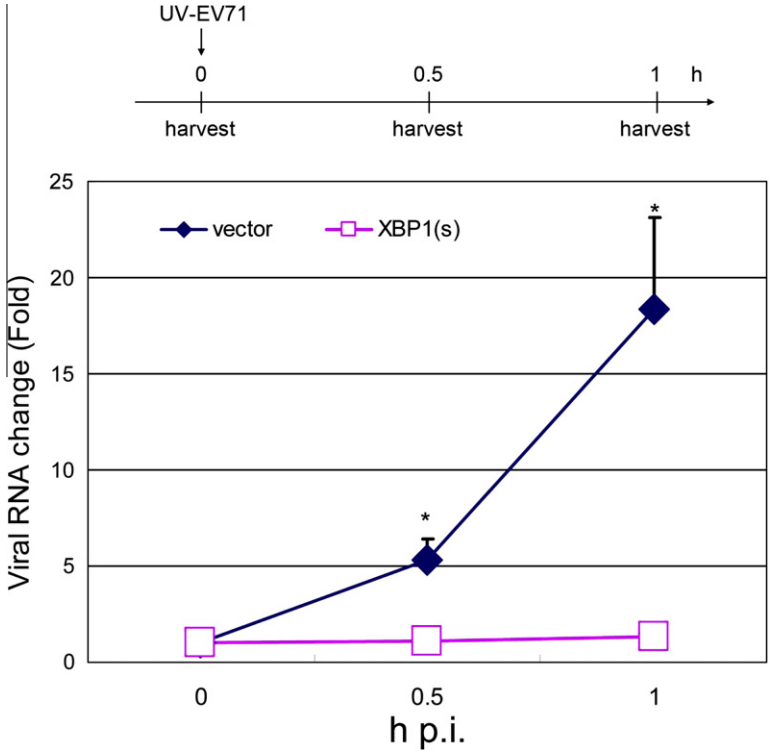


Fig. 4. XBP1-overexpressing RD cells show reduced viral entry of UV-irradiated EV71. EV71 (MOI 100) was irradiated by UV and added to cells transfected with XBP1 or a control vector, and the cells were harvested after 0, 0.5, and 1.0 h. Intracellular viral RNA level was measured by qPCR. To adjust for differences in viral binding in the two cell types, the ratio of viral RNA to the internal control was normalized to the RNA level at 0 h, arbitrarily set to 1. $^{*}p < 0.05$.

not affected by the virus itself. We demonstrated recently that EV71 infection upregulates several ER-resident chaperone genes, including BiP and calreticulin, both of which contain ERSE [20,21]. These chaperone proteins were upregulated by EV71, but this upregulation was not caused by an increase in RNA levels [12]. Chaperone genes such as BiP may contain an IRES structure, whose activity increases under stress [22] and which may escape cap-dependent translational shutoff. We cannot exclude the possibility that EV71 increases the stability of existing chaperone genes to facilitate the folding and assembly of rapidly synthesized viral proteins.

The inhibition of XBP1 by viral infection might be explained by the notion that XBP1 expression is unfavorable for viral replication. This speculation is supported by the inhibition of viral replication by the overexpression of XBP1 (Fig. 3A and B). Conversely, the reduced XBP1 expression by siRNA is advantageous to viral replication because it increases viral translation (Fig. 3C and D). Modulation of XBP1 signaling events by other viruses has also been observed. In HCMV-infected cells or in cells carrying HCV replicons, the transcriptional activity of XBP1 is inhibited despite the presence of significant levels of spliced XBP1 [23,24]. The suppression of IRE-XBP1 may promote HCV replication because the IRES-dependent translational activity of HCV increases in $IRE^{-/-}$MEF cells with a defective IRE-XPB1 pathway [24]. We found that XBP1 can inhibit EV71 entry, possibly by altering XBP1s transcriptional activity to regulate the expression of viral uptake-related proteins. It would be tempting to study these proteins in XBP1-overexpressing RD cells by transcriptomic or proteomic approaches.

Acknowledgments

This study was supported by Chang Gung Memorial Hospital (Grant numbers CMRPD 180072 and 190192) and by National Science Council (99-2321-B-001-035, 98-2311-B-182-003-MY3).

Appendix A. Supplementary data

Supplementary data associated with this article can be found, in the online version, at http://dx.doi.org/10.1016/j.bbrc.2012.03.094.

References

[1] H.P. Harding, Y. Zhang, D. Ron, Protein translation and folding are coupled by an endoplasmic-reticulum-resident kinase, Nature 397 (1999) 271–274.
[2] K. Haze, H. Yoshida, H. Yanagi, T. Yura, K. Mori, Mammalian transcription factor ATF6 is synthesized as a transmembrane protein and activated by proteolysis in response to endoplasmic reticulum stress, Mol. Biol. Cell. 10 (1999) 3787–3799.
[3] K. Mori, Tripartite management of unfolded proteins in the endoplasmic reticulum, Cell 101 (2000) 451–454.
[4] P. Walter, D. Ron, The unfolded protein response: from stress pathway to homeostatic regulation, Science 334 (2011) 1081–1086.
[5] H. Yoshida, T. Matsui, A. Yamamoto, T. Okada, K. Mori, XBP1 mRNA is induced by ATF6 and spliced by IRE1 in response to ER stress to produce a highly active transcription factor, Cell 107 (2001) 881–891.
[6] N.N. Iwakoshi, A.H. Lee, L.H. Glimcher, The X-box binding protein-1 transcription factor is required for plasma cell differentiation and the unfolded protein response, Immunol. Rev. 194 (2003) 29–38.
[7] H. Yoshida, T. Matsui, N. Hosokawa, R.J. Kaufman, K. Nagata, K. Mori, A time-dependent phase shift in the mammalian unfolded protein response, Dev. Cell 4 (2003) 265–271.
[8] A.H. Lee, N.N. Iwakoshi, L.H. Glimcher, XBP-1 regulates a subset of endoplasmic reticulum resident chaperone genes in the unfolded protein response, Mol. Cell Biol. 23 (2003) 7448–7459.
[9] J.Y. Lin, T.C. Chen, K.F. Weng, S.C. Chang, L.L. Chen, S.R. Shih, Viral and host proteins involved in picornavirus life cycle, J. Biomed. Sci. 16 (2009) 103.
[10] V.R. Racaniello, Picornaviridae: The viruses and their replication, in: P.M.H. David M Knipe, Malcolm A. Martin, Diane E. Griffin, Robert A. Lamb, Bernard Roizman, Stephen E Straus (Ed.), Fields Virology, Lippincott Williams & Wilkins, Philadelphia, 2007, pp. 795–838.
[11] B. He, Viruses, endoplasmic reticulum stress, and interferon responses, Cell Death Differ. 13 (2006) 393–403.
[12] J.R. Jheng, K.S. Lau, W.F. Tang, M.S. Wu, J.T. Horng, Endoplasmic reticulum stress is induced and modulated by enterovirus 71, Cell Microbiol. 12 (2010) 796–813.

[13] B.W. Wu, T.L. Pan, Y.L. Leu, Y.K. Chang, P.J. Tai, K.H. Lin, J.T. Horng, Antiviral effects of *Salvia miltiorrhiza* (Danshen) against enterovirus 71, Am. J. China Med. 35 (2007) 153–168.
[14] W.F. Tang, S.Y. Yang, B.W. Wu, J.R. Jheng, Y.L. Chen, C.H. Shih, K.H. Lin, H.C. Lai, P. Tang, J.T. Horng, Reticulon 3 binds the 2C protein of enterovirus 71 and is required for viral replication, J. Biol. Chem. 282 (2007) 5888–5898.
[15] W.R. Wong, Y.Y. Chen, S.M. Yang, Y.L. Chen, J.T. Horng, Phosphorylation of PI3K/Akt and MAPK/ERK in an early entry step of enterovirus 71, Life Sci. 78 (2005) 82–90.
[16] M. Calfon, H. Zeng, F. Urano, J.H. Till, S.R. Hubbard, H.P. Harding, S.G. Clark, D. Ron, IRE1 couples endoplasmic reticulum load to secretory capacity by processing the XBP-1 mRNA, Nature 415 (2002) 92–96.
[17] M.A. Beck, N.M. Chapman, B.M. McManus, J.C. Mullican, S. Tracy, Secondary enterovirus infection in the murine model of myocarditis. Pathologic and immunologic aspects, Am. J. Pathol. 136 (1990) 669–681.
[18] C.U. Hellen, M. Facke, H.G. Krausslich, C.K. Lee, E. Wimmer, Characterization of poliovirus 2A proteinase by mutational analysis: residues required for autocatalytic activity are essential for induction of cleavage of eukaryotic initiation factor 4F polypeptide p220, J. Virol. 65 (1991) 4226–4231.
[19] K. Yamamoto, H. Yoshida, K. Kokame, R.J. Kaufman, K. Mori, Differential contributions of ATF6 and XBP1 to the activation of endoplasmic reticulum stress-responsive cis-acting elements ERSE, UPRE and ERSE-II, J. Biochem. (Tokyo) 136 (2004) 343–350.
[20] X. Chen, J. Shen, R. Prywes, The luminal domain of ATF6 senses endoplasmic reticulum (ER) stress and causes translocation of ATF6 from the ER to the Golgi, J. Biol. Chem. 277 (2002) 13045–13052.
[21] J. Shen, R. Prywes, ER stress signaling by regulated proteolysis of ATF6, Methods 35 (2005) 382–389.
[22] S. Cho, S.M. Park, T.D. Kim, J.H. Kim, K.T. Kim, S.K. Jang, BiP internal ribosomal entry site activity is controlled by heat-induced interaction of NSAP1, Mol. Cell Biol. 27 (2007) 368–383.
[23] J.A. Isler, A.H. Skalet, J.C. Alwine, Human cytomegalovirus infection activates and regulates the unfolded protein response, J. Virol. 79 (2005) 6890–6899.
[24] K.D. Tardif, K. Mori, R.J. Kaufman, A. Siddiqui, Hepatitis C virus suppresses the IRE1-XBP1 pathway of the unfolded protein response, J. Biol. Chem. 279 (2004) 17158–17164.

Please cite this article in press as: J.-R. Jheng et al., Inhibition of enterovirus 71 entry by transcription factor XBP1, Biochem. Biophys. Res. Commun. (2012), http://dx.doi.org/10.1016/j.bbrc.2012.03.094

Biochemical and Biophysical Research Communications 420 (2012) 888–894

Contents lists available at SciVerse ScienceDirect

Biochemical and Biophysical Research Communications

journal homepage: www.elsevier.com/locate/ybbrc

Galpha/LGN-mediated asymmetric spindle positioning does not lead to unequal cleavage of the mother cell in 3-D cultured MDCK cells

Zhuoni Xiao [a,b], Qingwen Wan [a], Quansheng Du [a,*], Zhen Zheng [a,*]

[a] Institute of Molecular Medicine and Genetics, Department of Neurology, Georgia Health Sciences University, 1120 15th Street, Augusta, GA 30912, United States
[b] Reproductive Medicine Center, Renmin Hospital of Wuhan University, Wuhan 430060, China

ARTICLE INFO

Article history:
Received 4 March 2012
Available online 24 March 2012

Keywords:
Gα
LGN
Cell division
Asymmetric spindle positioning
Cleavage furrow
Cytokinesis

ABSTRACT

The position of the mitotic spindle plays a key role in spatial control of cell division. It is generally believed that when a spindle is positioned asymmetrically in a dividing cell, the resulting daughter cells are usually unequal in size due to eccentric cleavage of the mother cell. Molecular mechanisms underlying the generation of unequal sized daughter cells have been extensively studied in *Drosophila* neuroblast and *Caenorhabditis elegans* zygote where the Gα subunit of the heterotrimeric G proteins and its binding partner – Pins in *Drosophila* and GPR-1/2 in *C. elegans* – are shown to be critical in governing spindle positioning and asymmetric cleavage of the mother cell. In mammalian system, although Gα and LGN (mammalian Pins homolog) are also required for spindle orientation, whether they can mediate asymmetric spindle positioning or asymmetric cleavage of the mother cell is not known. Here, by artificially targeting Gαi to the apical cortex in 3-D cultured MDCK cells, we established a system where asymmetric spindle positioning can be consistently induced. Interestingly, this asymmetrically positioned spindle does not lead to asymmetric cleavage; instead it results in equal sized daughter cells. Live cell time-lapse analysis revealed that anaphase spindle elongation compensated the original asymmetric spindle positioning. Our findings demonstrate that asymmetric spindle positioning does not necessarily lead to unequal sized daughter cells in mammalian system. We discuss potential mechanisms in generating unequal sized daughter cells.

Published by Elsevier Inc.

1. Introduction

Cells propagate their progenies through cell division. To generate identical daughter cells, the mother cells divide symmetrically by positioning the mitotic spindle at the center of the cell. The mitotic spindle then directs central cleavage furrow formation which leads to the production of two equal sized daughter cells that inherit identical set of genetic materials and cytoplasmic components. Another type of cell division, called asymmetric cell division, is usually utilized by stem/progenitor cells to generate different daughter cells with distinct cell fates [1]. Asymmetric cell division usually results in the generation of unequal sized daughter cells.

It is generally believed that the position of mitotic spindle dictates the relative size of the daughter cells: a centrally located spindle leads to an equal cleavage, whereas an eccentrically located spindle results in an unequal cleavage, therefore generates unequal sized daughter cells [2–4]. Spindle positioning is achieved through interactions between astral microtubules and the cell cortex [5]. Recent studies suggest that receptor-independent G-protein signaling is a major regulator of spindle positioning in model systems including *Caenorhabditis elegans* and *Drosophila* [3,6]. Cortical Gα and its binding partner GPR-1/2 (in *C. elegans*) or Pins (in *Drosophila*) are the key players for generating asymmetric spindle positioning and subsequent unequal sized daughter cells [6]. In *C. elegans* zygote, Gα and GPR-1/2 are enriched at the posterior cell cortex where they serve as force generators, probably through cytoplasmic dynein, to produce stronger pulling forces on astral microtubules and lead to spindle displacement towards this side of the cell [7–9]. Such asymmetric spindle positioning leads to the production of a larger anterior and a smaller posterior daughter cell. In *Drosophila* neuroblast, apically localized Gα and Pins are required for spindle positioning and the generation of unequal sized daughters – a larger apical daughter cell that remains to be

Abbreviations: Gα, the alpha subunit of heterotrimeric G proteins; Pins, partner of inscuteable; LGN, mammalian homologue of Pins; 3-D, three dimensional; MDCK, Madin Darby canine kidney; Crb3, Crumb3.

* Corresponding authors. Address: Institute of Molecular Medicine and Genetics, Department of Neurology, Georgia Health Sciences University, 1120 15th Street, CA-2010, Augusta, GA 30912, United States. Fax: +1 706 721 0340.

E-mail addresses: qdu@georgiahealth.edu (Q. Du), zzheng@georgiahealth.edu (Z. Zheng).

0006-291X/$ - see front matter Published by Elsevier Inc.
http://dx.doi.org/10.1016/j.bbrc.2012.03.095

a neuroblast and a smaller basal ganglion mother cell [10–13]. In mammalian system, Gα and LGN (mammalian homologue of Pins) are also involved in regulating spindle orientation during neurogenesis, epidermal differentiation, epithelial morphogenesis and dermomyotome development [14–20]. However, whether Gα/LGN complex can direct asymmetric spindle positioning and asymmetric cleavage of the mother cell in mammalian system is not known.

Using an apically located protein Crumb3 (Crb3) as a vehicle, we have successfully targeted ectopically expressed Gαi1 and endogenous LGN to the apical cell membrane in 3-D cultured MDCK epithelial cells [20]. Here, we report that the apical Gαi1/LGN complex not only redirects the mitotic spindle orientation from perpendicular to parallel to the apical–basal axis, but also consistently positioned the metaphase spindle asymmetrically toward the apical cell membrane. Such a reproducible and biologically relevant system allowed us to test whether asymmetric spindle positioning leads to the generation of unequal sized daughter cells. By analyzing fixed cysts samples and live cell imaging of the cell division process, surprisingly, we found that Gαi1/LGN-mediated asymmetric spindle positioning does not result in asymmetric cleavage of the mother cell; instead, the mother cell eventually generates two equal sized daughter cells. Our findings challenge the general opinion that asymmetric spindle positioning leads to unequal sized daughter cells.

2. Materials and methods

2.1. Antibodies

The following antibodies were used: mouse anti-α-tubulin (Sigma–Aldrich), rabbit anti-γ-tubulin (Invitrogen), mouse anti-β-catenin (BD); and secondary Alexa 488, Alexa 594, Alexa 680 (Invitrogen), and IRDye800 (Rockland) conjugated goat anti-mouse or rabbit antibodies. Hoechst 33342 (Invitrogen) was used for DNA staining.

2.2. Cell culture and stable cell lines

MDCK cells were cultured in DMEM supplemented with 10% fetal calf serum and penicillin/streptomycin (100 IU/ml and 100 mg/ml, respectively) at 37 °C in a humidified 5% CO_2 atmosphere. Stable Tet-Off inducible MDCK Crb3-Venus-Gαi1 cell line was generated as described previously [20]. Briefly, Crb3 cDNA was first cloned in pTRE2Hyg vector. Venus was then cloned downstream of, and in frame with Crb3 to make pTRE2Crb3-Venus. cDNA encoding Gαi1 were inserted in pTRE2Crb3-Venus to generate pTRE2Crb3-Venus-Gαi1, and the plasmid was transfected into MDCK T23 cells and stable clones were selected using hygromycin. For the Crb3-Venus-Gαi1/mCherry-α-tubulin cell line, the mCherry-α-tubulin cassette was released from pmCherry-α-tubulin-IRES-puro2 plasmid (Addgene plasmid 21043) and cloned into pcDNA3.1/Zeo (Invitrogen) to generate pcDNA3.1-mCherry-α-tubulin-zoe. The plasmid was transfected into Crb3-Venus-Gai1 cell line in the presence of doxycycline and selected by Zeocin (Invitrogen).

2.3. 3-D culture

The 3-D culture of MDCK cells in matrigel was performed as previously described [20]. Briefly, cells were trypsinized and resuspended to single cell suspension of 4×10^4 cells/ml in 2% matrigel (BD). 400 μl of cells were plated in each well of 8-well Lab-Tek II chamber slides (Thermo Fisher Scientific) precoated with 30 μl of matrigel. Cells were grown for 3–4 days.

2.4. Western blot analysis

Cells were washed with cold PBS and collected in cell lysis buffer (25 mM HEPES, pH 7.4, 150 mM NaCl, 0.5% Triton X-100, 0.5 mM EDTA, 5 mM $MgCl_2$, 1 mM DTT, 1 mM PMSF, 10 μg/ml leupeptin, and 20 μg/ml aprotinin). Cell debris was removed by centrifugation at 14,000 rpm for 20 min at 4 °C. SDS sample buffer was added to equal amounts of cell lysate and proteins were separated by SDS–PAGE, transferred onto nitrocellulose membranes, and analyzed with anti-α-tubulin antibody.

2.5. Immunofluorescence microscopy

Cysts images were captured on a confocal microscope (510 LSM; Carl Zeiss, Inc.) using a Plan Apochromat 63×/1.4 NA oil objectives (Carl Zeiss, Inc.) and analyzed using the LSM Image Examiner and Image J software. To quantitate spindle and spindle pole to cell cortex distances, γ-tubulin staining was used to visualize spindle poles. To quantitate the areas of daughter cells, β-catenin staining was used to mark the cell border. Standard deviation was calculated, and statistical significance was determined by Student's *t* test.

2.6. Time-lapse analysis

Time-lapse analysis was performed on a LSM 7 Live laser-scanning confocal microscope (Carl Zeiss, Inc.), with a plan-Apochromat 63×/1.4 oil objective. Since the mCherry-α-tubulin forms mitotic spindle only during mitosis, it is easy to identify mitotic cells in the cysts. The images were acquired every 10 s with ZEN 2009 software (Carl Zeiss, Inc.).

3. Results

3.1. Apical targeting of Gαi1/LGN leads to asymmetric spindle positioning during cystogenesis of MDCK cells

Organotypic 3-D culture of MDCK cells phenocopies many aspects of *in vivo* cystogenesis and has been used as a model system to study epithelial morphogenesis *in vitro*. Using such a system, we showed previously that LGN plays a critical role in directing spindle orientation during epithelial morphogenesis [20]. During cystogenesis, atypical protein kinase C-mediated apical exclusion leads to restricted lateral cortical localization of LGN which directs spindle orientation to be perpendicular to the apical-basal axis [20,21]. To test the effect of apical mistargeting of LGN on spindle orientation and cystogenesis, we generated inducible MDCK cell lines expressing a Crumbs3-fused wild type Gαi1 (Crb3-Venus-Gαi1). Ectopic expression of Crb3-Venus-Gαi1 resulted in apical localization of the fusion protein which, in turn recruits endogenous LGN to the apical cell cortex during cystogenesis [20]. Such artificial apical targeting of endogenous LGN led to a complete reversion of the mitotic spindle axis – from perpendicular to parallel to the apical-basal axis – and profound cystogenesis defects [20]. Interestingly, when carefully examining Crb3-Venus-Gαi1 cysts stained with anti-α-tubulin antibody, we noticed that except for reorientation, the spindle appeared to be always positioned asymmetrically towards the apical cell cortex (Fig. 1B). To confirm such observation, we stained the cysts with anti-γ-tubulin antibody (Fig. 1C) and measured the distances between spindle poles to the apical or basal cell membrane, respectively, as depicted in Fig. 1D. Indeed, the distance from the apical spindle pole to apical cell membrane is significant shorter than that from the basal spindle pole to the basal membrane (Fig. 1E). When doxycycline was present in the medium to suppress the expression of Crb3-Venus-Gαi1, the

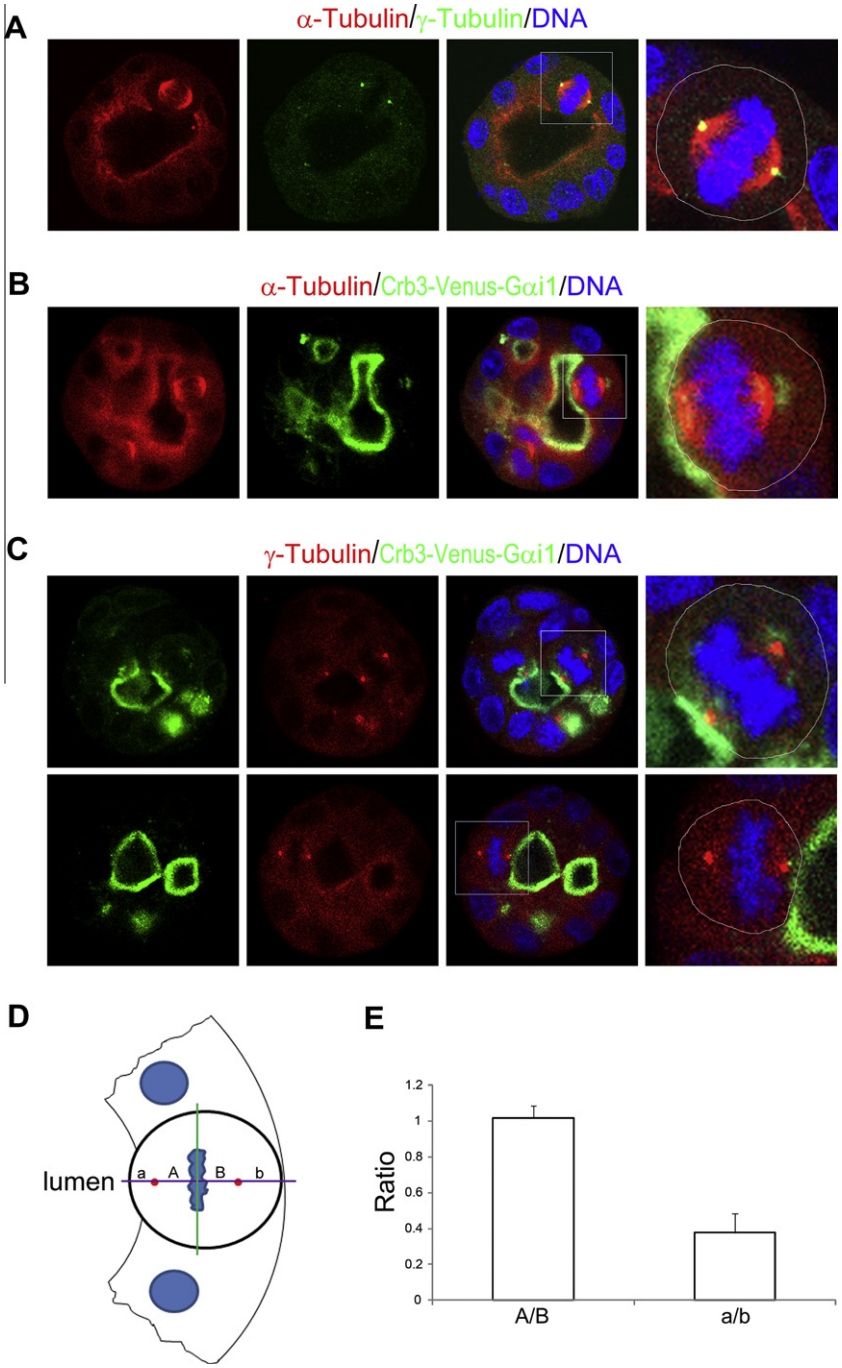


Fig. 1. Apical targeting of Gαi1 results in asymmetric spindle positioning. Stable Tet-Off MDCK cells expressing Crb3-Venus-Gαi1 were cultured in the presence (A. +Dox) or absence (B, C. −Dox) of doxycycline in matrigel for 3 days to allow 3-D cystogenesis. (A) Cysts were fixed and stained with anti-α-tubulin (red) and anti-γ-tubulin (green) antibodies. DNA was stained with Hoechst 33342. (B) Cysts were fixed and stained with anti-α-tubulin (red) antibody. DNA was stained with Hoechst 33342. (C) Cysts were fixed and stained with anti-γ-tubulin (red) antibody. DNA was stained with Hoechst 33342. Single confocal images were shown in A, B and C, white lines were drawn to outline the mitotic cell in A, B and C. (D) Schematic illustration for the measurement of relative spindle length and spindle positioning. Apical cell surface is facing the lumen. For each metaphase cell, two lines were drawn, one crossing the two spindle poles and the other along the long axis of the chromosome. The crossing point of the two lines was defined as "*O*". The distance from apical spindle pole to "*O*" was defined as "*A*" while the distance from basal spindle pole to "*O*" as "*B*". Similarly, the distance from apical spindle pole to apical cell cortex is defined as "*a*" while the distance from the basal spindle pole to basal cell cortex as "*b*". (E) Quantitation of *A*/*B* and *a*/*b* ratio as indicated in (*D*). $n = 30$. Error bars represent SD (Standard Deviation).

mitotic spindle positioned perpendicular to the apical-basal axis and in the center of the cell (Fig. 1A). Importantly, in dividing Crb3-Venus-Gαi1 cells, besides spindle misorientation and mispositioning, we did not observe obvious defect in spindle organization and chromosome alignment (Fig. 1B). Thus, apical targeting of Gαi1/LGN complex led to asymmetric spindle positioning; further support the hypothesis that this complex could generate pulling forces on astral microtubules.

3.2. Asymmetric spindle positioning generates equal sized daughter cells

During asymmetric cell division of *Drosophila* neuroblast, apically localized Gα and Pins are involved in generating unequally sized apical and basal spindles as well as astral microtubules [10,13]. We wondered whether similar outcome could be observed in our system. We carefully compared the apical and basal spindle

length by measuring the distances from the apical or basal spindle poles to the center of aligned chromosome (Fig. 1D). No obvious difference in length between apical and basal spindles was observed (Fig. 1E). We were not able to analyze astral microtubules due to the limited image resolution in 3-D cysts.

As asymmetrically localized Gα/Pins or Gα/GPR-1,2 led to asymmetric cleavage of *Drosophila* neuroblast and *C. elegans* zygote, we wondered whether Gαi1/LGN-mediated asymmetric spindle positioning also led to asymmetric cleavage of the mother cell in our system. Surprisingly, when we viewed telophase daughter cells, we did not observe obvious size difference between apical and basal daughter cells (Fig. 2A). To more precisely compare daughter cell size, we stained the cysts with anti-β-catenin antibody to mark the cell border (Fig. 2B). Again, the metaphase spindle is apparently asymmetrically positioned towards the apical cell cortex (Fig. 2B). We then measured and compared the area of telophase daughter cells. Indeed, there is no significant difference in daughter cell sizes (Fig. 2C; the area ratio of apical to basal cell is 1.05 ± 0.08, $n = 20$).

3.3. Anaphase spindle elongation compensates the original asymmetric spindle positioning

How could apparent asymmetric spindle positioning end up with equal sized daughter cells? The best way to answer this question is to monitor the detailed process of cell division in our system. We then generated double stable cell lines by introducing mCherry-α-tubulin into Crb3-Venus-Gαi1 cell line, so we can monitor the mitotic spindle movement in live cells. Western blot analysis indicated that mCherry-α-tubulin was expressed at a level that is comparable to endogenous α-tubulin in the cell line we generated (Fig. 3A).

We performed time-lapse analysis of mitotic cells in 3-D cultured cysts. First, we grew Crb3-Venus-Gαi1/mCherry-α-tubulin cells in 3-D culture in the presence of doxycycline to inhibit the ectopic expression of Crb3-Venus-Gαi1. The cells propagated nicely into single-lumened cysts, just like control MDCK cells (data not shown). Live cell analysis confirmed previous results that the mitotic spindle aligned predominantly perpendicular to the apical basal axis of the cell [20]. Although slight oscillation of the spindle axis was observed, the cell eventually divided along the planar axis. During anaphase when spindle elongation occurs, the two spindle poles move at similar speed towards the lateral cell cortex (Fig. 3B, Movie 1). Next, we grew Crb3-Venus-Gαi1/mCherry-α-tubulin cells in 3-D culture in the absence of doxycycline to allow the expression of Crb3-Venus-Gαi1. Not surprisingly, the mitotic spindle rotated from perpendicular to parallel to the apical basal axis of the cell, and always positioned asymmetrically towards apically localized Crb3-Venus-Gαi1 (Fig. 3C). When the cells entered anaphase, apical and basal spindle elongated at similar speed. Strikingly, accompanying spindle elongation, the basal spindle pole appeared to be pushed towards the basal cortex while the apical spindle pole did not show apparent movement (Fig. 3C, Movie 2). When the basal spindle pole almost reached the cell cortex, cleavage furrow started to form in the middle of the cell and eventually led to the production of equal sized daughter cells (Fig. 3C, Movie 2). Such pattern of spindle pole movement was observed in multiple cells and quantitation of the distance from spindle poles to cell cortex at different time points revealed that the basal spindle pole was initially far away from the basal cortex, and this distance was consistent through metaphase; when cell entered anaphase, this distance was shortened gradually until it was close to that of from apical spindle pole to the apical cell cortex (Fig. 3D). We conclude that anaphase spindle elongation compensates the original asymmetric spindle positioning in our system.

4. Discussion

Mechanisms of asymmetric spindle positioning and cell division have been intensely studied in the *C. elegans* zygote and *Drosophila* neuroblast [1,3,22]. Although most of the identified molecules that are involved in the regulation of asymmetric cell division are conserved in the two systems, there are obvious differences between the two types of cells in the ways of producing unequal sized daughter cells. In *Drosophila* neuroblast, asymmetric cell division involves differential spindle length regulation – the apical spindle is longer than the basal spindle during anaphase [13]. It also involves asymmetric spindle positioning – the spindle is positioned closer to the basal cell cortex, probably due to asymmetric astral microtubule nucleation [10]. Such asymmetry in spindle length and overall spindle positioning leads to the asymmetric cleavage and appears to rely on redundant Par3/Insc and Pins/Gα pathways [10,12]. In *C. elegans* zygote, right after metaphase onset, a so-called spindle displacement, featured by the movement of the entire spindle towards the posterior cell cortex in a Gα/GPR-1,2 dependent manner, results in the asymmetric positioning of the spindle and subsequent asymmetric cleavage of the zygote [22]. No obvious difference in terms of the anterior and posterior spindle length is observed, although the length difference between anterior and posterior astral microtubules is apparent [23].

In mammalian system, the Gα/LGN complex is also required for directing spindle orientation during asymmetric cell division of neuronal and epidermal progenitor cells [16–18]. However, asymmetric spindle positioning and asymmetric cleavage of the mother cell have not been reported in both systems, probably due to technical difficulties for *in vivo* analysis in mammals. So far, there is no mammalian system that can consistently produce asymmetric spindle positioning without compromising normal spindle organization and subsequent cell division. We have now, for the first time, established such a system. Artificially targeting of Gαi1 to the apical cell membrane led to apical recruitment of endogenous LGN, which mimics the asymmetric localization of this protein complex in *Drosophila* neuroblast and *C. elegans* zygote. Indeed, apically localized Gαi1/LGN can redirect spindle orientation from perpendicular to parallel to the apical-basal axis during cystogenesis, suggesting a conserved function for this complex in directing spindle orientation. Intriguingly, asymmetric localization of Gαi1/LGN complex also leads to asymmetric spindle positioning within the cell – the spindle is always positioned towards the apical cell cortex, which is similar to the spindle displacement in *C. elegans* zygote. Unexpectedly, however, Gαi1/LGN-mediated asymmetric spindle positioning in our system does not lead to asymmetric cleavage of the mother cell; instead, it generates two equal sized daughter cells. Careful time-lapse analysis revealed that anaphase spindle elongation gradually compensates the initial asymmetric localization of the metaphase spindle.

We believe that our system is different from *Drosophila* neuroblast, although the role of asymmetrically localized Gαi1/LGN in directing spindle orientation is conserved. First, we did not observe differential spindle lengthening in our system either during metaphase or anaphase. Second, we did not see the robust apical astral microtubule nucleation as observed in anaphase neuroblast. In *Drosophila* neuroblast, the asymmetric spindle lengthening and astral microtubule nucleation is regulated by redundant Gα/Pins and Par3/Insc pathways [12]. In our system, Insc may not be expressed (data not shown); and Par3 also localizes differently – at tight junctions rather than at the apical membrane. Par3 and Insc may modulate the interaction between Pins and other proteins [24] which may contribute to spindle length regulation. Alternatively, in our system, Gαi1 is fused with Crb3-Venus which may interfere with the normal signaling property of Gαi1 that is required for spindle

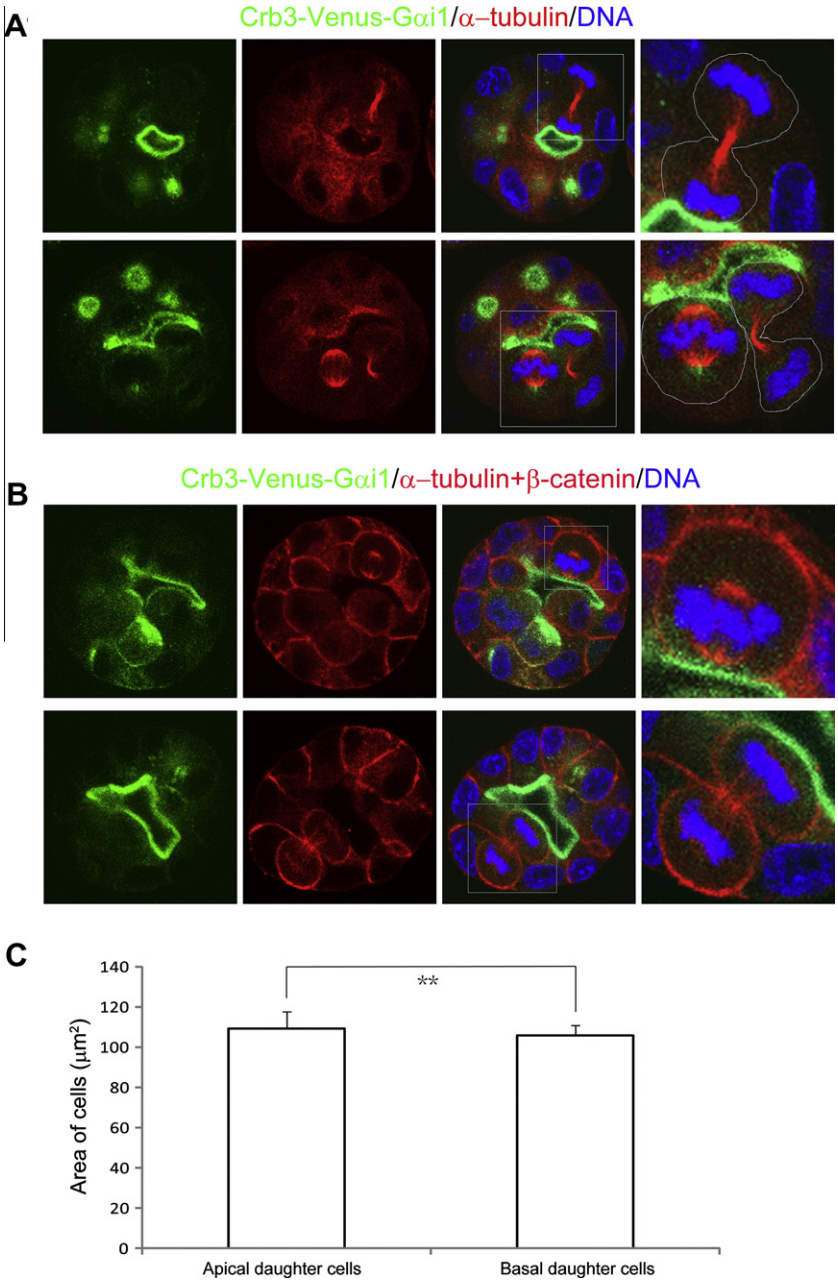


Fig. 2. Asymmetric spindle positioning does not lead to the production of unequally sized daughter cells. (A), (B) Stable Tet-Off MDCK cells expressing Crb3-Venus-Gα1 were cultured in the absence of doxycycline in matrigel for 3 days to allow 3-D cystogenesis. Cysts were fixed and stained with anti-α-tubulin antibody (A, red) or anti-α-tubulin plus anti-β-catenin antibodies (B, red). DNA was stained with Hoechst 33342. Single confocal images were shown, white lines were drawn to outline the mitotic cell in A. (C) Quantitation of daughter cell area. $^{**}P > 0.5$.

length control or astral microtubule nucleation. It is also possible that some basally localized proteins, which are absent in our system, are involved in shortening the basal spindle in neuroblast. Further studies are needed to distinguish these possibilities.

Our system is more like *C. elegans* zygote where mitotic spindle is displaced towards asymmetrically localized Gα/GPR-1,2. One obvious difference, however, is that *C. elegans* zygote is almost 3 times larger than MDCK cells. Such size provides more than enough space for anaphase spindle elongation in *C. elegans*, and the two spindle poles are far away from the cell cortex when cytokinesis is initiated. In most mammalian cells, especially for those that round up during mitosis, anaphase spindle elongation pushes the spindle poles towards the cell cortex and the maximum spindle length is almost equal to the length of the cell body. We speculate that if the mitotic cells in our system were larger than the maximum length of the anaphase spindle, we would predict asymmetric cleavage and the production of unequal sized daughter cells, as the central spindle, which plays a dominant role in dictating cleavage furrow formation in mammalian cells, would still be eccentrically positioned when cleavage furrow starts to form.

Our study also suggests that the timing of cleavage furrow formation must be tightly regulated in our system – the cleavage furrow starts to form only when the basal spindle pole has moved to be close enough to the basal cell cortex. If the cleavage furrow started to form before the basal spindle pole reached the cell cortex, it might also end up with asymmetric cleavage. Such timing may involve the interaction between astral microtubules and cortical cues.

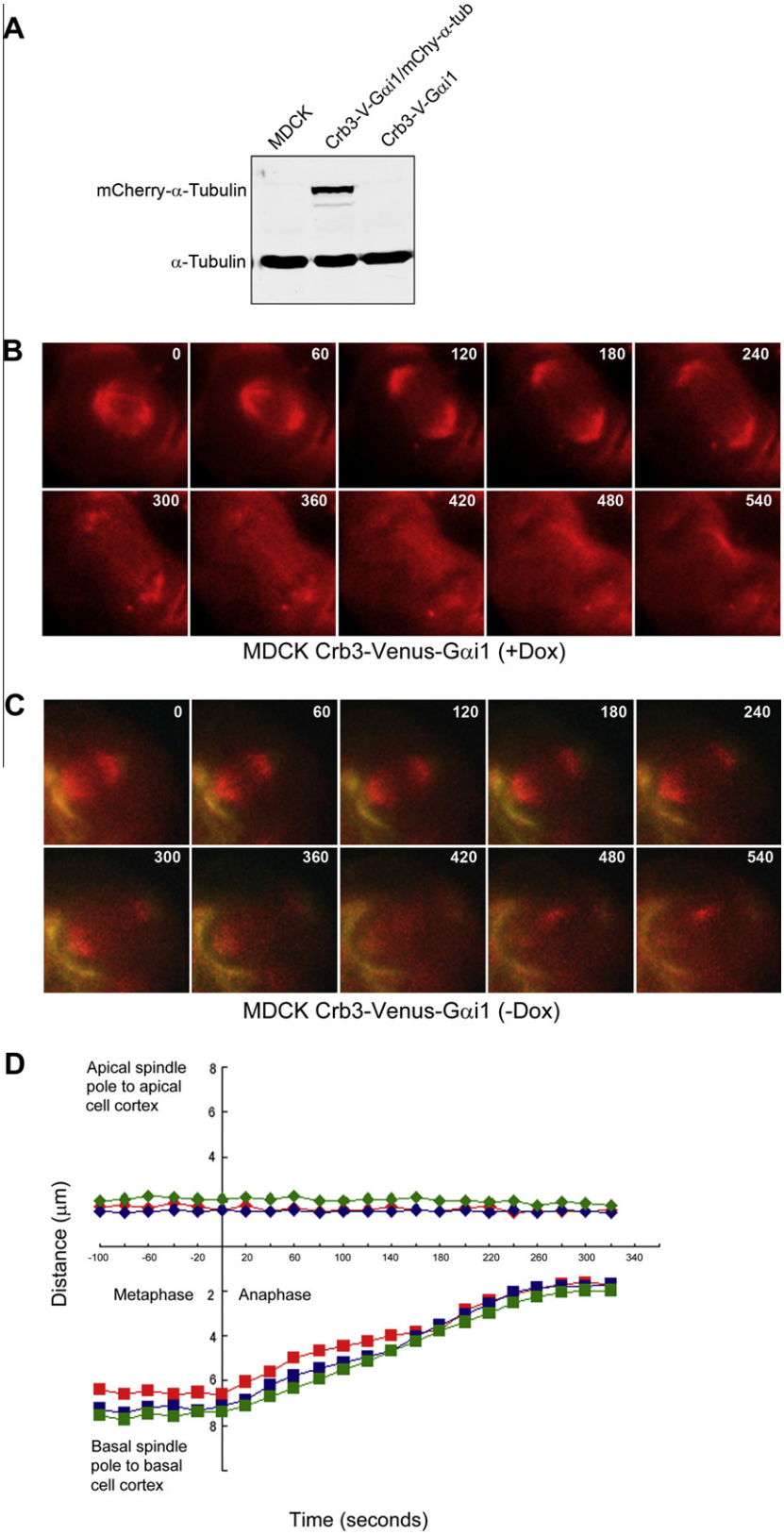


Fig. 3. Timelapse analysis of spindle movement in 3-D cultured cysts. (A). Western blot analysis of mCherry-α-tubulin expression. Equal amounts of cell lysates from parental MDCK T23, MDCK T23 Crb3-Venus-Gαi1 and MDCK T23 Crb3-Venus-Gαi1/mCherry-α-tubulin cells were subjected to western blot analysis using anti-α-tubulin antibody. (B). Fluorescent images from time-lapse analysis of mitotic Crb3-Venus-Gαi1/mCherry-α-tubulin cell in 3-D cyst in the presence of doxycycline. Time points are shown as seconds. (C). Fluorescent images from time-lapse analysis of mitotic Crb3-Venus-Gαi1/mCherry-α-tubulin cell in 3-D cyst in the absence of doxycycline. Time points are shown as seconds. (D). Quantitative analysis of fluorescent images in C. Distances from apical spindle pole to the apical cortex and distances from basal spindle pole to basal cortex were measured at different time points during cell division. Results from three different cells are marked by different colors.

Taken together, we propose that the lack of differential spindle lengthening, the limited size of the mother cell and the regulated timing of cleavage furrow formation may underlie the eventual symmetric cleavage and the generation of equal sized daughter cells in our system, although the metaphase spindle was initially asymmetrically positioned. Our study suggests that asymmetric spindle positioning does not necessary lead to the production of unequal sized daughter cells.

Acknowledgments

We thank Dr. Daniel Gerlich for providing the pmCherry-α-tubulin-IRES-puro2 plasmid. This work was supported by grants from National Institutes of Health (GM079506) and American Cancer Society (RSG0717601CSM) to Q. Du.

Appendix A. Supplementary data

Supplementary data associated with this article can be found, in the online version, at doi:10.1016/j.bbrc.2012.03.095.

References

[1] K.H. Siller, C.Q. Doe, Spindle orientation during asymmetric cell division, Nat. Cell Biol. 11 (2009) 365–374.
[2] M. Glotzer, Cleavage furrow positioning, J. Cell Biol. 164 (2004) 347–351.
[3] E.K. McCarthy, B. Goldstein, Asymmetric spindle positioning, Curr. Opin. Cell Biol. 18 (2006) 79–85.
[4] R. Rappaport, Repeated furrow formation from a single mitotic apparatus in cylindrical sand dollar eggs, J. Exp. Zool. 234 (1985) 167–171.
[5] P. Gonczy, Mechanisms of spindle positioning: focus on flies and worms, Trends Cell Biol. 12 (2002) 332–339.
[6] Y. Bellaiche, M. Gotta, Heterotrimeric G proteins and regulation of size asymmetry during cell division, Curr. Opin. Cell Biol. 17 (2005) 658–663.
[7] S.W. Grill, J. Howard, E. Schaffer, E.H. Stelzer, A.A. Hyman, The distribution of active force generators controls mitotic spindle position, Science 301 (2003) 518–521.
[8] T. Nguyen-Ngoc, K. Afshar, P. Gonczy, Coupling of cortical dynein and G alpha proteins mediates spindle positioning in *Caenorhabditis elegans*, Nat. Cell Biol. 9 (2007) 1294–1302.
[9] C. Couwenbergs, J.C. Labbe, M. Goulding, T. Marty, B. Bowerman, M. Gotta, Heterotrimeric G protein signaling functions with dynein to promote spindle positioning in *C. elegans*, J. Cell Biol. 179 (2007) 15–22.
[10] Y. Cai, F. Yu, S. Lin, W. Chia, X. Yang, Apical complex genes control mitotic spindle geometry and relative size of daughter cells in *Drosophila* neuroblast and pI asymmetric divisions, Cell 112 (2003) 51–62.
[11] N. Fuse, K. Hisata, A.L. Katzen, F. Matsuzaki, Heterotrimeric G proteins regulate daughter cell size asymmetry in *Drosophila* neuroblast divisions, Curr. Biol. 13 (2003) 947–954.
[12] Y. Izumi, N. Ohta, A. Itoh-Furuya, N. Fuse, F. Matsuzaki, Differential functions of G protein and Baz-aPKC signaling pathways in *Drosophila* neuroblast asymmetric division, J. Cell Biol. 164 (2004) 729–738.
[13] J.A. Kaltschmidt, C.M. Davidson, N.H. Brown, A.H. Brand, Rotation and asymmetry of the mitotic spindle direct asymmetric cell division in the developing central nervous system, Nat. Cell Biol. 2 (2000) 7–12.
[14] R. Ben-Yair, N. Kahane, C. Kalcheim, LGN-dependent orientation of cell divisions in the dermomyotome controls lineage segregation into muscle and dermis, Development 138 (2011) 4155–4166.
[15] Q. Du, I.G. Macara, Mammalian Pins is a conformational switch that links NuMA to heterotrimeric G proteins, Cell 119 (2004) 503–516.
[16] D. Konno, G. Shioi, A. Shitamukai, A. Mori, H. Kiyonari, T. Miyata, F. Matsuzaki, Neuroepithelial progenitors undergo LGN-dependent planar divisions to maintain self-renewability during mammalian neurogenesis, Nat. Cell Biol. 10 (2008) 93–101.
[17] T. Lechler, E. Fuchs, Asymmetric cell divisions promote stratification and differentiation of mammalian skin, Nature 437 (2005) 275–280.
[18] E. Peyre, F. Jaouen, M. Saadaoui, L. Haren, A. Merdes, P. Durbec, X. Morin, A lateral belt of cortical LGN and NuMA guides mitotic spindle movements and planar division in neuroepithelial cells, J. Cell Biol. 193 (2011) 141–154.
[19] S.E. Williams, S. Beronja, H.A. Pasolli, E. Fuchs, Asymmetric cell divisions promote notch-dependent epidermal differentiation, Nature 470 (2011) 353–358.
[20] Z. Zheng, H. Zhu, Q. Wan, J. Liu, Z. Xiao, D.P. Siderovski, Q. Du, LGN regulates mitotic spindle orientation during epithelial morphogenesis, J. Cell Biol. 189 (2010) 275–288.
[21] Y. Hao, Q. Du, X. Chen, Z. Zheng, J.L. Balsbaugh, S. Maitra, J. Shabanowitz, D.F. Hunt, I.G. Macara, Par3 controls epithelial spindle orientation by aPKC-mediated phosphorylation of apical Pins, Curr. Biol. 20 (2010) 1809–1818.
[22] M. Galli, S. van den Heuvel, Determination of the cleavage plane in early *C. elegans* embryos, Annu. Rev. Genet. 42 (2008) 389–411.
[23] C.R. Cowan, A.A. Hyman, Asymmetric cell division in *C. elegans*: cortical polarity and spindle positioning, Annu. Rev. Cell Dev. Biol. 20 (2004) 427–453.
[24] J. Zhu, W. Wen, Z. Zheng, Y. Shang, Z. Wei, Z. Xiao, Z. Pan, Q. Du, W. Wang, M. Zhang, LGN/mInsc and LGN/NuMA complex structures suggest distinct functions in asymmetric cell division for the Par3/mInsc/LGN and Galphai/LGN/NuMA pathways, Mol. Cell 43 (2011) 418–431.

Biochemical and Biophysical Research Communications 420 (2012) 895–900

Contents lists available at SciVerse ScienceDirect

Biochemical and Biophysical Research Communications

journal homepage: www.elsevier.com/locate/ybbrc

Identification of distinct physiochemical properties of toxic prefibrillar species formed by Aβ peptide variants

Anna-Lena Göransson [a], K. Peter R. Nilsson [b], Katarina Kågedal [c], Ann-Christin Brorsson [a,*]

[a] Division of Molecular Biotechnology, Department of Physics, Chemistry and Biology, Linköping University, Sweden
[b] Division of Organic Chemistry, Department of Physics, Chemistry and Biology, Linköping University, Sweden
[c] Department of Clinical and Experimental Medicine, Linköping University, Sweden

ARTICLE INFO

Article history:
Received 13 March 2012
Available online 27 March 2012

Keywords:
Alzheimer's disease
Amyloid-β peptide
Fluorescence spectroscopy
Cell toxicity
Protein aggregation

ABSTRACT

The formation of amyloid-β peptide (Aβ) aggregates at an early stage during the self-assembly process is an important factor in the development of Alzheimer's disease. The toxic effect is believed to be exerted by prefibrillar species of Aβ. It is therefore important to identify which prefibrillar species are toxic and characterize their distinct properties. In the present study, we investigated the *in vitro* aggregation behavior of Aβ-derived peptides possessing different levels of neurotoxic activity, using fluorescence spectroscopy in combination with transmission electron microscopy. The toxicity of various Aβ aggregates was assessed by using cultures of human neuroblastoma cells. Through combined use of the fluorescence probe 8-anilino-1-napthalenesulfonate (ANS) and the novel luminescent probe pentamer formyl thiophene acetic acid (p-FTAA), we were able to identify those Aβ peptide-derived prefibrillar species which exhibited cellular toxicity. In particular, species, which formed early during the aggregation process and showed strong p-FTAA and ANS fluorescence, were the species that possessed toxic activities. Moreover, by manipulating the aggregation conditions, it was possible to change the capacity of the Aβ peptide to form nontoxic versus toxic species.

© 2012 Elsevier Inc. All rights reserved.

1. Introduction

Misfolded proteins are involved in several diseases, e.g., Huntington's disease, Parkinson's disease, Creutzfeldt–Jakob disease and Alzheimer's disease (AD) [1]. These disorders are associated with the presence of protein deposits comprising amyloid fibrils. It is important to increase our understanding of the molecular processes involved in misfolding and aggregation of proteins in order to understand how these events are connected to the pathogenesis of diseases. The aggregation of the Aβ peptide into plaques has long been considered the key neuropathological hallmark of AD [2]. Aβ peptides are produced in the brain by proteolytic cleavage of the amyloid precursor protein (APP) by β- and γ-secretases [3]. Depending on the site of cleavage, different sized Aβ peptides are generated, with $Aβ_{40}$ and $Aβ_{42}$ being the most commonly occurring Aβ isoforms. $Aβ_{42}$ has a higher propensity to form prefibrillar and fibrillar aggregates than $Aβ_{40}$ and has also been reported to be more toxic [4]. Furthermore, it has been shown that an increased ratio of $Aβ_{42}$ to $Aβ_{40}$ correlates with an increased risk of subsequently developing AD [5]. Monomeric Aβ aggregates into insoluble fibrils via different soluble intermediates [6]. To date, the main consensus is that early formed oligomeric intermediates (prefibrillar species) are the critical entities which cause cellular damage, and they may be the key effectors of pathogenicity in AD [7]. Thus, it is important to identify which prefibrillar species are directly involved in cellular damage and determine their distinct biophysical properties.

Like many of the diseases associated with misfolded proteins, AD has both sporadic and inherited forms. One example of familial AD is the mutation E22G of $Aβ_{42}$ (also known as the Arctic mutation), which causes early onset of the disease [8]. The Arctic mutation accelerates the protein aggregation process and, in particular, accelerates the formation of prefibrillar species [8], further supporting the notion that these early formed prefibrillar species exert the neurotoxic activity. In recent studies, we have shown that the Arctic peptide is more neurotoxic than $Aβ_{42}$ when expressed in the central nervous system of *Drosophila melanogaster* [4,9]. It was also found that a single-point mutation, I31E, introduced into the Arctic

Abbreviations: AD, Alzheimer's disease; Aβ, amyloid-β peptide; APP, amyloid precursor protein; TEM, transmission electron microscopy; ANS, 8-anilino-1-napthalensulfonate; ThT, thioflavin T; p-FTAA, pentamer formyl thiophene acetic acid; $pFTAA^+$ species, species recognized by pFTAA; ThT^+ species, species recognized by ThT.

* Corresponding author. Address: Division of Molecular Biotechnology, Department of Physics, Chemistry and Biology, Linköping University, SE-581 83 Linköping, Sweden. Fax: +46 13 281399.

E-mail addresses: anngo@ifm.liu.se (A.-L. Göransson), petni@ifm.liu.se (K. Peter R. Nilsson), katarina.kagedal@liu.se (K. Kågedal), anki@ifm.liu.se (A.-C. Brorsson).

0006-291X/$ - see front matter © 2012 Elsevier Inc. All rights reserved.
http://dx.doi.org/10.1016/j.bbrc.2012.03.097

peptide (henceforth denoted the Rescue variant), abolishes the pathogenicity by significantly reducing the propensity to form prefibrillar aggregates.

In the present study, we investigated how differences in toxic behavior between $A\beta_{42}$, Arctic ($A\beta_{42}$ E22G) and Rescue ($A\beta_{42}$ E22G/I31E) related to the propensity of these peptides to form different protein aggregates by characterizing the *in vitro* aggregation behavior of these variants using fluorescent probes and fluorescence spectroscopy in combination with cell toxicity studies and transmission electron microscopy (TEM). The formation of amyloid fibrils was essentially probed by thioflavin T (ThT) fluorescence [10], and the hydrophobic properties of aggregated species were investigated using ANS fluorescence [11]. A novel luminescent probe, p-FTAA, was used to identify species which were not efficiently recognized by ThT, since it has been shown earlier that p-FTAA is a useful probe for detecting prefibrillar non-thioflavinophilic protein aggregates [12]. The aim was to carefully decipher the biophysical properties of aggregated species generated by the three selected peptides and identify the prefibrillar structures that are associated with neurodegeneration.

2. Materials and methods

2.1. Preparation of the Aβ peptides

Synthetic $A\beta_{42}$, $A\beta_{42}$ E22G and $A\beta_{42}$ E22G/I31E (Bachem, Weil am Rhein, Germany) were dissolved in trifluoroacetic acid and sonicated on ice for 20 s. The trifluoroacetic acid was removed by lyophilization, the peptide was dissolved in 1,1,1,3,3,3-hexafluoro-2-propanol and then divided into aliquots. The 1,1,1,3,3,3-hexafluoro-2-propanol was removed by rotary evaporation at room temperature, and the quantity of peptide in the aliquots was determined with the Bradford *DC* protein Assay (Bio-Rad Laboratories, Hemel Hempstead, UK).

2.2. Fluorescence measurements

Aβ samples were dissolved to a concentration of 20 μM ($A\beta_{42}$) or 30 μM ($A\beta_{42}$ E22G and $A\beta_{42}$ E22G/I31E) in 50 mM Na_2PO_4 (pH 7.4). The fluorescence probes ThT, p-FTAA and ANS were used at concentrations of 0.2 μM (p-FTAA), 0.5 μM (ThT), 100 μM (ANS-measurements of $A\beta_{42}$) and 50 μM (ANS-measurements of $A\beta_{42}$ E22G and $A\beta_{42}$ E22G/I31E). Samples were incubated under quiescent conditions at 37 °C in a Tecan Safire 2 plate reader. Peptide solutions of $A\beta_{42}$ E22G and $A\beta_{42}$ E22G/I31E, with a concentration of 20 μM, were also incubated at 30 °C under shaking conditions. Fluorescence intensities were recorded by excitation at 375 nm (ANS) or 440 nm (ThT and p-FTAA), and emission spectra were recorded between 470 and 550 nm. The fluorescence profile data presented were obtained from selected curves, representing at least three replicates.

2.3. Transmission electron microscopy

Carbon-coated nickel grids were charged with UV light for 5 min. Ten microliters of the peptide sample was dispensed onto the grid. After 2 min, the liquid was removed by blotting with a filter paper. The grid was washed with two aliquots of 10 μl dH_2O. Staining was performed using 10 μl 2% uranyl-acetate for 2 min, and then the grid was blotted dry. The dry grid was stored in a grid box until it was viewed with a JEOL 1230 TEM (Jeol Ltd.; Tokyo, Japan) equipped with an ORIUS SC 1000 CCD camera.

2.4. Cell culture and viability measurement

Aβ samples were dissolved to a concentration of 30 μM in 50 mM Na_2PO_4 (pH 7.4) and incubated at 37 °C. Human SH-SY5Y neuroblastoma cells were cultured in Minimum Essential Medium (MEM) Glutamax (Invitrogen, Paisley, UK), which was supplemented with 10% calf serum (PAA Laboratories, Pasching, Austria), 2 mM glutamine, 50 IU/ml penicillin-G and 50 mg/ml streptomycin (Lonza, Bazel, Switzerland). Prior to experiments, the cells were differentiated by treating them with 10 μM retinoic acid (Sigma Aldrich, St. Louis, MO, USA) for 7 days. The cells were trypsinized and seeded in culture plates at a density of 90,000 cells/cm^2 and subsequently exposed to 3 μM Aβ in serum-free medium for 6 days. After treatment, cell cultures were morphologically examined in a phase contrast microscope and viability was measured using XTT (Roch, Germany) according to instructions from the company.

2.5. Statistical analysis

Statistical significance was determined using the Kruskal–Wallis multiple comparison test followed by the Mann–Whitney *U*-test. Differences were considered significant when $p \leqslant 0.005$.

3. Results and discussion

3.1. Aggregation of $A\beta_{42}$

We first examined fibril formation of $A\beta_{42}$ to compare the aggregation behavior of this peptide with the more toxic Arctic variant and the essentially nontoxic Rescue variant [9]. Fig. 1A shows the aggregation of the $A\beta_{42}$ peptide probed by ThT, p-FTAA and ANS fluorescence under quiescent incubation. At the start of the aggregation process, species were formed that were recognized by all three probes. Comparison of the p-FTAA and ThT fluorescence profiles showed that the p-FTAA signal increased more rapidly than the ThT signal and reached a maximum value after 5 h followed by a slow decrease. In contrast, the ThT fluorescence signal increased continuously throughout the experiment. These observations suggest that efficient fluorescence from p-FTAA or ThT were achieved when different aggregated Aβ species were present during the aggregation process. Initially, one type of species which gave rise to strong emission from p-FTAA (these species are henceforth denoted p-$FTAA^+$) formed rapidly, giving rise to a rapid increase in the p-FTAA signal. Another type of species which yielded strong ThT fluorescence (these species are henceforth denoted ThT^+) formed more slowly as shown by the gradual increase in the ThT signal. TEM images at the end of the aggregation experiment confirmed fibril formation in the presence of both probes (Fig. 1B and C). Indeed, the morphologies of the fibrils formed in the presence of ThT and p-FTAA were very similar, comprising predominantly of twisted fibrils of μm length scale. The results suggest that the p-FTAA fluorescence curve initially reflects the rapid formation of p-$FTAA^+$ prefibrillar species, which are later converted to mature twisted ThT^+ fibrils, as reflected by the steady decrease in the p-FTAA fluorescence and increase in the ThT fluorescence observed after 5 h and during the remaining timepoints in the experiment. In agreement with the p-FTAA fluorescence profile, a rapid increase in the ANS fluorescence signals was also observed, indicating that the p-$FTAA^+$ species formed had exposed hydrophobic surfaces. TEM images recorded during this increase revealed a mixture of globular structures (Fig. 1D, black arrow), filaments of various lengths and long fibrils (Fig. 1D, dashed black arrow and white arrow, respectively). After 5 h, when the p-FTAA fluorescence had started to decrease, the ANS signal continued to show a small and steady increase during the remaining time of the

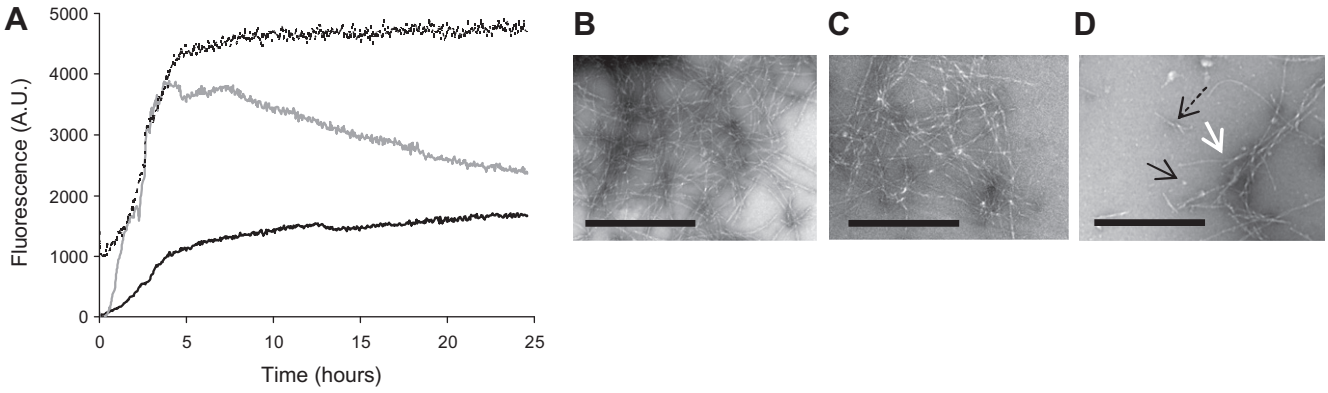


Fig. 1. Aggregation of $A\beta_{42}$ under quiescent incubation probed by ThT, p-FTAA and ANS fluorescence in combination with TEM. The progression of the aggregation probed by ThT (black line), p-FTAA (gray line) and ANS (dotted line) (A). TEM images of peptide samples taken at the end of the aggregation experiments in the presence of ThT (B) and p-FTAA (C). TEM image of peptide sample incubated without probes after 2.5 h (D). Black arrow indicates globular structures, dashed black arrow indicates filaments and white arrow indicates fibrils. Scale bar = 500 nm.

experiment, in agreement with the ThT fluorescence profile. Thus, both the p-FTAA$^+$ prefibrillar species, which formed at the start of aggregation, and the mature ThT$^+$ fibrils, which accumulated by the end of the experiment, had exposed hydrophobic surfaces.

3.2. Characterization of the aggregation process for Arctic and Rescue under quiescent conditions

When probing the aggregation process of Arctic using ThT, p-FTAA and ANS, a fluorescence signal from both ANS and p-FTAA was already observed at the start of the experiment, indicating that p-FTAA$^+$ hydrophobic prefibrillar species appeared immediately after dissolving the peptide in the buffer (Fig. 2A). During the aggregation process, the p-FTAA signal reached a maximum value at 15 h, followed by a gradual decrease, whereas the ANS signal increased in parallel to the p-FTAA signal for the first 15 h and then continued to increase during the remainder of the experiment. The ThT fluorescence signal gradually increased from the start of aggregation to the end of the experiment. Overall, the Arctic fluorescence profiles showed similarities to the $A\beta_{42}$ fluorescence profiles, where the early formed p-FTAA$^+$ hydrophobic prefibrillar species were later converted into ThT$^+$ matured amyloid fibrils with exposed hydrophobic surfaces.

The Rescue aggregation profiles, probed by ThT, p-FTAA and ANS showed a lag phase followed by a growth phase ending with a plateau (Fig. 2B). Here, the magnitudes observed for the fluorescence

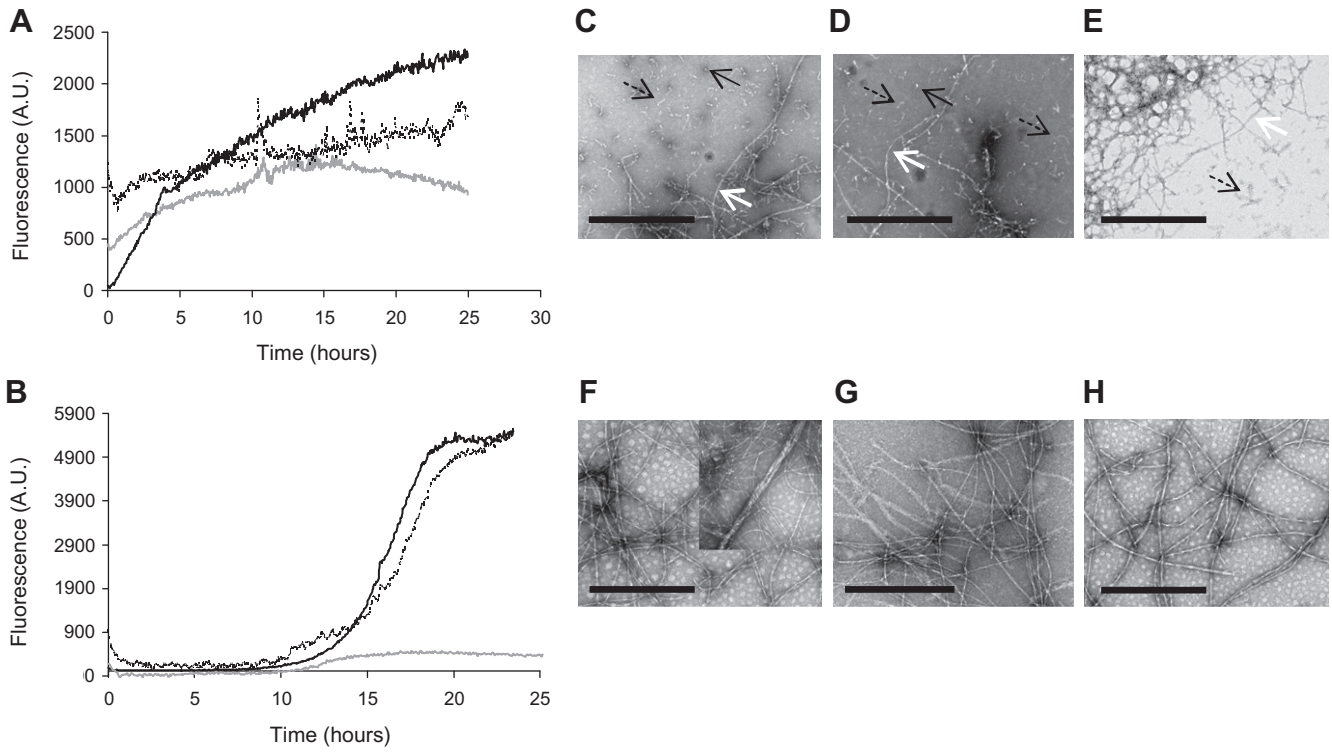


Fig. 2. Aggregation of Arctic and Rescue under quiescent incubation probed by ThT, p-FTAA and ANS fluorescence in combination with TEM. Aggregation of Arctic (A) and Rescue (B) probed by ThT (black line), p-FTAA (gray line) and ANS (dotted line). TEM images recorded at the end of the aggregation experiments of Arctic aggregates in the presence of ThT (C), p-FTAA (D) and ANS (E) and of Rescue aggregates in the presence of ThT (F), p-FTAA (G) and ANS (H). Black arrows indicate globular structures, dashed black arrows indicate short filaments and white arrows indicate long fibrils. Scale bar = 500 nm.

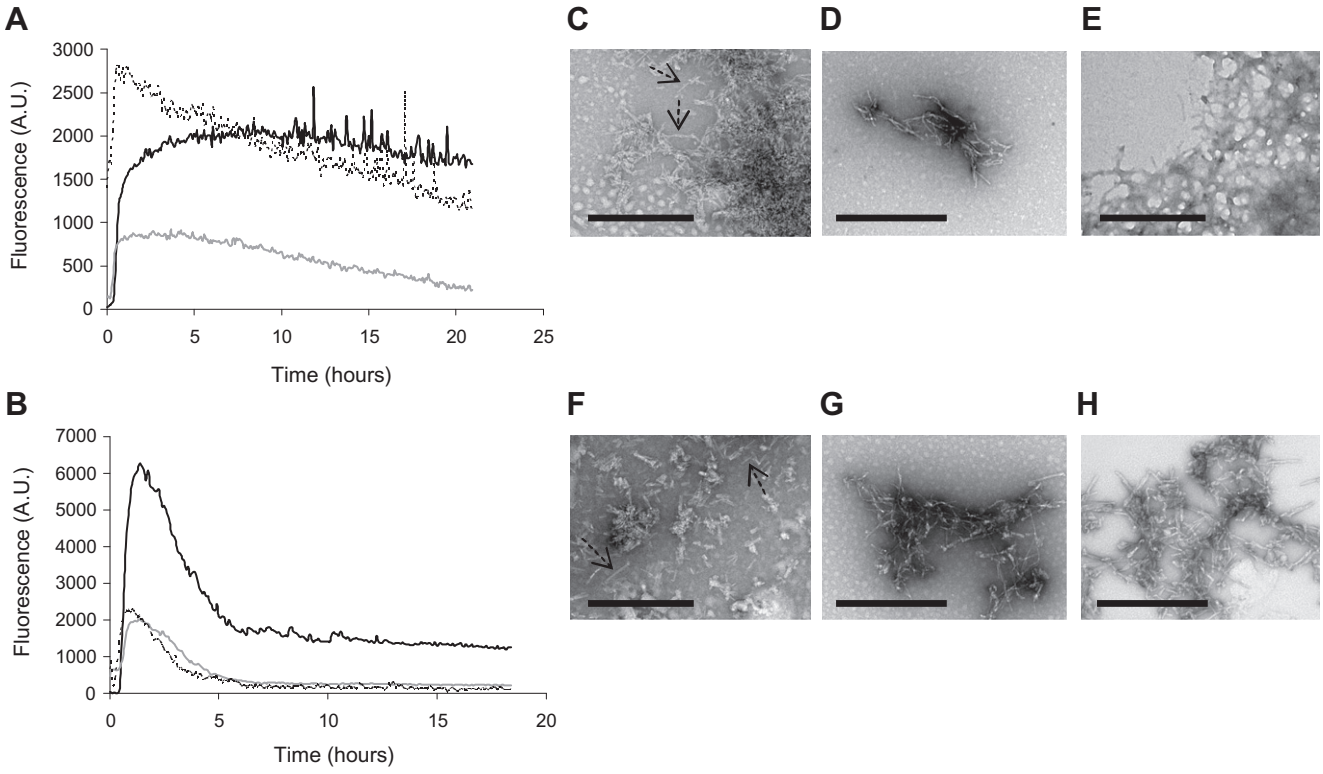


Fig. 3. Aggregation of Arctic and Rescue under shaken conditions probed by ThT, p-FTAA and ANS fluorescence in combination with TEM. Aggregation of Arctic (A) and Rescue (B) probed by ThT (black line), p-FTAA (gray line) and ANS (dotted line). TEM images recorded at the end of the aggregation experiments of Arctic aggregates in the presence of ThT (C), p-FTAA (D) and ANS (E) and of Rescue aggregates in the presence of ThT (F), p-FTAA (G) and ANS (H). Dashed black arrows indicate filaments of various lengths. Scale bar = 500 nm.

signals differed dramatically; the p-FTAA signals were very low compared to the ThT and ANS signals. Apparently, the Rescue peptide is able to form aggregates that give rise to strong ThT and ANS fluorescence but less fluorescence from p-FTAA. The presence of a lag phase in the p-FTAA and ANS profiles of the Rescue peptide implies that if p-FTAA$^+$ hydrophobic prefibrillar species were formed, they must exist at a very low concentration, which, in combination with the late onset of ThT fluorescence, indicates that the initial formation of fibrillar species occurred from a low concentration pool of prefibrillar species. The parallel increase in the ThT and ANS fluorescence profiles demonstrates that the ThT$^+$ species formed had exposed hydrophobic surfaces.

TEM images taken at the end of the aggregation experiments show the morphology of aggregates formed in the presence of ThT, p-FTAA and ANS for both Arctic (Fig. 2C–E) and Rescue (Fig. 2F–H). In line with previous observation [9], a large amount of prefibrillar species were detected for the Arctic peptide, including globular structures (Fig. 2C and D, black arrows) and short curvilinear filaments (Fig. 2C–E, dashed black arrows) together with long fibrils (Fig. 2C–E, white arrows). The large quantity of prefibrillar species accumulated for the Arctic peptide was most likely responsible for the distinct p-FTAA signal intensities found for this peptide. The p-FTAA profile of the Arctic peptide showed that the amount of prefibrillar species reached a maximum at around 15 h, followed by a decrease in the pool of prefibrillar species, of which a fraction was converted into more mature fibrils. The residual p-FTAA fluorescence observed at later times was most probably due to the remaining prefibrillar species, which can be seen in the TEM image (Fig. 2D). The observed fibrils gave rise to the ThT signal, which increased over time in the Arctic ThT profile (Fig. 2A and C). In contrast to the Arctic peptide, the Rescue peptide only gave an accumulation of mature fibrils with a twisted appearance (Fig. 2F–H), which were able to form intertwined structures composed of several fibrils (Fig. 2F, inset), and no prefibrillar species were observed in the samples. The absence of prefibrillar species in the TEM images supports the fluorescence data, where no p-FTAA$^+$ prefibrillar species were detected. As for $A\beta_{42}$ and Arctic, the mature Rescue fibrils were well recognized by ThT and ANS (Fig. 3B, F and H).

3.3. Characterization of the aggregation process for Arctic and Rescue under shaken conditions

Stirring and shaking protein samples during aggregation can affect amyloid fibril formation and change the properties of the resulting aggregated species [13]. Therefore, we next examined the aggregation properties of Arctic and Rescue under conditions in which the samples were shaken. At the start of the aggregation process for the Arctic peptide, species were formed which were recognized by ThT, p-FTAA and ANS (Fig. 3A), reflecting the formation of ThT$^+$ and p-FTAA$^+$ aggregates with exposed hydrophobic patches. After reaching a maximum fluorescence value after only 30 min, both the p-FTAA and ANS signals then declined during the remaining timepoints. The maximum fluorescence value of the ThT signal was reached after around 5 h and then remained fairly constant during the remainder of the experiment. These data indicate rapid formation of p-FTAA$^+$ hydrophobic prefibrillar species, which are later converted to ThT$^+$ species with exposed hydrophobic surfaces as revealed by the significant ANS signal at the end of the experiment.

A TEM image recorded at the end of the aggregation experiment shows the accumulation of filaments with various lengths (Fig. 3C, dashed black arrows) along with more amorphous assemblies in the presence of ThT. A TEM image of accumulated aggregates at

the end of the experiment in the presence of p-FTAA shows the presence of short filaments, which were stacked together (Fig. 3D). These species showed no increase in fluorescence from p-FTAA since the p-FTAA signal obtained at the end of the experiment was relatively low (Fig. 3A). The aggregates that accumulated in the presence of ANS under shaken conditions were rather amorphous (Fig. 3E). The results suggest that these structures contain exposed hydrophobic patches, which allow ANS to bind.

The Rescue peptide initially formed species very rapidly, which were recognized by ThT, p-FTAA and ANS (Fig. 3B). Thus, in contrast to quiescent conditions, the Rescue peptide formed both prefibrillar and fibrillar species under shaken conditions. However, the signals due to all three probes declined very quickly and reached a steady level after about 5 h. At the end of the experiment, only a low signal due to ThT was observed. Thus, the early formed ThT^+ and p-$FTAA^+$ aggregates containing hydrophobic patches were rapidly converted to aggregates that showed no fluorescence from p-FTAA and ANS and only to small extent fluorescence from ThT. A TEM image taken at the end of the aggregation experiment shows the accumulation of short filaments together with more amorphous assemblies in the presence of ThT (Fig. 3F, dashed black arrows). Assemblies accumulated in the presence of p-FTAA consisted of short and thin filaments that were stacked together (Fig. 3G), whereas the filaments accumulated in the presence of ANS were somewhat thicker (Fig. 3H).

3.4. Cell toxicity of aggregated species

To elucidate the toxicity of different aggregated species, their effects on cellular viability were examined. In parallel, the peptide samples were examined by TEM. We found that species that formed immediately after dissolving the Arctic peptide in the buffer (0 h of incubation) decreased cellular viability to about 40% of the control (Fig. 4A and B). A TEM image captured immediately after dissolving the Arctic peptide in the buffer revealed the presence of globular species of different sizes together with larger amorphous aggregates (Fig. 4C, black and dashed white arrows, respectively). After incubation of the peptide for 30 h under quiescent conditions, short curvilinear filaments were found to be the dominant species in the sample (Fig. 4E, dashed black arrows) along with a few more well-defined fibrils (Fig. 4E, white arrow). These species could not be linked to cell toxicity since no significant reduction in cellular viability was detected (Fig. 4A and D).

Surprisingly, we found that the Rescue peptide, which does not exert any significant toxicity when expressed in *Drosophila* [4,9], was able to induce cell death when aggregated under defined conditions. Specifically, aggregates that formed after 1 h under shaken conditions decreased the cellular viability to about 60% of the control (Fig. 4A and F). A TEM image captured after 1 h under shaken conditions reveals the formation of a substantial amount of prefibrillar species, including small globular and thin filamentous structures together with a few fibrils (Fig. 4G, black, dashed black and white arrows, respectively). A TEM image of species formed immediately after dissolving the peptide shows a small amount of tiny globular species and amorphous aggregates (Fig. 4I, black and dashed white arrow, respectively), whereas long mature fibrils were observed after incubation of the peptide for 30 h under quiescent conditions (Fig. 4K). These species could not be linked to cell toxicity since no significant reduction in cellular viability was detected for these samples (Fig. 4A, H and J).

The cell toxicity data clearly reveal that the Rescue peptide is able to form cytotoxic aggregates after 1 h under shaken conditions. Interestingly, the corresponding TEM image at this timepoint shows the presence of a substantial amount of prefibrillar species (Fig. 4G). Moreover the fluorescence profiles for the aggregation

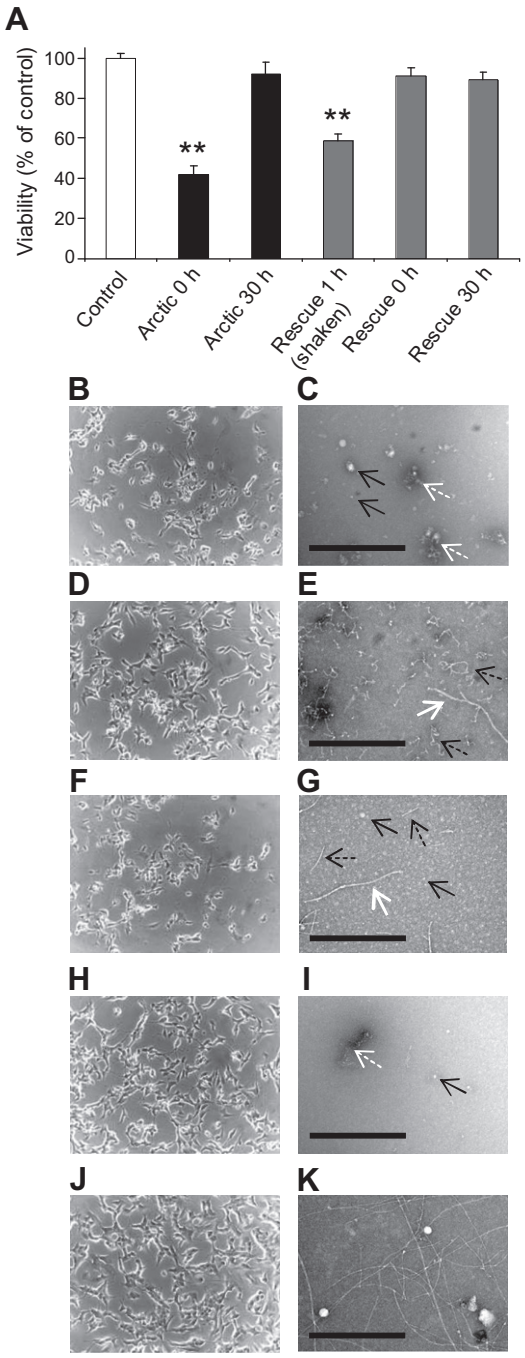


Fig. 4. Cell toxicity and TEM images of different Aβ aggregates. (A) Viability of human SH-SY5Y neuroblastoma cells after exposure to Aβ using the XTT viability assay. Viability is expressed as percentage of untreated cultures (control), $n = 3$. Images of cells after exposure to aggregates of the Arctic peptide formed at 0 h (B) and after 30 h (D) incubation under quiescent conditions. Images of cells after exposure to aggregates of the Rescue peptide formed after 1 h (F) incubation under shaking conditions, and at 0 h (H) and after 30 h (J) incubation under quiescent conditions. TEM images of the Arctic peptide at 0 h (C) and after 30 h (E) incubation under quiescent conditions. TEM images of the Rescue peptide after 1 h (G) incubation under shaking conditions, and at 0 h (I) and after 30 h (K) incubation under quiescent conditions. Black arrows indicate globular species, dashed white arrows indicate amorphous aggregates, dashed black arrows indicate short filaments and white arrows indicate fibrils. Scale bar = 500 nm. Asterisks indicate significant decreased cellular viability. $^{**}p \leqslant 0.005$.

of the Rescue peptide under shaken conditions reveal the presence of early formed species that gave rise to p-FTAA and ANS fluorescence (Fig. 3B). Consequently, the p-$FTAA^+$ hydrophobic prefibrillar

species that were formed under these conditions seem to be responsible for the cell toxicity mediated by the Rescue peptide.

3.5. In vivo and in vitro toxicity directly correlate with distinct physiochemical properties of the prefibrillar species

It is apparent that there is a clear link between neurodegenerative properties of the Aβ peptide in the central nervous system of *Drosophila* and the propensity of the peptide to form prefibrillar assemblies at an early stage of the aggregation process. Importantly, these prefibrillar species are characterized by strong fluorescence from p-FTAA and by having exposed hydrophobic surfaces as probed by ANS. The studied peptides were chosen because they have been shown to have different effects on fly longevity when expressed in the central nervous system of *D. melanogaster* [4,9]. In those studies, it was found that the Arctic peptide causes severe neurodegeneration, which manifested as a 74% reduction in longevity compared to flies expressing the nontoxic $A\beta_{40}$ peptide. The $A\beta_{42}$ peptide reduced the longevity by 36%, whereas no significant signs of neurodegeneration were observed for the Rescue peptide. The results of the present study show that under quiescent conditions, the two neurotoxic Aβ peptides $A\beta_{42}$ and Arctic form p-FTAA$^+$ prefibrillar species with exposed hydrophobic surfaces at the start of the aggregation process. Under these conditions, the nontoxic Rescue peptide did not form prefibrillar species that resulted in fluorescence from p-FTAA or ANS, nor did it form aggregates that could induce cell death. Taken together, these findings strongly suggest that the observed p-FTAA$^+$ hydrophobic prefibrillar species are responsible for the neurotoxic effect of $A\beta_{42}$ and Arctic seen both in the cell- and in the *Drosophila* model. Interestingly, by performing the aggregation of the Rescue peptide under shaken conditions species were formed that gave rise to p-FTAA and ANS fluorescence and were able to induce cell death. Thus, the cell toxicity is clearly dependent on formation of defined p-FTAA$^+$ hydrophobic prefibrillar species. The neurotoxic properties of the Aβ peptide must be linked to the propensity of the peptide to form aggregates that possess certain properties in terms of size and biophysical parameters which are required for cell toxicity. It has previously been suggested that the exposure of hydrophobic surfaces is crucial for the toxicity of protein oligomers and of Aβ aggregates promoting interference of the aggregates with membrane structures [14,15]. Our results strongly support these findings and, in addition, show that p-FTAA can be used to probe early formed prefibrillar species that are linked to cell toxicity.

Acknowledgments

We thank Prof. Bengt-Harald Jonsson for valuable discussions and Mildred Otieno and Daniel Kanmert for technical assistance. This work was supported by the Swedish National Graduate School in Science, Technology and Mathematics Education Research (FontD) (A.-L.G.), the Swedish Alzheimer's Foundation and by Söderberg foundation (A.-C.B.).

References

[1] C.M. Dobson, The structural basis of protein folding and its links with human disease, Philos. Trans. R. Soc. Lond. B Biol. Sci. 356 (2001) 133–145.
[2] J.A. Hardy, G.A. Higgins, Alzheimer's disease: the amyloid cascade hypothesis, Science 256 (1992) 184–185.
[3] M.S. Wolfe, S.Y. Guenette, APP at a glance, J. Cell Sci. 120 (2007) 3157–3161.
[4] L.M. Luheshi, G.G. Tartaglia, A.-C. Brorsson, et al., Systematic *in vivo* analysis of the intrinsic determinants of amyloid β pathogenicity, PLoS Biol. 5 (2007) e290.
[5] S. Kumar-Singh, J. Theuns, B. Van Broeck, et al., Mean age-of-onset of familial Alzheimer disease caused by presenilin mutations correlates with both increased Aβ42 and decreased Aβ40, Hum. Mutat. 27 (2006) 686–695.
[6] D.M. Walsh, A. Lomakin, G.B. Benedek, et al., Amyloid β-protein fibrillogenesis. Detection of a protofibrillar intermediate, J. Biol. Chem. 272 (1997) 22364–22372.
[7] J.P. Cleary, D.M. Walsh, J.J. Hofmeister, et al., Natural oligomers of the amyloid-β protein specifically disrupt cognitive function, Nat. Neurosci. 8 (2005) 79–84.
[8] C. Nilsberth, A. Westlind-Danielsson, C.B. Eckman, et al., The 'Arctic' APP mutation (E693G) causes Alzheimer's disease by enhanced Aβ protofibril formation, Nat. Neurosci. 4 (2001) 887–893.
[9] A.-C. Brorsson, B. Bolognesi, G.G. Tartaglia, et al., Intrinsic determinants of neurotoxic aggregate formation by the amyloid β peptide, Biophys. J. 98 (2010) 1677–1684.
[10] H. LeVine III, W. Ronald, Quantification of β-sheet amyloid fibril structures with thioflavin T, Methods Enzymol. (1999) 274–284.
[11] L. Stryer, The interaction of a naphthalene dye with apomyoglobin and apohemoglobin: a fluorescent probe of non-polar binding sites, J. Mol. Biol. 13 (1965) 482–495.
[12] P. Hammarström, R. Simon, S. Nyström, et al., A fluorescent pentameric thiophene derivative detects *in vitro*-formed prefibrillar protein aggregates, Biochemistry 49 (2010) 6838–6845.
[13] W.-F. Xue, A.L. Hellewell, W.S. Gosal, et al., Fibril fragmentation enhances amyloid cytotoxicity, J. Biol. Chem. 284 (2009) 34272–34282.
[14] B. Bolognesi, J.R. Kumita, T.P. Barros, et al., ANS binding reveals common features of cytotoxic amyloid species, ACS Chem. Biol. 5 (2010) 735–740.
[15] S. Campioni, B. Mannini, M. Zampagni, et al., A causative link between the structure of aberrant protein oligomers and their toxicity, Nat. Chem. Biol. 6 (2010) 140–147.

Biochemical and Biophysical Research Communications 420 (2012) 901–906

Contents lists available at SciVerse ScienceDirect

Biochemical and Biophysical Research Communications

journal homepage: www.elsevier.com/locate/ybbrc

Designation of enzyme activity of glycine-*N*-acyltransferase family genes and depression of glycine-*N*-acyltransferase in human hepatocellular carcinoma

Moe Matsuo [a], Kensuke Terai [b], Noriaki Kameda [b], Aya Matsumoto [a], Yumiko Kurokawa [a], Yuichi Funase [a], Kazuko Nishikawa [c], Naoki Sugaya [a], Nobuyuki Hiruta [b], Toshihiko Kishimoto [a,d,*]

[a] Department of Biomolecular Science, Faculty of Science, Toho University, 2-2-1 Miyama, Funabashi, Chiba 274-8510, Japan
[b] Pathology, Toho University Medical Center, Sakura Hospital, 564-1 Shimo-shizu, Sakura 285-8741, Japan
[c] Sumitomo Electric Industries, Ltd., 1 Taya-cho, Sakae-ku, Yokohama 244-8588, Japan
[d] Proteome Analysis Center, Faculty of Science, Toho University, 2-2-1 Miyama, Funabashi, Chiba 274-8510, Japan

ARTICLE INFO

Article history:
Received 6 March 2012
Available online 27 March 2012

Keywords:
Conjugation
Glycine-*N*-acyltransferase
Glutamine-*N*-acyltransferase
Hepatocellular carcinoma
Human

ABSTRACT

The human glycine-*N*-acyltransferase (hGLYAT) gene and two related-genes (GLYATL1 and GLYATL2) were isolated. Human GLYAT, GLYATL1, and GLYATL2 cDNAs were isolated and shown to encode polypeptides of 295, 302, and 294 amino acids, respectively. GLYAT catalyzes glycine-*N*-acyltransfer reaction with benzoyl-CoA acting as a typical aralkyl transferase, while GLYATL1 catalyzed glutamine-*N*-acyltransfer reaction with phenylacetyl-CoA as an arylacetyl transferase. GLYAT was shown to be expressed specifically in the liver and kidney, and the cellular localization of GLYAT protein was restricted to the mitochondria. Interestingly, labeling using highly affinity purified anti-GLYAT antibody revealed that GLYAT expression was suppressed in all hepatocellular carcinomas, but not in other liver diseases. hGLYAT repression in cancerous cells in the liver was controlled at the transcriptional level. hGLYAT is a good candidate as a novel marker of hepatocellular carcinoma and may be a key molecule in the transition between differentiation and carcinogenesis of liver cells.

© 2012 Elsevier Inc. All rights reserved.

1. Introduction

In mammals, a number of aliphatic and aromatic monocarboxylic acid xenobiotics are conjugated with amino acids, and the resulting peptides appear as excretory products in the urine and bile. This process is physiologically important in detoxification and shows species specificity with respect to both the acyl and amino acid components of peptides. Conjugation involves a two-step pathway, initiated by the activation of carboxylic acid to the coenzyme A thioester by a medium-chain fatty acyl: CoA ligase (adenosine monophosphate; EC 6.2.1.2) [1]. The mitochondrial glycine *N*-acyltransferase (GLYAT, EC 2.3.1.13) then transfers the acyl group to the amino terminus of glycine [1,2]. This enzyme is different from bile acid CoA: amino acid *N*-acyltransferase (EC 2.3.1.65), which conjugates the bile acids with taurine or glycine and is localized in peroxisomes and microsomes [3]. Two distinct GLYATs with different substrate specificities, *i.e.*, aralkyl and arylacetyl, have been isolated and characterized biochemically from cattle's [4], and GLYAT proteins have been biochemically identified from the liver and kidneys of human [5–7], monkey [5], rat [8], and pig [1]. Two bovine GLYAT genes were cloned, and shown to have similar structures [9,10]. Recently, a human GLYAT constitute gene cluster was identified on 11q12.1 containing two homologous genes, GLYATL1 and GLYATL2 [11,12]. GLYATL1 and GLYATL2 were suggested to be localized to the endoplasmic reticulum (ER). However, their functions and biological roles have yet to be investigated in detail.

Sodium benzoate therapy is used to treat congenital hyperamminemias and nonketotic hyperglycinemia [13]. In patients, sodium benzoate is used to divert ammonium nitrogen to hippurate (benzoyl glycine) synthesis and reduce the frequency of hyperammonemic attacks. These investigations suggested that glycine conjugation by GLYAT plays a pivotal role in nitrogen metabolism in the body. Rat HP33, which that was strongly induced in rat hepatocellular carcinoma (HCC), was show to have a high degree of sequence identity to GLYAT [14]. Moreover, human glycine *N*-methyltransferase expression was shown to be reduced in HCC [15]. These studies suggested that GLYAT and GLYAT-related factors may be involved in diseases such as HCC.

In the present study, we isolated and compared the cDNAs of three human GLYAT-related factors, *i.e.*, GLYAT, GLYATL1, and GLYATL2. Our results indicated that GLYAT and GLYATL1 had benzoyl-CoA glycine *N*-acyltransferase and phenylacetyl-CoA glutamine *N*-acyltransferase activities, respectively, while GLYATL2 did not show distinct enzyme activity under our experimental

* Corresponding author at: Department of Biomolecular Science, Faculty of Science, Toho University, 2-2-1 Miyama, Funabashi, Chiba 274-8510, Japan. Fax: +81 47 472 8510.
E-mail address: kisimoto@biomol.sci.toho-u.ac.jp (T. Kishimoto).

0006-291X/$ - see front matter © 2012 Elsevier Inc. All rights reserved.
http://dx.doi.org/10.1016/j.bbrc.2012.03.099

conditions. GLYAT expression was specific for the liver and kidney, and its expression was restricted to the mitochondria. The level of GLYAT expression was markedly reduced in all hepatocellular carcinomas tested. These results indicated that GLYAT plays pivotal roles in xenobiotic metabolism in the mitochondria of liver cells, and that its expression is specifically suppressed in HCC.

2. Materials and methods

2.1. Cloning and expression of genes

Human GLYAT, GLYATL1, and GLYATL2 cDNAs were isolated by PCR from human liver cDNA (Clontech, Palo Alto, CA). All cDNAs were introduced into the pET3a vector (Novagen, San Diego, CA) with a FLAG-6× His tag on their N-termini. Proteins were expressed in *Escherichia coli* BL21 (DE3) pLysS (Stratagene, La Jolla, CA). All transformants were cultured in LB medium containing 100 mg/mL ampicillin and 50 mg/mL chloramphenicol at 37 °C. When the optical density at 600 nm (OD_{600}) reached 0.4, proteins were induced by 0.5 mM IPTG for 90 min, extracted by sonication with three 30-s pulses in lysis buffer (10 mM sodium phosphate, pH 6.0, 10% glycerol, 0.1% Nonidet P40, 0.5 M NaCl, 20 mM 2-mercaptethanol, 1 mM phenylmethylsulfonyl fluoride, one tablet/50 mL Complete™ EDTA-Free; Roche, Basel, Switzerland) on ice, and ultracentrifugation at 30000 rpm (82000*g*) for 30 min at 4 °C using a Beckman Ti 50 angle rotor (Beckman, Fullerton, CA). The supernatants were purified with Ni–NTA agarose (Qiagen, Valencia, CA), and GLYAT was then further purified with anti-FLAG M2 agarose (Sigma, St. Louis. MO). All recombinant proteins were dialyzed against phosphate buffered saline (PBS), and stored at −80 °C. The protein concentration and purity was determined by comparing a known concentration of BSA on SDS–PAGE by staining with Coomassie Brilliant Blue R-250.

2.2. Enzyme assays

Amino acid *N*-acyltransferase activity was measured by monitoring the amino acid-dependent release of coenzyme A (CoASH) at 412 nm with 5,5′-dithio-bis(2-nitrobezoic acid) (DTNB). Assays were performed under the conditions described previously [8]. Briefly, the reaction mixture contained 0.3 M Tris–HCl (pH 8.0), 0.3 mM DTNB, and 4.0 μg/mL of enzyme protein in a total volume of 50 μL. The two substrates, benzoyl-CoA and glycine, were varied over the ranges of 470–4700 μM and 40–200 mM, respectively, to determine the apparent K_m and V_m values. The time courses of reactions were monitored by ARVO multilabel counter (Pharmacia, Upsalla, Sweden) at 37 °C. To examine the substrate specificity, benzoyl- and phenylacetyl-CoA were used at 100 μM, and glycine, glutamine, and taurine were used at 100 mM in a total volume of 50 μL. After 30 min of reaction at 37 °C, absorbance at 412 nm was measured using an Ultrospec 2000 spectrophotometer (Pharmacia). Enzyme units were determined as generation of CoA-SH nmol per minute per mg of enzyme protein.

2.3. Mitochondrial localization assay

Human GLYAT localization was determined by indirect immunostaining and biochemical fractionation. C-terminal HA-tagged hGLYAT in pcDNA3.1 expression vector or control vector was transfected into HeLa cells. After 48 h, cells were stained with anti-HA antibody (Roche) and MitoTracker (Invitrogen), and examined by confocal microscopy (FV1000-D; Olympus). Biochemical mitochondria fractionation was performed using a Dounce homogenization and centrifugation with a Mitochondria Isolation Kit for Mammalian Cells (Thermo Scientific). Fractionated mitochondria and cytosol protein solutions and whole-cell extract from transfected HeLa cells obtained 48 h after transfection were analyzed by Western blotting with anti-HA, anti-Mn-SOD (mitochondrial superoxide dismutase 2; Abcam), and anti-β-actin (Sigma) antibodies.

2.4. Quantitative RT-PCR

Real-time quantitative reverse transcriptase polymerase chain reaction (qRT-PCR) was performed by the ΔΔCt method with Taqman probe or CYBR Green staining. Human GLYAT level was normalized relative to the β-actin or GAPDH as an internal control. Tissue specificity was determined using a human multi-tissue cDNA panel 1 (Clontech). Comparison of hGLYAT expression between non-cancerous and cancerous cells was performed with cDNA prepared from test specimens excised from patients with informed consent.

2.5. Immunohistochemistry

Test specimens were prepared from tissues excised from patients with informed consent. All excised tissue specimens were fixed with formalin, embedded in paraffin, and sliced with a microtome at a thickness of 3 μm. After stretching and removal of paraffin, the specimens were stained with hematoxylin & eosin (H&E) and affinity purified with anti-GLYAT antibody.

3. Results and discussion

3.1. Identification of human glycine acyltransferase family genes

First, we attempted to isolate the full-length human GLYAT (hGLYAT) cDNA by the rapid amplification of cDNA ends (RACE) technique. Isolated hGLYAT cDNA was 1150 nucleotides in length, and encoded a predicted protein product of 295 amino acids. The poly(A) signal sequence (AATAAA) was observed at positions 1103–1108. Based on the hGLYAT sequence, we identified hGLYAT-related genes, isolated their cDNAs by PCR, confirmed their sequences, and examined their similarity by multiple alignment (Fig. S1). Human GLYAT showed 39.0% and 40.5% identity to hGLYATL1 and GLYATL2, respectively. Moreover, hGLYATL1 showed 49.0% identity to hGLYATL2. Human GLYAT most closely resembled rat HP33 and bovine glycine acyltransferases (bGLYATs) (Fig. S1).

3.2. Enzyme activity of hGLYAT and hGLYATL1 proteins

Next, the enzyme activities of three affinity-purified recombinant proteins were examined using amino acids (glycine and glutamine) and acyl-CoAs (benzoyl- and phenylacetyl-CoA) as substrates (Table 1). hGLYAT showed the highest activity to benzoyl-CoA as an acyl donor and glycine as acyl acceptor. Moreover,

Table 1
Enzyme activity of human GLYAT family proteins (unit/mg protein).

Acceptor	Donor	GLYAT	GLYATL1	GLYATL2
Glycine	Benzoyl-CoA	0.434 ± 0.02	0.027 ± 0.004	0.030 ± 0.004
	Phenylacetyl-CoA	0.095 ± 0.005	0.085 ± 0.004	0.102 ± 0.005
Glutamine	Benzoyl-CoA	0.105 ± 0.005	0.101 ± 0.005	0.113 ± 0.006
	Phenylacetyl-CoA	0.089 ± 0.004	0.603 ± 0.03	0.083 ± 0.01

1 U: 1 nmol of acyl residues tranferred to the acceptor amino acid per minute.
Purities of recombinant proteins used were >90% for GLYAT, and >85% for GLYATL1 and GLYATL2 (data not shown).

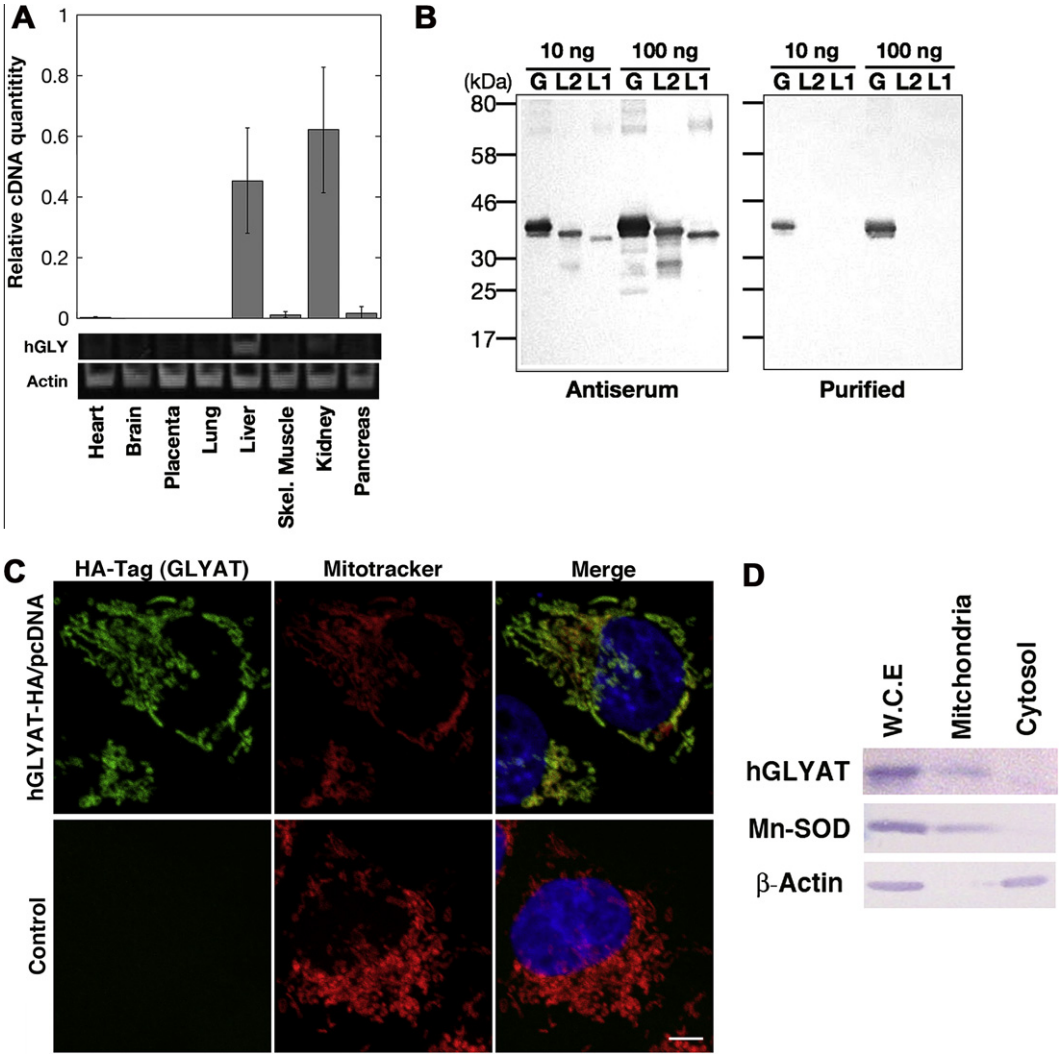


Fig. 1. Localization of human GLYAT mRNA and protein. (A) Human GLYAT mRNA expression in eight human tissues. qRT-PCR results determined by the ΔΔCt method with Taqman probe. After 40 cycles of PCR, amplified hGLYAT (hGLY) and β-actin (Actin) target sequences were analyzed by polyacrylamide gel electrophoresis. (B) Western blots of staining with anti-human GLYAT antiserum and affinity-purified anti-human GLYAT antibody. Anti-human GLYAT antiserum was preabsorbed to human GLYATL1 and GLYATL2 columns. Subsequently, preabsorbed antiserum was purified with a human GLYAT protein column. The antiserum and antibody were used at a dilution of 1000×. To judge cross-reactivity for GLYATL1 and GLYATL2, 10 ng and 100 ng of GLYAT, GLYATL1, and GLYATL2 proteins were used for blotting. Lanes G, L2, and L1 indicate GLYAT, GLYATL2, and GLYATL1, respectively. (C) Immunostaining of HeLa cells transfected with human GLYAT expression vector. Human GLYAT and mitochondria were stained with Alexafluor 488 (green) and MitoTracker (red), respectively. Scale bar indicates 10 μm. (D) Western blotting analyses of hGLYAT localization. Mn-SOD and β-actin were used as mitochondrial and cytosolic markers, respectively. W.C.E. indicates whole-cell extract of HA-tagged hGLYAT transfected HeLa cells.

in the case of glutamine as an acceptor, hGLYAT showed favorable catalysis of benzoyl-CoA over phenylacetyl-CoA. These results suggested that hGLYAT is a typical aralkyl transferase. hGLYATL1 most effectively catalyzed phenylacetyl-CoA and glutamine, indicating that hGLYATL1 is a human arylacetyl transferase [5]. This is the first report to identify a human glutamine *N*-acyltransferase gene, and this finding is consistent with the coexistence of glycine and glutamine *N*-acyltransferase activity in the mitochondrial fractions from human and monkey liver [5]. Moreover, these results suggested that glutamine *N*-acyltransferase evolved from glycine *N*-acyltransferase by gene duplication and gained glutamine binding affinity through the process of evolution from mammals to primates. GLYATL2 did not show significant enzymatic activity under the conditions used in this study. GLYATL2 also did not show activity with taurine as an acyl acceptor (data not shown). These results were in good agreement with those of Waluk et al. [12] indicating that GLYATL2 mainly catalyzes conjugation with long chain fatty acid-CoA and glycine. The results of multiple alignment analysis (Fig. S1) showed that bGLYAT (glycine acceptor) was more similar to hGLYAT (aralkyl transferase; glycine acceptor) in the 128–178 region than the corresponding region of bGLYATL1 (arylacetyl transferase; glutamine acceptor) at 128–180. Moreover, bGLYAT (arylacetyl transferase) was irreversibly inhibited by sulfhydryl reagent, while aralkyl bGLYAT was not [4], and the corresponding amino acid residue associated with the enzyme activity to sulfhydryl modification was cysteine at position 130 of arylacetyl bGLYAT. These results suggested that the active center of hGLYAT is localized within aa 128–178, which was important for glycine binding and acyl residue transfer. Moreover, if aa 128–178 of hGLYAT was responsible for glycine binding, the region consisting of aa 128–180 of hGLYATL1 was suggested to be the glutamine binding region.

Based on the sequence identity to hepatocellular carcinoma-related HP33 and enzyme activity for glycine conjugation, we were interested in hGLYAT with regard to its relation with human liver disease.

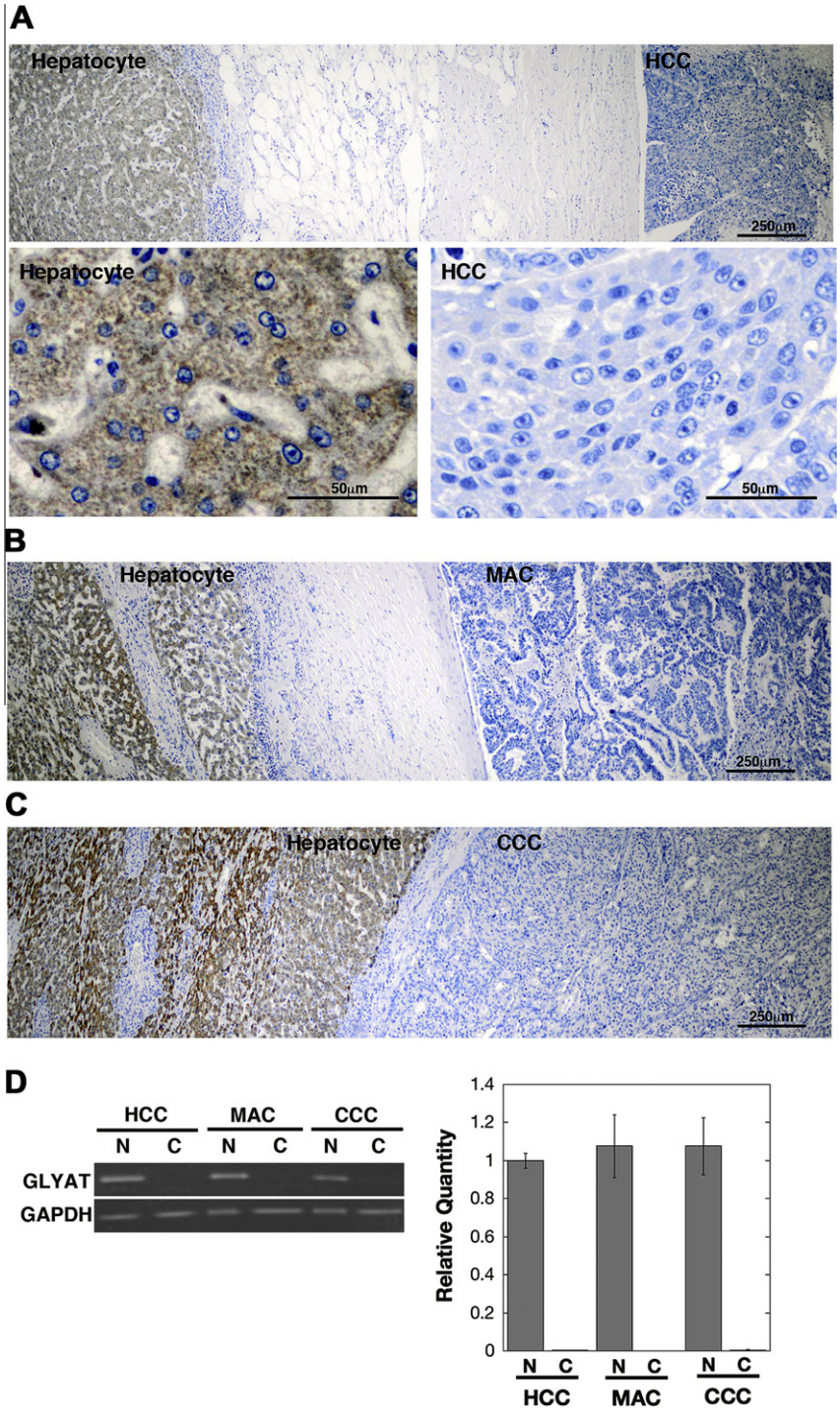


Fig. 2. Immunohistochemistry of various human liver specimens. (A) Upper panel: photograph of a human HCC specimen containing cancerous cells with a noncancerous border region through the fibrous capsule between them stained with affinity-purified anti-human GLYAT antibody (brown) and hematoxylin (blue). Lower left panel: higher resolution photograph of noncancerous region (Hepatocyte) of human HCC specimen. Lower right panel: higher resolution photograph of human HCC region of a specimen stained with affinity-purified anti-human GLYAT antibody (brown) and hematoxylin (blue). (B) Photograph of a human liver metastatic adenocarcinoma specimen containing cancerous cells with a noncancerous border region. The noncancerous region was stained brown with anti-GLYAT antibody. MAC: metastatic adenocarcinoma. (C) photograph of a human CCC specimen containing cancerous cells with a noncancerous border region. The noncancerous region was stained brown with anti-GLYAT antibody. CCC: cholangiocellular carcinoma. (D) qRT-PCR results between noncancerous and cancerous cells in HCC, MAC, and CCC corresponding to Fig. 2A–C, respectively. Human GLYAT expression was normalized relative to GAPDH cDNA in the same samples.

From the results shown in Table 1, we characterized GLYAT activity with benzoyl-CoA and glycine (Fig. S2). Lineweaver–Burk plot analyses suggested that the K_m values for benzoyl-CoA and glycine of hGLYAT were 209 and 26.6 mM, respectively, and the V_m value was 807 nmol/min/mg hGLYAT. The K_m for benzoyl-CoA was very smaller to that of hGLYAT purified from the liver (57.9 mM) [16], and V_m was about 1/20th that of hGLYAT from the liver (17.1 μmol/min/mg protein) [16]. The observed V_m was

Table 2
Summary of GLYAT expression in human liver disease.

	Positive	Weakly positive	Negative
HCC	0/41	9/41	32/41
CCC	0/6	0/6	6/6
Colon cancer metastasis	0/6	0/6	6/6
Chronic hepatitis	60/60	0/60	0/60

larger than that of bovine liver GLYAT and smaller than that of human liver GLYAT. These differences may be caused by differences in proteins used (recombinant hGLYAT with peptide tag and hGLYAT purified from liver). This enzyme assay indicated that hGLYAT catalyses a sequential bi-bi reaction and not a ping-pong bi-bi reaction.

3.3. Tissue-specific expression of hGLYAT

We performed qRT-PCR analyses to characterize the tissue specificity of hGLYAT gene expression. This tissue specificity was not the same as those of hGLYATL1 and hGLYATL2 [11,12], and was the same as that reported previously for rat HP33 [14]. Human GLYAT was shown to be expressed predominantly in the liver and kidney (Fig. 1A). Northern blotting analysis indicated that human GLYAT mRNA was about 1.2 kb in length (Fig. S3), which was identical to the length of the cDNA.

3.4. Human GLYAT is localized to mitochondria

GLYAT was shown to function as a glycine acyltransferase in the mitochondria of liver and kidney cells using biochemically purified protein prepared from the tissues. However, there was no direct evidence for the cellular localization of hGLYAT, and we prepared a specific anti-hGLYAT antibody to analyze the cellular localization of hGLYAT protein (Fig. 1B and C). Anti-hGLYAT antiserum was affinity-purified with recombinant hGLYAT protein after preabsorption with hGLYATL1 and hGLYATL2 proteins (Fig. 1B). Before purification, anti-hGLYAT antiserum showed severe cross-reactivity for hGLYATL1 and hGLYATL2 proteins (Fig. 1B Antiserum). However, after preabsorption and affinity purification, anti-hGLYAT antibody reacted solely with hGLYAT protein (Fig. 1B purified).

The cellular localization of hGLYAT was analyzed in HeLa cells (Fig. 1C). These cells did not show detectable endogenous hGLYAT protein expression on Western blotting analysis (data not shown). Therefore, we performed transient expression of hGLYAT in HeLa cells, followed by immunostaining (Fig. 1C). In the transfected cells, hGLYAT localization was restricted to fibrous structures in the cytosol that were coincident with the mitochondrial space stained with MitoTracker. Moreover, we examined hGLYAT localization by biochemical fractionation (Fig. 1D). Human GLYAT was clearly concentrated in the mitochondrial fraction (Fig. 1D, Mn-SOD) and not in the cytosol (Fig. 1D, β-Actin). These observations were consistent with previous results of the biochemical fractionation of human GLYAT from the liver [5].

3.5. GLYAT expression was reduced in hepatocellular carcinoma

Previous studies indicated that GLYAT was involved in the metabolic processing of xenobiotics in the liver, and rat HP33, which showed the highest degree of identity to hGLYAT, was induced in hepatocellular carcinoma (HCC) caused by metabolic intermediates of carcinogens. The results suggested that hGLYAT may be related to human HCC or other liver diseases. Therefore, we investigated hGLYAT expression and localization in specimens from various human diseases, such as HCC and hepatitis of various origins (Fig. 2 and Table 2). Typical hGLYAT expression in HCC tissues indicated that hGLYAT protein was expressed in noncancerous hepatocytes and disappeared in cancerous HCC cells (Fig. 2A upper panel). In noncancerous cells of HCC specimen, hGLYAT was localized in granular structures consistent with the mitochondrial space in the cytosol (Fig. 2A lower left). This observation corresponded to the localization in HeLa cells (Fig. 1C), and hGATF localization was observed in mitochondria in both liver cells and cultured cells. hGLYAT expression was not detected in cancerous cells from the same specimen (Fig. 2A lower right). Moreover, we used 103 specimens of a variety of liver diseases for analyses of hGLYAT expression and localization. Unexpectedly based on the rat HP33 results, hGLYAT protein was not detected or was detected only weakly in 78% and 22% of 41 HCC specimens, respectively (Table 2). Six samples of colon cancer metastasis (metastatic adenocarcinoma, MAC) to the liver (Fig. 2B) and six samples of cholangiocellular carcinoma (CCC) (Fig. 2C) as control tumors were completely negative for hGLYAT expression (Table 2). The results shown in Fig. 2A–C indicate marked differences in staining at the border between cancerous and noncancerous regions. Cancerous cells showing weak hGLYAT expression were very rare (Fig. S4), and noncancerous cells showed higher levels of hGLYAT expression than cancerous cells in all specimens examined (Table 2). These results indicated that hGLYAT expression was downregulated in all cases of HCC and other liver cancers. To investigate the cause of hGLYAT downregulation in cancerous cells, we performed qRT-PCR to determine hGLYAT expression in noncancerous and cancerous liver cells (Fig. 2D). All cancerous samples examined (HCC, MAC, and CCC) showed marked repression of hGLYAT expression, while all noncancerous samples showed similar and significant hGLYAT expression. Transcriptome analysis of HCC caused by hepatitis B virus infection indicated that hGLYAT expression was depressed in HCC [17]. These results suggested that repression of hGLYAT expression was mainly regulated at the transcriptional level. Moreover, we found no significant relationship between GLYAT expression and the degree of HCC differentiation. Interestingly, GLYAT expression was positive in all of 60 samples from chronic hepatitis patients with various etiologies, such as hepatitis A, B, and C virus infections, alcohol abuse, and autoimmune hepatitis (Table 2). These observations showed that GLYAT was constantly expressed in the noncancerous hepatocytes regardless of their status as normal or hepatitis cells with various origins. GLYAT may be expressed in differentiated hepatocytes and repressed in dedifferentiated cells, such as cancerous cells in the liver. These results strongly suggested that hGLYAT is a good candidate as a novel HCC marker. We propose that hGLYAT may be a key molecule in the transition between differentiation and carcinogenesis of liver cells.

Database linking and accession numbers

Human Glycine *N*-acyltransferase (GLYAT): GenBank ID: AB665285.

Human GLYATL1: GenBank ID: AB207212 registered as human GATF-C mRNA.

Human GLYATL2: GenBank ID: AB207211 registered as human GATF-B mRNA.

Acknowledgments

We thank Dr. M. Sone (Toho University) for useful assistance and discussion for qRT-PCR and Dr. Y. Makino and Dr. S. Niwa for detailed discussions.

Appendix A. Supplementary data

Supplementary data associated with this article can be found, in the online version, at http://dx.doi.org/10.1016/j.bbrc.2012.03.099.

References

[1] D. Schachter, J.V. Taggart, Benzoyl coenzyme A and hippurate synthesis, J. Biol. Chem. 203 (1953) 925–934.
[2] D. Schachter, J.V. Taggart, Glycine *N*-acylase: purification and properties, J. Biol. Chem. 208 (1954) 263–275.
[3] K. Solaas, A. Ulvestad, O. Soreide, B.F. Kase, Subcellular organization of bile acid amidation in human liver: a key issue in regulating the biosynthesis of bile salts, J. Lipid Res. 41 (2000) 1154–1162.
[4] D.L. Nandi, S.V. Lucas, L.T. Webster Jr., Benzoyl-coenzyme A:glycine *N*-acyltransferase and phenylacetyl-coenzyme A:glycine *N*-acyltransferase from bovine liver mitochondria. Purification and characterization, J. Biol. Chem. 254 (1979) 7230–7237.
[5] L.T. Webster, U.A. Siddiqui, S.V. Lucas, J.M. Strong, J.J. Mieyal, Identification of separate acyl- CoA:glycine and acyl-CoA:L-glutamine *N*-acyltransferase activities in mitochondrial fractions from liver of rhesus monkey and man, J. Biol. Chem. 251 (1976) 3352–3358.
[6] Y.R. Mawal, I.A. Qureshi, An immunodetection method for the quantitation of human acyl CoA:glycine *N*-acyltransferase in biological samples, Biochem. Mol. Biol. Int. 34 (1994) 595–601.
[7] N. Gregersen, S. Kolvraa, P.B. Mortensen, Acyl-CoA: glycine *N*-acyltransferase: in vitro studies on the glycine conjugation of straight- and branched-chained acyl-CoA esters in human liver, Biochem. Med. Metab. Biol. 35 (1986) 210–218.
[8] S. Kolvraa, N. Gregersen, Acyl-CoA:glycine *N*-acyltransferase: organelle localization and affinity toward straight- and branched-chained acyl-CoA esters in rat liver, Biochem. Med. Metab. Biol. 36 (1986) 98–105.
[9] D.A. Vessey, E. Lau, Determination of the sequence of the aralkyl acyl-CoA:amino acid *N*-acyltransferase from bovine liver mitochondria, J. Biochem. Toxicol. 11 (1996) 211–215.
[10] D.A. Vessey, E. Lau, Determination of the sequence of the arylacetyl acyl-CoA:amino acid *N*-acyltransferase from bovine liver mitochondria and its homology to the aralkyl acyl-CoA:amino acid *N*-acyltransferase, J. Biochem. Mol. Toxicol. 12 (1998) 275–279.
[11] H. Zhang, Q. Lang, J. Li, Z. Zhong, F. Xie, G. Ye, B. Wan, L. Yu, Molecular cloning and characterization of a novel human glycine-*N*-acyltransferase gene GLYATL1, which activates transcriptional activity of HSE pathway, Int. J. Mol. Sci. 8 (2007) 433–444.
[12] D.P. Waluk, N. Schultz, M.C. Hunt, Identification of glycine *N*-acyltransferase-like 2 (GLYATL2) as a transferase that produces *N*-acyl glycines in humans, FASEB J. 24 (2010) 2795–2803.
[13] B.A. Barshop, J. Breuer, J. Holm, J. Leslie, W.L. Nyhan, Excretion of hippuric acid during sodium benzoate therapy in patients with hyperglycinaemia or hyperammonaemia, J. Inherit. Metab. Dis. 12 (1989) 72–79.
[14] T. Nakadai, T. Kishimoto, Y. Miyazawa, N. Okada, Y. Makino, T. Obinata, T. Tamura, HP33: hepatocellular carcinoma-enriched 33-kDa protein with similarity to mitochondrial N-acyltransferase but localized in a microtubule-dependent manner at the centrosome, J. Cell. Sci. 112 (Pt 9) (1999) 1353–1364.
[15] Y.M. Chen, J.Y. Shiu, S.J. Tzeng, L.S. Shih, Y.J. Chen, W.Y. Lui, P.H. Chen, Characterization of glycine-*N*-methyltransferase-gene expression in human hepatocellular carcinoma, Int. J. Cancer 75 (1998) 787–793.
[16] Y.R. Mawal, I.A. Qureshi, Purification to homogeneity of mitochondrial acyl coa:glycine *n*-acyltransferase from human liver, Biochem. Biophys. Res. Commun. 205 (1994) 1373–1379.
[17] X.R. Xu, J. Huang, Z.G. Xu, B.Z. Qian, Z.D. Zhu, Q. Yan, T. Cai, X. Zhang, H.S. Xiao, J. Qu, F. Liu, Q.H. Huang, Z.H. Cheng, N.G. Li, J.J. Du, W. Hu, K.T. Shen, G. Lu, G. Fu, M. Zhong, S.H. Xu, W.Y. Gu, W. Huang, X.T. Zhao, G.X. Hu, J.R. Gu, Z. Chen, Z.G. Han, Insight into hepatocellular carcinogenesis at transcriptome level by comparing gene expression profiles of hepatocellular carcinoma with those of corresponding noncancerous liver, Proc. Natl. Acad. Sci. USA 98 (2001) 15089–15094.

Biochemical and Biophysical Research Communications 420 (2012) 907–912

Contents lists available at SciVerse ScienceDirect

Biochemical and Biophysical Research Communications

journal homepage: www.elsevier.com/locate/ybbrc

Heteroplasmy levels of mtDNA1555A>G mutation is positively associated with diverse phenotypes and mutation transmission in a Chinese family

Shan-Shan Shen, Chang Liu, Zhi-Yong Xu, Yu-Hua Hu, Guo-Feng Gao, Sha-Yan Wang *

Shenzhen People's Hospital, Clinical Medical College of Jinan University, Dongmen North Rd. 1017, Shenzhen 518020, PR China

ARTICLE INFO

Article history:
Received 15 March 2012
Available online 27 March 2012

Keywords:
Hereditary hearing loss
mtDNA 1555A>G mutation
Heteroplasmy
Eastern Asian
Clinical phenotype
Mutation transmission

ABSTRACT

The mtDNA 1555A>G mutation was considered to be one of the most common causes of aminoglycoside-induced and non-syndromic hearing loss. However, this mutation was always found in homoplasmy with high phenotypic heterogeneity. Recently this mutation in heteroplasmy has been reported in several studies. In the present study, we have collected a large Chinese family harboring heteroplasmic mtDNA 1555A>G mutation with diverse clinical phenotypes. To investigate the relationship between the mutation load and the severity of hearing loss under Eastern Asian background, we performed clinical, molecular, genetic and phylogenic analysis. This pedigree was characterized by coexistence of eight subjects with homoplasmic mutation and ten subjects with various degrees of heteroplasmy, and the results suggested that there was a strong correlation between the mutation load and the severity/age-onset of hearing loss ($r = 0.758$, $p < 0.001$). We noticed that the mutation level of offspring was associated with their mothers' in this pedigree, which indicated that maybe exist a regular pattern during the process of the heteroplasmic transmission. In addition, analysis of the complete mtDNA genome of this family revealed that it belonged to Eastern Asian haplogroup B4C1. In addition, a rare homoplasmic mtDNA 9128T>C variant was identified, it located at a strictly conserved site of mtDNA ATP6 gene.

© 2012 Elsevier Inc. All rights reserved.

1. Introduction

Mitochondria are essential organelles in cells as they are responsible not only for the generation of cellular energy in the form of ATP by oxidative phosphorylation, but also for the control of apoptosis. Mitochondrial DNA (mtDNA) mutations are important causes of human diseases and are associated with various forms of clinical abnormalities, including hearing loss, neuropathies, myopathies, diabetes and so on [1]. As previous reports suggested, mutations in mtDNA were responsible for aminoglycoside-induced and non-syndromic hearing loss. Prezant et al. [2] first described the single-nucleotide alteration 1555A>G in the highly conserved decoding site of the mtDNA 12S rRNA gene [2]. Subsequently, it was founded in many families of various ethnic backgrounds all over the world [3–8]. In contrast to other mutations associated with mitochondrial diseases, which were frequently heteroplasmic, the 1555A>G mutation had always been found in homoplasmy. However, the clinical phenotype varies considerably among matrilineal relatives within families or among different families, it exhibited a wide spectrum of clinical manifestations in the mode of expressivity, aminoglycoside susceptibility, age of onset, course and progression of the disease, while the homoplasmic 1555A>G mutation was insufficient to give a reasonable explanation about the variable phenotypes of deafness.

Recently, some researches have found that the mtDNA 1555A>G mutation could also be heteroplasmic. El-Schahwi et al. [9] first reported the mtDNA 1555A>G mutation in heteroplasmy in three Spanish subjects, with the mutation load ranging from 85% to 94% [9]. Del Castillo et al. [10] detected six Spanish families with sensorineural hearing loss, a total of 19 subjects harbored 1555A>G mutation in heteroplasmy [10]. They also have found that patients carrying less than 20% of mutant copies were either asymptomatic or with a mild hearing loss, whereas heteroplasmic subjects with mutant loads higher than 52% suffered from moderate to severe hearing loss. As these reports, all of these patients with 1555A>G mutation in heteroplasmy were collected from Spanish pedigrees. However, as mentioned above, these pedigrees were Caucasus origins. Only a few sporadic cases have been reported based on the Asians, [11,12] but the relationship between the mutation loads and the clinical phenotype under the East Asians background was still in the veil. Therefore, it is of vital necessity to collect more pedigrees which segregating the mtDNA 1555A>G mutation in heteroplasmy, then to evaluate the correlation between the mutation load and the severity of hearing loss in East Asians according to the mtDNA phylogenetic tree.

In the present study, we investigated the genetic and clinical characterization of a three-generation Chinese family segregating

* Corresponding author. Fax: +86 755 25633958.
E-mail address: shayanw@yahoo.com (S.-Y. Wang).

0006-291X/$ - see front matter © 2012 Elsevier Inc. All rights reserved.
http://dx.doi.org/10.1016/j.bbrc.2012.03.100

the 1555A>G mutation in heteroplasmy, which displayed incomplete penetrance and variable expressivity of hearing loss. An identical 1555A>G mutation was performed by PCR-RFLP and direct sequencing in all members of this pedigree. Furthermore, denaturing high performance liquid chromatography (DHPLC) was developed to confirm the heteroplasmy and quantification the mutation load. We also performed a mutational analysis of the entire mitochondrial genome and related nuclear gene.

2. Materials and methods

2.1. Subjects and audiological examinations

A three-generation Chinese pedigree with 18 maternal members was collected from Shanxi province (Fig. 1). All of them were identified through the otology clinic at Shenzhen People's Hospital, Second Clinical Medical College of Jinan University. Hearing impairment as a sole clinical phenotype was only present in the maternal lineage of this pedigree. A comprehensive clinical history was also collected, including information on severity and age of onset of hearing impairment, the exposure to different kinds of ototoxic substances such as aminoglycosides, and any other medical diagnoses of relevance. Appropriate audiological examinations were carried out with pure-tone audiometry (PTA). PTA was calculated from the average of audiometric thresholds at 500, 1000, 2000, 4000 and 8000 Hz. The degree of hearing impairment was classified as follows: normal hearing <26 dB; mild hearing loss: 26–40 dB; moderate hearing loss: 41–70 dB; severe hearing loss: 71–90 dB; profound: >91 dB. Peripheral blood samples were obtained from all participating family members, and DNA extraction was performed by standard procedures using QIAamp DNA Blood Mini kit (Qiagen, Germany). The maternal member's spouses in this pedigree were detected as the negative control. Informed consent was obtained from each individual according to the approval of the ethic committees of Shenzhen People's Hospital.

2.2. Detection of mtDNA 1555A>G mutation

Screening for the 1555A>G mutation was carried out using PCR-RFLP method. A 463 bp fragment of mitochondrial DNA encompassing the 1555A>G site was amplified by the method described elsewhere, [13] followed by digestion with restriction endonuclease Alw26 *I*. In the wild type allele, digestion resulted in two fragments of 339 and 124 bp. The mutation destroyed the restriction site, resulting in just one 463 bp fragment, [5] subsequently, PCR amplification products were purified and analyzed by direct sequencing using an ABI 3130 Sequencer. The obtained sequences were compared with the revised Cambridge reference sequence (GenBank accession number NC_001807) [14].

2.3. Quantification of the mtDNA 1555A>G mutation load

The proportion of mutant copies was quantified by the DHPLC method with the 3500- HT WAVE nucleic acid fragment analysis system (Transgenomic, Crewe, UK). Briefly, a 279 bp fragment was amplified using the primers; forward: 5′-GCTCAGCCTATATACCGCCATCTTCAGCAA-3′ and reverse: 5′-CAAGTCGTAACATGGTAAGTGTACTGGAAA-3′. The quantification method was applied as described previously [15]. DNA samples from wild-type individual and carrier of 1555A>G mutation were amplified using the same primers as for the DHPLC analysis. The resulting PCR-amplified fragments were purified and cloned into pGEM-T vector (Promega, Madison, WI), then the plasmids of all colonies were sequenced to identify the two clones, one with the wild-type genotype and another with the 1555A>G mutation. The wild-type and mutated DNA were mixed to generate samples with the 1555A>G mutation present at gradient levels ranging from 0% to 100%, a standard curve was built for the proportion of the mutation. Each sample was analyzed in triplicate.

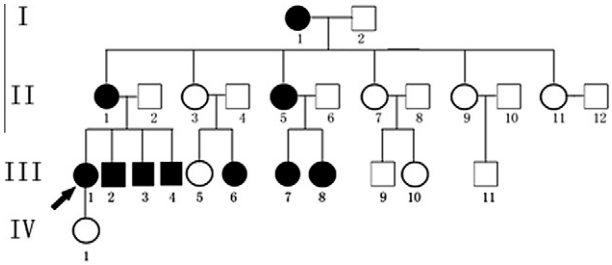


Fig. 1. Pedigree of a three-generation Chinese Han family that harbors the mtDNA 1555A>G mutation with aminoglycoside-induced and nonsyndronic hearing loss, the IV-1 was too young to do audiological examine.

2.4. Sequencing for the entire mitochondrial genome and defining haplogroup

The entire mitochondrial genome of the proband and one affected matrilineal relative I-1 were amplified in 24 overlapping fragments by using of sets of the light-strand and the heavy-strand oligonucleotide primers that could cover the entire mitochondrial DNA [16]. Each fragment was purified and subsequently submitted for sequence analysis. The resultant sequence data were assembled and compared with the revised Cambridge reference sequence and assigned to the Asian mitochondrial haplogroups by using the nomenclature of mitochondrial haplogroup [17,18]. Then, the presence of the secondary deafness-associated mutations were detected, which may interact with 1555A>G mutation and affect clinical manifestations.

2.5. Mutational analysis of GJB2 gene

The DNA fragment spanning the entire coding region of the GJB2 gene was amplified by PCR using the following oligodeoxy nucleotides: forward: 5′-TCTTTTCCAGAGCAAACCGCC-3′ and reverse: 5′-TGAGCACGGGTTGCCTCATC-3′. PCR amplification and subsequent sequencing analysis were performed as described above [7]. The results were compared with the wild type GJB2 sequence (GenBank accession number: M86849) to identify the mutations.

3. Results

3.1. Clinical presentation

The proband of this family, patient III-1, a 28-year-old woman, had suffered from deafness since half of a year old after taking regular doses of Gentamycin administration (3–5 mg/kg/dose every 8 h) for two weeks. Audiological evaluation showed that she exhibited profound mixed hearing impairment (91 and 98 dB at right ear and left ear, respectively). Her family history showed a typical pattern of maternal inheritance (Figs. 1 and 2). Four members (I-1, II-5 and III-2, 8) affected sensorineural hearing impairment and another six subjects (II-1 and III-1, 3, 4, 6, 7) with mixed hearing impairment. The proband's grandmother (I-1) was a 73-year-old woman with moderate sensorineural deafness and had a clear history of aminoglycoside exposure. In the second generation, all of them (excepted subject II-3) had a history of exposure to aminoglycosides. Only subjects II-1 and II-5 were affected by severe mixed type deafness and mild bilateral sensorineural deafness, respectively. Conversely,

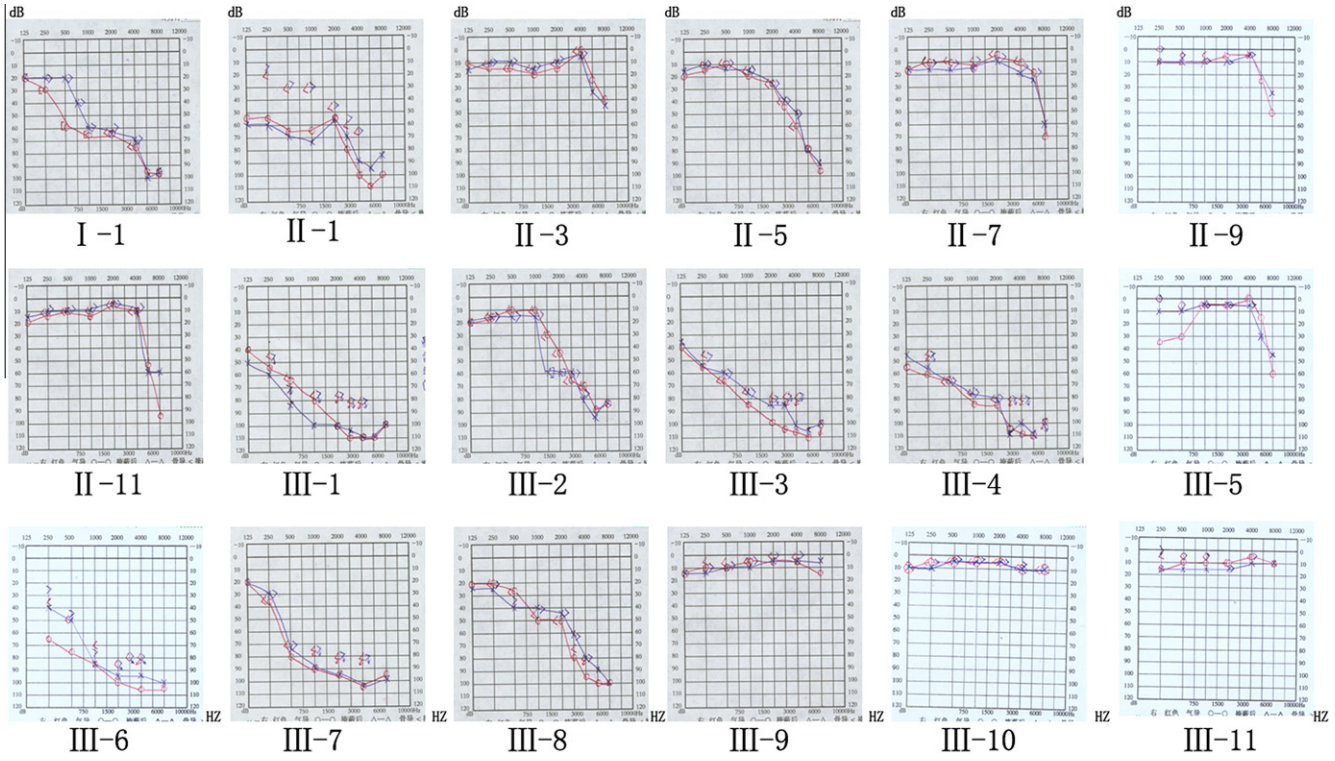


Fig. 2. Pure tone audiometries of the three-generation pedigree maternal subjects. Hearing level (in dB) is plotted vs. sound frequency (in HZ).

Table 1
Summary of clinical data and molecular evaluation for 18 maternal members in the Chinese pedigree with mtDNA 1555A>G mutation.

Sample	Gender	Age (year)	Age of onset	Use of aminoglycosides	PTA (dB) left ear	PTA (dB) right ear	HL degree	A1555G (G%)
I1	F	73	50–60	Yes	62	72	Moderate bilateral sensorineural deafness	70.60
II1	F	53	4	Yes	75	77	Severe mixed type deafness	97.90
II3	F	48	–	No	17	18	Normal	85.30
II5	F	44	Unclear	Yes	39	42	Mild bilateral sensorineural deafness	70.70
II7	F	41	–	Yes	24	22	Normal	49.80
II9	F	38	–	Yes	14	16	Normal	49.60
II11	F	35	–	Yes	19	27	Normal	49.50
III1	F	28	1.5	Yes	98	91	Profound mixed type deafness	100
III2	M	26	Unclear	No	51	44	Moderate bilateral sensorineural deafness	100
III3	M	24	3	Yes	84	91	Severe mixed type deafness	100
III4	M	20	3	Yes	84	89	Severe mixed type deafness	100
III5	F	26	–	No	14	20	Normal	100
III6	F	20	1.5	Yes	85	94	Severe mixed type deafness	100
III7	F	16	2	Yes	93	93	Profound mixed type deafness	100
III8	F	13	Unclear	No	61	64	Moderate bilateral sensorineural deafness	100
III9	M	11	–	No	7	8	Normal	14.80
III10	F	4	–	No	13	9	Normal	11.90
III11	M	9	–	No	7	7	Normal	19.40

other three subjects (II-7, 9 and 11) had normal hearing for low and middle frequencies, but suffered from a mild hearing loss for high frequencies. In the third generation, five subjects (III-1, 3, 4, 6 and 7) displayed severe or profound hearing loss with the records of aminoglycoside treatment. In the absence of aminoglycosides, three subjects (III-2, 5 and 8) showed normal or moderate hearing, and had obvious loss at 1000–8000 Hz frequencies, the remaining subjects (III-9, 10 and 11) showed absolutely normal hearing at all frequencies. We did not found deafness in the control subjects. The exact timing of aminoglycoside exposure, audiometric configuration and severity of deafness were shown in Table. 1.

3.2. Detection and quantification of mtDNA 1555A>G mutation

To detect the 1555A>G mutation, the PCR-RFLP analysis and the direct sequencing method were applied. As showed in Fig. 3A, 16 out of 18 maternally related family members were positive for the 1555A>G mutation, which was heteroplasmic in seven members. To verify the 1555A>G mutation, PCR amplification products were purified and analyzed by direct sequencing. From the results we could find that the PCR-RFLP analysis results were confirmed by direct sequencing of the corresponding PCR product (Fig. 3B).

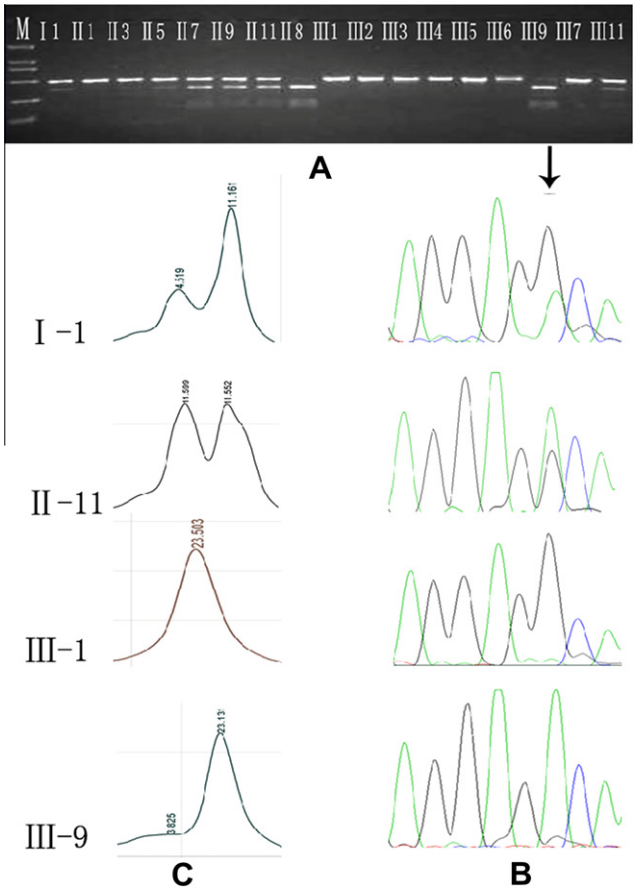


Fig. 3. PCR analysis for the mtDNA 1555A>G mutation in members of shanxi pedigree. (A) PCR products around 1555A>G region were digested with Alw26 I. In the wild-type allele, digestion results in two fragments; whereas the mutant DNA destroys the restriction site, resulting in one 463 bp fragment. (B) Sequence of one mutant subject (patient III-1), two heteroplasmic subjects (patient I-1 and II-11) and a wild-type subject (patient III-9). (C) DHPLC profiles observed in the samples.

In this study, the DHPLC method was applied to identify the level of heteroplasmy. As the results shown, ten subjects were heteroplasmic and mutant copies ranged from 11.9% to 97.9%, eight subjects with the mutation in homoplasmy. Compared with the results of PCR-RFLP and direct sequencing, three additional subjects (III-9, 10 and II-1) were detected out with heteroplasmic mutation, which were considered as normal or carrying with homoplasmic mutation (Table. 1 and Fig. 3C).

3.3. Sequence analysis for the entire mitochondrial genome

To assess the association of mitochondrial haplotype and mtDNA variants with the phenotypic expression of 1555A>G mutation, the entire mitochondrial genome of proband and I-1 were sequenced for haplogroup analysis and to screen other mtDNA variants. From the results, we could find that the sequence information about entire mitochondrial genome of the proband which carried with homoplasmic mutation was remarkably matched with heteroplasmic subject I-1. As the results shown, the mtDNA of this Chinese pedigree harbored variant 16189T>C, 8281–8289d, 16217T>C, 16274G>A, 15346>A, 3497C>T and other specific mutations. According to the Eastern Asian mtDNA tree, this suggested for their haplogroup B4c1 status. Besides, the subjects also exhibited a set of mtDNA polymorphisms including 27 known variants and 4 novel variants (Table. 2). About the novel four variants, these were the 8860A>G (T112A) and the 9128T>C (I201T) in the ATP6 gene, together with the 14766C>T (T7I) and the 15326A>G (T194A) in the cyto b gene. However, these mutations seemed to be missense. These variants in RNAs and polypeptides were further evaluated by phylogenetic analysis among 100 organisms. Of them, 9128T>C mutation in the ATP6 gene showed evolutionary conservation. Furthermore, all the pedigree members were used direct sequencing to determine the mutation 9128T>C (I201T) and appeared to be homoplasmic.

Table 2
Sequence variants found in the mitochondrial DNA (mtDNA) of 1555A>G carriers.

Locus	Position (np)	Replacement	Previously reported
12S rRNA	750	A to G	Yes
	1119	T to C	Yes
	1438	A to G	Yes
	1555	A to G	Yes
16S rRNA	2706	A to G	Yes
	3435	C to T	Yes
	3497	C to T	Yes
	3571	C to T	Yes
ND2	4769	A to G	Yes
CO1	7028	C to T	Yes
NC7	8281	del 9 bp	Yes
ATP6	8860[a]	A to G	Yes
	9128[a]	T to C	Yes
ND4	11440	C to T	Yes
	11719	G to A	Yes
ND6	14544	G to A	Yes
Cyt b	14766[a]	C to T	Yes
	15326[a]	A to G	Yes
	15346	G to A	Yes

[a] Novel mitochondrial DNA sequence variants found in this work.

3.4. Mutational analysis of GJB2 gene

To examine if the mutation of nuclear gene GJB2 contributed to the deafness phenotype, we performed mutational screening of GJB2 gene in 18 matrilineal relatives. Four mutations (79G>A, 257G>C, 258C>G and 34lA>G) in GJB2 gene were found in this Chinese pedigree, which existed in the other normal Chinese subjects. However, none of significant variants in GJB2 gene was found in these matrilineal relatives.

4. Discussion

In the present study, we detected a three-generation Chinese pedigree segregating the mtDNA 1555A>G mutation in heteroplasmy with a diverse spectrum of hearing levels ranging from normal to profound deafness. It showed a strong familial clustering of deafness accompanied by different degrees of mutation load, and characterized by a more serve loss of hearing at high frequencies. Furthermore, we have found eight subjects with 1555A>G mutation in homoplasmy, and ten subjects with various degrees in heteroplasmic mutation by DHPLC method, it was reported that this method could rapidly and sensitively detect the mutant level ranged from 5% to most 100% [15]. As the results shown, subject II-1 was detected as a homoplasmic carrier and other two subjects (III-9 and III-10) showed complete wild-type genotype by PCR-RFLP and direct sequencing. However, with DHPLC method we found they carried 97.9% and 14.8%, 11.9% of mtDNA 1555A>G mutation load, respectively. It suggested that DHPLC could be used as a routine method for detecting mtDNA heteroplasmic mutation.

From the clinical evaluations (Fig. 1, Table. 1), we noticed that the susceptibility to aminoglycoside antibiotics in this pedigree

was gradually raised. It seemed to be lower correlation between the severity of hearing loss and the history of aminoglycoside exposure in the first and second generation members, almost of them had a history of aminoglycoside exposure (excepted subject II-3), but were asymptomatic and mild deafness respectively (excepted subjects II-1). However, subject II-1 was treated with streptomycin for Otitis media at the age of four years old and the Otitis media could be as one of the factors for her deafness. As regard the third generation, the patients suffered from severe or profound hearing impairment after using the aminoglycoside (III-1, 3, 4, 6 and 7), it showed the higher positive susceptibility to aminoglycoside. The remaining carriers without history of aminoglycoside which suffered from mild or moderate hearing loss (III-2, 5 and 8), and three were asymptomatic (III-9, 10, 11).

Heteroplasmy extensively presents in mitochondrial genetics, hence the proportion of mutant mtDNA in any cell or tissue may be extremely variable. When it exceeds a certain threshold, the wild-type mtDNA can no longer 'complement' the effects of the coexisting mutated and will be expressed phenotypically as a cellular dysfunction leading to disease [19]. Among the numerous reported mitochondrial diseases by mitochondrial DNA point mutations, 3243A>G and 1555A>G were the most common pathogenic mutations [3,20]. The heteroplasmic level of the 3243A>G mutation was positively associated with clinical severity [21]. Here, we investigated the effect of 1555A>G heteroplasmy mutation on the severity and the age-of-onset of hearing loss. Among these subjects with heteroplasmy, subjects (III-9, 10 and 11) carrying mutant copies less than 19.4% were asymptomatic, with percentages of mutant copies about 50%, subjects (II-7, 9 and 11) had normal hearing for low and middle frequencies, but suffered from obvious hearing loss for high frequencies. The remaining three subjects (I-1, II-1 and 5), with percentages of mutant copies more that 70%, suffered from moderate or severe hearing loss. Conversely, the remaining eight subjects carrying the mutation in homoplasmy, five of them (the proband III-1 and III-3, 4, 6, 7) had the earliest age-of-onset and severe/profound hearing loss after using aminoglycoside, three others (III-2, 5 and 8) not explored to aminoglycoside, showed normal or moderate hearing loss, but an obvious loss at high frequencies. These results demonstrated that the heteroplasmic level of 1555A>G mutation was correlated with the severity of deafness. A statistic analysis of our data showed correlation coefficient between the mutation load and the hearing threshold was 0.758, with $p < 0.001$ (two-sided), this indicated a higher percentage of mutant mtDNA was associated with greater severity. It was consistent with previous studies which as part of a study on the Europeans mtDNA phylogeny [9,10,15]. Meanwhile, it was similar to the character of the heteroplasmy mtDNA 3243A>G mutation to diabetes on the clinical phenotype.

The heteroplasmic level of 1555A>G mutation not only had a strong relationship with the clinical presentations, but also displayed major effluences on the heteroplasmy transmission. During the process of the mtDNA transmitted through generations, the proportions of mutant mtDNA transmitted from a heteroplasmic mother to different offspring were variable. After we took into account about our pedigree, the heteroplasmic mother (I-1) had six daughters, all of them with different heteroplasmic levels ranged from 49.5% to 97.9%. However, we notice that the mutant levels of them was: II-1(97.9%)>II-3(85.3%)>II-5(70.7%)>II-7(49.8%)>II-9(49.6%)>II-11(49.5%). It seemed that the child-bearing age of the mother maybe have some influences on the mutant level of her offspring, with the increasing of her age, the heteroplasmic level was getting more and more lower. In addition, we noticed an interesting phenomenon that the wild-type and mutated mtDNA appeared to be more homogeneous in the younger members of the family during the process of the mtDNA transmitted from the second to the third generation. In the third generation, when the mutation loads of their mother were higher than 70% (II-1, 3, 5, mutation ranged from 70.7% to 97.9%), the mutation loads of the offspring tended to more higher, and even to the homogeneous (III1–8). On the contrary, when the mutation loads of mother were lower than 50% (II-7 and II-9, with 49.8% and 49.6% of mutant copies), the mutant levels of offspring tended to more lower and even close to normal (III-9, 10 and 11, mutant copies ranging from 11.9% to 19.4%). It showed that the heteroplasmic levels of offspring could be impacted by the mother', and there may exist a regular pattern in the transfer process of mtDNA 1555A>G heteroplasmic mutations.

While the evidence indicated that the 1555A>G mutation was a main factor associated with the aminoglycoside-induced and nonsyndromic hearing loss, other modifier factors such as some nuclear genes and mitochondrial variants/haplotypes may contribute to various penetrances and expressivities of hearing loss among the families [11]. To identify the mitochondrial haplotype of this pedigree and further understand the role of other mitochondrial modifiers in the phenotypic manifestation of the mutation associated deafness, we sequenced the entire mitochondrial genome of proband and subject I-1, and also sequenced the nuclear gene GJB2 of all the maternal members. As shown in Table. 2, there was a set of sequence variations in the mtDNA of this Chinese pedigree. Through the analysis of these specific mutations, we found this pedigree belonged to haplogroups B4C1, a common Eastern Asian subhaplogroup (Fig. 4). While the Spanish families carrying the same heteroplasmic 1555A>G mutation belonged to Caucasian origin [9,10,15]. It illustrated that the mtDNA 1555A>G heteroplasmy also presented in East Asian haplogroup. In addition, we also found a rare mutation-9128T>C (I201T), which presented in homoplasmy only in the maternal lineage. Through the phylogenetic analysis

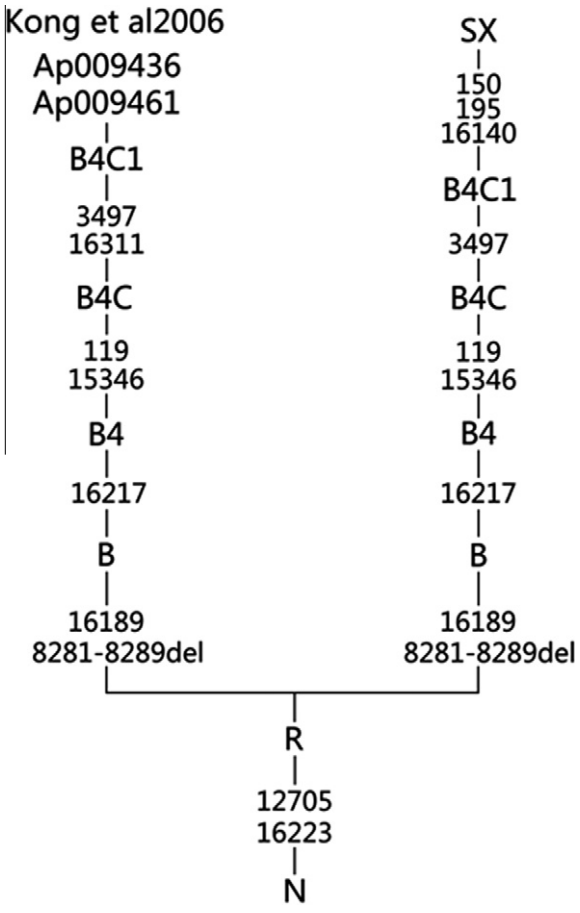


Fig. 4. Classification tree of the pedigree using the mtDNA phylogenetic tree.

among 100 organisms, this position localized at highly conserved nucleotides of ATP6 gene and was strictly conserved among 89 organisms. Since the 9128T>C (I201T) was an unclassified mutation and coexistence with the 1555A>G mutation in all maternal members, it could be speculated that the homoplasmy I201T might affect the phenotype expression and the penetrance of hearing loss. For the nuclear gene GJB2, we did not find significant mutation about it. Indeed, the absence of variant in the GJB2 gene in those subjects with hearing impairment indicated that the GJB2 gene may not be a modifier of the phenotypic effects of the 1555A>G mutation in this pedigree.

In summary, our results systematically indicated that there was a strong correlation between the severity of hearing loss with the 1555A>G mutation load ($r = 0.758$). It suggested that this phenomenon was not only a specific problem just existed in Spanish/European branch, but also existed in the East Asians background. Besides, we found that the levels of 1555A>G mutation of the offspring seemed to be associated with that of their mothers, that maybe exist a regular pattern during the process of the heteroplasmic transmission. Therefore, it has been shown that different mtDNA 1555A>G heteroplasmic levels determined or contributed to variable clinical manifestations and mutation transmission from the mother to their offspring. The mechanisms about how the heteroplasmic 1555A>G mutation segregated and fixed through generation may need further research. Nuclear gene GJB2 may not have effluences on the phenotypic expression of the 1555A>G mutation in this Chinese family. The role of the rare variant mtDNA 9128T>C localized at ATP6 gene seemed to be questionable and need further validation.

Acknowledgment

This project was supported by Science Foundation of Guangdong Province (No. 2009B030801233).

References

[1] D.C. Wallace, Mitochondrial diseases in man and mouse, Science 283 (1999) 1482–1488.
[2] T.R. Prezant, J.V. Agapian, M.C. Bohlman, et al., Mitochondrial ribosomal RNA mutation associated with both antibiotic induced and non-syndromic deafness, Nat. Genet. 4 (1993) 289–294.
[3] G. Matthijs, S. Claes, B. Longo-Bbenza, et al., Non-syndromic deafness associated with a mutation and a polymorphism in the mitochondrial 12S ribosomal RNA gene in a large Zairean pedigree, Eur. J. Hum. Genet. 4 (1996) 46–51.
[4] R.A. Casano, Y. Bykhovskaya, D.F. Johnson, et al., Hearing loss due to the mitochondrial M.1555A>G mutation in Italian families, Am. J. Med. Genet. 79 (1998) 388–391.
[5] X. Estivill, N. Govea, E. Barceló, et al., Familial progressive sensorineural deafness is mainly due to the mtDNA A1555G mutation and is enhanced by treatment with aminoglycosides, Am. J. Hum. Genet. 62 (1998) 27–35.
[6] S. Kupka, T. Tóth, M. Wróbel, et al., Mutation A1555G in the 12S rRNA gene and its epidemiological importance in German Hungarian and Polish patients, Hum. Mutat. 19 (2002) 308–309.
[7] R. Li, G. Xing, M. Yan, et al., Cosegregation of insertion at position 961 with A1555G mutation of mitochondrial 12S rRNA gene in a large Chinese family with maternally inherited hearing loss, Am. J. Med. Genet. 124A (2004) 113–117.
[8] E. Ballana, E. Morales, R. Rabionet, et al., Mitochondrial 12S rRNA gene mutations affect RNA secondary structure and lead to variable penetrance in hearing impairment, BBRC 341 (2006) 950–957.
[9] M. El-Schahawi, A. López de Munain, A.M. Sarrazin, et al., Two large Spanish pedigrees with nonsyndromic sensorineural deafness and the mtDNA mutation at mt 1555 in the 12S rRNA gene: evidence of heteroplasmy, Neurology 48 (1997) 453–456.
[10] F.J. Del Castillo, M. Rodriguez-Ballesteros, Y. Martin, et al., Heteroplasmy for the 1555A>G mutation in the mitochondrial 12 S rRNA gene in six Spanish families with non-syndromic hearing loss, J. Med. Genet. 40 (2003) 632–636.
[11] Y. Bai, Z. Wang, W. Dai, et al., A six-generation Chinese family in haplogroup B4C1C exhibits high penetrance of 1555A>G-induced hearing Loss, BMC Med. Genet. 11 (2010) 129.
[12] Q.S. Ou, Z.J. Cheng, B. Yang, et al., Analysis of the ratio of mitochondrial DNA with A1555G mutant to wild type in deaf patients of Fujian province in China by a new method and its relationship with the severity of hearing loss, Chin. Med. J. 124 (2011) 3347–3352.
[13] H.J. Yuan, J.Y. Cao, W.W. Guo, et al., Mutation analysis of mitochondrial 12S and 16S ribosomal RNA genes for aminoglycoside-induced deafness, Med. J. Chin. PLA. 29 (2004) 587–590.
[14] R.M. Andrews, I. Kubacka, P.F. Chinnery, et al., Reanalysis and revision of the Cambridge reference sequence for human mitochondrial DNA, Nat. Genet. 23 (1999) 147.
[15] E. Ballana, N. Govea, R. de Cid, et al., Detection of unrecognized low-level mtDNA heteroplasmy may explain the variable phenotypic expressivity of apparently homoplasmic mtDNA mutations, Hum. Mutat. 29 (2008) 248–257.
[16] M.J. Rieder, S.L. Taylor, V.O. Tobe, et al., Automating the identification of DNA variations using quality-based fluorescence re-sequencing: analysis of the human mitochondrial genome, Nucleic Acids Res. 26 (1998) 967–973.
[17] Q.P. Kong, H.J. Bandelt, C. Sun, et al., Updating the East Asian mtDNA phylogeny: a pre-requisite for the identification of pathogenic mutations, Hum. Mol. Genet. 15 (2006) 2076–2086.
[18] F. Chen, S.Y. Wang, R.Z. Zhang, et al., Analysis of mitochondrial DNA polymorphisms in Guangdong Han Chinese, Forensic. Sci. Int. Genet. 2 (2008) 150–153.
[19] R. Rossignol, B. Faustin, C. Rocher, et al., Mitochondrial threshold effects, Biochem. 370 (2003) 751–762.
[20] J.M. Van den Ouweland, H.H. Lemkes, W. Ruitenbeek, et al., Mutation in mitochondrial $tRNA^{Leu}$ (UUR) gene in a large pedigree with maternally transmitted type II diabetes mellitus and deafness, Nat. Genet. 1 (1992) 368–371.
[21] C. Olsson, B. Zethelius, M. Lagerström-Fermér, et al., Level of heteroplasmy for the mitochondrial mutation A3243G correlates with age at onset of diabetes and deafness, Hum. Mutat. 12 (1998) 52–58.

Biochemical and Biophysical Research Communications 420 (2012) 913–917

Contents lists available at SciVerse ScienceDirect

Biochemical and Biophysical Research Communications

journal homepage: www.elsevier.com/locate/ybbrc

Hypoxia-inducible Factor 1 regulated ARC expression mediated hypoxia induced inactivation of the intrinsic death pathway in p53 deficient human colon cancer cells

Jin-e Ao [a,1], Liang-hong Kuang [b,1], Yu Zhou [c], Rong Zhao [d], Chang-ming Yang [c,*]

[a] *Department of Pathology, Jingmen Hubei Province First Peoples' Hospital, Jingmen, Hubei, China*
[b] *Department of Neurology, Huangshi Central Hospital, Huangshi, Hubei, China*
[c] *Department of Anesthesiology, Jingmen Hubei Province First Peoples' Hospital, Jingmen, Hubei, China*
[d] *Department of Anesthesiology, Huangshi Central Hospital, Huangshi, Hubei, China*

ARTICLE INFO

Article history:
Received 16 March 2012
Available online 27 March 2012

Keywords:
Hypoxia
HIF-1α
ARC
Colon cancer cells
Apoptosis

ABSTRACT

Apoptosis repressor with caspase recruitment domain (ARC), an anti-apoptotic protein, plays an important role in the regulation of apoptosis by blocking both the extrinsic and intrinsic death pathways. However, its regulatory mechanism remains largely undefined. Here, we reported that hypoxia up-regulated the expression of ARC in p53 deficient human colon cancer cells. Moreover, ARC is a direct target of the *hypoxia-inducible factor 1 (HIF-1)*, a key transcriptional factor for the cellular response to hypoxia. Silencing the expression of HIF-1α in SW480 colon cancer cells by RNA interference abolished hypoxia induced ARC expression. Using luciferase reporter and ChIP assay, we showed that HIF-1α directly bound to hypoxia-responsive element located at −419 to −414 of ARC gene, which is essential for *HIF-1*-induced expression. As a result of the increased ARC expression, TRAIL-induced apoptosis was reduced by hypoxia. These discoveries would shed novel insights on the mechanisms for ARC expression regulation and hypoxia induced inactivation of the intrinsic death pathway.

© 2012 Elsevier Inc. All rights reserved.

1. Introduction

Carcinogenesis often involves defects in apoptosis [1]. Apoptosis is a highly regulated cell suicide process that is mediated through two central pathways: the extrinsic pathway involving death receptors and the intrinsic pathway involving the mitochondria/endoplasmic reticulum [2]. In contrast to most apoptosis inhibitors, which interfere with circumscribed portions of either the extrinsic or intrinsic death pathways, ARC (apoptosis repressor with caspase recruitment domain) antagonizes both central apoptosis pathways [3,4]. ARC suppresses the extrinsic pathway by directly binding to Fas, FADD, and procaspase-8 [3–5]. ARC inhibits the intrinsic pathway by directly binding to Bax and p53 [6]. The ability of ARC to interrupt both extrinsic and intrinsic apoptosis pathways makes it a stronger cell death inhibitor.

Hypoxia is defined as oxygen deficiency in tissues and is common place in solid tumors due to the outgrowth of tumor over supporting vasculature. Intratumoral hypoxia is a hallmark of solid cancer [7]. A hypoxic microenvironment initiates multiple cellular responses, including proliferation and angiogenesis, resulting in the development and progression of cancer. The homeostatic response to hypoxia is predominantly mediated by the transcription factor hypoxia-inducible factor (HIF)-1 which is a heterodimer that consists of a HIF-1α subunit and a HIF-1β subunit [8]. HIF-1β is constitutively expressed and HIF-1α which determines HIF-1 activity is highly regulated within cells in response to hypoxia. Under normoxic conditions, HIF-1α is hydroxylated and degraded rapidly via von Hippel–Lindau (VHL) mediated ubiquitin-proteasome pathway whereas it becomes stabilized and is rapidly accumulated in cell under hypoxic conditions [9]. This active transcription factor recognizes and binds to the hypoxia-response elements. Then HIF-1 activates transcription of its target genes that allow for adaptation to hypoxia [10]. As a result of hypoxia and genetic mutations, HIF-1α is over-expressed in many human cancers [11,12] including colon cancer [13].

Here, we show that both the mRNA and protein levels of ARC are markedly increased in p53 deficient human colon cancer cell lines in response to hypoxia. We also suggest that ARC is a direct target gene of *HIF-1*. As a result of the increased ARC expression, TRAIL-induced apoptosis was reduced by hypoxia. Our findings thus link hypoxia signaling with the ARC anti-apoptosis process, which have profound biological and therapeutic implications for colon cancer.

2. Material and methods

2.1. Cell culture

HT-29, DLD-1, SW620 and SW480 cell lines were cultured in RPMI-1640 or Dulbecco's modified Eagle's medium (Sigma–Aldrich,

* Corresponding author.
E-mail address: hbjmyangcm@hotmail.com (C.-m. Yang).
[1] These authors contributed equally to this article.

0006-291X/$ - see front matter © 2012 Elsevier Inc. All rights reserved.
http://dx.doi.org/10.1016/j.bbrc.2012.03.101

St Louis, MI) supplemented with 10% fetal bovine serum (FBS; Gibco BRL, Gaithersburg, MD). For hypoxic exposure, cells were cultured in a hypoxia incubator (Thermo Electron, Forma, MA) in an atmosphere that consists of 94% N_2, 5% CO_2 and 1% O_2.

2.2. Reagents

The following antibodies were purchased: anti-HIF-1α (Cell Signaling), anti-ARC (Abcam), and anti-actin (Sigma). TRAIL was purchased from Abcam.

2.3. Cell transfection with siRNA

Cells were plated on to six well plates grown to 50% confluence and then transfected with 25 nM siGENOME non-targeting siRNA, human HIF-1α siGENOME SMART pool or human ARC siGENOME SMART pool (Thermo Fisher Scientific) using DharmaFECT 1 transfection reagent according to the manufacturer's protocol. After 24 h incubation under normoxia, the transfection medium was replaced with complete medium and the cells were incubated under hypoxia for the indicated time. Total RNA and cell lysates were collected for Real-time PCR and western blot analysis, respectively.

2.4. RNA extraction, cDNA synthesis and Real-time analysis

Total RNAs were isolated from tissues or cells by TRIzol reagent, and reverse transcriptions were performed by Takara RNA PCR kit (Takara, China) following the manufacturer's instructions. In order to quantitate the transcripts of the interest genes, real-time PCR was performed using a SYBR Green Premix Ex Taq (Takara, Japan) on Light Cycler 480 (Roche, Switzerland). The primer sequences used are available upon request.

2.5. Apoptosis assay

Annexin-V assay was carried out by Annexin V-FITC Apoptosis Detection Kit according to manufacturer's instruction (BD, San Diego, CA). Briefly, cells were collected, washed twice with PBS, resuspended in binding buffer and incubated with Annexin V-FITC at room temperature for 10 min, followed by addition of propidium iodide (PI) for additional 5 min. Fluorescent intensities were determined on flow cytometry (Beckman Coulter, Miami, FL).

2.6. Western blot

Tissues and cells were lysed in radioimmunoprecipitation (RIPA) buffer containing 50 mM Tris–HCl, 150 mM NaCl, 5 mM $MgCl_2$, 2 mM EDTA, 1 mM NaF, 1% NP40 and 0.1% SDS. Protein expression levels were quantitated with use of Image J.

2.7. Luciferase assays

Human ARC promoter was cloned into PGL4.15 plasmid (Promega). All the transient transfections were performed by Lipofectamin 2000 (invitrogen), according to the manufacturer's instructions. For luciferase reporter assay, HEK293T cells were seeded in 24-well plates and transfected with the indicated plasmids. Cells were harvested 36 h after transfection. Luciferase activity was measured using the Dual Luciferase Reporter Assay System (Promega, USA).

2.8. ChIP assays

A chromatin immunoprecipitation (ChIP) assay kit was used (Upstate, USA). In brief, SW480 cells were fixed with formaldehyde. DNA was sheared to fragments at 200–1000 bp using sonications. The chromatin was incubated and precipitated with antibodies

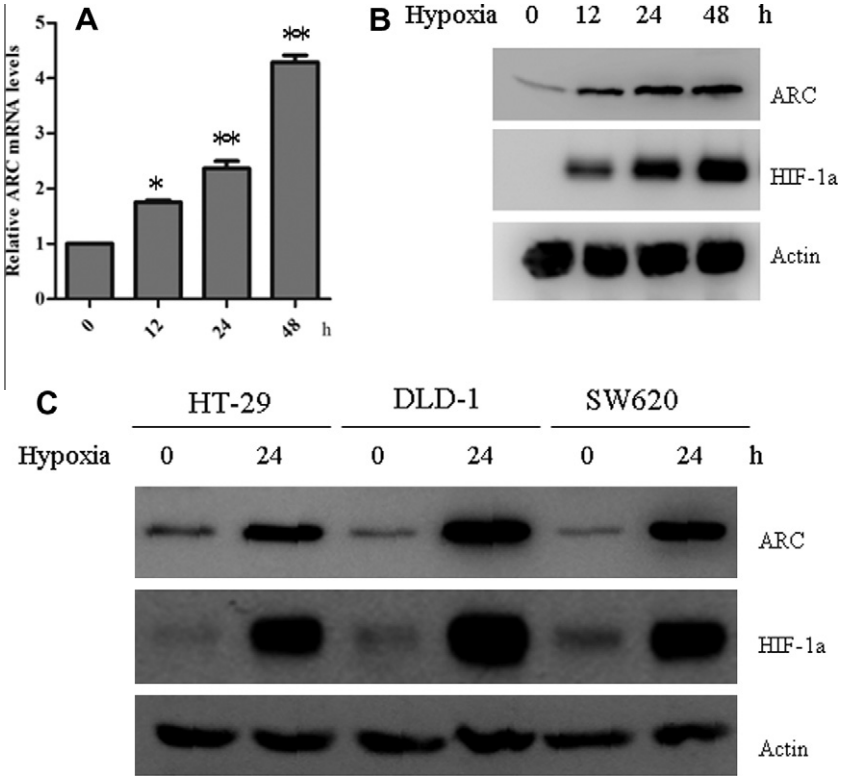


Fig. 1. Hypoxic induces ARC mRNA and protein expression in colon cancer cells. (A) mRNA levels of ARC from SW480 colon cancer cells incubated with 1% O_2 for the indicated time points. (B) SW480 cells were incubated with 1% O_2 for the indicated time points and analyzed by western blot (WB) with the indicated antibodies. (C) HT-29, DLD-1 and SW620 cells were incubated with 1% O_2 for the indicated time points and analyzed by WB with the indicated antibodies.

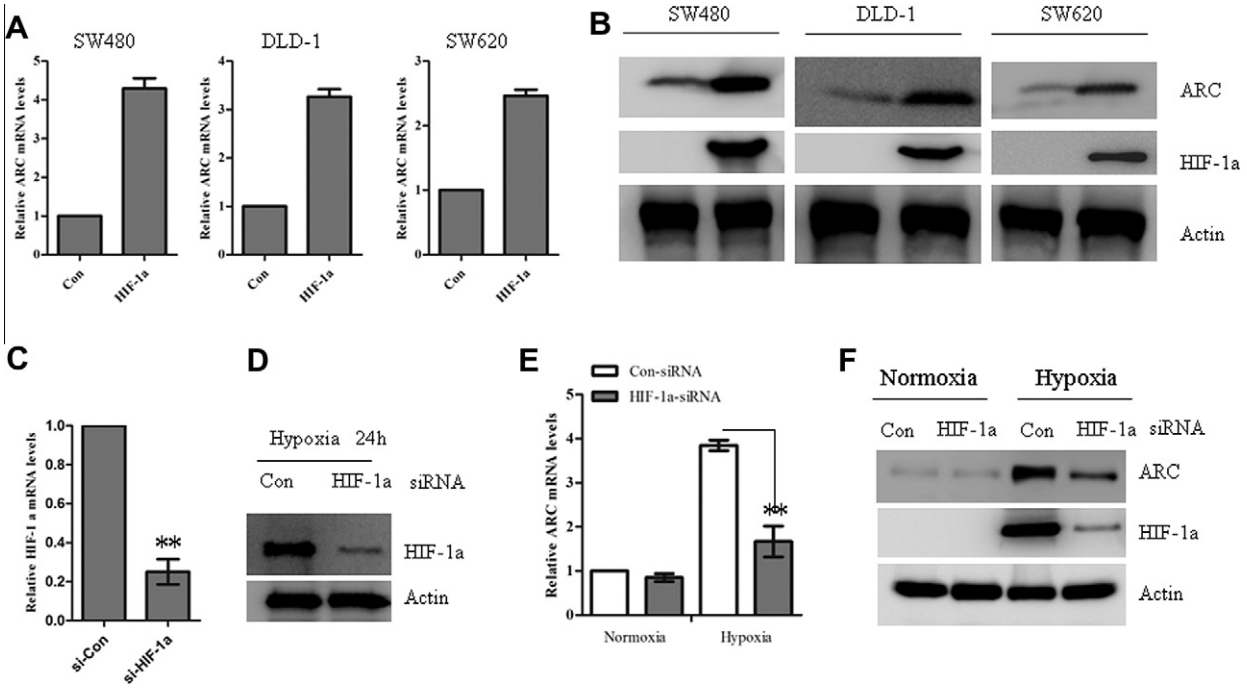


Fig. 2. *HIF-1* mediates hypoxia-induced ARC expression. (A) mRNA levels of ARC from SW480, DLD-1 and SW620 cells transfected with or with HIF-1α. (B) SW480, DLD-1 and SW620 cells were transfected with or with HIF-1α and analyzed by WB with the indicated antibodies. (C) ARC mRNA levels from SW480 cells transfected with non-targeting or HIF-1α siRNAs. (D) ARC protein levels from SW480 cells transfected with non-targeting or HIF-1α siRNAs. (E) SW480 cells transfected with non-targeting or HIF-1α siRNAs were incubated with normoxia or hypoxia, the mRNAs levels of ARC were checked by Realtime-PCR. (F) SW480 cells transfected with non-targeting or HIF-1α siRNAs were incubated with normoxia or hypoxia and analyzed by WB with the indicated antibodies.

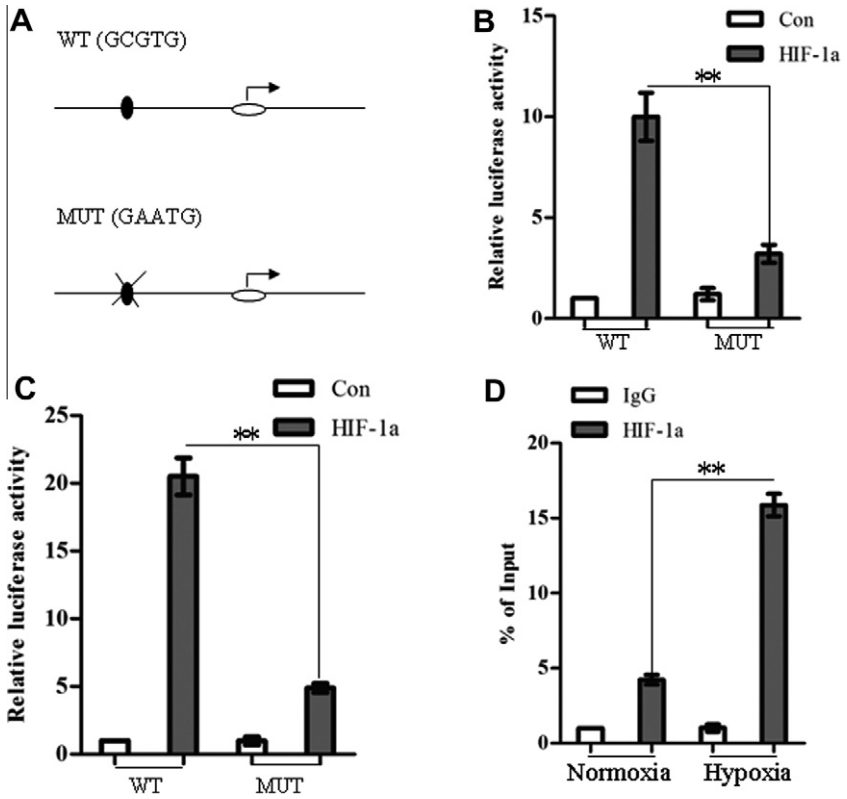


Fig. 3. HIF-1α activates ARC expression through bound to its promoter region. (A) Schematic diagrams of the regulating sequences with the putative HRE (black ovals) of ARC. The empty circles represented their transcriptional start point. Mut: CG was changed into AA. (B) SW480 cells were transfected with the putative ARC HRE-luciferase reporter plasmids in the absence or presence of HIF-1α plasmid. After 36 h of transfection, the luciferase activity was measured using Dual Luciferase Reporter Assay System. Transfection efficiency was normalized by Renilla luciferase expression, and the results are presented as activation over that for an empty vector. (C) The luciferase activity was measured in SW620 cells with the methods described in (B). (D) Two antibodies (anti-IgG and anti-HIF-1α) were used in the ChIP assays using SW480 cells incubated with or without hypoxia.

against the indicated antibodies or IgG (Santa Cruz, USA). Then, Real-time PCR for the HRE in the promotor was performed with specific primers: 5′-agctgctgcacccaccccca-3′ and 5′-tgtcttcttcc ttggtggtc-3′.

2.9. Statistical analysis

Values were shown as mean ± SEM. Statistical differences were determined by a Student's *t* test. Statistical significance is displayed as $^{*}(P < 0.05)$ or $^{**}(P < 0.01)$.

3. Results

3.1. Hypoxia induces ARC mRNA and protein expression in colon cancer cells

Since hypoxia is a common feature of the microenvironment of solid tumors, it is important to detect whether hypoxia promotes the expression of ARC in colon cancer cells. First, SW480 colon cancer cells were incubated with 1% O_2 for different time points and the ARC messenger RNA (mRNA) and protein levels were tested by quantitative Real-time PCR and western blot, respectively. The results showed that both mRNA and protein of ARC were significantly up-regulated by hypoxia in a time-dependent manner (Fig. 1A and B). In order to rule out cell type-specific effect, several colon cancer cell lines including HT-29, DLD-1 and SW620 were incubated with 1% O_2 for 24 h. As shown in Fig. 1B, hypoxia treatment led to the accumulation of ARC in these cells. Taken together, these data suggested hypoxia regulated the expression of ARC in colon cancer cell lines.

3.2. HIF-1 mediates hypoxia-induced ARC expression

HIF-1 is a global transcriptional regulator of the hypoxic response [10]. To test whether HIF-1 also mediates hypoxia-related increase of ARC, HIF-1α-expressing plasmid was transiently transfected into SW480, DLD-1 and SW620 cell lines. Notably, ectopic expression of HIF-1α could significantly up-regulate ARC expression in these cell lines (Fig. 2A and B). To determine the role of *HIF-1* in the regulation of the expression of ARC, SW480 cells were transfected with siRNA targeting HIF-1α or non-targeting siRNA to knock down HIF-1α. The inhibition rate was evaluated by Real-time PCR and western blot (Fig. 2C and D). As expected, ARC mRNA and protein levels were markedly decreased when HIF-1α was silenced under normoxic and hypoxic conditions (Fig. 2E and F).

3.3. HIF-1α activates ARC expression by binding to its promoter region

We next determined whether *HIF-1* could be a transcriptional regulator of ARC gene. There is one potential HRE at 0.4 kb region upstream to the transcription start site of ARC (−419 5′-GCGTG-3′ −414) (Fig. 3A). SW480 cells were transfected with a reporter vector encoding luciferase under control of the ARC promoter (WT-Luc). Concurrent expression of HIF-1α with the ARC reporter construct increased ARC promoter activity, which was abrogated by mutation of this *HIF-1* DNA-binding site (CG-AA) in the ARC promoter (Mut-Luc) (Fig. 3B). The stimulatory effect of HIF-1α on

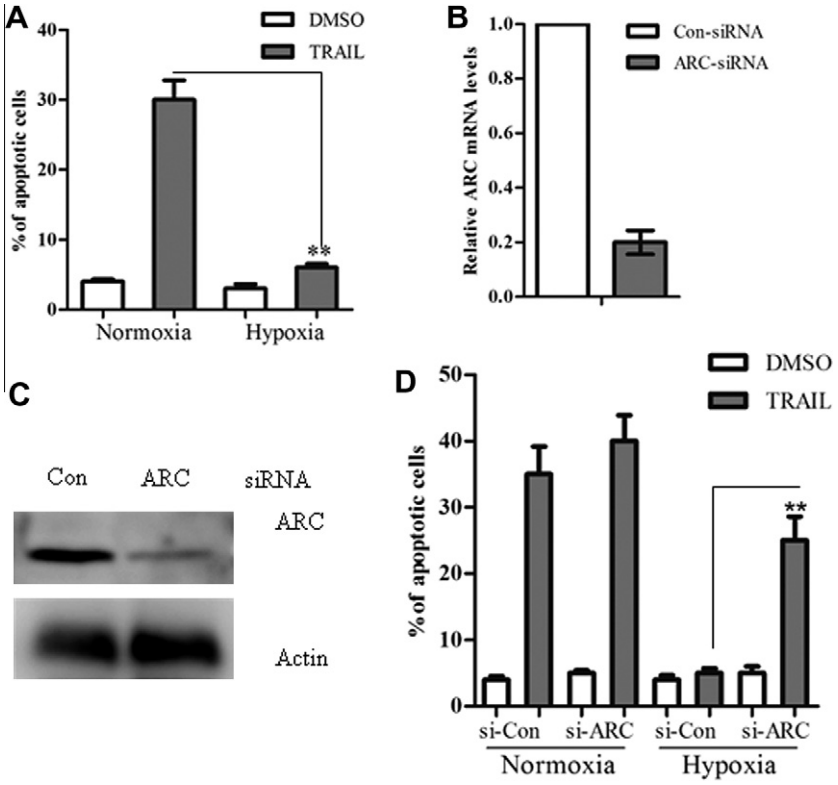


Fig. 4. Hypoxia-inhibited Bax translocation during TRAIL-induced cell death was mediated by ARC. (A) Effect of hypoxia on TRAIL-induced apoptosis. SW480 cells were exposed to normoxia or hypoxia for 24 h and coincubated with recombinant TRAIL protein (200 ng/ml) for 4 h. The apoptotic cells were detected by Annexin-V and PI staining. The data presented the percentages of apoptotic cells. $^{**}p < 0.01$. SW480 cells treated with TRAIL under hypoxia vs normaoxia. (B) ARC mRNA levels from SW480 cells transfected with non-targeting or ARC siRNAs. (C) SW480 cells were transfected with non-targeting or ARC siRNAs and analyzed by WB with the indicated antibodies. (D) SW480 cells transfected with non-targeting or ARC siRNAs were exposed to normoxia or hypoxia for 24 h and coincubated with soluble recombinant human TRAIL (200 ng/ml) for an additional 4 h. The apoptotic cells were detected by Annexin-V and PI staining. The data presented the percentages of apoptotic cells. $^{**}p < 0.01$. SW480 cells transfected with ARC siRNA treated with TRAIL under hypoxia vs SW480 cells transfected with non-targeting siRNA treated with TRAIL under hypoxia.

ARC promoter activity was also shown in SW620 cells (Fig. 3C). We next carried out chromatin immunoprecipitation (ChIP) assays to assess whether HIF-1α directly binds to the ARC promoter region. Indeed, HIF-1α protein bound to the ARC promoter region and this binding was significantly increased in SW480 cells incubated with hypoxia (Fig. 3D).

3.4. Hypoxia-inhibited TRAIL-induced apoptosis was mediated by ARC

Hypoxia inhibits TRAIL-induced apoptosis by blocking the translocation of Bax from cytosol to the mitochondria in tumor cells [14,15]. ARC has been shown to be able to interact with Bax to prevent Bax conformational activation and translocation to the mitochondria [6]. Therefore, we hypothesized that HIF-1α induced ARC expression may contribute to hypoxia inhibited TRAIL-induced apoptosis. In consistent with previous reports, TRAIL induced significant apoptosis in SW480 cells and SW620 cells under normoxia condition, whereas this phenomenon was dramatically abolished when cells were incubated under hypoxia condition (Fig. 4A and data not shown). To investigate whether ARC plays a role in hypoxia-inhibited TRAIL-induced apoptosis, we utilized siRNA to knock down the expression of ARC in SW480 colon cancer cells. The inhibition rate was evaluated by Real-time PCR and western blot (Fig. 4B and C). As depicted in Fig. 4D, ARC silencing significantly inhibited hypoxia-inhibited TRAIL-induced apoptosis. Taken together, our results linked hypoxia response with the ARC anti-apoptosis process.

4. Discussion

In the present study, we show that HIF-1α is required for ARC expression in human colon cancer cells. We provided evidence that ARC is a direct target gene of HIF-1. Hypoxia and ectopically expressed HIF-1α protein significantly increased ARC expression at both mRNA and protein levels in all colon cancer cell lines tested. Then, silencing of HIF-1α by specific siRNA antagonized hypoxia-induced ARC expression. Moreover, using luciferase reporter and ChIP assay, we showed that HIF-1α directly bound to the HRE located at −419 to −414 of ARC gene, which is essential for *HIF-1*-induced expression. As a result of the increased ARC expression, TRAIL-induced apoptosis was reduced by hypoxia.

Because of the unique anti-apoptosis roles of ARC, its expression should be tightly regulated [16]. It has been reported that DNA damage agent doxorubicin and p53 could negatively regulate ARC expression [17]. The ubiquitin E3 ligase MDM2 is also reported to be a critical regulator of ARC at protein level [18]. In order to avoid the regulation of ARC by p53 during hypoxia, in this study we utilized p53 deficient or mutated colon cancers including SW620 and SW480 cells to test the effect of HIF-1α on the regulation of ARC. Interestingly, Ras has been shown to regulate ARC abundance through effects on both transcription and protein stability [19]. Knockdown of endogenous N-Ras in colon cancer cells significantly reduces ARC mRNA and protein levels. Ras also stabilizes ARC protein by suppressing its polyubiquitination and subsequent proteasomal degradation. It would be interesting to understand the role of MDM2 in Ras mediated ARC stabilization.

In summary, these discoveries would shed new insights on the mechanisms for ARC expression regulation and hypoxia induced inactivation of the intrinsic death pathway. Ultimately, these data may provide the rationale for the development of ARC inhibitors as efficient anti-cancer drugs.

References

[1] F.H. Igney, P.H. Krammer, Death and anti-death: tumour resistance to apoptosis, Nat. Rev. Cancer 2 (2002) 277–288.
[2] G. Kroemer, L. Galluzzi, C. Brenner, Mitochondrial membrane permeabilization in cell death, Physiol. Rev. 87 (2007) 99–163.
[3] T. Koseki, N. Inohara, S. Chen, G. Nunez, ARC, an inhibitor of apoptosis expressed in skeletal muscle and heart that interacts selectively with caspases, Proc. Natl. Acad. Sci. USA 95 (1998) 5156–5160.
[4] Y.J. Nam, K. Mani, A.W. Ashton, C.F. Peng, B. Krishnamurthy, Y. Hayakawa, P. Lee, S.J. Korsmeyer, R.N. Kitsis, Inhibition of both the extrinsic and intrinsic death pathways through nonhomotypic death-fold interactions, Mol. Cell 15 (2004) 901–912.
[5] D.G. Jo, J.I. Jun, J.W. Chang, Y.M. Hong, S. Song, D.H. Cho, S.M. Shim, H.J. Lee, C. Cho, D.H. Kim, Y.K. Jung, Calcium binding of ARC mediates regulation of caspase 8 and cell death, Mol. Cell Biol. 24 (2004) 9763–9770.
[6] A.B. Gustafsson, J.G. Tsai, S.E. Logue, M.T. Crow, R.A. Gottlieb, Apoptosis repressor with caspase recruitment domain protects against cell death by interfering with Bax activation, J. Biol. Chem. 279 (2004) 21233–21238.
[7] K. Ruan, G. Song, G. Ouyang, Role of hypoxia in the hallmarks of human cancer, J. Cell Biochem. 107 (2009) 1053–1062.
[8] G.L. Wang, B.H. Jiang, E.A. Rue, G.L. Semenza, Hypoxia-inducible factor 1 is a basic-helix-loop-helix-PAS heterodimer regulated by cellular O2 tension, Proc. Natl. Acad. Sci. USA 92 (1995) 5510–5514.
[9] P.H. Maxwell, M.S. Wiesener, G.W. Chang, S.C. Clifford, E.C. Vaux, M.E. Cockman, C.C. Wykoff, C.W. Pugh, E.R. Maher, P.J. Ratcliffe, The tumour suppressor protein VHL targets hypoxia-inducible factors for oxygen-dependent proteolysis, Nature 399 (1999) 271–275.
[10] A. Zagorska, J. Dulak, HIF-1: the knowns and unknowns of hypoxia sensing, Acta Biochim. Pol. 51 (2004) 563–585.
[11] H. Zhong, A.M. De Marzo, E. Laughner, M. Lim, D.A. Hilton, D. Zagzag, P. Buechler, W.B. Isaacs, G.L. Semenza, J.W. Simons, Overexpression of hypoxia-inducible factor 1alpha in common human cancers and their metastases, Cancer Res. 59 (1999) 5830–5835.
[12] A. Giaccia, B.G. Siim, R.S. Johnson, HIF-1 as a target for drug development, Nat. Rev. Drug Discov. 2 (2003) 803–811.
[13] B. Krishnamachary, S. Berg-Dixon, B. Kelly, F. Agani, D. Feldser, G. Ferreira, N. Iyer, J. LaRusch, B. Pak, P. Taghavi, G.L. Semenza, Regulation of colon carcinoma cell invasion by hypoxia-inducible factor 1, Cancer Res. 63 (2003) 1138–1143.
[14] S.H. Han, M. Kim, K. Park, T.H. Kim, D.W. Seol, Blockade of processing/activation of caspase-3 by hypoxia, Biochem. Biophys. Res. Commun. 375 (2008) 684–688.
[15] M. Kim, S.Y. Park, H.S. Pai, T.H. Kim, T.R. Billiar, D.W. Seol, Hypoxia inhibits tumor necrosis factor-related apoptosis-inducing ligand-induced apoptosis by blocking Bax translocation, Cancer Res. 64 (2004) 4078–4081.
[16] C.M. Medina-Ramirez, S. Goswami, T. Smirnova, D. Bamira, B. Benson, N. Ferrick, J. Segall, J.W. Pollard, R.N. Kitsis, Apoptosis Inhibitor ARC Promotes Breast Tumorigenesis, Metastasis, and Chemoresistance, Cancer Res. 71 (2011) 7705–7715.
[17] Y.Z. Li, D.Y. Lu, W.Q. Tan, J.X. Wang, P.F. Li, p53 initiates apoptosis by transcriptionally targeting the antiapoptotic protein ARC, Mol. Cell Biol. 28 (2008) 564–574.
[18] R.S. Foo, L.K. Chan, R.N. Kitsis, M.R. Bennett, Ubiquitination and degradation of the anti-apoptotic protein ARC by MDM2, J. Biol. Chem. 282 (2007) 5529–5535.
[19] L. Wu, Y.J. Nam, G. Kung, M.T. Crow, R.N. Kitsis, Induction of the apoptosis inhibitor ARC by Ras in human cancers, J. Biol. Chem. 285 (2010) 19235–19245.

Biochemical and Biophysical Research Communications 420 (2012) 918–925

Contents lists available at SciVerse ScienceDirect

Biochemical and Biophysical Research Communications

journal homepage: www.elsevier.com/locate/ybbrc

Porphyromonas gingivalis lipopolysaccharide induces miR-146a without altering the production of inflammatory cytokines

Tomoyuki Honda, Naoki Takahashi, Sayuri Miyauchi, Kazuhisa Yamazaki *

Center for Transdisciplinary Research, Niigata University, Niigata, Japan
Laboratory of Periodontology and Immunology, Department of Oral Health and Welfare, Niigata University, Faculty of Dentistry, Niigata, Japan

ARTICLE INFO

Article history:
Received 16 March 2012
Available online 27 March 2012

Keywords:
miR-146a
Porphyromonas gingivalis
LPS
THP-1

ABSTRACT

Lipopolysaccharide (LPS) from *Porphyromonas gingivalis*, an oral Gram-negative bacterium, acts as a virulence factor for periodontal disease. Although *P. gingivalis* LPS does not induce proinflammatory cytokines as strongly as *Escherichia coli* LPS, it is still able to exploit negative Toll-like receptor (TLR) regulatory pathways and facilitate pathogen persistence. Recent reports suggest that microRNAs (miRNAs) are also involved in the regulation of TLR signaling. Here, we demonstrate that *P. gingivalis* LPS strongly induces miRNA-146a expression in THP-1 cells and THP-1-derived macrophages. However, the inhibition or overexpression of miR-146a, through the transfection of a specific inhibitor or precursor, respectively, had little effect on cytokine production in macrophages stimulated with *P. gingivalis* LPS. Moreover, the expression of interleukin-1 associated-kinase-1 (IRAK-1) and tumor-necrosis factor (TNF) receptor-associated factor-6 (TRAF6), potential target molecules of miR-146a, were not affected by the stimulation with *P. gingivalis* LPS. Because TLR signaling induces various negative regulators, these results call into question the role of miR-146a in cells stimulated with TLR ligands.

© 2012 Elsevier Inc. All rights reserved.

1. Introduction

The inflammatory response is central to effective host defense against invading pathogens that are primarily recognized by Toll-like receptors (TLRs). TLRs activate signaling pathways that induce the expression of immune and proinflammatory genes. However, an uncontrolled inflammatory response resulting in the inappropriate production of proinflammatory cytokines is detrimental to the host cells. Therefore, TLR signaling is tightly regulated at multiple levels by various negative regulators, such as interleukin-1 associated-kinase-M (IRAK-M) and suppressor of cytokine signaling-1 (SOCS1) [1,2].

In a previous study, we demonstrated that lipopolysaccharide (LPS) from *Porphyromonas gingivalis*, a common periodontopathic bacterium, specifically induced IRAK-M, which then suppressed the dissociation of IRAK-1 from its receptor complex, resulting in escape from subsequent degradation [3]. During chronic infection with this bacterium in periodontal tissue, this activity may serve as a mechanism of escape from immune surveillance. In addition, *P. gingivalis* can instigate subversive crosstalk between TLR2 and other innate receptors to blunt the antimicrobial response mediated by TLR2 [4]. These findings suggest that *P. gingivalis* has evolved to evade host immune systems.

MicroRNAs (miRNAs) are a newly identified class of endogenous small (18–25 nt long) noncoding RNAs that post-transcriptionally regulate gene expression by forming imperfect base pairs with sequences in the 3′ UTR of target mRNAs to prevent protein synthesis by repressing translation or inducing mRNA degradation [5,6]. More than 1000 miRNAs have been identified in mammals (miRBase v.18) [7], and they have been found to be associated with diverse biological processes, such as cell differentiation, metabolism, tumorigenesis, and immunity [8–10]. During innate immune response activation in response to enterobacterial LPS, changes in the expression of selected miRNAs, namely miR-146a [11], miR-155 [12], and miR-9 [13], have been observed in monocytic cell lines and mouse macrophages. These events could be involved in the negative regulation of TLR-signaling pathways, which is followed by the suppression of the inflammatory response. However, only limited data are available that describe the effects of *P. gingivalis* on the expression of miRNAs, particularly miR-146a. Nahid et al. demonstrated that *P. gingivalis* LPS continuously amplified the miR-146a level, which is inversely correlated to TNF-α production in THP-1 monocytes [14]. The same group showed that oral inoculation with a combination of *P. gingivalis*, *Treponema denticola* and *Tannerella forsythia* induced elevated expression of miR-146a in the maxillae and spleens of infected mice, and the expression of miR-146a was negatively correlated with that of TNF-α [15].

* Corresponding author. Address: Laboratory of Periodontology and Immunology, Department of Oral Health and Welfare, Niigata University, Faculty of Dentistry, 5274 Gakkocho 2-ban-cho, Chu-o-ku, Niigata 951-8514, Japan. Fax: +81 25 227 0744.
E-mail address: kaz@dent.niigata-u.ac.jp (K. Yamazaki).

0006-291X/$ - see front matter © 2012 Elsevier Inc. All rights reserved.
http://dx.doi.org/10.1016/j.bbrc.2012.03.102

To further clarify the role of miR-146a in periodontitis, the effect of *P. gingivalis* LPS on the expression of miR-146a was examined in THP-1 monocytes, and the subsequent effect of miR-146a on proinflammatory cytokine expression was analyzed by loss- and gain-of-function experiments. Interestingly, although *P. gingivalis* LPS upregulated the expression of miR-146a in THP-1 monocytes, the induction of miR-146a did not strongly suppress the production of proinflammatory cytokines.

2. Materials and methods

2.1. Reagents and antibodies

LPS from *P. gingivalis* 381 was kindly provided by Hidefumi Kumada and Toshio Umemoto (Department of Microbiology, Kanagawa Dental University, Yokosuka, Japan), and the LPS from *Escherichia coli* O111:B4 and phorbol myristic acetate (PMA) were purchased from Sigma–Aldrich (St. Louis, MO). $Pam_3CysSerLys4$ (Pam_3CSK4) was purchased from EMC microcollections (Tübingen, Germany). Anti-miR miRNA Inhibitors and Pre-miR miRNA Precursor Molecules were purchased from Ambion (Austin, TX). Anti-human IRAK-1 (H-273), anti-human TRAF6 (H-274, Santa Cruz Biotechnology, Santa Cruz, CA), anti-human GAPDH (ab8245; Abcam, Cambridge, UK), and the ECL Plus Western Blotting Reagent Pack (GE Healthcare, Buckinghamshire, UK) were used for Western blotting.

2.2. Cell preparation and culture

The monocytic cell line THP-1, maintained as described previously [3], was incubated in a 24-well culture plate (TPP, Trasadingen, Switzerland) at a concentration of 1×10^6 cells/ml in medium without FCS. After 12 h of incubation, the cells were stimulated with various doses of *P. gingivalis* LPS (0.001–10 μg/ml) for 4, 8 and 12 h or other TLR ligands (1.0 μg/ml) for 8 h.

For miRNA loss- and gain-of-function experiments, THP-1 cells were incubated for 48 h in a 24-well culture plate at a concentration of 5×10^5 cells/ml in medium supplemented with 10 ng/ml PMA to induce differentiation into macrophage-like cells (hereafter referred to as "macrophages") prior to stimulation.

2.3. miRNA microarray analysis

Total RNA was isolated from unstimulated and stimulated THP-1 cells using TRIzol reagent (Invitrogen, Carlsbad, CA). The RNA samples were labeled and hybridized using a commercial kit (Agilent Technologies, Santa Clara, CA) according to the manufacturer's protocol. Hybridization was carried out on Agilent human miRNA microarrays (Release 12.0), which were subsequently scanned with an Agilent DNA Microarray Scanner (model G2565CA).

2.4. Quantification of miRNA and mRNA expression

For quantitative analysis of miRNA expression, real-time RT-PCR was performed using the TaqMan MicroRNA Reverse Transcription Kit, the TaqMan microRNA Assay (primer/probe sets for miRNAs) and the TaqMan Universal PCR Master Mix (Applied Biosystems, Foster City, CA) according to the manufacturer's protocols.

For mRNA analysis, cDNA was synthesized as described previously [3], and amplified using TaqMan Gene Expression Assay primer/probe sets for mRNAs (Applied Biosystems) and EagleTaq Master Mix (Roche Molecular Systems, Branchburg, NJ) according to the manufacturers' instructions.

PCR reactions were conducted using the ABI PRISM 7900 HT sequence detection system (Applied Biosystems) and ABI PRISM SDS 2.0 software (Applied Biosystems). The relative expression level of each miRNA and mRNA was normalized to that of the appropriate internal control (RNU44 for miRNA, GAPDH for mRNA) using the $2^{-\Delta\Delta}C_t$ cycle threshold method [16].

2.5. Transfection with miRNA inhibitor and precursor

Macrophages were washed extensively with RPMI 1640 and cultured further in medium without FCS and antibiotics for 12 h. The cells were then transfected with 50 nM inhibitor for 8 h or 50 nM precursor for 24 h using siPORT NeoFX Transfection Agent (Ambion) according to the manufacturer's instructions, followed by exposure to stimulants for various lengths of time at a concentration of 0.1 μg/ml. Random-sequence inhibitors or precursors were transfected as matched controls. The doses of the inhibitor and precursor were selected based on preliminary experiments.

2.6. Western blotting

The cells were washed twice with ice-cold PBS, and the protein was extracted using M-PER Mammalian Protein Extraction Reagent supplemented with Halt Protease Inhibitor Cocktail and Halt Phosphatase Inhibitor Cocktail (Pierce Biotechnology, Rockford, IL, USA). The protein concentration was determined using the Pierce BCA Protein Assay Kit (Pierce Biotechnology).

Ten micrograms of each sample was solubilized by SDS sample buffer, separated by SDS–PAGE, transferred to PVDF membranes (Millipore Co., Bedford, MA), and Western blotted with each antibody. The proteins were detected using ECL Plus Western blotting detection reagents (GE Healthcare) and a LumiVision PRO 400EX (Aisin Seiki, Aichi, Japan).

2.7. Cytokine assay

The levels of TNF-α, IL-1β and IL-6 in the supernatants of each macrophage culture were determined using commercially available ELISA kits (Pierce Biotechnology) according to the manufacturer's instructions.

2.8. Statistical analysis

All experiments were performed in triplicate or quadruplicate wells for each set of conditions and were repeated at least twice. The results were expressed as the mean ± standard deviation (SD). When two groups were compared, an unpaired *t*-test was used. Multiple comparisons were performed by ANOVA-Williams test. Probability values of <0.05 were considered statistically significant.

3. Results

3.1. miRNA expression profile in P. gingivalis LPS-stimulated THP-1 cells

Microarray analysis demonstrated that eight miRNAs were upregulated, and two miRNAs were downregulated, with a greater than 2-fold change compared with unstimulated controls. Among the upregulated miRNAs, miR-146a was substantially and significantly induced by stimulation with *P. gingivalis* LPS ($p = 0.00137$, unpaired *t*-test). Although the expression level of miR-155 was relatively high relative to that of other miRNAs, the stimulatory effect of *P. gingivalis* LPS was very weak (Supplementary Fig. 1).

Consistent with the microarray findings, quantitative RT-PCR demonstrated that the expression of miR-146a was increased by *P. gingivalis* LPS in a dose- and time-dependent manner, with the

maximal response observed at a dose of 1 μg/ml LPS and stimulation for 8 h (Fig. 1A). Although the rate of upregulation by *P. gingivalis* LPS tended to be higher than that induced by the same dose of *E. coli* LPS, no significant difference was observed between the effects of *P. gingivalis* and *E. coli* (Fig. 1B). Furthermore, although the expression of miR-155 was also elevated by stimulation with *P. gingivalis* LPS, the degree of elevation was much lower than that of miR-146a (Fig. 1B). Therefore, only miR-146a was analyzed further.

3.2. The effects of miR-146a on P. gingivalis LPS-induced inflammatory cytokines

To clarify the functional role of miR-146a in the production of inflammatory cytokines in response to *P. gingivalis* LPS, we performed loss- and gain-of-function experiments using a miR-146a inhibitor and a miR-146a precursor, respectively. To activate the inflammatory response to *P. gingivalis* LPS, we used THP-1-derived macrophages. The constitutive expression of miR-146a in THP-1 cells was increased by 7-fold by differentiation (data not shown).

Transfection with a miR-146a inhibitor modestly decreased the constitutive expression of miR-146a compared to transfection with a control inhibitor. The stimulatory effect of *P. gingivalis* LPS on miR-146a expression was significantly suppressed (Fig. 2A). There were, however, no apparent effects of miR-146a knockdown on the mRNA or protein levels of inflammatory cytokines that are induced by *P. gingivalis* LPS and other TLR ligands (Fig. 2B and Supplementary Fig. 2B). TNF-α mRNA and IL-6 protein levels were rather slightly, but significantly downregulated when stimulated with *P. gingivalis* LPS (at 4 and 12 h, respectively; Fig. 2B).

Transfection with a miR-146a precursor significantly increased the expression of endogenous miR-146a (Fig. 3A and Supplementary Fig. 3A). The overexpression of miR-146a significantly reduced the stimulatory effects of *P. gingivalis* LPS on the IL-6 mRNA levels at 8 and 12 h but not the stimulatory effects on the TNF-α or IL-1β mRNA levels at all stimulation times. As with the mRNA levels, the protein levels of IL-6 were significantly lower in the miR-146a precursor-transfected culture compared with the control precursor-transfected culture. The IL-1β protein levels were only affected by the overexpression of miR-146a at the 12 h stimulation. In contrast, the TNF-α protein levels were significantly downregulated by miR-146a overexpression by the stimulation with *P. gingivalis* LPS, despite few change of the mRNA levels (Fig. 3B). Similar findings were observed for the stimulation by other TLR ligands (Supplementary Fig. 3B).

3.3. Effects of miR-146a on the expression of IRAK-1 and TRAF6

IRAK-1 and TRAF6 have been identified as potential molecular targets of miR-146 through experiments with 3′ UTR luciferase

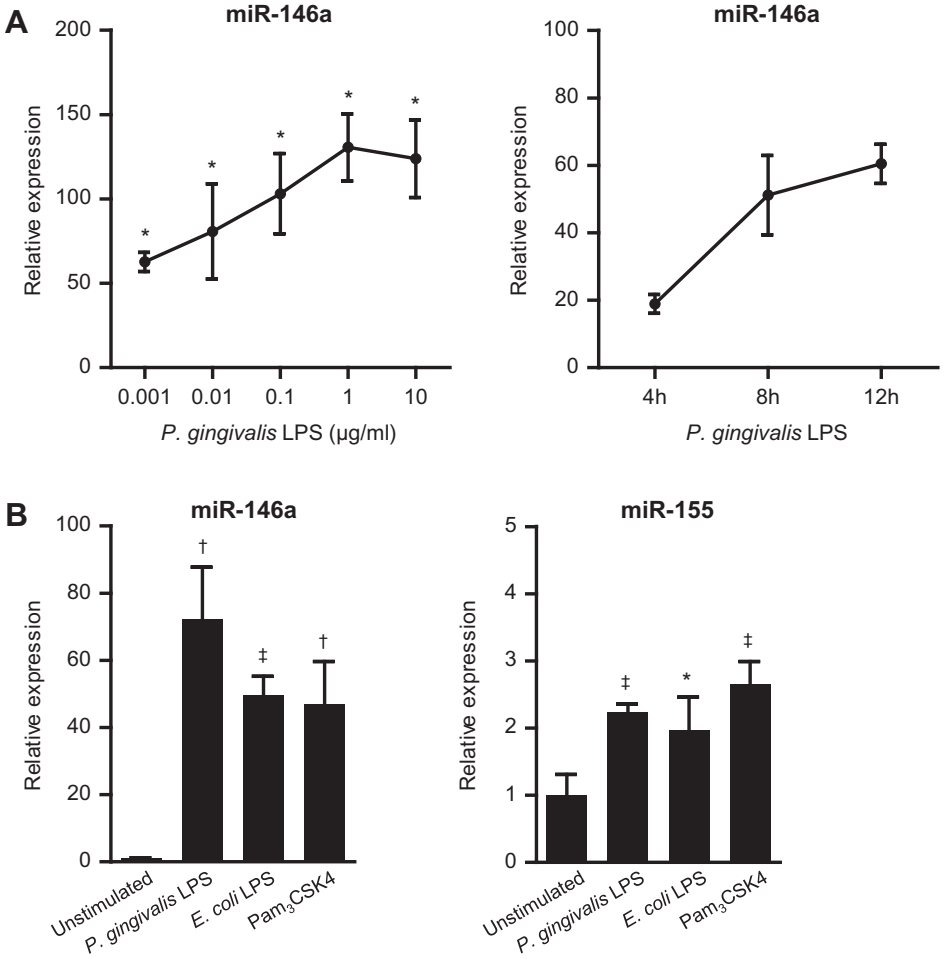


Fig. 1. The effects of stimulation with *P. gingivalis* LPS or TLR ligands on the expression of miRNAs in THP-1 cells. (A) After stimulation with various doses of *P. gingivalis* LPS for 8 h (left) or 1 μg/ml of *P. gingivalis* LPS for the indicated times (right), miR-146a expression was analyzed by quantitative RT-PCR. (B) After stimulation with the indicated stimulants at a concentration of 1 μg/ml for 8 h, the expression levels of miR-146a and miR-155 were analyzed by quantitative RT-PCR. The results shown are the mean ± SD of triplicate cultures from a representative experiment. The expression levels of the miRNAs in unstimulated cultures were set to one. $^{*}p < 0.05$; $^{\dagger}p < 0.005$; $^{\ddagger}p < 0.0005$ vs. unstimulated cultures.

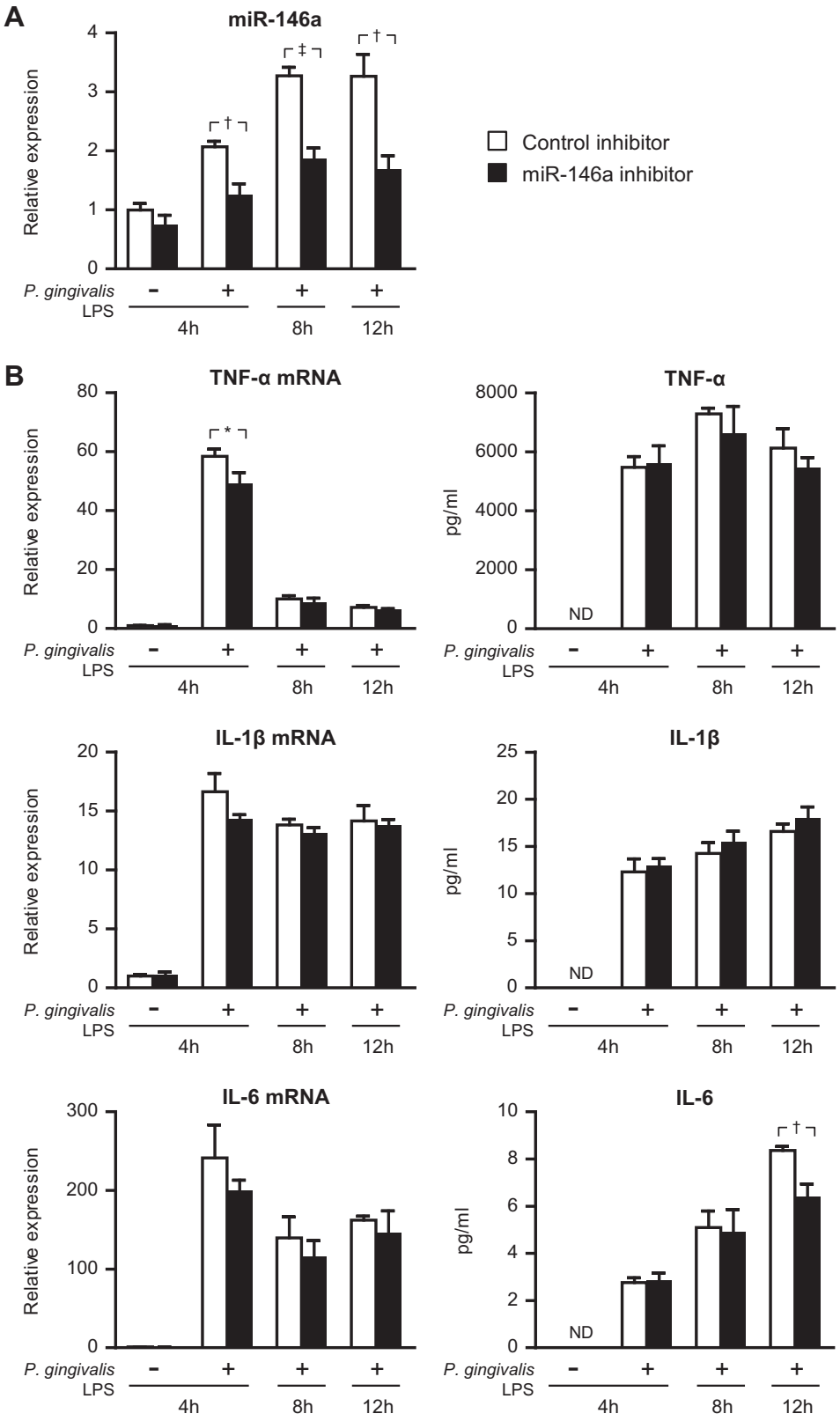


Fig. 2. Specific suppression of miR-146a by transfection of a miR-146a inhibitor and the effects of miR-146a on the production of inflammatory cytokines. Macrophages were transfected with a negative control inhibitor or a miR-146a-specific inhibitor at a concentration of 50 nM for 8 h and then were stimulated with 0.1 μg/ml of *P. gingivalis* LPS for the indicated times. The expression levels of the miR-146a, TNF-α, IL-1β and IL-6 mRNAs were analyzed by quantitative RT-PCR (A and B). The levels of TNF-α, IL-1β and IL-6 in the culture supernatants were analyzed by ELISA (B). The results shown are the mean ± SD of triplicate cultures from a representative experiment. The expression levels in unstimulated cultures were set to one. $^{*}p < 0.05$; $^{\dagger}p < 0.005$; $^{\ddagger}p < 0.0005$. ND, not detected.

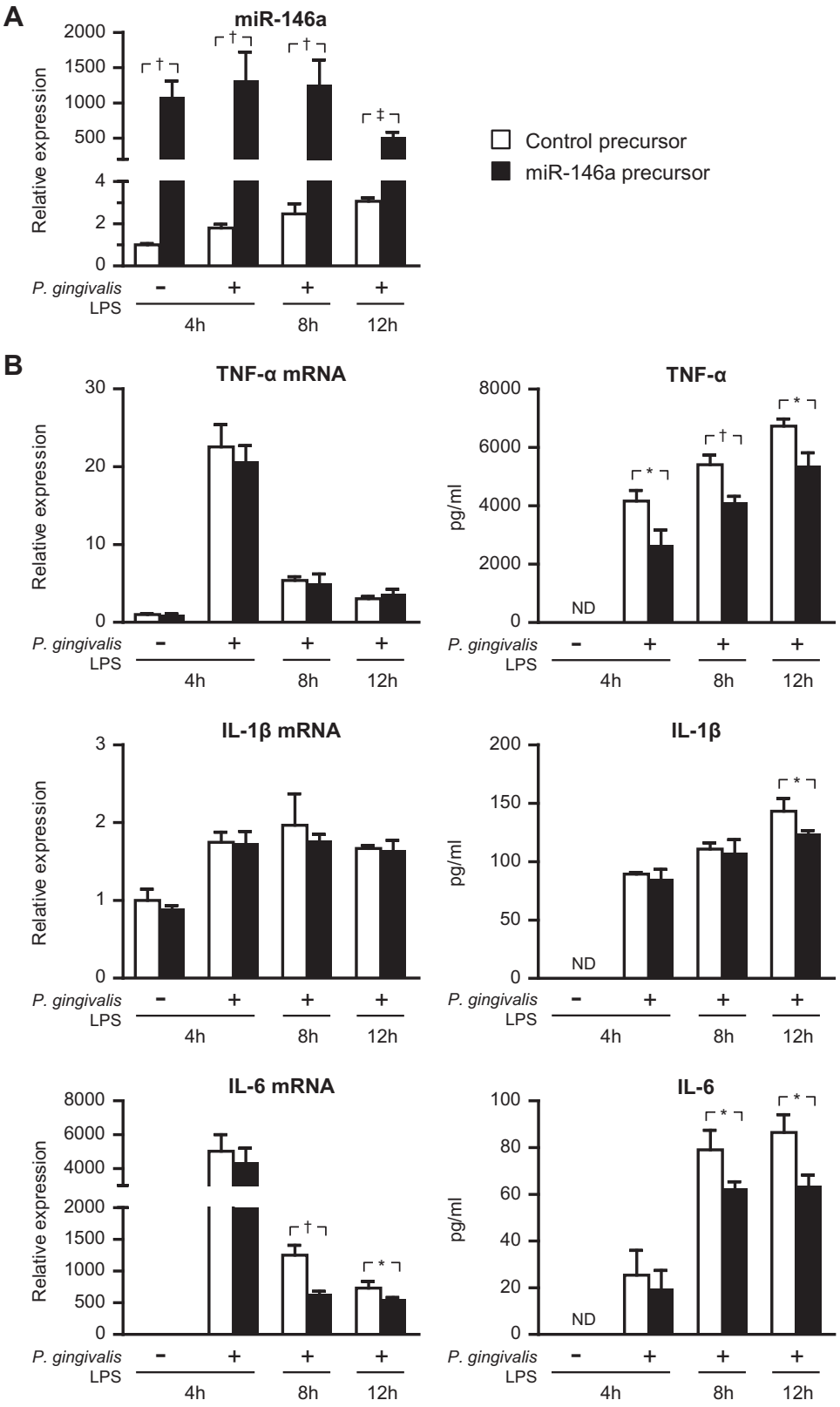


Fig. 3. Overexpression of miR-146a by transfection with a miR-146a precursor and its effects on the production of inflammatory cytokines. Macrophages were transfected with a negative control precursor or a miR-146a precursor at a concentration of 50 nM for 24 h and then were stimulated with 0.1 μg/ml of *P. gingivalis* LPS for the indicated times. The expression levels of the miR-146a, TNF-α, IL-1β and IL-6 mRNAs were analyzed by quantitative RT-PCR (A and B). The levels of TNF-α, IL-1β and IL-6 in the culture supernatants were analyzed by ELISA (B). The results shown are the mean ± SD of triplicate cultures from a representative experiment. The gene expression levels in unstimulated cultures were set to one. $^{*}p < 0.05$; $^{\dagger}p < 0.005$; $^{\ddagger}p < 0.0005$. ND, not detected.

reporters. Therefore, we investigated whether miR-146a negatively regulates the expression of IRAK-1 and TRAF6 and subsequent cytokine production in *P. gingivalis* LPS-stimulated macrophages.

As shown in Fig. 4A, macrophages transfected with a miR-146a inhibitor exhibited no apparent changes in the mRNA levels of IRAK-1 and TRAF6, with or without stimulation. Although there were subtle but significant changes in the IRAK-1 and TRAF6 mRNA levels after transfection with miR-146a in some cases, these changes were not reflected in the protein levels (Fig. 4B).

Transfection with the miR-146a precursor did not affect the IRAK-1 or TRAF6 mRNA or protein levels (Fig. 4C and D), but this transfection did attenuate the level of cytokine production in re-

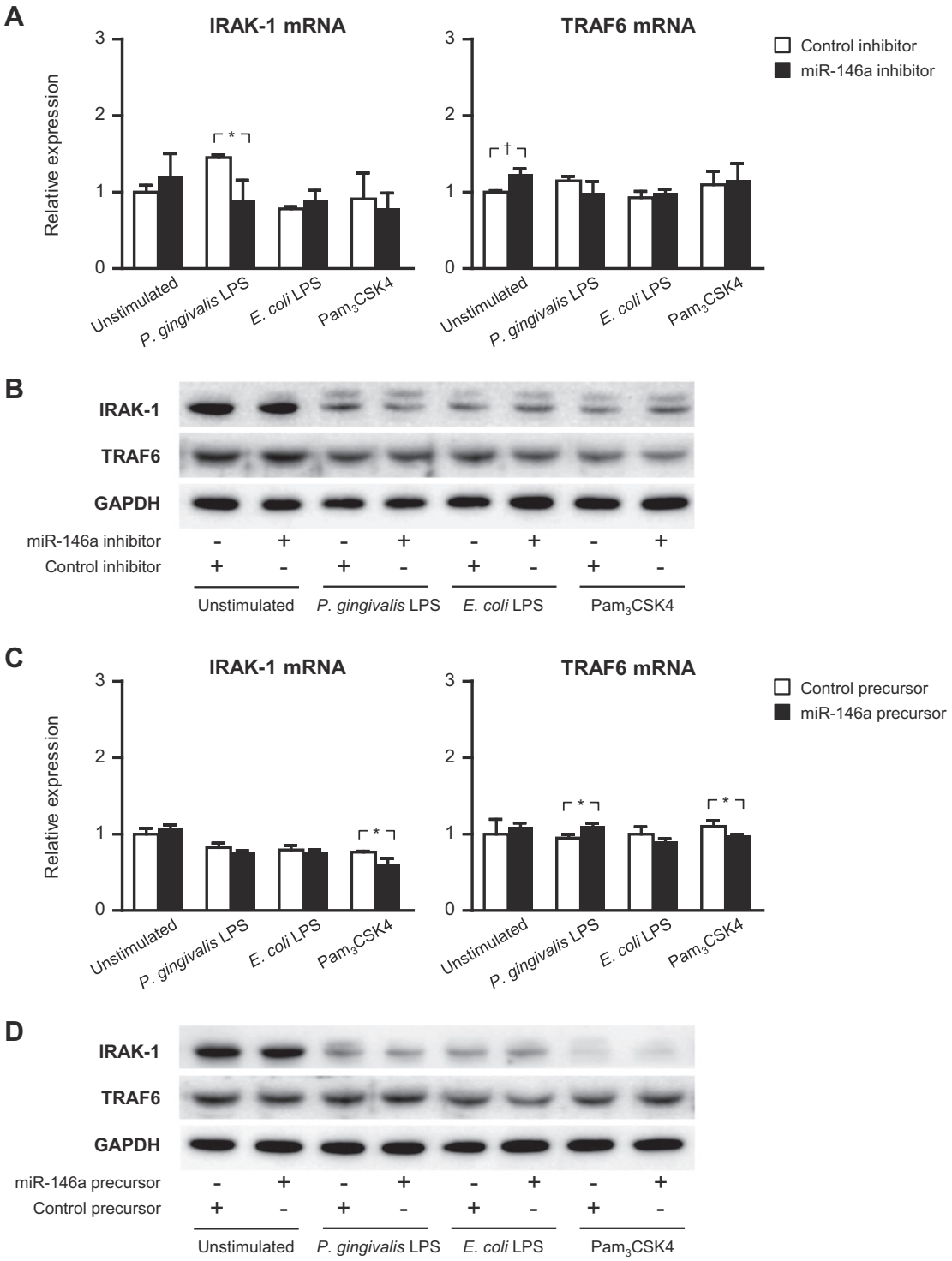


Fig. 4. The effects of miR-146a on the expression of IRAK-1 and TRAF6. Macrophages were transfected with a negative control inhibitor or a miR-146a-specific inhibitor (A and B) or with a negative control precursor or a miR-146a precursor (C and D). After transfection, the cells either were left unstimulated or were stimulated with the indicated stimulants at a concentration of 0.1 μg/ml for 8 h. The mRNA and protein levels of IRAK-1 and TRAF6 were analyzed by quantitative RT-PCR (A and C) and Western blotting (B and D), respectively. The results shown are the mean ± SD of triplicate cultures from a representative experiment. The gene expression levels in unstimulated cultures were set to one. $^{*}p < 0.05$; $^{\dagger}p < 0.005$.

sponse to stimulation with *P. gingivalis* LPS and other TLR ligands (Fig. 3B and Supplementary Fig. 3B).

4. Discussion

P. gingivalis pathogenicity is partly attributed to mechanisms that disturb the host immune response by upregulating a negative regulator of TLR signaling, IRAK-M [3], or by exploiting the complement system [17]. Recent work has shown that miRNAs not only participate in the regulation of developmental events, but also affect the outcome of immune responses to infection [10]. Therefore, we assumed that miRNA expression induced by *P. gingivalis* infection might be exploited to ensure the survival of this bacterium in the periodontium, resulting in low-grade but sustained inflammation.

As observed after *E. coli* LPS stimulation [11], miR-146a was the most prominent miRNA induced in THP-1 cells by stimulation with *P. gingivalis* LPS. However, in contrast to *E. coli* LPS, *P. gingivalis* LPS did not affect miR-132 and miR-155 expression in stimulated THP-1 cells. Moreover, the stimulatory effect of *P. gingivalis* LPS on miR-146a expression tended to be greater than that of *E. coli* LPS. Thus, different LPSs may modulate cell function by inducing different miRNAs, and this difference may be dependent on cell type.

miR-146a was first identified by Taganov et al. and was suggested to be an endotoxin-responsive gene that controlled TLR and cytokine signaling by downregulating IRAK-1 and TRAF6 [11]. Several reports support a regulatory mechanism that functions through negative feedback regulation in various infection models. Although our results showing that *P. gingivalis* LPS upregulates miR-146a in monocytes are consistent with those of Nahid et al. [14], these functional analyses of *P. gingivalis* LPS-induced miR-146a demonstrated quite different findings. Nahid et al. showed that the upregulation of miR-146a by *P. gingivalis* LPS was negatively correlated with TNF-α release from THP-1 cells, whereas our results demonstrated essentially no effect of miR-146a induction on TNF-α expression at either the mRNA or protein level. One possible reason for this discrepancy is that the effect of miR-146a was assayed in macrophages derived by differentiation from THP-1 cells in our study, whereas Nahid et al. used undifferentiated cells. The induction of differentiation using PMA elevated the miR-146a expression by 7-fold. This could explain the lower suppressive effect (approximately 50%) of miR-146a inhibitor transfection in our study relative to that observed for the same treatment in THP-1 cells, in which the inhibition efficiency of even the lower inhibitor concentration (40 nM vs. 50 nM) was >90% [14].

In a pioneering study [11], the function of miR-146a was predicted by searching for target sequences and subsequently analyzing the post-transcriptional repression of the target molecules using reporter assays. However, the downstream cytokine production was not analyzed. In the present study, functional analyses revealed that the suppression of miR-146a had almost no effect on the production of proinflammatory cytokines in macrophages. In line with our results, Liu et al. demonstrated that infection of the gastric epithelium cell line GES-1 with *Helicobacter pylori* upregulated miR-146a expression but that transfection of an miR-146a inhibitor did not affect infection-induced IL-8, MIP-3α, or GRO-α mRNA expression [18]. In contrast, Nahid et al. showed that the inhibition of miR-146a expression increased the TNF-α response to TLR ligands, including *P. gingivalis* LPS at a concentration of 1 μg/ml, by approximately 20% [14]. Although these findings seem to be contradictory to our results, there are several important differences between the two studies. Notably, the dose of *P. gingivalis* LPS used in their study was 10-fold higher than that used in our study, and macrophages are more responsive to TLR ligands than are THP-1 cells. As mentioned above, basal miR-146a expression may be much higher in macrophages than in undifferentiated monocytes, and the effects of miR-146a inhibitor transfection may therefore be diminished in macrophages.

It has been reported that the overexpression of miR-146a through precursor transfection effectively suppresses proinflammatory cytokine production in *P. gingivalis* LPS-stimulated THP-1 cells [14] and *H. pylori*-infected GES-1 cells [18]. In the present study, although transfection with the miR-146a precursor effectively upregulated the expression of functional miR-146a by >1000-fold, the degree of suppression of cytokine production was less than the >50% suppression observed in other studies. The precise reasons for this difference are not clear but may be related to differences in cell type and differentiation stage.

The mechanisms by which miR-146a suppresses TLR signaling are reported to involve the downregulation of IRAK-1 and TRAF6 [19]. Therefore, it is important to confirm that *P. gingivalis* LPS-induced miR-146a is involved in this process. In the present study, although miR-146a inhibitor transfection significantly downregulated the level of IRAK-1 mRNA expression, this change was not obviously reflected at the protein level in *P. gingivalis* LPS-stimulated macrophages, and no change in TRAF6 mRNA or protein expression was observed. The pattern of IRAK-1 protein expression observed in our study is consistent with that reported by Nahid et al., who showed that there was no difference in IRAK-1 protein levels between unstimulated and *P. gingivalis* LPS-stimulated THP-1 cells [14]. The same group also demonstrated that stimulation with *Salmonella* LPS induced robust miR-146a expression and a concomitant decrease in the IRAK-1 protein level in THP-1 cells [20]. The difference in IRAK-1 protein expression between *P. gingivalis* LPS-stimulated macrophages and *Salmonella* LPS-simulated THP-1 cells could be due to a difference in the IRAK-M-inducing activity of the LPSs of the two bacteria. IRAK-M is a negative regulator of the TLR signaling pathway in monocytes and macrophages [21]. During TLR signal transduction, IRAK-1 is phosphorylated by IRAK-4 and then, together with transiently associated TRAF6, translocates to the cell membrane, where it is subsequently degraded [22]. Therefore, LPS stimulation of TLR-expressing cells results in a reduction in the level of IRAK-1 protein, irrespective of miR-146a expression. However, it is known that IRAK-M inhibits the translocation and subsequent degradation of IRAK-1 [21]. We previously demonstrated that *P. gingivalis* LPS preferentially induced IRAK-M and that induced IRAK-M suppressed the dissociation of IRAK-1 from its receptor complex, preventing its subsequent degradation [3]. Therefore, it is assumed that miR-146a expression was strongly induced in both *Salmonella* LPS-stimulated monocytes and *P. gingivalis* LPS-stimulated macrophages, but IRAK-M expression may be higher in *P. gingivalis* LPS-stimulated cells than in *Salmonella* LPS-stimulated cells. This difference could account for the difference in IRAK-1 protein expression. In support of our findings, Perry et al. demonstrated that neither IRAK-1 nor TRAF6 mRNA expression was altered in IL-1β-stimulated lung alveolar epithelial cells, even though miR-146a was upregulated [23].

The overexpression of miR-146a also had little effect on IRAK-1 or TRAF6 expression level, irrespective of the presence or absence of TLR ligand stimulation. In contrast, Liu et al. [18] and Nahid et al. [14] showed that miR-146a overexpression decreased both the IRAK-1 and TRAF6 protein levels in unstimulated cells. However, it is not clear how TLR ligand stimulation affects IRAK-1 and TRAF6 expression when miR-146a is overexpressed.

In conclusion, it is evident that TLR ligand stimulation induces robust miR-146a expression, not only in monocytes and macrophages but also in other TLR-expressing cells. Loss-of-function and gain-of-function experiments suggest that this molecule can act as a negative regulator of TLR signaling by suppressing IRAK-1 and TRAF6. However, the ultimate effects of miR-146a activity appear to vary based on cell type and other factors. Single miRNAs

have been reported to have multiple target molecules [24], and miR-146a may have other targets. Moreover, in the TLR signaling pathway, a number of negative regulators that are affected by TLR ligand stimulation, such as IRAK-M, may account for the findings described above. Further studies are clearly needed to clarify the exact role of miR-146a in infection and inflammation.

Acknowledgments

This study was supported by the Japanese Society for the Promotion of Science (23390476 and 23659974 for K.Y., 21792112 and 23792470 for T.H.), the Young Researcher Overseas Visits Program for Vitalizing Brain Circulation (S2203), and the Promotion of Niigata University Research Project.

Appendix A. Supplementary data

Supplementary data associated with this article can be found, in the online version, at http://dx.doi.org/10.1016/j.bbrc.2012.03.102.

References

[1] F.Y. Liew, D. Xu, E.K. Brint, L.A. O'Neill, Negative regulation of Toll-like receptor-mediated immune responses, Nat. Rev. Immunol. 5 (2005) 446–458.
[2] J. Wang, Y. Hu, W.W. Deng, B. Sun, Negative regulation of Toll-like receptor signaling pathway, Microbes Infect. 11 (2009) 321–327.
[3] H. Domon, T. Honda, T. Oda, H. Yoshie, K. Yamazaki, Early and preferential induction of IL-1 receptor-associated kinase-M in THP-1 cells by LPS derived from *Porphyromonas gingivalis*, J. Leukoc. Biol. 83 (2008) 672–679.
[4] G. Hajishengallis, M. Wang, S. Liang, M. Triantafilou, K. Triantafilou, Pathogen induction of CXCR4/TLR2 cross-talk impairs host defense function, Proc. Natl. Acad. Sci. USA 105 (2008) 13532–13537.
[5] D.P. Bartel, MicroRNAs: genomics, biogenesis, mechanism, and function, Cell 116 (2004) 281–297.
[6] M.R. Fabian, N. Sonenberg, W. Filipowicz, Regulation of mRNA translation and stability by microRNAs, Annu. Rev. Biochem. 79 (2010) 351–379.
[7] A. Kozomara, S. Griffiths-Jones, miRBase: integrating microRNA annotation and deep-sequencing data, Nucleic Acids Res. 39 (2011) D152–157.
[8] V. Ambros, The functions of animal microRNAs, Nature 431 (2004) 350–355.
[9] R.I. Gregory, R. Shiekhattar, MicroRNA biogenesis and cancer, Cancer Res. 65 (2005) 3509–3512.
[10] K.D. Taganov, M.P. Boldin, D. Baltimore, MicroRNAs and immunity: tiny players in a big field, Immunity 26 (2007) 133–137.
[11] K.D. Taganov, M.P. Boldin, K.J. Chang, D. Baltimore, NF-κB-dependent induction of microRNA miR-146, an inhibitor targeted to signaling proteins of innate immune responses, Proc. Natl. Acad. Sci. USA 103 (2006) 12481–12486.
[12] R.M. O'Connell, K.D. Taganov, M.P. Boldin, G. Cheng, D. Baltimore, MicroRNA-155 is induced during the macrophage inflammatory response, Proc. Natl. Acad. Sci. USA 104 (2007) 1604–1609.
[13] F. Bazzoni, M. Rossato, M. Fabbri, D. Gaudiosi, M. Mirolo, L. Mori, N. Tamassia, A. Mantovani, M.A. Cassatella, M. Locati, Induction and regulatory function of miR-9 in human monocytes and neutrophils exposed to proinflammatory signals, Proc. Natl. Acad. Sci. USA 106 (2009) 5282–5287.
[14] M.A. Nahid, M. Satoh, E.K. Chan, Mechanistic role of microRNA-146a in endotoxin-induced differential cross-regulation of TLR signaling, J. Immunol. 186 (2011) 1723–1734.
[15] M.A. Nahid, M. Rivera, A. Lucas, E.K. Chan, L. Kesavalu, Polymicrobial infection with periodontal pathogens specifically enhances microRNA miR-146a in ApoE$^{-/-}$ mice during experimental periodontal disease, Infect. Immun. 79 (2011) 1597–1605.
[16] K.J. Livak, T.D. Schmittgen, Analysis of relative gene expression data using real-time quantitative PCR and the $2^{-\Delta\Delta CT}$ method, Methods 25 (2001) 402–408.
[17] M. Wang, J.L. Krauss, H. Domon, K.B. Hosur, S. Liang, P. Magotti, M. Triantafilou, K. Triantafilou, J.D. Lambris, G. Hajishengallis, Microbial hijacking of complement-Toll-like receptor crosstalk, Sci. Signal. 3 (2010) ra11.
[18] Z. Liu, B. Xiao, B. Tang, B. Li, N. Li, E. Zhu, G. Guo, J. Gu, Y. Zhuang, X. Liu, H. Ding, X. Zhao, H. Guo, X. Mao, Q. Zou, Up-regulated microRNA-146a negatively modulate *Helicobacter pylori*-induced inflammatory response in human gastric epithelial cells, Microbes Infect. 12 (2010) 854–863.
[19] M.P. Boldin, K.D. Taganov, D.S. Rao, L. Yang, J.L. Zhao, M. Kalwani, Y. Garcia-Flores, M. Luong, A. Devrekanli, J. Xu, G. Sun, J. Tay, P.S. Linsley, D. Baltimore, MiR-146a is a significant brake on autoimmunity, myeloproliferation, and cancer in mice, J. Exp. Med. 208 (2011) 1189–1201.
[20] M.A. Nahid, K.M. Pauley, M. Satoh, E.K. Chan, MiR-146a is critical for endotoxin-induced tolerance: implication in innate immunity, J. Biol. Chem. 284 (2009) 34590–34599.
[21] K. Kobayashi, L.D. Hernandez, J.E. Galan, C.A. Janeway Jr., R. Medzhitov, R.A. Flavell, IRAK-M is a negative regulator of Toll-like receptor signaling, Cell 110 (2002) 191–202.
[22] Z. Jiang, J. Ninomiya-Tsuji, Y. Qian, K. Matsumoto, X. Li, Interleukin-1 (IL-1) receptor-associated kinase-dependent IL-1-induced signaling complexes phosphorylate TAK1 and TAB2 at the plasma membrane and activate TAK1 in the cytosol, Mol. Cell. Biol. 22 (2002) 7158–7167.
[23] M.M. Perry, S.A. Moschos, A.E. Williams, N.J. Shepherd, H.M. Larner-Svensson, M.A. Lindsay, Rapid changes in microRNA-146a expression negatively regulate the IL-1beta-induced inflammatory response in human lung alveolar epithelial cells, J. Immunol. 180 (2008) 5689–5698.
[24] L.P. Lim, N.C. Lau, P. Garrett-Engele, A. Grimson, J.M. Schelter, J. Castle, D.P. Bartel, P.S. Linsley, J.M. Johnson, Microarray analysis shows that some microRNAs downregulate large numbers of target mRNAs, Nature 433 (2005) 769–773.

Biochemical and Biophysical Research Communications 420 (2012) 926–930

Contents lists available at SciVerse ScienceDirect

Biochemical and Biophysical Research Communications

journal homepage: www.elsevier.com/locate/ybbrc

Detection of asymmetric distribution of phospholipids by fluorescence resonance energy transfer

Yoko Nishimura, Satoshi Tadokoro, Masahiko Tanaka, Naohide Hirashima *

Graduate School of Pharmaceutical Sciences, Nagoya City University, 3-1, Tanabe-dori, Mizuho-ku, Nagoya 467-8603, Japan

ARTICLE INFO

Article history:
Received 17 March 2012
Available online 26 March 2012

Keywords:
Lipid asymmetry
Flip-flop
Fluorescence resonance energy transfer

ABSTRACT

It is well established that the plasma membrane exhibits an asymmetric distribution of lipids between the inner and outer leaflets of the lipid bilayer. Recent studies suggest that the asymmetric distribution changes locally and temporarily, accompanied by cellular events. However, available methods to detect lipid asymmetry lack spatio-temporal resolution. As a technique of potential use for real-time imaging of lipid asymmetry, we a novel method that utilizes fluorescence resonance energy transfer (FRET) between NBD-labeled phospholipids (donor) and extracellular rhodamine (acceptor). When cell apoptosis was induced by staurosporine, the fluorescence intensity of NBD-labeled phosphatidylserine decreased owing to FRET from NBD to rhodamine. This method provides a simple way to detect lipid asymmetry and may be useful for observing dynamic changes in asymmetric distribution of lipids.

© 2012 Elsevier Inc. All rights reserved.

1. Introduction

It has been well-documented that the plasma membrane exhibits an asymmetric distribution of phospholipids between the two leaflets of the bilayer. Aminophospholipids such as phosphatidylserine (PS) and phosphatidylethanolamine (PE) reside in the inner leaflet of the plasma membrane, while phosphatidylcholine (PC) and sphingomyelin (SM) are distributed in the outer leaflet [1–4]. The physiological significance of this asymmetric distribution is not well understood, but the translocation of PS from the inner to the outer leaflet was observed during apoptosis and platelet activation [5–7]. Several recent studies have suggested that the asymmetric distribution of phospholipids and transbilayer movement of phospholipids are involved in a wide range of cellular events such as cell division [8,9] and antigen recognition [10]. We reported that rapid scrambling of phospholipids in the plasma membrane occurred during the exocytotic release of acetylcholine from nerve terminals prepared from the electric organs of electric ray [11]. We also reported that asymmetric distribution is associated with exocytototic release in mast cells [12]. These observations imply that asymmetric distribution and transbilayer movements of phospholipids may mediate other biological events.

Several methods have been developed for investigating the asymmetric distribution of lipids [13]. Some utilize membrane impermeable reagents to modify phospholipids in the outer leaflet, allowing their discrimination from lipids in the inner leaflet. Aminophospholipids in the outer leaflet are modified by trinitrobenzenesulfonic acid [14] and phospholipids in the outer leaflet are converted to lysophospholipids by phospholipase A2 [15]. Labeled lipids have been used to detect asymmetric distribution of lipids. They are labeled by radioisotope, fluorescence, and spin probe methods [16–18], followed by a back exchange method to extract the labeled lipids in the outer leaflet with bovine serum albumin (BSA) [19], but centrifugation is required to separate the extracted lipids and time resolution is low. McIntyre and Sleight developed a method, without back exchange, using dithionite to quench the fluorescence of lipids in the outer leaflet [20]. For the detection of phosphatidylserine translocated to the outer leaflet, annexin V is often used [21].

However, the methods described above do not satisfy the requirement of detecting the asymmetric distribution of lipids that is expected in various cellular events, because changes in the transbilayer distribution may occur transiently or in limited areas of the plasma membrane. To monitor the asymmetric distribution of phospholipids at higher spatio-temporal resolution, fluorescence-based techniques that do not rely on back exchange and the use of a quencher are desirable, since they support real-time imaging of lipid asymmetry with a fluorescence microscope. Here we report the development of a similar method.

2. Materials and methods

2.1. Cell culture

Chinese hamster ovary cells (CHO-K1) were cultured in F-12 culture medium (Gibco, Grand Island, NY, USA) supplemented with

* Corresponding author. Fax: +81 52 836 3414.
E-mail address: hirashim@phar.nagoya-cu.ac.jp (N. Hirashima).

0006-291X/$ - see front matter © 2012 Elsevier Inc. All rights reserved.
http://dx.doi.org/10.1016/j.bbrc.2012.03.106

10% fetal bovine serum (Biological Industries, Beit HaEmek, Israel). at 37 °C in a humidified atmosphere with 5% CO_2.

2.2. Fluorescence imaging

Fluorescence-labeled phospholipids, NBD-PC (1-palmitoyl-2-[6-[(7-nitro-2-1,3-benzoxadiazol-4-yl)amino]hexanoyl]-*sn*-glycero-3-phosphocholine) and NBD-PS (1-palmitoyl-2-[6-[(7-nitro-2-1,3-benzoxadiazol-4-yl)amino]hexanoyl]-*sn*-glycero-3-phospho-L-serine) were purchased from Avanti Polar Lipids (Birmingham, AL, USA). NBD-PC or NBD-PE in chloroform was dried with nitrogen gas and chloroform was removed by a rotary evaporator under reduced pressure. HEPES buffer (140 mM NaCl, 5 mM KCl, 1 mM $CaCl_2$, 0.6 mM $MgCl_2$, 0.1% BSA, and 10 mM HEPES, pH 7.5) was added to a thin film of fluorescence-labeled phospholipids. Samples were vortexed vigorously to obtain a lipid suspension. CHO-K1 cells (1×10^5 cells) were plated in a ZOG-3 glass-bottom chamber (Elekon Science; Chiba, Japan) and incubated for 18 h. Cells were washed with HEPES buffer and incubated with the suspension of fluorescence-labeled phospholipids for 10 min at 15 °C [22]. After two washes of cells with HEPES buffer, fluorescence images were obtained using a confocal laser scanning microscope (LSM-510; Carl Zeiss, Göttingen, Germany) with a 63× objective lens (Plan-Apochromat 63×/1.4 oil). Samples were excited at 488 nm with an Ar laser and fluorescence was observed through an LP 560 filter. To observe rhodamine, sulforhodamine B (Sigma, St. Louis, MO, USA) in HEPES buffer was added to the glass-bottom chamber, and samples were excited at 543 nm with a He–Ne laser and fluorescence was observed through an LP 560 filter.

2.3. Flow cytometry

Externalized PS and membrane permeability were measured by flow cytometry (FACSort; Becton Dickinson, Franklin Lakes, NJ, USA) using annexin V-EGFP and propidium iodide (PI) (Annexin V-EGFP Apoptosis Detection kit, Medical & Biological Laboratories, Nagoya, Japan), following the manufacturer's instructions [23].

2.4. FRET

FRET was estimated using a spectrofluorometer equipped with a personal computer (RF-5300PC, Shimadzu, Kyoto, Japan). Fluorescence spectra of NBD before and after addition of sulforhodamine B (final concentration = 0.67 nM) were obtained by excitation at 488 nm. To induce apoptosis, cells were treated with staurosporine (Merck Chemicals, Darmstadt, Germany). Efficiency of FRET (Ef) was calculated by the equation:

$$Ef = (Flb - Fla)/Flb$$

where Flb and Fla denote fluorescence intensity at 530 nm before and after addition of rhodamine, respectively.

3. Results and discussion

3.1. Detection of lipid asymmetry by FRET-based technique

We aimed to develop a fluorescence resonance energy transfer (FRET)-based technique to detect the asymmetric distribution of phospholipids in the plasma membrane. Fig. 1 shows the schematic representation of the technique. Transbilayer movement

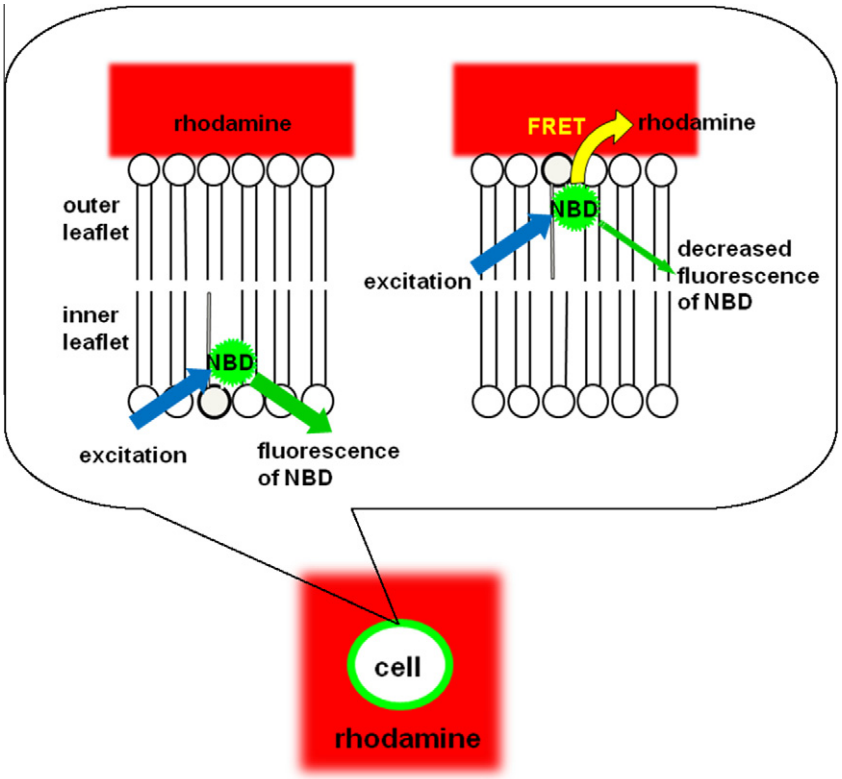


Fig. 1. Schematic representation of a method detecting lipid asymmetry by FRET. NBD-labeled lipids are introduced into the plasma membrane. The labeled lipids are distributed in either the outer or inner leaflet of the plasma membrane. When present in the extracellular solution, rhodamine (red) serves as an acceptor of energy from excited NBD (green). When the labeled lipids reside in the inner leaflet (left), the efficiency of FRET is low. In contrast, when the labeled lipids reside in the outer leaflet (right), the FRET efficiency increases owing to the shorter distance between NBD and rhodamine, resulting in a decrease in the fluorescence intensity of NBD.

of phospholipids produces changes in the distance between a phospholipid molecule and the extracellular solution, such that phospholipids in the outer leaflet are closer to the extracellular solution than those in the inner leaflet. Accordingly, when fluorescence-labeled phospholipids are introduced into the plasma membrane in the presence of fluorophores in the extracellular solution, the flip-flop of phospholipids causes a change in the efficiency of FRET between fluorophores of the labeled phospholipids and the extracellular solution.

We used NBD-labeled phospholipid as a FRET donor in the presence of rhodamine, a FRET acceptor, in the extracellular solution. If NBD-labeled phospholipid resides in the outer leaflet facing the extracellular solution, the efficiency of FRET is higher than when the NBD-labeled phospholipid is in the inner leaflet facing the cytoplasm. In this system, FRET is observed only as a decreased fluorescence intensity of NBD, because an increase in the fluorescence intensity of rhodamine, which is abundant in the extracellular solution, is considered negligible.

3.2. Distribution of fluorescence-labeled phospholipids and rhodamine

First, we observed the intracellular distribution of fluorescence-labeled phospholipids by confocal laser scanning microscopy. Fluorescence-labeled phospholipid, NBD-PC (1-palmitoyl-2-[6-[(7-nitro-2-1,3-benzoxadiazol-4-yl)amino]hexanoyl]-*sn*-glycero-3-phosphocholine) or NBD-PS (1-palmitoyl-2-[6-[(7-nitro-2-1, 3-benzoxadiazol-4-yl)amino]hexanoyl]-*sn*-glycero-3-phospho-L-serine) was applied to CHO-K1 cells extracellularly. Fig. 2A and B shows the intracellular distribution of NBD-PC and NBD-PS, respectively. NBD-PC was distributed in the plasma membrane, while NBD-PS was distributed in the plasma membrane and cytoplasm. NBD-PS integrated into the plasma membrane seemed to be transported to the inner leaflet and distributed in the cytoplasm. Next we examined the distribution of the water-soluble fluorescent dye sulforhodamine B. As shown in Fig. 2C, rhodamine remained in the extracellular solution and was not internalized into the cells up to 1 h after addition of rhodamine. Thus, energy transfer from NBD to rhodamine occurs mainly between NBD in the plasma membrane and extracellular rhodamine; the contribution of internalized NBD to the FRET can be considered negligible.

3.3. Induction of externalization of PS by apoptosis

To determine whether or not the FRET-based method can detect changes in lipid asymmetry in the plasma membrane, we observed the externalization of PS to the outer leaflet in apoptotic cells. It has been reported that apoptosis can be induced by various ways. In the present study, we used staurosporine to induce apoptosis to CHO-K1 cells. Externalized PS was detected using annexin V-EGFP by flow cytometry. Cells were incubated with staurosporine for the indicated periods. As shown in Fig. 3A and B, PS was transported to the outer leaflet depending on the incubation time with staurosporine. These data are consistent with previous reports [24,25]. Membrane permeability was also checked by measuring internalization of PI (Fig. 3C and D). We found that incubation with staurosporine for 24 h caused damage to the plasma membrane (green

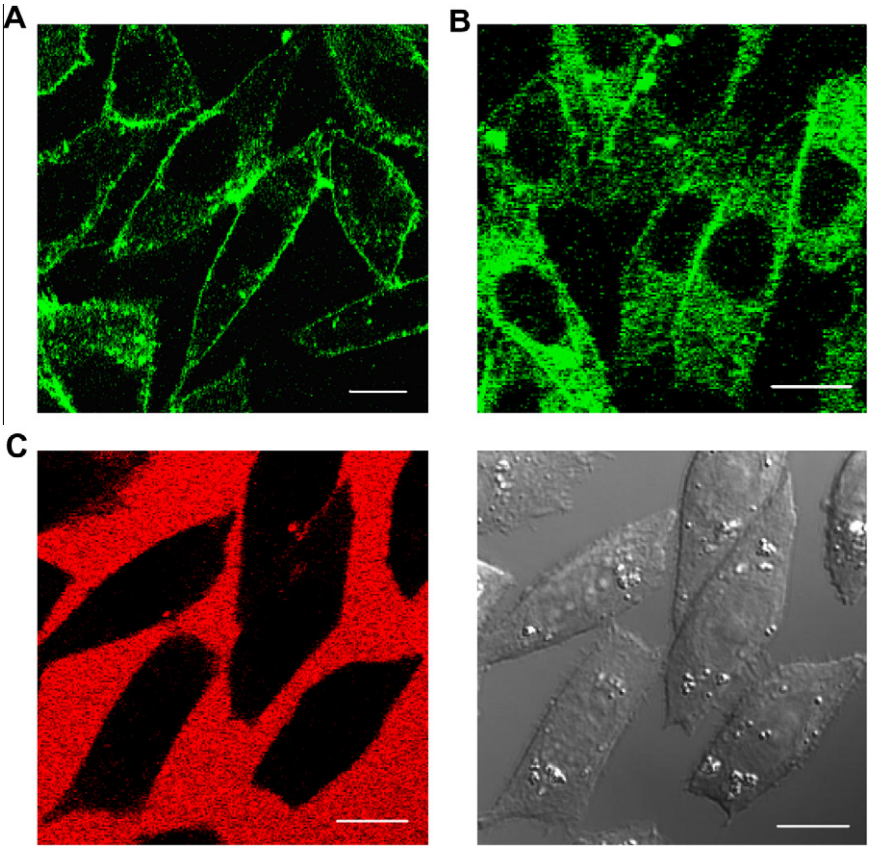


Fig. 2. Distribution of fluorescence-labeled lipids and rhodamine. (A) Intracellular distribution of NBD-PC. CHO-K1 cells were incubated with NBD-PC for 10 min at 15 °C. After washing with HEPES buffer, fluorescence images were obtained using a confocal laser scanning microscope. Scale bar indicates 10 μm. (B) Intracellular distribution of NBD-PS. Scale bar indicates 10 μm. (C) Left panel: fluorescence image of CHO-K1 cells in the presence of sulforhodamine B (1 μM) in the extracellular solution. Right panel: differential interference image of the same field. Scale bar indicates 10 μm.

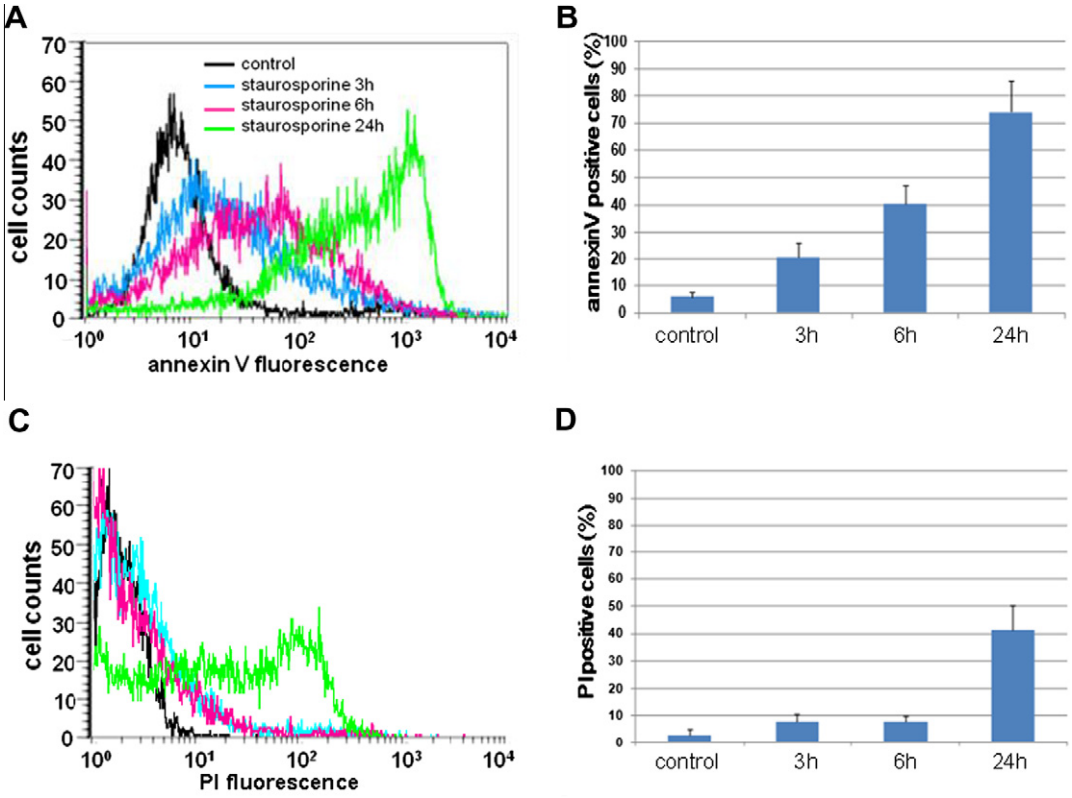


Fig. 3. Externalization of PS induced by staurosporine. (A) CHO-K1 cells were incubated with staurosporine for the indicated periods and externalized PS was estimated using annexin V-EGFP by flow cytometry (0 h: black line, 3 h: blue line, 6 h: red line, 24 h: green). (B) Percentage of annexin V-positive cells was estimated from 3 independent experiments. Values indicate mean ± S.E.M (n = 3). (C) CHO-K1 cells were incubated with staurosporine for the indicated periods and membrane permeability was estimated by PI (0 h: black line, 3 h: blue line, 6 h: red line, 24 h: green). (D) Percentage of PI-positive cells was estimated from 3 independent experiments. Values indicate mean ± S.E.M (n = 3).

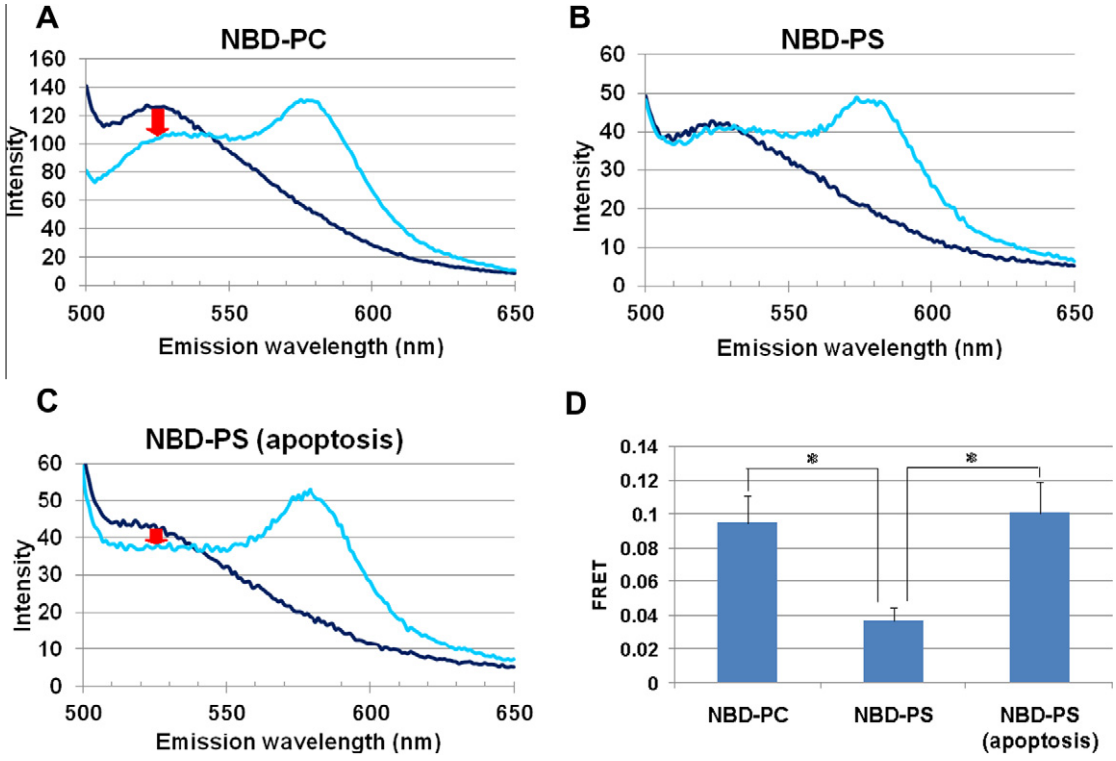


Fig. 4. Detection of lipid asymmetry by FRET. (A and B) Fluorescence-labeled phospholipids were introduced into CHO-K1 cells. Fluorescence spectra of NBD-labeled PC (A) and PS (B), before (blue) and after (light blue) addition of rhodamine excited at 488 nm are shown. (C) Fluorescence spectra of NBD-labeled PS in cells following staurosporine-induced apoptosis. A significant decrease in the fluorescence intensity of NBD caused by FRET is indicated by a red arrow. (D) Efficiency of FRET estimated from fluorescence intensity at 530 nm. Values indicate mean ± S.E.M. (n = 3), $^*P < 0.05$ by Student's t test.

line), allowing permeation of PI. Accordingly, in the subsequent experiments, we incubated cells with staurosporine for 5 h.

3.4. Change in FRET efficiency due to transbilayer movement of phospholipids

As mentioned previously, energy transfer from NBD to rhodamine is detected as a decrease in fluorescence intensity of NBD. We obtained fluorescence spectra of NBD conjugated with phospholipids. FRET was induced by addition of rhodamine. Fig. 4A shows the fluorescence spectra of NBD-PC, which resides in the outer leaflet of the plasma membrane. A significant decrease in the fluorescence intensity of NBD around 530 nm was observed after addition of rhodamine. In contrast, no significant decrease of NBD fluorescence was observed for NBD PS, which resides in the inner leaflet (Fig. 4B). When cell apoptosis was induced by staurosporine, the decrease in fluorescence intensity of NBD was reduced (Fig. 4C), reflecting externalization of PS to the outer leaflet. The efficiency of FRET is summarized in Fig. 4D.

These results indicate that the efficiency of FRET between fluorescence-labeled phospholipids and extracellular rhodamine reflects the asymmetric distribution of lipids. This technique provides a simple method for monitoring change in the asymmetric distribution of lipids. Furthermore, it would be possible to monitor localized changes in asymmetric distribution of lipids by measuring the fluorescence spectrum of the region of interest in the plasma membrane using a confocal microscope with spectral imaging capability.

References

[1] J.A.F. Op den Kamp, Lipid asymmetry in membranes, Annu. Rev. Biochem. 48 (1979) 47–71.
[2] P.F. Devaux, Static and dynamic lipid asymmetry in cell membranes, Biochemistry 30 (1991) 1163–1173.
[3] A. Zachowski, Phospholipids in animal eukaryotic membranes: transverse asymmetry and movement, Biochem. J. 294 (1993) 1–14.
[4] B. Fadeel, D. Xue, The ins and outs of phospholipid asymmetry in the plasma membrane: roles in health and disease, Crit. Rev. Biochem. Mol. Biol. 44 (2009) 264–277.
[5] V.A. Fadok, D.L. Bratton, D.M. Rose, A. Pearson, R.A. Ezekewitz, P.M. Henson, A receptor for phosphatidylserine-specific clearance of apoptotic cells, Nature 405 (2000) 85–90.
[6] V.A. Fadok, A. de Cathelineau, D.L. Daleke, P.M. Henson, D.L. Bratton, Loss of phospholipid asymmetry and surface exposure of phosphatidylserine is required for phagocytosis of apoptotic cells by macrophages and fibroblasts, J. Biol. Chem. 276 (2001) 1071–1077.
[7] E.F. Smeets, P. Comfurius, E.M. Bevers, R.F. Zwaal, Calcium-induced transbilayer scrambling of fluorescent phospholipid analogs in platelets and erythrocytes, Biochim. Biophys. Acta 1195 (1994) 281–286.
[8] K. Emoto, T. Kobayashi, A. Yamaji, H. Aizawa, I. Yahara, K. Inoue, M. Umeda, Redistribution of phosphatidylethanolamine at the cleavage furrow of dividing cells during cytokinesis, Proc. Natl. Acad. Sci. USA 93 (1996) 12867–12872.
[9] K. Emoto, M. Umeda, An essential role for a membrane lipid in cytokinesis. Regulation of contractile ring disassembly by redistribution of phosphatidylethanolamine, J. Cell Biol. 149 (2000) 1215–1224.
[10] K. Fischer, S. Voelkl, J. Berger, R. Andreesen, T. Pomorski, A. Mackensen, Antigen recognition induces phosphatidylserine exposure on the cell surface of human CD8+ T cells, Blood 108 (2006) 4094–4101.
[11] D.-S. Lee, N. Hirashima, Y. Kirino, Rapid transbilayer phospholipid redistribution associated with exocytotic release of neurotransmitters from cholinergic nerve terminals isolated from electric ray Narke japonica, Neurosci. Lett. 291 (2000) 21–24.
[12] N. Kato, M. Nakanishi, N. Hirashima, Transbilayer asymmetry of phospholipids in the plasma membrane regulates exocytotic release in mast cells, Biochemistry 41 (2002) 8068–8074.
[13] P.F. Devaux, P. Fellmann, P. Hervé, Investigation on lipid asymmetry using lipid probes: comparison between spin-labeled lipids and fluorescent lipids, Chem. Phys. Lipids 116 (2002) 115–134.
[14] R.M. Buckland, G.K. Radda, C.D. Shennan, Accessibility of phospholipids in the chromaffin granule membrane, Biochim. Biophys. Acta 513 (1978) 321–337.
[15] L. Herbette, J.K. Blasie, P. Defoor, S. Fleischer, R.J. Bick, W.B. Van Winkle, C.A. Tate, M.L. Entman, Phospholipid asymmetry in the isolated sarcoplasmic reticulum membrane, Arch. Biochem. Biophys. 234 (1984) 235–242.
[16] K. Anzai, Y. Yoshioka, Y. Kirino, Novel radioactive phospholipid probes as a tool for measurement of phospholipid translocation across biomembranes, Biochim. Biophys. Acta 1151 (1993) 69–75.
[17] J. Connor, K. Gillum, A.J. Schroit, Maintenance of lipid asymmetry in red blood cells and ghosts: effect of divalent cations and serum albumin on the transbilayer distribution of phosphatidylserine, Biochim. Biophys. Acta 1025 (1990) 82–86.
[18] M. Seigneuret, P.F. Devaux, ATP-dependent asymmetric distribution of spin-labeled phospholipids in the erythrocyte membrane: relation to shape changes, Proc. Natl. Acad. Sci. USA 81 (1984) 3751–3755.
[19] M. Bitbol, P.F. Devaux, Measurement of outward translocation of phospholipids across human erythrocyte membrane, Proc. Natl. Acad. Sci. USA 85 (1988) 6783–6787.
[20] J.C. McIntyre, R.G. Sleight, Fluorescence assay for phospholipid membrane asymmetry, Biochemistry 30 (1991) 11819–11827.
[21] J. Dachary-Prigent, J.M. Freyssinet, J.M. Pasquet, J.C. Carron, A.T. Nurden, Annexin V as a probe of aminophospholipid exposure and platelet membrane vesiculation: a flow cytometry study showing a role for free sulfhydryl groups, Blood 81 (1993) 2554–2565.
[22] T.A. Endo, T. Kobayashi, K. Ohki, A Chinese hamster ovary cell mutant resistant to phosphatidylserine is defective in transbilayer movement of cell surface phosphatidylserine, Exp. Cell Res. 228 (1996) 341–346.
[23] S.J. Martin, C.P. Reutelingsperger, A.J. McGahon, J.A. Rader, R.C. van Schie, D.M. LaFace, D.R. Green, Early redistribution of plasma membrane phosphatidylserine is a general feature of apoptosis regardless of the initiating stimulus: inhibition by overexpression of Bcl-2 and Abl, J. Exp. Med. 182 (1995) 1545–1556.
[24] T. Godard, E. Deslandes, P. Lebaily, C. Vigreux, F. Sichel, J.M. Poul, P. Gauduchon, Early detection of staurosporine-induced apoptosis by comet and annexin V assays, Histochem. Cell Biol. 112 (1999) 155–161.
[25] P.A. Grandmaison, T.S. Nanowski, J.E. Vance, Externalization of phosphatidylserine during apoptosis does not specifically require either isoform of phosphatidylserine synthase, Biochim. Biophys. Acta 1636 (2004) 1–11.

Biochemical and Biophysical Research Communications 420 (2012) 931–936

Contents lists available at SciVerse ScienceDirect

Biochemical and Biophysical Research Communications

journal homepage: www.elsevier.com/locate/ybbrc

Dicer has a crucial role in the early stage of adipocyte differentiation, but not in lipid synthesis, in 3T3-L1 cells

Yuri Fujimoto [a], Yoshimi Nakagawa [b,*], Akiko Shingyouchi [a], Naoko Tokushige [a], Noriko Nakanishi [a], Aoi Satoh [a], Takashi Matsuzaka [a], Kiyo-aki Ishii [a], Hitoshi Iwasaki [a], Kazuto Kobayashi [a], Shigeru Yatoh [a], Hiroaki Suzuki [a], Naoya Yahagi [a], Osamu Urayama [b], Nobuhiro Yamada [a], Hitoshi Shimano [a]

[a] Department of Internal Medicine (Metabolism and Endocrinology), Faculty of Medicine, University of Tsukuba, 1-1-1 Tennodai, Tsukuba, Ibaraki 305-8575, Japan
[b] Department of Diagnostic Biochemistry, Faculty of Medicine, University of Tsukuba, 1-1-1 Tennodai, Tsukuba, Ibaraki 305-8575, Japan

ARTICLE INFO

Article history:
Received 20 March 2012
Available online 26 March 2012

Keywords:
MicroRNA
Dicer
Adipogenesis
Adipocyte differentiation
Lipid synthesis

ABSTRACT

Dicer is a rate-limiting enzyme for microRNA (miRNA) synthesis. To determine the effects of Dicer on adipogenesis, we performed stage-specific knockdown of Dicer using adenovirus encoding short-hairpin RNAi against Dicer in 3T3-L1 cells. When cells were infected with the adenovirus before induction of adipocyte differentiation, Dicer RNAi suppressed the gene expression of inducers of adipocyte differentiation such as PPARγ, C/EBPα, and FAS in 3T3-L1 cells during adipocyte differentiation. Concurrently, both adipocyte differentiation and cellular lipid accumulation were cancelled by Dicer RNAi when compared with control RNAi. Meanwhile, we addressed the roles of Dicer in lipid synthesis and accumulation in the final stages of differentiation. When the differentiated cells at day 4 after induction of differentiation were infected with adenovirus Dicer RNAi, cellular lipid accumulation was unchanged. Consistent with this, Dicer RNAi had no effects on the expression of genes related to cellular lipid accumulation, including PPARγ and FAS. Thus, Dicer controls proadipogenic genes such as C/EBPα and PPARγ in the early, but not in the late, stage of adipogenesis via regulation of miRNA synthesis.

© 2012 Elsevier Inc. All rights reserved.

1. Introduction

MicroRNAs (miRNAs) are short noncoding RNA molecules composed of approximately 22 nucleotides that function through the posttranscriptional cleavage and translational suppression of their target mRNAs. Thus, miRNAs play important roles in gene expression. Some reports have suggested that miRNAs function in various diseases such as cancer, cardiovascular, obesity, and diabetes. miRNA genes are typically transcribed by RNA polymerase II to generate a long primary miRNA. The hairpin structures within the pri-miRNA are recognized by both the RNase III enzyme Drosha and the double-stranded RNA-binding domain protein DGCR8 also termed Pasha. DGCR8/Pasha takes Drosha to the pri-miRNA, for Drosha to cleave, resulting in a precursor miRNA. Next, the RNase III enzyme Dicer cleaves the pre-miRNA to generate a 22nt mature miRNA duplex. Dicer is one of the rate-limiting enzymes in miRNA biogenesis. Deficiency of Dicer inhibits miRNA synthesis. Some reports have shown that conditional ablation of Dicer in mice results in dysfunction of numerous cellular and developmental processes, including in pancreatic β-cells, muscle cells, and adipocytes [1,2].

The process of adipocyte proliferation and differentiation has been extensively characterized in the cultures of the preadipocyte clonal cell line, mouse 3T3-L1 cells [3]. Adipogenesis requires a sequence of events including growth arrest of proliferating preadipocytes, coordinated reentry into the cell cycle with limited clonal expansion, and growth arrest before terminal differentiation, during which lipid accumulation occurs. Adipogenesis is regulated by adipogenic transcription factors such as peroxisome proliferator-activated receptor-γ (PPARγ), CCAAT/enhancer-binding proteins (C/EBPs), Krüppel-like factors (KLFs), and sterol regulatory element-binding proteins (SREBPs) [4].

Differences in miRNAs between preadipocytes and mature adipocytes were identified, suggesting potential roles for miRNA during adipocyte differentiation [5]. It was reported that some miRNAs regulate various processes during adipogenesis [6,7]. For example, ectopic expressions of miR-103 and miR-143 induce adipocyte differentiation and accumulation of lipid in cells accompanied by increased expression of adipogenesis-related molecules such as PPARγ, fatty acid-binding protein 4 (FABP4), and GLUT4 [8]. Reversely, miR-27a suppresses adipocyte differentiation via suppression of C/EBPα and expression of PPARγ [9]. miRNAs have both positive and negative functions in adipocyte differentiation. Using adipocyte-specific Dicer knockout mice, Mudhasani et al. showed that Dicer was required for the differentiation of

* Corresponding author. Fax: +81 29 853 3174.
E-mail address: yosshy@md.tsukuba.ac.jp (Y. Nakagawa).

0006-291X/$ - see front matter © 2012 Elsevier Inc. All rights reserved.
http://dx.doi.org/10.1016/j.bbrc.2012.03.110

preadipocytes into mature adipocytes [10]. However, the stage-specific effects of Dicer on adipogenesis remains unclear.

In this study, we infected 3T3-L1 cells with adenoviruses encoding Dicer RNAi both before and after differentiation to determine the stage-specific effects of Dicer on adipogenesis.

2. Methods

2.1. Cell culture and adipocyte differentiation

3T3-L1 cells were maintained in high-glucose Dulbecco's modified Eagle's medium (DMEM) with 10% FBS in 5% CO_2. The cells were cultured to confluence. After 2 days, the medium was replaced with high-glucose DMEM containing 5 μg/mL insulin, 1 μM dexamethasone, and 0.5 mM IBMX (Day 0). After 48 h, the medium was changed to high-glucose DMEM containing 5 μg/mL insulin (Day 2). The medium was renewed every other day [5]. For the adipocyte differentiation study, 3T3-L1 cells at day -2 after induction of differentiation were infected with adenovirus (1000 OPU/cell) and incubated for 8 days. For the late stage of differentiation study, 3T3-L1 cells at day 4 after induction of differentiation were infected with adenovirus (1000 OPU/cell) and incubated for 6 days.

2.2. Oil Red O staining

3T3-L1 cells were fixed with 10% formalin for 10 min. The fixed cells were stained with 0.3% Oil Red O/isopropanol solution for 20 min. The stained cytosolic triglycerides were visualized and images captured by phase contrast microscopy. To quantify the cellular triglycerides, the stained cells were eluted with isopropanol and the OD values detected by spectrophotometry at a wavelength of 490 nm.

2.3. Preparation of adenovirus

RNAi adenovirus vectors, RNAi-LacZ (LacZi), mouse Dicer RNAi-345 (345i) 5′-GCAACAAGAAGCAATTCAT-3′ and mouse Dicer RNAi-1594 (1594i) 5′-GAAAGAAGATACACAGCAG-3′ were constructed with a BLOCK-iT™ U6 RNAi Entry Vector Kit and a BLOCK-iT™ Adenoviral RNAi Expression System (Invitrogen). Each adenoviral vector was propagated in 293A cells and purified by cesium chloride density centrifugation [11].

2.4. Real-time PCR

Total RNA was prepared from 3T3-L1 cells using Trizol Reagent (Life Technologies). For gene expression analysis, total RNA was reverse transcribed using a High Capacity cDNA Reverse Transcription Kit (Life Technologies) and subjected to real-time PCR using a KAPA SYBR Fast qPCR Kit (Kapa Biosystems) and TaqMan probes (Life Technologies). The following primers were used for this analysis: p21 Fwd, 5′-gtacttcctctgccctgctg-3′ and p21 Rv, 5′-tctgcgcttggagtga taga-3′; C/EBPα Fwd, 5′-gcgcaagagccgagataaag-3′ and C/EBPα Rv, 5′-cggtcattgtcactggtcaact-3′; C/EBPβ Fwd, 5′-cgcctttagacccatgga ag-3′ and C/EBPβ Rv, 5′-cccgtaggccaggcagt-3′; Dicer Fwd, 5′-aaga cttggagtacggctgcct-3′ and Dicer Rv, 5′-tctctgcgtctggatggtcaa-3′; FAS Fwd, 5′-atcctggaacgagaacacgatct-3′ and FAS Rv, 5′-agagacgt gtca ctcctggactt-3′; PPARγ2 Fwd, 5′-aactctgggagattctcctgttga-3′ and PPA Rγ2 Rv, 5′-gaagtgctcataggcagtgcat-3′; cyclophilin Fwd, 5′-tggc tca-cagttcttcataacca-3′ and cyclophilin Rv, 5′-atgacatccttcagtggctt gtc-3′. Gene expression was normalized to cyclophilin expression. For miRNA expression analysis, total RNA was reverse transcribed using a TaqMan™ microRNA Reverse Transcription Kit and subjected to real-time PCR using a TaqMan™ microRNA Assay Kit for mmu-miR-27a and mmu-miR-103 (Applied Biosystems). Reactions were performed using an Applied Biosystems 7300 Real-Time PCR System. miRNA expression was normalized to snRNA U6 expression. Data were analyzed using the comparative CT method.

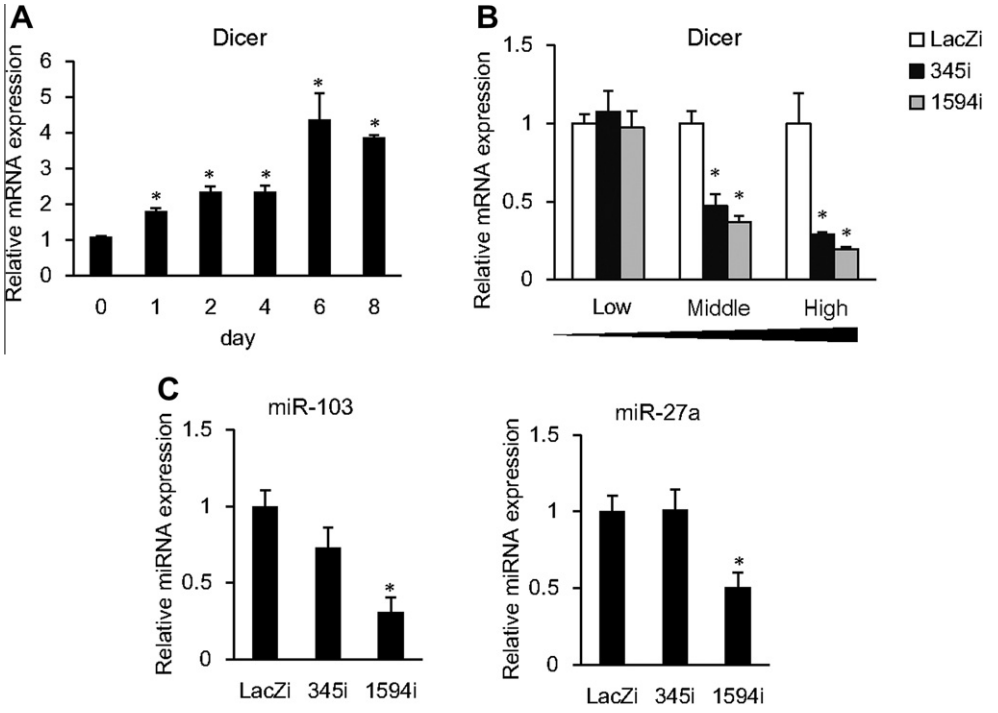


Fig. 1. Dicer RNAi suppresses Dicer and miRNA expression. (A) Changes in Dicer expression in differentiating 3T3-L1 cells. Total RNA was isolated from cells at indicated days of differentiation and subjected to real-time PCR. $n = 4$ per group, $^*p < 0.05$ vs. day 0. (B, C) Efficiency of Dicer knockdown in 3T3-L1 cells infected with Dicer RNAi 345 (345i) and Dicer RNAi 1594 (1594i) adenoviruses (Low, 100 OPU/cell; Middle, 500 OPU/cell; and High, 1000 OPU/cell). Total RNA was isolated after 2 days' infection. Gene expressions of Dicer1 (B) and of miR-27a and miR-103 (C) were estimated by real-time PCR. $n = 4$ per group, $^*p < 0.05$ vs. LacZi as control.

2.5. Statistical analysis

Data were expressed as the mean ± SEM. Statistical significance was assessed using the *t* test.

3. Results

3.1. Dicer mRNA is induced during adipocyte differentiation in 3T3-L1 cells

We first checked the expression pattern of Dicer during adipocyte differentiation in 3T3-L1 preadipocyte cells. Differentiation of the cells into mature adipocytes was induced by dexamethasone, IBMX, and insulin. The cells were collected at days 0, 1, 2, 4, 6, and 8 after induction. Total RNA was isolated from cells and subjected to real-time PCR to evaluate the levels of Dicer mRNA. Dicer mRNA was gradually but significantly increased during differentiation of 3T3-L1 cells (Fig. 1A), suggesting a relationship between Dicer expression and adipocyte differentiation.

3.2. Knockdown of Dicer suppresses adipocyte differentiation and lipid accumulation in 3T3-L1 cells

To determine the role of Dicer in adipocyte differentiation, we constructed an adenovirus encoding short-hairpin RNAi against Dicer (Ad-Dicer RNAi). We evaluated the knockdown efficiency of Ad-Dicer RNAi (345i, 1594i) against endogenous Dicer expression. 3T3-L1 cells were infected with adenoviral LacZi and Dicer RNAi 345i and 1594i, collected at day 2 after infection, and subjected to real-time PCR. Both Ad-Dicer RNAi 345i and Ad-Dicer RNAi 1459i efficiently suppressed the expression of endogenous Dicer in the adenovirus in a dose-dependent manner (Fig. 1B). As Dicer is a rate-limiting enzyme for miRNA synthesis, we checked the expression of adipocyte-specific miRNAs in these cells. Ad-Dicer RNAi 1594i could efficiently suppress the expression of miRNAs including miR-27a and miR-103, but Ad-Dicer RNAi 345i did not (Fig. 1C).

To determine the effects of Dicer on adipogenesis, we infected adenoviral Dicer RNAi into 3T3-L1 cells 2 days before induction of differentiation, and the cells were induced by dexamethasone, IBMX, and insulin. The cells were fixed and stained with Oil Red O at day 8 after induction. The cells infected with both Ad-Dicer RNAi 345i and Ad-Dicer RNAi 1594i did not stain well with Oil Red O when compared with the cells infected with LacZi (Fig. 2A). To quantify the amount of lipid accumulation, the Oil Red O-stained cells were destained with isopropanol and the amount of staining was quantified. Both Ad-Dicer RNAi 345i and Ad-Dicer RNAi 1594i significantly inhibited lipid accumulation when compared with Ad-lacZ RNAi as the control (Fig. 2B). These results indicated that Dicer had an important role in adipocyte differentiation and lipid accumulation in 3T3-L1 cells when cells were infected with Dicer RNAi adenovirus before induction of differentiation.

3.3. Dicer RNAi suppresses gene expression related to adipocyte differentiation in 3T3-L1 cells

To determine the effects of Dicer deficiency on gene expression during adipocyte differentiation, 3T3-L1 cells were infected with adenovirus encoding 2 types of Dicer RNAi 2 days before induction of differentiation. Total RNA was isolated during differentiation and subjected to real-time PCR. Dicer expression was apparently reduced in Dicer RNAi-infected cells during adipocyte differentiation (Fig. 3A). C/EBPβ functions at the early stage of adipogenesis, whereas p21 functions at the entry stage into clonal expansion of adipogenesis [12]. Therefore, both molecules function in the relatively early stages of adipogenesis. These molecules were apparently not altered by either LacZi or Dicer RNAi from day 0 to day 2 after induction (Fig. 3A). Consistent with the reduction in Dicer mRNA, the levels of C/EBPα and PPARγ, both inducers of adipocyte differentiation, were significantly reduced in cells infected with Dicer RNAi adenovirus during differentiation (Fig. 3A). Together with the reduction in Oil Red O staining in cells infected with Dicer RNAi adenovirus (Fig. 2), the expression levels of FAS as the rate-limiting enzyme in lipogenesis were remarkably suppressed from 4 days after induction when compared with LacZi (Fig. 3A). To confirme whether miRNA synthesis was suppressed in Dicer knockdown cells, We determined the levels of miR-27a and miR-103 at day 8 after induction of differentiation. The levels of miR-27a expression were not changed in cells infected with both Dicer RNAi adenoviruses, whereas miR-103 expression was significantly reduced (Fig. 3B). Although Dicer is an important molecule for miRNA synthesis, it has been reported that Dicer is not required for the generation of all miRNAs [13,14].

3.4. Dicer is not required for lipid accumulation in differentiated 3T3-L1 cells

Next, we sought to determine the role of Dicer in lipid synthesis and accumulation in differentiated 3T3-L1 cells. The cells were

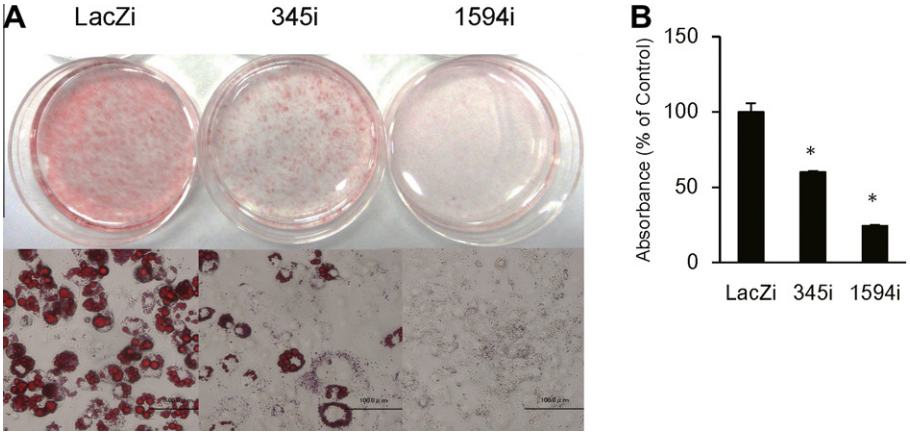


Fig. 2. Inhibition of adipocyte differentiation by Dicer knockdown. (A) Preadipocyte 3T3-L1 cells were infected with adenoviral LacZi and Dicer RNAi at day-2. Oil Red O staining of cells was performed at day 8 after induction of adipocyte differentiation. (B) Quantification of Oil Red O was measured at 490 nm. $n = 4$ per group, $^{*}p < 0.05$ vs. LacZi as control.

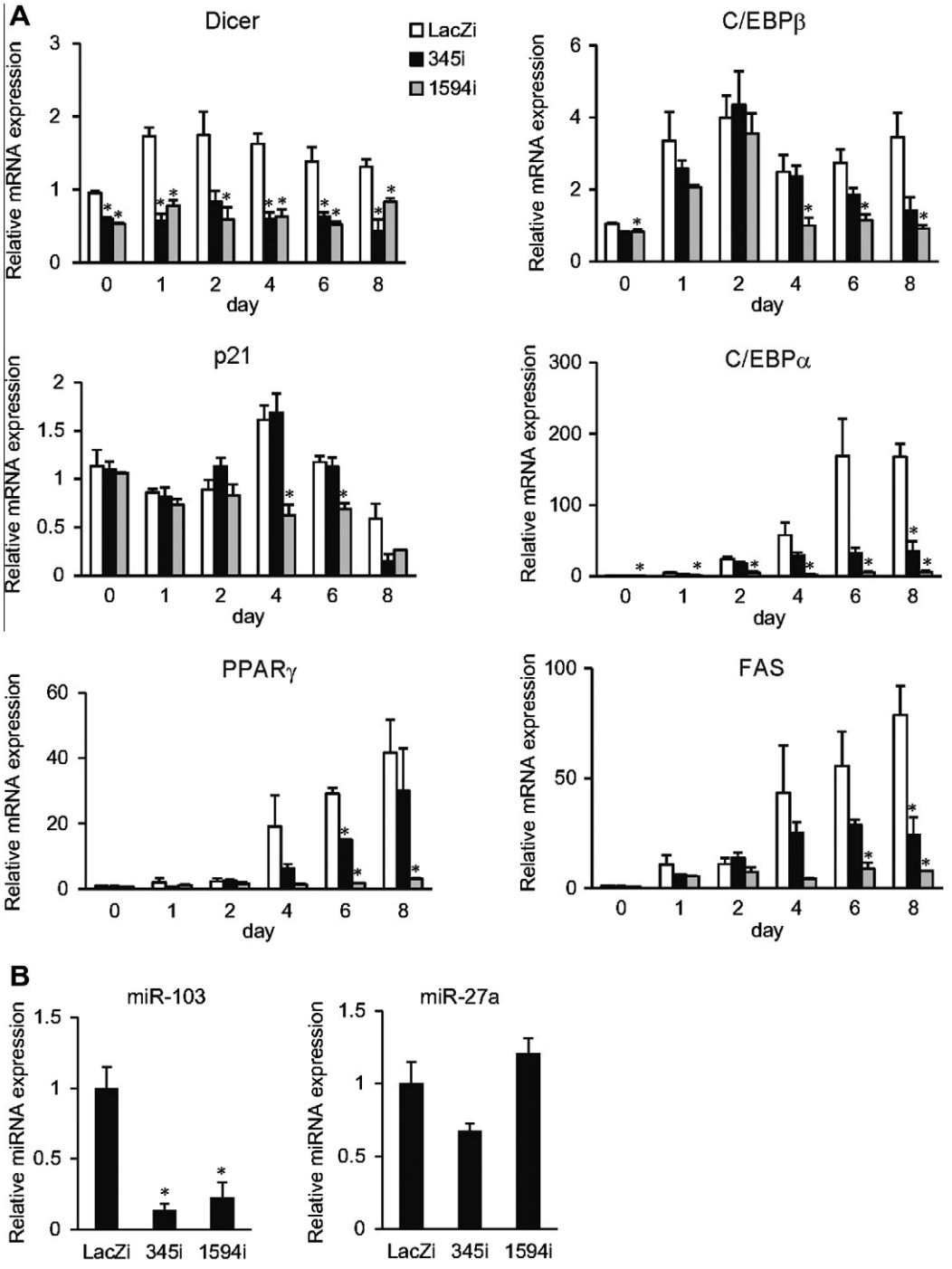


Fig. 3. Gene expression in 3T-L1 cells infected with Dicer RNAi adenovirus during adipocyte differentiation Preadipocyte 3T3-L1 cells were infected with adenovirus LacZi and Dicer RNAi at day-2. (A) Time course analysis of mRNA expression in 3T3-L1 cells was determined at indicated days after induction of adipocyte differentiation, as estimated by real-time PCR. (B) Expressions of miR-27a and miR-103 at day 8 after induction of differentiation were estimated by real-time PCR. $n = 3$ per group, $^{*}p < 0.05$ vs. LacZi.

infected with adenoviral LacZi or Dicer RNAi at day 4 after induction of differentiation and incubated for an additional 6 days. To evaluate adipocyte differentiation and lipid accumulation in the differentiated cells, we stained the cells with Oil Red O. The cells infected with both Dicer RNAi adenoviruses were well stained to the same levels as those in the Ad-LacZi-infected cells (Fig. 4A). Consistent with these results, the levels of adipogenic gene expression including PPARγ and FAS were also not changed (Fig. 4B). This finding indicates that Dicer knockdown has no effect on lipid synthesis or lipid accumulation in the late stage of differentiation.

4. Discussion

miRNAs play important roles in posttranscriptional gene regulation. miRNAs are involved in the regulatory network of many biological processes including adipocyte differentiation. Most miRNAs are generated by a conserved mechanism involving 2 RNase III enzymes, Drosha and Dicer. Dicer has crucial roles in the development of cells, such as skin and muscle angiogenesis. miRNA play regulatory roles in many biological processes associated with obesity, including adipocyte differentiation, insulin

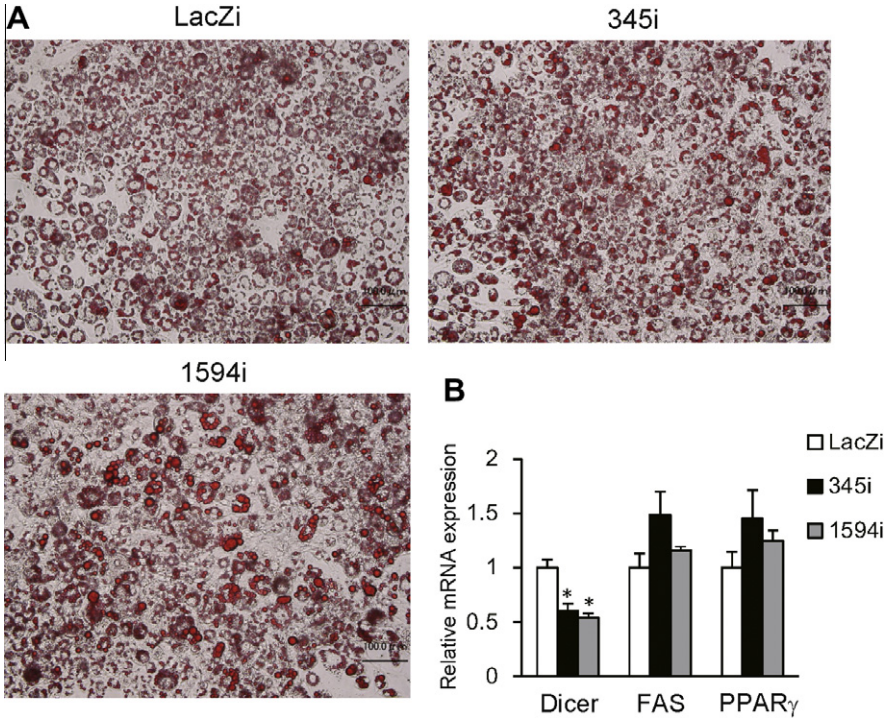


Fig. 4. Dicer has no effect on differentiated 3T3-L1 cells. 3T3-L1 cells were infected with Dicer RNAi adenovirus at day 4 after induction of differentiation. (A) Oil Red O staining was performed at day 6 after infection. (B) Gene expression in cells was estimated by real-time PCR at day 6 after infection. $n = 4$, $^{*}p < 0.05$ vs. LacZi.

action, and fat metabolism [15]. Recent studies have shown that the expression of miRNAs is dysregulated in obese adipose tissue [5]. During adipogenesis, the expression of Dicer mRNA was gradually but significantly induced (Fig. 1A). MiRNAs could accelerate or inhibit the differentiation and regulate the development of adipocytes [6,7]. However, the stage-specific role of Dicer on adipogenesis remains unclear.

Adipocyte differentiation consists of growth arrest of proliferating preadipocytes (day 0), coordinated reentry into the cell cycle with clonal expansion stage (days 1–2), postmitotic growth arrest (days 3–4), and its associated terminal differentiation (days 4–10) [12]. C/EBPβ, known to function in the early stage of adipogenesis and to directly induce PPARγ expression, was not altered in cells infected with Dicer RNAi when compared with control RNAi from day 0 to day 2 (Fig. 3A). p21 is induced by Foxo1 and implicated in the entry of adipocytes into the clonal expansion stage of adipogenesis. The ablation of Dicer in embryonic fibroblasts upregulated the $p19^{arf}$-p53 pathway, resulting in increased p21 expression [16]. However, Dicer RNAi had no effects on p21 expression from day 0 to day 2 (Fig. 3A). These findings indicated that Dicer has no direct function in proliferation and clonal expansion. Ad-Dicer RNAi suppressed the expression of the proadipogenic gene PPARγ during adipogenesis (Fig. 3A), and other proadipogenic genes, such as C/EBPα, and the lipid synthesis gene, FAS (Fig. 3A). As PPARγ and C/EBPα are mutually activated during adipocyte differentiation, promoting adipogenesis and lipid synthesis, Dicer RNAi could halt the positive feedback loop between PPARγ and C/EBPα. It was conceivable that the suppression of proadipogenic gene expression by Dicer knockdown was due to the change in regulatory genes other than C/EBPβ that induce adipogenesis.

Different miRNAs have proadipogenic and antiadipogenic effects in adipogenesis. MiR-27 has inhibitory effects on adipogenesis by repressing the expression of adipogenic transcription factors such as C/EBPα and PPARγ [9,17]. Reversely, miR-103 has proadipogenic roles in adipogenesis. The overexpression of miR-103 increased triglyceride accumulation and upregulated the expression of adipogenic transcription factors [8]. Although Dicer is required for miRNA synthesis, the knockdown of Dicer downregulated the expression of miR-103, but not of miR-27a (Fig. 3B). It is possible that the inhibitory effects of Dicer knockdown on adipogenesis were due to the suppression of the proadipogenic miRNA miR-103, not of the antiadipogenic miRNA miR-27a.

Dicer affected adipocyte differentiation and lipid accumulation before induction of adipocyte differentiation. But whether Dicer has direct effects on lipid accumulation in the late stages of adipocyte differentiation remained unclear. Our data indicated that Dicer has no effects on lipid accumulation or gene expression via direct regulation of the expression of PPARγ and FAS in the late stage of differentiation. These findings suggest that miRNA has no effect on the late stage of adipocyte differentiation.

In this study, we determined the roles of Dicer in the adipogenesis of 3T3-L1 cells by knocking it down at two different stages: before and after adipocyte differentiation. Dicer might have important roles in the expression of adipogenic genes including PPARγ and C/EBPα via regulation of the expression of miRNAs at the early, but not the late, stage of adipocyte differentiation. The transcriptional and translational processes during adipogenesis were dysregulated by Dicer deficiency, resulting in suppression of adipogenesis. Therefore, we need identify the miRNAs that are important during adipocyte differentiation and reveal their functions in adipogenesis.

Acknowledgment

We thank F Miyamasu for critical reading of the manuscript. This work was supported by Grants-in-Aid from The Japanese Ministry of Science, Education, Culture and Technology.

References

[1] K.S. Harris, Z. Zhang, M.T. McManus, B.D. Harfe, X. Sun, Dicer function is essential for lung epithelium morphogenesis, Proc. Natl. Acad. Sci. USA 103 (2006) 2208–2213.

[2] J.F. Chen, E.P. Murchison, R. Tang, T.E. Callis, M. Tatsuguchi, Z. Deng, M. Rojas, S.M. Hammond, M.D. Schneider, C.H. Selzman, G. Meissner, C. Patterson, G.J. Hannon, D.Z. Wang, Targeted deletion of Dicer in the heart leads to dilated cardiomyopathy and heart failure, Proc. Natl. Acad. Sci. USA 105 (2008) 2111–2116.
[3] N. Inoue, N. Yahagi, T. Yamamoto, M. Ishikawa, K. Watanabe, T. Matsuzaka, Y. Nakagawa, Y. Takeuchi, K. Kobayashi, A. Takahashi, H. Suzuki, A.H. Hasty, H. Toyoshima, N. Yamada, H. Shimano, Cyclin-dependent kinase inhibitor, p21WAF1/CIP1, is involved in adipocyte differentiation and hypertrophy, linking to obesity, and insulin resistance, J. Biol. Chem. 283 (2008) 21220–21229.
[4] E.D. Rosen, B.M. Spiegelman, Molecular regulation of adipogenesis, Annu. Rev. Cell Dev. Biol. 16 (2000) 145–171.
[5] N. Nakanishi, Y. Nakagawa, N. Tokushige, N. Aoki, T. Matsuzaka, K. Ishii, N. Yahagi, K. Kobayashi, S. Yatoh, A. Takahashi, H. Suzuki, O. Urayama, N. Yamada, H. Shimano, The up-regulation of microRNA-335 is associated with lipid metabolism in liver and white adipose tissue of genetically obese mice, Biochem. Biophys. Res. Commun. 385 (2009) 492–496.
[6] J.M. Romao, W. Jin, M.V. Dodson, G.J. Hausman, S.S. Moore, L. Guan le, MicroRNA regulation in mammalian adipogenesis, Exp. Biol. Med. (Maywood). 236 (2011) 997–1004.
[7] R.A. McGregor, M.S. Choi, MicroRNAs in the regulation of adipogenesis and obesity, Curr. Mol. Med. 11 (2011) 304–316.
[8] H. Xie, B. Lim, H.F. Lodish, MicroRNAs induced during adipogenesis that accelerate fat cell development are downregulated in obesity, Diabetes 58 (2009) 1050–1057.
[9] S.Y. Kim, A.Y. Kim, H.W. Lee, Y.H. Son, G.Y. Lee, J.W. Lee, Y.S. Lee, J.B. Kim, MiR-27a is a negative regulator of adipocyte differentiation via suppressing PPARgamma expression, Biochem. Biophys. Res. Commun. 392 (2010) 323–328.
[10] R. Mudhasani, A.N. Imbalzano, S.N. Jones, An essential role for Dicer in adipocyte differentiation, J. Cell Biochem. 110 (2010) 812–816.
[11] Y. Nakagawa, H. Shimano, T. Yoshikawa, T. Ide, M. Tamura, M. Furusawa, T. Yamamoto, N. Inoue, T. Matsuzaka, A. Takahashi, A.H. Hasty, H. Suzuki, H. Sone, H. Toyoshima, N. Yahagi, N. Yamada, TFE3 transcriptionally activates hepatic IRS-2, participates in insulin signaling and ameliorates diabetes, Nat. Med. 12 (2006) 107–113.
[12] J. Nakae, T. Kitamura, Y. Kitamura, W.H. Biggs 3rd, K.C. Arden, D. Accili, The forkhead transcription factor Foxo1 regulates adipocyte differentiation, Dev. Cell 4 (2003) 119–129.
[13] I. Gerin, G.T. Bommer, C.S. McCoin, K.M. Sousa, V. Krishnan, O.A. MacDougald, Roles for miRNA-378/378* in adipocyte gene expression and lipogenesis, Am. J. Physiol. Endocrinol. Metab. 299 (2010) E198–206.
[14] J.M. Cummins, Y. He, R.J. Leary, R. Pagliarini, L.A. Diaz Jr., T. Sjoblom, O. Barad, Z. Bentwich, A.E. Szafranska, E. Labourier, C.K. Raymond, B.S. Roberts, H. Juhl, K.W. Kinzler, B. Vogelstein, V.E. Velculescu, The colorectal microRNAome, Proc. Natl. Acad. Sci. USA 103 (2006) 3687–3692.
[15] J. Krutzfeldt, M. Stoffel, MicroRNAs: a new class of regulatory genes affecting metabolism, Cell Metab. 4 (2006) 9–12.
[16] R. Mudhasani, Z. Zhu, G. Hutvagner, C.M. Eischen, S. Lyle, L.L. Hall, J.B. Lawrence, A.N. Imbalzano, S.N. Jones, Loss of miRNA biogenesis induces p19Arf-p53 signaling and senescence in primary cells, J. Cell Biol. 181 (2008) 1055–1063.
[17] Q. Lin, Z. Gao, R.M. Alarcon, J. Ye, Z. Yun, A role of miR-27 in the regulation of adipogenesis, FEBS. J. 276 (2009) 2348–2358.

Biochemical and Biophysical Research Communications 420 (2012) 937

Contents lists available at SciVerse ScienceDirect

Biochemical and Biophysical Research Communications

journal homepage: www.elsevier.com/locate/ybbrc

Letter to the Editor

TRPM8 antagonists and their emerging role in the modulation of pain and allodynia

To the Editor,

I read with great interest the recent article by Pedretti et al. in a recent issue of your esteemed journal [1]. The article is highly thought provoking. Interestingly, the past few years have seen the emergence of a number of novel new TRPM8 antagonists that play a major role in managing pain and allodynia.

For instance, M8-B is a relatively new and highly effective TRPM8 antagonist [2]. M8-B acts by decreasing the expression of c-Fos in neural tissue. 5-Benzyloxytryptamine 19 is another remerging TRPM8 antagonist as is JNJ-39267631 [3,4]. JNJ-39267631 specifically reverses neuropathic cold allodynia.

Similarly, tetrahydroisoquinoline 87 is another new type of TRPM8 antagonist that is chemically a "fused piperidine" derivative [5]. The good thing about tetrahydroisoquinoline 87 is that it can be administered orally. Other emerging TRPM8 antagonists that hold significant potential in reducing cancer induced allodynia include BCTC and capsazepine [6]. The last two act on TRPV1 receptors too besides showing antagonist effects on TRPM8 receptors.

Most malignancies are associated with severe allodynia. The fact that TRPM8 antagonists have an attenuating effect on carcinomas such as prostate carcinoma and oral squamous cell carcinomas besides mitigating pain increases their therapeutic significance in oncology. Further studies are needed to fully elaborate and harness the anti-proliferative and anti-nociceptive effects of TRPM8 antagonists in oncology.

References

[1] A. Pedretti, A. Labozzetta, M. Lo Monte, A.R. Beccari, A. Moriconi, G. Vistoli, Exploring the activation mechanism of TRPM8 channel by targeted MD simulations, Biochem. Biophys. Res. Commun. 414 (2011) 14–19.
[2] M.C. Almeida, T. Hew-Butler, R.N. Soriano, et al., Pharmacological blockade of the cold receptor TRPM8 attenuates autonomic and behavioral cold defenses and decreases deep body temperature, J. Neurosci. 32 (2012) 2086–2099.
[3] J. DeFalco, D. Steiger, M. Dourado, D. Emerling, M.A. Duncton, 5-Benzyloxytryptamine as an antagonist of TRPM8, Bioorg. Med. Chem. Lett. 20 (2010) 7076–7079.
[4] R.W. Colburn, J.M. Matthews, N. Qin, Y. Liu, Small-molecule TRPM8 antagonist JNJ-39267631 reverses neuropathy-induced cold allodynia in rats, in: 12th IASP World Congress.
[5] N.A. Tamayo, Y. Bo, V. Gore, et al., Fused piperidines as a novel class of potent and orally available transient receptor potential melastatin type 8 (TRPM8) antagonists, J. Med. Chem. 55 (2012) 1593–1611.
[6] A. Weil, S.E. Moore, N.J. Waite, A. Randall, M.J. Gunthorpe, Conservation of functional and pharmacological properties in the distantly related temperature sensors TRVP1 and TRPM8, Mol. Pharmacol. 68 (2005) 518–527.

M.D. Shailendra Kapoor
Mechanicsville, VA 23111,
United States
E-mail address: shailendrakapoor@yahoo.com

0006-291X/$ - see front matter © 2012 Elsevier Inc. All rights reserved.
http://dx.doi.org/10.1016/j.bbrc.2012.03.116

Biochemical and Biophysical Research Communications 420 (2012) 938

Contents lists available at SciVerse ScienceDirect

Biochemical and Biophysical Research Communications

journal homepage: www.elsevier.com/locate/ybbrc

Corrigendum

Corrigendum to "A natural squamosamide derivative FLZ inhibits homocysteine-induced rat brain microvascular endothelial cells dysfunction" [Biochem. Biophys. Res. Commun. 417 (2012) 1176–1181]

Rui-xia Kang, Jian-jun Zhang *

State Key Laboratory of Bioactive Substance and Function of Natural Medicines, Department of Pharmacology, Institute of Materia Medica, Chinese Academy of Medical Sciences and Peking Union Medical College, No. 2, Xiannongtan Road, Beijing 100050, China

The authors regret an error in the affiliation information in the published paper. The affiliation line is correct as it appears above.

DOI of original article: http://dx.doi.org/10.1016/j.bbrc.2011.12.094
* Corresponding author. Fax: +86 10 63182392.
E-mail address: jjzhang@imm.ac.cn (J.-j. Zhang).

0006-291X/$ - see front matter © 2012 Elsevier Inc. All rights reserved.
http://dx.doi.org/10.1016/j.bbrc.2012.03.043

Biochemical and Biophysical Research Communications 420 (2012) 939

Contents lists available at SciVerse ScienceDirect

Biochemical and Biophysical Research Communications

journal homepage: www.elsevier.com/locate/ybbrc

Erratum

Erratum to "Sorafenib down-regulates c-IAP expression post-transcriptionally in hepatic carcinoma cells to suppress apoptosis" [Biochem. Biophys. Res. Commun. 418 (2012) 531–536]

Xi-feng Li [1], Ren-yan Gong [1], Meng Wang, Zhen-lin Yan, Bo Yuan, Kui Wang *, Le-hua Shi *

Eastern Hepatobiliary Surgery Hospital, Second Military Medical University, Shanghai, China

The publisher regrets an error in the author line, which appears correctly above.

DOI of original article: http://dx.doi.org/10.1016/j.bbrc.2012.01.060
* Corresponding authors.
E-mail addresses: wangkui021@gmail.com (K. Wang), shilh12@126.com (L.-h. Shi).
[1] These authors contributed equally to this work.

0006-291X/$ - see front matter © 2012 Elsevier Inc. All rights reserved.
http://dx.doi.org/10.1016/j.bbrc.2012.03.042

Biochemical and Biophysical Research Communications

Wolfgang Baumeister
Abteilung Molekulare Strukturbiologie
Max-Planck-Institut für Biochemie
Martinsried
Germany

Ernesto Carafoli
Dipartimento di Chimica Biologica
Università degli Studi di Padova
Padua
Italy

Chin Ha Chung
School of Biological Sciences
College of Natural Sciences
Seoul National University
Seoul
Republic of Korea

Barry Halliwell
Biochemistry Department
National University of Singapore
Singapore
Singapore

Cecilia Hidalgo
Faculty of Medicine
University of Chile
Santiago
Chile

James D. Jamieson
MD/PhD Program
Yale University School of Medicine
New Haven, Connecticut
USA

Hans Jornvall
Department of Medical Biochemistry and Biophysics
Karolinska Institutet
Stockholm
Sweden

Claude Klee
Laboratory of Biochemistry
National Cancer Institute
National Institutes of Health
Bethesda, Maryland
USA

Guido Kroemer
INSERM, U848
Institut Gustave Roussy
Villejuif
France

M. Daniel Lane
Department of Biological Chemistry
The Johns Hopkins University
Baltimore, Maryland
USA

William J. Lennarz
Editor-in-Chief
Department of Biochemistry and Cell Biology
State University of New York at Stony Brook
Stony Brook, New York
USA

Masami Muramatsu
Research Center for Genomic Medicine
Saitama Medical School
Saitama
Japan

Davis Ng
Temasek Life Sciences Laboratory
National University of Singapore
Singapore
Singapore

Sten Orrenius
Institutet of Environmental Medicine
Karolinska Institutet
Stockholm
Sweden

Jacques Pouysségur
UMR 6543 CNRS
Centre Antoine Lacassagne
Nice
France

Kiyoshi Takatsu
Department of Immunology
Institute of Medical Science
University of Tokyo
Tokyo
Japan

Naoyuki Taniguchi
RIKEN Advanced Science Institute
Wako
Japan

Anna Tramontano
Department of Biochemical Sciences "Rossi Fanelli"
University of Rome "La Sapienza"
Rome
Italy

Correspondence regarding production may be sent to:

Biochemical and Biophysical Research Communications, Elsevier Inc.

525 B Street, Suite 1800, San Diego, California 92101-4495, USA
Telephone +1 (619) 699-6857, Fax +1 (619) 699-6859, E-mail bbrc@elsevier.com

0006-291X(20120420)420:4;1-U

Cover photo. The cover photo graphic is taken from figure 1A of the paper 'Susceptibility of Antiviral Drugs Against 2009 Influenza A (H1N1) Virus' published in the journal (BBRC Volume 385, pages 390–394). It is reproduced by kind permission of the authors – Supot Hannongbua, et al.